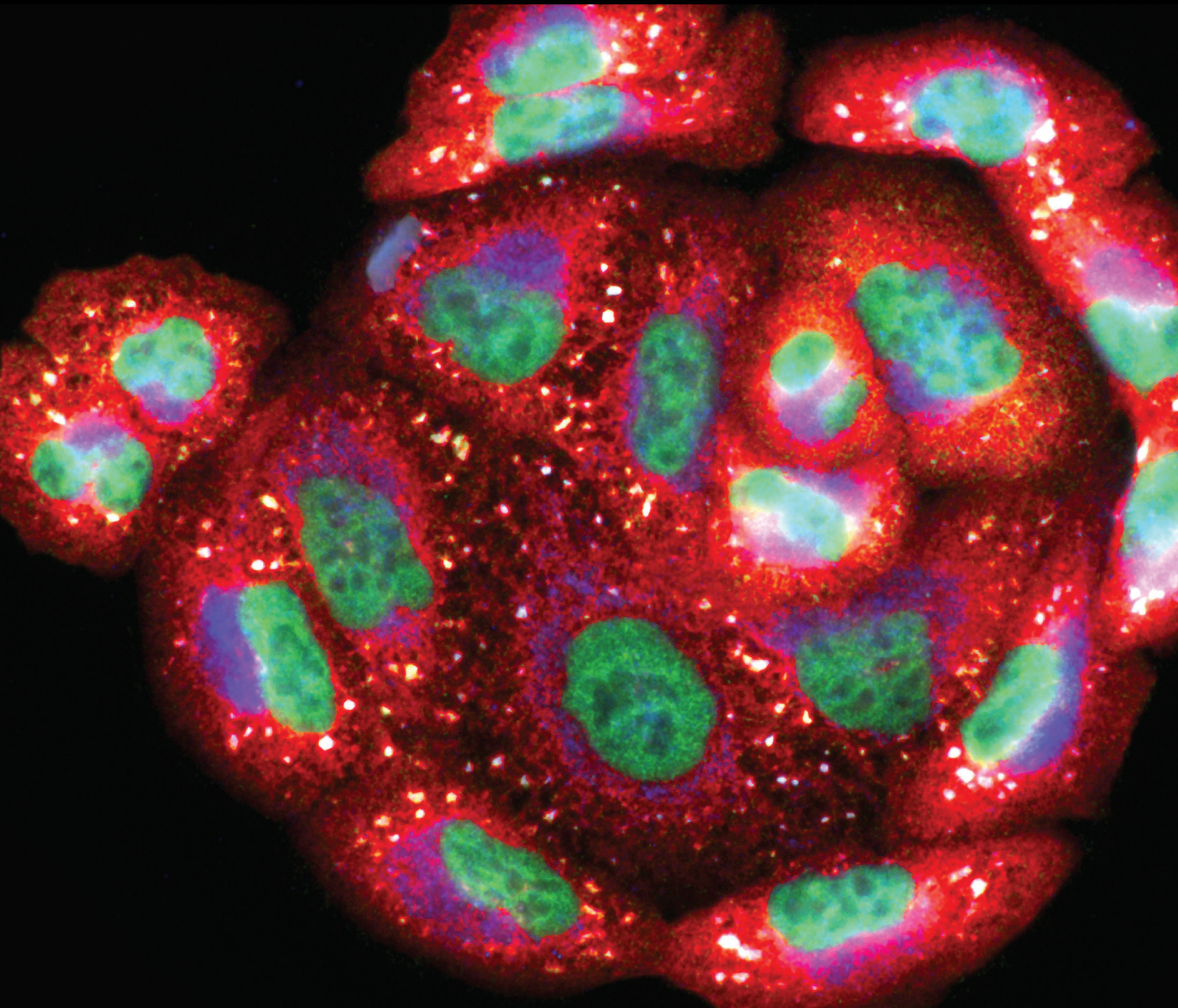


Oxidative Stress in Cardio-Oncology

Lead Guest Editor: Shao Liang

Guest Editors: Gemma A. Figtree and Xinyong Cai



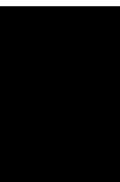
Oxidative Stress in Cardio-Oncology

Oxidative Medicine and Cellular Longevity

Oxidative Stress in Cardio-Oncology

Lead Guest Editor: Shao Liang

Guest Editors: Gemma A. Figtree and Xinyong Cai



Copyright © 2023 Hindawi Limited. All rights reserved.

This is a special issue published in "Oxidative Medicine and Cellular Longevity" All articles are open access articles distributed under the Creative Commons Attribution License, which permits unrestricted use, distribution, and reproduction in any medium, provided the original work is properly cited.

Chief Editor

Jeannette Vasquez-Vivar, USA

Associate Editors

Amjad Islam Aqib, Pakistan
Angel Catalá , Argentina
Cinzia Domenicotti , Italy
Janusz Gebicki , Australia
Aldrin V. Gomes , USA
Vladimir Jakovljevic , Serbia
Thomas Kietzmann , Finland
Juan C. Mayo , Spain
Ryuichi Morishita , Japan
Claudia Penna , Italy
Sachchida Nand Rai , India
Paola Rizzo , Italy
Mithun Sinha , USA
Daniele Vergara , Italy
Victor M. Victor , Spain

Academic Editors

Ammar AL-Farga , Saudi Arabia
Mohd Adnan , Saudi Arabia
Ivanov Alexander , Russia
Fabio Altieri , Italy
Daniel Dias Rufino Arcanjo , Brazil
Peter Backx, Canada
Amira Badr , Egypt
Damian Bailey, United Kingdom
Rengasamy Balakrishnan , Republic of Korea
Jiaolin Bao, China
Ji C. Bihl , USA
Hareram Birla, India
Abdelhakim Bouyahya, Morocco
Ralf Braun , Austria
Laura Bravo , Spain
Matt Brody , USA
Amadou Camara , USA
Marcio Carochio , Portugal
Peter Celec , Slovakia
Giselle Cerchiaro , Brazil
Arpita Chatterjee , USA
Shao-Yu Chen , USA
Yujie Chen, China
Deepak Chhangani , USA
Ferdinando Chiaradonna , Italy

Zhao Zhong Chong, USA
Fabio Ciccarone, Italy
Alin Ciobica , Romania
Ana Cipak Gasparovic , Croatia
Giuseppe Cirillo , Italy
Maria R. Ciriolo , Italy
Massimo Collino , Italy
Manuela Corte-Real , Portugal
Manuela Curcio, Italy
Domenico D'Arca , Italy
Francesca Danesi , Italy
Claudio De Lucia , USA
Damião De Sousa , Brazil
Enrico Desideri, Italy
Francesca Diomede , Italy
Raul Dominguez-Perles, Spain
Joël R. Drevet , France
Grégory Durand , France
Alessandra Durazzo , Italy
Javier Egea , Spain
Pablo A. Evelson , Argentina
Mohd Farhan, USA
Ioannis G. Fatouros , Greece
Gianna Ferretti , Italy
Swaran J. S. Flora , India
Maurizio Forte , Italy
Teresa I. Fortoul, Mexico
Anna Fracassi , USA
Rodrigo Franco , USA
Juan Gambini , Spain
Gerardo García-Rivas , Mexico
Husam Ghanim, USA
Jayeeta Ghose , USA
Rajeshwary Ghosh , USA
Lucia Gimeno-Mallench, Spain
Anna M. Giudetti , Italy
Daniela Giustarini , Italy
José Rodrigo Godoy, USA
Saeid Golbidi , Canada
Guohua Gong , China
Tilman Grune, Germany
Solomon Habtemariam , United Kingdom
Eva-Maria Hanschmann , Germany
Md Saquib Hasnain , India
Md Hassan , India

Tim Hofer , Norway
John D. Horowitz, Australia
Silvana Hrelia , Italy
Dragan Hrnčić, Serbia
Zebo Huang , China
Zhao Huang , China
Tariq Hussain , Pakistan
Stephan Immenschuh , Germany
Norsharina Ismail, Malaysia
Franco J. L. , Brazil
Sedat Kacar , USA
Andleeb Khan , Saudi Arabia
Kum Kum Khanna, Australia
Neelam Khaper , Canada
Ramoji Kosuru , USA
Demetrios Kouretas , Greece
Andrey V. Kozlov , Austria
Chan-Yen Kuo, Taiwan
Gaocai Li , China
Guoping Li , USA
Jin-Long Li , China
Qiangqiang Li , China
Xin-Feng Li , China
Jialiang Liang , China
Adam Lightfoot, United Kingdom
Christopher Horst Lillig , Germany
Paloma B. Liton , USA
Ana Lloret , Spain
Lorenzo Loffredo , Italy
Camilo López-Alarcón , Chile
Daniel Lopez-Malo , Spain
Massimo Lucarini , Italy
Hai-Chun Ma, China
Nageswara Madamanchi , USA
Kenneth Maiese , USA
Marco Malaguti , Italy
Steven McAnulty, USA
Antonio Desmond McCarthy , Argentina
Sonia Medina-Escudero , Spain
Pedro Mena , Italy
V́ctor M. Mendoza-Núñez , Mexico
Lidija Milkovic , Croatia
Alexandra Miller, USA
Sara Missaglia , Italy

Premysl Mladenka , Czech Republic
Sandra Moreno , Italy
Trevor A. Mori , Australia
Fabiana Morroni , Italy
Ange Mouithys-Mickalad, Belgium
Iordanis Mourouzis , Greece
Ryoji Nagai , Japan
Amit Kumar Nayak , India
Abderrahim Nemmar , United Arab Emirates
Xing Niu , China
Cristina Nocella, Italy
Susana Novella , Spain
Hassan Obied , Australia
Pál Pacher, USA
Pasquale Pagliaro , Italy
Dilipkumar Pal , India
Valentina Pallottini , Italy
Swapnil Pandey , USA
Mayur Parmar , USA
Vassilis Paschalis , Greece
Keshav Raj Paudel, Australia
Ilaria Peluso , Italy
Tiziana Persichini , Italy
Shazib Pervaiz , Singapore
Abdul Rehman Phull, Republic of Korea
Vincent Pialoux , France
Alessandro Poggi , Italy
Zsolt Radak , Hungary
Dario C. Ramirez , Argentina
Erika Ramos-Tovar , Mexico
Sid D. Ray , USA
Muneeb Rehman , Saudi Arabia
Hamid Reza Rezvani , France
Alessandra Ricelli, Italy
Francisco J. Romero , Spain
Joan Roselló-Catafau, Spain
Subhadeep Roy , India
Josep V. Rubert , The Netherlands
Sumbal Saba , Brazil
Kunihiro Sakuma, Japan
Gabriele Saretzki , United Kingdom
Luciano Saso , Italy
Nadja Schroder , Brazil

Anwen Shao , China
Iman Sherif, Egypt
Salah A Sheweita, Saudi Arabia
Xiaolei Shi, China
Manjari Singh, India
Giulia Sita , Italy
Ramachandran Srinivasan , India
Adrian Sturza , Romania
Kuo-hui Su , United Kingdom
Eisa Tahmasbpour Marzouni , Iran
Hailiang Tang, China
Carla Tatone , Italy
Shane Thomas , Australia
Carlo Gabriele Tocchetti , Italy
Angela Trovato Salinaro, Italy
Rosa Tundis , Italy
Kai Wang , China
Min-qi Wang , China
Natalie Ward , Australia
Grzegorz Wegrzyn, Poland
Philip Wenzel , Germany
Guangzhen Wu , China
Jianbo Xiao , Spain
Qiongming Xu , China
Liang-Jun Yan , USA
Guillermo Zalba , Spain
Jia Zhang , China
Junmin Zhang , China
Junli Zhao , USA
Chen-he Zhou , China
Yong Zhou , China
Mario Zoratti , Italy

Contents

Retracted: Mild Hypothermia Promotes Ischemic Tolerance and Survival of Neural Stem Cell Grafts by Enhancing Global SUMOylation

Oxidative Medicine and Cellular Longevity

Retraction (1 page), Article ID 9894206, Volume 2023 (2023)

Retracted: Protective Effects of *Amauroderma rugosum* on Doxorubicin-Induced Cardiotoxicity through Suppressing Oxidative Stress, Mitochondrial Dysfunction, Apoptosis, and Activating Akt/mTOR and Nrf2/HO-1 Signaling Pathways

Oxidative Medicine and Cellular Longevity

Retraction (1 page), Article ID 9861059, Volume 2023 (2023)

Retracted: Ginsenoside Rg3 Alleviates Antithyroid Cancer Drug Vandetanib-Induced QT Interval Prolongation

Oxidative Medicine and Cellular Longevity

Retraction (1 page), Article ID 9858040, Volume 2023 (2023)

Retracted: Cryptotanshinone Protects against PCOS-Induced Damage of Ovarian Tissue via Regulating Oxidative Stress, Mitochondrial Membrane Potential, Inflammation, and Apoptosis via Regulating Ferroptosis

Oxidative Medicine and Cellular Longevity

Retraction (1 page), Article ID 9875726, Volume 2023 (2023)

Retracted: Perioperative Management and Long-Term Outcomes in Ocular Cicatricial Pemphigoid Patients Undergoing Cataract Surgery

Oxidative Medicine and Cellular Longevity

Retraction (1 page), Article ID 9826796, Volume 2023 (2023)

Retracted: The Establishment of a Mouse Model for Degenerative Kyphoscoliosis Based on Senescence-Accelerated Mouse Prone 8

Oxidative Medicine and Cellular Longevity

Retraction (1 page), Article ID 9753462, Volume 2023 (2023)

Retracted: Characterization of the Prognostic Values of CXCL Family in Epstein-Barr Virus Associated Gastric Cancer

Oxidative Medicine and Cellular Longevity

Retraction (1 page), Article ID 9808937, Volume 2023 (2023)

Retracted: Modified Trabeculectomy versus Glaucoma Drainage Implant Surgery: A Retrospective Comparative Study for Refractory Glaucoma Treatment

Oxidative Medicine and Cellular Longevity

Retraction (1 page), Article ID 9798673, Volume 2023 (2023)

Retracted: Potential Benefits of Music Therapy on Stroke Rehabilitation

Oxidative Medicine and Cellular Longevity

Retraction (1 page), Article ID 9873067, Volume 2023 (2023)

Retracted: Fibroblasts in Scar Formation: Biology and Clinical Translation

Oxidative Medicine and Cellular Longevity

Retraction (1 page), Article ID 9868570, Volume 2023 (2023)

Retracted: The Correlation between the Increased Expression of Aquaporins on the Inner Limiting Membrane and the Occurrence of Diabetic Macular Edema

Oxidative Medicine and Cellular Longevity

Retraction (1 page), Article ID 9835497, Volume 2023 (2023)

Retracted: Comparative Analysis of Early Clinical Features and Complications of Different Types of Acute Pancreatitis

Oxidative Medicine and Cellular Longevity

Retraction (1 page), Article ID 9830716, Volume 2023 (2023)

Retracted: Clinical Efficacy of PEG-IFN α -2a and PEG-IFN α -2b in the Treatment of Hepatitis B e Antigen-Positive Hepatitis B and Their Value in Improving Inflammatory Factors and Hemodynamics in Patients: A Comparative Study

Oxidative Medicine and Cellular Longevity

Retraction (1 page), Article ID 9828565, Volume 2023 (2023)

Retracted: A Novel Approach Combined with MIPO Technique for the Treatment of Type C Pilon Fractures

Oxidative Medicine and Cellular Longevity

Retraction (1 page), Article ID 9827528, Volume 2023 (2023)

Retracted: Glymphatic System: Emerging Therapeutic Target for Neurological Diseases

Oxidative Medicine and Cellular Longevity



Retraction (1 page), Article ID 9806739, Volume 2023 (2023)

Retracted: An Enhanced Priori Knowledge GAN for CT Images Generation of Early Lung Nodules with Small-Size Labelled Samples

Oxidative Medicine and Cellular Longevity


Retraction (1 page), Article ID 9797608, Volume 2023 (2023)

[Retracted] The Establishment of a Mouse Model for Degenerative Kyphoscoliosis Based on Senescence-Accelerated Mouse Prone 8

Zongshan Hu , Ziyang Tang, Abdukahar Kiram, Jie Li, Hui Xu, Yanjie Xu, Huiming Jiang, Zezhang Zhu, Yong Qiu, and Zhen Liu 

Research Article (7 pages), Article ID 7378403, Volume 2022 (2022)

[Retracted] Comparative Analysis of Early Clinical Features and Complications of Different Types of Acute Pancreatitis

Hongsheng Wu, Keqiang Ma, Biling Liao, Tengfei Ji, Shengmin Zhang, and Tiansheng Cao 

Research Article (9 pages), Article ID 3771610, Volume 2022 (2022)



Contents

[Retracted] Potential Benefits of Music Therapy on Stroke Rehabilitation

Chengyan Xu, Zixia He, Zhipeng Shen , and Fei Huang 



Review Article (11 pages), Article ID 9386095, Volume 2022 (2022)

[Retracted] A Novel Approach Combined with MIPO Technique for the Treatment of Type C Pilon Fractures

Youhao Chen, Haoming Wang, Nan Li, Lixin Xu, Feng Liu, Qiu Xu, Qiang Zhou , and Xiaohua Chen 




Research Article (10 pages), Article ID 7427255, Volume 2022 (2022)

[Retracted] An Enhanced Priori Knowledge GAN for CT Images Generation of Early Lung Nodules with Small-Size Labelled Samples

Xun Wang , Zhiyong Yu, Lisheng Wang, and Pan Zheng 


Research Article (9 pages), Article ID 2129303, Volume 2022 (2022)

[Retracted] Glymphatic System: Emerging Therapeutic Target for Neurological Diseases

Xianjun Xuan , Guoyi Zhou, Caihong Chen, Anwen Shao , Yunxiang Zhou , Xiaobo Li, and Jiaqi Zhou

Review Article (14 pages), Article ID 6189170, Volume 2022 (2022)

[Retracted] Clinical Efficacy of PEG-IFN α -2a and PEG-IFN α -2b in the Treatment of Hepatitis B e Antigen-Positive Hepatitis B and Their Value in Improving Inflammatory Factors and Hemodynamics in Patients: A Comparative Study

Nina Jia , Wei Gao, Xiaohong Fan, Hong Gao, Xueqing Li, Biantao Mi, and Jie Yang



Research Article (10 pages), Article ID 3185320, Volume 2022 (2022)

[Retracted] Characterization of the Prognostic Values of CXCL Family in Epstein–Barr Virus Associated Gastric Cancer

Li Mu, Shun Hu, Guoping Li, Ping Wu, Caihong Ren, Taiyu Lin, and Sheng Zhang 


Research Article (24 pages), Article ID 2218140, Volume 2022 (2022)

[Retracted] Protective Effects of *Amauroderma rugosum* on Doxorubicin-Induced Cardiotoxicity through Suppressing Oxidative Stress, Mitochondrial Dysfunction, Apoptosis, and Activating Akt/mTOR and Nrf2/HO-1 Signaling Pathways

Jingjing Li , Yanfen Cheng, Renkai Li, Xiaoping Wu, Chengwen Zheng, Polly Ho-Ting Shiu, Jacqueline Cho-Ki Chan, Panthakarn Rangsinth, Conghui Liu, Susan Wai-Sum Leung, Simon Ming-Yuen Lee, Chen Zhang, Chaomei Fu, Jinming Zhang, Timothy Man-Yau Cheung, and George Pak-Heng Leung 




Research Article (24 pages), Article ID 9266178, Volume 2022 (2022)

[Retracted] Mild Hypothermia Promotes Ischemic Tolerance and Survival of Neural Stem Cell Grafts by Enhancing Global SUMOylation



Heng Cai, Xiaofang Ma, Dading Lu, Liangyu Chen, Xiyun Bian, Nan Zhang, Wei Tang, Xiaozhi Liu, and Zhiqing Li 

Research Article (13 pages), Article ID 6503504, Volume 2022 (2022)

[Retracted] Modified Trabeculectomy versus Glaucoma Drainage Implant Surgery: A Retrospective Comparative Study for Refractory Glaucoma Treatment

Yuan He , Beilei He , Zhi Ji, Ruixue Zhang , Zhuoya Quan , Guijun Xie, and Xiaoli Pu
Research Article (15 pages), Article ID 3050007, Volume 2022 (2022)


[Retracted] Fibroblasts in Scar Formation: Biology and Clinical Translation

Huan Qian , Yihan Shan, Ruicheng Gong, Danfeng Lin, Mengwen Zhang, Chen Wang, and Lu Wang 
Review Article (11 pages), Article ID 4586569, Volume 2022 (2022)

[Retracted] Perioperative Management and Long-Term Outcomes in Ocular Cicatricial Pemphigoid Patients Undergoing Cataract Surgery

Yuan He , Zhuoya Quan , Ruixue Zhang , Zhi Ji, Jun Jia, Huifeng Liu, Chuntao Zhang, Beilei He, Yuan Ren, and Yun Feng 
Research Article (24 pages), Article ID 2496649, Volume 2022 (2022)





[Retracted] The Correlation between the Increased Expression of Aquaporins on the Inner Limiting Membrane and the Occurrence of Diabetic Macular Edema

Yiqi Chen, Huan Chen, Chenxi Wang, Jiafeng Yu, Jiwei Tao, Jianbo Mao, and Lijun Shen 
Research Article (11 pages), Article ID 7412208, Volume 2022 (2022)



[Retracted] Cryptotanshinone Protects against PCOS-Induced Damage of Ovarian Tissue via Regulating Oxidative Stress, Mitochondrial Membrane Potential, Inflammation, and Apoptosis via Regulating Ferroptosis

Honglin Liu , Jiani Xie , Limin Fan , Yue Xia , Xia Peng , Jianhua Zhou , and Xiaorong Ni 
Research Article (21 pages), Article ID 8011850, Volume 2022 (2022)

***Nauclea orientalis* (L.) Bark Extract Protects Rat Cardiomyocytes from Doxorubicin-Induced Oxidative Stress, Inflammation, Apoptosis, and DNA Fragmentation**

Jayasinghe A. N. Sandamali , Ruwani P. Hewawasam , Kamani A. P. W. Jayatilaka , and Lakmini K. B. Mudduwa 
Research Article (19 pages), Article ID 1714841, Volume 2022 (2022)

[Retracted] Ginsenoside Rg3 Alleviates Antithyroid Cancer Drug Vandetanib-Induced QT Interval Prolongation

Juan Zhang, Dan Luo, Fang Li, Zhiyi Li, Xiaoli Gao, Jie Qiao, Lin Wu , and Miaoling Li 
Research Article (14 pages), Article ID 3520034, Volume 2021 (2021)

Retraction

Retracted: Mild Hypothermia Promotes Ischemic Tolerance and Survival of Neural Stem Cell Grafts by Enhancing Global SUMOylation

Oxidative Medicine and Cellular Longevity

Received 26 December 2023; Accepted 26 December 2023; Published 29 December 2023

Copyright © 2023 Oxidative Medicine and Cellular Longevity. This is an open access article distributed under the Creative Commons Attribution License, which permits unrestricted use, distribution, and reproduction in any medium, provided the original work is properly cited.

This article has been retracted by Hindawi, as publisher, following an investigation undertaken by the publisher [1]. This investigation has uncovered evidence of systematic manipulation of the publication and peer-review process. We cannot, therefore, vouch for the reliability or integrity of this article.

Please note that this notice is intended solely to alert readers that the peer-review process of this article has been compromised.

Wiley and Hindawi regret that the usual quality checks did not identify these issues before publication and have since put additional measures in place to safeguard research integrity.

We wish to credit our Research Integrity and Research Publishing teams and anonymous and named external researchers and research integrity experts for contributing to this investigation.

The corresponding author, as the representative of all authors, has been given the opportunity to register their agreement or disagreement to this retraction. We have kept a record of any response received.

References

- [1] H. Cai, X. Ma, D. Lu et al., “Mild Hypothermia Promotes Ischemic Tolerance and Survival of Neural Stem Cell Grafts by Enhancing Global SUMOylation,” *Oxidative Medicine and Cellular Longevity*, vol. 2022, Article ID 6503504, 13 pages, 2022.

Retraction

Retracted: Protective Effects of *Amauroderma rugosum* on Doxorubicin-Induced Cardiotoxicity through Suppressing Oxidative Stress, Mitochondrial Dysfunction, Apoptosis, and Activating Akt/mTOR and Nrf2/HO-1 Signaling Pathways

Oxidative Medicine and Cellular Longevity

Received 26 December 2023; Accepted 26 December 2023; Published 29 December 2023

Copyright © 2023 Oxidative Medicine and Cellular Longevity. This is an open access article distributed under the Creative Commons Attribution License, which permits unrestricted use, distribution, and reproduction in any medium, provided the original work is properly cited.

This article has been retracted by Hindawi, as publisher, following an investigation undertaken by the publisher [1]. This investigation has uncovered evidence of systematic manipulation of the publication and peer-review process. We cannot, therefore, vouch for the reliability or integrity of this article.

Please note that this notice is intended solely to alert readers that the peer-review process of this article has been compromised.

Wiley and Hindawi regret that the usual quality checks did not identify these issues before publication and have since put additional measures in place to safeguard research integrity.

We wish to credit our Research Integrity and Research Publishing teams and anonymous and named external researchers and research integrity experts for contributing to this investigation.

The corresponding author, as the representative of all authors, has been given the opportunity to register their agreement or disagreement to this retraction. We have kept a record of any response received.

References

- [1] J. Li, Y. Cheng, R. Li et al., "Protective Effects of *Amauroderma rugosum* on Doxorubicin-Induced Cardiotoxicity through Suppressing Oxidative Stress, Mitochondrial Dysfunction, Apoptosis, and Activating Akt/mTOR and Nrf2/HO-1 Signaling Pathways," *Oxidative Medicine and Cellular Longevity*, vol. 2022, Article ID 9266178, 24 pages, 2022.

Retraction

Retracted: Ginsenoside Rg3 Alleviates Antithyroid Cancer Drug Vandetanib-Induced QT Interval Prolongation

Oxidative Medicine and Cellular Longevity

Received 26 December 2023; Accepted 26 December 2023; Published 29 December 2023

Copyright © 2023 Oxidative Medicine and Cellular Longevity. This is an open access article distributed under the Creative Commons Attribution License, which permits unrestricted use, distribution, and reproduction in any medium, provided the original work is properly cited.

This article has been retracted by Hindawi, as publisher, following an investigation undertaken by the publisher [1]. This investigation has uncovered evidence of systematic manipulation of the publication and peer-review process. We cannot, therefore, vouch for the reliability or integrity of this article.

Please note that this notice is intended solely to alert readers that the peer-review process of this article has been compromised.

Wiley and Hindawi regret that the usual quality checks did not identify these issues before publication and have since put additional measures in place to safeguard research integrity.

We wish to credit our Research Integrity and Research Publishing teams and anonymous and named external researchers and research integrity experts for contributing to this investigation.

The corresponding author, as the representative of all authors, has been given the opportunity to register their agreement or disagreement to this retraction. We have kept a record of any response received.

References

- [1] J. Zhang, D. Luo, F. Li et al., "Ginsenoside Rg3 Alleviates Antithyroid Cancer Drug Vandetanib-Induced QT Interval Prolongation," *Oxidative Medicine and Cellular Longevity*, vol. 2021, Article ID 3520034, 14 pages, 2021.

Retraction

Retracted: Cryptotanshinone Protects against PCOS-Induced Damage of Ovarian Tissue via Regulating Oxidative Stress, Mitochondrial Membrane Potential, Inflammation, and Apoptosis via Regulating Ferroptosis

Oxidative Medicine and Cellular Longevity

Received 26 September 2023; Accepted 26 September 2023; Published 27 September 2023

Copyright © 2023 Oxidative Medicine and Cellular Longevity. This is an open access article distributed under the Creative Commons Attribution License, which permits unrestricted use, distribution, and reproduction in any medium, provided the original work is properly cited.

This article has been retracted by Hindawi following an investigation undertaken by the publisher [1]. This investigation has uncovered evidence of one or more of the following indicators of systematic manipulation of the publication process:

- (1) Discrepancies in scope
- (2) Discrepancies in the description of the research reported
- (3) Discrepancies between the availability of data and the research described
- (4) Inappropriate citations
- (5) Incoherent, meaningless and/or irrelevant content included in the article
- (6) Peer-review manipulation

The presence of these indicators undermines our confidence in the integrity of the article's content and we cannot, therefore, vouch for its reliability. Please note that this notice is intended solely to alert readers that the content of this article is unreliable. We have not investigated whether authors were aware of or involved in the systematic manipulation of the publication process.

Wiley and Hindawi regrets that the usual quality checks did not identify these issues before publication and have since put additional measures in place to safeguard research integrity.

We wish to credit our own Research Integrity and Research Publishing teams and anonymous and named external researchers and research integrity experts for contributing to this investigation.

The corresponding author, as the representative of all authors, has been given the opportunity to register their

agreement or disagreement to this retraction. We have kept a record of any response received.

References

- [1] H. Liu, J. Xie, L. Fan et al., "Cryptotanshinone Protects against PCOS-Induced Damage of Ovarian Tissue via Regulating Oxidative Stress, Mitochondrial Membrane Potential, Inflammation, and Apoptosis via Regulating Ferroptosis," *Oxidative Medicine and Cellular Longevity*, vol. 2022, Article ID 8011850, 21 pages, 2022.

Retraction

Retracted: Perioperative Management and Long-Term Outcomes in Ocular Cicatricial Pemphigoid Patients Undergoing Cataract Surgery

Oxidative Medicine and Cellular Longevity

Received 26 September 2023; Accepted 26 September 2023; Published 27 September 2023

Copyright © 2023 Oxidative Medicine and Cellular Longevity. This is an open access article distributed under the Creative Commons Attribution License, which permits unrestricted use, distribution, and reproduction in any medium, provided the original work is properly cited.

This article has been retracted by Hindawi following an investigation undertaken by the publisher [1]. This investigation has uncovered evidence of one or more of the following indicators of systematic manipulation of the publication process:

- (1) Discrepancies in scope
- (2) Discrepancies in the description of the research reported
- (3) Discrepancies between the availability of data and the research described
- (4) Inappropriate citations
- (5) Incoherent, meaningless and/or irrelevant content included in the article
- (6) Peer-review manipulation

The presence of these indicators undermines our confidence in the integrity of the article's content and we cannot, therefore, vouch for its reliability. Please note that this notice is intended solely to alert readers that the content of this article is unreliable. We have not investigated whether authors were aware of or involved in the systematic manipulation of the publication process.

Wiley and Hindawi regrets that the usual quality checks did not identify these issues before publication and have since put additional measures in place to safeguard research integrity.

We wish to credit our own Research Integrity and Research Publishing teams and anonymous and named external researchers and research integrity experts for contributing to this investigation.

The corresponding author, as the representative of all authors, has been given the opportunity to register their agreement or disagreement to this retraction. We have kept a record of any response received.

References

- [1] Y. He, Z. Quan, R. Zhang et al., "Perioperative Management and Long-Term Outcomes in Ocular Cicatricial Pemphigoid Patients Undergoing Cataract Surgery," *Oxidative Medicine and Cellular Longevity*, vol. 2022, Article ID 2496649, 24 pages, 2022.

Retraction

Retracted: The Establishment of a Mouse Model for Degenerative Kyphoscoliosis Based on Senescence-Accelerated Mouse Prone 8

Oxidative Medicine and Cellular Longevity

Received 26 September 2023; Accepted 26 September 2023; Published 27 September 2023

Copyright © 2023 Oxidative Medicine and Cellular Longevity. This is an open access article distributed under the Creative Commons Attribution License, which permits unrestricted use, distribution, and reproduction in any medium, provided the original work is properly cited.

This article has been retracted by Hindawi following an investigation undertaken by the publisher [1]. This investigation has uncovered evidence of one or more of the following indicators of systematic manipulation of the publication process:

- (1) Discrepancies in scope
- (2) Discrepancies in the description of the research reported
- (3) Discrepancies between the availability of data and the research described
- (4) Inappropriate citations
- (5) Incoherent, meaningless and/or irrelevant content included in the article
- (6) Peer-review manipulation

The presence of these indicators undermines our confidence in the integrity of the article's content and we cannot, therefore, vouch for its reliability. Please note that this notice is intended solely to alert readers that the content of this article is unreliable. We have not investigated whether authors were aware of or involved in the systematic manipulation of the publication process.

Wiley and Hindawi regrets that the usual quality checks did not identify these issues before publication and have since put additional measures in place to safeguard research integrity.

We wish to credit our own Research Integrity and Research Publishing teams and anonymous and named external researchers and research integrity experts for contributing to this investigation.

The corresponding author, as the representative of all authors, has been given the opportunity to register their agreement or disagreement to this retraction. We have kept a record of any response received.

References

- [1] Z. Hu, Z. Tang, A. Kiram et al., "The Establishment of a Mouse Model for Degenerative Kyphoscoliosis Based on Senescence-Accelerated Mouse Prone 8," *Oxidative Medicine and Cellular Longevity*, vol. 2022, Article ID 7378403, 7 pages, 2022.

Retraction

Retracted: Characterization of the Prognostic Values of CXCL Family in Epstein–Barr Virus Associated Gastric Cancer

Oxidative Medicine and Cellular Longevity

Received 8 August 2023; Accepted 8 August 2023; Published 9 August 2023

Copyright © 2023 Oxidative Medicine and Cellular Longevity. This is an open access article distributed under the Creative Commons Attribution License, which permits unrestricted use, distribution, and reproduction in any medium, provided the original work is properly cited.

This article has been retracted by Hindawi following an investigation undertaken by the publisher [1]. This investigation has uncovered evidence of one or more of the following indicators of systematic manipulation of the publication process:

- (1) Discrepancies in scope
- (2) Discrepancies in the description of the research reported
- (3) Discrepancies between the availability of data and the research described
- (4) Inappropriate citations
- (5) Incoherent, meaningless and/or irrelevant content included in the article
- (6) Peer-review manipulation

The presence of these indicators undermines our confidence in the integrity of the article's content and we cannot, therefore, vouch for its reliability. Please note that this notice is intended solely to alert readers that the content of this article is unreliable. We have not investigated whether authors were aware of or involved in the systematic manipulation of the publication process.

Wiley and Hindawi regrets that the usual quality checks did not identify these issues before publication and have since put additional measures in place to safeguard research integrity.

We wish to credit our own Research Integrity and Research Publishing teams and anonymous and named external researchers and research integrity experts for contributing to this investigation.

The corresponding author, as the representative of all authors, has been given the opportunity to register their agreement or disagreement to this retraction. We have kept a record of any response received.

References

- [1] L. Mu, S. Hu, G. Li et al., "Characterization of the Prognostic Values of CXCL Family in Epstein–Barr Virus Associated Gastric Cancer," *Oxidative Medicine and Cellular Longevity*, vol. 2022, Article ID 2218140, 24 pages, 2022.

Retraction

Retracted: Modified Trabeculectomy versus Glaucoma Drainage Implant Surgery: A Retrospective Comparative Study for Refractory Glaucoma Treatment

Oxidative Medicine and Cellular Longevity

Received 8 August 2023; Accepted 8 August 2023; Published 9 August 2023

Copyright © 2023 Oxidative Medicine and Cellular Longevity. This is an open access article distributed under the Creative Commons Attribution License, which permits unrestricted use, distribution, and reproduction in any medium, provided the original work is properly cited.

This article has been retracted by Hindawi following an investigation undertaken by the publisher [1]. This investigation has uncovered evidence of one or more of the following indicators of systematic manipulation of the publication process:

- (1) Discrepancies in scope
- (2) Discrepancies in the description of the research reported
- (3) Discrepancies between the availability of data and the research described
- (4) Inappropriate citations
- (5) Incoherent, meaningless and/or irrelevant content included in the article
- (6) Peer-review manipulation

The presence of these indicators undermines our confidence in the integrity of the article's content and we cannot, therefore, vouch for its reliability. Please note that this notice is intended solely to alert readers that the content of this article is unreliable. We have not investigated whether authors were aware of or involved in the systematic manipulation of the publication process.

In addition, our investigation has also shown that one or more of the following human-subject reporting requirements has not been met in this article: ethical approval by an Institutional Review Board (IRB) committee or equivalent, patient/participant consent to participate, and/or agreement to publish patient/participant details (where relevant).

Wiley and Hindawi regrets that the usual quality checks did not identify these issues before publication and have since put additional measures in place to safeguard research integrity.

We wish to credit our own Research Integrity and Research Publishing teams and anonymous and named external researchers and research integrity experts for contributing to this investigation.

The corresponding author, as the representative of all authors, has been given the opportunity to register their agreement or disagreement to this retraction. We have kept a record of any response received.

References

- [1] Y. He, B. He, Z. Ji et al., "Modified Trabeculectomy versus Glaucoma Drainage Implant Surgery: A Retrospective Comparative Study for Refractory Glaucoma Treatment," *Oxidative Medicine and Cellular Longevity*, vol. 2022, Article ID 3050007, 15 pages, 2022.

Retraction

Retracted: Potential Benefits of Music Therapy on Stroke Rehabilitation

Oxidative Medicine and Cellular Longevity

Received 1 August 2023; Accepted 1 August 2023; Published 2 August 2023

Copyright © 2023 Oxidative Medicine and Cellular Longevity. This is an open access article distributed under the Creative Commons Attribution License, which permits unrestricted use, distribution, and reproduction in any medium, provided the original work is properly cited.

This article has been retracted by Hindawi following an investigation undertaken by the publisher [1]. This investigation has uncovered evidence of one or more of the following indicators of systematic manipulation of the publication process:

- (1) Discrepancies in scope
- (2) Discrepancies in the description of the research reported
- (3) Discrepancies between the availability of data and the research described
- (4) Inappropriate citations
- (5) Incoherent, meaningless and/or irrelevant content included in the article
- (6) Peer-review manipulation

The presence of these indicators undermines our confidence in the integrity of the article's content and we cannot, therefore, vouch for its reliability. Please note that this notice is intended solely to alert readers that the content of this article is unreliable. We have not investigated whether authors were aware of or involved in the systematic manipulation of the publication process.

Wiley and Hindawi regrets that the usual quality checks did not identify these issues before publication and have since put additional measures in place to safeguard research integrity.

We wish to credit our own Research Integrity and Research Publishing teams and anonymous and named external researchers and research integrity experts for contributing to this investigation.

The corresponding author, as the representative of all authors, has been given the opportunity to register their agreement or disagreement to this retraction. We have kept a record of any response received.

References

- [1] C. Xu, Z. He, Z. Shen, and F. Huang, "Potential Benefits of Music Therapy on Stroke Rehabilitation," *Oxidative Medicine and Cellular Longevity*, vol. 2022, Article ID 9386095, 11 pages, 2022.

Retraction

Retracted: Fibroblasts in Scar Formation: Biology and Clinical Translation

Oxidative Medicine and Cellular Longevity

Received 1 August 2023; Accepted 1 August 2023; Published 2 August 2023

Copyright © 2023 Oxidative Medicine and Cellular Longevity. This is an open access article distributed under the Creative Commons Attribution License, which permits unrestricted use, distribution, and reproduction in any medium, provided the original work is properly cited.

This article has been retracted by Hindawi following an investigation undertaken by the publisher [1]. This investigation has uncovered evidence of one or more of the following indicators of systematic manipulation of the publication process:

- (1) Discrepancies in scope
- (2) Discrepancies in the description of the research reported
- (3) Discrepancies between the availability of data and the research described
- (4) Inappropriate citations
- (5) Incoherent, meaningless and/or irrelevant content included in the article
- (6) Peer-review manipulation

The presence of these indicators undermines our confidence in the integrity of the article's content and we cannot, therefore, vouch for its reliability. Please note that this notice is intended solely to alert readers that the content of this article is unreliable. We have not investigated whether authors were aware of or involved in the systematic manipulation of the publication process.

Wiley and Hindawi regrets that the usual quality checks did not identify these issues before publication and have since put additional measures in place to safeguard research integrity.

We wish to credit our own Research Integrity and Research Publishing teams and anonymous and named external researchers and research integrity experts for contributing to this investigation.

The corresponding author, as the representative of all authors, has been given the opportunity to register their agreement or disagreement to this retraction. We have kept a record of any response received.

References

- [1] H. Qian, Y. Shan, R. Gong et al., "Fibroblasts in Scar Formation: Biology and Clinical Translation," *Oxidative Medicine and Cellular Longevity*, vol. 2022, Article ID 4586569, 11 pages, 2022.

Retraction

Retracted: The Correlation between the Increased Expression of Aquaporins on the Inner Limiting Membrane and the Occurrence of Diabetic Macular Edema

Oxidative Medicine and Cellular Longevity

Received 1 August 2023; Accepted 1 August 2023; Published 2 August 2023

Copyright © 2023 Oxidative Medicine and Cellular Longevity. This is an open access article distributed under the Creative Commons Attribution License, which permits unrestricted use, distribution, and reproduction in any medium, provided the original work is properly cited.

This article has been retracted by Hindawi following an investigation undertaken by the publisher [1]. This investigation has uncovered evidence of one or more of the following indicators of systematic manipulation of the publication process:

- (1) Discrepancies in scope
- (2) Discrepancies in the description of the research reported
- (3) Discrepancies between the availability of data and the research described
- (4) Inappropriate citations
- (5) Incoherent, meaningless and/or irrelevant content included in the article
- (6) Peer-review manipulation

The presence of these indicators undermines our confidence in the integrity of the article's content and we cannot, therefore, vouch for its reliability. Please note that this notice is intended solely to alert readers that the content of this article is unreliable. We have not investigated whether authors were aware of or involved in the systematic manipulation of the publication process.

In addition, our investigation has also shown that one or more of the following human-subject reporting requirements has not been met in this article: ethical approval by an Institutional Review Board (IRB) committee or equivalent, patient/participant consent to participate, and/or agreement to publish patient/participant details (where relevant).

Wiley and Hindawi regrets that the usual quality checks did not identify these issues before publication and have since put additional measures in place to safeguard research integrity.

We wish to credit our own Research Integrity and Research Publishing teams and anonymous and named external researchers and research integrity experts for contributing to this investigation.

The corresponding author, as the representative of all authors, has been given the opportunity to register their agreement or disagreement to this retraction. We have kept a record of any response received.

References

- [1] Y. Chen, H. Chen, C. Wang et al., "The Correlation between the Increased Expression of Aquaporins on the Inner Limiting Membrane and the Occurrence of Diabetic Macular Edema," *Oxidative Medicine and Cellular Longevity*, vol. 2022, Article ID 7412208, 11 pages, 2022.

Retraction

Retracted: Comparative Analysis of Early Clinical Features and Complications of Different Types of Acute Pancreatitis

Oxidative Medicine and Cellular Longevity

Received 1 August 2023; Accepted 1 August 2023; Published 2 August 2023

Copyright © 2023 Oxidative Medicine and Cellular Longevity. This is an open access article distributed under the Creative Commons Attribution License, which permits unrestricted use, distribution, and reproduction in any medium, provided the original work is properly cited.

This article has been retracted by Hindawi following an investigation undertaken by the publisher [1]. This investigation has uncovered evidence of one or more of the following indicators of systematic manipulation of the publication process:

- (1) Discrepancies in scope
- (2) Discrepancies in the description of the research reported
- (3) Discrepancies between the availability of data and the research described
- (4) Inappropriate citations
- (5) Incoherent, meaningless and/or irrelevant content included in the article
- (6) Peer-review manipulation

The presence of these indicators undermines our confidence in the integrity of the article's content and we cannot, therefore, vouch for its reliability. Please note that this notice is intended solely to alert readers that the content of this article is unreliable. We have not investigated whether authors were aware of or involved in the systematic manipulation of the publication process.

Wiley and Hindawi regrets that the usual quality checks did not identify these issues before publication and have since put additional measures in place to safeguard research integrity.

We wish to credit our own Research Integrity and Research Publishing teams and anonymous and named external researchers and research integrity experts for contributing to this investigation.

The corresponding author, as the representative of all authors, has been given the opportunity to register their agreement or disagreement to this retraction. We have kept a record of any response received.

References

- [1] H. Wu, K. Ma, B. Liao, T. Ji, S. Zhang, and T. Cao, "Comparative Analysis of Early Clinical Features and Complications of Different Types of Acute Pancreatitis," *Oxidative Medicine and Cellular Longevity*, vol. 2022, Article ID 3771610, 9 pages, 2022.

Retraction

Retracted: Clinical Efficacy of PEG-IFN α -2a and PEG-IFN α -2b in the Treatment of Hepatitis B e Antigen-Positive Hepatitis B and Their Value in Improving Inflammatory Factors and Hemodynamics in Patients: A Comparative Study

Oxidative Medicine and Cellular Longevity

Received 1 August 2023; Accepted 1 August 2023; Published 2 August 2023

Copyright © 2023 Oxidative Medicine and Cellular Longevity. This is an open access article distributed under the Creative Commons Attribution License, which permits unrestricted use, distribution, and reproduction in any medium, provided the original work is properly cited.

This article has been retracted by Hindawi following an investigation undertaken by the publisher [1]. This investigation has uncovered evidence of one or more of the following indicators of systematic manipulation of the publication process:

- (1) Discrepancies in scope
- (2) Discrepancies in the description of the research reported
- (3) Discrepancies between the availability of data and the research described
- (4) Inappropriate citations
- (5) Incoherent, meaningless and/or irrelevant content included in the article
- (6) Peer-review manipulation

The presence of these indicators undermines our confidence in the integrity of the article's content and we cannot, therefore, vouch for its reliability. Please note that this notice is intended solely to alert readers that the content of this article is unreliable. We have not investigated whether authors were aware of or involved in the systematic manipulation of the publication process.

Wiley and Hindawi regrets that the usual quality checks did not identify these issues before publication and have since put additional measures in place to safeguard research integrity.

We wish to credit our own Research Integrity and Research Publishing teams and anonymous and named external researchers and research integrity experts for contributing to this investigation.

The corresponding author, as the representative of all authors, has been given the opportunity to register their

agreement or disagreement to this retraction. We have kept a record of any response received.

References

- [1] N. Jia, W. Gao, X. Fan et al., "Clinical Efficacy of PEG-IFN α -2a and PEG-IFN α -2b in the Treatment of Hepatitis B e Antigen-Positive Hepatitis B and Their Value in Improving Inflammatory Factors and Hemodynamics in Patients: A Comparative Study," *Oxidative Medicine and Cellular Longevity*, vol. 2022, Article ID 3185320, 10 pages, 2022.

Retraction

Retracted: A Novel Approach Combined with MIPO Technique for the Treatment of Type C Pilon Fractures

Oxidative Medicine and Cellular Longevity

Received 1 August 2023; Accepted 1 August 2023; Published 2 August 2023

Copyright © 2023 Oxidative Medicine and Cellular Longevity. This is an open access article distributed under the Creative Commons Attribution License, which permits unrestricted use, distribution, and reproduction in any medium, provided the original work is properly cited.

This article has been retracted by Hindawi following an investigation undertaken by the publisher [1]. This investigation has uncovered evidence of one or more of the following indicators of systematic manipulation of the publication process:

- (1) Discrepancies in scope
- (2) Discrepancies in the description of the research reported
- (3) Discrepancies between the availability of data and the research described
- (4) Inappropriate citations
- (5) Incoherent, meaningless and/or irrelevant content included in the article
- (6) Peer-review manipulation

The presence of these indicators undermines our confidence in the integrity of the article's content and we cannot, therefore, vouch for its reliability. Please note that this notice is intended solely to alert readers that the content of this article is unreliable. We have not investigated whether authors were aware of or involved in the systematic manipulation of the publication process.

In addition, our investigation has also shown that one or more of the following human-subject reporting requirements has not been met in this article: ethical approval by an Institutional Review Board (IRB) committee or equivalent, patient/participant consent to participate, and/or agreement to publish patient/participant details (where relevant).

Wiley and Hindawi regrets that the usual quality checks did not identify these issues before publication and have since put additional measures in place to safeguard research integrity.

We wish to credit our own Research Integrity and Research Publishing teams and anonymous and named external

researchers and research integrity experts for contributing to this investigation.

The corresponding author, as the representative of all authors, has been given the opportunity to register their agreement or disagreement to this retraction. We have kept a record of any response received.

References

- [1] Y. Chen, H. Wang, N. Li et al., "A Novel Approach Combined with MIPO Technique for the Treatment of Type C Pilon Fractures," *Oxidative Medicine and Cellular Longevity*, vol. 2022, Article ID 7427255, 10 pages, 2022.

Retraction

Retracted: Glymphatic System: Emerging Therapeutic Target for Neurological Diseases

Oxidative Medicine and Cellular Longevity

Received 1 August 2023; Accepted 1 August 2023; Published 2 August 2023

Copyright © 2023 Oxidative Medicine and Cellular Longevity. This is an open access article distributed under the Creative Commons Attribution License, which permits unrestricted use, distribution, and reproduction in any medium, provided the original work is properly cited.

This article has been retracted by Hindawi following an investigation undertaken by the publisher [1]. This investigation has uncovered evidence of one or more of the following indicators of systematic manipulation of the publication process:

- (1) Discrepancies in scope
- (2) Discrepancies in the description of the research reported
- (3) Discrepancies between the availability of data and the research described
- (4) Inappropriate citations
- (5) Incoherent, meaningless and/or irrelevant content included in the article
- (6) Peer-review manipulation

The presence of these indicators undermines our confidence in the integrity of the article's content and we cannot, therefore, vouch for its reliability. Please note that this notice is intended solely to alert readers that the content of this article is unreliable. We have not investigated whether authors were aware of or involved in the systematic manipulation of the publication process.

Wiley and Hindawi regrets that the usual quality checks did not identify these issues before publication and have since put additional measures in place to safeguard research integrity.

We wish to credit our own Research Integrity and Research Publishing teams and anonymous and named external researchers and research integrity experts for contributing to this investigation.

The corresponding author, as the representative of all authors, has been given the opportunity to register their agreement or disagreement to this retraction. We have kept a record of any response received.

References

- [1] X. Xuan, G. Zhou, C. Chen et al., "Glymphatic System: Emerging Therapeutic Target for Neurological Diseases," *Oxidative Medicine and Cellular Longevity*, vol. 2022, Article ID 6189170, 14 pages, 2022.

Retraction

Retracted: An Enhanced Priori Knowledge GAN for CT Images Generation of Early Lung Nodules with Small-Size Labelled Samples

Oxidative Medicine and Cellular Longevity

Received 1 August 2023; Accepted 1 August 2023; Published 2 August 2023

Copyright © 2023 Oxidative Medicine and Cellular Longevity. This is an open access article distributed under the Creative Commons Attribution License, which permits unrestricted use, distribution, and reproduction in any medium, provided the original work is properly cited.

This article has been retracted by Hindawi following an investigation undertaken by the publisher [1]. This investigation has uncovered evidence of one or more of the following indicators of systematic manipulation of the publication process:

- (1) Discrepancies in scope
- (2) Discrepancies in the description of the research reported
- (3) Discrepancies between the availability of data and the research described
- (4) Inappropriate citations
- (5) Incoherent, meaningless and/or irrelevant content included in the article
- (6) Peer-review manipulation

The presence of these indicators undermines our confidence in the integrity of the article's content and we cannot, therefore, vouch for its reliability. Please note that this notice is intended solely to alert readers that the content of this article is unreliable. We have not investigated whether authors were aware of or involved in the systematic manipulation of the publication process.

In addition, our investigation has also shown that one or more of the following human-subject reporting requirements has not been met in this article: ethical approval by an Institutional Review Board (IRB) committee or equivalent, patient/participant consent to participate, and/or agreement to publish patient/participant details (where relevant).

Wiley and Hindawi regrets that the usual quality checks did not identify these issues before publication and have since put additional measures in place to safeguard research integrity.

We wish to credit our own Research Integrity and Research Publishing teams and anonymous and named external researchers and research integrity experts for contributing to this investigation.

The corresponding author, as the representative of all authors, has been given the opportunity to register their agreement or disagreement to this retraction. We have kept a record of any response received.

References

- [1] X. Wang, Z. Yu, L. Wang, and P. Zheng, "An Enhanced Priori Knowledge GAN for CT Images Generation of Early Lung Nodules with Small-Size Labelled Samples," *Oxidative Medicine and Cellular Longevity*, vol. 2022, Article ID 2129303, 9 pages, 2022.

Retraction

Retracted: The Establishment of a Mouse Model for Degenerative Kyphoscoliosis Based on Senescence-Accelerated Mouse Prone 8

Oxidative Medicine and Cellular Longevity

Received 26 September 2023; Accepted 26 September 2023; Published 27 September 2023

Copyright © 2023 Oxidative Medicine and Cellular Longevity. This is an open access article distributed under the Creative Commons Attribution License, which permits unrestricted use, distribution, and reproduction in any medium, provided the original work is properly cited.

This article has been retracted by Hindawi following an investigation undertaken by the publisher [1]. This investigation has uncovered evidence of one or more of the following indicators of systematic manipulation of the publication process:

- (1) Discrepancies in scope
- (2) Discrepancies in the description of the research reported
- (3) Discrepancies between the availability of data and the research described
- (4) Inappropriate citations
- (5) Incoherent, meaningless and/or irrelevant content included in the article
- (6) Peer-review manipulation

The presence of these indicators undermines our confidence in the integrity of the article's content and we cannot, therefore, vouch for its reliability. Please note that this notice is intended solely to alert readers that the content of this article is unreliable. We have not investigated whether authors were aware of or involved in the systematic manipulation of the publication process.

Wiley and Hindawi regrets that the usual quality checks did not identify these issues before publication and have since put additional measures in place to safeguard research integrity.

We wish to credit our own Research Integrity and Research Publishing teams and anonymous and named external researchers and research integrity experts for contributing to this investigation.

The corresponding author, as the representative of all authors, has been given the opportunity to register their agreement or disagreement to this retraction. We have kept a record of any response received.

References

- [1] Z. Hu, Z. Tang, A. Kiram et al., "The Establishment of a Mouse Model for Degenerative Kyphoscoliosis Based on Senescence-Accelerated Mouse Prone 8," *Oxidative Medicine and Cellular Longevity*, vol. 2022, Article ID 7378403, 7 pages, 2022.

Research Article

The Establishment of a Mouse Model for Degenerative Kyphoscoliosis Based on Senescence-Accelerated Mouse Prone 8

Zongshan Hu ^{1,2}, Ziyang Tang,² Abdukahar Kiram,¹ Jie Li,¹ Hui Xu,¹ Yanjie Xu,¹ Huiming Jiang,² Zezhang Zhu,^{1,2} Yong Qiu,^{1,2} and Zhen Liu ^{1,2}

¹Division of Spine Surgery, Department of Orthopedic Surgery, Nanjing Drum Tower Hospital, The Affiliated Hospital of Nanjing University Medical School, China

²Division of Spine Surgery, Department of Orthopedic Surgery, Nanjing Drum Tower Hospital, The Clinical College of Nanjing Medical University, China

Correspondence should be addressed to Zhen Liu; drluozhen@163.com

Zongshan Hu and Ziyang Tang contributed equally to this work.

Received 26 April 2022; Revised 8 June 2022; Accepted 14 June 2022; Published 20 July 2022

Academic Editor: Shao Liang

Copyright © 2022 Zongshan Hu et al. This is an open access article distributed under the Creative Commons Attribution License, which permits unrestricted use, distribution, and reproduction in any medium, provided the original work is properly cited.

Objective. Degenerative kyphoscoliosis (DKS) is a complex spinal deformity associated with degeneration of bones, muscles, discs, and facet joints. The aim of this study was to establish an animal model of degenerative scoliosis that recapitulates key pathological features of DKS and to validate the degenerative changes in senescence-accelerated mouse prone 8 (SAMP8) mice. **Methods.** Thirty male mice were divided into 2 groups: 10 bipedal C57BL/6J mice were used as the control group, and 20 bipedal SAMP8 mice were used as the experimental group. Mice were bipedalized under general anesthesia. The incidence of scoliosis and bone quality was determined using radiographs and in vivo micro-CT images 4, 8, and 12 weeks after surgery, respectively. Histomorphological studies of muscle samples were performed after sacrifice at 12 weeks after surgery. **Results.** On the 12th week, the incidence rates of kyphosis in C57BL/6J and SAMP8 groups were 50% and 100%, respectively. Overall, the incidence and angle of kyphosis were significantly higher in the bipedal SAMP8 group compared to the C57BL/6J group ($44.7^\circ \pm 6.2^\circ$ vs. $84.3^\circ \pm 10.3^\circ$, $P < 0.001$). Based on 3D reconstruction of the entire spine, degeneration of the intervertebral disc was observed in bipedal SAMP8 mice, including the reduction of disc height and the formation of vertebral osteophytes. The bone volume ratio (BV/TV) was significantly suppressed in the bipedal SAMP8 group compared with the bipedal C57BL/6J group. In addition, HE staining and Mason staining of the paraspinal muscle tissue showed chronic inflammation and fibrosis in the muscles of the bipedal SAMP8 group. **Conclusions.** The SAMP8 mouse model can be taken as a clinically relevant model of DKS, and accelerated aging of the musculoskeletal system promotes the development of kyphosis.

1. Introduction

Degenerative kyphoscoliosis (DKS) is a coronal deviation of the spine, prevalent in the elderly. Most DKS cases occur in the lumbar segment of the spine (the Cobb angle of the coronal plane $> 10^\circ$) [1, 2]. DKS involves progressive and asymmetric degeneration of the intervertebral discs, facet joints, and other structural spinal components, often resulting in nerve compression [3]. The reported incidence of DKS was 0.087%, and the median age was 64.9 ± 9.4 years. The incidence is significantly higher in older women than

in older men [4, 5]. With the gradual aging of the population, DKS seriously affects the quality of life of the elderly and poses a threat to the life of the elderly [6].

With the increase in DKS patients, in order to better understand the pathogenesis of DKS, animal models of scoliosis have been established using different animals, such as Sprague-Dawley (SD) rats [7], pigs [8], goats [9], C57BL/6 mice [10], and baboons [11]. A mouse model of DKS using heparin has also been recently reported. Heparin increased the incidence of scoliosis in C57BL/6J biped mice and resulted in more severe deformity in a relatively short period

of time [12]. The occurrence of DKS is age-related. It is common in middle-aged and elderly people. The mean age of the patients was approximately 60 years [13]. The accelerated aging mouse (SAM) established by Takahashi is the only mammalian model currently used to study accelerated aging. These mammals include SAMP1, SAMP6, SAMP8, SAMP10, SAMR1, and others [14]. SAMP1 mice are commonly used to study animal models of senile amyloidosis [15]. SAMP6 mice have been developed as a spontaneous experimental model of senile osteoporosis [16]. SAMP8 mice are a model for studying the effects of aging on cardiovascular health [17] and neurodegenerative diseases [18]. Notably, SAMP8 mice are frequently used to study neurodegenerative diseases, but they can also be used to study degenerative joint diseases [19]. Studies have shown that SAMP8 mice may simultaneously develop sarcopenia, osteoporotic fractures, and other symptoms [20]. Sarcopenia affects muscle performance and is considered a major cause of functional limitation and exercise dependence in older adults with osteoporosis [21]. Osteoporosis is a cause of DKS. However, the association between sarcopenia, osteoporosis, and DKS remains unclear, in part due to the lack of relevant animal models to study. Therefore, in this study, we aimed to construct an animal model of DKS through SAMP8 mice and to explore the relevant clinical manifestations of the model animals of DKS.

2. Materials and Methods

2.1. Animal. Adult male C57BL/6J mice ($N = 10$, 10-12 weeks old, 20-24 g body weight) and male SAMP8 mice ($N = 20$, 20-21 weeks old, 22-25 g body weight) were obtained from Nanjing University Medicine obtained from the Animal Experiment Center of the Chinese Academy of Sciences. Animals were housed under standard conditions (12 h light/dark cycle, 22-25°C, 50% relative humidity) with free access to food and water. The protocol of animal experiments has been approved by the Animal Care Committee of Nanjing University School of Medicine (approval number MSNU20210013), and the animal experiments were carried out in accordance with the National Institutes of Health Guidelines for the Care and Use of Laboratory Animals.

2.2. The Construction of the Bipedal Upright Model. C57BL/6J and SAMP8 mice were anesthetized by intraperitoneal injection of 3% sodium phenobarbital (30 mg/kg). After anesthesia, the skin of the mice was incised in the supine position at the level of the scapulae of both forelimbs. Both forelimbs were securely ligated with silk thread above the proximal skin edge. Then, the distal limb is excised, and the bleeding is appropriately stopped. The skin is sutured, and the stump is buried. The tail was firmly ligated and then removed. Finally, a bipedal mouse model was constructed. After surgery, animals are housed in specially designed cages to recover for 3 to 5 days. In the cage, the mice had to stand up to feed and remain standing for 2 weeks. Monthly, X-rays of the entire spine were performed. Twelve weeks later, mice were anesthetized with 3% sodium phenobarbital (30 mg/kg)

and sacrificed and underwent X-ray, micro-CT, and histological examinations (Figure 1).

2.3. X-Ray Examination. Twelve weeks after surgery, mice were placed supine on a camera table under anesthesia. Take anterior, posterior, and lateral radiographs of the animal. Observe the spine curve. Spinal curvature was measured by the Cobb method (Cobb $> 10^\circ$ represents scoliosis). The Cobb angle of each group of mice was measured.

2.4. Micro-CT. Twelve weeks after surgery, mice were anesthetized with 3% sodium phenobarbital intraperitoneally. The spines of mice were harvested, and the continuity and integrity of the spines were maintained. The soft tissue surrounding the spine was removed and fixed in 4% paraformaldehyde for 24 h. The ratio of bone volume to total volume (BV/TV, %) was examined using micro-CT (Belgium Skyscan, Skyscan-1076) and scanned with 50 kV and 200 μ A settings and a 0.5 mm aluminum filter. Resolution is adjusted to 26.6 microns per pixel. Each rotation step is 0.70 degrees over a range of 180 degrees. The binarized 3D image was generated with CTvox (version 2.4) [22].

2.5. H&E Staining. Mice were anesthetized by intraperitoneal injection of 3% sodium phenobarbital. After anesthesia, mice were sacrificed by cervical dislocation. The paraspinal muscle tissue of mice in each group was taken and fixed in formalin for 1 day. Tissues were embedded in paraffin, sliced (4 μ m thick), and baked in a constant temperature oven (65°C) for 6 h. Sections were routinely dewaxed, hydrated, stained with H&E, sealed with neutral glue, and observed under a microscope (Leica, Germany).

2.6. Masson Staining. Collagen fibers and muscle fibers in mouse paraspinal muscle tissue were examined using a Masson staining kit (Solarbio, Beijing, China) according to the manufacturer's protocol. The morphology of each slice was observed using a Leica DMI6000 B microscope (Leica, Germany).

2.7. Statistical Analysis. Statistical analysis was performed using SPSS 17.0 software (SPSS Inc., Chicago, IL, USA). Measurement data are expressed as mean \pm standard deviation (SD). Differences between two groups were compared by the independent t -test, and differences among multiple groups were compared by one-way ANOVA. $P < 0.05$ was considered statistically significant.

3. Results

3.1. The X-Ray Examination and Micro-CT Evaluation of Spinal Deformities in SAMP8 Mice. We constructed C57BL/6J and SAMP8 mouse DKS models, respectively. After twelve weeks, the mice were assessed for scoliosis by X-ray. The results showed that 50% of C57 mice developed kyphosis with an angle of $44.7^\circ \pm 6.2$. All SAMP8 mice developed kyphosis with a Cobb angle of $84.3^\circ \pm 10.3^\circ$. Overall, the incidence of kyphosis was higher in the SAMP8 group than in the C57 group (Figure 2(a), $P < 0.001$). Spinal

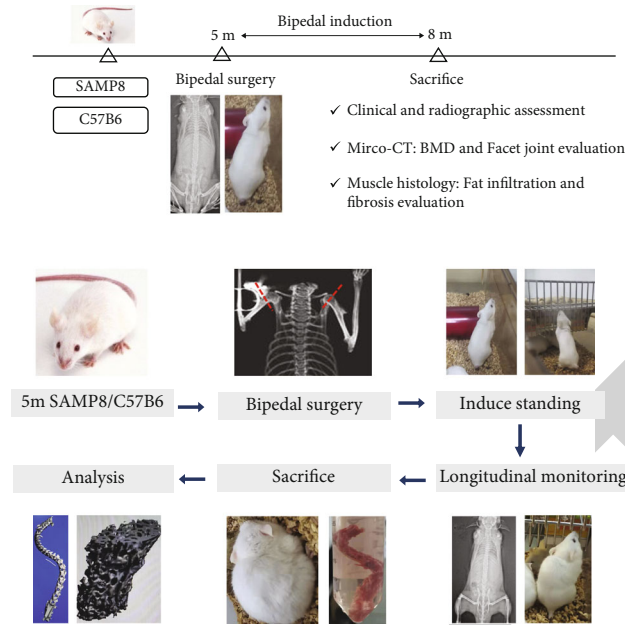


FIGURE 1: The schematic diagrams of experimental designs.

deformities were further investigated using micro-CT. 3D reconstruction images showed that SAMP8 mice exhibited more severe kyphosis, decreased intervertebral height, and vertebral osteophyte formation. The bone volume ratio (BV/TV) of the SAMP8 group was significantly lower than that of the C57 group (Figures 2(b) and 2(c), $P < 0.001$).

3.2. The Histological Changes of SAMP8 Mice. Inflammation and muscle fibrosis in paraspinal muscle tissue of C57BL/6J and SAMP8 mice were examined by HE staining and Masson staining. HE staining showed that adipocytes and inflammatory cells were more concentrated in the muscle tissue of SAMP8 mice compared with C57BL/6J mice. Masson staining showed that the area of adipose and fibrotic tissue increased in the paraspinal muscle tissue of SAMP8 mice, suggesting significant chronic inflammation and fibrosis in their muscles (Figure 3).

4. Discussion

The lateral deviation of the spine usually occurs after age 50. As the population ages, the incidence of DKS also increases [2, 23]. The etiology of the disease remains poorly understood, but the most common causes include osteoporosis and degenerative disc disease [24]. Surgery is currently the most common strategy for the treatment of DKS. However, surgery is indicated for patients with moderate symptoms, large or progressive deformity, moderate spinal or foraminal stenosis, or sagittal imbalance. It is not suitable for patients with mild symptoms and less stable deformity but without sagittal imbalance or moderate stenosis, especially in elderly patients with multiple complications [25]. Therefore, establishing a suitable animal model will lay the foundation for studying the pathogenesis and treatment strategies of DKS. In this study, we used SAMP8 mice to establish a bipedal

erection model. Our results showed that the incidence and angle of kyphosis were significantly higher in the bipedal SAMP8 group than in the C57BL/6J group, suggesting that the SAMP8 mouse model can be used as a clinical research model for DKS.

The SAM model was first established in 1981 and includes 9 major SAMP subtypes and 3 major aging-accelerated mouse resistance (SAMR) subtypes. Each subtype exhibits characteristic symptoms. Recently, SAMP8 mice have attracted the attention of gerontological studies due to their characteristic learning and memory impairment in old age [26]. SAMP8 mice are widely used in the study of aging-related diseases such as AD [27], cardiovascular disease [28], and age-related hearing loss [29]. More importantly, when SAMP8 mice underwent ovariectomy (OVX-SAMP8) 4 months after birth, osteoporosis was rapidly induced and bone mineral content was greatly reduced [30]. However, this study only focused on female mice, and secondary osteoporosis is caused by a lack of estrogen. Myofibrillar protein was significantly attenuated in skeletal muscle of SAMP8 mice compared to control SAMR1 mice [31, 32]. DKS usually occurs in elderly patients. Sarcopenia and osteoporosis are significantly associated with DKS [33, 34]. Therefore, SAMP8 mice can better mimic the development of DKS.

X-ray and micro-CT can be used for the diagnosis of DKS in clinical practice. In the case of osteoporosis and intervertebral disc degeneration, the morphological changes determined by X-ray are very important for the judgment of the diagnosis. Therefore, X-rays cannot be replaced by bone mineral measurements, CT, MR, or other imaging techniques. Micro-CT is a nondestructive 3D imaging technique that can generate nondestructive 3D images of trabecular bone microstructure, demonstrate the microstructure of trabecular bone, and determine bone parameters. The X-ray

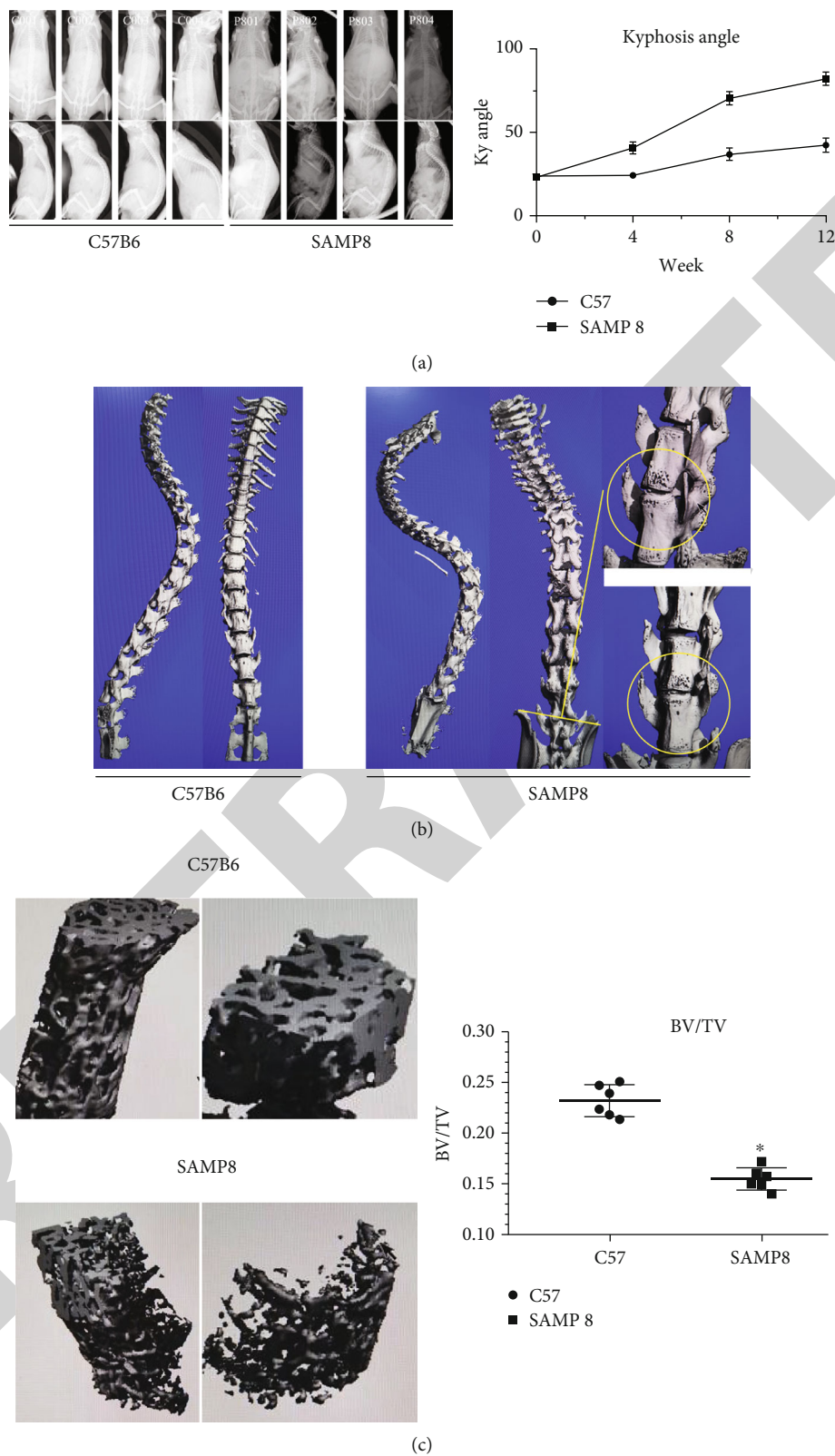


FIGURE 2: X-ray and micro-CT assessment of spinal deformities in SAMP8 mice. (a) X-ray examination of mouse spine morphology and calculation of mouse Cobb angle. $*P < 0.001$, $n = 10$ /group. (b, c) Micro-CT was used to assess trabecular bone microstructure in mice by 3D imaging and to measure the bone volume ratio (BV/TV). $*P < 0.001$, $n = 8$ /group.

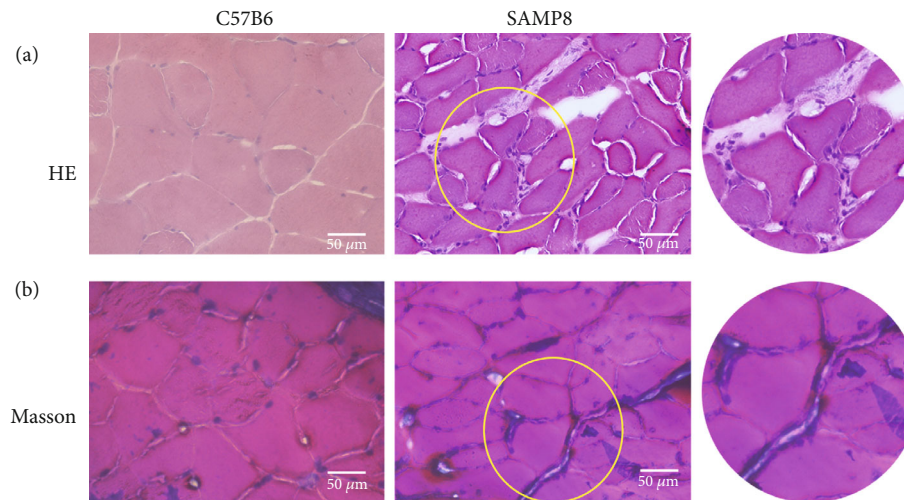


FIGURE 3: Histological changes in SAMP8 mice. (a) HE staining to examine chronic adipose proliferation in mouse paraspinal muscle tissue. (b) Masson staining to measure collagen fibers and muscle fibers in paraspinal muscle tissue in mice. Scale = 50 μm .

films are reflected in the scoliosis model established using FGFR3^{-/-} mice; the spines of FGFR3^{-/-} mice showed a clear curve and a larger Cobb angle. Micro-CT showed sparse pyramidal foramen structure, decreased BV/TV ratio, and significantly increased vertebral body length in FGFR3^{-/-} mice [35]. Here, we harvested the entire spine of the mice following 12-week modeling. X-ray films suggested that 50% of C57 mice developed kyphosis with an angle of $44.7^\circ \pm 6.2$, and 100% of SAMP8 mice manifested kyphosis with a Cobb angle of $84.3^\circ \pm 10.3$. Micro-CT further examined spinal deformities. 3D reconstructed images displayed that the kyphosis of SAMP8 mice was much more severe, and the BV/TV ratio of the SAMP8 group was considerably lower than that of C57 group. All these findings demonstrated that we successfully established a DKS mouse model in SAMP8 mice by making them stand upright on two feet.

The muscles that attach to the spine, the paraspinal muscles, play a vital role in maintaining the function of the spine and the entire body. Spinal lesions can directly lead to changes in the structure and function of the paraspinal muscles. Alterations in muscle structure and function, especially fatty infiltration and fibrosis, are clearly associated with spinal disorders [36]. An increasing number of studies have shown that in patients with DKS, the cross-sectional area of the lumbar erector spinae and psoas major is significantly thinner, and pathological assessment shows muscle atrophy, necrosis, and hyaline fibrosis, while muscle fat infiltration and inflammatory cell infiltration are more pronounced [37–39]. Therefore, we also performed pathological examination of the paraspinal muscle tissue of DKS mice by HE staining and Masson staining. The results showed an increase in adipocytes and inflammatory cells in the muscle tissue of SAMP8 mice. Masson staining showed that the area of adipose and fibrotic tissue in the paraspinal muscle tissue of SAMP8 mice was enlarged, indicating obvious muscle fibrosis. These findings further confirm the reliability of the DKS model using SAMP8 mice.

5. Conclusion

In conclusion, we successfully established an animal model of DKS using SAMP8 mice. X-ray films, micro-CT, and related histological examinations confirmed the validity of the model. We provide a reliable animal model for further study of DKS. However, the number of mouse samples in our study was not sufficient. Therefore, we will increase our sample in the next study to further confirm the validity of the DKS model using SAMP8 mice.

Data Availability

All data were included in the manuscript.

Conflicts of Interest

The authors declare that they have no conflicts of interest.

Authors' Contributions

Zongshan Hu and Ziyang Tang contributed equally to this work.

Acknowledgments

This work was supported by the National Natural Science Foundation of China (NSFC) (No. 82072518), the Nanjing Medical Science and Technique Development Foundation (No. QRX17126) funds, the Jiangsu Provincial Key Medical Center, and the China Postdoctoral Science Foundation (2021M701677).

References

- [1] M. Aebi, "The adult scoliosis," *European Spine Journal*, vol. 14, no. 10, pp. 925–948, 2005.

- [2] C. B. Tribus, "Degenerative lumbar scoliosis: evaluation and management," *The Journal of the American Academy of Orthopaedic Surgeons*, vol. 11, no. 3, pp. 174–183, 2003.
- [3] S. Kotwal, M. Pumberger, A. Hughes, and F. Girardi, "Degenerative scoliosis: a review," *HSS Journal*, vol. 7, no. 3, pp. 257–264, 2011.
- [4] C. L. García-Ramos, C. A. Obil-Chavarría, D. D. Molina-Choez, and A. Reyes-Sánchez, "Epidemiological and radiological profile of patients with degenerative scoliosis: 20 year experience at a referral institute," *Acta Ortopédica Mexicana*, vol. 32, no. 2, pp. 60–64, 2018.
- [5] N. G. Wang, Y. P. Wang, G. X. Qiu et al., "Radiological evaluation of intervertebral angles on short-segment fusion of degenerative lumbar scoliosis," *Zhonghua Wai Ke Za Zhi*, vol. 48, no. 7, pp. 506–510, 2010.
- [6] C. McDaniels-Davidson, A. Davis, D. Wing et al., "Kyphosis and incident falls among community-dwelling older adults," *Osteoporosis International*, vol. 29, no. 1, pp. 163–169, 2018.
- [7] Y. Wang, X. D. Yi, and C. D. Li, "Suppression of mTOR signaling pathway promotes bone marrow mesenchymal stem cells differentiation into osteoblast in degenerative scoliosis: in vivo and in vitro," *Molecular Biology Reports*, vol. 44, no. 1, pp. 129–137, 2017.
- [8] F. Accadbled, J. M. Laffosse, T. Odent, A. Gomez-Brouchet, J. S. de Gauzy, and P. Swider, "Influence of growth modulation on the effective permeability of the vertebral end plate. A porcine experimental scoliosis model," *Clinical Biomechanics*, vol. 26, no. 4, pp. 337–342, 2011.
- [9] K. J. Hunt, J. T. Braun, and B. A. Christensen, "The effect of two clinically relevant fusionless scoliosis implant strategies on the health of the intervertebral disc: analysis in an immature goat model," *Spine (Phila Pa 1976)*, vol. 35, no. 4, pp. 371–377, 2010.
- [10] L. A. Nasto, K. Ngo, A. S. Leme et al., "Investigating the role of DNA damage in tobacco smoking-induced spine degeneration," *The Spine Journal*, vol. 14, no. 3, pp. 416–423, 2014.
- [11] W. C. Lauerma, R. C. Platenberg, J. E. Cain, and V. F. Deeney, "Age-related disk degeneration," *Journal of Spinal Disorders*, vol. 5, no. 2, pp. 170–174, 1992.
- [12] L. Jie, L. Na, C. Jiayu et al., "Establishment of degenerative scoliosis model in aged bipedal mice with heparin," *Annals of Orthopaedic Surgery in China*, vol. 26, no. 17, pp. 1605–1608, 2018.
- [13] T. Ailon, C. I. Shaffrey, L. G. Lenke, J. S. Harrop, and J. S. Smith, "Progressive spinal kyphosis in the aging population," *Neurosurgery*, vol. 77, Supplement 1, pp. S164–S172, 2015.
- [14] R. Takahashi, "Anti-aging studies on the senescence accelerated mouse (SAM) strains," *Yakugaku zasshi: Journal of the Pharmaceutical Society of Japan*, vol. 130, no. 1, pp. 11–18, 2010.
- [15] M. Umezawa, K. Tatsumatsu, T. Korenaga et al., "Dietary fat modulation of apo A-II metabolism and prevention of senile amyloidosis in the senescence-accelerated mouse," *Journal of Lipid Research*, vol. 44, no. 4, pp. 762–769, 2003.
- [16] K. Azuma, Q. Zhou, and K. Y. Kubo, "Morphological and molecular characterization of the senile osteoporosis in senescence-accelerated mouse prone 6 (SAMP6)," *Medical Molecular Morphology*, vol. 51, no. 3, pp. 139–146, 2018.
- [17] V. Karuppagounder, S. Arumugam, S. S. Babu et al., "The senescence accelerated mouse prone 8 (SAMP8): a novel murine model for cardiac aging," *Ageing Research Reviews*, vol. 35, pp. 291–296, 2017.
- [18] M. M. Akbor, J. Kim, M. Nomura, J. Sugioka, N. Kurosawa, and M. Isobe, "A candidate gene of Alzheimer diseases was mutated in senescence-accelerated mouse prone (SAMP) 8 mice," *Biochemical and Biophysical Research Communications*, vol. 572, pp. 112–117, 2021.
- [19] K. Matsubara, M. Okuda, S. Shibata et al., "The delaying effect of alpha-glycerophosphocholine on senescence, transthyretin deposition, and osteoarthritis in senescence-accelerated mouse prone 8 mice," *Bioscience, Biotechnology, and Biochemistry*, vol. 82, no. 4, pp. 647–653, 2018.
- [20] N. Zhang, S. K. H. Chow, K. S. Leung, H. H. Lee, and W. H. Cheung, "An animal model of co-existing sarcopenia and osteoporotic fracture in senescence accelerated mouse prone 8 (SAMP8)," *Experimental Gerontology*, vol. 97, pp. 1–8, 2017.
- [21] P. P. Coll, S. Phu, S. H. Hajjar, B. Kirk, G. Duque, and P. Taxel, "The prevention of osteoporosis and sarcopenia in older adults," *Journal of the American Geriatrics Society*, vol. 69, no. 5, pp. 1388–1398, 2021.
- [22] H. K. Kim, O. Aruwajoye, D. Sucato et al., "Induction of SHP2 deficiency in chondrocytes causes severe scoliosis and kyphosis in mice," *Spine*, vol. 38, no. 21, pp. E1307–E1312, 2013.
- [23] K. Chen, J. Zhao, Y. Yang et al., "Global research trends of adult degenerative scoliosis in this decade (2010-2019): a bibliometric study," *European Spine Journal*, vol. 29, no. 12, pp. 2970–2979, 2020.
- [24] S. D. Daffner and A. R. Vaccaro, "Adult degenerative lumbar scoliosis," *American Journal of Orthopedics (Belle Mead, N.J.)*, vol. 32, no. 2, pp. 77–82, 2003.
- [25] P. G. Chen, M. D. Daubs, S. Berven et al., "Surgery for degenerative lumbar scoliosis," *Spine*, vol. 41, no. 10, pp. 910–918, 2016.
- [26] D. A. Butterfield and H. F. Poon, "The senescence-accelerated mouse prone mouse (SAMP8): a model of age-related cognitive decline with relevance to alterations of the gene expression and protein abnormalities in Alzheimer's disease," *Experimental Gerontology*, vol. 40, no. 10, pp. 774–783, 2005.
- [27] K. Lok, H. Zhao, H. Shen et al., "Characterization of the APP/PS1 mouse model of Alzheimer's disease in senescence accelerated background," *Neuroscience Letters*, vol. 557, pp. 84–89, 2013.
- [28] V. V. Giridharan, V. Karuppagounder, S. Arumugam et al., "3, 4-Dihydroxybenzalacetone (DBL) prevents aging-induced myocardial changes in senescence-accelerated mouse-prone 8 (SAMP8) mice," *Cell*, vol. 9, no. 3, p. 597, 2020.
- [29] A. Marie, P. Larroze-Chicot, S. Cosnier-Pucheu, and S. Gonzalez-Gonzalez, "Senescence-accelerated mouse prone 8 (SAMP8) as a model of age-related hearing loss," *Neuroscience Letters*, vol. 656, pp. 138–143, 2017.
- [30] W. C. Lo, J. F. Chiou, J. G. Gelovani et al., "Transplantation of embryonic fibroblasts treated with platelet-rich plasma induces osteogenesis in SAMP8 mice monitored by molecular imaging," *Journal of Nuclear Medicine*, vol. 50, no. 5, pp. 765–773, 2009.
- [31] T. Sato, Y. Ito, and T. Nagasawa, "L-Lysine suppresses myofibrillar protein degradation and autophagy in skeletal muscles of senescence-accelerated mouse prone 8," *Biogerontology*, vol. 18, no. 1, pp. 85–95, 2017.
- [32] N. Zhang, Y. N. Chim, J. Wang, R. M. Y. Wong, S. K. H. Chow, and W. H. Cheung, "Impaired fracture healing in sarcoosteoporotic mice can be rescued by vibration treatment

Retraction

Retracted: Comparative Analysis of Early Clinical Features and Complications of Different Types of Acute Pancreatitis

Oxidative Medicine and Cellular Longevity

Received 1 August 2023; Accepted 1 August 2023; Published 2 August 2023

Copyright © 2023 Oxidative Medicine and Cellular Longevity. This is an open access article distributed under the Creative Commons Attribution License, which permits unrestricted use, distribution, and reproduction in any medium, provided the original work is properly cited.

This article has been retracted by Hindawi following an investigation undertaken by the publisher [1]. This investigation has uncovered evidence of one or more of the following indicators of systematic manipulation of the publication process:

- (1) Discrepancies in scope
- (2) Discrepancies in the description of the research reported
- (3) Discrepancies between the availability of data and the research described
- (4) Inappropriate citations
- (5) Incoherent, meaningless and/or irrelevant content included in the article
- (6) Peer-review manipulation

The presence of these indicators undermines our confidence in the integrity of the article's content and we cannot, therefore, vouch for its reliability. Please note that this notice is intended solely to alert readers that the content of this article is unreliable. We have not investigated whether authors were aware of or involved in the systematic manipulation of the publication process.

Wiley and Hindawi regrets that the usual quality checks did not identify these issues before publication and have since put additional measures in place to safeguard research integrity.

We wish to credit our own Research Integrity and Research Publishing teams and anonymous and named external researchers and research integrity experts for contributing to this investigation.

The corresponding author, as the representative of all authors, has been given the opportunity to register their agreement or disagreement to this retraction. We have kept a record of any response received.

References

- [1] H. Wu, K. Ma, B. Liao, T. Ji, S. Zhang, and T. Cao, "Comparative Analysis of Early Clinical Features and Complications of Different Types of Acute Pancreatitis," *Oxidative Medicine and Cellular Longevity*, vol. 2022, Article ID 3771610, 9 pages, 2022.

Research Article

Comparative Analysis of Early Clinical Features and Complications of Different Types of Acute Pancreatitis

Hongsheng Wu, Keqiang Ma, Biling Liao, Tengfei Ji, Shengmin Zhang, and Tiansheng Cao 

Department of Hepatobiliary Pancreatic Surgery, Affiliated Huadu Hospital, Southern Medical University, Guangzhou, 510800 Guangdong Province, China

Correspondence should be addressed to Tiansheng Cao; caotiansheng2088@sina.com

Received 7 March 2022; Revised 16 May 2022; Accepted 25 May 2022; Published 25 June 2022

Academic Editor: Shao Liang

Copyright © 2022 Hongsheng Wu et al. This is an open access article distributed under the Creative Commons Attribution License, which permits unrestricted use, distribution, and reproduction in any medium, provided the original work is properly cited.

Background. Acute pancreatitis (AP) is a common surgical acute abdomen. Different kinds of pancreatitis may have different pathophysiological characteristics each other. The objective of this research was to investigate the early clinical features and complications of different types of acute pancreatitis. **Methods.** 787 AP patients admitted in the Huadu District People's Hospital of Guangzhou during January 2009 and December 2019 were analyzed retrospectively. Among 787 AP patients, 520 (66.1%) were biliary AP (group I), 69 (8.7%) were alcoholic AP (group II), and 198 (25.2%) were hypertriglyceridemic AP (group III). According to the local and systemic complications and mortality in the early stage, we compared and analyzed the clinical characteristics and prognosis of different types of pancreatitis. **Results.** Mild acute pancreatitis accounted for the highest proportion (79.4%) in group I, while moderately severe acute pancreatitis in group II (36.2%) and severe acute pancreatitis in group III (62.6%). In terms of severity score of the pancreatitis, the average scores of BISAP, Ranson, APACHE-II, and MCTSI of the patients in group III were the highest ($p < 0.01$). The incidence of acute peripancreatic fluid collection and infectious pancreatic necrosis was the highest in group III. The incidences of acute necrotic collection, pancreatic pseudocyst, and walled-off necrosis in group III were significantly higher than those in the other two groups ($p < 0.01$). The incidences of systemic inflammatory response syndrome, sepsis, multiple organ failure, intra-abdominal hypertension, and mortality were highest in group III. **Conclusions.** There is an upward trend of the incidence rate of hypertriglyceridemic AP in recent years; it has been gradually developed into the second type of acute pancreatitis which is second only to the acute biliary pancreatitis. It is worthy to pay more and more attentions to it due to the feature of its younger onset, high incidence of complications, and high mortality.

1. Introduction

Acute pancreatitis (AP) is caused by abnormal activation of digestive enzymes from pancreas which lead to self-digestion of pancreas and peripancreatic organs under various pathogenic factors. Although the etiology of AP is various and complicated, however, among all of these etiologies, biliary stones, alcoholism, and hyperlipidemia are the three main causes which lead to AP. Based on the etiology of AP, acute biliary pancreatitis and alcoholic pancreatitis are the two major causes of acute pancreatitis from the developed coun-

tries at present, and two types of these acute pancreatitis accounts for about 80% of the incidence rate of acute pancreatitis [1]. In China, these two kinds of pancreatitis were the most common clinical types of AP in the past. However, in recent years, with the improvement of people's living quality and the changes of diet styles increasingly, the incidence rate of hypertriglyceridemia caused by lipid metabolism disorders has been increasing year by year, which makes the acute pancreatitis caused by hypertriglyceridemia rapidly increase in recent years, and had become one of the common causes of AP [2–5]. The characteristics of its rapid

TABLE 1: Basic clinical data of three groups of AP patients.

Typing of AP	Group I (<i>n</i> = 520)	Group II (<i>n</i> = 69)	Group III (<i>n</i> = 198)	<i>p</i> value
Sex (male/female)	141/379 (27.1/72.9)	67/2 (97.1/2.9)	162/36 (81.8/18.2)	<0.01 ^Φ
Age	65.0 ± 3.4	46.0 ± 2.8	38.0 ± 2.4	<0.01 ^Φ
Pulse rate at admission (time/min)	92.0 ± 3.5	101.0 ± 3.2	126.0 ± 4.2	<0.01 ^Φ
Respiratory rate at admission (time/min)	17.0 ± 1.2	19.0 ± 1.5	25.0 ± 1.4	<0.01 [§]
WBC (×10 ⁹ /L)	12.3 ± 1.5	14.4 ± 1.4	15.8 ± 1.2	0.167
CRP (mg/L)	45.0 ± 12.3	68.0 ± 16.7	123.0 ± 24.2	<0.01
Serum creatinine (μmol/L)	62.0 ± 7.8	65.0 ± 8.2	125.0 ± 19.8	<0.01 [§]
BUN (mmol/L)	5.4 ± 0.5	6.7 ± 0.7	27 ± 2.5	<0.01 [§]
Blood glucose (mmol/L)	6.3 ± 0.4	7.1 ± 0.5	14.5 ± 2.0	<0.01 [§]
Serum amylase (U/L)	987.0 ± 23.1	1023.0 ± 45.3	1110.0 ± 68.2	0.231
Serum calcium (mmol/L)	2.6 ± 0.3	2.4 ± 0.4	1.9 ± 0.2	0.472
Arterial pH	7.4 ± 0.2	7.4 ± 0.1	7.3 ± 0.3	0.564
Serum triacylglycerol (mmol/L)	1.7 ± 0.3	2.2 ± 0.5	21.4 ± 5.5	<0.01 [§]

Group I: acute biliary pancreatitis; group II: acute alcoholic pancreatitis; group III: hypertriglyceridemic pancreatitis; WBC: White blood cell; CRP: C-reactive protein; BUN: blood urea nitrogen. ^Φ*p* < 0.01: the difference between any two groups was statistically significant. [§]*p* < 0.01: the difference between group III and group I or group II was statistically significant.

TABLE 2: Results of clinical classification and severity score of three groups of AP patients.

Typing of AP	Group I (<i>n</i> = 520)	Group II (<i>n</i> = 69)	Group III (<i>n</i> = 198)	<i>p</i> value
Clinical classification				
MAP	413 (79.4)	21 (30.4)	21 (10.6)	<0.01 ^Φ
MSAP	75 (14.4)	25 (36.2)	53 (26.8)	<0.01 ^Φ
SAP	32 (6.2)	23 (33.4)	124 (62.6)	<0.01 ^Φ
BISAP score ($\bar{x} \pm s, d$)	2.1 ± 0.8	2.4 ± 1.3	4.5 ± 1.2	<0.01 [§]
Ranson score ($\bar{x} \pm s, d$)	2.5 ± 0.3	2.8 ± 0.1	5.9 ± 0.4	<0.01 [§]
APACHE-II score ($\bar{x} \pm s, d$)	8.4 ± 1.6	15.2 ± 2.3	20.12 ± 3.1	<0.01 ^Φ
MCTSI score ($\bar{x} \pm s, d$)	3.5 ± 0.8	6.4 ± 1.1	9.2 ± 1.3	<0.01 ^Φ

Group I: acute biliary pancreatitis; group II: acute alcoholic pancreatitis; group III: hypertriglyceridemic pancreatitis; MAP: mild acute pancreatitis; MSAP: moderately severe acute pancreatitis; SAP: severe acute pancreatitis; APACHE-II: acute physiology and chronic health evaluation; MCTSI: modified computed tomography severity index. ^Φ*p* < 0.01: the difference between any two groups was statistically significant. [§]*p* < 0.01: the difference between group III and group I or group II was statistically significant.

and serious illness, its poor prognosis, and its high mortality rate had attracted the attention of clinicians. Although self-digestion of pancreas and peripancreatic tissue by abnormal activation of pancreatic digestive enzymes is the common feature of acute pancreatitis, however, due to the diversity of etiology of AP, pathophysiological characteristics of acute pancreatitis caused by different etiology may be different [6, 7]. Therefore, it is still unclear whether the diversity of AP etiology affects the incidence of complications in early stage or influenced severity of illness or determines the prognosis. Therefore, the motivation of our study is to explore the relationships between the characteristics of acute pancreatitis and the clinical types of AP and provide theoretical basis for the treatment and prevention of clinical pancreatitis. Thus, we analyzed the data of the AP patients which were admitted in a single medical center during the past 10 years retrospectively and reported.

2. Materials and Methods

2.1. Materials. 787 AP patients admitted to the Guangzhou Huadu District People's Hospital from 2008 to 2018 were enrolled in this research, and all the patients were hospitalized with acute abdominal pain as the main clinical symptom. After admission, they had been made a diagnosis of AP according to the following characteristics (meets all three): (1) abdominal pain; (2) serum amylase level was more than three times higher than the upper limit of normal value; (3) abdominal CT examination showed that the pancreas was swollen with varying degree. From all of the patients, there were 376 males and 411 females with a sex ratio of 1:1.09 and an average age of 49.7 ± 3.2 years. Among them, 520 cases (66.1%) were acute biliary AP (group I), 69 (8.7%) were alcoholic AP (group II), and 198 (25.2%) were hypertriglyceridemic AP (group III).

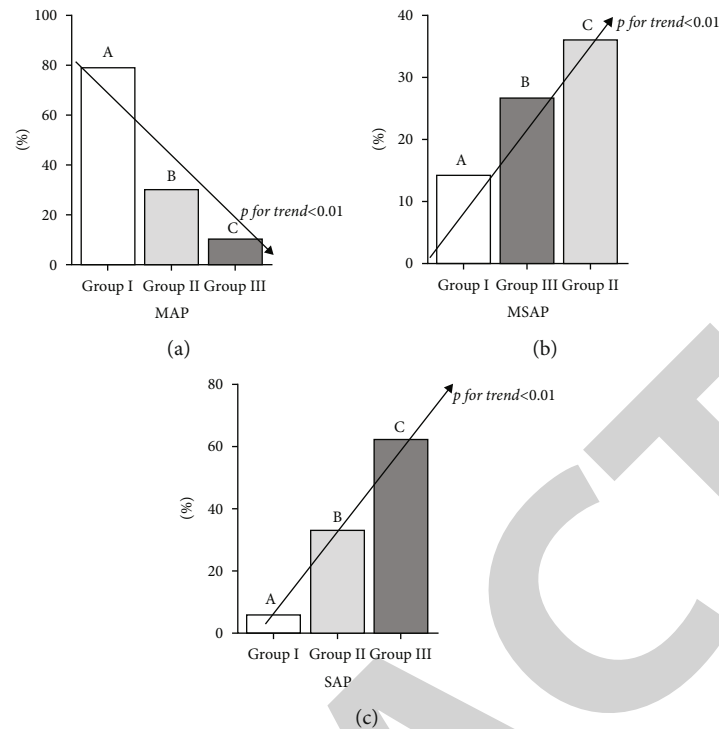


FIGURE 1: Comparison of clinical classification of three groups of AP patients. (a) Mild acute pancreatitis patients; (b) moderately severe acute pancreatitis patients; (c) severe acute pancreatitis patients; there was no significant difference between groups with the same letters and hand significant difference between the groups with different letters. p for trend: Cuzick trend chi-square test (multiple groups).

According to different types of AP, diagnostic criteria of acute biliary pancreatitis [8], with clinical manifestations of AP, B-ultrasound, CT or MRCP imaging, or endoscopy showed biliary stones. The diagnostic criteria of alcohol-related pancreatitis [9] were as follows: patients with AP clinical symptoms and signs, alcoholic pancreatitis generally requires drinking more than eight alcoholic drinks/day (>100 g/d) for more than 5 years, or drinking alcohol one week before onset of the disease and excluding other etiologies which lead to AP. The diagnostic criteria of hypertriglyceridemic AP are as follows [10]: patients with AP clinical symptoms and signs and the serum triglyceride ≥ 1000 mg/dL in the acute setting. Exclusion criteria are as follows: other types of etiologies which lead to AP, any severe systemic illness, and those with incomplete case files. The basic clinical data of this study is shown in Table 1. This study was approved by the ethics committee of our hospital; due to this was a retrospective study, our ethics committee granted an authorisation to waive written informed consent from patients.

2.2. Methods

2.2.1. Patients. According to the classifications from the latest Chinese guidelines for the diagnosis and treatment of acute pancreatitis [11], patients with AP were divided into three groups: acute biliary AP (group I), alcoholic AP (group II), and hypertriglyceridemic AP (group III). The clinical characteristics, clinical classification, bedside index for severity in acute pancreatitis (BISAP) score [12], APACHE-II

score [13], Ranson score [14] for severity assessment, modified CT severity index (MCTSI) score [15], and early local and systemic complications were statistically analyzed from each group. Multiple scoring systems were used to evaluate the severity and prognosis of AP. The early local complications included the following: (1) acute peripancreatic fluid collection (APFC) [16]: CT scan imaging feature indicated fluid accumulation with uniform signal and lack of intact capsule in the space of intrapancreatic or peripancreatic tissue; (2) acute necrotic collection (ANC) [17]: ultrasound or MRI indicated necrotic tissue contains in the liquid collection; (3) pancreatic pseudocyst (PPC) [18]: ultrasonography, CT scan, or MRI manifestation showed pancreatic cystic mass, containing pancreatic secretion, granulation tissue, and fibrous tissue; (4) walled-off necrosis (WON) [19]; and (5) infected pancreatic necrosis (IPN) [20]: the indication of the CT scan had typical “bubble sign” around the pancreas. Early systemic complications included the following: (1) systemic inflammatory response syndrome (SIRS) [21], (2) organ failure (OF); and (3) sepsis.

2.3. Statistical Analysis. SPSS 12.0 medical statistical software (SPSS, Inc., Chicago, IL, USA) was used for data statistics, continuous data were tested for normal distribution and were expressed in mean differences \pm standard deviation ($\bar{x} \pm s$), and t -test was used for comparison; the comparison of dichotomous data was presented as n (%), and chi-square test was performed for comparison. When comparison involved beyond two groups, Cuzick trend chi-square test (multiple groups) was used. For all the statistical tests,

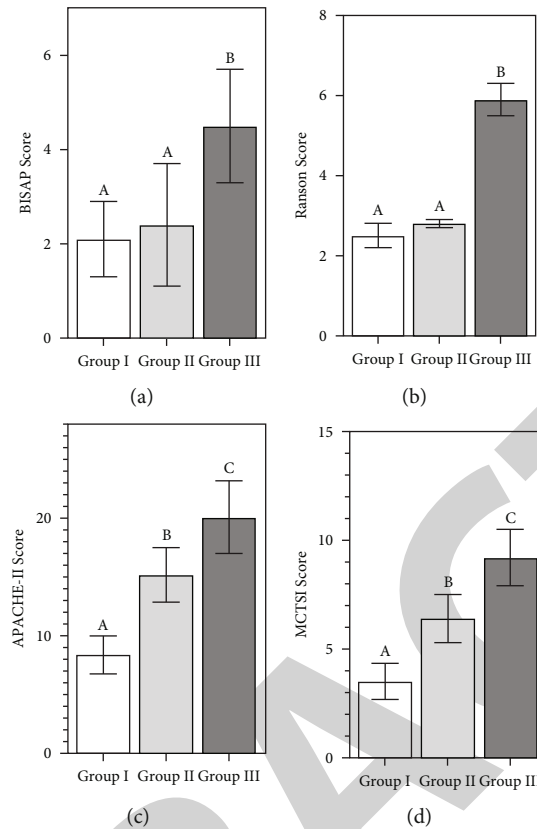


FIGURE 2: Comparison of severity score of three groups of AP patients. (a) BISAP score of three groups; (b) Ranson score of three groups; (c) APACHE-II score of three groups; (d) MCTSI score of three groups; there was no significant difference between groups with the same letters and hand significant difference between the groups with different letters.

a 0.05 significance level was used to claim a statistically significant effect.

3. Results

3.1. Clinical Type of AP between Three Groups. Among 520 AP patients in group I, there were 413 cases (79.4%) of MAP, 75 cases (14.4%) of MSAP, and 32 cases (6.2%) of SAP; among 69 AP patients in group II, there were 21 cases (30.4%) of MAP, 25 cases (36.2%) of MSAP, and 23 cases (33.4%) of SAP; for group III, there were 21 cases (10.6%) of MAP, 53 cases (26.8%) of MSAP, and 124 (62.6%) cases of SAP. The ratios of MAP from group I, group II, and group III were 79.4%, 30.4%, and 10.6%, respectively, and there had the difference between the three groups which was statistically significant ($p < 0.01$). The results of clinical classification between the three groups are shown in Table 2.

3.2. Severity Scores of Different Types of AP between Three Groups. The average BISAP scores of AP patients from group I, group II, and group III were 2.1 ± 0.8 , 2.4 ± 1.3 , and 4.5 ± 1.2 , respectively; the average BISAP score of group III was significantly higher than that in group I and group II ($p < 0.01$); average Ranson score of three groups were 2.5 ± 0.3 , 2.8 ± 0.1 , and 5.9 ± 0.4 , respectively; average Ranson score of group III was significantly higher than that in group I and group II ($p < 0.01$); the average APACHE-II score of

three groups were 8.4 ± 1.6 , 15.2 ± 2.3 , and 20.12 ± 3.1 , respectively; AP patients from the group III had the significantly higher APACHE-II score than that from the other groups ($p < 0.01$); the average MCTSI scores of the three groups were 3.5 ± 0.8 , 6.4 ± 1.1 , and 9.2 ± 1.3 , respectively; similarly, AP patients from the group III had the significantly higher MCTSI score than that from the other groups, and the difference was statistically significant ($p < 0.01$). The results of severity scores of three groups are shown in Table 2; the comparison of clinical classification and severity score between three groups was shown in Figures 1 and 2.

3.3. Comparison of Early Local and Systemic Complications among the Three Groups. From the comparison of local complications in early stage, among these complications, APFC complicated in group I, group II, and group III was 17.1%, 65.2%, and 88.9%; ANC complicated in three groups were 12.5%, 11.6%, and 66.7%; PPC complicated in three groups were 4.0%, 4.3%, and 44.9%; WON complicated in three groups were 1.5%, 2.9%, and 39.4%; IPN complicated in three groups were 0.4%, 2.9%, and 32.8%, respectively. The trend chi-square test result indicated that the difference of incidence of APFC, WON, and IPN was statistically significant between three groups each other ($p < 0.01$); for ANC and PPC, incidences occurred in group III were significantly higher than in group I or group II ($p < 0.01$). The incidences of systemic complications in early stage of AP

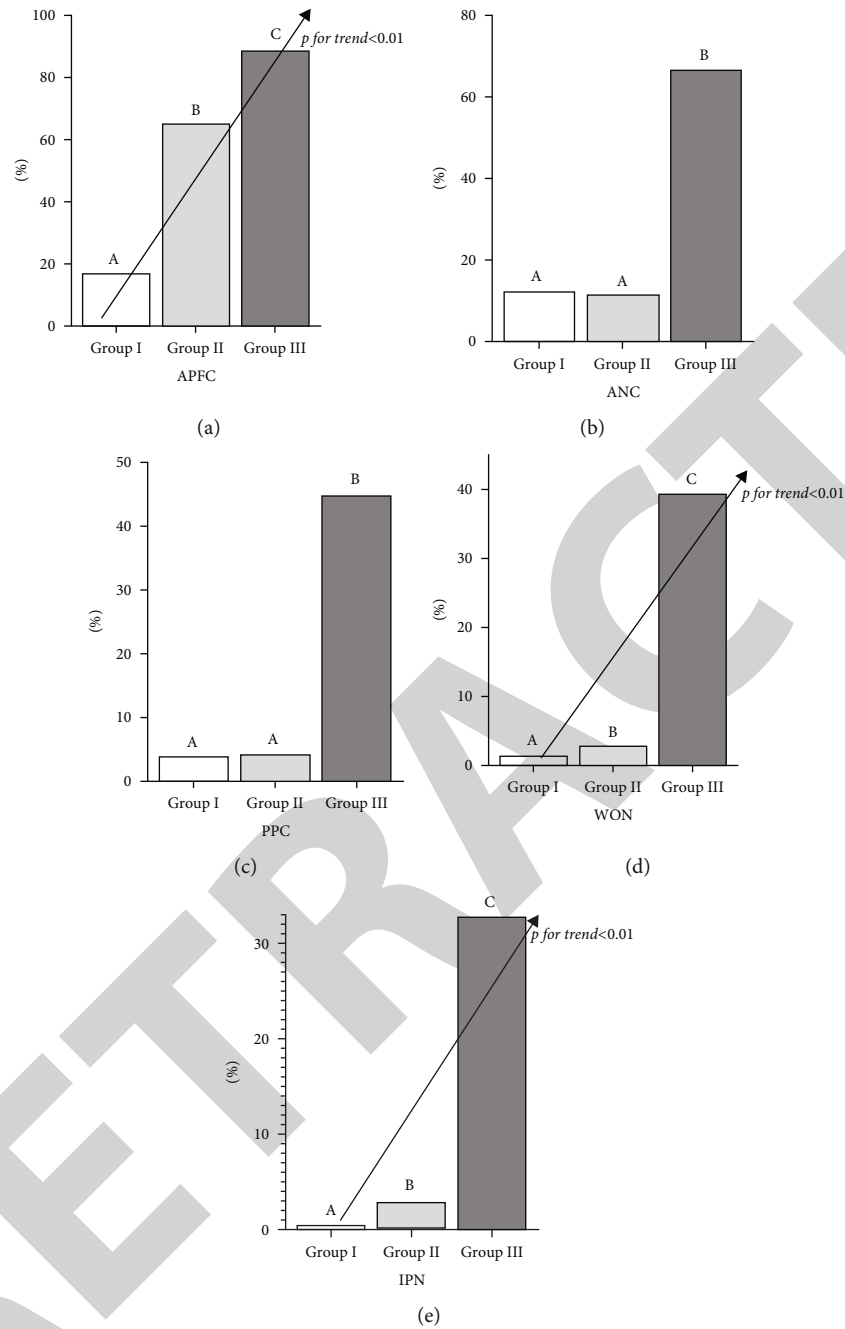


FIGURE 3: Comparison of local complications between three groups of AP patients in early stage. (a) The incidence rate of APFC in three groups; (b) the incidence rate of ANC in three groups; (c) the incidence rate of PPC in three groups; (d) the incidence rate of WON in three groups; (e) the incidence rate of IPN in three groups; there was no significant difference between groups with the same letters and hand significant difference between the groups with different letters. p for trend: Cuzick trend chi-square test (multiple groups).

from groups I, II, and III were (40.8% vs. 39.1% vs. 94.4%), organ failure (3.1% vs. 7.2% vs. 88.4%), sepsis (0.4% vs. 2.9% vs. 6.1%), intraperitoneal hypertension (1.3% vs. 50.7% vs. 85.4%), and mortality (0.4% vs. 1.4% vs. 4.0%); comparisons indicated incidences of early systemic complications and mortality were statistically significant between three groups each other ($p < 0.01$). The comparison of the results of early local and systemic complication mortality among the three groups is shown in Figures 3 and 4.

4. Discussion

Since updated through the Pancreatic Branch Committee of Chinese Medical Association from 2013, the guidance about AP diagnosis and treatment had been improved obviously, and the rationalization and standardization of the treatment for acute pancreatitis significantly reduced the mortality rate in China. However, as a common surgical acute abdomen, the mortality rate of MSAP and SAP is still about 5.9%

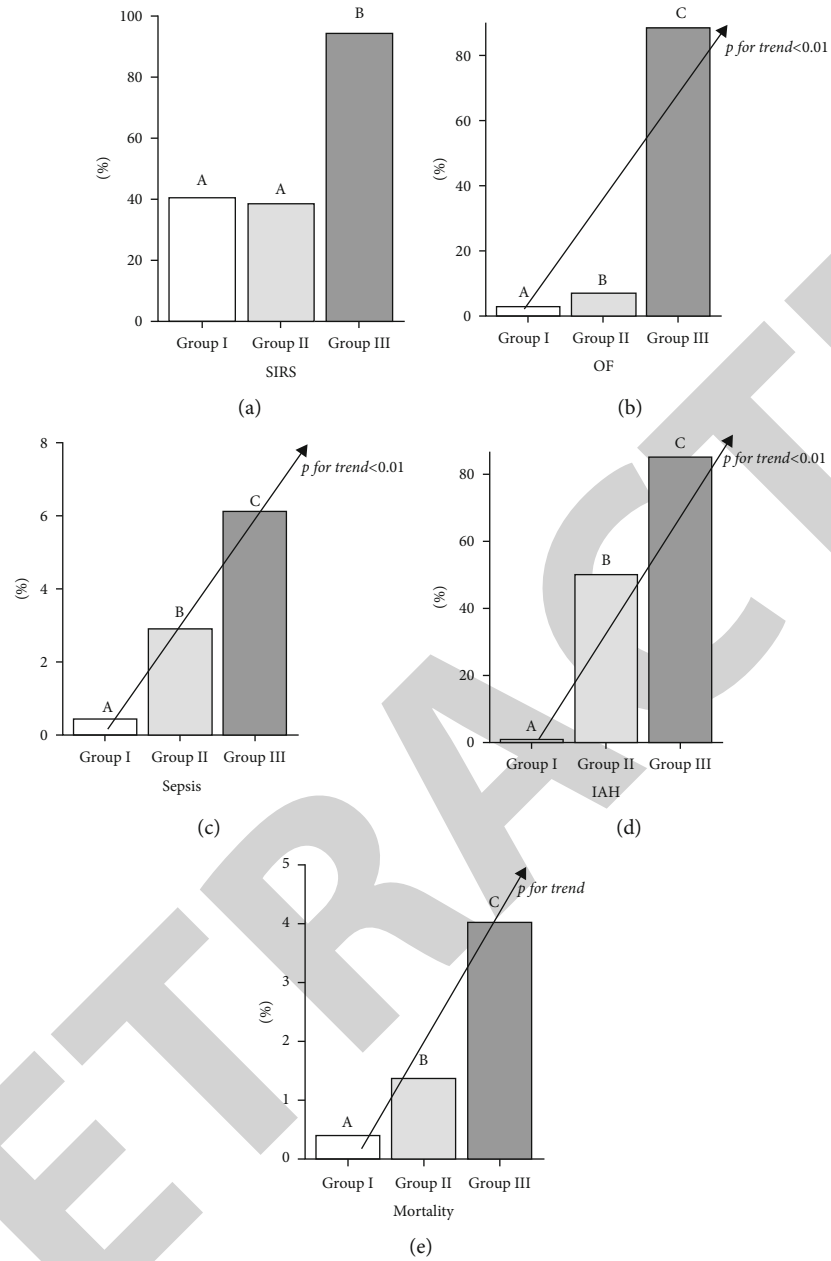


FIGURE 4: Comparison of systemic complications and mortality between three groups of AP patients in early stage. (a) The incidence rate of SIRS in three groups; (b) the incidence rate of OF in three groups; (c) the incidence rate of sepsis in three groups; (d) the incidence rate of IAH in three groups; (e) the mortality rate in three groups; there was no significant difference between groups with the same letters and hand significant difference between the groups with different letters. p for trend: Cuzick trend chi-square test (multiple groups).

[11]. The irrecoverable organ function and uncontrollable infection are the main factors which cause death [22–25]; meanwhile, local and systemic complications caused by acute pancreatitis prolong the hospitalization time and increase the medical expenses [26, 27]; especially for SAP, the incidence of local complications was as high as 59% [28] and has the highest mortality among all types of AP. Therefore, under this situation, clinical surgeons should pay more and more attentions of illness assessment in early stage, organ function protection, infections control, and complications prevention of patients with acute pancreatitis.

The pathogenesis of ABP is due to the obstruction of the common bile or pancreatic duct by the stones from biliary system, which leads to the increase of pancreatic duct pressure, thereby result in activation of pancreatic digestive enzymes [29, 30]. Due to most of the bile duct stones can be proved from the patient's history or hospital auxiliary examination such as B-ultrasound, CT, or MR, therefore, ABP has the definite etiology and early surgery or endoscopic ERCP removal of stones from the bile-pancreatic duct can achieve the purpose of treatment [31–33], and the endocrine and exocrine functions of pancreas were not

significantly affected in most mild or moderate AP patients after the etiology was removed [34]. From the research of complications and prognosis of severe BAP, the result of Barauskas et al. [35] indicated that although there was no significant difference about severity scoring between acute biliary AP and alcoholic AP, however, the incidence of complications such as intra-abdominal hypertension (IAH), abdominal compartment syndrome (ACS), and pancreatic necrosis was significantly lower in acute biliary AP than in alcoholic AP, and the mortality was significantly lower than that in alcoholic AP.

Alcoholic AP defined as damage of pancreatic cytotoxic action from the alcohol and its metabolites from the long-term large-scale alcohol intake [36, 37], due to the long-term and high alcohol consumption, most of this kind of patients complicate with chronic pancreatitis or pancreatic fibrosis [38, 39] and even involve other organs such as alcoholic liver damage [40] or chronic renal damage [41]. Therefore, once acute alcoholic pancreatitis occurs, local or systemic complications are more likely to arise from other organs damage aggravation and even lead to multiple organ failure. Several clinical studies [42, 43] have shown that compared with ABP, alcoholic AP, alcoholic AP had higher incidence of complications and poor prognosis. From this study, the results indicated that incidences of local complications in early stage such as APFC, WON, and IPN were significantly higher in alcoholic AP than those in ABP; similarly, systemic incidences of complications of MODS, SIRS, and sepsis were higher in alcoholic AP, and the difference was statistically significant. It was proved the proposition that compared with ABP, alcoholic pancreatitis had the worse illness and poor prognosis.

Hypertriglyceridemic pancreatitis is a kind of acute pancreatitis caused by the abnormal high serum triglyceride; due to the disorder of lipid metabolism, it is often combined with other endocrine metabolic disorders [44]. Hitherto, the pathogenesis of hypertriglyceridemic pancreatitis is not very unclear; however, it is clear that high concentration of TG in serum can activate pancreatic lipase and produce a large amount of free fatty acids which may damage the capillaries and cell membrane of the pancreas; this process may release cytokines and inflammatory mediators, which can lead to pancreatitis [3]. With its acute onset, severe illness, high incidence of complications, and poor prognosis, hypertriglyceridemic pancreatitis is often complicated with systemic inflammatory response syndrome (SIRS) and even multiple organ dysfunction syndrome (MODS) in the early stage [45–47]. In this study, hypertriglyceridemic AP accounted for the highest proportion in SAP, and BISAP, Ranson, APACHE-II, and MCTSI scores were significantly higher in hypertriglyceridemic AP than the other two groups, which indicated that hypertriglyceridemic AP was serious and complex in clinical practice. In terms of complications, both of the early local and systemic complications of hypertriglyceridemic AP were significantly higher than those of acute biliary AP and alcoholic AP, and the mortality rate was significantly higher than the other two groups; the difference was statistically significant. Several clinical researches [3, 48–50] indicated that from the comparison

of severity and complications between different types of AP, hypertriglyceridemic AP had higher rate of complication incidences and mortality than other types of AP; this was highly in coincidence with the results of our study, and it was worth noting that with the increasing number of hypertriglyceridemia patients, the incidence of hypertriglyceridemic AP is rising, and age of onset is becoming younger and younger increasingly [51]. In some areas of China, the incidence rate of hypertriglyceridemic AP even exceeds alcoholic AP and had become the second type of AP next to the ABP [52].

5. Conclusions

In conclusion, the difference in etiology had obvious influence on the complications and prognosis of AP patients. The incidence rate of hypertriglyceridemic AP is increasing and becoming younger and its local and systemic complications and mortality are significantly higher than those of other types of acute pancreatitis. The presented study still have room for improvement, the risk factors for different type of AP need to be further investigate, and proper advise for the invention and treatment of AP can be put up with. Therefore, a comprehensive investigation of the pathogenesis and management of AP is needed. Meanwhile, the high-fat diet control, aerobic exercise recommendation, and early intervention of hyperlipidemia have important implication for preventing hypertriglyceridemic AP.

Data Availability

The simulation experiment data used to support the findings of this study are available from the corresponding author upon request.

Ethical Approval

This study is a retrospective research, and there is no change in the treatment plan of the patient during the research process, which will not cause harm to the patient, and the study has been approved by the ethics committee.

Conflicts of Interest

The authors have no personal, financial, or other conflicts to disclose.

Authors' Contributions

Hongsheng Wu and Keqiang Ma contributed to design of this study. Tiansheng Cao conceived and designed the study and revised the manuscript critically. Biling Liao, Tengfei Ji, and Shengmin Zhang contributed to the collection of data of this research. All authors read and approved the final manuscript.

Acknowledgments

We thank the Department of Medical Records Management of Affiliated Huadu Hospital, Southern Medical University,

for providing case information for this research and assistant Lei Yu for the statistics guidance. The funds for research design, data collection, and data analysis in this study are from the internal medicine research fund of the Affiliated Huadu Hospital, Southern Medical University (no. 2020A01).

References

- [1] S. E. Roberts, S. Morrison-Rees, A. John, J. G. Williams, T. H. Brown, and D. G. Samuel, "The incidence and aetiology of acute pancreatitis across Europe," *Pancreatology*, vol. 17, no. 2, pp. 155–165, 2017.
- [2] D. Yadav and A. B. Lowenfels, "Trends in the epidemiology of the first attack of acute pancreatitis: a systematic review," *Pancreas*, vol. 33, no. 4, pp. 323–330, 2006.
- [3] P. Valdivielso, A. Ramírez-Bueno, and N. Ewald, "Current knowledge of hypertriglyceridemic pancreatitis," *European Journal of Internal Medicine*, vol. 25, no. 8, pp. 689–694, 2014.
- [4] P. Rawla, T. Sunkara, K. C. Thandra, and V. Gaduputi, "Hypertriglyceridemia-induced pancreatitis: updated review of current treatment and preventive strategies," *Clinical Journal of Gastroenterology*, vol. 11, no. 6, pp. 441–448, 2018.
- [5] Y. Zheng, Z. Zhou, H. Li et al., "A multicenter study on etiology of acute pancreatitis in Beijing during 5 years," *Pancreas*, vol. 44, no. 3, pp. 409–414, 2015.
- [6] H. Xu, Y. Li, J. Yan et al., "Severity analysis of acute pancreatitis based on etiology," *Zhonghua Yi Xue Za Zhi*, vol. 94, no. 41, pp. 3220–3223, 2014.
- [7] Y. Zhu, X. Pan, H. Zeng et al., "A study on the etiology, severity, and mortality of 3260 patients with acute pancreatitis according to the revised Atlanta classification in Jiangxi, China over an 8-year period," *Pancreas*, vol. 46, no. 4, pp. 504–509, 2017.
- [8] Z. M. Hazem, "Acute biliary pancreatitis: diagnosis and treatment," *Saudi Journal of Gastroenterology*, vol. 15, no. 3, pp. 147–155, 2009.
- [9] P. Chowdhury and P. Gupta, "Pathophysiology of alcoholic pancreatitis: an overview," *World Journal of Gastroenterology: WJG*, vol. 12, no. 46, pp. 7421–7427, 2006.
- [10] W. Tsuang, U. Navaneethan, L. Ruiz, J. B. Palascak, and A. Gelrud, "Hypertriglyceridemic pancreatitis: presentation and management," *Official Journal of the American College of Gastroenterology*, vol. 104, no. 4, pp. 984–991, 2009.
- [11] X. Bai, M. Jin, H. Zhang, B. Lu, H. Yang, and J. Qian, "Evaluation of Chinese updated guideline for acute pancreatitis on management of moderately severe and severe acute pancreatitis," *Pancreatology*, vol. 20, no. 8, pp. 1582–1586, 2020.
- [12] M. Gompertz, L. Fernandez, I. Lara, J. P. Miranda, C. Mancilla, and Z. Berger, "Bedside index for severity in acute pancreatitis (bisap) score as predictor of clinical outcome in acute pancreatitis: retrospective review of 128 patients," *Revista Médica de Chile*, vol. 140, no. 8, pp. 977–983, 2012.
- [13] Z. Jin, H. Liu, X. Wang et al., "Predictive values of apache-o, apache-ii, ranson and balthazar ct scoring system on prognosis of acute pancreatitis," *Chinese Journal of Hepatobiliary Surgery*, pp. 680–683, 2012.
- [14] P. Aphinives, C. Karunasumetta, V. Bhudhisawasdi, and O.-t. Saesaew, "Acute pancreatitis: assessment severity with ranson score and ct evaluation," *Journal of the Medical Association of Thailand*, vol. 94, p. 437, 2011.
- [15] A. Harshit Kumar and M. S. Griwan, "A comparison of apache ii, bisap, ranson's score and modified ctsi in predicting the severity of acute pancreatitis based on the 2012 revised Atlanta classification," *Gastroenterology Report*, vol. 6, no. 2, pp. 127–131, 2018.
- [16] M. Bezmarević, S. M. van Dijk, R. P. Voermans, H. C. van Santvoort, M. G. Besselink, and Dutch Pancreatitis Study Group, "Management of (peri) pancreatic collections in acute pancreatitis," *Visceral Medicine*, vol. 35, no. 2, pp. 91–96, 2019.
- [17] B. Mallick, N. Dhaka, P. Gupta et al., "An audit of percutaneous drainage for acute necrotic collections and walled off necrosis in patients with acute pancreatitis," *Pancreatology*, vol. 18, no. 7, pp. 727–733, 2018.
- [18] W. Udeshika, H. Herath, S. Dassanayake, S. Pahalagamage, and A. Kulatunga, "A case report of giant pancreatic pseudocyst following acute pancreatitis: experience with endoscopic internal drainage," *BMC Research Notes*, vol. 11, no. 1, pp. 1–9, 2018.
- [19] S. S. Rana, "An overview of walled-off pancreatic necrosis for clinicians," *Expert Review of Gastroenterology & Hepatology*, vol. 13, no. 4, pp. 331–343, 2019.
- [20] Z. Zheng, J. Lu, F. Cao et al., "'One-step' approach versus 'step-up' approach minimally invasive treatment for infected pancreatic necrosis: a study protocol for a single-center, prospective, randomized controlled trial," *BMC Gastroenterology*, vol. 22, no. 1, pp. 1–11, 2022.
- [21] R. K. Chakraborty and B. Burns, *Systemic Inflammatory Response Syndrome*, StatPearls Publishing, 2019.
- [22] Q. Qiu, Y.-j. Nian, Y. Guo et al., "Development and validation of three machine-learning models for predicting multiple organ failure in moderately severe and severe acute pancreatitis," *BMC Gastroenterology*, vol. 19, no. 1, pp. 1–9, 2019.
- [23] M. G. Raraty, S. Connor, D. N. Criddle, R. Sutton, and J. P. Neoptolemos, "Acute pancreatitis and organ failure: pathophysiology, natural history, and management strategies," *Current Gastroenterology Reports*, vol. 6, no. 2, pp. 99–103, 2004.
- [24] H. Tian, L. Chen, X. Wu et al., "Infectious complications in severe acute pancreatitis: pathogens, drug resistance, and status of nosocomial infection in a university-affiliated teaching hospital," *Digestive Diseases and Sciences*, vol. 65, no. 7, pp. 2079–2088, 2020.
- [25] M. Werge, S. Novovic, P. N. Schmidt, and L. L. Gluud, "Infection increases mortality in necrotizing pancreatitis: a systematic review and meta-analysis," *Pancreatology*, vol. 16, no. 5, pp. 698–707, 2016.
- [26] T. J. Howard, E. A. Wiebke, G. Mogavero et al., "Classification and treatment of local septic complications in acute pancreatitis," *The American Journal of Surgery*, vol. 170, no. 1, pp. 44–50, 1995.
- [27] A. Lancaster and M. Zwijacz, "Acute pancreatitis and fluid-filled collections: etiology and endoscopic management," *Gastroenterology Nursing*, vol. 42, no. 5, pp. 417–419, 2019.
- [28] M.-C. Pintado, M. Trascasa, C. Arenillas et al., "New Atlanta classification of acute pancreatitis in intensive care unit: complications and prognosis," *European Journal of Internal Medicine*, vol. 30, pp. 82–87, 2016.
- [29] C.-L. Liu, C.-M. Lo, and S.-T. Fan, "Acute biliary pancreatitis: diagnosis and management," *World Journal of Surgery*, vol. 21, no. 2, pp. 149–154, 1997.
- [30] G.-J. Wang, C.-F. Gao, D. Wei, C. Wang, and S.-Q. Ding, "Acute pancreatitis: etiology and common pathogenesis,"

Retraction

Retracted: Potential Benefits of Music Therapy on Stroke Rehabilitation

Oxidative Medicine and Cellular Longevity

Received 1 August 2023; Accepted 1 August 2023; Published 2 August 2023

Copyright © 2023 Oxidative Medicine and Cellular Longevity. This is an open access article distributed under the Creative Commons Attribution License, which permits unrestricted use, distribution, and reproduction in any medium, provided the original work is properly cited.

This article has been retracted by Hindawi following an investigation undertaken by the publisher [1]. This investigation has uncovered evidence of one or more of the following indicators of systematic manipulation of the publication process:

- (1) Discrepancies in scope
- (2) Discrepancies in the description of the research reported
- (3) Discrepancies between the availability of data and the research described
- (4) Inappropriate citations
- (5) Incoherent, meaningless and/or irrelevant content included in the article
- (6) Peer-review manipulation

The presence of these indicators undermines our confidence in the integrity of the article's content and we cannot, therefore, vouch for its reliability. Please note that this notice is intended solely to alert readers that the content of this article is unreliable. We have not investigated whether authors were aware of or involved in the systematic manipulation of the publication process.

Wiley and Hindawi regrets that the usual quality checks did not identify these issues before publication and have since put additional measures in place to safeguard research integrity.

We wish to credit our own Research Integrity and Research Publishing teams and anonymous and named external researchers and research integrity experts for contributing to this investigation.

The corresponding author, as the representative of all authors, has been given the opportunity to register their agreement or disagreement to this retraction. We have kept a record of any response received.

References

- [1] C. Xu, Z. He, Z. Shen, and F. Huang, "Potential Benefits of Music Therapy on Stroke Rehabilitation," *Oxidative Medicine and Cellular Longevity*, vol. 2022, Article ID 9386095, 11 pages, 2022.

Review Article

Potential Benefits of Music Therapy on Stroke Rehabilitation

Chengyan Xu,¹ Zixia He,² Zhipeng Shen ¹ and Fei Huang ³

¹Department of Neurosurgery, The Children's Hospital Zhejiang University School of Medicine, National Clinical Research Center for Child Health, Hangzhou, China

²Department of Outpatient, The Children's Hospital Zhejiang University School of Medicine, National Clinical Research Center for Child Health, Hangzhou, China

³Department of Science and Education, Hangzhou Women's Hospital, Hangzhou Maternity and Child Health Care Hospital, Hangzhou, China

Correspondence should be addressed to Zhipeng Shen; shenzp@zju.edu.cn and Fei Huang; 601506529@qq.com

Received 26 April 2022; Revised 15 May 2022; Accepted 24 May 2022; Published 15 June 2022

Academic Editor: Shao Liang

Copyright © 2022 Chengyan Xu et al. This is an open access article distributed under the Creative Commons Attribution License, which permits unrestricted use, distribution, and reproduction in any medium, provided the original work is properly cited.

Stroke is associated with a high rate of disability and mortality, and survivors are usually accompanied with dysphagia, aphasia, motor dysfunction, cognitive impairment, depression, and other complications. In the past decades, many studies have been conducted to reveal the pathogenesis and pathological mechanisms of stroke. Furthermore, treatment methods have been developed that contribute to the elevated survival rate of stroke patients. Early rehabilitation poststroke is starting to be recognized as important and has been receiving increasing attention in order to further improve the quality of life of the patients. As an emerging method of poststroke rehabilitation, music therapy can help attenuate dysphagia and aphasia, improve cognition and motor function, alleviate negative moods, and accelerate neurological recovery in stroke patients. This review helps summarize the recent progress that has been made using music therapy in stroke rehabilitation and is aimed at providing clinical evidence for the treatment of stroke patients.

1. Introduction

Stroke is a severe cerebrovascular disease that is associated with high morbidity, mortality, and disability. It seriously affects the daily lives of the patients and imposes a heavy burden on families and society. There are approximately 16 million people that suffer from stroke per year worldwide, of whom 5.7 million die and about 5 million become disabled [1]. The incidence of stroke in China is approximately 1000/100,000 per year, and the mortality rate is approximately 150/100,000 per year [2, 3]. Globally, China is a country that has the highest lifetime risk of stroke, as well as the heaviest disease burden. Stroke can cause dysphagia, aphasia, motor dysfunction, cognitive impairment, mood disorders, and other complications [4–7]. The neurological damage that is caused by stroke often cannot be completely recovered. With early intervention and rehabilitation, impaired neurological function can be restored to a certain extent at dif-

ferent stages of stroke, which mainly depends on the plasticity and functional reorganization of the brain [8–10]. Therefore, in order to conduct reasonable rehabilitation treatment for stroke patients, it is important to have the maximum curative effect, reduce the treatment cost, and alleviate the family and social burden of diseases.

Music therapy is a systematic treatment method that utilizes music elements as an intervention to improve patients' neurological function and mood status [11, 12]. Many studies have applied music therapy during rehabilitation of stroke, which has led to the achievement of a good effect [13, 14]. Due to its safety, it is low cost, convenient, simple, and easy to implement. It has good efficacy and is easily accepted by patients. Music therapy has started to receive more attention and application in stroke rehabilitation. This review summarizes and provides direction for the role of music therapy in the rehabilitation of stroke patients.

2. Music Therapy and Beneficial Effect on Neurological Disease

Music therapy mainly strengthens patients' perception of sound through rhythm and melody of music and improves patients' language understanding ability through lyrics and singing, as well as speech frequency and rhythm [15, 16]. The anatomical basis of music therapy is mainly the different processing of music by the brain hemispheres, with the left brain responsible for understanding lyrics and distinguishing rhythms, while the right brain deals with melody [17, 18]. Music therapy is comprised of two different types, the active type and the passive type. Active music therapy refers to when patients directly participate in singing, playing instruments, or moving with music during therapy. Passive music therapy, also known as sensory music therapy, allows patients to listen to familiar music. Passively listening to music has no special requirements, but it can create an environment that allows people to feel comfortable and safe [19–21]. For music selection, music with a strong sense of rhythm is chosen during active music therapy, while music is selected mainly based on personal preference during passive music therapy. Music selection and treatment plan design tend to be diverse, according to the degree of disease, the patient's age, gender, and cultural background [22–24].

Music therapy often exerts a beneficial effect on many neurological diseases, including neuropsychiatric disorders, chronic neurodegenerative diseases, epilepsy, and acute brain injury [25–27]. Many random clinical trials have been carried out and have provided strong evidence for the effectiveness of music therapy during disease remission. A clinical trial including 60 patients found that integration of music therapy with family recollection can help regulate physiological parameters. Hence, it is recommended to use this cost-effective therapy as a supplementary treatment for patients with traumatic brain injury [28]. Another study in which traumatic brain injury patients receive three months of neurological music therapy intervention has shown that there are enhanced executive functions and fine-grained neuroanatomical changes in the prefrontal areas [29]. Rhythmic auditory stimulation, as an important style of music therapy, can help improve the effect of gait training by reshaping the sensorimotor rhythms and strengthens frontal-temporal connectivity. Thus, this activity is able to sustain gait improvement in Parkinson's disease patients [30]. Furthermore, music therapy exerts a positive effect on the cognitive function of the patients with Alzheimer's disease and regulates factors that are related to sleep, mood, and quality of life [31, 32]. One of the most well-studied areas of music therapy is its application in neuropsychiatric diseases. Music therapy can help alleviate various types of anxiety, including preoperative anxiety [33, 34] and serious or long illness-induced anxiety [35, 36]. However, opposite results have demonstrated that music does not reduce anxiety among women receiving radiation therapy for cancer [37], which may be due to differences in the music therapy interval and initiation time. However, additional studies are required to discover the best path to decrease anxiety through music therapy. Music has been shown to relieve depressive symptoms across a number of clinical studies [38,

39]. A randomized controlled trial with 18 major depressive disorder patients who listen to 10 Hz beat-embedded music therapy in combination with classical therapy showed no significant differences of depression scale, quality of life, and medication adherence compared to the control group [40]. Lu et al. revealed that psychiatric symptoms and depression status of schizophrenia patients are improved after using group music therapy, indicating that music therapy may be economical and an easily implemented method that improves mood and mental state [41]. It is important to note that during music therapy, the choice of music and the degree of the patients' illness all have an effect on treatment.

3. The Role of Music Therapy in the Rehabilitation Poststroke

3.1. Music Therapy Improves Dysphagia Poststroke. Dysphagia, a common complication of stroke, is mainly characterized by dysphonia, dysarthria, abnormal spontaneous cough, salivation, and choking after swallowing and is particularly common among the elderly [42, 43]. About 28%–67% of stroke patients tend to develop dysphagia [44], among which the incidence of dysphagia after stroke is 41% during the acute stage and 16% in the chronic stage [45]. Dysphagia can cause serious complications, including aspiration pneumonia, electrolyte disorders, and malnutrition. Additionally, stroke patients with dysphagia tend to develop psychological problems (i.e., fear of eating, anxiety, and depression), which seriously affect the patients' quality of life. Early rehabilitation plays an important role during the recovery of patients with dysphagia. Previous studies have discovered that swallowing training, acupuncture, electrical stimulation, transcranial magnetic stimulation, and other means can help stroke patients improve dysphagia and swallowing dysfunction [46–48].

In recent years, a large number of clinical studies have suggested that music therapy can effectively improve patients' dysphagia poststroke. A clinical study enrolled six stroke patients with mixed dysarthria. All patients underwent individual music therapy sessions. The duration of each session was 30 minutes, and 12 sessions in total were conducted. The maximum phonation time, fundamental frequency, average intensity, and sequential motion rates were increased after music therapy, indicating that music therapy can improve speech motor coordination, including respiration, phonation, articulation, resonance, and prosody [49]. Another study investigated the effect of vocal exercises and singing on intelligibility and speech naturalness among patients with acquired dysarthria, following traumatic brain injury or stroke. Each patient implemented 24 individual music therapy sessions within eight weeks. The content of music training included therapeutic singing using familiar songs, oral motor respiratory exercises, rhythmic and melodic articulation exercises, rhythmic speech cuing, and vocal intonation therapy. Functional speech intelligibility and speech naturalness were significantly improved after completing treatment, which demonstrates that timely and continuous vocal exercises and singing may help accelerate the recovery of speech after stroke [50]. A music-enhanced swallowing protocol was developed in a preliminary study conducted by Kim, among which eight stroke patients participated. After six sessions of

therapy, oral motor control, laryngeal elevation, breathing, and swallowing functions of the patients were enhanced by improving oral motor control, which suggests the effectiveness of music therapy in stroke rehabilitation [51]. The number of participants in most current studies is small, and the data are from a single center. Multicenter large-scale clinical trials are needed in the future to further substantiate the effect of music therapy on the improvement of dysphagia after stroke.

3.2. Music Therapy Promotes Recovery of Motor Function Poststroke. Motor dysfunction is one of the most common complications following stroke, which manifests as numbness and weakness of the limbs and even paralysis or spasms [13, 52]. Motor dysfunction can seriously affect the quality of life and social participation of stroke patients. Rehabilitation of motor function after stroke is a progressive and dynamic process and mainly includes exercise training, drug therapy, and psychological counseling. A variety of innovative neurorehabilitation strategies are emerging tools that will help improve motor function after stroke [53]. Music therapy, as a novel method, provides a new way for the motor function rehabilitation of stroke patients. By listening to music or singing songs, it can help promote neural plasticity, regulate neural networks and signal transduction, and achieve the purpose of improving patients' motor function [54, 55].

Exercise training is an important rehabilitation measure that is utilized for the treatment of stroke patients with motor dysfunction. During treatment, music with a strong sense of rhythm is generally helpful for rehabilitation of motor function [56]. The motor system is sensitive to auditory stimulation, and music rhythms can excite motor neurons in order to cause the muscles to move in a natural and ideal way, improving the rhythm of action and quality of action completion. It also enhances the effect of exercise therapy in order to promote the recovery of the patients' limb motor function. Playing musical instruments or pulling an arm trainer with rhythmic music can help increase the frequency and fluency of finger movements, as well as upper extremity function [57–59], which can cause excitability changes in the motor cortex. In addition, studies have validated that adding sound feedback during exercise training can increase auditory input of the patients, which can help improve excitation of the motor cortex, promote brain function remodeling, and achieve auditory motor function integration [60]. Moreover, functional magnetic resonance imaging (MRI) suggests that one of the effects of music-supported therapy is task-dependent coupling of auditory and motor cortical areas [61].

As limb motor dysfunction in stroke patients can lead to gait impairment, many scholars focus on the impact of music therapy on gait training in stroke patients [62]. Patients that receive music motor feedback training have experienced a significant improvement in stride length and gait speed compared to routine gait training without music. Even after removing the external pacer, the gait of the patients may be improved to some extent through memory of music and rhythm [62]. In addition, studies have highlighted that patients that receive rhythmic auditory stimulation have significantly improved step velocity, stride frequency, symmetry and length, and balance function and trunk control, regardless of the type of rhythmic

stimuli [63–66]. Previous studies have also discovered that rhythmic auditory stimulation can improve the gait of patients with acute, subacute, or chronic stroke [67, 68]. However, choosing the most appropriate music type, which involves considering rhythm, strength, and frequency, for stroke patients at different stages, remains to be further studied. The potential mechanism underlying music therapy-induced benefits have been extensively studied, and the results demonstrate that music therapy can enhance the effect of gait training by improving psychology and cognition, regulating neurotransmitter delivery, and enhancing the plasticity of the nervous system, as well as other mechanisms [69, 70].

The complex repair mechanism that is involved in limb dysfunction has not been clearly defined. Therefore, it is necessary to fully assess the degree and type of limb dysfunction among different stroke patients and explore its possible pathological mechanisms and risk factors. The period, course of treatment, intensity, and frequency of music therapy, as well as the combined rehabilitation therapy plan, are significantly different in current studies. Furthermore, various music therapy plans, evaluation index, and measurement scales are utilized in studies that are conducted across different centers. Therefore, standardized multicenter trials need to be carried out in the future to improve the clinical efficacy of music therapy in motor recovery after stroke. Additionally, the treatment plan should be rationally optimized to meet the individual needs of each patient.

3.3. Music Therapy Attenuates Aphasia Poststroke. Poststroke aphasia refers to a focal brain injury caused by stroke, leading to the destruction of cortical and subcortical structural networks within the dominant hemisphere of language. Thereby, it causes impaired or permanent loss of the production and understanding of language symbols, as well as language dysfunction during listening, speaking, reading, or writing [71, 72]. Aphasia is one of the important manifestations of neurological impairment after stroke. Aphasia has a high incidence during stroke and seriously affects the communication ability of the patients, aggravates neurological dysfunction, and brings great mental and economic burden to patients, families, and society. Medication, speech and language therapy, behavioral therapy, noninvasive brain stimulation, and other therapeutic strategies have been developed in order to decrease the incidence and alleviate the degree of aphasia poststroke [73–76].

Neuroimaging studies have discovered that there is an overlap between the brain regions that are activated during speech and singing, which suggests that singing and speech share some common neural pathways [77–79]. Music therapy is introduced during treatment of aphasia after stroke through carefully designed music experience, which stimulates the damaged brain language function area, regulates neuroplasticity changes within the language network, and promotes the recovery of speech function [80, 81]. Melodic intonation therapy (MIT) is the most popular and effective music therapy that is applied to aphasia poststroke (Table 1). It makes use of the patients' unimpaired singing ability to sing words and phrases during daily life with musical melody in order to improve patients' oral expression ability. Zhang et al. discovered that music therapy-based MIT can have a positive impact on the

TABLE 1: The application of melodic intonation therapy (MIT) in aphasia poststroke.

Participants	Intervention of MIT	Evaluation	Findings	References
The intervention group ($n = 20$; 16 males, 4 females) and the control group ($n = 20$; 15 males, 5 females)	Intervention group receives MIT treatment for 30 min/day, five times a week for 8 weeks	Boston diagnostic aphasia examination, Hamilton anxiety scale, and Hamilton depression scale	MIT has a better effect in fluency, spontaneous naming, object naming, reaction naming, and sentence completing, with a time accumulation effect	[82]
A 63-year-old man, 10 years poststroke, presented with a mild to moderate nonfluent aphasia	Receives MIT treatment 50 min twice weekly and attends a 4 hr socialization program once per week	Apraxia battery for adults, and Boston diagnostic aphasia evaluation	Integration of MIT by adding musical elements improves speech and expressive language skills, combined with a group socialization program	[104]
20 stroke patients with poststroke nonfluent aphasia	Receives MIT treatment for 12 sessions over six weeks	Communicative activity log questionnaire, Boston diagnostic aphasia examination	MIT may have a beneficial effect on the communication skills of stroke patients with nonfluent aphasia	[84]
17 patients with chronic (>1 year) poststroke aphasia. 10 in the MIT group and 7 in the control group	Receives 6 weeks intensive MIT (5 h/week)	Aachen aphasia test, Amsterdam-Nijmegen everyday language test, and Sabadel story retell task	MIT shows limited and temporary effect, suggesting that MIT exerts better effect for chronic aphasia in earlier stages poststroke	[105]
Six patients with severe nonfluent aphasia poststroke	Receives melodic-rhythmic therapy (a modified MIT) treatment 4 days a week for 16 weeks, with sessions of 30-40 min	Aachen aphasia test	MIT significantly improves the ability of spontaneous speech	[85]
Three participants with chronic poststroke Broca's aphasia	Receives MIT treatment in hourly sessions, 3 days per week for 6 weeks	Percent correct information units in connected speech, number of correct syllables in the trained and nontrained sentences, and visual analog mood scales	Combination of rhythm and pitch induces the strongest generalization effect to nontrained stimuli and connected speech. No significant effect in motor-speech agility or mood	[106]
Two patients with nonfluent aphasia poststroke	rTMS therapy (consisted of 3 treatment sessions) followed by 40 min of MIT	Western aphasia battery, fMRI	One patient has improvement in verbal fluency and repetition of phrases, while the other patient has no significant improvement. Neural activity changes are observed in the left Broca's area and right Broca's homolog	[107]
27 participants with subacute severe nonfluent aphasia poststroke	Receives MIT treatment in hourly sessions, 5 h per week for 6 weeks	Aachen aphasia test, semantic association task	MIT treatment has an improvement in verbal communication and language repetition	[108]
A patient with severe nonfluent aphasia poststroke	Receives intensive adapted MIT, attending five, 1.5-hour treatment sessions per week for 16 weeks	fMRI, DTI, and speech and language tasks	MIT induces functional and structural changes in a right hemisphere fronto-temporal network	[109]
30 acute stroke patients with nonfluent aphasia, 14 in the control group, and 16 in the treatment group	Receives a 10 to 15 min MIT session	Western aphasia battery	Significant immediate improvements in speech output after one session of MMIT training	[110]

TABLE 1: Continued.

Participants	Intervention of MIT	Evaluation	Findings	References
Six patients with nonfluent aphasia at least 1 year postonset of first ischemic stroke	Treatment sessions are administered one per day for 3 consecutive days. The stimulation period of tDCS lasts for 20 min and combines with 20 min MIT	Boston diagnostic aphasia examination, verbal fluency tests	Transcranial direct current stimulation plus MIT contributes to significant improvements in fluency of speech, by enhancing activity in a right hemisphere sensorimotor network for articulation	[111]
Six patients with nonfluent aphasia at least 1 year postonset of first left hemisphere stroke	Receives an intense fashion with 75–80 daily therapy sessions	MRI and DTI; behavioral tests include number of correct information units/min produced during spontaneous speech, picture descriptions, and descriptions of common procedures	MTI increases the number of arcuate fasciculus fibers and arcuate fasciculus volume and improves the speech outcome	[112]

language function of stroke patients that suffer from aphasia in the Chinese population [82], and similar effects are observed in the Greek [83], Spanish [84], Italians [85], and other populations, which indicates that MIT therapy has a good therapeutic effect in the population across different regions. A systematic review, including six clinical trials involving 115 patients, was aimed at evaluating the effectiveness of music therapy in the recovery of language function in poststroke aphasia. The data reveal that MIT can improve functional communication, repetition, and naming of patients but does not improve comprehension [80]. Another recently published systematic review retrieves MIT-related literature, including 39 randomized controlled trials that focus on MIT intervention among patients with aphasia in the stroke recovery period. The results demonstrate the beneficial effect of MIT on language rehabilitation. However, further MRI studies have been recommended that can help determine the clinical evidence and intervention targets of MIT and help provide clear neural circuit prompts and predict models used for MIT intervention [86]. Lim et al. demonstrate that neurologic music therapy and speech language therapy are both effective treatments for poststroke aphasic patients during the chronic stage, and the former is effective in the subacute stage of stroke [87]. Therefore, it is important to choose the appropriate music therapy strategy for stroke patients at different stages, which is worthy of further study. Moreover, due to the variety of music intervention modes for aphasia, future studies need to further standardize intervention methods and clarify the measurement indicators (i.e., spontaneous speech, fluency, repetition, and naming) in order to clarify the effect of music therapy and develop a more appropriate treatment plan.

3.4. Music Therapy Enhances Cognitive Recovery Poststroke. Poststroke cognitive impairment refers to a series of cognitive damages with different symptoms and severity after stroke. Due to the influence of multiple factors, including etiology, type, location, and complications of stroke, the clinical manifestations of cognitive dysfunction after stroke are multiple and are associated with memory disorders, learning ability disorders, attention disorders, sensory and perceptual disorders, personality changes, and behavioral abnormalities [4, 88–91]. The manifestations of poststroke cognitive impairment are not single but actually often overlap and interact with each other in complex ways. Cognitive rehabilitation is the systematic use of medical and rehabilitation therapy to improve the daily living activities and delay further aggravation of cognitive impairment, daily living ability, and limb function of stroke. On the basis of evaluation of the patients' brain injury and cognitive function, the therapeutic activity system is formulated with a goal of improving cognitive function. Hence, the behavior pattern acquired before is reconstructed or a new correct cognitive pattern is established in order to compensate for changes in the brain and body. Current clinical treatment for poststroke cognitive impairment includes drug therapy, computer-assisted cognitive rehabilitation, physical therapy, noninvasive brain stimulation, and traditional Chinese medicine [92–95].

Recently, studies have shown that music therapy, regardless of playing a musical instrument or listening to music or

singing, can improve cognitive function of stroke patients [96, 97]. Early music intervention for patients with stroke is beneficial for long-term plasticity changes of sensory and perceptual processes and promotes the recovery of cognitive function. Rosemann et al. have proposed that deficits in memory or attention do not contribute to music perception impairment after stroke [98]. Vocal music can help improve memory recovery after stroke, as vocal music engages extensive and bilateral networks within the brain observed by functional magnetic resonance imaging, which may stimulate structural and functional plasticity changes in brain neural networks that are crucial for emotional processing and memory [99, 100]. One clinical trial with 15 subjects was in a face-to-face interview after a four-week multimodal rehabilitation program, including music therapy. The participants stated that they had a positive experience with cognitive and emotional improvements [101]. Similarly, a prospective randomized study that was conducted in Greece enrolled 65 stroke patients and discovered that music-based exercise programs have beneficial effects on the mood status of stroke patients and that the combination of exercise training and music treatment with familiar music had a better recovery effect [102]. Interestingly, different types of music exposure have different effects on poststroke cognitive impairment. Audiobook listening has been found to be associated with a positive distraction from thoughts and worries. Furthermore, mindful music listening is tightly associated with relaxation and concentration and strengthened attentional control. Music listening is also correlated with increased activity, memory reminiscence, and positive mood [103]. Therefore, the forms of music or sound input should be selected according to the main symptoms and severity of cognitive dysfunction in order to achieve the best therapeutic effect.

4. Conclusion

Overall, studies have demonstrated that music therapy in rehabilitation of stroke can help improve dysphagia, enhance the effect of limb motor exercise training, promote speech function recovery, and improve cognitive impairment. The mechanism of neurologic functional recovery after stroke is complex, and existing rehabilitation techniques are mainly focused on limb motor therapy and the recovery of brain function on the damaged side. As the integrity of the human brain function depends on close contact and interaction between the hemispheres, poststroke rehabilitation should not only enhance the recovery of the brain function on the injured side but also pay attention to the contralateral side in order to stimulate the hemispheres connectivity, resulting in an improvement in the integration of the entire brain function. Music therapy can improve neurological function by enhancing the neuroplasticity and neural networks of the brain. However, specific neurobiological mechanisms remain to be further explored.

Thus far, the effect of music therapy on rehabilitation following stroke has been gradually confirmed in clinic, and the therapy is simple, safe, and easy to accept. However, the patients' number of current clinical studies is small, and large-scale randomized controlled trials are needed. Moreover, the potential mechanisms of music therapy, implementation process, outcome evaluation, and treatment mode need to be

further studied. In addition, as a kind of rehabilitation method, music therapy has a long treatment cycle and high requirements for patient compliance. And at present, the whole world is still short of professional music therapists, which need to cultivate more qualified therapists through international cooperation and exchange.

Data Availability

No data were used to support this study.

Conflicts of Interest

The authors declare that there are no potential conflicts of interest.

Authors' Contributions

Chengyan Xu wrote the manuscript. Zixia He, Zhipeng Shen, and Fei Huang revised the manuscript. All authors approved the final version.

References

- [1] K. Strong, C. Mathers, and R. Bonita, "Preventing stroke: saving lives around the world," *Lancet Neurology*, vol. 6, no. 2, pp. 182–187, 2007.
- [2] Y. J. Wang, Z. X. Li, H. Q. Gu et al., "China Stroke Statistics 2019: A report from the national center for healthcare quality management in neurological diseases, China National Clinical Research Center for Neurological Diseases, the Chinese Stroke Association, National Center for Chronic and Non-communicable Disease Control and Prevention, Chinese Center for Disease Control and Prevention and Institute for Global Neuroscience and Stroke Collaborations," *Stroke and Vascular Neurology*, vol. 5, no. 3, pp. 211–239, 2020.
- [3] "Global, regional, and national age-sex specific mortality for 264 causes of death, 1980–2016: a systematic analysis for the global burden of disease study 2016," *Lancet*, vol. 390, no. 10100, pp. 1151–1210, 2017.
- [4] N. S. Rost, A. Brodtmann, M. P. Pase et al., "Post-stroke cognitive impairment and dementia," *Circulation Research*, vol. 130, no. 8, pp. 1252–1271, 2022.
- [5] C. A. Jones, C. M. Colletti, and M. C. Ding, "Post-stroke dysphagia: recent insights and unanswered questions," *Current Neurology and Neuroscience Reports*, vol. 20, no. 12, p. 61, 2020.
- [6] N. Cichon, L. Wlodarczyk, J. Saluk-Bijak et al., "Novel advances to post-stroke aphasia pharmacology and rehabilitation," *Journal of Clinical Medicine*, vol. 10, no. 17, p. 3778, 2021.
- [7] M. L. Hackett, S. Köhler, J. T. O'Brien, and G. E. Mead, "Neuropsychiatric outcomes of stroke," *Lancet Neurology*, vol. 13, no. 5, pp. 525–534, 2014.
- [8] C. M. Stinear, C. E. Lang, S. Zeiler, and W. D. Byblow, "Advances and challenges in stroke rehabilitation," *Lancet Neurology*, vol. 19, no. 4, pp. 348–360, 2020.
- [9] P. Langhorne, J. Bernhardt, and G. Kwakkel, "Stroke rehabilitation," *Lancet*, vol. 377, no. 9778, pp. 1693–1702, 2011.
- [10] B. H. Dobkin, "Strategies for stroke rehabilitation," *Lancet Neurology*, vol. 3, no. 9, pp. 528–536, 2004.
- [11] J. Grau-Sánchez, T. F. Münte, E. Altenmüller, E. Duarte, and A. Rodríguez-Fornells, "Potential benefits of music playing in stroke upper limb motor rehabilitation," *Neuroscience and Biobehavioral Reviews*, vol. 112, pp. 585–599, 2020.
- [12] J. Loewy, "Music therapy as a potential intervention for sleep improvement," *Nature and Science of Sleep*, vol. Volume 12, pp. 1–9, 2020.
- [13] F. Xiong, X. Liao, J. Xiao et al., "Emerging limb rehabilitation therapy after post-stroke motor recovery," *Frontiers in Aging Neuroscience*, vol. 14, article 863379, 2022.
- [14] A. Street, J. Zhang, S. Pethers, L. Wiffen, K. Bond, and H. Palmer, "Neurologic music therapy in multidisciplinary acute stroke rehabilitation: could it be feasible and helpful?," *Topics in Stroke Rehabilitation*, vol. 27, no. 7, pp. 541–552, 2020.
- [15] P. Kulkarni, O. Duffy, J. Synnott, W. G. Kernohan, and R. McNaney, "Speech and language practitioners' experiences of commercially available voice-assisted technology: web-based survey study," *JMIR Rehabilitation and Assistive Technologies*, vol. 9, no. 1, article e29249, 2022.
- [16] H. Mayer-Benarous, X. Benarous, F. Vonthron, and D. Cohen, "Music therapy for children with autistic spectrum disorder and/or other neurodevelopmental disorders: a systematic review," *Frontiers in Psychiatry*, vol. 12, article 643234, 2021.
- [17] P. Albouy, L. Benjamin, B. Morillon, and R. J. Zatorre, "Distinct sensitivity to spectrotemporal modulation supports brain asymmetry for speech and melody," *Science*, vol. 367, no. 6481, pp. 1043–1047, 2020.
- [18] T. Chabin, L. Pazart, and D. Gabriel, "Vocal melody and musical background are simultaneously processed by the brain for musical predictions," *Annals of the New York Academy of Sciences*, 2022.
- [19] L. Montello and E. E. Coons, "Effects of active versus passive group music therapy on preadolescents with emotional, learning, and behavioral disorders," *Journal of Music Therapy*, vol. 35, no. 1, pp. 49–67, 1999.
- [20] T. McPherson, D. Berger, S. Alagapan, and F. Fröhlich, "Active and passive rhythmic music therapy interventions differentially modulate sympathetic autonomic nervous system activity," *Journal of Music Therapy*, vol. 56, no. 3, pp. 240–264, 2019.
- [21] K. A. Lynch, N. Emard, K. T. Liou et al., "Patient perspectives on active vs. passive music therapy for cancer in the inpatient setting: a qualitative analysis," *Journal of Pain and Symptom Management*, vol. 62, no. 1, pp. 58–65, 2021.
- [22] C. Freitas, J. F. Fernández-Company, M. F. Pita, and M. García-Rodríguez, "Music therapy for adolescents with psychiatric disorders: an overview," *Clinical Child Psychology and Psychiatry*, vol. 13591045221079161, p. 135910452210791, 2022.
- [23] S. Kim and H. Jeong, "Effects of patient-selected music listening on the pain and anxiety of patients undergoing hemodialysis: a randomized controlled trial," *Healthcare*, vol. 9, no. 11, p. 1437, 2021.
- [24] G. Lu, R. Jia, D. Liang, J. Yu, Z. Wu, and C. Chen, "Effects of music therapy on anxiety: a meta-analysis of randomized controlled trials," *Psychiatry Research*, vol. 304, p. 114137, 2021.
- [25] L. Gassner, M. Geretsegger, and J. Mayer-Ferbas, "Effectiveness of music therapy for autism spectrum disorder,

- dementia, depression, insomnia and schizophrenia: update of systematic reviews,” *European Journal of Public Health*, vol. 32, no. 1, pp. 27–34, 2022.
- [26] O. Brancatisano, A. Baird, and W. F. Thompson, “Why is music therapeutic for neurological disorders? The Therapeutic Music Capacities Model,” *Neuroscience & Biobehavioral Reviews*, vol. 112, pp. 600–615, 2020.
- [27] A. J. Sihvonen, T. Särkämö, V. Leo, M. Tervaniemi, E. Altenmüller, and S. Soinila, “Music-based interventions in neurological rehabilitation,” *Lancet Neurology*, vol. 16, no. 8, pp. 648–660, 2017.
- [28] R. Froutan, M. Eghbali, S. H. Hoseini, S. R. Mazloom, M. S. Yekaninejad, and R. Boostani, “The effect of music therapy on physiological parameters of patients with traumatic brain injury: a triple-blind randomized controlled clinical trial,” *Complementary Therapies in Clinical Practice*, vol. 40, p. 101216, 2020.
- [29] S. T. Siponkoski, N. Martínez-Molina, L. Kuusela et al., “Music therapy enhances executive functions and prefrontal structural neuroplasticity after traumatic brain injury: evidence from a randomized controlled trial,” *Journal of Neurotrauma*, vol. 37, no. 4, pp. 618–634, 2020.
- [30] R. S. Calabrò, A. Naro, S. Filoni et al., “Walking to your right music: a randomized controlled trial on the novel use of treadmill plus music in Parkinson's disease,” *Journal of Neuroengineering and Rehabilitation*, vol. 16, no. 1, p. 68, 2019.
- [31] K. E. Innes, T. K. Selfe, K. Brundage et al., “Effects of meditation and music-listening on blood biomarkers of cellular aging and Alzheimer's disease in adults with subjective cognitive decline: an exploratory randomized clinical trial,” *Journal of Alzheimer's Disease*, vol. 66, no. 3, pp. 947–970, 2018.
- [32] J. Lyu, J. Zhang, H. Mu et al., “The effects of music therapy on cognition, psychiatric symptoms, and activities of daily living in patients with Alzheimer's disease,” *Journal of Alzheimer's Disease*, vol. 64, no. 4, pp. 1347–1358, 2018.
- [33] K. Wakana, Y. Kimura, Y. Nitta, and T. Fujisawa, “The effect of music on preoperative anxiety in an operating room: a single-blind randomized controlled trial,” *Anesthesia Progress*, vol. 69, no. 1, pp. 24–30, 2022.
- [34] D. Reynaud, N. Bouscaren, V. Lenclume, and M. Boukerrou, “Comparing the effects of self-selected MUsic versus predetermined music on patient ANXIety prior to gynaecological surgery: the MUANX randomized controlled trial,” *Trials*, vol. 22, no. 1, p. 535, 2021.
- [35] Y. İriağaç, E. Çavdar, K. Karaboyun, O. Avci, N. Tuna, and E. S. Şeber, “The influence of visual objects and music on anxiety levels of breast cancer patients scheduled to experience chemotherapy for the first time: a prospective randomized clinical study,” *Support Care Cancer*, vol. 30, no. 5, pp. 4355–4362, 2022.
- [36] H. Cheng, G. Breitbart, L. Giordano, D. Richmand, and G. Wong, “Music in the wound care center: effects on anxiety levels and blood pressure measurements in patients receiving standard care,” *Wound Management & Prevention*, vol. 67, no. 4, pp. 16–22, 2021.
- [37] L. O'Steen, N. A. Lockney, C. G. Morris, V. Johnson-Mallard, D. Pereira, and R. J. Amdur, “A prospective randomized trial of the influence of music on anxiety in patients starting radiation therapy for cancer,” *International Journal of Radiation Oncology • Biology • Physics*, vol. 109, no. 3, pp. 670–674, 2021.
- [38] P. Atiwannapat, P. Thaipisuttikul, P. Poopityastaporn, and W. Katekaew, “Active versus receptive group music therapy for major depressive disorder—a pilot study,” *Complementary Therapies in Medicine*, vol. 26, pp. 141–145, 2016.
- [39] J. Fachner, C. Gold, and J. Erkkilä, “Music therapy modulates fronto-temporal activity in rest-EEG in depressed clients,” *Brain Topography*, vol. 26, no. 2, pp. 338–354, 2013.
- [40] P. Daengruan, R. Chairat, R. Jenraumjit et al., “Effectiveness of receptive music therapy with imbedded 10 Hz binaural beats compared with standard care for patients with major depressive disorder: a randomized controlled trial,” *Complementary Therapies in Medicine*, vol. 61, p. 102765, 2021.
- [41] S. F. Lu, C. H. Lo, H. C. Sung, T. C. Hsieh, S. C. Yu, and S. C. Chang, “Effects of group music intervention on psychiatric symptoms and depression in patient with schizophrenia,” *Complementary Therapies in Medicine*, vol. 21, no. 6, pp. 682–688, 2013.
- [42] E. Michou, S. Mistry, S. Jefferson, P. Tyrrell, and S. Hamdy, “Characterizing the mechanisms of central and peripheral forms of neurostimulation in chronic dysphagic stroke patients,” *Brain Stimulation*, vol. 7, no. 1, pp. 66–73, 2014.
- [43] G. D. Carnaby, L. LaGorio, S. Silliman, and M. Cray, “Exercise-based swallowing intervention (McNeill dysphagia therapy) with adjunctive NMES to treat dysphagia post-stroke: a double-blind placebo-controlled trial,” *Journal of Oral Rehabilitation*, vol. 47, no. 4, pp. 501–510, 2020.
- [44] H. G. Seo, B. M. Oh, and T. R. Han, “Swallowing kinematics and factors associated with laryngeal penetration and aspiration in stroke survivors with dysphagia,” *Dysphagia*, vol. 31, no. 2, pp. 160–168, 2016.
- [45] J. A. Logemann, “Dysphagia: evaluation and treatment,” *Folia Phoniatrica et Logopaedica*, vol. 47, no. 3, pp. 140–164, 1995.
- [46] R. Dziewas, R. Stellato, I. van der Tweel et al., “Pharyngeal electrical stimulation for early decannulation in tracheotomised patients with neurogenic dysphagia after stroke (PHAST-TRAC): a prospective, single-blinded, randomised trial,” *Lancet Neurology*, vol. 17, no. 10, pp. 849–859, 2018.
- [47] J. W. Park, Y. Kim, J. C. Oh, and H. J. Lee, “Effortful swallowing training combined with electrical stimulation in post-stroke dysphagia: a randomized controlled study,” *Dysphagia*, vol. 27, no. 4, pp. 521–527, 2012.
- [48] J. W. Park, J. C. Oh, J. W. Lee, J. S. Yeo, and K. H. Ryu, “The effect of 5Hz high-frequency rTMS over contralesional pharyngeal motor cortex in post-stroke oropharyngeal dysphagia: a randomized controlled study,” *Neurogastroenterology and Motility*, vol. 25, no. 4, pp. e250–e324, 2013.
- [49] S. J. Kim and U. Jo, “Study of accent-based music speech protocol development for improving voice problems in stroke patients with mixed dysarthria,” *NeuroRehabilitation*, vol. 32, no. 1, pp. 185–190, 2013.
- [50] J. Tamplin, “A pilot study into the effect of vocal exercises and singing on dysarthric speech,” *NeuroRehabilitation*, vol. 23, no. 3, pp. 207–216, 2008.
- [51] S. J. Kim, “Music therapy protocol development to enhance swallowing training for stroke patients with dysphagia,” *Journal of Music Therapy*, vol. 47, no. 2, pp. 102–119, 2010.
- [52] Q. Lv, G. Xu, Y. Pan et al., “Effect of acupuncture on neuroplasticity of stroke patients with motor dysfunction: a meta-analysis of fMRI studies,” *Neural Plasticity*, vol. 2021, Article ID 8841720, 10 pages, 2021.

- [53] C. C. Huo, Y. Zheng, W. W. Lu et al., "Prospects for intelligent rehabilitation techniques to treat motor dysfunction," *Neural Regeneration Research*, vol. 16, no. 2, pp. 264–269, 2021.
- [54] E. Segura, J. Grau-Sánchez, D. Sanchez-Pinsach et al., "Designing an app for home-based enriched music-supported therapy in the rehabilitation of patients with chronic stroke: a pilot feasibility study," *Brain Injury*, vol. 35, no. 12-13, pp. 1585–1597, 2021.
- [55] C. R. Phang, L. W. Ko, W. C. Chang, K. H. Yu, and C. H. Chen, "Immediate plasticity of parietal-frontocentral functional connections in music-reality based post-stroke rehabilitation," in *2021 43rd Annual International Conference of the IEEE Engineering in Medicine & Biology Society (EMBC)*, pp. 5828–5831, Mexico, 2021.
- [56] P. Douglass-Kirk, M. Grierson, N. S. Ward et al., "Real-time auditory feedback may reduce abnormal movements in patients with chronic stroke," *Disability and Rehabilitation*, pp. 1–7, 2022.
- [57] J. L. Amengual, N. Rojo, M. V. de Las Heras et al., "Sensorimotor plasticity after music-supported therapy in chronic stroke patients revealed by transcranial magnetic stimulation," *PLoS One*, vol. 8, no. 4, p. e61883, 2013.
- [58] N. Schaffert, T. Braun Janzen, R. Ploigt, S. Schlüter, V. Vuong, and M. H. Thaut, "Development and evaluation of a novel music-based therapeutic device for upper extremity movement training: a pre-clinical, single-arm trial," *PLoS One*, vol. 15, no. 11, article e0242552, 2020.
- [59] C. M. Haire, L. Tremblay, V. Vuong et al., "Therapeutic instrumental music training and motor imagery in post-stroke upper-extremity rehabilitation: a randomized-controlled pilot study," *Archives of Rehabilitation Research and Clinical Translation*, vol. 3, p. 100162, 2021.
- [60] E. Altenmüller, J. Marco-Pallares, T. F. Münte, and S. Schneider, "Neural reorganization underlies improvement in stroke-induced motor dysfunction by music-supported therapy," *Annals of the New York Academy of Sciences*, vol. 1169, no. 1, pp. 395–405, 2009.
- [61] N. Rojo, J. Amengual, M. Juncadella et al., "Music-supported therapy induces plasticity in the sensorimotor cortex in chronic stroke: a single-case study using multimodal imaging (fMRI-TMS)," *Brain Injury*, vol. 25, no. 7-8, pp. 787–793, 2011.
- [62] M. Schauer and K. H. Mauritz, "Musical motor feedback (MMF) in walking hemiparetic stroke patients: randomized trials of gait improvement," *Clinical Rehabilitation*, vol. 17, no. 7, pp. 713–722, 2003.
- [63] Y. Lee and S. Shin, "Improvement of gait in patients with stroke using rhythmic sensory stimulation: a case-control study," *Journal of Clinical Medicine*, vol. 11, no. 2, p. 425, 2022.
- [64] S. Gonzalez-Hoelling, C. Bertran-Noguer, G. Reig-Garcia, and R. Suñer-Soler, "Effects of a music-based rhythmic auditory stimulation on gait and balance in subacute stroke," *International Journal of Environmental Research and Public Health*, vol. 18, no. 4, p. 2032, 2021.
- [65] M. H. Thaut, A. K. Leins, R. R. Rice et al., "Rhythmic auditory stimulation improves gait more than NDT/Bobath training in near-ambulatory patients early poststroke: a single-blind, randomized trial," *Neurorehabilitation and Neural Repair*, vol. 21, no. 5, pp. 455–459, 2007.
- [66] Y. Cha, Y. Kim, S. Hwang, and Y. Chung, "Intensive gait training with rhythmic auditory stimulation in individuals with chronic hemiparetic stroke: a pilot randomized controlled study," *NeuroRehabilitation*, vol. 35, no. 4, pp. 681–688, 2014.
- [67] L. D. Crosby, J. S. Wong, J. L. Chen, J. Grahn, and K. K. Patterson, "An initial investigation of the responsiveness of temporal gait asymmetry to rhythmic auditory stimulation and the relationship to rhythm ability following stroke," *Frontiers in Neurology*, vol. 11, article 517028, 2020.
- [68] M. H. Thaut, G. C. McIntosh, and R. R. Rice, "Rhythmic facilitation of gait training in hemiparetic stroke rehabilitation," *Journal of the Neurological Sciences*, vol. 151, no. 2, pp. 207–212, 1997.
- [69] W. L. Magee, I. Clark, J. Tamplin, J. Bradt, and Cochrane Stroke Group, "Music interventions for acquired brain injury," *Cochrane Database of Systematic Reviews*, vol. 2017, no. 1, p. Cd006787, 2017.
- [70] J. Bradt, W. L. Magee, C. Dileo, B. L. Wheeler, and E. McGilloway, "Music therapy for acquired brain injury," *Cochrane Database of Systematic Reviews*, vol. 7, p. Cd006787, 2010.
- [71] E. Vitti and A. E. Hillis, "Treatment of post-stroke aphasia: a narrative review for stroke neurologists," *International Journal of Stroke*, vol. 16, no. 9, pp. 1002–1008, 2021.
- [72] J. D. Stefaniak, A. D. Halai, and M. A. Lambon Ralph, "The neural and neurocomputational bases of recovery from post-stroke aphasia," *Nature Reviews. Neurology*, vol. 16, no. 1, pp. 43–55, 2020.
- [73] S. Saxena and A. E. Hillis, "An update on medications and noninvasive brain stimulation to augment language rehabilitation in post-stroke aphasia," *Expert Review of Neurotherapeutics*, vol. 17, no. 11, pp. 1091–1107, 2017.
- [74] J. Fridriksson and A. E. Hillis, "Current approaches to the treatment of post-stroke aphasia," *J Stroke*, vol. 23, no. 2, pp. 183–201, 2021.
- [75] M. C. Brady, H. Kelly, J. Godwin, P. Enderby, and P. Campbell, "Speech and language therapy for aphasia following stroke," *Cochrane Database of Systematic Reviews*, vol. 2016, no. 6, p. Cd000425, 2016.
- [76] S. M. Sheppard and R. Sebastian, "Diagnosing and managing post-stroke aphasia," *Expert Review of Neurotherapeutics*, vol. 21, no. 2, pp. 221–234, 2021.
- [77] C. Y. Wan, K. Demaine, L. Zipse, A. Norton, and G. Schlaug, "From music making to speaking: engaging the mirror neuron system in autism," *Brain Research Bulletin*, vol. 82, no. 3-4, pp. 161–168, 2010.
- [78] N. Martínez-Molina, S. T. Siponkoski, A. Pitkäniemi et al., "Neuroanatomical correlates of speech and singing production in chronic post-stroke aphasia," *Brain Commun*, vol. 4, no. 1, p. fcac001, 2022.
- [79] J. C. Whitehead and J. L. Armony, "Singing in the brain: neural representation of music and voice as revealed by fMRI," *Human Brain Mapping*, vol. 39, no. 12, pp. 4913–4924, 2018.
- [80] Q. Liu, W. Li, Y. Yin et al., "The effect of music therapy on language recovery in patients with aphasia after stroke: a systematic review and meta-analysis," *Neurological Sciences*, vol. 43, no. 2, pp. 863–872, 2022.
- [81] A. J. Sihvonen, P. Ripollés, V. Leo et al., "Vocal Music Listening Enhances Post-Stroke Language Network Reorganization," *ENEURO*, vol. 8, no. 4, p. ENEURO.0158–ENEU21.2021, 2021.

- [82] X. Y. Zhang, W. Y. Yu, W. J. Teng et al., “Effectiveness of melodic intonation therapy in Chinese mandarin on non-fluent aphasia in patients after stroke: a randomized control trial,” *Frontiers in Neuroscience*, vol. 15, article 648724, 2021.
- [83] M. Martzoukou, A. Nousia, G. Nasios, and S. Tsiouris, “Adaptation of melodic intonation therapy to Greek: a clinical study in Broca's aphasia with brain perfusion SPECT validation,” *Frontiers in Aging Neuroscience*, vol. 13, article 664581, 2021.
- [84] A. M. Haro-Martínez, G. Lubrini, R. Madero-Jarabo, E. Díez-Tejedor, and B. Fuentes, “Melodic intonation therapy in post-stroke nonfluent aphasia: a randomized pilot trial,” *Clinical Rehabilitation*, vol. 33, no. 1, pp. 44–53, 2019.
- [85] M. D. Cortese, F. Riganello, F. Arcuri, L. M. Pignataro, and I. Buglione, “Rehabilitation of aphasia: application of melodic-rhythmic therapy to Italian language,” *Frontiers in Human Neuroscience*, vol. 9, p. 520, 2015.
- [86] X. Zhang, J. Li, and Y. Du, “Melodic intonation therapy on non-fluent aphasia after stroke: a systematic review and analysis on clinical trials,” *Frontiers in Neuroscience*, vol. 15, p. 753356, 2021.
- [87] K. B. Lim, Y. K. Kim, H. J. Lee et al., “The therapeutic effect of neurologic music therapy and speech language therapy in post-stroke aphasic patients,” *Annals of Rehabilitation Medicine*, vol. 37, no. 4, pp. 556–562, 2013.
- [88] Y. Y. Huang, S. D. Chen, X. Y. Leng et al., “Post-stroke cognitive impairment: epidemiology, risk factors, and management,” *Journal of Alzheimer's Disease*, vol. 86, no. 3, pp. 983–999, 2022.
- [89] J. S. Lim, J. J. Lee, and C. W. Woo, “Post-stroke cognitive impairment: pathophysiological insights into brain disconnectome from advanced neuroimaging analysis techniques,” *J Stroke*, vol. 23, no. 3, pp. 297–311, 2021.
- [90] M. Brainin, J. Tuomilehto, W. D. Heiss et al., “Post-stroke cognitive decline: an update and perspectives for clinical research,” *European Journal of Neurology*, vol. 22, no. 229–238, pp. e213–e226, 2015.
- [91] H. Shim, “Vascular cognitive impairment and post-stroke cognitive deficits,” *Current Neurology and Neuroscience Reports*, vol. 14, no. 1, p. 418, 2014.
- [92] P. Nie, F. Liu, S. Lin et al., “The effects of computer-assisted cognitive rehabilitation on cognitive impairment after stroke: a systematic review and meta-analysis,” *Journal of Clinical Nursing*, vol. 31, no. 9–10, pp. 1136–1148, 2022.
- [93] C. Y. Hung, X. Y. Wu, V. C. Chung, E. C. Tang, J. C. Wu, and A. Y. Lau, “Overview of systematic reviews with meta-analyses on acupuncture in post-stroke cognitive impairment and depression management,” *Integr Med Res*, vol. 8, no. 3, pp. 145–159, 2019.
- [94] W. Shen, X. Fan, L. Wang, and Y. Zhang, “Traditional Chinese medicine for post-stroke cognitive impairment: a systematic review and meta-analysis,” *Frontiers in Pharmacology*, vol. 13, p. 816333, 2022.
- [95] T. Hara, A. Shanmugalingam, A. McIntyre, and A. M. Burhan, “The effect of non-invasive brain stimulation (NIBS) on attention and memory function in stroke rehabilitation patients: a systematic review and meta-analysis,” *Diagnostics (Basel)*, vol. 11, no. 2, p. 227, 2021.
- [96] T. Särkämö, “Music for the ageing brain: cognitive, emotional, social, and neural benefits of musical leisure activities in stroke and dementia,” *Dementia (London)*, vol. 17, no. 6, pp. 670–685, 2018.
- [97] S. Baylan, R. Swann-Price, G. Peryer, and T. Quinn, “The effects of music listening interventions on cognition and mood post-stroke: a systematic review,” *Expert Review of Neurotherapeutics*, vol. 16, no. 11, pp. 1241–1249, 2016.
- [98] S. Rosemann, F. Brunner, A. Kastrup, and M. Fahle, “Musical, visual and cognitive deficits after middle cerebral artery infarction,” *eNeurologicalSci*, vol. 6, pp. 25–32, 2017.
- [99] A. J. Sihvonen, V. Leo, P. Ripollés et al., “Vocal music enhances memory and language recovery after stroke: pooled results from two RCTs,” *Annals of Clinical Translational Neurology*, vol. 7, no. 11, pp. 2272–2287, 2020.
- [100] M. Suzuki, M. Kanamori, M. Watanabe et al., “Behavioral and endocrinological evaluation of music therapy for elderly patients with dementia,” *Nursing & Health Sciences*, vol. 6, no. 1, pp. 11–18, 2004.
- [101] P. Pohl, G. Carlsson, L. Bunketorp Käll, M. Nilsson, and C. Blomstrand, “Experiences from a multimodal rhythm and music-based rehabilitation program in late phase of stroke recovery - a qualitative study,” *PLoS One*, vol. 13, no. 9, article e0204215, 2018.
- [102] G. Fotakopoulos and P. Kotlia, “The value of exercise rehabilitation program accompanied by experiential music for recovery of cognitive and motor skills in stroke patients,” *Journal of Stroke and Cerebrovascular Diseases*, vol. 27, no. 11, pp. 2932–2939, 2018.
- [103] S. Baylan, M. McGinlay, M. MacDonald et al., “Participants' experiences of music, mindful music, and audiobook listening interventions for people recovering from stroke,” *Annals of the New York Academy of Sciences*, vol. 1423, no. 1, pp. 349–359, 2018.
- [104] D. Slavin and R. Fabus, “A case study using a multimodal approach to melodic intonation therapy,” *American Journal of Speech-Language Pathology*, vol. 27, no. 4, pp. 1352–1362, 2018.
- [105] I. Van Der Meulen, M. W. Van De Sandt-Koenderman, M. H. Heijnenbrok, E. Visch-Brink, and G. M. Ribbers, “Melodic intonation therapy in chronic aphasia: evidence from a pilot randomized controlled trial,” *Frontiers in Human Neuroscience*, vol. 10, p. 533, 2016.
- [106] A. Zumbansen, I. Peretz, and S. Hébert, “The combination of rhythm and pitch can account for the beneficial effect of melodic intonation therapy on connected speech improvements in Broca's aphasia,” *Frontiers in Human Neuroscience*, vol. 8, p. 592, 2014.
- [107] S. Al-Janabi, L. A. Nickels, P. F. Sowman, H. Burianová, D. L. Merrett, and W. F. Thompson, “Augmenting melodic intonation therapy with non-invasive brain stimulation to treat impaired left-hemisphere function: two case studies,” *Frontiers in Psychology*, vol. 5, p. 37, 2014.
- [108] I. van der Meulen, W. M. van de Sandt-Koenderman, M. H. Heijnenbrok-Kal, E. G. Visch-Brink, and G. M. Ribbers, “The efficacy and timing of melodic intonation therapy in subacute aphasia,” *Neurorehabilitation and Neural Repair*, vol. 28, no. 6, pp. 536–544, 2014.
- [109] L. Zipse, A. Norton, S. Marchina, and G. Schlaug, “When right is all that is left: plasticity of right-hemisphere tracts in a young aphasic patient,” *Annals of the New York Academy of Sciences*, vol. 1252, no. 1, pp. 237–245, 2012.
- [110] D. Conklyn, E. Novak, A. Boissy, F. Bethoux, and K. Chemali, “The effects of modified melodic intonation therapy on

Retraction

Retracted: A Novel Approach Combined with MIPO Technique for the Treatment of Type C Pilon Fractures

Oxidative Medicine and Cellular Longevity

Received 1 August 2023; Accepted 1 August 2023; Published 2 August 2023

Copyright © 2023 Oxidative Medicine and Cellular Longevity. This is an open access article distributed under the Creative Commons Attribution License, which permits unrestricted use, distribution, and reproduction in any medium, provided the original work is properly cited.

This article has been retracted by Hindawi following an investigation undertaken by the publisher [1]. This investigation has uncovered evidence of one or more of the following indicators of systematic manipulation of the publication process:

- (1) Discrepancies in scope
- (2) Discrepancies in the description of the research reported
- (3) Discrepancies between the availability of data and the research described
- (4) Inappropriate citations
- (5) Incoherent, meaningless and/or irrelevant content included in the article
- (6) Peer-review manipulation

The presence of these indicators undermines our confidence in the integrity of the article's content and we cannot, therefore, vouch for its reliability. Please note that this notice is intended solely to alert readers that the content of this article is unreliable. We have not investigated whether authors were aware of or involved in the systematic manipulation of the publication process.

In addition, our investigation has also shown that one or more of the following human-subject reporting requirements has not been met in this article: ethical approval by an Institutional Review Board (IRB) committee or equivalent, patient/participant consent to participate, and/or agreement to publish patient/participant details (where relevant).

Wiley and Hindawi regrets that the usual quality checks did not identify these issues before publication and have since put additional measures in place to safeguard research integrity.

We wish to credit our own Research Integrity and Research Publishing teams and anonymous and named external

researchers and research integrity experts for contributing to this investigation.



The corresponding author, as the representative of all authors, has been given the opportunity to register their agreement or disagreement to this retraction. We have kept a record of any response received.

References

- [1] Y. Chen, H. Wang, N. Li et al., "A Novel Approach Combined with MIPO Technique for the Treatment of Type C Pilon Fractures," *Oxidative Medicine and Cellular Longevity*, vol. 2022, Article ID 7427255, 10 pages, 2022.

Research Article

A Novel Approach Combined with MIPO Technique for the Treatment of Type C Pilon Fractures

Youhao Chen,¹ Haoming Wang,^{1,2,3} Nan Li,¹ Lixin Xu,^{1,3} Feng Liu,¹ Qiu Xu,⁴ Qiang Zhou ,² and Xiaohua Chen ^{1,3}

¹Department of Orthopedics, Chongqing University Three Gorges Hospital, Chongqing 404000, China

²Department of Orthopedics, The Third Affiliated Hospital of Chongqing Medical University, Chongqing 401120, China

³Chongqing Municipality Clinical Research Center for Geriatric Diseases, Chongqing University Three Gorges Hospital, Chongqing 404000, China

⁴Health Center of Sunjia Town, Wanzhou District, Chongqing 404000, China

Correspondence should be addressed to Xiaohua Chen; chen13996510998@163.com

Received 16 March 2022; Revised 24 April 2022; Accepted 27 April 2022; Published 14 June 2022

Academic Editor: Shao Liang

Copyright © 2022 Youhao Chen et al. This is an open access article distributed under the Creative Commons Attribution License, which permits unrestricted use, distribution, and reproduction in any medium, provided the original work is properly cited.

Objective. Type C fracture is a complete intra-articular fracture, and the mainstay of treatment remains open reduction and internal fixation. The purpose of the study is to observe the clinical effect of an anterior ankle C approach (ankle-C) combined with minimal invasive plate osteosystems (MIPO) for tibial pilon fractures (AO/OTA 43C, combined with fibula fractures). **Methods.** A retrospective comparative analysis was performed on the clinical data of 33 patients with C-type pilon fractures (combined fibula fractures) admitted to our department from July 2018 to July 2021, including 12 cases treated with ankle-C (a-C) approach and 21 cases with conventional approach (including combined approach). All patients were followed up for over 6 months. Visual Analogue Scale (VAS), AOFAS Ankle-Hindfoot Scale (AOFAS-AHS), wound healing time, fracture healing time, and complications were used to evaluate the clinical efficacy. **Results.** The scores of VAS and AOFAS in the a-C group scored better than the conventional group ($P < 0.05$), especially in the extent of limited range of motion (LROM) of ankle dorsiflexion-plantarflexion in 1 month after operation and at the last follow-up ($P < 0.01$). Bone healing was achieved in both groups 6 months after operation, with no implant exposure or infection. Among them, 4 cases in the conventional approach group had wound healing time exceeding 2 weeks. **Conclusions.** For type C pilon fractures (combined with fibula fractures), ankle-C approach combined with MIPO technique has certain advantages in ankle function recovery and soft tissue repair, which provides an alternative for the treatment of type C pilon fractures.

1. Background

With the development of society, there are more and more patients with high-energy trauma. Pilon fractures, represented by falls from heights, are common in clinical practice, accounting for about 1% of lower limb fractures, most of which are complicated with fibular fractures (about 10-30% are open fractures) [1]. Pilon fracture has been studied for 110 years since Etienne Destot, a French physician, introduced the concept of pilon fracture in 1911 based on the mechanism of injury and fracture characteristics [2]. The treatment of complex pilon fractures has always been a difficult and controversial clinical problem. Due to the complexity of these fractures, which are

often associated with severe soft tissue injuries and multiple treatment complications, managing pilon fractures has been a challenge for orthopaedic trauma surgeons to this day [3]. According to AO classification [4], type C fracture is a complete intra-articular fracture, and the mainstay of treatment remains open reduction and internal fixation. There are some classic surgical approaches for pilon fractures, such as antero-medial, medial, anterolateral, lateral, posterolateral, combined approaches, or many modified ones based on some classic approaches, aiming at facilitating surgical exposure, reduction, and fixation and reducing incision complications [5]. From the earliest conservative treatment to open reduction and internal fixation, there are many incision complications in the

treatment of pilon fractures, especially the difficulty of incision closure after operation, necrosis, and infection of incision skin or local skin flap and even catastrophic complications such as amputation [6]. In order to reduce these complications, limited open reduction and internal fixation, external stent staging treatment with one-stage fixation or nonfixation of fibula, minimally invasive percutaneous plate technique (MIPO), and other related minimally invasive techniques [7–10] have been developed to provide clinicians with more choices for the management of complex pilon fractures.

The overall treatment principles of pilon fractures are to restore limb force line, good articular surface reduction, good joint matching, and strong fixation for early functional exercise [11]. Based on the above treatment principles, the author has made some reflections in clinical work on how to reduce the soft tissue complications and achieve the balance between bone and soft tissue while taking into account the reduction and fixation quality of fracture. Pilon fracture is divided into two parts: the metaphysis and the joint (including internal and external malleolus). The treatment of metaphysis fracture is mainly to restore fracture force line, which can be easily accomplished by closed reduction under C-arm fluoroscopy, and effective fixation can be completed by percutaneously inserting bone plates through the MIPO technique [12].

There has been no report on anterior ankle C approach in the treatment of tibial pilon fractures. Thus, the motivation and novelty of the study are to firstly evaluate the clinical effect of an anterior ankle C approach combined with minimal invasive plate osteosystems for tibial pilon fractures and hopefully provide a new efficient approach for clinical treatment. Hereby, we reported 33 patients with pilon fractures who have achieved good clinical effects after treatment with single incision, i.e., anterior ankle C-shaped incision approach combined with minimal invasive plate osteosystems (MIPO) technique in our hospital in recent years.

2. Data and Methods

2.1. Patients. Inclusion criteria are as follows: (1) tibial pilon fracture caused by violence, namely, AO/OTA43-C fracture; (2) open reduction and plate internal fixation; and (3) retrospective case-control study.

Exclusion criteria are as follows: (1) no fibular fracture; (2) open pilon fracture with Gustilo classification < III; (3) previous ipsilateral leg and ankle injuries and surgical history; (4) tibiofibula and ankle deformity; (5) other diseases that cannot tolerate surgery; and (6) defective follow-up data or follow-up time < 3 months.

From July 2018 to July 2021, 52 cases of type C pilon fractures surgically treated in the Chongqing University Three Gorges Hospital were selected, of which 33 cases were finally enrolled after screening according to the above eligibility criteria. Among them, there were 21 males (63.64%) and 12 females (36.36%), aged 41.9 ± 10.3 years (range: 22–55). This study was approved by Ethics Committee of Chongqing University Three Gorges Hospital as an exempt study without registration number.

2.2. Case Grouping. Twelve patients (male-to-female ratio, 7:5) who underwent surgical treatment through anterior ankle C-shaped approach combined with MIPO technique were included in the a-C group, with an average age of 38.40 ± 6.32 years (ranging from 22 to 43 years); 5 cases of 43-C1, 3 cases of C2, and 4 cases of C3 were determined based on the AO/OTA classification. And according to the Tscherne-Gotze classification of preoperative soft tissue trauma, there were 2, 7, 2, and 1 cases of grades 0, 1, 2, and 3, respectively. Twenty-one patients with regular longitudinal incision (including anterior internal, anterior-external, posterior-internal, and posterior-external approaches) with or without MIPO technique for open reduction and plate internal fixation were defined as the routine approach group, including 14 males and 7 females, with an average age of 41.50 ± 7.41 years (ranging from 26 to 55 years); OTA/AO classification identified 3 cases of 43-C1, 12 cases of C2, and 6 cases of C3. And according to Tscherne-Gotze classification of preoperative soft tissue trauma, there were 5 cases of grade 0, 10 cases of grade 1, 6 cases of grade 2, and 0 cases of grade 3. The research flow is shown in Figure 1.

2.3. Treatment Methods

2.3.1. Preoperative Plan. All patients underwent calcaneal traction after admission, with the traction weight being 1/12 to 1/8 of their body weight (to maintain a mild overtraction state). Full-length anteroposterior-lateral X-ray of the lower leg and 3-dimensional CT examination of the ankle were performed to classify the fracture and determine the mechanism of injury, and the corresponding internal fixation plan was developed according to the fracture type. All open wounds were treated by emergency debridement and suture. In the case of serous or bloody blisters, blister fluid was extracted, and the blister skin was preserved.

2.3.2. Surgical Plan. Cefazolin sodium (2.0 g intravenous drip) was applied 30 min before skin excision. All patients were subjected to spinal anesthesia with sciatic and saphenous nerve block. Patients were placed in a supine position with a tourniquet on the thigh root.

2.3.3. a-C Group. An arc-shaped surgical incision was made at 1 cm from the proximal end of the medial and lateral malleolar prominence to the upper site of the ankle mortise. Then, the skin, subcutaneous tissue, and deep fascia were cut, and the subcutaneous and deep fascia were sutured intermittently with 4-0 silk thread, which could play a role of distraction and avoid subcutaneous tissue undermining dissection during the operation, which could play a role of distraction while avoiding subcutaneous tissue segregation during operation. In this plane, care was taken to protect the medial great saphenous vein and lateral superficial peroneal nerve.

The deep anterior tibial tendon and extensor hallucis longus were exposed from the extensor digitorum tendon, and care was taken to protect the anterior tibial blood vessel and the deep peroneal nerve located below the extensor digitorum muscle. The medial side of the great saphenous vein was the “first window”, which can reveal the fracture of the distal medial malleolus. The “second window” was between

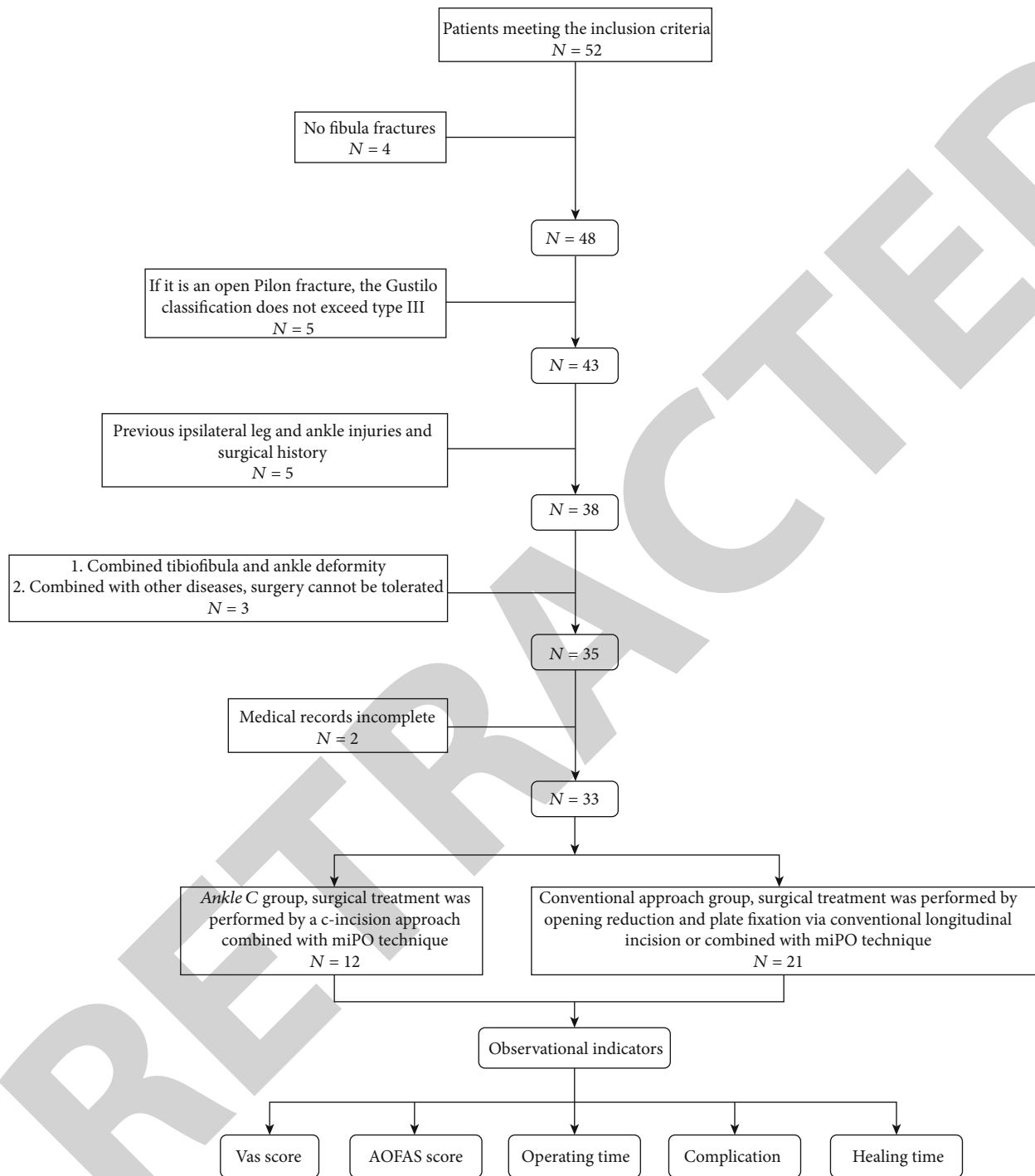


FIGURE 1: Research flow chart.

the great saphenous vein and the tibialis anterior tendon, which can expose the medial malleolus dome and the medial ankle mortise. The “third window” was between the extensor digitorum tendon and the extensor hallucis longus, which can expose the middle space of ankle mortise. The “fourth window” was between extensor digitorum tendon and superficial peroneal nerve, which can expose the lateral side of the ankle mortise and lateral dome. The lateral side of superficial peroneal nerve was the “fifth window”, which can expose distal tibial and fibular.

Under the second, third, and fourth windows, the anterior fracture block was opened with the anterior joint capsule or the inferior tibiofibular syndesmosis as the hinge, and the central collapsed articular surface and the intermediate die-punch fracture block were explored. Using the posterior malleolar fracture block as a reference, the die-punch fracture block was reduced, and bone grafting was determined according to the bone defect. Then, the central compressed articular surface was reduced; the anteriorly displaced fracture fragment was removed, followed by temporary fixation with Kirschner wire.



FIGURE 2: Schematic diagram of anterior ankle C-shaped incision. (a) Anterior ankle C-type incision: a transverse arc line was made from the medial and lateral malleolar prominence to the proximal 1 cm of the ankle joint. (b) Protection of the great saphenous vein, superficial peroneal nerve, tibialis anterior muscle, extensor hallucis longus, extensor digitorum longus, anterior tibial artery, and deep peroneal nerve. (c) The lateral window can expose the lateral border of trochlea tali. (d) The middle window can completely expose the fornix of the talus to provide 23 mm of operating space at the distal tibia. (e) The medial window can completely expose the medial malleolar prominence.

The medial-distal tibia and medial malleolus were exposed at the first and second windows and temporarily fixed with Kirschner wire after reduction. The distal lateral part of the tibia and the lateral malleolus were exposed at windows fourth and fifth, and the lateral malleolus fracture, Tillaux-Chaput bone block, and Wagstaff bone block were reduced. After satisfactory reduction of the articular surface and medial and lateral malleolus through C-arm fluoroscopy, the metaphyseal fracture was closed, and C-arm fluoroscopy was performed to confirm that the force line returned to normal.

Then, using MIPO technique, a medial malleolus screw or medial tibial plate was placed in the first window, an anterolateral plate or screw was placed in the third or fourth window, and a lateral malleolus plate or screw was placed in the fifth window. The distal screws of the bone plate were placed under direct vision, and the proximal screws were perforated. C-arm fluoroscopy was performed again to confirm the normal force line of the lower limbs, satisfactory reduction of the articular surface, and good joint matching, and limb movement was performed to confirm the stability of fracture fixation. Then, an

TABLE 1: Comparison of general data and perioperative indicators between the ankle-C approach group and the conventional approach group.

Variables	a-C approach group ($n = 12$)	Conventional approach group ($n = 21$)	P
Age (years, $\bar{x} \pm s$)	38.40 \pm 6.32	41.50 \pm 7.41	0.233
Gender (n (%))			0.632
Male	7 (58.3)	14 (66.7)	
Female	5 (41.7)	7 (33.3)	
Preoperative soft tissue trauma Tscherne-Gotze classification evaluation (n (%))			0.466
0	2 (16.7)	5 (23.8)	
1	7 (58.3)	10 (47.6)	
2	2 (16.7)	6 (28.6)	
3	1 (8.3)	0 (0)	
AO/OTA fracture classification (n (%))			0.125
C1	5 (41.7)	3 (14.3)	
C2	3 (25.0)	12 (57.1)	
C3	4 (33.3)	6 (28.6)	
Operation time (minutes, $\bar{x} \pm s$)	95.27 \pm 10.32	83.34 \pm 6.44	0.012
Complications (n (%))	0 (0)	4 (19.0)	0.107
Complete wound healing time (days, $\bar{x} \pm s$)	13.27 \pm 0.90	14.95 \pm 1.78	0.004
Complete healing time of fracture (months)	6.25 \pm 0.72	6.34 \pm 0.47	0.666

antifracture drainage tube was placed. If the aponeurosis was damaged during operation, conventional 4-0 absorbable suture was used for repair. Finally, the deep fascia, subcutaneous tissue, and skin were sutured layer by layer. The schematic diagram of anterior ankle C-shaped incision was shown in Figure 2.

2.3.4. Conventional Approach Group. According to the fracture site and fragmentation degree of distal tibia and fibula, classic surgical approaches were performed, including anterolateral, anteromedial, posteromedial, posterolateral, and combined approaches. MIPO technology [12] can also be used to assist plate implantation according to the patient's skin and soft tissue conditions. Conventional incision closure was performed after intraoperative radioscopic evaluation of fracture reduction and plate fixation.

2.3.5. Postoperative Plan. Incision healing was observed in all patients according to the incision management guidelines [13], and all patients were immobilized with plaster for 1 week. After 30 degrees of limb elevation, cefazolin sodium (2.0 g, iv drip) was used once after operation. Besides, 4000 U enoxaparin sodium [14] was subcutaneously injected daily for multimode combined analgesia. After surgery, the patient was instructed to perform active and passive functional exercises of the toes and isometric muscle contraction. The drainage tube was removed 24 hours after operation, and active and passive flexion and dorsiflexion exercises of the ankle joint were initiated after the plaster was removed 1 week postoperatively. The stitches were removed 12-14 days postoperatively, and the active exercise intensity of ankle joint was gradually increased 3 weeks after surgery until normal activities resumed. Partial weight-bearing exercise was started 6 weeks after X-ray review,

and full weight-bearing functional exercise was performed 3 months after gradual recovery shown by X-ray reexamination.

2.4. Endpoints. All patients were scored by Visual Analogue Scale (VAS) [15] and AOFAS Ankle-Hindfoot Scale (AOFAS-AHS) [16] before operation, 1 month after operation, and the last follow-up (≥ 6 months after operation). The ankle flexion-extension range of motion (ROM) was measured and recorded. At the last follow-up (≥ 6 months after operation), CT scanning was performed to evaluate bone healing. The operation time (OT), wound healing time, fracture healing time, and complications of patients were recorded. All the above data were analyzed statistically.

2.5. Statistical Processing. This is a retrospective case-control study. Data analysis was made by SPSS23.0 (SPSS, USA). Measurement data (age, OT, wound healing time, fracture healing time, VAS score, AOFAS-AHS score, and ankle flexion-extension range of motion) were tested by normal distribution first, and those who met were indicated by $\bar{x} \pm s$ and compared by independent sample t -test between groups. The categorical data were presented as n (%) and compared by χ^2 test. The comparison of VAS and AOFAS-AHS scores within the group was performed by paired sample t -test. Categorical variables (gender, complications, fracture classification, soft tissue classification) were compared by χ^2 test. The test level was $\alpha = 0.05$ (two-tailed). $P < 0.05$ were considered statistically significant.

3. Results

3.1. General Information and Perioperative Indicators. The comparison results of the general data and perioperative indicators between two groups are as shown in Table 1. The two



FIGURE 3: Typical case: male, 37 years old, type C3 fracture. (a) One week after the injury, the condition of soft tissue improved, and the time was ripe for surgery. (b) Preoperative X-ray and CT findings. (c) Intraoperative soft tissue protection and “window” application. (d) Intraoperative C-arm fluoroscopy, plate implantation, and suture. (e) Postoperative X-ray and CT examination results.

TABLE 2: Comparison of Visual Analogue Scale (VAS), AOFAS Ankle-Hindfoot Score (AOFAS-AHS), and ankle flexion-extension range of motion between the ankle-C approach group and the conventional approach group ($^{\circ}$ $\bar{x} \pm s$).

Groups	<i>n</i>	VAS (points)		AOFAS-AHS (points)		Ankle flexion-extension range of motion ($^{\circ}$)	
		Before surgery	1 month after surgery	Before surgery	At the last follow-up (≥ 6 months after surgery)	Before surgery	At the last follow-up (≥ 6 months after surgery)
a-C approach group	12	5.75 \pm 0.57	1.42 \pm 0.51*	12.08 \pm 1.31	70.25 \pm 2.38*	10.17 \pm 2.16	47.58 \pm 3.17*
Conventional approach group	21	5.71 \pm 0.71	2.05 \pm 0.82	12.05 \pm 1.46	68.05 \pm 3.35*	9.81 \pm 1.78	39.85 \pm 3.45*
<i>P</i>		0.904	0.023	0.944	0.036	0.612	0.000

* $P < 0.05$, compared to the same group before surgery; # $P < 0.05$, compared to the same group 1 month after surgery.

groups differed insignificantly in age, sex, Tscherne-Gotze classification, and AO/OTA fracture classification, complications and complete healing time of fracture. Meanwhile, evidently shorter OT was determined in a-C approach group with 95.27 ± 10.32 min compared with conventional approach group with 83.34 ± 6.44 min. Although there was no difference in the incidence of complications between the two groups, the time of wound healing in the a-C approach group was significantly reduced compared with the conventional approach group. A typical treatment case file of a 37-year-old male with type C3 fracture is shown in Figure 3.

3.2. VAS, AOFAS-AHS, and Ankle Flexion-Extension Range of Motion. As shown in Table 2, the VAS score, which showed no distinct difference between groups before surgery ($P > 0.05$), was lower in the a-C approach group at 1 month after operation ($P < 0.05$), while differed insignificantly between groups at the last follow-up ($P > 0.05$). The preoperative AOFAS-AHS score and the one at the last follow-up differed insignificantly between groups ($P > 0.05$), while the score was notably higher in the a-C approach group than in the conventional approach group at 1 month after operation ($P < 0.05$). In observation of the change of ankle flexion-extension range of motion, no distinct difference was observed in preoperative ankle flexion-extension ROM between groups ($P > 0.05$); however, in comparison with the conventional approach group, the ankle joint ROM in the a-C approach group was improved at 1 month after operation and the last follow-up (≥ 6 months after operation), especially at 1 month after operation ($P < 0.05$), with the ROM basically reached 70% of the normal.

3.3. Complications. There was no postoperative wound dehiscence or infection in the a-C group, except for one patient with light brown changes in the skin margin of the wound but it did not affect wound healing. Four patients in the conventional approach group developed wound-related complications after surgery. Two of them had an anterolateral incision, and the wound near the metaphysis was cracked about 4 cm, with a small amount of exudation and no steel plate exposure, which completely healed 7 days beyond the average healing time. Another two cases showed redness at the skin margin of the wound after surgery, with the appearance of blisters in the skin of the operative area due to high suture tension. After timely treatment, the skin healed completely 2-3 days beyond the average healing time.

4. Discussion

In the operation of open pilon fracture, the current classical surgical approaches cannot be fully applied, and in some patients with severe soft tissue injury, the risk of applying traditional large incision is also high. However, suture and fracture staging treatment strategy is associated with longer treatment time, increased treatment cost, increased risk of joint stiffness, and lower patient satisfaction. The traditional longitudinal incision has the problem of insufficient exposure of the left and right ankle mortise, especially the dome of the medial and lateral ankle mortise. And due to poor

exposure, satisfactory fracture reduction is often not achieved, increasing the incidence of traumatic arthritis. In addition, the tension of longitudinal incision is extremely high when suturing deep fascia after operation, and it is often difficult or impossible to suture. In patients with primary closure, the tension of incision is concentrated in the skin and subcutaneous, which affects the blood supply of soft tissue, resulting in significantly elevated risk of skin and soft tissue necrosis and infection [17]. And for some patients, incision closure cannot be completed in one stage due to excessive tension, with the need to place negative pressure devices such as VSD, and secondary closure or skin grafting and flap repair can only be performed after the swelling subsides [18].

In this study, the design concept of anterior ankle arc incision approach was that full exposure is required in the complex intra-articular fracture surgery, so we think of a transverse arc incision with the main purpose of revealing the joints. The tibialis anterior muscle group, blood vessels, and nerves of the ankle run longitudinally, along which the important soft tissues include the anteromedial great saphenous vein, the anterior tibial tendon, extensor hallucis longus, extensor digitorum tendon, anterior tibial artery and deep peroneal nerve in the middle, and the lateral superficial peroneal nerve. With the help of the concept of soft tissue "window" under the deep fascia, the ankle joint space can be exposed in all directions, and the fractures of internal and external malleolus and the central compression joint can be reduced and fixed under direct vision. In addition, the soft tissue of the anterior ankle arc incision is located in the depression of the foot and the lower leg, and the chance of soft tissue being traumatised is relatively smaller than that of the lower leg, which can completely avoid the severe soft tissue injury and the open wound on the inner and outer sides of the lower leg. Moreover, the transverse incision is along the dermatoglyphic direction, which also meets the requirements of surgical incision design.

From this study, the results showed that the scores of VAS and AOFAS in the a-C group scored better than the conventional group, especially in the extent of limited range of motion (LROM) of ankle dorsiflexion-plantarflexion in 1 month after operation and at the last follow-up. Meanwhile, bone healing was achieved in both groups 6 months after operation, with no implant exposure or infection. First of all, this incision is a single transverse incision, which avoids metaphyseal incision, protects the blood supply of metaphyseal fracture, and facilitates fracture healing. In addition, thanks to the concept of soft tissue windows, fractures at the joint, including the medial and lateral malleolus, are fully exposed, expanding the exposure range of the ankle mortise. In particular, due to the full exposure of the internal and external dome which is of reference significance for reduction, the articular surface of the posterior malleolus can be seen when the foot is pulled distally, which is of great help to anatomical reduction and improves the quality of reduction and fixation of the fracture under direct vision. In addition, the incision can be partially cut according to the fracture type.

The core advantage of this incision is the prognosis of soft tissue. First of all, the anterior ankle soft tissue is less likely to be injured during the original injury, and the soft tissue conditions are generally better [19]. The deep fascia

of C-shaped incision is a transverse incision, which takes the advantages of the transverse support band of tibialis anterior extensor and the thickness of deep fascia, contributing to small tension during suture or almost no suture tension in the ankle dorsiflexion position and easy closure of the incision [20]. In addition, because the tension is concentrated in the deep fascia layer, the skin and subcutaneous tissue can be sutured without tension, with little influence on soft tissue blood supply, and less chance of necrosis and infection. All the incisions in 12 patients healed in one stage without necrosis or infection, indicating that this incision has obvious advantages over traditional incision after soft tissue prevention.

Of course, this incision also has certain disadvantages. First of all, during skin incision, the anteromedial great saphenous vein and the anterolateral superficial peroneal nerve are prone to injury, so special attention should be paid to the protection during the operation. In addition, the Ankle-C approach only had an exposure range of 5-7cm from the center of the incision to the proximal and distal ends. and it could not fix the ankle from the rear, so it had strict indications.

5. Thoughts and Prospects

Since there are many therapeutic methods and incision approaches for pilon fractures, the indications of each surgical approach should be strictly controlled. For patients with intact posterior ankle or without open reduction and fixation, a single anterior transverse arc incision approach can be a new choice for clinicians and has obvious advantages in treating complex C2 and C3 pilon fractures. This article only makes a preliminary report on the clinical efficacy of this approach, with good results achieved in the study cases. However, the number of cases that can be summarized is still limited, which requires further demonstration through a large sample-size research for clinical promotion and application.

Data Availability

The simulation experiment data used to support the findings of this study are available from the corresponding author upon request.

Conflicts of Interest

The authors declare no competing interests.

Authors' Contributions

Youhao Chen and Haoming Wang contributed equally to this work.

Acknowledgments

This work was funded by the Chongqing Medical Scientific Research Project (joint project of Chongqing Health Commission and Science and Technology Bureau) (No. 2020FYYX211), the Medical Research Project of Wanzhou District, Chongqing (joint project of Health Commission and Science and Technol-

ogy Bureau) (No. wzstc-kw2020023, No. wzstc-kw2021018), and the Natural Science Foundation of Chongqing, China (No. cstc2021jcyj-msxmx0569).

References

- [1] J. Reátiga Aguilar, X. Rios, E. González Ederly, A. De La Rosa, and L. A. Ortega, "Epidemiological characterization of tibial plateau fractures," *Journal of Orthopaedic Surgery and Research*, vol. 17, no. 1, pp. 1–7, 2022.
- [2] A. Dwivedi, W. X. Jian, S. S. Dwivedi, N. R. Dwivedi, W. Han, and X. Peng, "Pilon fracture; an unsolved riddle an updated review," *IJCMR*, vol. 4, pp. 718–725, 2017.
- [3] B. N. Saad, J. M. Yingling, F. A. Liporace, and R. S. Yoon, "Pilon fractures: challenges and solutions," *Orthopedic Research and Reviews*, vol. 11, pp. 149–157, 2019.
- [4] J. Marsh, T. F. Slongo, J. Agel et al., "Fracture and dislocation classification compendium - 2007," *Journal of Orthopaedic Trauma*, vol. 21, pp. S1–S6, 2007.
- [5] J. Bear, N. Rollick, and D. Helfet, "Evolution in management of tibial pilon fractures," *Current Reviews in Musculoskeletal Medicine*, vol. 11, no. 4, pp. 537–545, 2018.
- [6] D. J. Cinats, T. Stone, D. Viskontas, and K. Apostle, "Osteonecrosis of the distal tibia after pilon fractures," *Foot and Ankle Surgery*, vol. 26, no. 8, pp. 895–901, 2020.
- [7] G. B. Kim, O.-J. Shon, and C. H. Park, "Treatment of AO/OTA type C pilon fractures through the anterolateral approach combined with the medial MIPO technique," *Foot & Ankle International*, vol. 39, no. 4, pp. 426–432, 2018.
- [8] A. Barış, E. Çirci, Z. Demirci, and Y. Öztürkmen, "Minimally invasive medial plate osteosynthesis in tibial pilon fractures: longterm functional and radiological outcomes," *Acta Orthopaedica et Traumatologica Turcica*, vol. 54, no. 1, pp. 20–26, 2020.
- [9] R. I. Davidovitch, R. Elkataran, S. Romo, M. Walsh, and K. A. Egol, "Open reduction with internal fixation versus limited internal fixation and external fixation for high grade pilon fractures (OTA type 43C)," *Foot & Ankle International*, vol. 32, no. 10, pp. 955–961, 2011.
- [10] K. Nozaka, N. Miyakoshi, H. Saito et al., "Effectiveness of Ili-zarov external fixation in elderly patients with pilon fractures," *Journal of Orthopaedic Science*, vol. 26, no. 2, pp. 254–260, 2021.
- [11] S.-B. Zhang, Y.-B. Zhang, S.-H. Wang et al., "Clinical efficacy and safety of limited internal fixation combined with external fixation for pilon fracture: a systematic review and meta-analysis," *Chinese Journal of Traumatology*, vol. 20, no. 2, pp. 94–98, 2017.
- [12] G. Vicenti, D. Bizzoca, V. S. Nappi et al., "The impact of lag screw in the healing time of distal tibia fractures treated with minimally invasive plate osteosynthesis: a randomized clinical trial," *Injury*, vol. 51, pp. S80–S85, 2020.
- [13] K. Yan, Z. Zongke, and Y. Huilin, "A guideline on the management of incisions for the enhanced recovery after orthopaedic surgery in China," *Chin J Bone Joint Surg*, vol. 11, pp. 3–10, 2018.
- [14] Y. Xu, J. Zhao, and Y. Chen, "Prevention of venous thrombo-embolism in patients undergoing major orthopedic surgery in China: a qualitative study of patients' perceptions," *Journal of Orthopaedic Surgery and Research*, vol. 13, no. 1, pp. 1–5, 2018.

Retraction

Retracted: An Enhanced Priori Knowledge GAN for CT Images Generation of Early Lung Nodules with Small-Size Labelled Samples

Oxidative Medicine and Cellular Longevity

Received 1 August 2023; Accepted 1 August 2023; Published 2 August 2023

Copyright © 2023 Oxidative Medicine and Cellular Longevity. This is an open access article distributed under the Creative Commons Attribution License, which permits unrestricted use, distribution, and reproduction in any medium, provided the original work is properly cited.

This article has been retracted by Hindawi following an investigation undertaken by the publisher [1]. This investigation has uncovered evidence of one or more of the following indicators of systematic manipulation of the publication process:

- (1) Discrepancies in scope
- (2) Discrepancies in the description of the research reported
- (3) Discrepancies between the availability of data and the research described
- (4) Inappropriate citations
- (5) Incoherent, meaningless and/or irrelevant content included in the article
- (6) Peer-review manipulation

The presence of these indicators undermines our confidence in the integrity of the article's content and we cannot, therefore, vouch for its reliability. Please note that this notice is intended solely to alert readers that the content of this article is unreliable. We have not investigated whether authors were aware of or involved in the systematic manipulation of the publication process.

In addition, our investigation has also shown that one or more of the following human-subject reporting requirements has not been met in this article: ethical approval by an Institutional Review Board (IRB) committee or equivalent, patient/participant consent to participate, and/or agreement to publish patient/participant details (where relevant).

Wiley and Hindawi regrets that the usual quality checks did not identify these issues before publication and have since put additional measures in place to safeguard research integrity.

We wish to credit our own Research Integrity and Research Publishing teams and anonymous and named external researchers and research integrity experts for contributing to this investigation.

The corresponding author, as the representative of all authors, has been given the opportunity to register their agreement or disagreement to this retraction. We have kept a record of any response received.

References

- [1] X. Wang, Z. Yu, L. Wang, and P. Zheng, "An Enhanced Priori Knowledge GAN for CT Images Generation of Early Lung Nodules with Small-Size Labelled Samples," *Oxidative Medicine and Cellular Longevity*, vol. 2022, Article ID 2129303, 9 pages, 2022.

Research Article

An Enhanced Priori Knowledge GAN for CT Images Generation of Early Lung Nodules with Small-Size Labelled Samples

Xun Wang ¹, Zhiyong Yu,¹ Lisheng Wang,¹ and Pan Zheng ²

¹College of Computer Science and Technology, China University of Petroleum (East China), Qingdao 266580, China

²University of Canterbury, Christchurch 8140, New Zealand

Correspondence should be addressed to Pan Zheng; pan.zheng@canterbury.ac.nz

Received 28 April 2022; Revised 19 May 2022; Accepted 31 May 2022; Published 14 June 2022

Academic Editor: Shao Liang

Copyright © 2022 Xun Wang et al. This is an open access article distributed under the Creative Commons Attribution License, which permits unrestricted use, distribution, and reproduction in any medium, provided the original work is properly cited.

The small size of labelled samples is one of the challenging problems in identifying early lung nodules from CT images using deep learning methods. Recent literature on the topic shows that deep convolutional generative adversarial network (DCGAN) has been used in medical data synthesis and gained some success, but does not demonstrate satisfactory results in synthesizing CT images. It primarily suffers from the problem of model convergence and is prone to mode collapse. In this paper, we propose a generative adversarial network (GAN) model with prior knowledge to generate CT images of early lung nodules from a small-size of labelled samples, i.e., SLS-PriGAN. Particularly, a knowledge acquisition network and a sharpening network are designed for priori knowledge learning and acquisition, and then, a GAN model is developed to produce CT images of early lung nodules. To validate our method, a general fast R-CNN network is trained using the CT images generated by SLS-PriGAN. The experiment result shows that it achieved a recognizing accuracy of 91%, a recall rate of 81%, and F1 score of 0.85 in identifying clinic CT images of early lung nodules. This provides a promising way of identifying early lung nodules from CT images using deep learning with small-size labelled samples.

1. Introduction

Neural networks, particularly deep learning models, have shown promising results in the field of cancer-targeted detection. Some studies have shown the ability of trained neural network models can reach the level of human physicians in lesion detection [1–4]. Almost all the methods are based on training with a large volume of datasets, which would fail when the amount of data is sparse and lacking [5, 6].

The small size of labelled samples has become one of the challenging problems in identifying early lung nodules from CT Images using deep learning technology. When there are a small number of patients screened for early pulmonary nodules, it is difficult to develop large datasets of CT images for the purpose of machine learning methods and model developments. It is formulated in [5, 7] that the small size

of labelled samples has become a natural barrier to the use of neural network models in medical imaging.

A common solution to this problem is to design data synthesis methods. A typical one is to process the data set image by using translation, rotation, flip, and zoom to achieve data augmentation. Such a method has some drawbacks. Due to their inherent characteristics, medical images tend to lose their original interpretation during the process. Moreover, it is difficult to add additional useful information to the dataset for the training of neural network algorithms. Usually, the datasets used by these networks have both input and expected output, and the difference between the generated and the expected output is defined as the loss function [8–11]. It is shown in [10] that when the original data is lost or unavailable, the generated images can be used to diagnose Alzheimer's disease. This kind of model requires a large amount of data for training, and the performance of the

network model on a small set of sample data is less accurate and sufficient.

Generative adversarial networks (GAN), which have a generator and a discriminator, are used to do data augmentation by learning statistical laws of the input data and generating data samples similar to the input data but not completely repeated [12]. In recent works, GAN and its variants are used in medical image generation. For instance, deep convolutional GAN (DCGAN) is proposed to synthesize realistic prostate disease plaques [13, 14], generate retinal images [15], and synthesize different types of plaques in liver CT [16]. In [17], DCGAN is used to generate high-resolution MR data with only a small number of samples. In 2019, progressive GAN is used to synthesize high-resolution images of skin lesions, which can “cheat” professional dermatologists [18]. Although CT images of lung cancer nodules can be generated by GAN [19], the synthetic lung cancer nodules are indistinguishable from real ones [20], even for radiologists [21]. Evidently, it is still difficult to generate high-resolution CT images of early lung nodules from a small size of labelled samples.

In this work, we developed a method to synthesize quality CT images of early lung nodules using a priori knowledge GAN model from small-size labelled samples. We designed the network to acquire some priori knowledge before executing the generation task. Especially, a knowledge acquisition network and a sharpening network are designed for priori knowledge acquisition, and then, a GAN model is developed to produce CT images of early lung nodules. The contributions of this work are as follows:

- (i) An autoencoder is developed for priori knowledge curation and to retain information on the spatial position, size and shape
- (ii) A priori knowledge sharpening layer is embedded to make the model converge quickly

As a result, the CT images generated by SLS-PriGAN are used to train a fast R-CNN network. It achieves a recognition accuracy of 91%, recall rate of 81%, and $F1$ score of 0.85 in identifying clinic CT images of early lung nodules. This provides an effective way of identifying early lung nodules from CT Images generated by deep learning methods with small size samples. It shows that the data enhancement and generation method based on GAN is feasible in alleviating the dilemma caused by the small number of samples.

It is worth noting that the prior knowledge GAN is a problem and domain-specific deep learning algorithm, which is different from the concept of “transfer learning.” Transfer learning uses a pretrained machine learning model for a new but similar problem.

2. Method

We herewith propose a GAN-based generative model, named, SLS-PriGAN, to generate high-resolution CT images of early lung nodules. As shown in Figure 1, the main network of our SLS-PriGAN is a stack of GAN networks, which

includes a generator, a discriminator, a priori knowledge generation module, and a fusion control module.

The generator accepts a random vector and integrates the output of priori knowledge module to synthesize the image. In image synthesis, a random control module is introduced to achieve the goal of diversification. If the random control module is removed, the generated image will be more inclined to the original image, and the randomness of the generated image will be destroyed. During data simulation, it is found that it is sufficient to use up to 2 random control modules. The discriminator network module reads both pseudo and actual images to analyze and understand their differences and eventually achieve the syntheses.

Incorporating priori knowledge into the generation module is one of the main contributions of SLS-PriGAN, which accelerates the convergence of the model and makes the synthesized image more realistic thus producing more accurate results.

2.1. The Generation Network with a Prior Knowledge. During generating process, it uses noise, such as image attributes and categories, to fit feature information. We need to adjust the distribution of high dimensional vectors from low dimensional vectors to synthesize high-resolution CT images, which is a challenge in the case of using small size labelled samples.

The design of the generation network is shown in Figure 2, which includes a knowledge acquisition network and a sharpening network.

The priori knowledge acquisition network is constructed by a convolutional autoencoder (CAE) [22]. The CAE is a structure composed of an encoder and a decoder, and it is trained by the reconstruction loss between the decoded data and the original data [23]. The training process of the CAE is shown in Figure 3. The autoencoder preserves the main features of an image and extract information by encoding and decoding the image.

Let x be the input image, h be the latent variable, and \hat{x} be the reconstructed image. Ideally, the reconstructed image of the training output should be similar to the original image. The encoder and decoder are represented by Equations (1) and (2), respectively:

$$h = \sigma_e(W_1x + b_1), \quad (1)$$

$$\hat{x} = \sigma_d(W_2h + b_2), \quad (2)$$

where W_1, b_1 are encoding weights and offsets, W_2, b_2 are decoding weights and offsets, and σ_e, σ_d are the nonlinear transformations used in the encoding and decoding processes. The convolutional autoencoder uses convolution to linearly transform the input signal and implements a weight sharing strategy. The reconstruction process is a linear combination of basic image blocks that are hidden and coded.

The encoder encodes the input high-dimensional data to obtain the expression of the low-dimensional hidden layer. The decoder decodes the low-dimensional hidden layer to reconstruct the high-dimensional output with the same size as the input. It is further handed over to the lower network to extract and express knowledge. We used variational

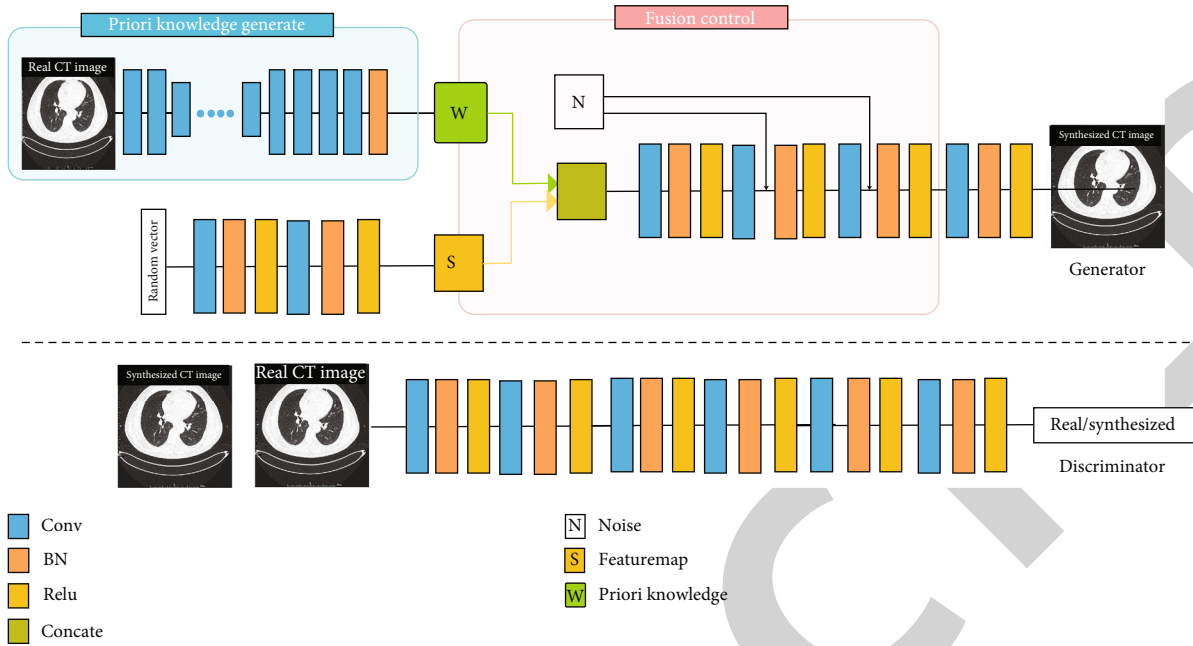


FIGURE 1: The overall design of SLS-PriGAN.

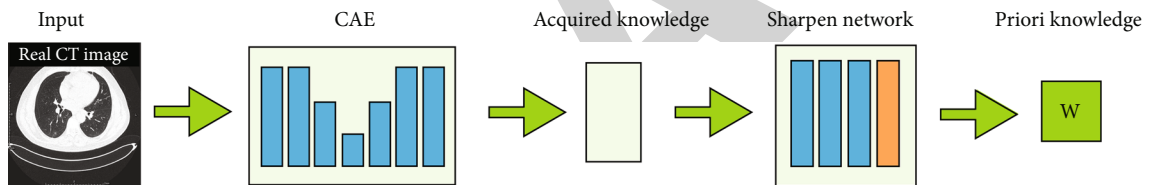


FIGURE 2: A priori knowledge generation network.

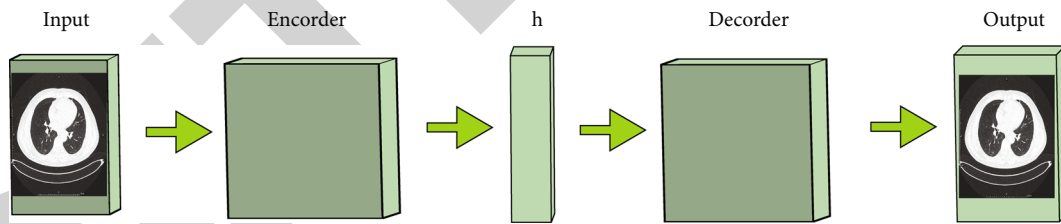


FIGURE 3: The convolutional autoencoder.

autoencoders (VAE) in SLS-PriGAN to extract priori knowledge. As shown in Figure 4, after passing through the VAE network, we can directly obtain superficial feature information about shape, size, etc. Our priori knowledge includes information such as the shape and size of the lungs. In addition, high-dimensional and abstract features will be extracted by the neural network.

The knowledge acquisition module further refines the acquired knowledge. Image feature learning is one of the important capabilities of convolutional neural networks (CNN). We access the knowledge sharpening module after acquiring a priori information in order to fully exploit the acquired knowledge features. The sharpening network prevents the collapse of the network. The priori knowledge is further extracted, and the global information of the original

image is retained. The priori knowledge module is able to overcome the notorious problems that GAN models often encounter, i.e., difficult to convergence and easy to collapse.

2.2. Fusion Control Network. A fusion control module is added to the generator, which implements the additions to the generator’s priori knowledge. As well, a random control module is applied to give the generated image a variety and authenticity of detailed information.

2.2.1. Integration of Prior Knowledge. The fusion control network is shown in Figure 5, which includes two parts: the fusion of priori knowledge W and the fusion of random noise N . As shown in Figure 5, we generally put through the priori knowledge in the 8×8 pixel resolution image

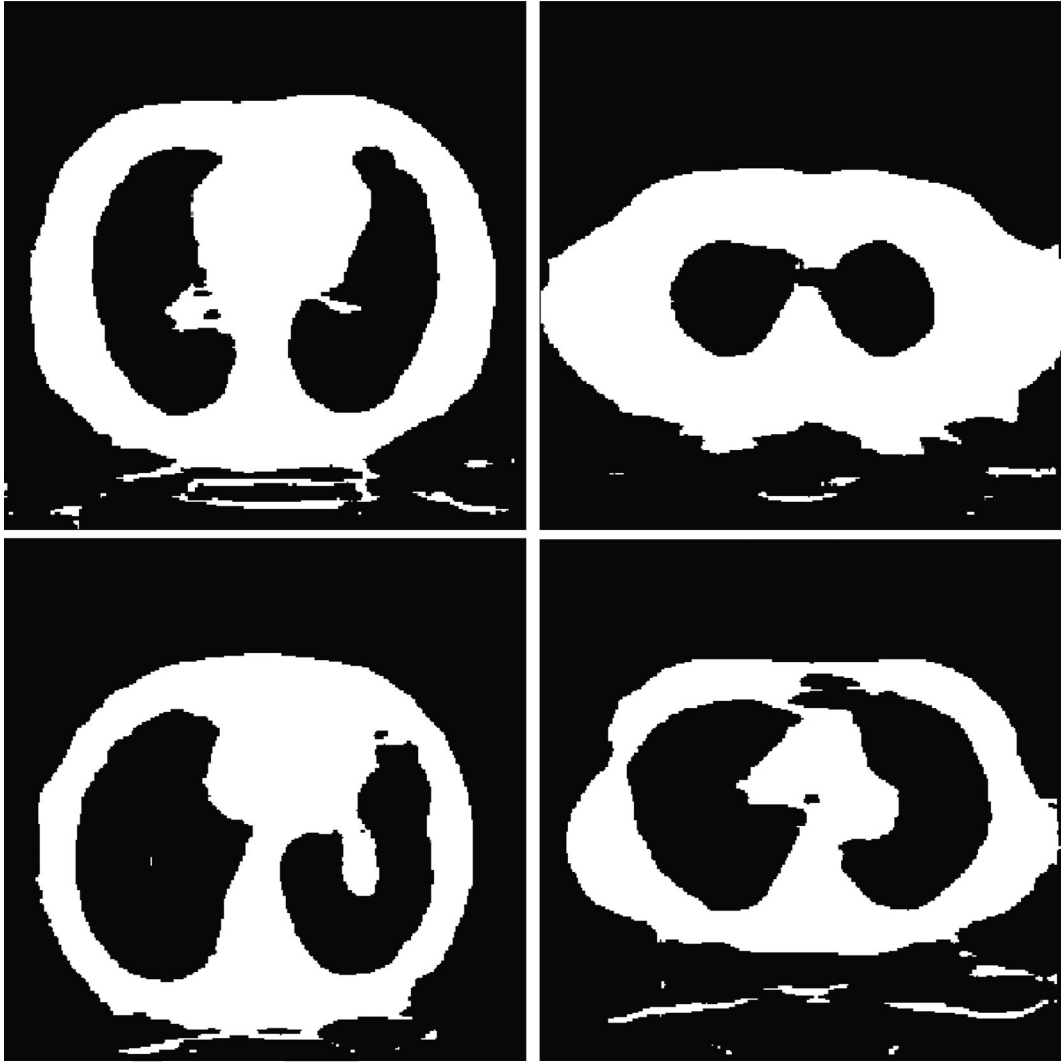


FIGURE 4: Our priori knowledge includes information such as the shape and size of the lungs.

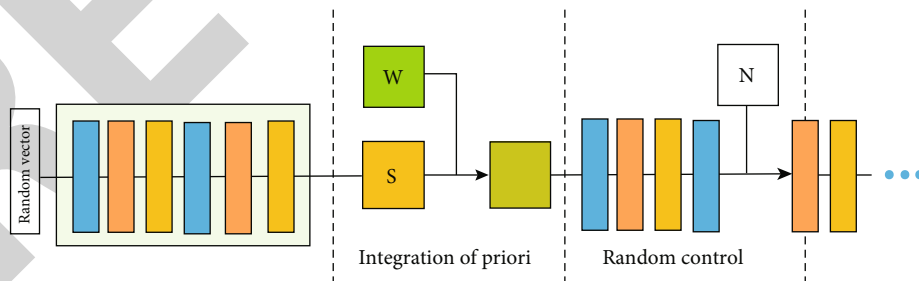


FIGURE 5: The details of the fusion control module.

synthesis process. The intermediate vector W is summed with the feature map S channel by channel, which realizes the control of the priori knowledge over the body structure of the generated image.

2.2.2. Random Control. The initial random noise input often makes the generated image closer to the real image. We

introduced random noises at different locations in the network to make the composite images more diverse. Generally, the lower layers of the network control the high-dimensional information of the generated image, such as the overall structure of the lungs. The relatively high layer tends to control the detailed information of the generated image, such as the information on lung nodules. We added scaled noises to

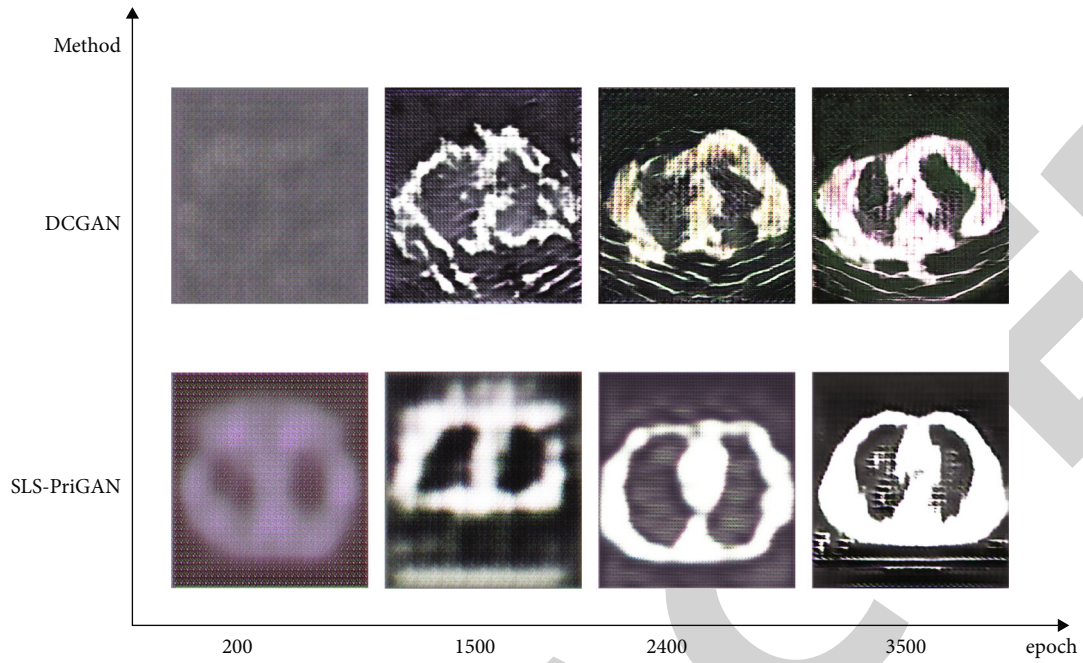


FIGURE 6: The training results of SLS-PriGAN comparing DCGAN, the results of 200, 1500, 2400, and 3500 epochs of training.

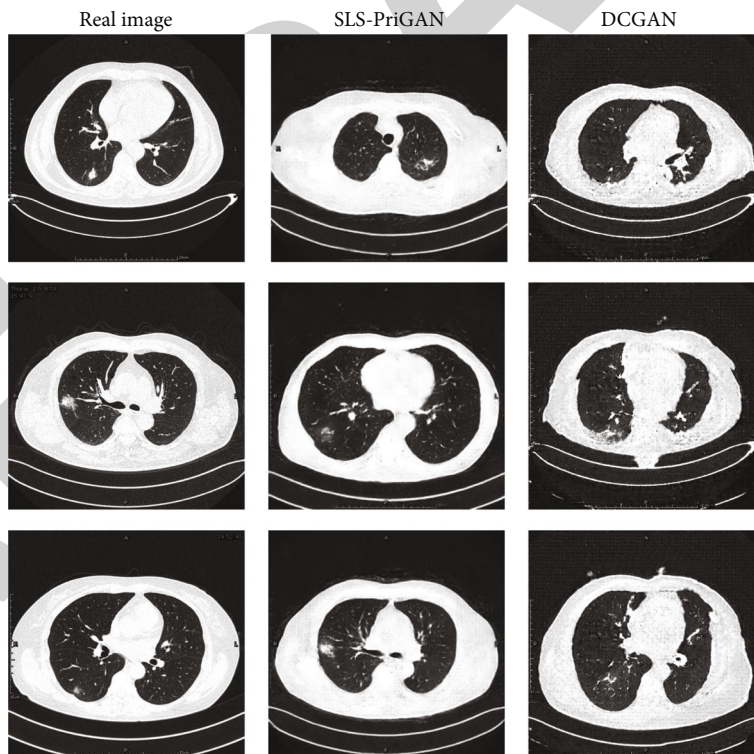


FIGURE 7: The generated result comparison with real CT images and DCGAN images.

each channel of the generation network at different resolution stages to make the noise only affect the subtle changes in the picture style and then obtain different visual expressions by changing the resolution level.

2.2.3. The Loss Function of the Network. The loss consists of two parts, which are from priori knowledge acquisition module and the generative adversarial network module. The loss can be calculated by Equation (3) [24, 25].

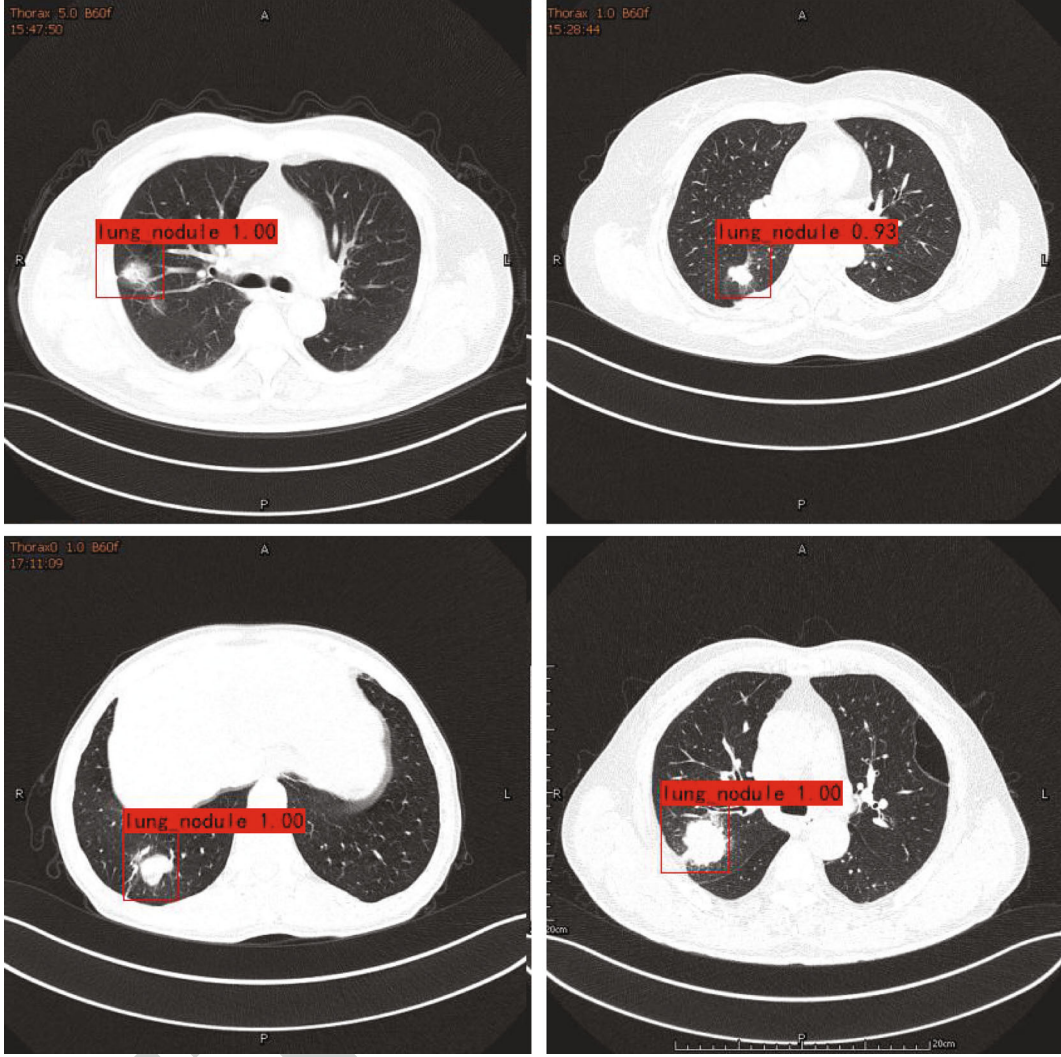


FIGURE 8: The lung nodule detection of the faster R-CNN on SLS-PriGAN generated images.

$$\text{Loss} = J_{\text{CAE}} + D_{\text{loss}} + G_{\text{loss}}. \quad (3)$$

D_{loss} and G_{loss} are the loss of discriminator and generator, respectively.

The purpose of the priori knowledge acquisition network is to minimize the error between input x and output \hat{x} . Therefore, the loss function that can be used is as follows:

$$J_{\text{CAE}}(W) = \sum(L(x, \hat{x})) + \lambda \|W\|_2^2. \quad (4)$$

Cross-entropy function L is taken as the loss function. The value of parameter λ ranges from 0 to 1, which is used to control the weight W . Using λ , we suppress the influence of static noise, improve the generalization ability of the model, and avoid overfitting. As for the second part, we use Wasserstein Gradient Penalty (WGAN-GP) [26] loss to make the model easy to train, which is as follows:

$$D_{\text{loss}} : E_{x \sim P_g}[D(x)] - E_{x \sim P_r}[D(x)] + \lambda E_{x \sim \chi} [\|\nabla_x D(x)\|_p] - 1, \quad (5)$$

$$G_{\text{loss}} : -E_{x \sim P_g}[D(x)]. \quad (6)$$

3. Experiments and Result Discussion

The study was approved by the ethical committee of The Third Hospital of Shandong Province. According to the ethical committee policy, this is a completely anonymous, retrospective study. All sensitive information of the data was removed. The experimental protocols were approved by the hospital, and all methods were carried out per relevant guidelines and regulations.

3.1. Training and Testing Dataset. The training and testing dataset of CT images are collected all from The Third Hospital of Shandong Province, China. We curated a total of 673 lung cancer CT images, among which 373 lung cancer

TABLE 1: The lung nodule detection results using faster R-CNN on synthesized data generated by SLS-PriGAN and DCGAN.

Train data	Method	Precision	Recall	F1
G_dataset1	SLS-PriGAN	0.91	0.81	0.85
G_dataset2	DCGAN	0.88	0.78	0.82
R_dataset	—	0.92	0.90	0.89

G_dataset1 and G_dataset2 are synthesized datasets generated by SLS-PriGAN and DCGAN, respectively. R_dataset is the real CT image data without any modification or synthesized data, which, in this case, can be considered as ground truth to benchmark with two other methods.

CT images are with nodules and selected as the training dataset. The location of the lesion in the CT image is marked by radiologists. The remaining 300 CT images of lung nodules were used as the test set for validation.

3.2. Image Synthesis. The structure of the SLS-PriGAN makes model training efficient by introducing a priori knowledge module and a random control module. It does not require redundant techniques hence avoiding possible model collapse. The model has achieved high-quality and high-resolution image generation compared to some work in the current literature, e.g., the method outperformed deep convolutional GAN (DCGAN), see Figure 6.

As shown in Figure 6, at the beginning of training, our SLS-PriGAN showed better fitting ability because of the integration of the priori knowledge. When the training epochs increased gradually, it exhibited a stronger convergence ability. At the epoch of 200, comparing to the DCGAN-generated image with a blurred piece, the synthetic image of the proposed method could be seen as a coarse outline. By epoch 3500, the images synthesized by the proposed method already have a clear lung outline, while DCGAN apparently fell into the trap of image style at epoch 1500 without further convergence.

Figure 7 shows a further qualitative result comparison, which shows that the SLS-PriGAN achieved better results than DCGAN when they were trained for the same number of times. After 47,000 iterations of training, DCGAN-generated images showed structural flaws. The proposed method retained the structural and content accuracy and generated images of higher quality with less significant noise. It is worth mentioning that during the training of DCGAN, the model collapse often occurred, and it was more difficult to synthesize better quality images, yet our network is not prone to such phenomenon. In addition, it is possible for the DCGAN generator to fool the discriminator with images that do not match the lung structure, which is due to the fact that DCGAN uses uncontrolled random noise, but SLS-PriGAN can obviate it.

3.3. Experimental Results. It is usually less possible to train an accurate recognition network model using only about 300 images and then recognize the remaining 300 CT images in the test set. With SLS-PriGAN, we generated 4000 CT images to enhance the training set. The generated training set is used to train a general faster R-CNN for lung nodule

recognition from CT images. It is shown, in Figure 8, that the results of the performance of the test set with 300 CT images of lung nodules. It achieved the recognizing accuracy of 91%, recall rate of 81%, and F1 score of 0.85 in identifying clinic CT images of early lung nodules. The detailed information can be found in Table 1.

Figure 8 shows the qualitative result of early lung nodule detection using Faster R-CNN working on the synthesized data produced by SLS-PriGAN. The four images were randomly selected; the numbers shown in the red labels are the probability of the presence of lung nodules, e.g., 0.93 means that there is a 93% chance of the detected object being a lung nodule.

4. Conclusion

In this paper, we propose an SLS-PriGAN model with prior knowledge to generate CT images of early lung nodules from small-size labelled samples. Specifically, a knowledge acquisition network and a sharpening network are designed for priori knowledge learning, and then, a GAN model is developed to produce CT images of early lung nodules. As a result, a general FR-CNN network is trained by the CT images generated SLS-PriGAN, and it achieved a recognizing accuracy of 91%, recall rate of 81%, and F1 score of 0.85 in identifying early lung nodules in clinic CT images. This provides a viable way of identifying early lung nodules from CT Images by deep learning with small-size labelled samples. Our study focused on CT images of lung nodules; it is believed that the proposed network model should perform equally well for other problems.

For future research, it is worth investigating the priori knowledge-driven learning strategies, as well as the other kind of cancers of CT images with a small size of labelled samples [27–29], feature-based approaches [30], and a transfer learning enhanced GAN [31].

Data Availability

Data are available from the authors upon reasonable request.

Disclosure

Funding was utilized to obtain research equipment. Funding body was not involved in the design of the study, the data collection, analysis and interpretation of data, or in writing the manuscript. No authors have any other industrial links or affiliations.

Conflicts of Interest

The authors declare that they have no conflicts of interest to report regarding the present study.

Acknowledgments

This work was funded and supported by the Natural Science Foundation of China (grant nos. 61873280, 61672033, 61672248, and 61972416), Taishan Scholarship (tsqn201812029), major projects of the National Natural

Science Foundation of China (grant no. 41890851), Natural Science Foundation of Shandong Province (no. ZR2019MF012), Foundation of Science and Technology Development of Jinan (201907116), and Fundamental Research Funds for the Central Universities (18CX02152A and 19CX05003A-6).

References

- [1] S. Wang, L. Dong, X. Wang, and X. Wang, "Classification of pathological types of lung cancer from CT images by deep residual neural networks with transfer learning strategy," *Open Medicine*, vol. 15, no. 1, pp. 190–197, 2020.
- [2] S. Pang, T. Ding, A. Rodríguez-Patón, T. Song, and Z. Pan, "A parallel bioinspired framework for numerical calculations using enzymatic P system with an enzymatic environment," *IEEE Access*, vol. 6, pp. 65548–65556, 2018.
- [3] T. Song, A. Rodríguez-Patón, P. Zheng, P. Zheng, and X. Zeng, "Spiking neural P systems with colored spikes," *IEEE Transactions on Cognitive and Developmental Systems*, vol. 10, no. 4, pp. 1106–1115, 2017.
- [4] T. Song, X. Zeng, P. Zheng, M. Jiang, and A. Rodríguez-Patón, "A parallel workflow pattern modeling using spiking neural P systems with colored spikes," *IEEE Transactions on Nanobiotechnology*, vol. 17, no. 4, pp. 474–484, 2018.
- [5] G. Litjens, T. Kooi, B. E. Bejnordi et al., "A survey on deep learning in medical image analysis," *Medical Image Analysis*, vol. 42, pp. 60–88, 2017.
- [6] N. Tajbakhsh, J. Y. Shin, S. R. Gurudu et al., "Convolutional neural networks for medical image analysis: full training or fine tuning?," *IEEE Transactions on Medical Imaging*, vol. 35, no. 5, pp. 1299–1312, 2016.
- [7] H. Greenspan, B. Van Ginneken, and R. M. Summers, "Guest editorial deep learning in medical imaging: overview and future promise of an exciting new technique," *IEEE Transactions on Medical Imaging*, vol. 35, no. 5, pp. 1153–1159, 2016.
- [8] W. Yang, Y. Chen, Y. Liu et al., "Cascade of multi-scale convolutional neural networks for bone suppression of chest radiographs in gradient domain," *Medical Image Analysis*, vol. 35, pp. 421–433, 2017.
- [9] K. Bahrami, F. Shi, I. Rekik, and D. Shen, "Convolutional Neural Network for Reconstruction of 7T-like Images from 3T MRI Using Appearance and Anatomical Features," in *Deep Learning and Data Labeling for Medical Applications*, pp. 39–47, Springer, Cham, 2016.
- [10] R. Li, W. Zhang, H. I. Suk et al., "Deep Learning Based Imaging Data Completion for Improved Brain Disease Diagnosis," in *International Conference on Medical Image Computing and Computer-Assisted Intervention*, pp. 305–312, Springer, Cham, 2014.
- [11] D. Nie, X. Cao, Y. Gao, L. Wang, and D. Shen, "Estimating CT Image from MRI Data Using 3D Fully Convolutional Networks," in *Deep Learning and Data Labeling for Medical Applications*, pp. 170–178, Springer, Cham, 2016.
- [12] I. Goodfellow, J. Pouget-Abadie, M. Mirza et al., "Generative adversarial nets," *Advances In Neural Information Processing Systems*, vol. 27, pp. 2672–2680, 2014.
- [13] Salome Kazemini, Christoph Baur, Arjan Kuijper et al., "GANs for medical image analysis," 2018, <http://arxiv.org/abs/1809.06222>.
- [14] A. Kitchen and J. Seah, "Deep generative adversarial neural networks for realistic prostate lesion MRI synthesis," 2017, <http://arxiv.org/abs/1708.00129>.
- [15] T. Schlegl, P. Seeböck, S. M. Waldstein, U. Schmidt-Erfurth, and G. Langs, "Unsupervised Anomaly Detection with Generative Adversarial Networks to Guide Marker Discovery," in *International conference on information processing in medical imaging*, pp. 146–157, Springer, Cham, 2017.
- [16] M. Frid-Adar, E. Klang, M. Amitai, J. Goldberger, and H. Greenspan, "Synthetic data augmentation using GAN for improved liver lesion classification," in *2018 IEEE 15th international symposium on biomedical imaging (ISBI 2018)*, pp. 289–293, Washington, DC, USA, 2018.
- [17] C. Bermudez, A. J. Plassard, L. T. Davis, A. T. Newton, S. M. Resnick, and B. A. Landman, "Learning implicit brain MRI manifolds with deep learning, medical imaging 2018: image processing," *International Society for Optics and Photonics*, vol. 10574, 2018.
- [18] C. Baur, S. Albarqouni, and N. Navab, "Melano GANs: high resolution skin lesion synthesis with GANs," 2018, <http://arxiv.org/abs/1804.04338>.
- [19] C. Baur, S. Albarqouni, and N. Navab, "Generating highly realistic images of skin lesions with GANs OR 2.0 Context-Aware Operating Theaters, Computer Assisted Robotic Endoscopy," in *Clinical Image-Based Procedures, and Skin Image Analysis*, pp. 260–267, Springer, Cham, 2018.
- [20] T. Karras, T. Aila, S. Laine, and J. Lehtinen, "Progressive growing of GANs for improved quality, stability, and variation," 2017, <http://arxiv.org/abs/1710.10196>.
- [21] M. J. M. Chuquicusma, S. Hussein, J. Burt, and U. Bagci, "How to fool radiologists with generative adversarial networks: a visual turing test for lung cancer diagnosis," in *IEEE 15th international symposium on biomedical imaging (ISBI 2018)*, pp. 240–244, Washington, DC, USA, 2018.
- [22] J. Masci, U. Meier, D. Cireşan, and J. Schmidhuber, "Stacked Convolutional Auto-Encoders for Hierarchical Feature Extraction," in *International conference on artificial neural networks*, pp. 52–59, Springer, Berlin, Heidelberg, 2011.
- [23] F. N. Yuan, L. Zhang, J. T. Shi, X. Xia, and G. Li, "Theories and applications of auto-encoder neural networks: a literature survey," *Chinese Journal of Computers*, vol. 42, no. 1, pp. 203–230, 2019.
- [24] A. B. L. Larsen, S. K. Sønderby, H. Larochelle, H. Larochelle, and O. Winther, "Autoencoding beyond pixels using a learned similarity metric," *Proceedings On Machine Learning*, vol. 48, pp. 1558–1566, 2016.
- [25] M. Arjovsky and L. Bottou, "Towards principled methods for training generative adversarial networks," 2017, <http://arxiv.org/abs/1701.04862>.
- [26] I. Gulrajani, F. Ahmed, M. Arjovsky, V. Dumoulin, and A. C. Courville, "Improved training of wasserstein GANs," *Advances In Neural Information Processing Systems*, vol. 30, pp. 5767–5777, 2017.
- [27] S. Pang, Y. Zhang, M. Ding, X. Wang, and X. Xie, "A deep model for lung cancer type identification by densely connected convolutional networks and adaptive boosting," *IEEE Access*, vol. 8, pp. 4799–4805, 2020.
- [28] X. Meng, X. Li, and X. Wang, "A computationally virtual histological staining method to ovarian cancer tissue by deep generative adversarial networks," *Computational and Mathematical Methods in Medicine*, vol. 2021, article 4244157, 2021.

Retraction

Retracted: Glymphatic System: Emerging Therapeutic Target for Neurological Diseases

Oxidative Medicine and Cellular Longevity

Received 1 August 2023; Accepted 1 August 2023; Published 2 August 2023

Copyright © 2023 Oxidative Medicine and Cellular Longevity. This is an open access article distributed under the Creative Commons Attribution License, which permits unrestricted use, distribution, and reproduction in any medium, provided the original work is properly cited.

This article has been retracted by Hindawi following an investigation undertaken by the publisher [1]. This investigation has uncovered evidence of one or more of the following indicators of systematic manipulation of the publication process:

- (1) Discrepancies in scope
- (2) Discrepancies in the description of the research reported
- (3) Discrepancies between the availability of data and the research described
- (4) Inappropriate citations
- (5) Incoherent, meaningless and/or irrelevant content included in the article
- (6) Peer-review manipulation

The presence of these indicators undermines our confidence in the integrity of the article's content and we cannot, therefore, vouch for its reliability. Please note that this notice is intended solely to alert readers that the content of this article is unreliable. We have not investigated whether authors were aware of or involved in the systematic manipulation of the publication process.

Wiley and Hindawi regrets that the usual quality checks did not identify these issues before publication and have since put additional measures in place to safeguard research integrity.

We wish to credit our own Research Integrity and Research Publishing teams and anonymous and named external researchers and research integrity experts for contributing to this investigation.

The corresponding author, as the representative of all authors, has been given the opportunity to register their agreement or disagreement to this retraction. We have kept a record of any response received.

References

- [1] X. Xuan, G. Zhou, C. Chen et al., "Glymphatic System: Emerging Therapeutic Target for Neurological Diseases," *Oxidative Medicine and Cellular Longevity*, vol. 2022, Article ID 6189170, 14 pages, 2022.

Review Article

Glymphatic System: Emerging Therapeutic Target for Neurological Diseases

Xianjun Xuan ¹, Guoyi Zhou,² Caihong Chen,¹ Anwen Shao ³, Yunxiang Zhou ⁴,
Xiaobo Li,¹ and Jiaqi Zhou⁵

¹Department of Neurology, Hangzhou Ninth People's Hospital, Hangzhou, China

²The Fourth School of Clinical Medicine, Zhejiang Chinese Medical University, Hangzhou, China

³Department of Neurosurgery, The Second Affiliated Hospital, School of Medicine, Zhejiang University, Hangzhou, China

⁴Department of Surgical Oncology, The Second Affiliated Hospital, School of Medicine, Zhejiang University, Hangzhou, China

⁵State Key Laboratory for Diagnosis and Treatment of Infectious Diseases, National Clinical Research Center for Infectious Diseases, Collaborative Innovation Center for Diagnosis and Treatment of Infectious Diseases, The First Affiliated Hospital, College of Medicine, Zhejiang University, China

Correspondence should be addressed to Xianjun Xuan; xianjunxjx@163.com and Anwen Shao; 21118116@zju.edu.cn

Received 27 April 2022; Revised 15 May 2022; Accepted 24 May 2022; Published 11 June 2022

Academic Editor: Shao Liang

Copyright © 2022 Xianjun Xuan et al. This is an open access article distributed under the Creative Commons Attribution License, which permits unrestricted use, distribution, and reproduction in any medium, provided the original work is properly cited.

The newly discovered glymphatic system acts as pseudolymphatic vessels subserving brain waste clearance and is functionally dependent on astrocytic aquaporin-4 channels. The glymphatic system primarily functions during sleep as an interchange between cerebrospinal fluid and interstitial fluid, with cerebrospinal fluid flowing into the parenchyma via the perivascular spaces and then exchanging with interstitial fluid. The discovery of meningeal lymphatics helps refine the conceptual framework of glymphatic pathway, as certain waste products collected alongside perivascular spaces ultimately drain into the cervical lymph nodes via meningeal lymphatics, whose function regulates the functioning of the glymphatic system. The glymphatic and meningeal lymphatic systems are critical for the homeostasis of central nervous system, and their malfunctions complicate cerebral dysfunction and diseases. The present review will shed light on the structure, regulation, functions, and interrelationships of the glymphatic system and meningeal lymphatics. We will also expound on their impairments and corresponding targeted intervention in neurodegenerative diseases, traumatic brain injury, stroke, and infectious/autoimmune diseases, offering valuable references for future research.

1. Introduction

Homeostasis is vital for tissue health. Excess fluid and soluble proteins from the interstitial tissue space are returned to the circulation via the lymphatic system in peripheral tissue and organs [1–3]. Although the central nervous system (CNS) has a high metabolic rate, it lacks a conventional lymphatic system, which has made brain waste clearance, cerebrospinal fluid (CSF)/interstitial fluid (ISF) outflow mechanisms, and neuromonitoring a realm of enigmas and mystery for a long time [2, 4]. Emerging studies have reported the existence of meningeal lymphatics and demonstrated that there is a perivascular pathway acting as pseudo-

lymphatic vessels for brain waste clearance. It functionally depends on aquaporin-4 (AQP4) channels, the main water channels of astrocytes, thereby referred to as a glial-lymphatic or glymphatic system [5–7]. This unravels several questions, casting a spotlight.

CSF and ISF constitute the extracellular fluid of the brain [8]. The former is mainly secreted by the choroid plexus and is considered the leading way to remove metabolic waste products from CNS [5, 9]. However, the latter may be secreted by blood-brain barrier (BBB) and surrounds the brain parenchyma, delivering fluid and solute to brain cells and directly removing waste products from those cells [10–13]. CSF and ISF exchange plays a pivotal role in the

waste clearance within CNS, including toxic proteins like amyloid β ($A\beta$) and tau [14]. Notably, the underlying mechanisms of extracellular fluid circulation and metabolism are strongly correlated with the glymphatic system and meningeal lymphatics, significantly affecting the waste clearance and fluid balance. Mechanically, the glymphatic system functions as an interchange between them and facilitates their exchange [6]. Meningeal lymphatics perform the function of CSF absorption and waste clearance, transporting immune cells and soluble substances to peripheral lymph nodes [15–17]. Generally, there are three pathways of CSF drainage: (1) CSF from the subarachnoid space drains directly into the blood via the arachnoid villi of the superior sagittal sinus, (2) CSF from the subarachnoid space drains into the lymph nodes via the subarachnoid spaces around the olfactory nerves and nasal lymphatics, and (3) meningeal lymphatics disgorge macromolecules and immune cells of CSF into the cervical lymph nodes [18–21].

Given their critical impact on the maintenance of CNS homeostasis, the impairments of glymphatic system and meningeal lymphatics may lead to cerebral dysfunction and diseases [8]. Increased evidence has revealed that the dysfunction of glymphatic/meningeal lymphatic system is implicated in various neurological diseases, such as Alzheimer's disease (AD), stroke, traumatic brain injury (TBI), and infectious/autoimmune diseases [21–25]. This study reviews the recent findings concerning characteristics, functions, and relationships of glymphatic system and meningeal lymphatics. We also elaborate on the crosstalk between glymphatic/meningeal lymphatic system and neurological disorders and discuss corresponding targeted interventions, which may lend significant therapeutic promise.

2. The Discoveries of Glymphatic and Meningeal Lymphatic Systems

2.1. Classical Model of the Circulation of Extracellular Fluid. It is traditionally thought that the choroid plexus secretes CSF. It then flows from lateral ventricles to the third ventricle through the foramen of Monro, subsequently passing across the aqueduct to the fourth ventricle, where CSF enters subarachnoid space through the apertures of Magendie and Luschka and is eventually absorbed into the blood at the arachnoid villi [9, 26]. However, there was no consensus on the mechanism for draining through arachnoid villi. Researchers did not find direct evidence to confirm the function of arachnoid villi [27, 28]. Ma et al. recently proposed that lymphatic outflow was the primary route to draining CSF [29]. In this model, the choroid plexus is the leading site of CSF formation, secreting approximately 80–90% of the total CSF [8, 30]. Unlike BBB, there are no tight junctions between the endothelial cells in the choroid plexus, which is beneficial to fluid infiltration in blood [2, 8]. However, tight junctions are present between epithelial cells to regulate CSF secretion [2, 8, 30]. The main driver of the CSF secretion is metabolic energy to fuel the Na-pump [31]. In addition to the osmotic pressure gradient, the high AQP1 expression at the apical membrane contributes to high fluid permeability [26]. Besides arachnoid villi, CSF absorption

can be achieved through two other routes: (1) passing along olfactory nerves across the cribriform plate to the nasal mucosa and then entering the cervical lymphatics or (2) flowing through the spinal nerve root into blood or lymph [10, 32].

Another type of extracellular fluid of the brain, ISF, is produced by the capillary-astrocyte complex of BBB, providing a necessary environment for brain cells [10, 12, 26]. ISF surrounds the brain parenchyma with the metabolic waste products of brain cells dissolved inside and drains to CSF to renew itself, while CSF acts like lymphatics and causes eventual waste removal from CNS [8]. Although CSF's clearance of waste from the brain is widely accepted, it remains unclear how CSF exchanges with ISF to remove metabolic waste products.

2.2. Novel Discoveries of the Circulation of Extracellular Fluid. Due to developing neuroanatomy, molecular biology, and neuroimaging, discoveries regarding the circulation of CSF and ISF have emerged. For instance, researchers have found that choroidectomy did not cure hydrocephalus, suggesting the existence of other CSF sources [10, 33]. Correspondingly, novel assumptions have been put forward. Brinker et al. proposed a model in which CSF and ISF are formed and absorbed directly in the capillaries rather than passing through the choroid plexus to arachnoid villi [26]. Nevertheless, this model was inadequate as CSF flow through the aqueduct was observed using magnetic resonance imaging (MRI) [34]. Some researchers combined the two abovementioned models to generate a new one, which was thought to provide new insights into CSF formation [2]. More attractively, recent work has demonstrated the presence of glymphatic and meningeal lymphatic systems, uncovering more precise mechanisms underlying the exchange and outflow of extracellular fluid.

2.3. The Discovery of the Glymphatic System. Recent discoveries about the brain's glymphatic system have garnered considerable debate [6, 17, 35]. Many details about glymphatic systems were described decades ago. For instance, Cserr et al. conducted several experimental studies by injecting traceable solutes into the brain to identify the pathway of fluid removal [36–38]. They also found that removal rates of traceable solutes were almost identical, regardless of the molecular size and weight [37, 38]. It was concluded that the communication of ISF and CSF occurred in a specialized pathway in the brain by convection [14]. Moreover, studies revealed that CSF could penetrate the brain parenchyma through perivascular space via convection [8, 39, 40]. However, this conclusion was questioned for decades before Iliff et al. made a breakthrough in 2012 [6, 14]. Iliff et al. used two-photon imaging and Tie2-GFP: NG2-DsRed double reporter mice to investigate the flow of CSF in the brain parenchyma [6]. They demonstrated CSF and ISF exchange and the efflux of mixed CSF and ISF out of the brain and the perivenous space.

Given that the function of this perivascular pathway was similar to that of the lymphatic system, with astrocytic AQP4 playing a crucial role in it, it was therefore termed the glial-lymphatic system or glymphatic system [6].

Notably, Carare et al. concluded that solutes drained out along the basement membranes of capillaries and arteries, flowing in the direction opposite to arterial blood [18]. The outflow pathway of glymphatic system remains a debate. Bakker et al. proposed that the existence of these two pathways, separated by meningeal sheets, could explain the debate [41]. They also proposed that different research methods might contribute to different findings [41]. However, this debate is yet to be settled by experiments.

The glymphatic system consists of periarterial CSF, flowing in the same direction as blood, propelled by the pulsatility of the arterial wall [42, 43]. CSF and ISF mix in a process aided by AQP4 water channels abundant at the vascular astrocytic end-feet [44]. The influx of fluid across BBB or extrachoroidal sources of CSF may also contribute to glymphatic flow [45–47]. CSF and ISF mixture leaves the brain via the perivascular space and along cranial and spinal nerves. This fluid is eventually transported out of CNS by traditional lymphatic vessels located in the meninges and the soft tissue surrounding the skull. The current wave of great interest in the glymphatic system is probably that the glymphatic system concept has articulated a function of the transport system by demonstrating its role in $A\beta$ clearance [6]. The glymphatic system clears key proteins involved in neurodegeneration. In contrast, inhibiting glymphatic system transport accelerates protein accumulation and cognitive decline in mouse models of Alzheimer's disease, traumatic brain injury, and Parkinson's disease [20, 25, 48], indicating that the glymphatic system is an attractive brain waste removal system.

2.4. The Discovery of Meningeal Lymphatics. In the 18th century, physician Paolo Mascagni discovered lymphatic vessels in the meninges and made people conscious of their existence [32]. However, his view was not initially understood and accepted by others [32]. Over the next 200 years, several studies suggesting the presence of lymphatic vessels in the meninges [49–51] appeared with questions [32]. Researchers recently confirmed Paolo's conjecture by detecting the lymphatic epithelial cell markers (e.g., LYVE-1, VEGFR3, PDPN, CCL21, and PROX1) in mouse meningeal vessels using immunofluorescence staining [15, 17]. Alitalo et al. addressed the existence of meningeal lymphatic vessels in CNS alongside the arteries, veins, and cranial nerves in mice [15]. It was further discovered that meningeal lymphatics exist not only in mice but also in other animals and humans [16, 32] (Table 1). Zhou et al. visualized the clearance of meningeal lymphatics based on brain 3-dimensional T1-weighted imaging in humans, which supported the existence of meningeal lymphatic vessels in the human CNS [52]. Furthermore, Louveau et al. showed that the characteristics of meningeal lymphatics are consistent with the initial lymphatic vessels, both lacking smooth muscle cells [17].

The brain was considered immune-privileged because of the absence of a lymphatic system in CNS [53]. The concept of CNS immune privilege was proposed for allografts surviving longer in the brain compared with the periphery [54]. Another experiment showed that skin allografts into the brain caused late graft rejection, consistent with the findings mentioned above [55]. However, recent evidence has over-

turned the idea that CNS lacks lymphatic vessels [16, 35]. The discovery of meningeal system makes CNS connected to peripheral lymphatics [54]. As discussed above, CSF drained antigens, activated T cells and other immune cells to cervical lymph nodes through the meningeal system, and then induced an immune response in cervical lymph nodes [4, 17, 54]. This may explain why allografts survived longer in the brain [4].

The meningeal system played a key role in immune surveillance. The immune cells and antigen-presenting cells (APCs) in CSF were drained to cervical lymph nodes via the meningeal system [54]. Antigens from the brain presented to the APCs activate immune cells such as T cells in lymph nodes and induce them to enter the brain across BBB using specific adhesins (ICAM-1 and VCAM-1) [54]. In addition, lymphatic endothelial cells of meningeal vessels contribute to the tolerance of T cells in CNS, which is vital in maintaining the homeostasis of CNS [53].

3. Glymphatic System and Meningeal Lymphatics

3.1. AQP4 in the Glymphatic System

3.1.1. The Distribution of AQP4. AQP4 is one of 14 aquaporins that are only found on astrocytes and are primarily found in their foot processes [10, 56, 57]. AQP4 is expressed as a tetramer [8]. There are two isoforms of AQP4, M1, and M23 [56]. The supramolecular structure assembled by M23 is called orthogonal arrays of particles (OAPs), which can enhance water permeability and promote the polarization of AQP4 to the astrocyte end-feet. Astrocytes stretch these particles to the microvessels to constitute the perivascular space and glial limiting membranes and sheathe the BBB [56, 57]. Moreover, AQP4 anchors to the dystrophin-associated protein complex (DAPC) attached to the perivascular glial basement membrane [8]. These characteristics reflect the high density of AQP4 in the perivascular space.

3.1.2. The Function of AQP4. AQP4 is a regulator for the transcellular transport of water and facilitates the rapid movement of water flow across the membrane [58]. The high AQP4 expression in perivascular space plays a vital role in the influx and efflux of the glymphatic pathway [6]. AQP4 reduces the resistance of CSF and ISF exchange in the glymphatic system [4, 6]. Iiff et al. found that the flow velocity of tracer solutes did not reduce in the periarterial space but significantly reduced when passing from the perivascular space to the interstitial space in AQP4-null mice, suggesting that AQP4 affects the fluid flow in this interface [6]. Additionally, the removal rates of interstitial solutes and $A\beta$ were reduced by 70% and 55%, implying that AQP4 is critical for the clearance of brain waste products [6]. These findings are consistent with other studies, revealing that the function of the glymphatic system mainly depends on AQP4 [59, 60].

3.2. The Driving Force of the Glymphatic System

3.2.1. The Driving Force. The fluid transportation of glymphatic system involves multiple mechanisms [8]. Iiff et al.

TABLE 1: Recently published human studies on the glymphatic system and meningeal lymphatics.

References	Year	Subjects or samples (list only human)	Imaging and mapping techniques	Main findings
Absinta et al. [16]	2017	5 healthy volunteers (three women, age range 28–53 years) and 3 healthy adult common marmosets (one female, two males, age range 4–11 years)	T2-FLAIR and T1-weighted black-blood MRI imaging, with gadolinium-based contrast agents	The existence of lymphatic vessels within the dura mater of human and nonhuman primates
Louveau et al. [17]	2015	9 autopsy specimens of human dura including the superior sagittal sinus	Leica TCS SP8 confocal system, Lyve-1 staining	The lymphatic structures were identified in two of nine human samples
Zhou et al. [52]	2020	35 patients (18 males, mean age: 52 years, age range: 21–71 years; 17 females, mean age: 58 years, age range: 18–79 years) with neurological disorders	Head T1-weighted imaging and head high-resolution T2-FLAIR MRI imaging, with contrast agent: gadodiamide	Glymphatic pathway and pMLVs might be impaired in the aging human brain; pMLVs are the downstream of the glymphatic pathway
Hasan-Olive et al. [59]	2019	Cortical brain biopsies of 30 iNPH patients (15 males and 15 females, mean age: 71 years) and 12 reference patients (6 males and 6 females, mean age: 44 years)	Semiquantitative immunogold electron microscopy	Perivascular AQP4 expression was attenuated in iNPH patients, potentially contributing to impaired glymphatic clearance
Kiviniemi et al. [62]	2016	9 healthy volunteers (5 females, age range: 21–30 years)	Novel multimodal ultrafast MREG technology	Three distinct pulsation mechanisms of the human glymphatic system coexist, and these pulsations can be separated using ultrafast MRI techniques

FLAIR: fluid-attenuation inversion recovery; MRI: magnetic resonance imaging; pMLVs: putative meningeal lymphatic vessels; iNPH: idiopathic normal pressure hydrocephalus; AQP4: aquaporin-4; MREG: magnetic resonance encephalography.

showed that ligation of the internal carotid artery reduced CSF influx while dopamine, an inotropic adrenergic agonist, increased it [42]. They suggested that cerebral arterial pulsation, including its amplitude and frequency, was a primary driving force for CSF influx in the glymphatic system [42]. This conclusion is further verified by Liu et al., who found that acute alcohol exposure reduced cerebral vascular pulsation, provoking the reduction of CSF influx in the glymphatic system [61]. Furthermore, the respiratory-related pulsatile cycle promotes the centripetal venous fluid flow, augmenting perivenous spaces and driving CSF outflow in the glymphatic system [62].

Intracranial pressure (ICP) is another driving force of the glymphatic system [58]. When CSF communicates with the outside, ICP decreases, and the solute clearance rate in the glymphatic system decreases significantly [58]. Meanwhile, ICP is related to the head posture, as it decreases when the head moves from supine to upright [58].

3.2.2. Action Time. The glymphatic system functioning is primarily active during sleep and is primarily suppressed during the awake state [8, 58]. CSF influx can be reduced by 95%, and $A\beta$ clearance can be slowed by half on awakening [63]. Xie et al. suggested that the state of consciousness determined the rate of solute clearance in the glymphatic system in mice rather than the circadian rhythm [63]. They also found that CSF influx increased after inhibiting the adrenergic signaling during wakefulness [63]. Consistent with this, another study found that the glymphatic transport increased by 32% in rats anesthetized with dexmedetomi-

dine, which lowers norepinephrine, plus low-dose isoflurane, which does not, compared with high-dose isoflurane only [64]. Adrenergic signaling activation in the awake state may affect the glymphatic pathway transport.

3.3. The Function of the Glymphatic System. As mentioned above, the glymphatic system is an interchange between CSF and ISF and facilitates their exchange to promote waste removal (Figure 1) [4, 6]. As a result, one of the most significant functions of glymphatic system is removing the metabolic waste products [8], which include $A\beta$ and tau and are associated with neurological diseases when accumulated from CNS [65]. The glymphatic system achieves the clearance of lactate from wakefulness to sleep [66].

The glymphatic system also serves as a key player in nutrient distribution [8], brain energy supply (via glucose delivery) [67], and lipid transport and signaling [68]. The diffusion of lipids in the glymphatic system is highly selective, which may be related to the high density of astrocyte-secreted lipoproteins and lipid transport carriers. In contrast, an impaired glymphatic system leads to unselective diffusion of lipid and abnormal astrocyte calcium signaling [68]. The glymphatic system can also facilitate the distribution of apolipoprotein E (ApoE) in the brain, which removes excess $A\beta$ and maintains brain homeostasis [2, 7]. Recent work found that fluid stress opened N-methyl-D-aspartic acid (NMDA) receptors in astrocytes, increasing calcium current, suggesting that the glymphatic system might play a role in mechanotransduction [8].

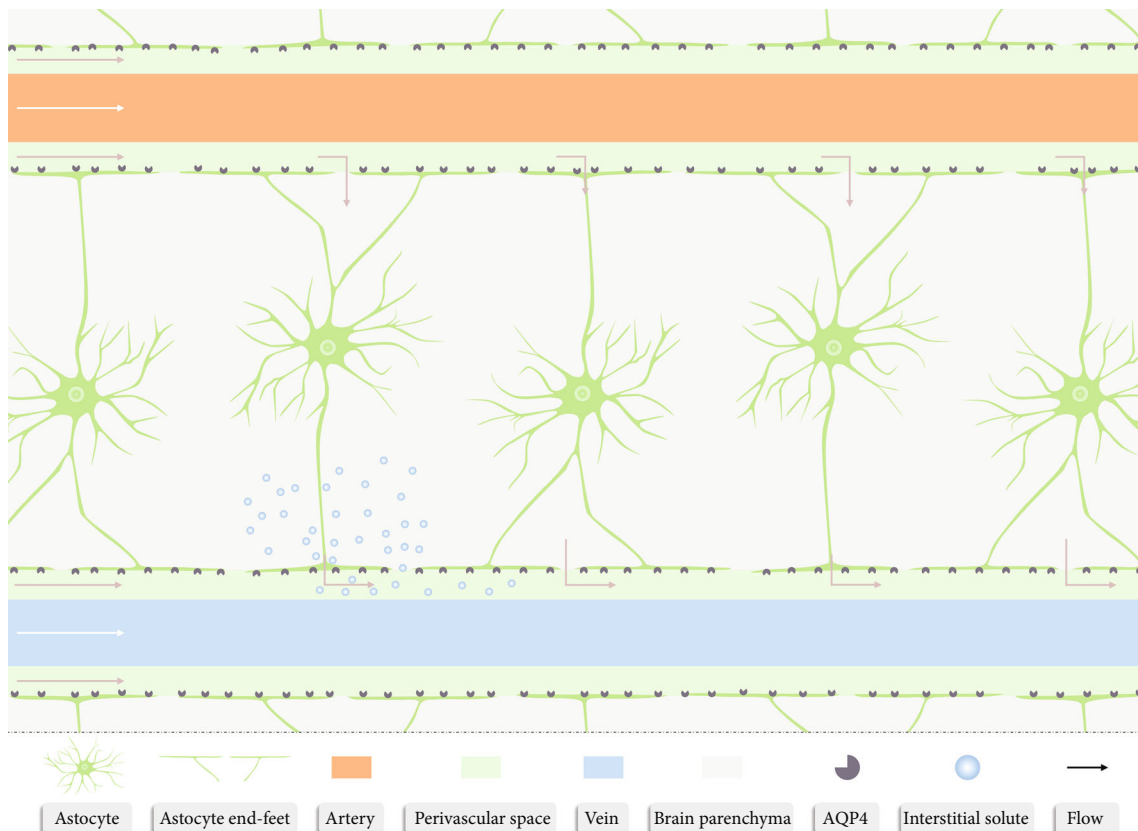


FIGURE 1: The glymphatic system functions as an interchange between cerebrospinal fluid (CSF) and interstitial fluid (ISF) and facilitates their exchange to promote waste removal. CSF within the subarachnoid space flows into the parenchyma via the periarterial space and subsequently exchanges with ISF, which is facilitated by astrocytic aquaporin-4 and drives the convective flow of interstitial solutes and ISF into perivenous spaces. Eventually, mixed CSF, ISF, and interstitial solutes flow along the perivenous space to remove metabolic waste products away from the brain parenchyma.

3.4. The Function of Meningeal Lymphatic System and Its Interaction with the Glymphatic System. The novel discovery of meningeal lymphatics as a complementary route for CSF and ISF clearance has attracted much attention [15, 17]. Alitalo et al. disclosed that meningeal lymphatics absorbed CSF from subarachnoid space and brain ISF via the glymphatic system, draining CSF directly into the deep cervical lymph nodes (dCLNs) in mice [15]. Their findings are consistent with those of Zhou et al. [52]. Notably, meningeal lymphatics played a crucial role in the clearance of macromolecules, whose clearance from CNS and transfer from the subarachnoid space into dCLNs could be attenuated and abrogated upon the aplasia of the meningeal lymphatic system [15]. After injecting Evans blue, Louveau et al. found that Evans blue appeared successively in meningeal lymphatics, dCLNs, and superficial cervical lymph nodes (sCLNs) in human samples and mice [17]. They concluded that meningeal lymphatics were the main pathway for draining specific solutes from CSF and ISF into dCLNs [4, 17]. However, Ma et al. declared perineural pathways to be a major route to drain solutes from the brain to dCLNs, as they found that P40D680, a kind of pegylated near-infrared tracers, drained along the perineural (e.g., olfactory nerve and optic nerve) pathway, while no signal was detected in the meningeal lymphatic vessels [29]. These contradictory

findings may be explained by the different tracers used, warranting further experiments to uncover the mystery.

CSF delivers cytokines, neurotransmitters, and hormones throughout the brain and removes metabolic waste products away from the brain parenchyma by exchanging with ISF via the glymphatic system [5, 6, 9, 53]. CSF is enriched with interstitial solutes and drains to the periphery mostly through meningeal lymphatics, which play an important role in macromolecule removal (Figure 2) [15]. Notably, the drainage of meningeal lymphatics is positively related to the CSF influx in the glymphatic system [20]. The glymphatic system functioning is regulated by the function of the meningeal lymphatic system [20]. The glymphatic and meningeal lymphatic systems are coupled in the exchange and circulation of the brain's extracellular fluid. The discovery of meningeal lymphatics helps refine the conceptual framework of the glymphatic pathway.

4. Glymphatic Pathway and Neurodegenerative Diseases

4.1. Neurodegenerative Diseases. Neurodegenerative diseases, a group of clinical diseases including AD, Parkinson's disease, and others, are characterized by the accumulation of pathological proteins, such as $A\beta$, tau, and α -synuclein

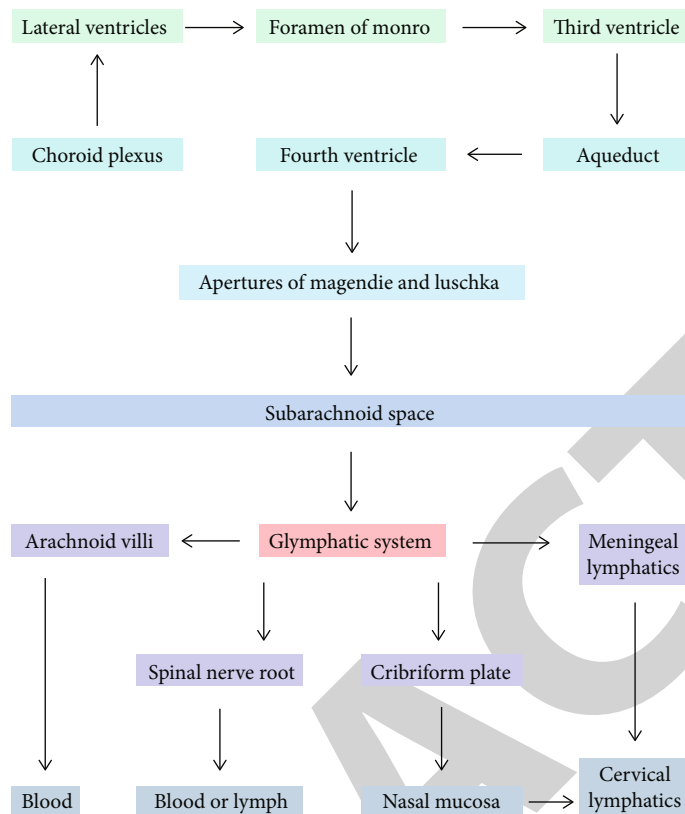


FIGURE 2: Schematic diagram of the circulation of cerebrospinal fluid (CSF) in the brain. CSF secreted by the choroid plexus flows into the subarachnoid space through the apertures of Magendie and Luschka of the fourth ventricle and then enters the perivascular spaces (glymphatic system). CSF collected alongside perivascular spaces ultimately drains into the periphery through meningeal lymphatics, arachnoid villi, the cribriform plate, and the spinal nerve root.

[2, 69]. AD is the most common neurodegenerative disease, affecting 10-30% of the population over the age of 65 [70]. AD is characterized as a chronic progressive disease that involves cognitive impairment and neuropsychiatric abnormalities [70], with a global burden of US\$ 818 billion in 2015, with a 35% increase over the previous five years [71]. AD is generally in an advanced stage when diagnosed [70]. Patients with different AD forms are often accompanied by dementia [72]. The median survival time for AD patients is approximately 7.1 years, an apparent reduction in life expectancy [70]. AD management mainly relies on pharmacotherapies, including NMDA receptor antagonists (e.g., memantine) and cholinesterase inhibitors (e.g., donepezil, galantamine, and rivastigmine). However, their efficacies are limited to slowing down the progress of cognitive impairment [72]. Therefore, novel therapeutics are urgently required.

4.2. Crosstalk between the Glymphatic Pathway and AD. AD is featured with the accumulation of amyloid plaques and neurofibrillary tangles of hyperphosphorylated protein tau [65, 69]. The hyperphosphorylated protein tau is often thought to be produced in the later stage of AD [73], and the accumulation of $A\beta$ is considered the predominant cause of AD [73]. $A\beta$ clearance involves a series of mechanisms, including phagocytosis by myelomonocytes, degradation by astrocytes and neurons, and drainage into the peripheral

circulation or lymphatic system via the BBB and glymphatic system [74, 75]. Although the drainage route through BBB into blood is responsible for 75% of $A\beta$ removal, the glymphatic pathway is an indispensable alternative route [32], and the impaired glymphatic system is adequate to yield a decreased clearance rate of $A\beta$ and tau [6, 75, 76]. The aggregation of $A\beta$ can inhibit the function of glymphatic system by constricting blood vessels, resulting in glymphatic influx suppression [77].

Moreover, the circulation of $A\beta$ in the brain is mediated by the glymphatic system, and prolonged circulation of $A\beta$ that has not been cleared in time may trigger the formation of amyloid plaques, which reduce the perivascular space of the glymphatic system, impairing the exchange efficiency of CSF and ISF [77]. In addition, amyloid plaques can lead to cerebral amyloid angiopathy (CAA) development [78, 79]. CAA boosts arteriosclerosis and reduces arterial pulsation [78, 79], which in turn further reduces the clearance efficiency of glymphatic system [75]. These discoveries suggest a vicious cycle in which $A\beta$ accumulation facilitates the dysfunction of glymphatic system, resulting in further reduced clearance of $A\beta$ and amyloid plaque formation [75]. The dysfunction of meningeal lymphatics also aggravates AD [20, 80], which is reflected by the critical role meningeal lymphatics play in CSF circulation and macromolecule clearance [4]. Altogether, the impairment of

glymphatic/meningeal lymphatic systems may be a risk factor for AD onset and development.

As a determinant of the function of glymphatic system, AQP4 regulates $A\beta$ removal [6, 48]. Iliff et al. found that $A\beta$ clearance decreased by 55% in AQP4 knockout mice [6]. Similarly, Xu et al. displayed that AQP4 knockout aggravated $A\beta$ accumulation and the cognitive impairment of $A\beta$ precursor protein/presenilin 1 mice, a pathological model of AD [48]. They also found that AQP4 knockout did not affect $A\beta$ formation and degradation [48]. Amyloid plaque deposition is mainly associated with the impairment of $A\beta$ clearance rather than the increase of $A\beta$ formation [58]. Moreover, aging is a significant predisposing factor for AD [81]. Although AQP4 expression can increase in the aging brain, the loss of perivascular AQP4 localization increases the vulnerability of the aging brain to the disaggregation of pathological proteins [82]. Zhou et al. demonstrated that the glymphatic system might be impaired in older people, which may accumulate $A\beta$ [52]. Notably, AQP4 and $A\beta$ aggregation also interact, forming a vicious circle. Long-term accumulation of $A\beta$ leads to the atrophy and malfunction of astrocytes, which in turn reduces the clearance of $A\beta$ [48]. Furthermore, amyloid plaque and reactive astrogliosis in AD pathology can inhibit AQP4 polarization to astrocyte end-feet, resulting in a decrease in $A\beta$ removal in the glymphatic system [48, 77].

Sleep deprivation has been revealed to increase AD susceptibility [83–85]. It can induce the impairment of glymphatic system functioning, leading to $A\beta$ accumulation and accelerating amyloid plaque formation [63, 85, 86]. Besides, sleep deprivation-induced glymphatic malfunction hinders ApoE delivery, reducing $A\beta$ clearance across BBB [87]. In addition, sleep deprivation is associated with $A\beta$ production [84]. Shorter sleep time and poor sleep quality can lead to higher levels of $A\beta$ burden [84]. Although we have explained that reduced $A\beta$ clearance mainly accounts for AD occurrence and development [58], we cannot rule out the role of increased $A\beta$ production in AD pathogenesis, which requires further investigation.

4.3. Glymphatic Pathway as a Novel Therapeutic Target for AD. The discovery of the glymphatic pathway provides promising strategies for treating AD [80]. The restoration of cerebral arterial pulsation in AD patients can preserve the driving force of the glymphatic system, holding a therapeutic potential [42, 75]. It is suggested that protecting smooth muscle cells to maintain pulsation may prevent AD [75, 88]. AQP4 polarization destroyed by AD in the astrocyte end-feet serves as a candidate mechanism for intervention. N-3 polyunsaturated fatty acids (PUFAs) have been demonstrated to protect the polarization of AQP4, increase $A\beta$ removal in the glymphatic system, and avoid amyloid plaque formation [89]. Melatonin can improve sleep quality, potentially enhancing the activation of the glymphatic system and increasing $A\beta$ removal [83, 90]. However, melatonin has not been revealed to significantly improve cognitive ability in AD patients [90]. More preclinical and clinical studies regarding the precise mechanisms of glymphatic malfunction in AD and related targeted therapy are required.

5. Glymphatic Pathway and Traumatic Brain Injury

5.1. Traumatic Brain Injury. TBI is the structural or functional disruption of the brain caused by external forces, which often occurs in soldiers and athletes [91–93]. TBI is now considered a public health crisis and a leading cause of death and disability worldwide [91, 92, 94]. TBI incidence is about 349 per 100000 persons per year, of which mild traumatic brain injury (mTBI) accounts for the majority, with an incidence of around 224 per 100000 persons per year [91, 92]. It is estimated that 50% of individuals would be affected by TBI in their lifetime [91]. TBI is a heterogeneous disease with diverse clinical manifestations, complicating the management strategies [92, 95]. This may be attributed to the complexity of the brain and the secondary injury [96]. So far, few effective TBI therapies have been developed [96–98]. TBI survivors usually suffer from various sequelae, including cerebrovascular disease, cerebral concussion, coma [98], and some chronic complications, such as neurodegenerative diseases [99] and sleep disorders [100, 101]. These sequelae impose a more significant burden on societies, patients, and families than TBI itself [98].

5.2. Crosstalk between Glymphatic Pathway and TBI. Growing evidence demonstrates that TBI is a risk factor for tauopathies, including AD, chronic traumatic encephalopathy (CTE), and frontal-temporal dementia (FTD) [102–104]. Tauopathy refers to the formation of neurofibrillary tangles (NFT) composed of hyperphosphorylated tau [105]. Mechanically, the glymphatic system is impaired in TBI, leading to the reduction of tau removal and ultimately aggravating the tauopathy [25].

Brain edema is a frequent manifestation of TBI, altering ICP and suppressing the glymphatic system [106]. After TBI, glial scars characterized by hypertrophic glial fibrillary acidic protein- (GFAP-) positive astrocytes and reactive astrogliosis surround the ipsilateral hemispheres, changing the polarization and localization of AQP4 to affect the clearance of glymphatic system, with the recovery time proportional to the severity of TBI [25, 107]. AQP4 expression may not fully recover after 28 days in severe TBI [93]. These post-TBI changes cause the dysfunction of the glymphatic system, resulting in decreased glymphatic influx and waste removal [2, 25]. TBI impairs the clearance of tau and increases the production of tau, further accumulating interstitial tau [108].

The dysfunctional glymphatic pathway is a key player in post-TBI neuroinflammation, a “double-edged sword” that may be beneficial, increasing debris clearance or harm and accelerating nerve cell death [109]. The increased waste due to the dysfunction of glymphatic system can trigger or enhance inflammatory responses [109]. Moreover, the altered association of meningeal vessels and peripheral lymphatics post-TBI may further lead to inflammatory disequilibrium and worse outcomes [109].

The recently discovered enlarged perivascular space (ePVS) may be a marker of the dysfunction of glymphatic clearance [110]. A positive correlation between sleep deprivation and ePVS has been observed in TBI [111]. Sleep

disturbances are prevalent following TBI, particularly in mTBI victims [112]. About 80% of mTBIs are linked to sleep disturbances, in which insomnia is the most common [113], underlying the impairments of glymphatic system post-TBI [63]. Sleep deprivation may trigger or aggravate other complications and sequelae of TBI, including neurodegenerative diseases [112].

5.3. Glymphatic Pathway as a Novel Therapeutic Target for TBI. Reactive astrogliosis is implicated in a myriad of pathologic mechanisms of TBI, including the loss of AQP4 polarization [25, 57]. Inhibiting reactive astrogliosis may restore the glymphatic system by keeping AQP4 polarized [25]. Studies have demonstrated the potential of stem cells in TBI treatment, and one of the mechanisms is that stem cells may inhibit the reactive astrogliosis by suppressing inflammatory response [114]. Moreover, recent work disclosed that post-TBI anesthetics increased the uptake of dendrimer nanoparticles enriched with anti-inflammation drugs in glial cells, thus enhancing the efficiency of drugs and leading to better restoration of the function of neuroglia and the glymphatic system [115]. However, this finding was obtained in cell experiments [115] and must be further validated *in vivo*. Furthermore, craniostomy, a novel surgical procedure, can recover ICP and the function of glymphatic system after TBI [106].

6. Glymphatic Pathway and Stroke

6.1. Stroke. Stroke, the second leading cause of death and the third leading cause of disability worldwide, can be classified into ischemic stroke and hemorrhagic stroke [116–118]. Stroke affects 13.7 million people every year worldwide, with a global annual cost of US\$ 34 billion [116, 119]. It is estimated that one in every four adults will experience a stroke during their lifetime [116]. Ischemic stroke accounts for 71% of global strokes [116]. The incidences of ischemic stroke in men and women are approximately 133 and 99 per 100,000 persons, respectively [117]. Hemorrhagic stroke includes subarachnoid hemorrhage (SAH) and intracranial hemorrhage (ICH), the incidences of which are 9.1 and 24.6 per 100,000 persons, respectively [120, 121]. The incidence and mortality of stroke have declined gradually over the past two decades [116, 117, 122]. However, the rate of mortality decline has slowed in recent years and is even increasing [119]. Stroke survivors may never fully recover neurological function [121]. The disability-adjusted life-year (DALY) due to stroke was 113 million in 2013 [117]. Therefore, stroke still poses a significant challenge for society. It is necessary to explore a new therapeutic approach.

6.2. Crosstalk between Glymphatic Pathway and Stroke. Studies have demonstrated that stroke impairs the glymphatic system [24, 123, 124]. Ischemic stroke induces the dysfunction 3 h postinjury by reduced vascular pulsation and occlusive perivascular space due to thrombus, while the recanalization of arteries after 24 h can recover the function of the glymphatic system [24]. Regarding SAH, the glymphatic system dysfunction occurs 24 h postonset [24]. The

impaired glymphatic system caused by SAH may be correlated with the occlusion by blood clots post SAH in the perivascular space, which affects CSF circulation [123]. Notably, ICH seems not to impair the function of glymphatic system [24]. As a result of the dysfunctional glymphatic system, CSF efflux turns to reduce, rendering ICP elevated, which parallels worse outcome poststroke [125]. In addition, A β accumulates poststroke, which accelerates the formation of amyloid plaques, CAA, and even dementia [124]. Dementia is one of the common complications of stroke; about a quarter of patients develop dementia three months after stroke onset [126]. In addition, the reduction of glymphatic system clearance after SAH can lead to delayed cerebral ischemia (DCI), which is associated with SAH prognosis [123].

A recent study by Mestre et al. has been cast in the spotlight and may revise our understanding of poststroke edema [127]. Cerebral edema is a prevalent complication of stroke, and its severity is related to patient outcomes [128]. Unexpectedly, Mestre et al. found that increased CSF influx via the glymphatic system was the leading cause of early stage edema after ischemic stroke [127]. Ischemic spreading depolarization, which contributes to the vasoconstriction of cerebral arteries, could change the pressure gradient, provoke ePVS, and double glymphatic influx [127]. In addition, they demonstrated that AQP4 deletion reduced cerebral edema caused by ischemic stroke [127]. However, AQP4 deletion impairs the clearance function of glymphatic system, which may lead to other complications [6]. Thus, the impact of glymphatic system on ischemia stroke under different stages may require further exploration.

Meningeal lymphatics play a vital role in the outcome of ischemic stroke [129, 130]. In addition to the impaired BBB, meningeal lymphatics represent another pathway for peripheral immune cells, such as T and B cells, to invade brain parenchyma and aggravate the neuroinflammation during ischemic stroke [131, 132]. Mast cells in the meninges may amplify the inflammation response and worsen the prognosis of stroke patients [132]. Moreover, the ingrown meningeal lymphangiogenesis into the injured brain parenchyma post vascular injury can increase the clearance of interstitial fluid to resolve cerebral edema and promote vascular regeneration [130]. Conversely, the hypoplasia of meningeal lymphatics does aggravate the severity of ischemic stroke in transient MACO [129]. Hence, it appears likely that meningeal lymphangiogenesis is linked to the outcome of ischemic stroke [129].

6.3. Glymphatic Pathway as a Novel Therapeutic Target for Stroke. Targeting the glymphatic system and meningeal lymphatics has the therapeutic potential for stroke and its complications and sequelae based on the roles mentioned above [129, 130]. Injection of tissue plasminogen activator can dissolve thrombus in vessels or perivascular space to recover the function of glymphatic pathway [24, 133]. The recovery of glymphatic system functioning is beneficial to A β clearance, and protein tau, among other interstitial solutes, reduces the incidence of poststroke dementia [124]. Moreover, dexmedetomidine administration holds the promise of reversing the impaired glymphatic system poststroke

[133]. In addition, increasing the plasma osmolality has been suggested to subserve the function of glymphatic system by accelerating glymphatic inflow speeds [134]. According to Mestre et al. [127], this may aggravate cerebral edema in the early stage of ischemic stroke, meriting further study.

7. Glymphatic Pathway and Infectious or Autoimmune Disease

Besides the diseases mentioned above, the glymphatic pathway is related to diseases, including infectious and autoimmune diseases. Microglia and type I astrocytes, the crucial innate immune cells that reside in CNS, are considered part of the glymphatic pathway [135], accounting for the close relationship between the glymphatic pathway and brain infection/inflammation [53, 135]. Recently, novel coronavirus- (SARS-CoV-2-) infected disease (COVID-19) started spreading worldwide. Lavi and Cong found that microglia and type I astrocytes infected with murine coronavirus (MHV-A 59), whose pathogenesis is similar to that of SARS-CoV-2, released proinflammatory cytokines, such as IL-1, IL-2, IL-6, TNF, and interferons [135], providing valuable insight into the crosstalk of glymphatic pathway and COVID-19.

Multiple sclerosis (MS), characterized by the invasion of auto-reactive T cells, is one of the common autoimmune diseases of CNS [21, 54]. Experimental autoimmune encephalomyelitis (EAE) is the most common animal model to explore the molecular immune in CNS [54]. Louveau et al. demonstrated that ablation of the meningeal lymphatics could prevent the interaction of T cells and APC and the activation of T cells in dCLNs, resulting in the reduced invasion of activated T cells into the brain and ameliorating the EAE [21]. They concluded that meningeal lymphatics played a critical role in the immune surveillance and the inflammatory response regulation of CNS [21]. As a result, meningeal lymphatics may be a therapeutic target for CNS autoimmune disease.

8. Conclusion

CSF has always been considered to play a vital role in CNS metabolism. The characterization of glymphatic/meningeal lymphatic system has led to a more nuanced understanding of the exchange and circulation of CSF and ISF in the brain. The glymphatic and meningeal lymphatic systems add to our understanding of metabolic waste drainage and immune privilege. However, more research is required for further understanding of these systems. The function of glymphatic system is linked to different physiological conditions, such as cerebral vascular pulsation, state of consciousness, and body posture, and is partially regulated by meningeal lymphatics. The glymphatic/meningeal lymphatic system clarifies the physiology of CNS metabolism and plays a vital role in the pathology of different neurological diseases, including neurodegenerative diseases, TBI, and stroke, serving as a promising target for intervention. However, most studies are limited to animal or cell experiments. More evidence is required to prove the similar effects of glymphatic pathway

in humans. Future research on the glymphatic pathway must demonstrate its pathological change in human diseases and provide novel therapies.

Abbreviations

A β :	Amyloid β
AD:	Alzheimer's disease
ApoE:	Apolipoprotein E
AQP:	Aquaporin
BBB:	Blood-brain barrier
CAA:	Amyloid angiopathy
COVID-19:	Novel coronavirus- (SARS-CoV-2-) infected disease
CNS:	Central nervous system
CSF:	Cerebrospinal fluid
CTE:	Chronic traumatic encephalopathy
DAPC:	Dystrophin-associated protein complex
DCI:	Delayed cerebral ischemia
dCLNs:	Deep cervical lymph nodes
ePVS:	Enlarged perivascular space
FTD:	Frontal-temporal dementia
GFAP:	Glial fibrillary acidic protein
ICH:	Subarachnoid hemorrhage
ICP:	Intracranial pressure
ISF:	Interstitial fluid
MCAO:	Middle cerebral artery occlusion
MRI:	Magnetic resonance imaging
mTBI:	Mild traumatic brain injury
NFT:	Neurofibrillary tangle
NMDA:	N-Methyl-D-aspartate acid
PUFAs:	Polyunsaturated fatty acids
SAH:	Subarachnoid hemorrhage
SAS:	Subarachnoid space
sCLNs:	Superficial cervical lymph nodes
SMC:	Smooth muscle cell
TBI:	Traumatic brain injury.

Data Availability

No data were used to support this study.

Conflicts of Interest

The authors declare that they have no competing interests.

Authors' Contributions

XJX and Guoyi Zhou wrote the paper and made the original figures. AWS, CHC, XBL, YXZ, and JQZ critically revised the texts and figures. All authors read and approved the final manuscript. Xianjun Xuan and Guoyi Zhou contributed equally to this manuscript.

Acknowledgments

This work was funded by the Scientific and Technology Project of Hangzhou Municipal Health Commission (A20220987).

References

- [1] J. E. Moore Jr. and C. D. Bertram, "Lymphatic system flows," *Annual Review of Fluid Mechanics*, vol. 50, no. 1, pp. 459–482, 2018.
- [2] N. A. Jessen, A. S. F. Munk, I. Lundgaard, and M. Nedergaard, "The glymphatic system: a beginner's guide," *Neurochemical Research*, vol. 40, no. 12, pp. 2583–2599, 2015.
- [3] T. P. Padera, E. F. Meijer, and L. L. Munn, "The lymphatic system in disease processes and cancer progression," *Annual Review of Biomedical Engineering*, vol. 18, no. 1, pp. 125–158, 2016.
- [4] A. Louveau, B. A. Plog, S. Antila, K. Alitalo, M. Nedergaard, and J. Kipnis, "Understanding the functions and relationships of the glymphatic system and meningeal lymphatics," *The Journal of Clinical Investigation*, vol. 127, no. 9, pp. 3210–3219, 2017.
- [5] M. Neuroscience Nedergaard, "Garbage truck of the brain," *Science*, vol. 340, no. 6140, pp. 1529–1530, 2013.
- [6] J. J. Iliff, M. Wang, Y. Liao et al., "A paravascular pathway facilitates CSF flow through the brain parenchyma and the clearance of interstitial solutes, including amyloid β ," *Science translational medicine*, vol. 4, no. 147, p. 147ra111, 2012.
- [7] T. M. Achariyar, B. Li, W. Peng et al., "Glymphatic distribution of CSF-derived apoE into brain is isoform specific and suppressed during sleep deprivation," *Molecular Neurodegeneration*, vol. 11, no. 1, p. 74, 2016.
- [8] B. A. Plog and M. Nedergaard, "The glymphatic system in central nervous system health and disease: past, present, and future," *Annual Review of Pathology*, vol. 13, no. 1, pp. 379–394, 2018.
- [9] H. H. Damkier, P. D. Brown, and J. Praetorius, "Cerebrospinal fluid secretion by the choroid plexus," *Physiological Reviews*, vol. 93, no. 4, pp. 1847–1892, 2013.
- [10] S. B. Hladky and M. A. Barrand, "Mechanisms of fluid movement into, through and out of the brain: evaluation of the evidence," *Fluids Barriers CNS*, vol. 11, no. 1, p. 26, 2014.
- [11] H. F. Cserr, C. J. Harling-Berg, and P. M. Knopf, "Drainage of brain extracellular fluid into blood and deep cervical lymph and its immunological significance," *Brain Pathology*, vol. 2, no. 4, pp. 269–276, 1992.
- [12] B. Bedussi, M. G. van Lier, J. W. Bartstra et al., "Clearance from the mouse brain by convection of interstitial fluid towards the ventricular system," *Fluids Barriers CNS*, vol. 12, p. 23, 2015.
- [13] S. B. Hladky and M. A. Barrand, "Fluid and ion transfer across the blood-brain and blood-cerebrospinal fluid barriers; a comparative account of mechanisms and roles," *Fluids Barriers CNS*, vol. 13, no. 1, p. 19, 2016.
- [14] N. J. Abbott, M. E. Pizzo, J. E. Preston, D. Janigro, and R. G. Thorne, "The role of brain barriers in fluid movement in the CNS: is there a 'glymphatic' system?," *Acta Neuropathologica*, vol. 135, no. 3, pp. 387–407, 2018.
- [15] A. Aspelund, S. Antila, S. T. Proulx et al., "A dural lymphatic vascular system that drains brain interstitial fluid and macromolecules," *Journal of Experimental Medicine*, vol. 212, no. 7, pp. 991–999, 2015.
- [16] M. Absinta, S. K. Ha, G. Nair et al., "Human and nonhuman primate meninges harbor lymphatic vessels that can be visualized noninvasively by MRI," *eLife*, vol. 6, 2017.
- [17] A. Louveau, I. Smirnov, T. J. Keyes et al., "Structural and functional features of central nervous system lymphatic vessels," *Nature*, vol. 523, no. 7560, pp. 337–341, 2015.
- [18] R. O. Carare, M. Bernardes-Silva, T. A. Newman et al., "Solutes, but not cells, drain from the brain parenchyma along basement membranes of capillaries and arteries: significance for cerebral amyloid angiopathy and neuroimmunology," *Neuropathology and Applied Neurobiology*, vol. 34, no. 2, pp. 131–144, 2008.
- [19] R. O. Weller, E. Djuanda, H. Y. Yow, and R. O. Carare, "Lymphatic drainage of the brain and the pathophysiology of neurological disease," *Acta Neuropathologica*, vol. 117, no. 1, pp. 1–14, 2009.
- [20] S. Da Mesquita, A. Louveau, A. Vaccari et al., "Functional aspects of meningeal lymphatics in ageing and Alzheimer's disease," *Nature*, vol. 560, no. 7717, pp. 185–191, 2018.
- [21] A. Louveau, J. Herz, M. N. Alme et al., "CNS lymphatic drainage and neuroinflammation are regulated by meningeal lymphatic vasculature," *Nature Neuroscience*, vol. 21, no. 10, pp. 1380–1391, 2018.
- [22] M. Xia, L. Yang, G. Sun, S. Qi, and B. Li, "Mechanism of depression as a risk factor in the development of Alzheimer's disease: the function of AQP4 and the glymphatic system," *Psychopharmacology*, vol. 234, no. 3, pp. 365–379, 2017.
- [23] L. H. M. Keir and D. P. Breen, "New awakenings: current understanding of sleep dysfunction and its treatment in Parkinson's disease," *Journal of Neurology*, vol. 267, no. 1, pp. 288–294, 2020.
- [24] T. Gaberel, C. Gakuba, R. Goulay et al., "Impaired glymphatic perfusion after strokes revealed by contrast-enhanced MRI: a new target for fibrinolysis?," *Stroke*, vol. 45, no. 10, pp. 3092–3096, 2014.
- [25] J. J. Iliff, M. J. Chen, B. A. Plog et al., "Impairment of glymphatic pathway function promotes tau pathology after traumatic brain injury," *The Journal of Neuroscience*, vol. 34, no. 49, pp. 16180–16193, 2014.
- [26] T. Brinker, E. Stopa, J. Morrison, and P. Klinge, "A new look at cerebrospinal fluid circulation," *Fluids Barriers CNS*, vol. 11, p. 10, 2014.
- [27] A. Zakharov, C. Papaiconomou, L. Koh, J. Djenic, R. Bozanovic-Sosic, and M. Johnston, "Integrating the roles of extracranial lymphatics and intracranial veins in cerebrospinal fluid absorption in sheep," *Microvascular Research*, vol. 67, no. 1, pp. 96–104, 2004.
- [28] J. G. McComb, "Recent research into the nature of cerebrospinal fluid formation and absorption," *Journal of Neurosurgery*, vol. 59, no. 3, pp. 369–383, 1983.
- [29] Q. Ma, B. V. Ineichen, M. Detmar, and S. T. Proulx, "Outflow of cerebrospinal fluid is predominantly through lymphatic vessels and is reduced in aged mice," *Nature Communications*, vol. 8, no. 1, p. 1434, 2017.
- [30] S. W. Bothwell, D. Janigro, and A. Patabendige, "Cerebrospinal fluid dynamics and intracranial pressure elevation in neurological diseases," *Fluids Barriers CNS*, vol. 16, no. 1, p. 9, 2019.
- [31] A. B. Steffensen, E. K. Oernbo, A. Stoica et al., "Cotransporter-mediated water transport underlying cerebrospinal fluid formation," *Nature Communications*, vol. 9, no. 1, p. 2167, 2018.
- [32] S. Da Mesquita, Z. Fu, and J. Kipnis, "The meningeal lymphatic system: a new player in neurophysiology," *Neuron*, vol. 100, no. 2, pp. 375–388, 2018.
- [33] T. H. Milhorat, "The third circulation revisited," *Journal of Neurosurgery*, vol. 42, no. 6, pp. 628–645, 1975.

- [34] G. A. Bateman and K. M. Brown, "The measurement of CSF flow through the aqueduct in normal and hydrocephalic children: from where does it come, to where does it go?," *Child's Nervous System*, vol. 28, no. 1, pp. 55–63, 2012.
- [35] A. Aspelund, S. Antila, S. T. Proulx et al., "A dural lymphatic vascular system that drains brain interstitial fluid and macromolecules," *The Journal of Experimental Medicine*, vol. 212, no. 7, pp. 991–999, 2015.
- [36] H. F. Cserr and L. H. Ostrach, "Bulk flow of interstitial fluid after intracranial injection of blue dextran 2000," *Experimental Neurology*, vol. 45, no. 1, pp. 50–60, 1974.
- [37] H. F. Cserr, D. N. Cooper, and T. H. Milhorat, "Flow of cerebral interstitial fluid as indicated by the removal of extracellular markers from rat caudate nucleus," *Experimental Eye Research*, vol. 25, pp. 461–473, 1977.
- [38] H. F. Cserr, D. N. Cooper, P. K. Suri, and C. S. Patlak, "Efflux of radiolabeled polyethylene glycols and albumin from rat brain," *The American Journal of Physiology*, vol. 240, no. 4, pp. F319–F328, 1981.
- [39] M. L. Rennels, T. F. Gregory, O. R. Blaumanis, K. Fujimoto, and P. A. Grady, "Evidence for a 'paravascular' fluid circulation in the mammalian central nervous system, provided by the rapid distribution of tracer protein throughout the brain from the subarachnoid space," *Brain Research*, vol. 326, no. 1, pp. 47–63, 1985.
- [40] M. L. Rennels, O. R. Blaumanis, and P. A. Grady, "Rapid solute transport throughout the brain via paravascular fluid pathways," *Advances in Neurology*, vol. 52, pp. 431–439, 1990.
- [41] E. N. Bakker, B. J. Bacskaï, M. Arbel-Ornath et al., "Lymphatic clearance of the brain: perivascular, paravascular and significance for neurodegenerative diseases," *Cellular and Molecular Neurobiology*, vol. 36, no. 2, pp. 181–194, 2016.
- [42] J. J. Iloff, M. Wang, D. M. Zeppenfeld et al., "Cerebral arterial pulsation drives paravascular CSF-interstitial fluid exchange in the murine brain," *The Journal of Neuroscience*, vol. 33, no. 46, pp. 18190–18199, 2013.
- [43] H. Mestre, J. Tithof, T. Du et al., "Flow of cerebrospinal fluid is driven by arterial pulsations and is reduced in hypertension," *Nature Communications*, vol. 9, no. 1, p. 4878, 2018.
- [44] H. Mestre, L. M. Hablitz, A. L. R. Xavier et al., "Aquaporin-4-dependent glymphatic solute transport in the rodent brain," *eLife*, vol. 7, 2018.
- [45] M. Klarica, M. Radoš, and D. Orešković, "The movement of cerebrospinal fluid and its relationship with substances behavior in cerebrospinal and interstitial fluid," *Neuroscience*, vol. 414, pp. 28–48, 2019.
- [46] D. Orešković, M. Radoš, and M. Klarica, "Cerebrospinal fluid secretion by the choroid plexus?," *Physiological Reviews*, vol. 96, no. 4, pp. 1661–1662, 2016.
- [47] H. F. Cserr, "Role of secretion and bulk flow of brain interstitial fluid in brain volume regulation," *Annals of the New York Academy of Sciences*, vol. 529, pp. 9–20, 1988.
- [48] Z. Xu, N. Xiao, Y. Chen et al., "Deletion of aquaporin-4 in APP/PS1 mice exacerbates brain A β accumulation and memory deficits," *Molecular Neurodegeneration*, vol. 10, p. 58, 2015.
- [49] V. Lecco, "Probable modification of the lymphatic fissures of the walls of the venous sinuses of the dura mater," *Archivio Italiano di Otologia, Rinologia e Laringologia*, vol. 64, no. 3, pp. 287–296, 1953.
- [50] M. Földi, A. Gellért, M. Kozma, M. Poberai, Ö. T. Zoltán, and E. Csanda, "New contributions to the anatomical connections of the brain and the lymphatic system," *Acta Anatomica (Basel)*, vol. 64, no. 4, pp. 498–505, 1966.
- [51] J. Li, J. Zhou, and Y. Shi, "Scanning electron microscopy of human cerebral meningeal stomata," *Annals of Anatomy-Anatomischer Anzeiger*, vol. 178, no. 3, pp. 259–261, 1996.
- [52] Y. Zhou, J. Cai, W. Zhang et al., "Impairment of the glymphatic pathway and putative meningeal lymphatic vessels in the aging human," *Annals of Neurology*, vol. 87, no. 3, pp. 357–369, 2020.
- [53] A. Louveau, T. H. Harris, and J. Kipnis, "Revisiting the mechanisms of CNS immune privilege," *Trends in Immunology*, vol. 36, no. 10, pp. 569–577, 2015.
- [54] N. Negi and B. K. Das, "CNS: not an immunoprivileged site anymore but a virtual secondary lymphoid organ," *International Reviews of Immunology*, vol. 37, no. 1, pp. 57–68, 2018.
- [55] P. B. Medawar, "Immunity to homologous grafted skin; the relationship between the antigens of blood and skin," *British Journal of Experimental Pathology*, vol. 27, no. 1, pp. 15–24, 1946.
- [56] S. Mader and L. Brimberg, "Aquaporin-4 water channel in the brain and its implication for health and disease," *Cell*, vol. 8, no. 2, p. 90, 2019.
- [57] Y. Zhou, A. Shao, Y. Yao, S. Tu, Y. Deng, and J. Zhang, "Dual roles of astrocytes in plasticity and reconstruction after traumatic brain injury," *Cell Communication and Signaling: CCS*, vol. 18, no. 1, p. 62, 2020.
- [58] H. Benveniste, X. Liu, S. Koundal, S. Sanggaard, H. Lee, and J. Wardlaw, "The glymphatic system and waste clearance with brain aging: a review," *Gerontology*, vol. 65, no. 2, pp. 106–119, 2019.
- [59] M. M. Hasan-Olive, R. Enger, H. A. Hansson, E. A. Nagelhus, and P. K. Eide, "Loss of perivascular aquaporin-4 in idiopathic normal pressure hydrocephalus," *Glia*, vol. 67, no. 1, pp. 91–100, 2019.
- [60] E. Mathieu, N. Gupta, A. Ahari, X. Zhou, J. Hanna, and Y. H. Yücel, "Evidence for cerebrospinal fluid entry into the optic nerve via a glymphatic pathway," *Investigative Ophthalmology & Visual Science*, vol. 58, no. 11, pp. 4784–4791, 2017.
- [61] Q. Liu, L. Yan, M. Huang et al., "Experimental alcoholism primes structural and functional impairment of the glymphatic pathway," *Brain, Behavior, and Immunity*, 2020.
- [62] V. Kiviniemi, X. Wang, V. Korhonen et al., "Ultra-fast magnetic resonance encephalography of physiological brain activity - glymphatic pulsation mechanisms?," *Journal of Cerebral Blood Flow and Metabolism*, vol. 36, no. 6, pp. 1033–1045, 2016.
- [63] L. Xie, H. Kang, Q. Xu et al., "Sleep drives metabolite clearance from the adult brain," *Science*, vol. 342, no. 6156, pp. 373–377, 2013.
- [64] H. Benveniste, H. Lee, F. Ding et al., "Anesthesia with dexmedetomidine and low-dose isoflurane increases solute transport via the glymphatic pathway in rat brain when compared with high-dose isoflurane," *Anesthesiology*, vol. 127, no. 6, pp. 976–988, 2017.
- [65] M. K. Rasmussen, H. Mestre, and M. Nedergaard, "The glymphatic pathway in neurological disorders," *The Lancet Neurology*, vol. 17, no. 11, pp. 1016–1024, 2018.
- [66] I. Lundgaard, M. L. Lu, E. Yang et al., "Glymphatic clearance controls state-dependent changes in brain lactate concentration,"

- Journal of Cerebral Blood Flow and Metabolism*, vol. 37, no. 6, pp. 2112–2124, 2017.
- [67] I. Lundgaard, B. Li, L. Xie et al., “Direct neuronal glucose uptake heralds activity-dependent increases in cerebral metabolism,” *Nature Communications*, vol. 6, p. 6807, 2015.
- [68] V. R. Thrane, A. S. Thrane, B. A. Plog et al., “Paravascular microcirculation facilitates rapid lipid transport and astrocyte signaling in the brain,” *Scientific Reports*, vol. 3, no. 1, p. 2582, 2013.
- [69] A. A. Davis, C. E. G. Leyns, and D. M. Holtzman, “Intercellular spread of protein aggregates in neurodegenerative disease,” *Annual Review of Cell and Developmental Biology*, vol. 34, pp. 545–568, 2018.
- [70] A. Manrique de Lara, L. Soto-Gómez, E. Núñez-Acosta, G. Saruwatari-Zavala, and M. E. Rentería, “Ethical issues in susceptibility genetic testing for late-onset neurodegenerative diseases,” *American Journal of Medical Genetics. Part B, Neuropsychiatric Genetics*, vol. 180, no. 8, pp. 609–621, 2019.
- [71] K. Tanabe, Y. Maeshima, Y. Sato, and J. Wada, “Antiangiogenic therapy for diabetic nephropathy,” *BioMed Research International*, vol. 2017, 2017.
- [72] J. Y. Szeto and S. J. Lewis, “Current treatment options for Alzheimer’s disease and Parkinson’s disease dementia,” *Current Neuropharmacology*, vol. 14, no. 4, pp. 326–338, 2016.
- [73] A. J. Smith and A. S. Verkman, “The “glymphatic” mechanism for solute clearance in Alzheimer’s disease: game changer or unproven speculation?,” *The FASEB Journal*, vol. 32, no. 2, pp. 543–551, 2018.
- [74] L. Zuroff, D. Daley, K. L. Black, and M. Koronyo-Hamaoui, “Clearance of cerebral A β in Alzheimer’s disease: reassessing the role of microglia and monocytes,” *Cellular and Molecular Life Sciences*, vol. 74, no. 12, pp. 2167–2201, 2017.
- [75] B. C. Reeves, J. K. Karimy, A. J. Kundishora et al., “Glymphatic system impairment in Alzheimer’s disease and idiopathic normal pressure hydrocephalus,” *Trends in Molecular Medicine*, vol. 26, no. 3, pp. 285–295, 2020.
- [76] I. F. Harrison, O. Ismail, A. Machhada et al., “Impaired glymphatic function and clearance of tau in an Alzheimer’s disease model,” *Brain*, vol. 143, no. 8, pp. 2576–2593, 2020.
- [77] W. Peng, T. M. Acharyar, B. Li et al., “Suppression of glymphatic fluid transport in a mouse model of Alzheimer’s disease,” *Neurobiology of Disease*, vol. 93, pp. 215–225, 2016.
- [78] R. O. Weller, A. Massey, T. A. Newman, M. Hutchings, Y. M. Kuo, and A. E. Roher, “Cerebral amyloid angiopathy: amyloid beta accumulates in putative interstitial fluid drainage pathways in Alzheimer’s disease,” *The American Journal of Pathology*, vol. 153, no. 3, pp. 725–733, 1998.
- [79] R. O. Weller, A. Massey, Y.-m. Kuo, and A. E. Roher, “Cerebral amyloid angiopathy: accumulation of A β in interstitial fluid drainage pathways in Alzheimer’s disease,” *Annals of the New York Academy of Sciences*, vol. 903, no. 1 VASCULAR FACT, pp. 110–117, 2000.
- [80] L. Wang, Y. Zhang, Y. Zhao, C. Marshall, T. Wu, and M. Xiao, “Deep cervical lymph node ligation aggravates AD-like pathology of APP/PS1 mice,” *Brain Pathology*, vol. 29, no. 2, pp. 176–192, 2019.
- [81] M. Valenza, R. Facchinetti, L. Steardo, and C. Scuderi, “Altered waste disposal system in aging and Alzheimer’s disease: focus on astrocytic aquaporin-4,” *Frontiers in Pharmacology*, vol. 10, p. 1656, 2019.
- [82] D. M. Zeppenfeld, M. Simon, J. D. Haswell et al., “Association of perivascular localization of aquaporin-4 with cognition and Alzheimer disease in aging brains,” *JAMA Neurology*, vol. 74, no. 1, pp. 91–99, 2017.
- [83] S. Cordone, L. Annarumma, P. M. Rossini, and L. de Genaro, “Sleep and β -amyloid deposition in Alzheimer disease: insights on mechanisms and possible innovative treatments,” *Frontiers in Pharmacology*, vol. 10, p. 695, 2019.
- [84] E. L. Boespflug and J. J. Iliff, “The emerging relationship between interstitial fluid-cerebrospinal fluid exchange, amyloid-beta, and sleep,” *Biological Psychiatry*, vol. 83, no. 4, pp. 328–336, 2018.
- [85] E. Shokri-Kojori, G. J. Wang, C. E. Wiers et al., “ β -Amyloid accumulation in the human brain after one night of sleep deprivation,” *Proceedings of the National Academy of Sciences of the United States of America*, vol. 115, no. 17, pp. 4483–4488, 2018.
- [86] J. E. Kang, M. M. Lim, R. J. Bateman et al., “Amyloid-beta dynamics are regulated by orexin and the sleep-wake cycle,” *Science*, vol. 326, no. 5955, pp. 1005–1007, 2009.
- [87] H. Wu, S. Dunnett, Y.-S. Ho, and R. C.-C. Chang, “The role of sleep deprivation and circadian rhythm disruption as risk factors of Alzheimer’s disease,” *Frontiers in Neuroendocrinology*, vol. 54, p. 100764, 2019.
- [88] S. J. van Veluw, S. S. Hou, M. Calvo-Rodriguez et al., “Vasomotion as a driving force for paravascular clearance in the awake mouse brain,” *Neuron*, vol. 105, no. 3, pp. 549–561.e5, 2020.
- [89] H. Ren, C. Luo, Y. Feng et al., “Omega-3 polyunsaturated fatty acids promote amyloid-beta clearance from the brain through mediating the function of the glymphatic system,” *The FASEB Journal*, vol. 31, no. 1, pp. 282–293, 2017.
- [90] E. Spinedi and D. P. Cardinali, “Neuroendocrine-metabolic dysfunction and sleep disturbances in neurodegenerative disorders: focus on Alzheimer’s disease and melatonin,” *Neuroendocrinology*, vol. 108, no. 4, pp. 354–364, 2019.
- [91] T. Mollayeva, S. Mollayeva, and A. Colantonio, “Traumatic brain injury: sex, gender and intersecting vulnerabilities,” *Nature Reviews. Neurology*, vol. 14, no. 12, pp. 711–722, 2018.
- [92] A. I. R. Maas, D. K. Menon, P. D. Adelson et al., “Traumatic brain injury: integrated approaches to improve prevention, clinical care, and research,” *The Lancet Neurology*, vol. 16, no. 12, pp. 987–1048, 2017.
- [93] M. J. Sullan, B. M. Asken, M. S. Jaffee, S. T. DeKosky, and R. M. Bauer, “Glymphatic system disruption as a mediator of brain trauma and chronic traumatic encephalopathy,” *Neuroscience and Biobehavioral Reviews*, vol. 84, pp. 316–324, 2018.
- [94] G. Quaglio, M. Gallucci, H. Brand, A. Dawood, and F. Cobello, “Traumatic brain injury: a priority for public health policy,” *Lancet Neurology*, vol. 16, no. 12, pp. 951–952, 2017.
- [95] A. E. Kline, J. B. Leary, H. L. Radabaugh, J. P. Cheng, and C. O. Bondi, “Combination therapies for neurobehavioral and cognitive recovery after experimental traumatic brain injury: is more better?,” *Progress in Neurobiology*, vol. 142, pp. 45–67, 2016.
- [96] M. Khaksari, Z. Soltani, and N. Shahrokhi, “Effects of female sex steroids administration on pathophysiologic mechanisms in traumatic brain injury,” *Translational Stroke Research*, vol. 9, no. 4, pp. 393–416, 2018.

- [97] B. Dang, W. Chen, W. He, and G. Chen, "Rehabilitation treatment and progress of traumatic brain injury dysfunction," *Neural Plasticity*, vol. 2017, 2017.
- [98] B. Roozenbeek, A. I. Maas, and D. K. Menon, "Changing patterns in the epidemiology of traumatic brain injury," *Nature Reviews. Neurology*, vol. 9, no. 4, pp. 231–236, 2013.
- [99] M. Cruz-Haces, J. Tang, G. Acosta, J. Fernandez, and R. Shi, "Pathological correlations between traumatic brain injury and chronic neurodegenerative diseases," *Transl Neurodegeneration*, vol. 6, p. 20, 2017.
- [100] R. J. Castriotta, M. C. Wilde, J. M. Lai, S. Atanasov, B. E. Masel, and S. T. Kuna, "Prevalence and consequences of sleep disorders in traumatic brain injury," *Journal of Clinical Sleep Medicine*, vol. 3, no. 4, pp. 349–356, 2007.
- [101] S. Barshikar and K. R. Bell, "Sleep disturbance after TBI," *Current Neurology and Neuroscience Reports*, vol. 17, no. 11, p. 87, 2017.
- [102] I. Moreno-Gonzalez and C. Soto, "Misfolded protein aggregates: mechanisms, structures and potential for disease transmission," *Seminars in Cell & Developmental Biology*, vol. 22, no. 5, pp. 482–487, 2011.
- [103] C. Soto, "Unfolding the role of protein misfolding in neurodegenerative diseases," *Nature Reviews. Neuroscience*, vol. 4, no. 1, pp. 49–60, 2003.
- [104] B. T. Hyman, J. C. Augustinack, and M. Ingelsson, "Transcriptional and conformational changes of the tau molecule in Alzheimer's disease," *Biochimica et Biophysica Acta*, vol. 1739, no. 2-3, pp. 150–157, 2005.
- [105] G. Edwards, J. Zhao, P. K. Dash, C. Soto, and I. Moreno-Gonzalez, "Traumatic brain injury induces tau aggregation and spreading," *Journal of Neurotrauma*, vol. 37, no. 1, pp. 80–92, 2020.
- [106] I. Cherian, M. Beltran, A. Landi, C. Alafaci, F. Torregrossa, and G. Grasso, "Introducing the concept of "CSF-shift edema" in traumatic brain injury," *Journal of Neuroscience Research*, vol. 96, no. 4, pp. 744–752, 2018.
- [107] Z. Ren, J. J. Iff, L. Yang et al., "'Hit & Run' model of closed-skull traumatic brain injury (TBI) reveals complex patterns of post-traumatic AQP4 dysregulation," *Journal of Cerebral Blood Flow and Metabolism*, vol. 33, no. 6, pp. 834–845, 2013.
- [108] S. Magnoni, T. J. Esparza, V. Conte et al., "Tau elevations in the brain extracellular space correlate with reduced amyloid- β levels and predict adverse clinical outcomes after severe traumatic brain injury," *Brain*, vol. 135, no. 4, pp. 1268–1280, 2012.
- [109] D. W. Simon, M. J. McGeachy, H. Bayır, R. S. Clark, D. J. Loane, and P. M. Kochanek, "The far-reaching scope of neuroinflammation after traumatic brain injury," *Nature Reviews. Neurology*, vol. 13, no. 3, pp. 171–191, 2017.
- [110] J. Ramirez, C. Berezuk, A. A. McNeely, F. Gao, J. McLaurin, and S. E. Black, "Imaging the perivascular space as a potential biomarker of neurovascular and neurodegenerative diseases," *Cellular and Molecular Neurobiology*, vol. 36, no. 2, pp. 289–299, 2016.
- [111] R. A. Opel, A. Christy, E. L. Boespflug et al., "Effects of traumatic brain injury on sleep and enlarged perivascular spaces," *Journal of Cerebral Blood Flow and Metabolism*, vol. 39, no. 11, pp. 2258–2267, 2019.
- [112] B. P. Lucke-Wold, K. E. Smith, L. Nguyen et al., "Sleep disruption and the sequelae associated with traumatic brain injury," *Neuroscience and Biobehavioral Reviews*, vol. 55, pp. 68–77, 2015.
- [113] H. J. Orff, L. Ayalon, and S. P. Drummond, "Traumatic brain injury and sleep disturbance: a review of current research," *The Journal of Head Trauma Rehabilitation*, vol. 24, no. 3, pp. 155–165, 2009.
- [114] Y. Zhou, A. Shao, W. Xu, H. Wu, and Y. Deng, "Advance of stem cell treatment for traumatic brain injury," *Frontiers in Cellular Neuroscience*, vol. 13, p. 301, 2019.
- [115] G. Kannan, S. P. Kambhampati, and S. R. Kudchadkar, "Effect of anesthetics on microglial activation and nanoparticle uptake: implications for drug delivery in traumatic brain injury," *Journal of Controlled Release*, vol. 263, pp. 192–199, 2017.
- [116] B. C. Campbell, D. A. De Silva, M. R. Macleod et al., "Ischaemic stroke," *Nature Reviews Disease Primers*, vol. 5, no. 1, pp. 1–22, 2019.
- [117] V. L. Feigin, B. Norrving, and G. A. Mensah, "Global burden of stroke," *Circulation Research*, vol. 120, no. 3, pp. 439–448, 2017.
- [118] Y. Zhang, X. Zhang, Q. Wei et al., "Activation of sigma-1 receptor enhanced pericyte survival via the interplay between apoptosis and autophagy: implications for blood-brain barrier integrity in stroke," *Translational Stroke Research*, vol. 11, no. 2, pp. 267–287, 2020.
- [119] A. K. Boehme, C. Esenwa, and M. S. Elkind, "Stroke risk factors, genetics, and prevention," *Circulation Research*, vol. 120, no. 3, pp. 472–495, 2017.
- [120] C. J. J. van Asch, M. J. A. Luitse, G. J. E. Rinkel, I. van der Tweel, A. Algra, and C. J. M. Klijn, "Incidence, case fatality, and functional outcome of intracerebral haemorrhage over time, according to age, sex, and ethnic origin: a systematic review and meta-analysis," *The Lancet Neurology*, vol. 9, no. 2, pp. 167–176, 2010.
- [121] A. Shao, Y. Zhou, Y. Yao, W. Zhang, J. Zhang, and Y. Deng, "The role and therapeutic potential of heat shock proteins in haemorrhagic stroke," *Journal of Cellular and Molecular Medicine*, vol. 23, no. 9, pp. 5846–5858, 2019.
- [122] M. Ezzati, Z. Obermeyer, I. Tzoulaki, B. M. Mayosi, P. Elliott, and D. A. Leon, "Contributions of risk factors and medical care to cardiovascular mortality trends," *Nature Reviews. Cardiology*, vol. 12, no. 9, pp. 508–530, 2015.
- [123] R. Goulay, J. Flament, M. Gauberti et al., "Subarachnoid hemorrhage severely impairs brain parenchymal cerebrospinal fluid circulation in nonhuman primate," *Stroke*, vol. 48, no. 8, pp. 2301–2305, 2017.
- [124] R. Goulay, L. Mena Romo, E. M. Hol, and R. M. Dijkhuizen, "From stroke to dementia: a comprehensive review exposing tight interactions between stroke and amyloid-beta formation," *Translational Stroke Research*, 2020.
- [125] M. S. Alshuhri, L. Gallagher, C. McCabe, and W. M. Holmes, "Change in CSF dynamics responsible for ICP elevation after ischemic stroke in rats: a new mechanism for unexplained END?," *Translational Stroke Research*, vol. 11, no. 2, pp. 310–318, 2020.
- [126] D. B. Back, K. J. Kwon, D. H. Choi et al., "Chronic cerebral hypoperfusion induces post-stroke dementia following acute ischemic stroke in rats," *Journal of Neuroinflammation*, vol. 14, no. 1, p. 216, 2017.
- [127] H. Mestre, T. Du, A. M. Sweeney et al., "Cerebrospinal fluid influx drives acute ischemic tissue swelling," *Science*, vol. 367, no. 6483, 2020.

Retraction

Retracted: Clinical Efficacy of PEG-IFN α -2a and PEG-IFN α -2b in the Treatment of Hepatitis B e Antigen-Positive Hepatitis B and Their Value in Improving Inflammatory Factors and Hemodynamics in Patients: A Comparative Study

Oxidative Medicine and Cellular Longevity

Received 1 August 2023; Accepted 1 August 2023; Published 2 August 2023

Copyright © 2023 Oxidative Medicine and Cellular Longevity. This is an open access article distributed under the Creative Commons Attribution License, which permits unrestricted use, distribution, and reproduction in any medium, provided the original work is properly cited.

This article has been retracted by Hindawi following an investigation undertaken by the publisher [1]. This investigation has uncovered evidence of one or more of the following indicators of systematic manipulation of the publication process:

- (1) Discrepancies in scope
- (2) Discrepancies in the description of the research reported
- (3) Discrepancies between the availability of data and the research described
- (4) Inappropriate citations
- (5) Incoherent, meaningless and/or irrelevant content included in the article
- (6) Peer-review manipulation

The presence of these indicators undermines our confidence in the integrity of the article's content and we cannot, therefore, vouch for its reliability. Please note that this notice is intended solely to alert readers that the content of this article is unreliable. We have not investigated whether authors were aware of or involved in the systematic manipulation of the publication process.

Wiley and Hindawi regrets that the usual quality checks did not identify these issues before publication and have since put additional measures in place to safeguard research integrity.

We wish to credit our own Research Integrity and Research Publishing teams and anonymous and named external researchers and research integrity experts for contributing to this investigation.

The corresponding author, as the representative of all authors, has been given the opportunity to register their

agreement or disagreement to this retraction. We have kept a record of any response received.

References

- [1] N. Jia, W. Gao, X. Fan et al., "Clinical Efficacy of PEG-IFN α -2a and PEG-IFN α -2b in the Treatment of Hepatitis B e Antigen-Positive Hepatitis B and Their Value in Improving Inflammatory Factors and Hemodynamics in Patients: A Comparative Study," *Oxidative Medicine and Cellular Longevity*, vol. 2022, Article ID 3185320, 10 pages, 2022.

Research Article

Clinical Efficacy of PEG-IFN α -2a and PEG-IFN α -2b in the Treatment of Hepatitis B e Antigen-Positive Hepatitis B and Their Value in Improving Inflammatory Factors and Hemodynamics in Patients: A Comparative Study

Nina Jia , Wei Gao, Xiaohong Fan, Hong Gao, Xueqing Li, Biantao Mi, and Jie Yang

Department of Gastroenterology, The Second Hospital of Shanxi Medical University, Taiyuan, 030001 Shanxi, China

Correspondence should be addressed to Nina Jia; jianina1109@126.com

Received 18 March 2022; Revised 24 April 2022; Accepted 27 April 2022; Published 11 June 2022

Academic Editor: Shao Liang

Copyright © 2022 Nina Jia et al. This is an open access article distributed under the Creative Commons Attribution License, which permits unrestricted use, distribution, and reproduction in any medium, provided the original work is properly cited.

Objective. To compare the merits and demerits of PEG-IFN α -2a and PEG-IFN α -2b for the treatment of hepatitis B e antigen (HBeAg)-positive chronic hepatitis B (CHB). **Methods.** Clinical files from eighty-four CHB patients admitted to the Second Hospital of Shanxi Medical University between January 2018 and January 2019 were retrospectively analyzed and assigned to two groups: group 2a treated with PEG-IFN α -2a and group 2b treated with PEG-IFN α -2b. The clinical efficacy was compared between the above two arms, and the liver function (ALT, AST, HA, LN, and IV-C), HBV-DNA, HBsAg, HBeAg, and inflammatory factors (IFs, IL-1 β , IL-6, IL-8, and TNF- α) were tested at 12 weeks (T1), 24 weeks (T2), and 48 weeks (T3). The alterations of hemodynamics (SBP, DBP, MAP, and CVP), cardiac function (LVEF and BNP), and the incidence of adverse reactions (ARs) during treatment were recorded. Finally, the patients were followed up for 2 years to investigate the quality of life (QOL) as well as the positive seroconversion rate of HBsAg and HBeAg. **Results.** The overall response rate was similar in the two arms ($P > 0.05$). After treatment, the liver function, HBV-DNA, HBsAg, HBeAg, IFs, hemodynamics, and cardiac function were enormously improved ($P < 0.05$), with faster improvement in group 2b compared with group 2a ($P < 0.05$). The investigation of ARs identified notably lower incidence rates of alopecia, thrombocytopenia, and granulocytopenia in group 2a as compared to group 2b ($P < 0.05$). The prognostic follow-up results revealed no distinct difference in the QOL score and the positive seroconversion rate of HBsAg and HBeAg ($P > 0.05$); however, the quantitative results of HBV-DNA, HBsAg, and HBeAg in group 2b were lower than those in group 2a ($P < 0.05$). **Conclusions.** Both PEG-IFN α -2a and PEG-IFN α -2b have excellent and stable therapeutic effects on HBeAg-positive CHB, among which PEG-IFN α -2b renders a faster treatment process but higher side effects, which can provide valuable references when choosing a treatment plan for CHB.

1. Introduction

Chronic hepatitis B (CHB), one of the most pervasive infectious diseases globally, is caused by hepatitis B virus (HBV) and is highly contagious [1]. As indicated by statistics, the number of known CHB patients worldwide continues to increase, with more than 260 million cases as of 2016 [2]. The incidence of CHB also varies greatly among different regions. In China, India, and other regions with large population density and base, the infection rate has increased significantly [3]. For example, there are over 70 million cases of HBV infection in China, of which more than 40% were

finally diagnosed as CHB [4]. At the early stage, CHB presents no other special clinical symptoms except dizziness and anorexia, which are often ignored by patients [5]. However, when there are obvious symptoms, the disease has usually progressed into the middle and late stage when pathological conditions such as liver fibrosis, liver dysfunction, failure, and even liver cancer may occur in patients [6]. On average, approximately 800,000 to 900,000 patients die each year from CHB, a two-to-fourfold increase in mortality compared to 2006, according to the study [7].

Currently, CHB treatment depends largely on conservative therapy, mainly through antiviral, immunomodulation,

anti-inflammatory, and liver protection methods to inhibit or eliminate HBV infection in the long term. Among them, nucleoside (acid) analogues and interferon (IFN) are all clinical treatments for CHB. Nucleoside (acid) analogues have excellent antiviral effect and good tolerance, but the treatment time is extremely long; Moreover, nucleoside (acid) analogues under selective pressure may cause virus variability resistance, resulting in virologic rebound and liver metabolic disturbance [8, 9]. IFN, on the other hand, plays an anti-HBV effect through the dual effects of HBV replication and immune regulation, with higher serological response and longer sustained virologic response, which is mainly related to molecular pathways. It has the same anti-HBV ability as nucleoside (acid) but faster antiviral effect, so it has been increasingly applied in CHB treatment in recent years [10, 11].

Currently, PEG-IFN α -2A and PEG-IFN α -2b are commonly used in clinical practice, both of which have well-documented therapeutic effects on CHB [12, 13]. However, the difference between the two types of IFN genes on CHB is still under debate, and there is no authoritative research that indicates which type is more suitable for CHB treatment. Furthermore, we found that previous studies on PEG-IFN α -2a and PEG-IFN α -2b in treating CHB mostly focused on patients' hepatitis virus infection, ignoring the changes of other vital signs [14, 15]. As we all know, pathological changes such as inflammatory factors (IFs) and hemodynamics are also important links in the occurrence of CHB, which are closely related to the pathology of infection. Thus, the motivation and novelty of this study are to compare the effect of PEG-IFN α -2a and PEG-IFN α -2b in treating CHB on the change of inflammatory factors and hemodynamics in patients, hopefully, to provide strong evidence for the treatment protocol of CHB.

With the increasing incidence of CHB and its major threat, it is necessary to find a suitable treatment for CHB as soon as possible. This study, undoubtedly, will provide more reliable and comprehensive experimental guidance for future treatment of CHB by investigating the impacts of PEG-IFN α -2a and PEG-IFN α -2b on clinical efficacy as well as the hemodynamics and IFs of patients with HBeAg-positive CHB.

2. Materials and Methods

2.1. Patient Data. The study population comprised 84 CHB patients admitted to the Second Hospital of Shanxi Medical University between January 2018 and January 2019. There were 49 males and 35 females, and the mean age was (47.6 \pm 7.4) years (range: 34-61). Ethical approval has been obtained for this study, all subjects were aware of the study and signed informed consent. The enrolled CHB patients were assigned to group 2b and group 2a according to treatment plan, with 42 cases in each group.

2.2. Eligibility Criteria. Inclusion criteria: (1) presence of clinical manifestations of CHB (constitutional symptoms, anorexia, nausea, jaundice, and right upper quadrant discomfort), together with the confirmed diagnosis of HBeAg-

positive CHB after second liver two half-and-half test in our hospital [16]; (2) >18 years old; (3) no liver cirrhosis; (4) complete case data; (5) willingness to participate in this study. Exclusion criteria: (1) hepatitis A, hepatitis C, or reinfection with other hepatitis viruses; (2) autoimmune liver diseases; (3) other cardiovascular and cerebrovascular diseases and hematopoietic system diseases; (4) neoplastic diseases; (5) drug-induced liver injury and alcoholic liver injury; (6) drug allergies; (7) pregnant and lactating women; (8) mental disorders; (9) referrals.

2.3. Treatment Methods. After admission, patients in both arms received routine examinations such as second liver two half-and-half and were treated accordingly. Group 2a: 180 μ g PEG-IFN α -2a (Shanghai Roche Pharmaceutical Ltd., SFDA Approval No. J20070055) was injected subcutaneously once a week. Group 2b: 180 μ g PEG-IFN α -2b (Xiamen Amoytop Biotech Co., Ltd., SFDA Approval No. S20174005) was injected subcutaneously weekly. Both arms were treated continuously for 48 weeks.

2.4. Blood Sample Collection. At 12 weeks (T1), 24 weeks (T2), and 48 weeks (T3) after treatment, 5 mL of fasting venous blood was extracted from patients into coagulation-promoting tubes, which were left at room temperature for 30 min and then centrifuged (1505 \times g, 4°C) to obtain serum to be refrigerated at -80°C.

2.5. Observational Indicators

2.5.1. Clinical Efficacy. Markedly effective was considered if the symptoms disappeared, the liver function recovered more than 50%, and the liver fibrosis indexes recovered to normal levels. Effective was translated in basically disappeared symptoms and a 10-50% recovery of the liver function. Failure to meet the above standards was considered ineffective. Total effective rate = (markedly effective + effective) cases/total cases \times 100%.

2.5.2. Liver Function. The contents of alanine aminotransferase (ALT) and aspartate aminotransferase (AST) were measured using an automatic biochemical analyzer (Sysmex Corporation, Kobe, Japan). (2) The determination of liver fibrosis indexes including hyaluronidase (HA), laminin (LN), type IV collagen (IV-C), and B-type natriuretic peptide (BNP) contents was realized by chemiluminescence. ALT, AST, HA, LN, and IV-C of patients in both arms were recorded at 12 T1, T2, and T3.

2.5.3. Marker Conversion. The detection of serum hepatitis B virus deoxyribonucleic acid (HBV DNA) employed PCR. ELISA was used for determining the expression of hepatitis B surface antigen (HBsAg) and hepatitis B e antigen (HBeAg). HBV-DNA, HBsAg, and HBeAg levels were quantified, and HBV-DNA (HBV - DNA quantification < 2.5 lg copies/mL is judged as HBV-DNA negative conversion), HBsAg, and HBeAg negative conversion ratios were calculated.

2.5.4. IFs. ELISA was used for determining the expression of hepatitis B surface antigen (HBsAg), hepatitis B e antigen

TABLE 1: Comparison of clinical baseline data [n(%)].

	Group 2a (n = 42)	Group 2b (n = 42)	t/ χ^2	P
Age (years, $\bar{x} \pm s$)	47.6 \pm 8.2	46.4 \pm 8.3	0.667	0.507
Gender [n(%)]			0.441	0.507
Male	23 (54.76)	26 (61.90)		
Female	19 (45.24)	16 (38.10)		
Family history of illness [n(%)]			0.124	0.724
Have	4 (9.52)	5 (11.90)		
Without	38 (90.48)	37 (88.10)		
History of liver disease [n(%)]			0.081	0.776
Have	8 (19.05)	7 (16.67)		
Without	34 (80.95)	35 (83.33)		
History of diabetes [n(%)]			0.223	0.637
Have	12 (28.57)	14 (33.33)		
Without	30 (71.43)	28 (66.67)		
History of hypertension [n(%)]			0.214	0.643
Have	15 (35.71)	13 (30.95)		
Without	27 (64.29)	29 (69.05)		
Smoking [n(%)]			0.449	0.503
Yes	18 (42.86)	15 (35.71)		
No	24 (57.14)	27 (64.29)		
Drinking [n(%)]			—	—
Yes	15 (35.71)	15 (35.71)		
No	27 (64.29)	27 (64.29)		
Living environment [n(%)]			0.343	0.558
City	34 (80.95)	36 (85.71)		
Countryside	8 (19.05)	6 (14.29)		

(HBeAg), as well as IFs IL-1 β , IL-6, IL-8, and TNF- α . The kits were supplied by Shanghai Enzyme Research Biotechnology Co., Ltd., and the operation procedure was carried out strictly in accordance with the instructions.

2.5.5. Hemodynamics and Cardiac Function. The left ventricular ejection fraction (LVEF) was measured by echocardiography. The left femoral artery was continuously monitored for mean arterial pressure (MAP), central venous pressure (CVP), systolic blood pressure (SBP), and diastolic blood pressure (DBP).

2.5.6. Safety. The incidence of adverse reactions (ARs) from admission to discharge was calculated. (8) Prognosis: the prognostic QOL score and positive seroconversion rate of HBsAg and HBeAg (the number of patients with positive HBsAg and HBeAg reexamination results) were recorded.

2.6. Follow-Up for Prognosis. Patients in both arms were followed up for 2 years via regular hospital reexamination. The 36-Item Short-Form Health Survey (SF-36) [17] was used to investigate patients' social functioning, role emotional, mental health, and vitality at the end of the 2-year

follow-up. Each dimension has a maximum score of 100, and a higher score indicates a better quality of life (QOL). In addition, patients were regularly reviewed for second liver two half-and-half.

2.7. Statistical Processing. The statistical method applied in this study was SPSS24.0. The enumeration data was recorded as [n(%)], and Chi-square test was used for comparison between groups. The measurement data were recorded in ($\bar{x} \pm s$); independent samples *t*-test and paired *t*-test were used for comparison among groups, and one-way analysis of variance and LSD post hoc test was used for comparison among multiple groups. A *P* value less than 0.05 was considered to be of statistical significance.

3. Results

3.1. Comparison of Clinical Baseline Data. In order to ensure the accuracy of the experimental results, we made a statistical comparison of the clinical baseline data of the two groups. The results identified no distinct difference in baseline data such as age and gender between the two arms (*P* > 0.05), suggesting comparability Table 1.

TABLE 2: Clinical efficacy [$n(\%)$].

	Markedly effective	Effective	Invalid	Total effective rate (%)
Group 2a ($n = 42$)	21 (50.00)	14 (33.33)	7 (16.67)	83.33
Group 2b ($n = 42$)	24 (57.14)	14 (33.33)	4 (9.52)	90.48
χ^2				0.942
P				0.332

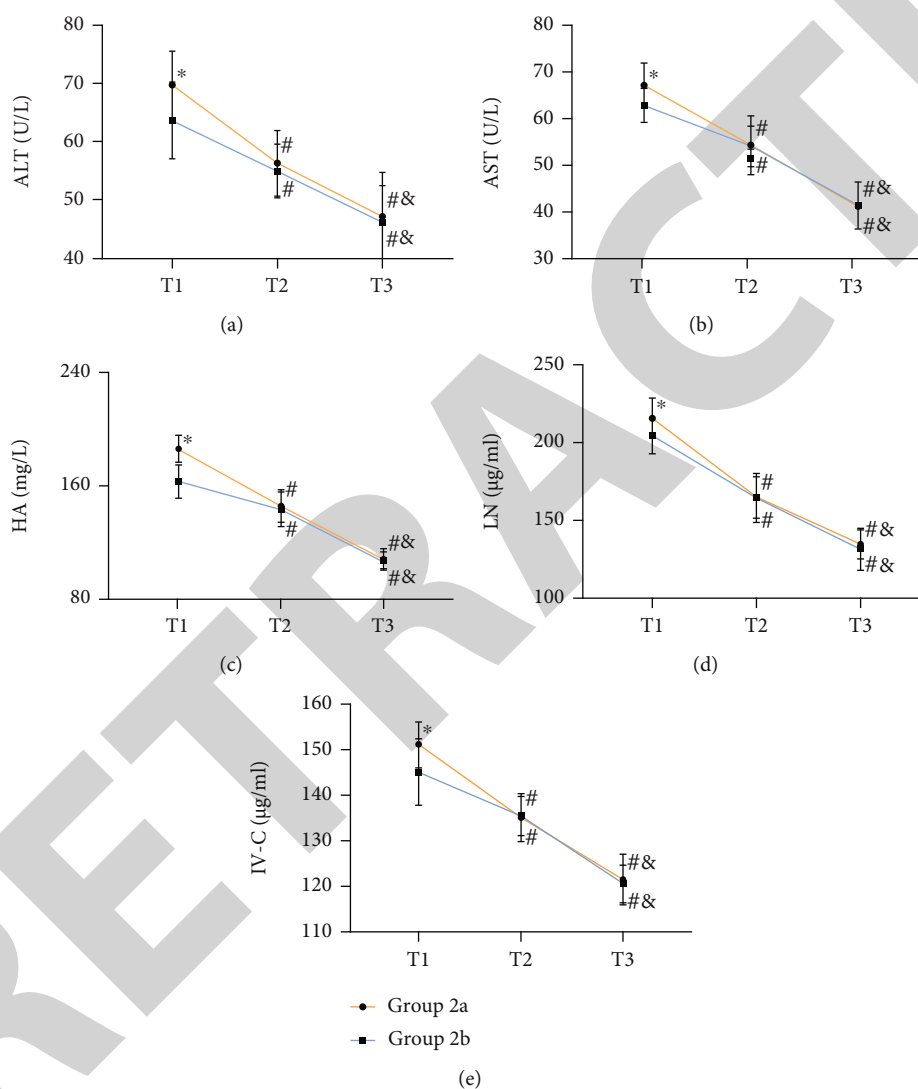


FIGURE 1: Comparison of liver function. (a) Comparison of ALT. (b) Comparison of AST. (c) Comparison of HA. (d) Comparison of LN. (e) Comparison of IV-C. Compared with 2b group, * $P < 0.05$. Compared with T1, # $P < 0.05$. Compared with T2, & $P < 0.05$.

3.2. *Comparison of Clinical Efficacy.* Total effective rate was not statistically different between group 2b (83.33%) and group 2a (90.48%) ($P > 0.05$) Table 2.

3.3. *Liver Function Comparison.* T2 and T3 had witnessed no statistical difference in ALT, AST, HA, LN, and IV-C between the two arms ($P > 0.05$). Whereas, at T1, the above liver function indexes were all lower in group 2b than in group 2a ($P < 0.05$). The liver function indexes of both

groups decreased gradually with the treatment time ($P < 0.05$) Figure 1.

3.4. *Comparison of Marker Conversion.* HBV-DNA, HBsAg, and HBeAg, which showed no evident difference between the two arms at T2 and T3 ($P > 0.05$), were lower in group 2b than in group 2a at T1 ($P < 0.05$). The quantitative detection results of HBV-DNA, HBsAg, and HBeAg in both groups showed a decreasing trend with the treatment time

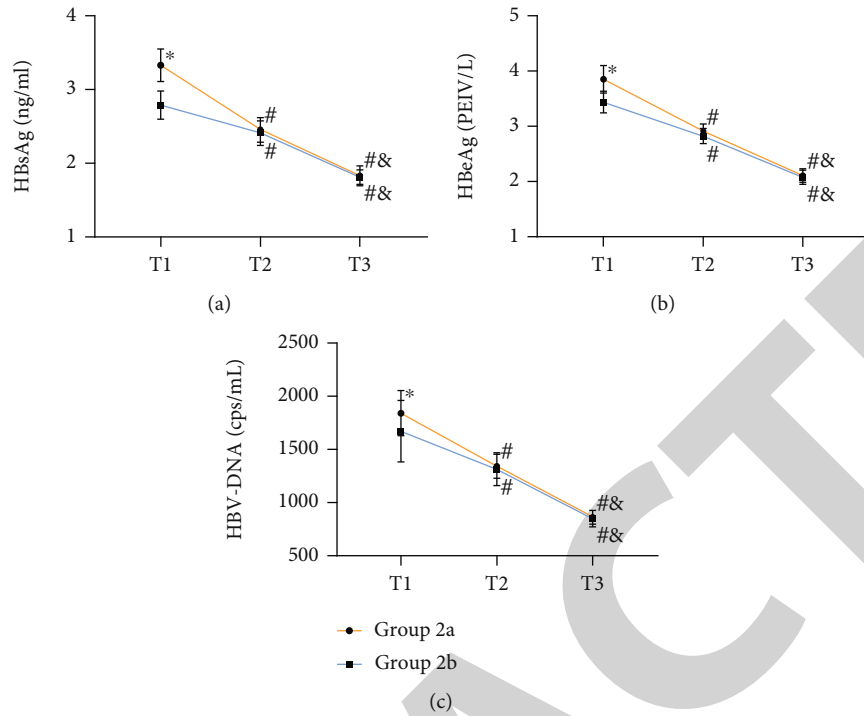


FIGURE 2: Comparison of marker conversion. (a) Comparison of quantitative results of HBsAg. (b) Comparison of quantitative results of HBeAg. (c) Comparison of quantitative results of HBV-DNA. Compared with 2b group, * $P < 0.05$. Compared with T1, # $P < 0.05$. Compared with T2, & $P < 0.05$.

TABLE 3: Comparison of marker conversion [$n(\%)$].

	Group 2a ($n = 42$)	Group 2b ($n = 42$)	χ^2	P
HBV-DNA negative conversion rate				
T1	8 (19.05)	13 (30.95)	1.587	0.208
T2	24 (57.14)	25 (59.52)	0.049	0.825
T3	34 (80.95)	36 (85.71)	0.343	0.558
HBsAg negative conversion rate				
T1	1 (2.38)	2 (4.76)	0.346	0.557
T2	3 (7.14)	4 (9.52)	0.156	0.693
T3	5 (11.90)	5 (11.90)	—	—
HBeAg negative conversion rate				
T1	8 (19.05)	10 (23.81)	0.283	0.595
T2	14 (33.33)	15 (35.71)	0.053	0.819
T3	22 (52.38)	24 (57.14)	0.192	0.661

($P < 0.05$). The two arms showed no evident difference in the negative conversion ratio of HBV-DNA, HBsAg, and HBeAg at T1, T2, and T3 ($P > 0.05$), as indicated by the statistical results of conversion (Figure 2 and Table 3).

3.5. Comparison of IFs. IL-1 β , IL-6, IL-8, and TNF- α , which differed insignificantly between the two arms at T3 ($P > 0.05$), were lower in group 2b versus group 2a at T1 and T2 ($P < 0.05$). In both arms, these IFs decreased gradually with the treatment time ($P < 0.05$) Figure 3.

3.6. Comparison of Hemodynamics. SBP and DBP showed no distinct difference between the two arms at T1, T2, and

T3 ($P > 0.05$); however, the MAP was higher and the CVP was lower in group 2b compared with group 2a ($P < 0.05$). During treatment, SBP and DBP of the two groups did not change significantly ($P > 0.05$), while MAP increased and CVP decreased gradually with the treatment time ($P < 0.05$) Figure 4.

3.7. Comparison of Cardiac Function. In the course of treatment, LVEF in both arms increased with the treatment time, while BNP decreased ($P < 0.05$). At T1, LVEF was significant higher in group 2b while the level of BNP was significant lower than in group 2a ($P < 0.05$) Figure 5.

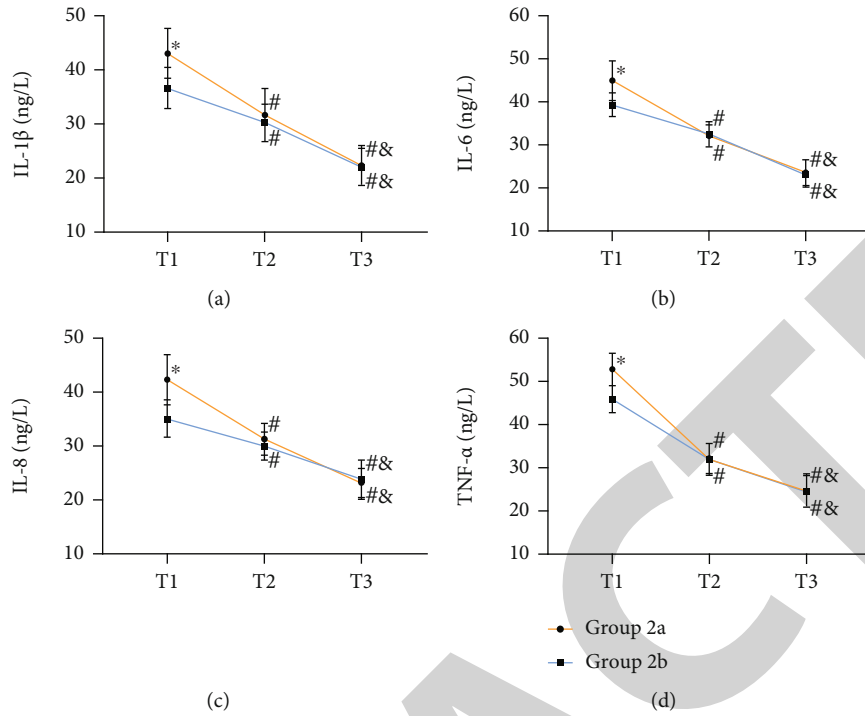


FIGURE 3: Comparison of inflammatory factors. (a) Comparison of IL-1β levels. (b) Comparison of IL-6 levels. (c) Comparison of IL-8 levels. (d) Comparison of TNF-α levels. Compared with 2b group, * $P < 0.05$. Compared with T1, # $P < 0.05$. Compared with T2, & $P < 0.05$.

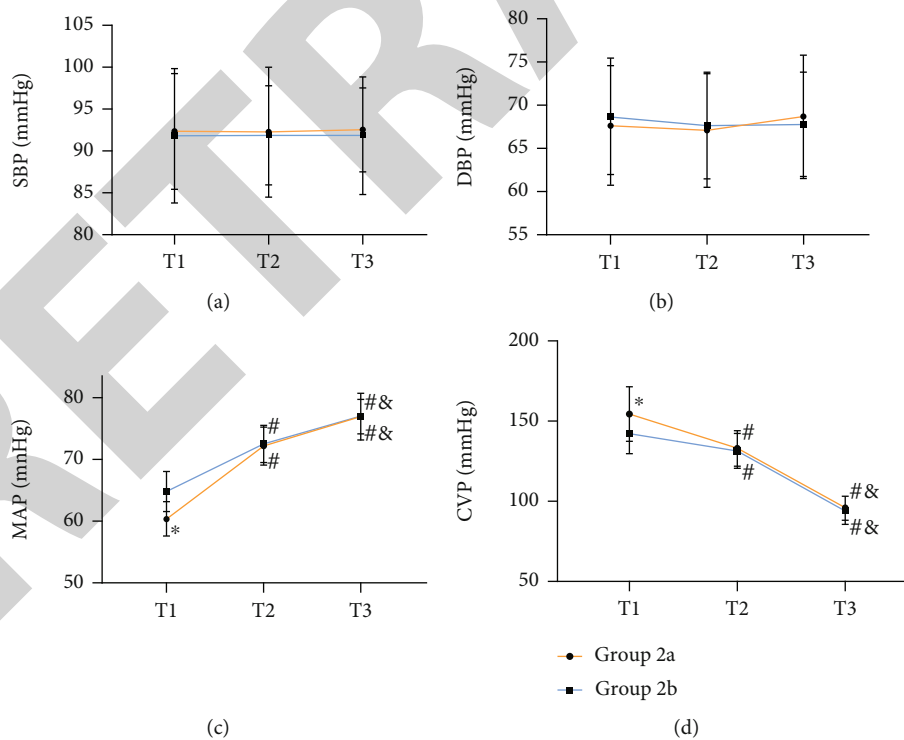


FIGURE 4: Comparison of hemodynamics. (a) Comparison of SBP. (b) Comparison of DBP. (c) Comparison of MAP. (d) Comparison of CVP. Compared with 2b group, * $P < 0.05$. Compared with T1, # $P < 0.05$. Compared with T2, & $P < 0.05$.

3.8. Comparison of Treatment Safety. Comparison was also made on the incidence of ARs during treatment. The two arms had similar cases of fever, fatigue, insomnia, skin itching, and

thyroid dysfunction ($P > 0.05$), while the cases with alopecia, thrombocytopenia, and granulocytopenia were fewer in group 2a compared with group 2b ($P < 0.05$) Table 4.

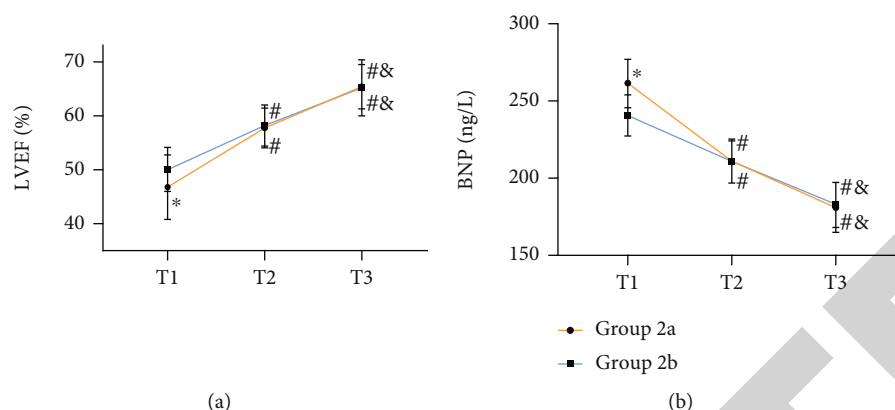


FIGURE 5: Comparison of cardiac function. (a) Comparison of LVEF. (b) Comparison of BNP. Compared with 2b group, $*P < 0.05$. Compared with T1, $^{\#}P < 0.05$. Compared with T2, $^{\&}P < 0.05$.

TABLE 4: Incidence of adverse reactions [n(%)].

	Fever	Fatigue	Thyroid dysfunction	Alopecia	Insomnia	Skin itching	Thrombocytopenia	Granulocytopenia
Group 2a (n = 42)	14 (33.33)	19 (45.24)	4 (9.52)	6 (14.29)	10 (23.81)	1 (2.38)	11 (26.19)	24 (57.14)
Group 2b (n = 42)	15 (35.71)	21 (50.00)	5 (11.90)	15 (35.71)	11 (26.19)	1 (2.38)	20 (47.62)	33 (78.57)
χ^2	0.053	0.191	0.124	5.143	0.063	—	4.141	4.421
P	0.819	0.662	0.724	0.023	0.801	—	0.042	0.036

3.9. Comparison of Prognosis. During the 2-year follow-up, 40 patients in group 2a and 41 patients in group 2b were successfully followed up. The positive seroconversion rate of HBsAg and HBeAg differed insignificantly between the two arms ($P > 0.05$) Figure 6.

4. Discussion

CHB, as a highly contagious and occult disease, should be brought to the forefront of the clinic and patients [18]. Although there are stable and effective vaccines for CHB, there is still a certain periodicity in the existence of CHB vaccines in humans. Research indicates that people need to be vaccinated again 10-15 years after CHB vaccination to maintain the integrity of CHB antibodies [19]. However, most patients ignore the time of CHB vaccine revaccination, resulting in HBV infection in the process of antibody failure [20]. Therefore, reducing the threat of CHB lies in improving people's awareness of vaccination and preventing HBV infection on the one hand and in getting timely and effective clinical treatment on the other hand. PEG-IFN α -2a and PEG-IFN α -2b are currently the main clinical treatment options for CHB, and the merits and demerits of the two have always been an urgent issue to be verified in clinical research. This study, by comparing the efficacy of PEG-IFN α -2a and PEG-IFN α -2b in the treatment of HBeAg-positive CHB patients, is of important reference significance for future clinical selection of therapeutic drugs.

In this study, we first compared the clinical efficacy and found no difference in the overall response rate between the

two arms, which suggested that both PEG-IFN α -2a and PEG-IFN α -2b had excellent therapeutic effects on CHB. Dogan et al. [12] compared the efficacy of pegylated interferon α -2a and α -2b in chronic hepatitis B patients and found that there were no significant differences between Peg-IFN α -2a and Peg-IFN α -2b treatment groups in achieving an SVR and undetectable HBV-DNA levels. Besides, the efficacy of PEG-IFN α -2a and PEG-IFN α -2b as the most commonly used drugs for treating CHB has been verified in many studies [21, 22], so the results obtained in this research are not out of expectation. Whereas, the merits and demerits of the two treatments need to be confirmed through various investigations. Furthermore, the liver function recovery was investigated. The results showed that after treatment, the indexes of liver function injury in both groups showed a decreasing trend, which further proved the therapeutic effect of both treatments on liver function. At T1, however, the reduction of ALT, AST, HA, LN, and IV-C was more significant in group 2b, suggesting that PEG-IFN α -2b could repair patients' liver function more quickly. At the same time, the detection results of CHB markers conversion showed that the negative conversion ratio of HBV-DNA, HBsAg, and HBeAg was consistent in the two groups after treatment; however, at T1, group 2b had lower HBV-DNA, HBsAg, and HBeAg as indicated by the quantitative test results with more patients showing complete response. As we all know, the key to the treatment of CHB lies in the inhibition of HBV-DNA polymerase activity [23]. HBsAg is the surface antigen of HBV-DNA particles, which can accelerate HBV maturation and complexity, while HBeAg is a soluble

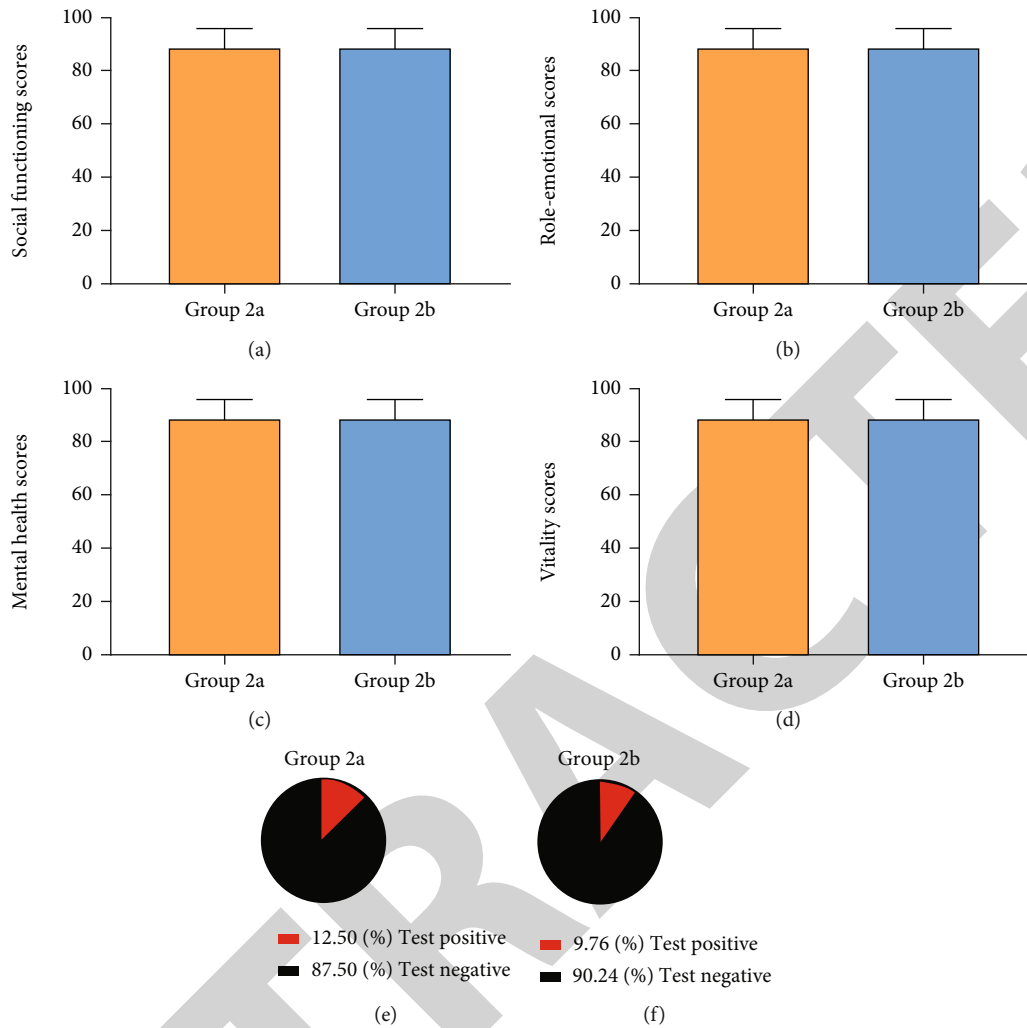


FIGURE 6: Comparison of prognosis. (a) Comparison of social functioning scores. (b) Comparison of role-emotional scores. (c) Comparison of mental health scores. (d) Comparison of vitality scores. (e) Comparison of positive seroconversion rate of HBsAg. (f) Comparison of positive seroconversion rate of HBeAg.

protein that can reflect HBV replication [24]. PEG-IFN α -2a and PEG-IFN α -2b are produced by combining polyethylene glycol molecules with a certain molecular weight on the basis of α -IFN, which can improve HBV-specific antibody levels in patients by enhancing oxidative metabolism, membrane depolarization, and phagocytosis [25].

Therefore, under the same pathway of action, we speculated that the reason for the difference between the two groups might be related to the molecular weight of the two kinds of IFN genes. PEG-IFN α -2a has a large molecular weight of about 40KD and better protection of IFN, so its blood concentration is more stable and its half-life is longer. However, due to its large molecular weight, PEG-IFN α -2a is mainly concentrated in blood and liver tissues after being injected into human body [26]. Because of this, some PEG-IFN α -2a drugs cannot be metabolized completely *in vivo* as the individual blood volume varies, so the liver function repair of some patients is slow in the initial use process. PEG-IFN α -2b, on the other hand, is only 12KD and has a wider distribution in the body. After injection, it can com-

plete drug metabolism in blood, muscle, tissue, fat, and even cells [27], so it has a more rapid and significant effect on patients at the initial stage of use.

In addition, continuous HBV replication and the resulting immune-mediated response are important factors leading to hepatocyte inflammatory necrosis and hepatofibrosis. Excessive inflammatory reaction and fibrosis of hepatocytes will further destroy hepatocytes [28]. Therefore, in the treatment of CHB, anti-inflammatory effect is also one of the most important links. In this study, PEG-IFN α -2b showed faster inhibition of inflammation, which may also be related to our above inference. The occurrence of inflammatory reaction is a complicated pathological process, in which IFs are dominant, and cytokines such as monocytes and eosinophils are also involved [29]. As aforementioned, PEG-IFN α -2a works only in liver and blood and does not affect the activity cycle of cells, so its anti-inflammatory response is not as significant as PEG-IFN α -2b, an IFN gene involved in the cell life cycle. Similarly, the liver, as the most important metabolic organ in the human body, has a vital

influence on the hemodynamics of the human body, and the most direct effect of hemodynamics is on the pumping capacity of the heart [30, 31]. While comparing the hemodynamic and cardiac functions of the two groups, we also found that PEG-IFN α -2b had a more significant improvement effect on MAP, CVP, LVEF, and BNP at the initial stage of treatment. This also verified our point of view again, indicating that PEG-IFN α -2b had a more comprehensive and rapid action in humans. However, a higher incidence of alopecia, thrombocytopenia, and granulocytopenia was identified in group 2b than in group 2a, suggesting a higher safety profile for PEG-IFN α -2a. It is also because PEG-IFN α -2a can be completely metabolized by the liver after the interference effect is completed, while PEG-IFN α -2b has a certain inhibitory effect on more cytokines, thus contributing to the reduction of such cells. It is also possible that PEG-IFN α -2b contains a higher number of IFN molecules (specific activity) per milligram of protein (PEG-IFN α -2b has a specific activity of 108 versus 107 of PEG-IFN α -2a) [32].

Finally, the follow-up results revealed no difference in the prognostic QOL and recurrence of CHB between the two arms, indicating that both treatments had stable long-term effect and high application value. However, through previous studies, we also found that the production rate of neutralizing antibodies against PEG-IFN α -2b was only about 3%, while that of PEG-IFN α -2a was about 6%-10% [33], which indicated that PEG-IFN α -2b was more effective in the long-term treatment of CHB. In our research, there was no difference in the prognosis between the two groups, which may be due to the small difference in the rate of neutralizing antibody production between the two groups on the one hand, or the chance caused by the short follow-up time or the small number of cases on the other hand.

However, the study still has some limitations, and due to the small base of research participants, we need to further expand the sample size to improve the comprehensiveness of experimental results. In addition, this paper proposed that the molecular weight difference between PEG-IFN α -2a and PEG-IFN α -2b was responsible for the differential performance of CHB treatment, which needs to be confirmed by further *in vitro* experiments, and the underlying mechanism needs to be clarified. In the future, we will conduct more in-depth and comprehensive experimental analysis on the treatment of CHB to obtain more effective experimental results for clinical reference.

5. Conclusion

Both PEG-IFN α -2a and PEG-IFN α -2b have excellent and stable therapeutic effects on HBeAg-positive CHB, among which PEG-IFN α -2b has a faster therapeutic process but higher side effects. These findings can provide reference for future clinical treatment of CHB.

Data Availability

The simulation experiment data used to support the findings of this study are available from the corresponding author upon request.

Conflicts of Interest

The authors declare no competing interests.

References

- [1] A. S. Lok, B. J. McMahon, R. S. Brown Jr. et al., "Antiviral therapy for chronic hepatitis B viral infection in adults: a systematic review and meta-analysis," *Hepatology*, vol. 63, no. 1, pp. 284–306, 2016.
- [2] N. A. Terrault, N. H. Bzowej, K.-M. Chang et al., "Aasld guidelines for treatment of chronic hepatitis B," *Hepatology*, vol. 63, no. 1, pp. 261–283, 2016.
- [3] K. R. Mysore and D. H. Leung, "Hepatitis B and C," *Clinics in Liver Disease*, vol. 22, no. 4, pp. 703–722, 2018.
- [4] T. J. Liang, "Hepatitis B: the virus and disease," *Hepatology*, vol. 49, no. S5, pp. S13–S21, 2009.
- [5] R. G. Gish, B. D. Given, C.-L. Lai et al., "Chronic hepatitis B: virology, natural history, current management and a glimpse at future opportunities," *Antiviral Research*, vol. 121, pp. 47–58, 2015.
- [6] J. Zhang, S. Lin, D. Jiang et al., "Chronic hepatitis B and non-alcoholic fatty liver disease: conspirators or competitors?," *Liver International*, vol. 40, no. 3, pp. 496–508, 2020.
- [7] Y. Y. Zhang and K. Q. Hu, "Rethinking the pathogenesis of hepatitis b virus (HBV) infection," *Journal of Medical Virology*, vol. 87, no. 12, pp. 1989–1999, 2015.
- [8] L.-Y. Mak, W.-K. Seto, J. Fung, and M.-F. Yuen, "Use of hbsag quantification in the natural history and treatment of chronic hepatitis B," *Hepatology International*, vol. 14, no. 1, pp. 35–46, 2020.
- [9] O. Paccoud, L. Surgers, and K. Lacombe, "Hepatitis B virus infection: natural history, clinical manifestations and therapeutic approach," *La Revue de Médecine Interne*, vol. 40, no. 9, pp. 590–598, 2019.
- [10] Y.-F. Shih and C.-J. Liu, "Hepatitis C virus and hepatitis b virus co-infection," *Viruses*, vol. 12, no. 7, p. 741, 2020.
- [11] F.-K. Zhang, "Interferon-alfa in the treatment of chronic hepatitis B," *Hepatobiliary & Pancreatic Diseases International*, vol. 3, no. 3, pp. 337–340, 2004.
- [12] U. B. Dogan, N. Golge, and M. S. Akin, "The comparison of the efficacy of pegylated interferon α -2a and α -2b in chronic hepatitis B patients," *European Journal of Gastroenterology & Hepatology*, vol. 25, no. 11, pp. 1312–1316, 2013.
- [13] G. Gao, X. Xu, Y. Hu, and H. Yan, "Study on the relationship between hepatitis b virus genotypes and the effect of polyethylene glycol-interferon-alpha therapy on hbeag-positive chronic hepatitis B," *Zhonghua Nei Ke Za Zhi*, vol. 52, no. 12, pp. 1009–1012, 2013.
- [14] M. W. Fried, T. Piratvisuth, G. K. Lau et al., "Hbeag and hepatitis b virus DNA as outcome predictors during therapy with peginterferon alfa-2a for hbeag-positive chronic hepatitis B," *Hepatology*, vol. 47, no. 2, pp. 428–434, 2008.
- [15] H. Liang, Y. Liu, X. Jiang et al., "Impact of hepatic steatosis on the antiviral effects of peg-ifna-2a in patients with chronic hepatitis B and the associated mechanism," *Gastroenterology Research and Practice*, vol. 2020, 10 pages, 2020.
- [16] P. Lampertico, K. Agarwal, T. Berg et al., "EASL 2017 clinical practice guidelines on the management of hepatitis B virus infection," *Journal of Hepatology*, vol. 67, no. 2, pp. 370–398, 2017.

Retraction

Retracted: Characterization of the Prognostic Values of CXCL Family in Epstein–Barr Virus Associated Gastric Cancer

Oxidative Medicine and Cellular Longevity

Received 8 August 2023; Accepted 8 August 2023; Published 9 August 2023

Copyright © 2023 Oxidative Medicine and Cellular Longevity. This is an open access article distributed under the Creative Commons Attribution License, which permits unrestricted use, distribution, and reproduction in any medium, provided the original work is properly cited.

This article has been retracted by Hindawi following an investigation undertaken by the publisher [1]. This investigation has uncovered evidence of one or more of the following indicators of systematic manipulation of the publication process:

- (1) Discrepancies in scope
- (2) Discrepancies in the description of the research reported
- (3) Discrepancies between the availability of data and the research described
- (4) Inappropriate citations
- (5) Incoherent, meaningless and/or irrelevant content included in the article
- (6) Peer-review manipulation

The presence of these indicators undermines our confidence in the integrity of the article's content and we cannot, therefore, vouch for its reliability. Please note that this notice is intended solely to alert readers that the content of this article is unreliable. We have not investigated whether authors were aware of or involved in the systematic manipulation of the publication process.

Wiley and Hindawi regrets that the usual quality checks did not identify these issues before publication and have since put additional measures in place to safeguard research integrity.

We wish to credit our own Research Integrity and Research Publishing teams and anonymous and named external researchers and research integrity experts for contributing to this investigation.

The corresponding author, as the representative of all authors, has been given the opportunity to register their agreement or disagreement to this retraction. We have kept a record of any response received.

References

- [1] L. Mu, S. Hu, G. Li et al., "Characterization of the Prognostic Values of CXCL Family in Epstein–Barr Virus Associated Gastric Cancer," *Oxidative Medicine and Cellular Longevity*, vol. 2022, Article ID 2218140, 24 pages, 2022.

Research Article

Characterization of the Prognostic Values of CXCL Family in Epstein–Barr Virus Associated Gastric Cancer

Li Mu, Shun Hu, Guoping Li, Ping Wu, Caihong Ren, Taiyu Lin, and Sheng Zhang 

Department of Pathology, The First Affiliated Hospital of Fujian Medical University, Fuzhou, Fujian 350005, China

Correspondence should be addressed to Sheng Zhang; hudan199112@126.com

Received 1 March 2022; Revised 12 April 2022; Accepted 18 April 2022; Published 1 June 2022

Academic Editor: Shao Liang

Copyright © 2022 Li Mu et al. This is an open access article distributed under the Creative Commons Attribution License, which permits unrestricted use, distribution, and reproduction in any medium, provided the original work is properly cited.

Background. CXCL family is a class of secreted growth factors signaling through G-protein-coupled receptors, and abnormal expression is associated with the growth and progression of many tumors. However, their prognostic value has been poorly studied in Epstein–Barr virus- (EBV-) associated gastric cancer (EBVaGC). Therefore, it is of great significance to explore the prognostic value of the CXCL family in EBVaGC. **Methods.** CXCL family mRNA expression was analyzed in STAD data from The Cancer Genome Atlas (TCGA). Kaplan–Meier Plotter was used to assess the prognostic value of the CXCL family. Transcription factors (TFs) and miRNAs associated with the CXCL family were identified by TFCheckpoint, miRWalk, and ViRBase databases. The prognostic model was evaluated using the EBVaGC patient cohort GSE51575. **Results.** The mRNA expression of CXCL1/3/5/6/8/9/10/11/16 was significantly upregulated, while the expression of CXCL12/14 was downregulated in EBVaGC compared with normal tissues from TCGA-STAD. The mRNA expressions of CXCL9, CXCL10, CXCL11, and CXCL17 in EBVaGCs were higher than those in EBVnGCs, but the mRNA expressions of CXCL6, CXCL12, and CXCL17 were lower than those in EBVnGCs. The mRNA expression levels of CXCL9, CXCL10, and CXCL11 in EBVaGCs were higher than those in EBVnGCs regardless of the tumor stage. High mRNA expression of CXCL8 was associated with better OS in patients with EBVaGC, while high expression of CXCL9 was associated with better OS in patients with EBVnGC. We obtained 10 candidate potential transcription factors (TFs) associated with CXCLs: OTOP3, NKX6-2, NKX2-2, FEV, SMYD1, TRIMSO, TBX10, CDX1, SLC26A3, and ARC. 576 miRNA–mRNA interactions were obtained. Among them, 65 miRNAs were predicted to be correlated with CXCL6, CXCL9, CXCL10, and CXCL11. Similar to the results of TCGA-STAD, the GSE51575 dataset also showed that the mRNA expression levels of CXCL1/3/9/10/11/16 were markedly enhanced in EBVaGC tissues compared with corresponding normal gastric mucosa tissues, while the mRNA expression levels of CXCL12/14 were significantly reduced. The mRNA expression levels of CXCL3/9/10/11/13/17 were increased in EBVaGC compared with EBVnGC tissues. **Conclusions.** The expression differences of CXCL family members are closely associated with the progression of EBVaGC. Expression of CXCL9/10/11/17 mRNA may be a promising prognostic indicator for EBVaGC patients.

1. Introduction

Gastric cancer (GC) ranks fifth and fourth in global morbidity and mortality, respectively, with more than 1 million new cases and an estimated 769,000 deaths by 2020 (equivalent to 1 in 13 deaths globally) [1–3]. Due to aging population, the number of newly diagnosed cancers worldwide is expected to triple by 2050 [4]. Gastric cancer is twice as common in men as it is in women, with the highest incidence in Asia and Eastern Europe, while rates are generally low in North America and northern

Europe. Gastric cancer occurs mainly in developing countries. The prognosis is poor when gastric cancer progresses [5–7].

Epstein–Barr virus (EBV) is human herpesvirus type IV. 90%–95% of humans have a history of invisible infection, which is closely related to the occurrence of human cancer [8]. Since Burke et al. first reported the correlation between Epstein–Barr virus and gastric cancer in 1990 [9], more and more evidence has confirmed the key role of EBV in the formation and development of GC, and a series of studies have been carried out, and various related theories have

been put forward [10, 11]. However, the relationship and mechanism between Epstein-Barr virus infection and the pathogenesis of gastric cancer have not been fully elucidated so far. Therefore, it is of great significance to clarify the role of EBV infection in carcinogenesis and prognosis of gastric cancer.

Chemokines are small cytokines or signaling proteins secreted by cells, with small molecular weight (about 8-10kDa), mainly consisting of four subfamilies: CXC, CC, CX3C, and XC [11]. Chemokines exert their biological effects through interactions with G-protein linked transmembrane receptors (chemokine receptors) and participate in the proliferation, invasion, and metastasis of tumor cells [12]. Among them, CXC-motif chemokine ligand (CXCL) family is involved in regulating immune cell activity, inducing tumor cell migration, and regulating tumor cell proliferation and neoplastic microvascular formation, which is closely related to tumor occurrence and development [13, 14]. CXCL family contains CXCL1, CXCL2, CXCL3, CXCL4, CXCL5, CXCL6, CXCL7, CXCL8, CXCL9, CXCL10, CXCL11, CXCL12, CXCL13, CXCL14, CXCL15, CXCL16, and CXCL17, involved in the invasion and metastasis of gastric cancer [15–17]. However, the role of CXCL family in the pathogenesis and prognosis of EBVaGC has not been clarified so far.

Recently, more and more studies have shown that CXCL family members can be used as targets for GC therapy, and the construction of CXCL family gene regulatory network is of great significance to comprehensively analyze the prognostic value of CXCL in EBVaGC [18–20]. With the increasing availability of expression databases from cancers, it is possible to extract and integrate databases to investigate the occurrence and progression of cancer. In this study, we evaluated the expression differences and prognostic value of CXCL family in public databases through comprehensive bioinformatics methods, providing new ideas for further research on regulatory mechanism and targeted therapy in EBVaGC.

2. Methods

2.1. Gastric Cancer mRNA Expression Dataset Collection and Data Standardization. The mRNA expression profiles and corresponding clinical data of 618 GC patients were obtained from TCGA Gastric adenocarcinoma (TCGA-STAD) cohort of Xena download at the University of California, Santa Cruz (UCSC). According to exclusion criteria presented in the literature [21], patients with preoperative chemotherapy, targeted therapy, radiotherapy, lack of clinical staging, and lack of mRNA expression were excluded. After clinical data standardization, genomic data of 223 gastric cancers or normal gastric mucosa tissues were obtained, including 23 EBVaGCs, 200 EBVnGCs, and 26 normal gastric mucosa tissues. Table 1 shows corresponding clinical information.

2.2. Data Processing. The sample data collected above were used for gene expression analysis. First, DESeq2 software package was used to standardize the original count data. Then, DESeq2 software package was used to carry out difference analysis on the normalized count data. Using corrected P values (P -adj) < 0.05 and multiples of changes \log_2 fold

TABLE 1: Clinicopathological characteristics of EBVaGC and EBVnGC in TCGA-STAD.

	EBVaGC ($n = 23$)	EBVnGC ($n = 200$)
Age	63.0 \pm 11.6	65.8 \pm 10.6
Gender		
Male	19	119
Female	4	81
Tumor location		
Gastric fundus	5	26
Gastric body	9	47
Gastric antrum	6	80
Cardia	3	39
Stomach, NOS		8
Histological type		
Papillary adenocarcinoma		3
Adenocarcinoma, mixed type		1
Tubular adenocarcinoma	4	26
Adenocarcinoma, NOS	11	85
Adenocarcinoma, diffuse	6	33
Adenocarcinoma, intestinal type	2	36
Signet ring cell carcinoma		2
Mucinous adenocarcinoma		14
AJCC pathological stage		
I	1	30
II	7	78
III	13	74
IV	2	18
Prognosis		
Survival	16	128
Death	7	71
Unknown		1

change ≥ 1 or ≤ -1 as thresholds, differentially expressed genes with significant changes were screened between EBVaGC and normal gastric mucosa, as well as between EBVaGC and EBVnGC, and volcano maps were drawn. Next, CXCL family members were screened. The mRNA expression levels of all CXCL between EBVaGC and normal gastric mucosa, as well as between EBVaGC and EBVnGC, were, respectively, displayed. Each figure was a box plot of mRNA expression level and overlaid a scatter plot of CXCL expression level in each sample.

The expression changes of CXCL mRNA in different clinical stages of GC were analyzed. Stages I and II were defined as the low-stage group, and stages III and IV were defined as the high-stage group. The expression changes of 14 CXCL family members in different clinical stages were displayed.

2.3. Prognostic Value of CXCL Family Members between EBVaGC and EBVnGC. The prognostic value of CXCL family members in EBVaGC was evaluated by using Kaplan-Meier

Plotter (<https://www.kmplot.com>) [22]. Taking the median value of each CXCL in the sample as the threshold value, the CXCL was divided into two groups of high expression or low expression, and the P value of log-rank was calculated. Survival data and the optimal cut-off value were confirmed according to the algorithms embedded in the KM plotter.

2.4. PPI Network Construction. STRING (<https://string-db.org/>) is a website about protein interactions (PPI). In this study, we collected and integrated different expressions and potential interactions of CXCL family members in EBVaGC through PPI network analysis and constructed a PPI network of coexpressed genes.

2.5. Microarray Data Processing. GSE51575 collected from the GEO database is an mRNA profiling for EBVaGC (<http://www.ncbi.nlm.nih.gov/geo/>). GSE51575 microarray data (GPL13607 platform) contained a total of 26 patients which were divided into 14 EBVnGC and 12 EBVaGC. The probe symbols were transformed into gene symbols. The original data were introduced into R software for data normalization. One patient (GSM1248661) was deleted because his gastric cancer tissue data migrated to the normal tissue range, and his paired normal gastric mucosa tissue data were also deleted (GSM1248660). Finally, 25 patients were enrolled, including 14 patients with EBVnGC and matched normal gastric mucosa and 11 patients with EBVaGC and matched normal gastric mucosa. The cut-off criteria were set to $P\text{value} < 0.05$, and $|\log_2 \text{fold change}| \geq 1.5$ was regarded as differentially expressed genes (DEGs). DEGs were recognized by the Limma package.

The mRNA data of CXCL were extracted from the database. The differences between EBVaGC/EBVnGC and its corresponding normal gastric mucosa and between EBVaGC and EBVnGC and between paired normal gastric mucosa of EBVaGC and EBVnGC were analyzed.

2.6. Statistical Analysis. SPSS 20.0 and GraphPad Prism 5.0 software (GraphPad, La Jolla, CA, USA) was employed for statistical analysis. The unpaired Student t -test was employed to compare the means between groups. Pearson correlation analysis is used for correlation analysis. P values < 0.05 were considered significant.

3. Results

3.1. CXCL Family Members Are Significantly Overexpressed in GC. In this study, TCGA-STAD was used to verify the mRNA expression of CXCL family members in EBVaGC. By downloading clinical information of TCGA-STAD, genomic data of 223 cases of GC and 26 cases of normal gastric mucosa were obtained. In GCs, 23 cases were EBVaGC, and 200 cases were EBVnGC. Based on DESeq2 algorithm, volcano map showed the differentially expressed genes (DEGs) between EBVaGC and normal gastric mucosa (Figure 1(a)) and between EBVnGC and normal gastric mucosa (Figure 1(b)).

Next, we analyzed the difference of CXCL family mRNA expression between EBVaGC or EBVnGC and normal gastric mucosa. Results show that CXCL1, CXCL3, CXCL5, CXCL6,

CXCL8, CXCL9, CXCL10, CXCL11, and CXCL16 mRNA expressions were significantly higher in EBVaGC (Figure 1(c)) and EBVnGC (Figure 1(d)); on the contrary, CXCL12, CXCL14, and CXCL17 mRNA expression decreased. Our results confirmed that mRNA expression of most CXCL family members was drastically elevated in EBVaGC.

3.2. Relationship between mRNA Expression of CXCL Family Members and EBV Infection in GCs. We further studied the mRNA expression differences of CXCL family members between EBVaGC and EBVnGC. After data normalization, DEGs were identified between 23 EBVaGCs and 200 EBVnGCs with $FDR \leq 0.05$ and $|\log_2 FC| \geq 1$. A volcano map of DEGs was showed in Figure 2(a). Our results showed that the mRNA expressions of CXCL9, CXCL10, CXCL11, and CXCL17 in EBVaGCs were higher than those in EBVnGCs, but the mRNA expressions of CXCL6 and CXCL12 in EBVaGCs were lower than those in EBVnGCs (Figure 2(b)). The results of TCGA-STAD data analysis showed that the mRNA expression of CXCL family members was significantly correlated with EBV infection in GCs.

3.3. Relationship between mRNA Expression of CXCL Family Members and Tumor Stage in EBVaGCs Based on TCGA-STAD. Figure 3 shows that the mRNA expression of CXCL family members was closely related to the clinical stage of EBVaGC. The mRNA expression levels of CXCL9, CXCL10, and CXCL11 in EBVaGCs were higher than those in EBVnGCs regardless of the early or late stage of tumors.

3.4. Prognostic Value of CXCL Family Members in GCs. Using KM Plotter, we evaluated the prognostic value of CXCL mRNA expression in GC with or without EBV infection. As shown in Figure 4, high CXCL8 mRNA expression was significantly associated with better OS in patients with EBVaGC ($P = 0.027$), while high CXCL9 mRNA expression was significantly associated with better OS in patients with EBVnGC ($P = 0.049$). The results also showed that mRNA expression of other CXCL family members was not associated with survival.

3.5. Gene Network and Interaction Analysis of CXCL Family Members in EBVaGC. We performed PPI network analysis in STRING to further explore the potential interaction between differentially expressed CXCLs and adjacent genes in EBVaGC. PPI network consists of 176 nodes and 117 edges (Figure 5(a)). Then, the TFCheckpoint database was used to identify potential transcription factors (TFs) linked to CXCL family members in PPI network, and 10 candidate TFs were obtained: OTOP3, NKX6-2, NKX2-2, FEV, SMYD1, TRIMSO, TBX10, CDX1, SLC26A3, and ARC. Results from KinG database showed that these TFs are not kinases. No EBVaGC-associated kinases act on the CXCL family. Overall, no predicted kinases were associated with CXCL family members in EBVaGC. Our study further explored potential miRNAs that may be predicted in relation to members of the CXCL family. The miRNAs associated with CXCL family members in the PPI network were then explored using miRWalk and ViRBase databases, and 576 miRNA-mRNA interactions were obtained. Among them, 65 miRNAs were predicted to be correlated with CXCL6, CXCL9,

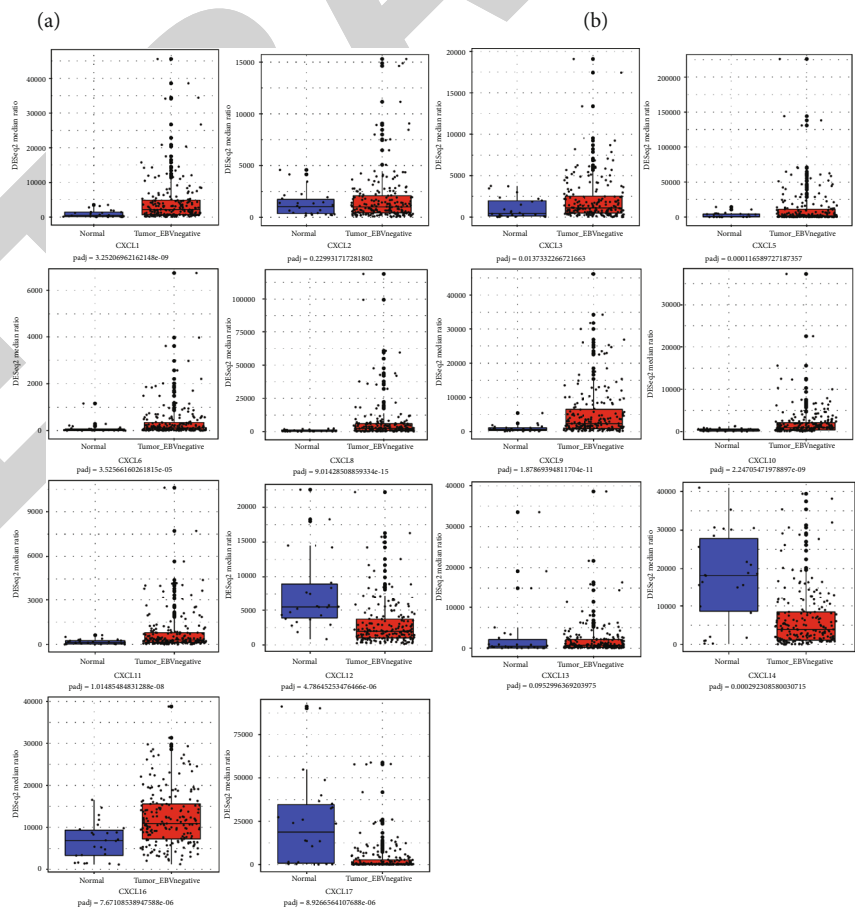
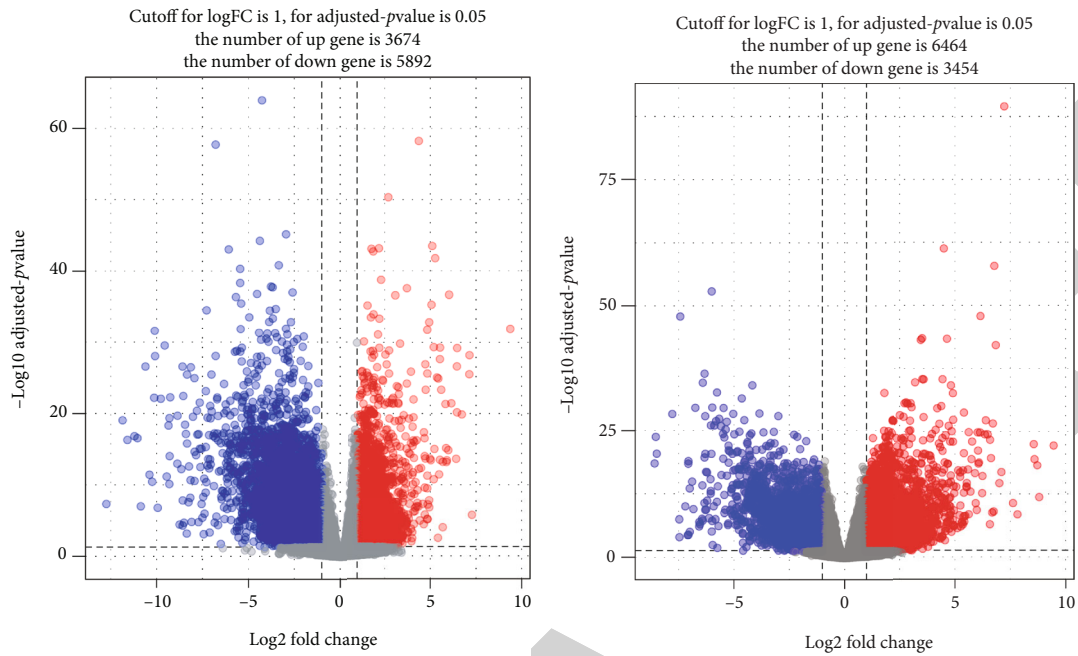


FIGURE 1: Continued.

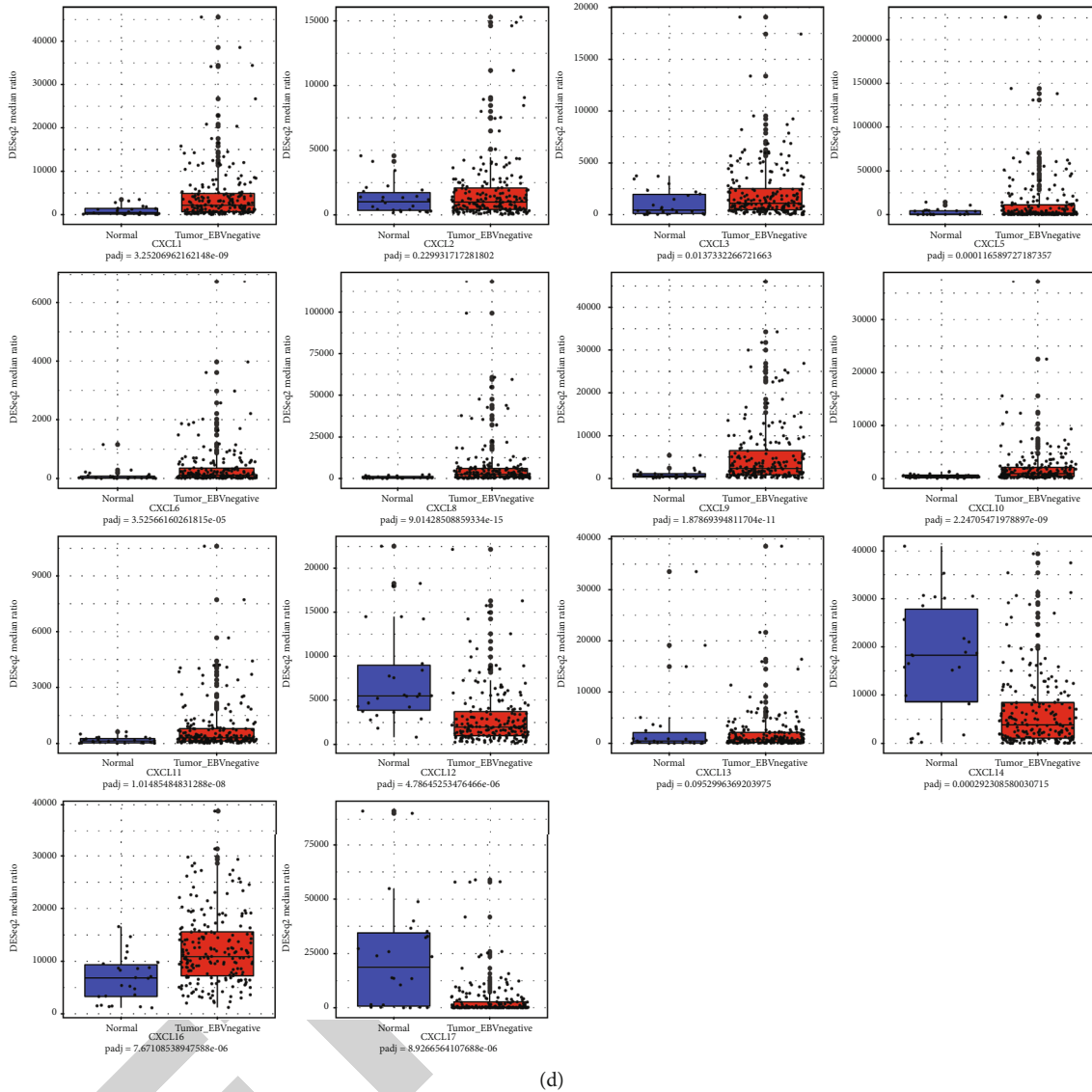


FIGURE 1: CXCL family members markedly overexpressed in EBVaGC. (a, b) Volcano plot. DEGs were selected using P value < 0.05 and $|\log_2 \text{fold change}| \geq 1.5$. (c) The mRNA expression of CXCL members between EBVaGC and normal tissues; $*P < 0.05$. (d) The mRNA expression of CXCL members between EBVnGC and normal tissues; $*P < 0.05$.

CXCL10, and CXCL11 (Figure 5(b)). In addition, this PPI network with transcription factors and miRNAs was divided into four small graphs centered on CXCL6, CXCL9, CXCL10, and CXCL11 (Figures 5(c)–5(f)).

3.6. Validation of the Prognostic Value of EBVaGC Datasets from the GEO Database (GSE51575). We validated the prognostic model using the EBVaGC patient cohort GSE51575 dataset. The GSE51575 dataset from the GEO cohort contained 26 patients with gastric cancer, including 14 EBVnGC and its paired normal gastric mucosa and 12 EBVaGC and its paired normal gastric mucosa. The gene expression level of GSE51575 was standardized by quartile partition method, and the standardization results are shown in Figure 6(a). The density profile shows an approximate normal distribution (Figure 6(b)). UMAP showed that the data of 1 gastric cancer sample (GSE 1248661) was deviated to range of nor-

mal gastric mucosa and deleted, and its paired normal gastric mucosa (GSE 1248660) was also deleted (Figure 6(c)). After the exclusion of two samples, the data were standardized again (Figures 6(d) and 6(e)). We found that all samples met expectations through UMAP diagnostic RAM. Finally, 25 patients were obtained for follow-up analysis, including 14 EBVnGC and its paired normal gastric mucosa and 11 EBVaGC and its paired normal gastric mucosa (Figures 6(f) and 6(g)). mRNA data of CXCL family members were extracted and analyzed. Figure 7 shows CXCL mRNA expression levels between EBVaGC and corresponding normal gastric mucosa. We found that the mRNA expression levels of CXCL1/3/9/10/11/16 were markedly enhanced in EBVaGC tissues compared with corresponding normal gastric mucosa tissues, which was similar to TCGA-STAD. By contrast, the mRNA expression levels of CXCL12/14 were significantly reduced in EBVaGC compared with corresponding normal

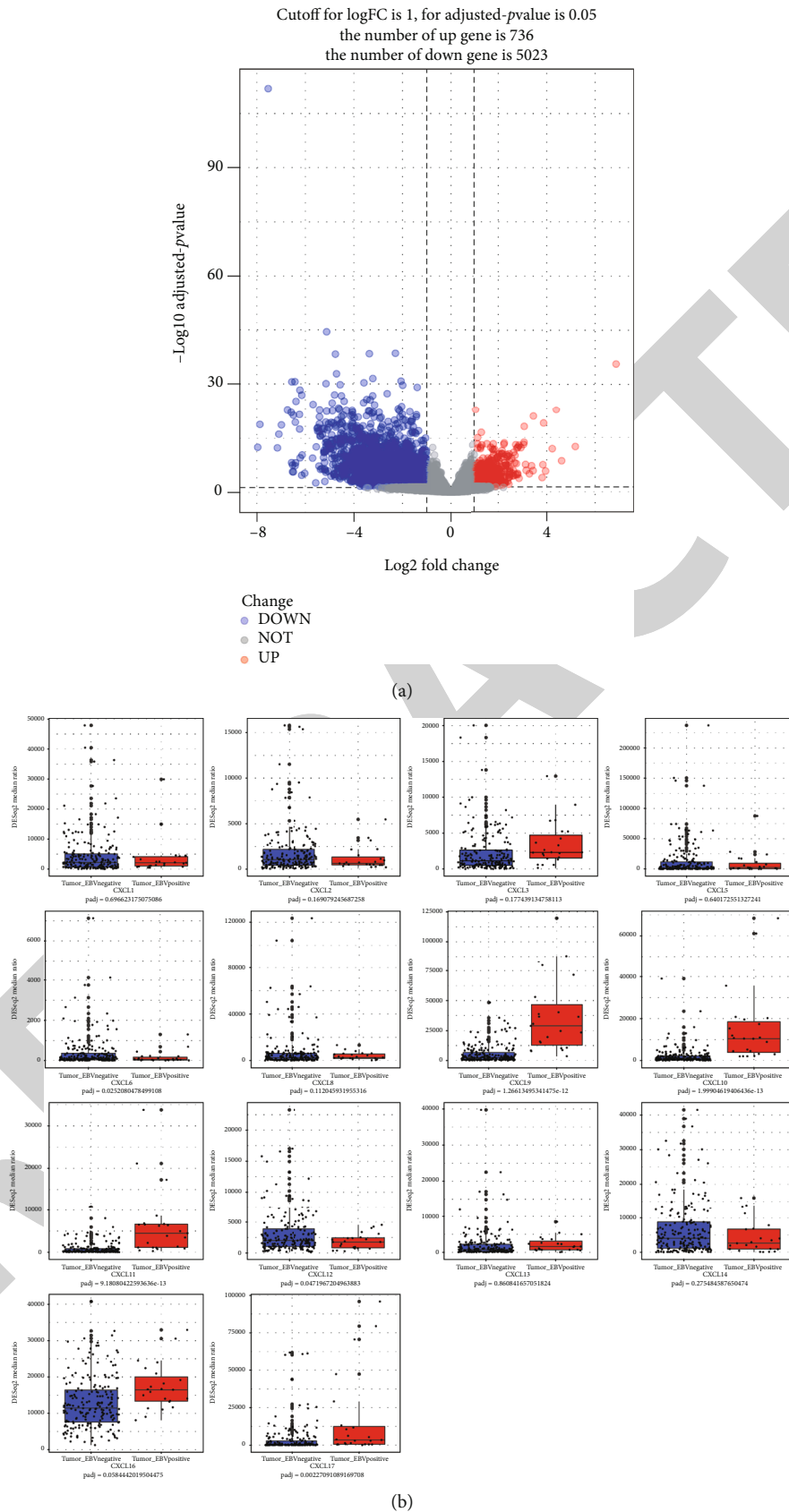


FIGURE 2: The relationship between CXCL family members and EBV infection in GCs. (a) Volcano plot. DEGs were selected using P value < 0.05 and $|\log_2 \text{fold change}| \geq 1.5$. (b) The mRNA expression of CXCL members between EBVaGC and EBVnGC; * $P < 0.05$.

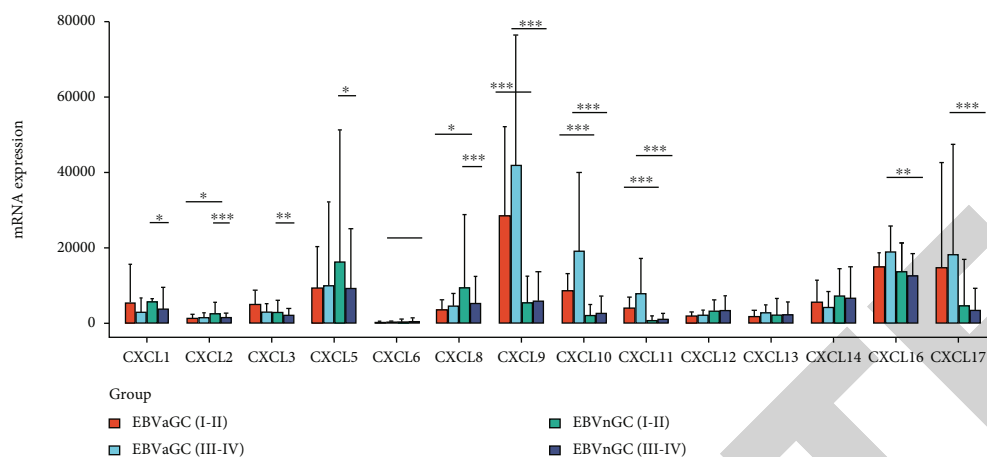


FIGURE 3: Relationship between mRNA expression of CXCL family members and tumor stage in EBVaGCs based on TCGA-STAD.

gastric mucosa tissues. Moreover, the mRNA expression levels of CXCL10/11/13/17/3/9 were markedly increased in EBVaGC compared with EBVnGC tissues.

Similar to TCGA results, the GSE51575 dataset also showed that the mRNA expression of CXCL family members was closely related to the clinical staging of EBVaGC. The mRNA expression of CXCL 9/10/11/17 was higher in EBVaGC than that in EBVnGC. Moreover, the validation data for GSE51575 showed no significant difference in mRNA expression levels of CXCL family members among the three subtypes of EBVaGC.

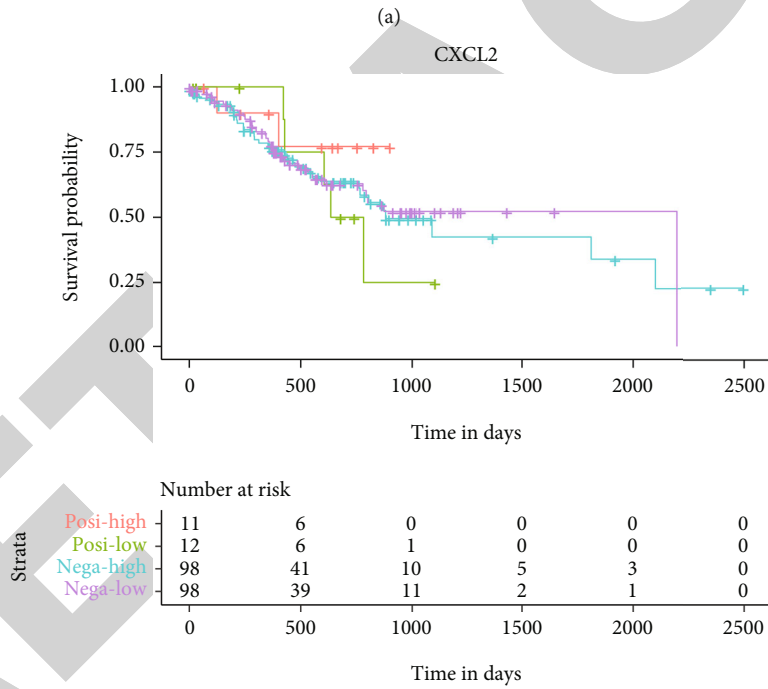
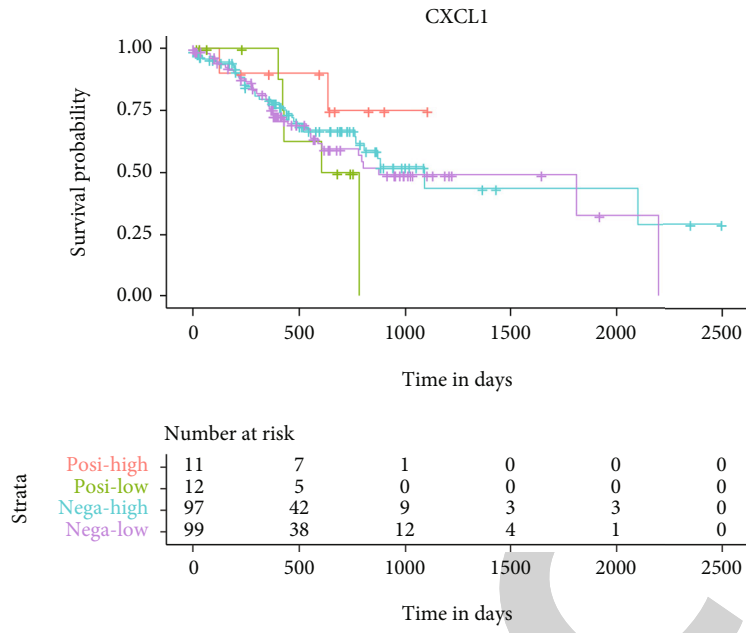
4. Discussion

The chemokine superfamily is a large family of small-molecule cytokine proteins with chemotactic activity. It consists of about 50 endogenous chemokine ligands and 20 G protein-coupled 7 transmembrane signaling receptors, whose homologous receptors are expressed by cancer cells and stromal cells. Chemokines can be divided into CXC, CC, XC, and CX3C subtypes according to the differences in the relative positions of the first two of the four conservative cysteines, among which CC and CXC chemokines are the majority. Several chemokines can bind to the same receptor, and one chemokine can bind to many receptors, therefore, resulting in many combinations and many biological results. Chemokines are important for tumor growth and development. Chemokines by adjusting the stem cell characteristics of tumor cells, inducing cancer cell proliferation, prevent cancer cell apoptosis and directly control the growth of tumor. Chemokines can affect tumor stromal cells and induce tumor microenvironment cells to release growth factor and angiogenesis factor to adjust the new angiogenesis. Neurogenesis and fibrogenesis indirectly regulate tumor growth [23–25].

In addition to their role in regulating leukocyte transport, CXC chemokines are usually accompanied by a series of molecular and biological changes during the genesis and development of tumor cells. CXC chemokine subfamily is closely related to immune response to tumor and biological behavior of tumor. CXC chemokines can regulate the cell

transformation of tumor cells, change the angiogenic environment, promote the growth of local tumor cells, enter the circulatory system through the invasion of extracellular matrix (ECM) and vascular basement membrane, and eventually metastasize to distant organs. CXC chemokines have been shown to be closely involved in the growth, invasion, and metastasis of tumors [26].

Gastric cancer is a solid tumor in which the extracellular stroma is composed of endothelial cells, fibroblasts, lymphocytes, neutrophils, and macrophages. All of these cells are involved in chemokine production [27]. CXC chemokines and their receptors are widely expressed in gastric cancer and participate in the invasion and metastasis of gastric cancer, which is related to prognosis [28]. Chen et al. included 69 patients with gastric cancer in a single-center prospective study and detected the concentrations of chemokines in peripheral blood and tumor drainage blood, and the patients were followed up for 6 years. The results showed that the concentrations of CXCL1, CXCL2, CXCL4, CXCL5, CXCL7, CXCL8, CXCL9, CXCL10, CXCL12, CXCL13, and CXCL14 in peripheral blood and tumor drainage blood were significantly higher than those in patients without recurrence. Inhibition of CXCL1-14 expression by siRNA in HGC27 cells showed that the migration ability of most cell lines was significantly inhibited. These results suggest that the CXCL chemokine family plays an important role in the pathogenesis of gastric cancer and can be used as a marker for the occurrence and development of gastric cancer [29]. Raja et al. used tissue microarray by immunohistochemistry to study the expression of chemokines and other markers in gastric cancer tissues and analyzed the expression levels of related markers in the epithelium and stroma and their correlation with patient characteristics and prognosis. The results showed that CXCL8, CXCL9, CXCL10, and other markers were increased in gastric cancer stroma compared with normal tissues. The expression of IGFBP3, CXCL8, TIMP1, CCL4, and SPP1 in the stroma was associated with intestinal-type gastric cancer. Kaplan-Meier analysis showed that high expression of PDGFRB and CXCL8 in epithelial cells was associated with poor disease-free survival and



(b)

FIGURE 4: Continued.

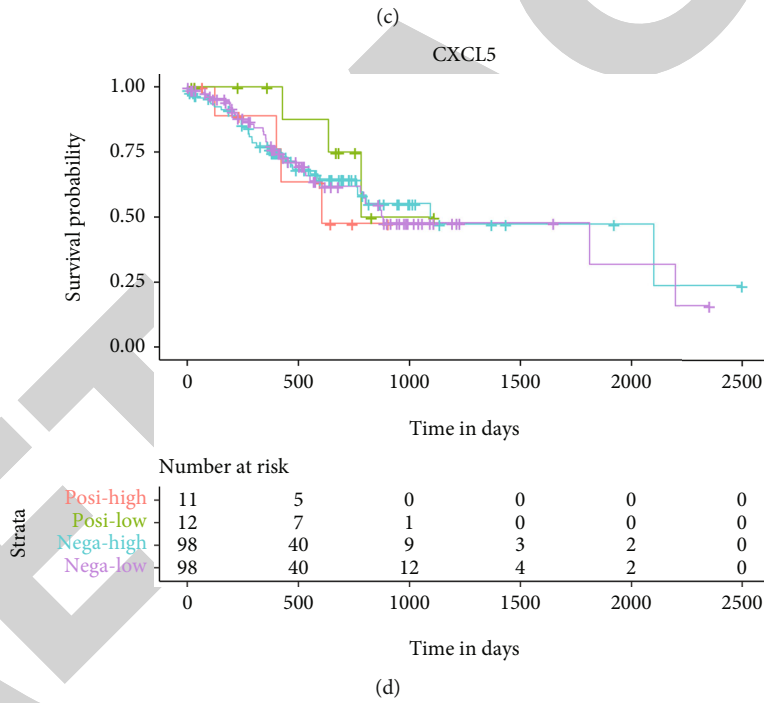
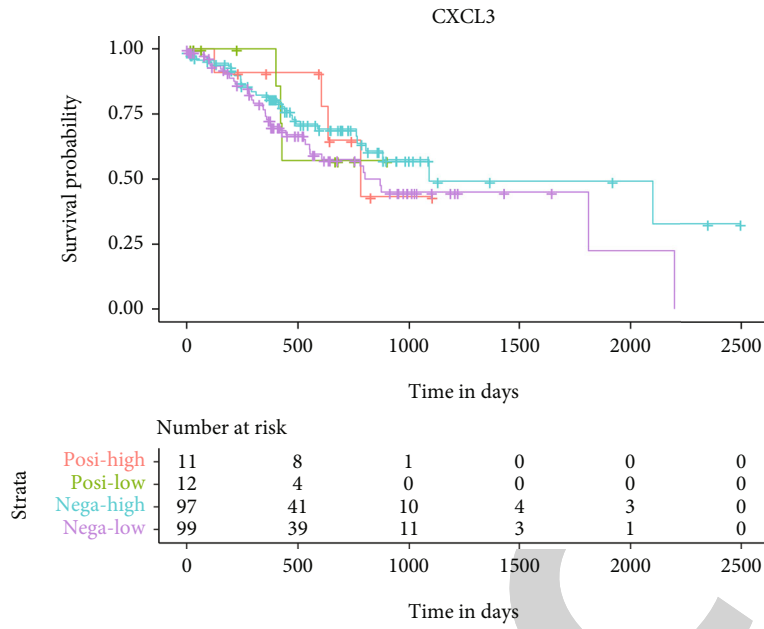
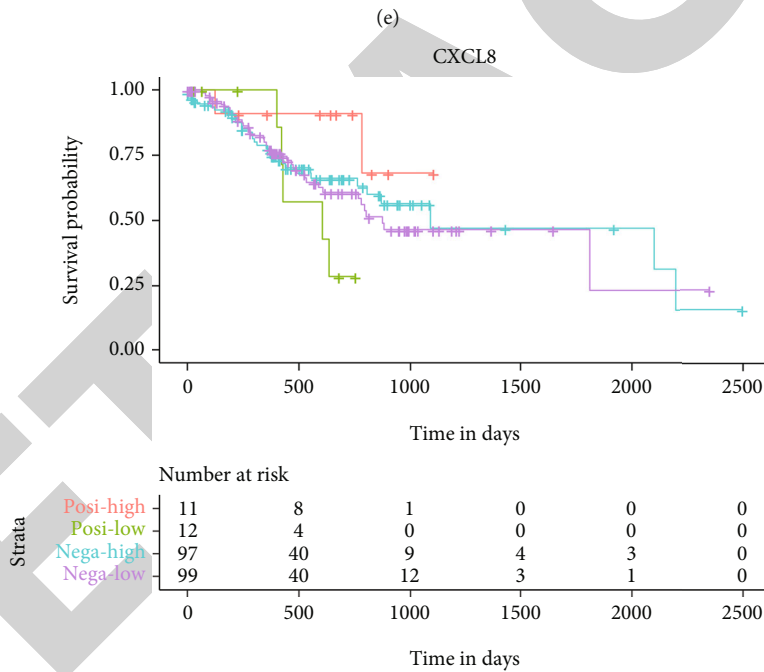
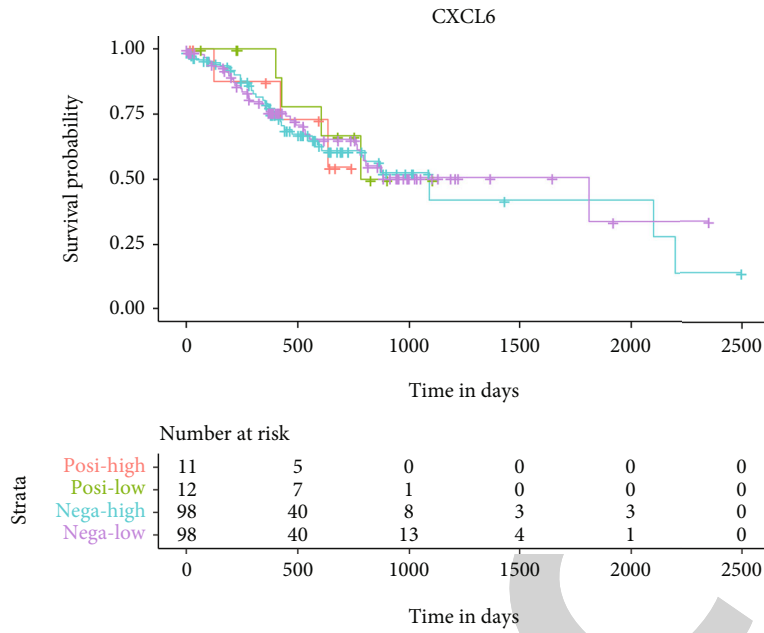
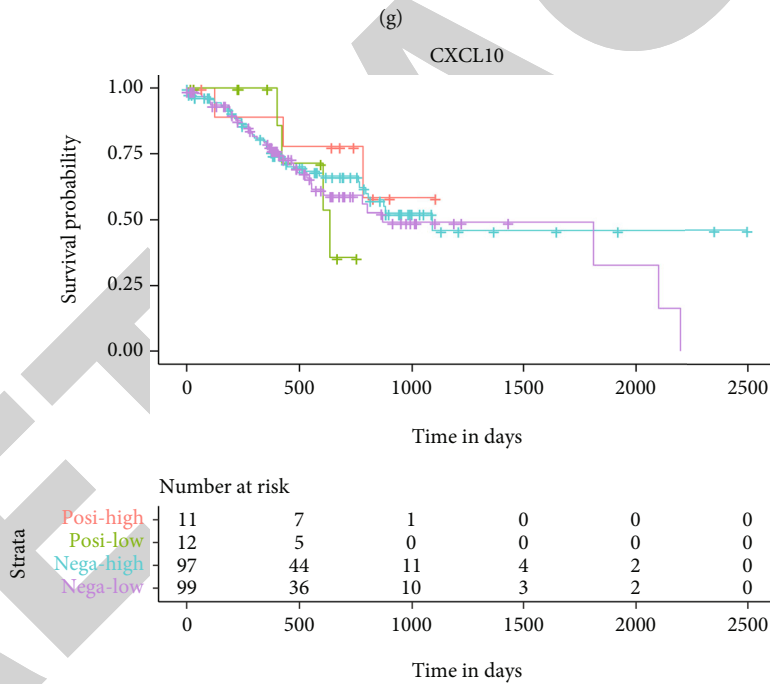
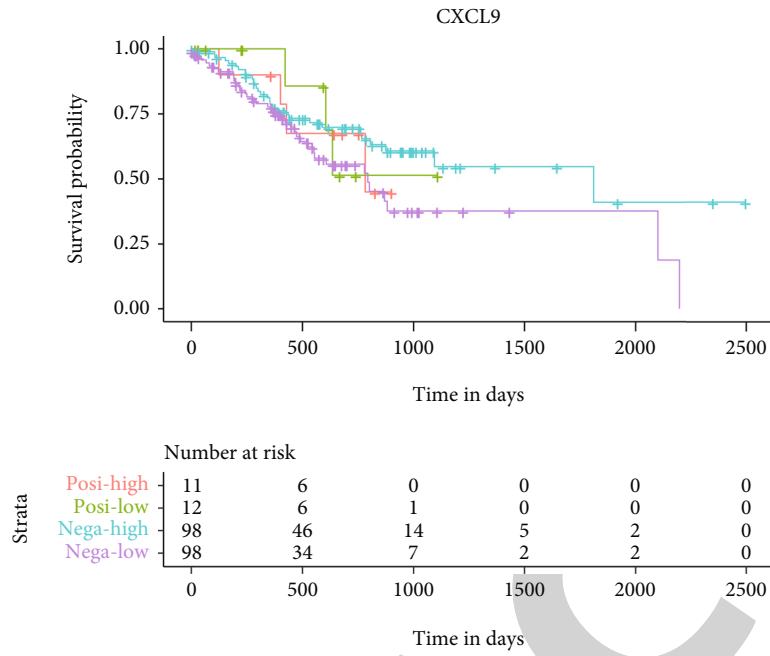


FIGURE 4: Continued.



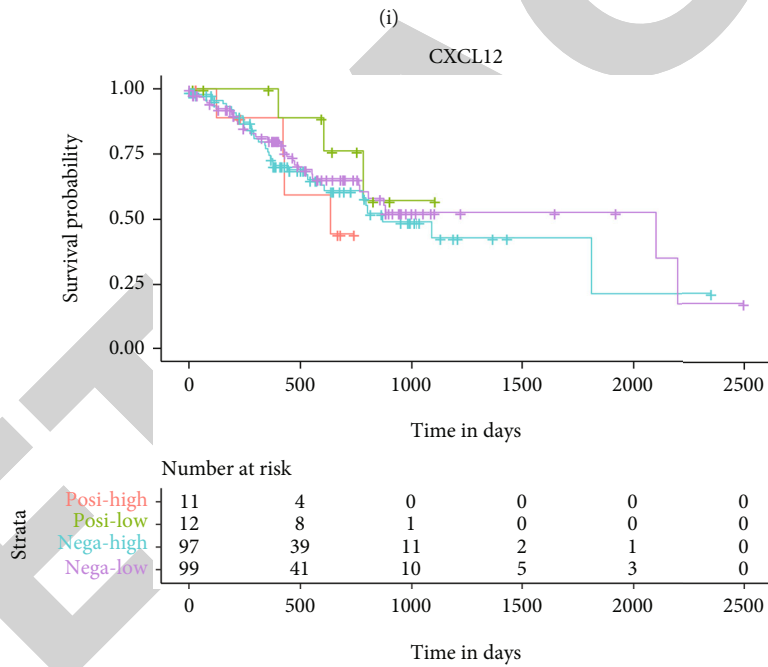
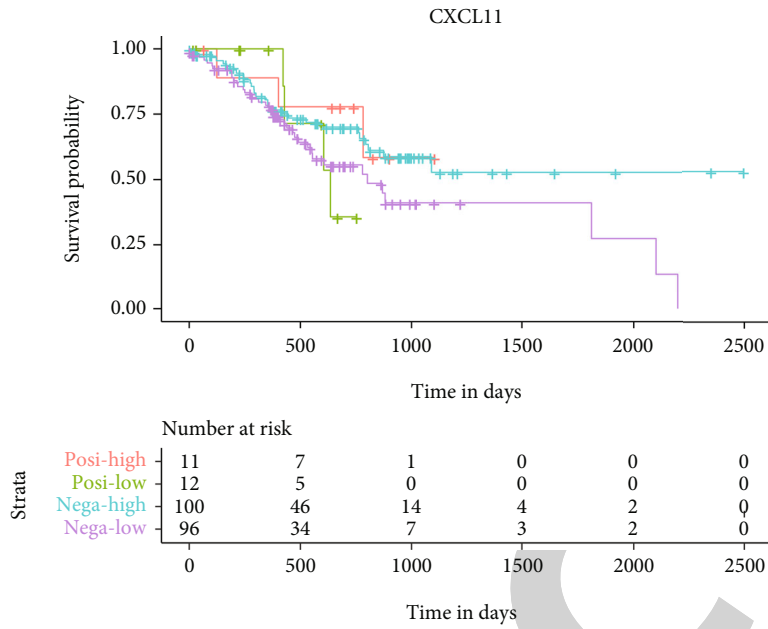
(f)

FIGURE 4: Continued.



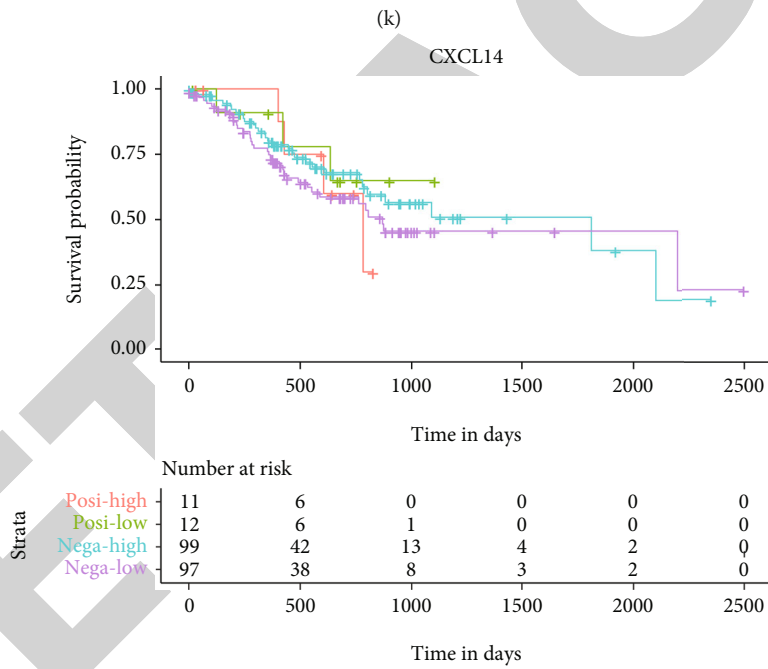
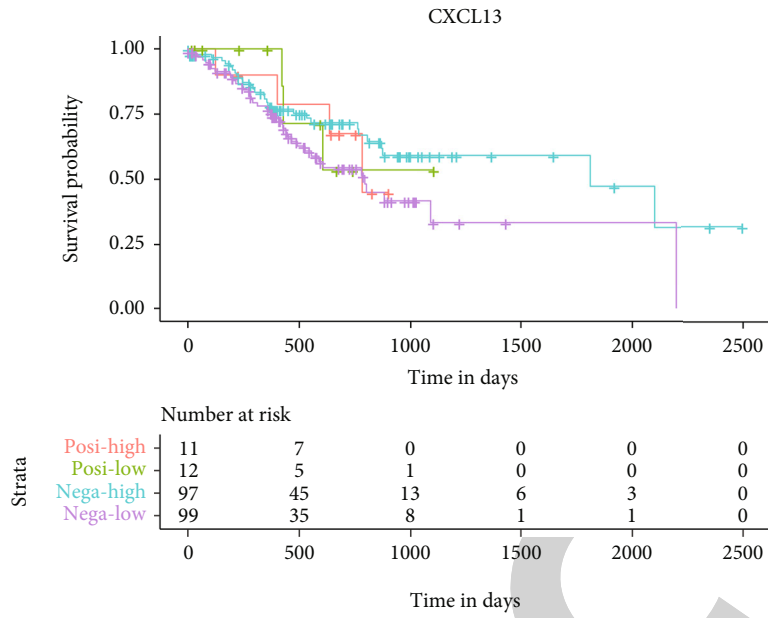
(h)

FIGURE 4: Continued.



(j)

FIGURE 4: Continued.



(l)

FIGURE 4: Continued.

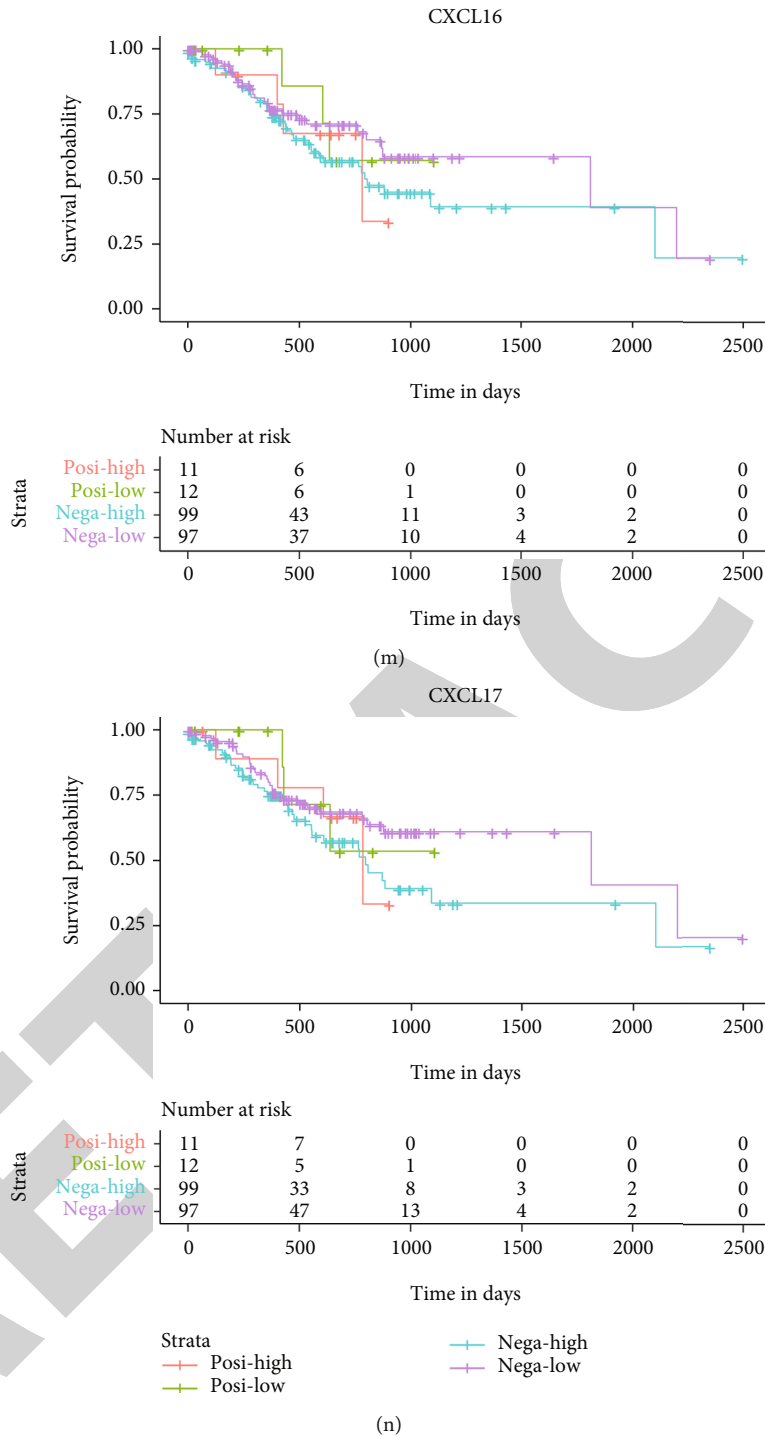


FIGURE 4: Prognostic values of CXCL family members in GCs. (a–n) The prognostic values of CXCL members in EBVaGC and EBVnGC by the KM plotter.

overall survival [30]. Wei et al. used immunohistochemistry to detect the expression of CXCL13 in gastric cancer tissues. Low CXCL13 expression was found to be associated with longer survival in stage T2-4 patients [31]. Lee et al. studied the effect of Escin on the migration and invasion of AGS human gastric cancer cells. It was found that Escin decreased the production of soluble C-X-C motif chemokine (CXCL) 16 but increased the expression of transmembranous

CXCL16 and inhibited the migration and invasion of AGS cells. The results suggest that CXCL16/CXCR6 axis can be used as an Escin agent to exert its potential as an antimetastasis agent in gastric cancer [32].

Epstein-Barr virus belongs to γ -herpesvirus; the population infection rate is up to 90%-95%; it is the most asymptomatic infection of B cells and has lifetime existence. Infection of Epstein-Barr virus is associated with the

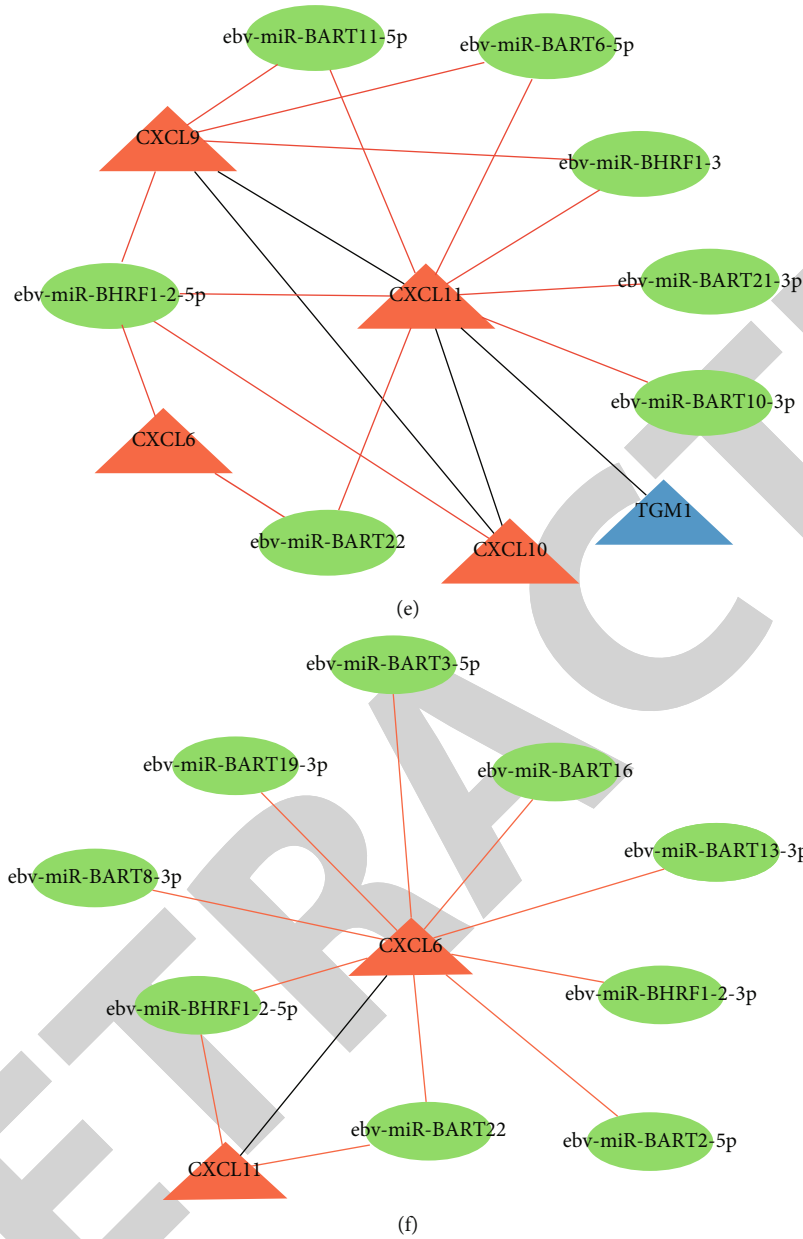
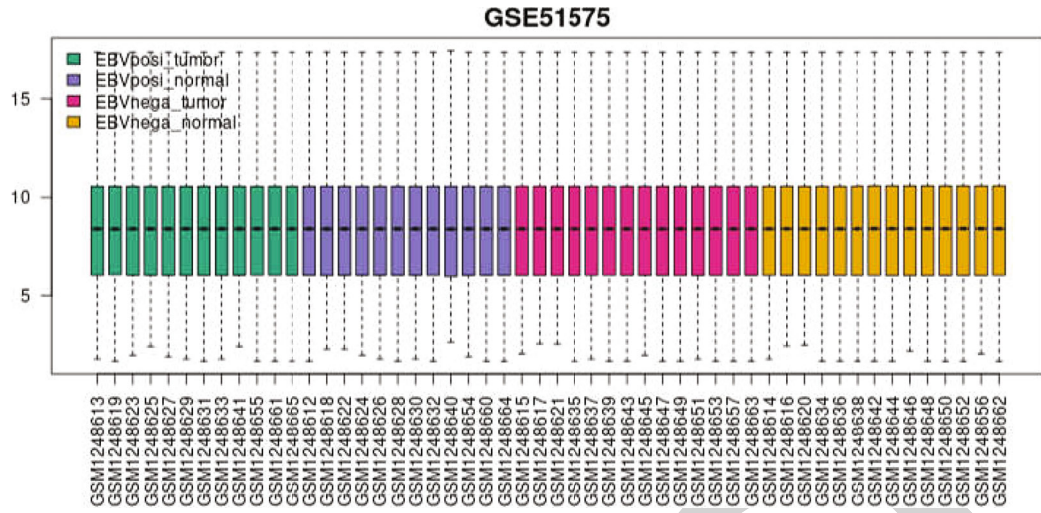


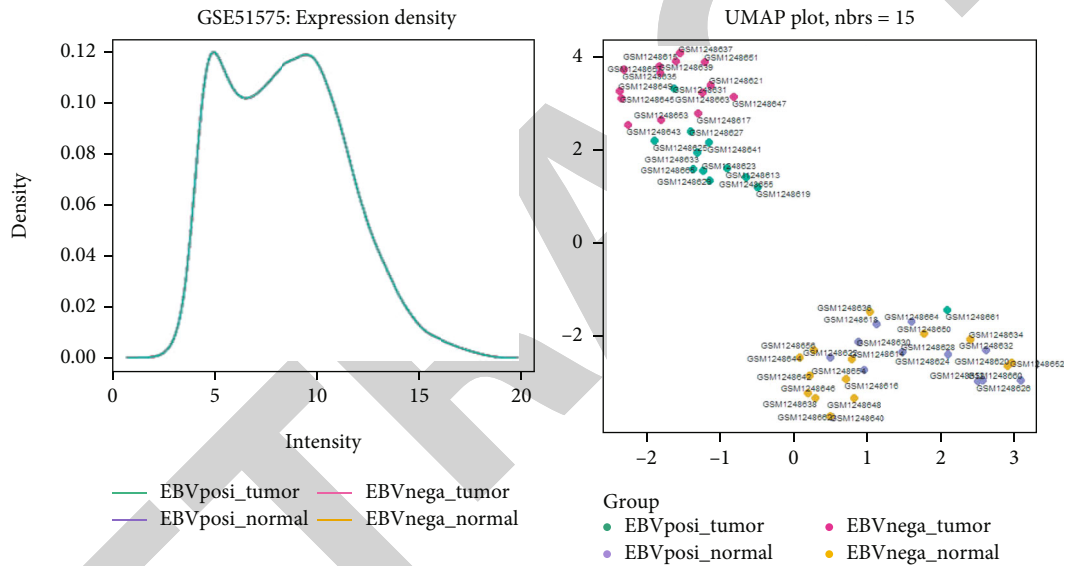
FIGURE 5: Analysis of gene network and interaction of CXCL family members in EBVaGC. (a) The PPI network of CXCL family members and their similar transcription factors and kinases. (b) The PPI network of CXCL family members and their similar miRNAs. (c–f) The PPI network of CXCL family members and their similar transcription factors and miRNAs.

occurrence and development of some human malignant tumors, such as lymphomas (Burkitt lymphoma, Hodgkin lymphoma, and NK/T lymphoma), and some epithelial tumors, such as nasopharyngeal cancer and gastric cancer. In 1990, Burke et al. first proved the existence of Epstein-Barr virus infection in gastric lymphoepitheliomatoid carcinoma [9], and in 1993, Tokunaga et al. confirmed that EBV-positive gastric cancer cells were defined as EBV-associated gastric cancer (EBVaGC) [9, 10]. Previous studies have found that Epstein-Barr virus can induce changes in the expression of chemokines and surface adhesion elements in infected epithelial and B cells, contributing to immune avoidance, antia-

poptosis, and cell proliferation functions, thereby affecting the progression of Epstein-Barr virus-associated tumors. EBV infection of nasopharyngeal epithelial cells activates the NF- κ B and STAT3 pathways, resulting in increased secretion of many inflammatory cytokines and chemokines [33]. A comprehensive array analysis of gene expression patterns in the ENKTL-NT cell line revealed that some interesting molecules, such as intracellular/cell-surface molecules, cytokines, chemokines, and miRNAs, were upregulated or downregulated, and some were directly involved in the proliferation and invasion of lymphoma by additional in vivo and in vitro assays [34]. However, the biological role and prognostic value

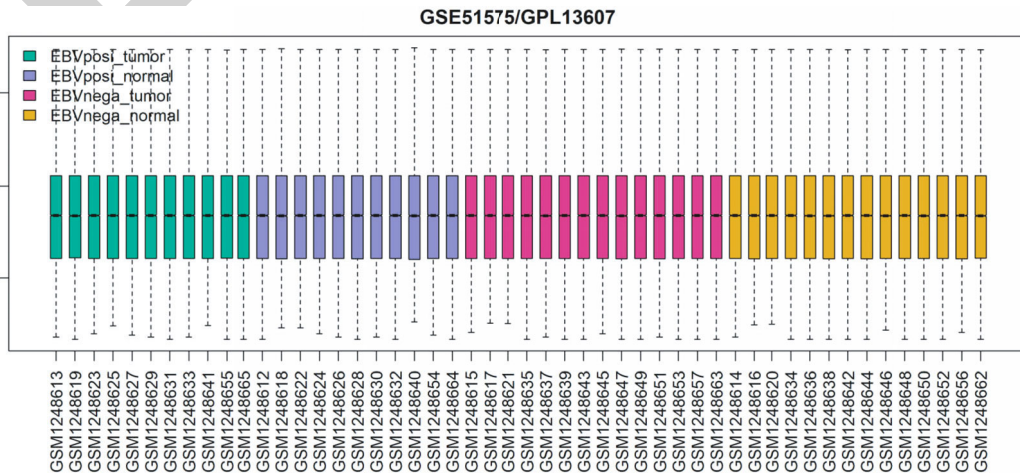


(a)



(b)

(c)



(d)

FIGURE 6: Continued.

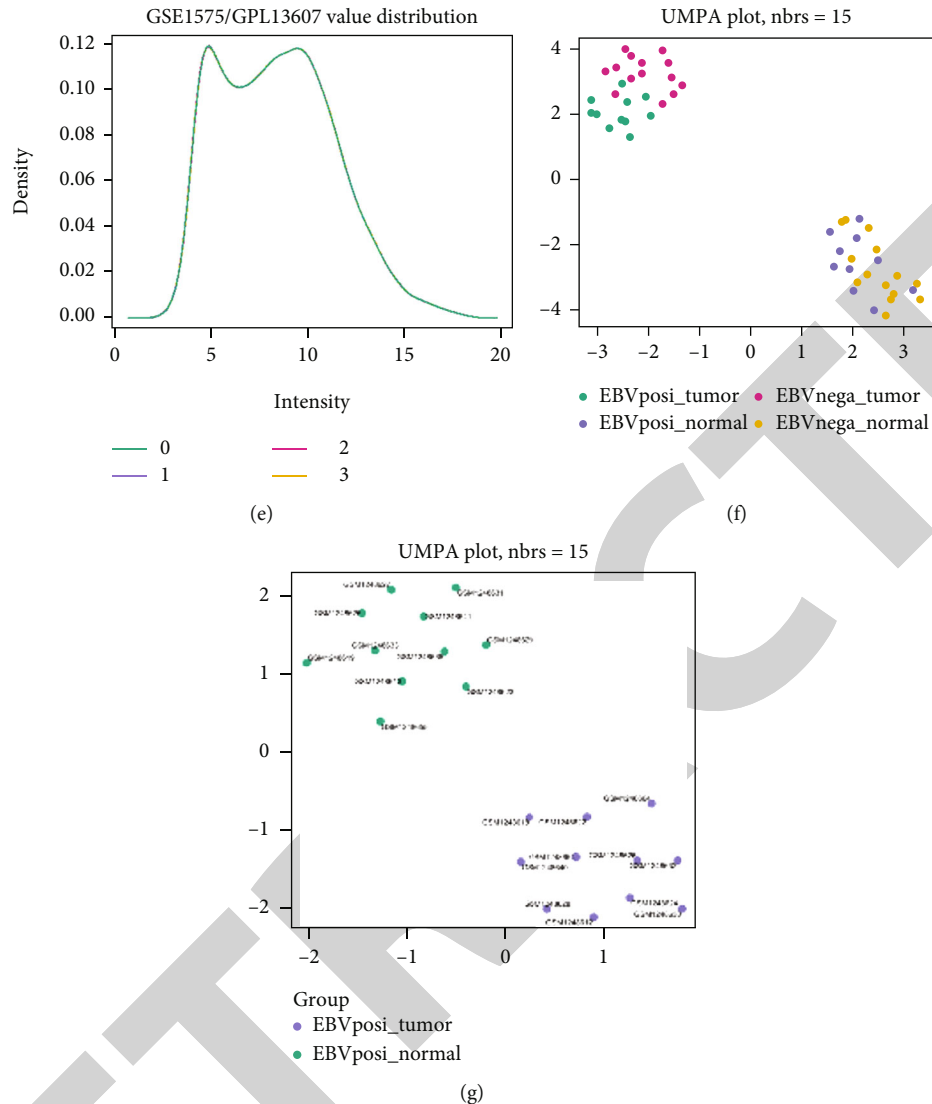


FIGURE 6: GSE51575 data standardization. (a–c) Show the box diagram, density distribution diagram, and UMAP diagram of GSE51575 data before standardization. GSM1248661 does not meet expectations and should be removed. Meanwhile, its control sample GSM1248660 was also deleted. (d–g) Show the box diagram, density distribution diagram, and UMAP diagram after data normalization. All samples met expectations and could be used for subsequent analysis.

of chemokines in Epstein-Barr virus associated gastric cancer have not been systematically evaluated.

Here, we explore the prognostic value of CXCL mRNA expression in patients with EBV-associated gastric cancer based on the clinical information of TCGA-STAD. The results showed that compared with normal gastric mucosa of TCGA-STAD, the mRNA expression of CXCL1/3/5/6/8/9/10/11/16 in EBVaGC was significantly upregulated, while the mRNA expression of CXCL12/14/17 was downregulated. In addition, the mRNA expression of CXCL9/10/11/17 in EBVaGC patients was higher than that in EBVnGC patients, and the mRNA expression of CXCL6/12 was lower than that in EBVnGC patients. We further investigated the relationship between mRNA expression of CXCL family members and stage of EBVaGCs. We found that the mRNA expression of CXCL family members was closely related to the clinical staging of EBVaGC, and the expression of CXCL 6/9/10/

11 mRNA was higher in advanced EBVaGC. Previous studies have shown that CXCL expression is involved in growth regulation, invasion, and metastasis of gastric cancer. A recent study highlighted CXCL as a biomarker and prognostic value for GC. Our study evaluated the prognostic value of CXCL mRNA expression in GC using KM plotter, regardless of EBV infection. We found that high CXCL8 mRNA expression was associated with better OS in EBVaGC patients, while high CXCL9 mRNA expression was significantly associated with better OS in EBVnGC patients.

In addition, we used the Retrieval interaction Gene database (STRING) to evaluate protein interaction (PPI) information and further explore the potential interaction between the differentially expressed CXCL in EBVaGC and adjacent genes. Using TFCheckpoint database, we identified 10 candidate's TF similar to members of the family of CXCL, including OTOP3, NKX6-2, NKX2-2, FEV, SMYD1, TRIMSO, TBX10, CDX1,

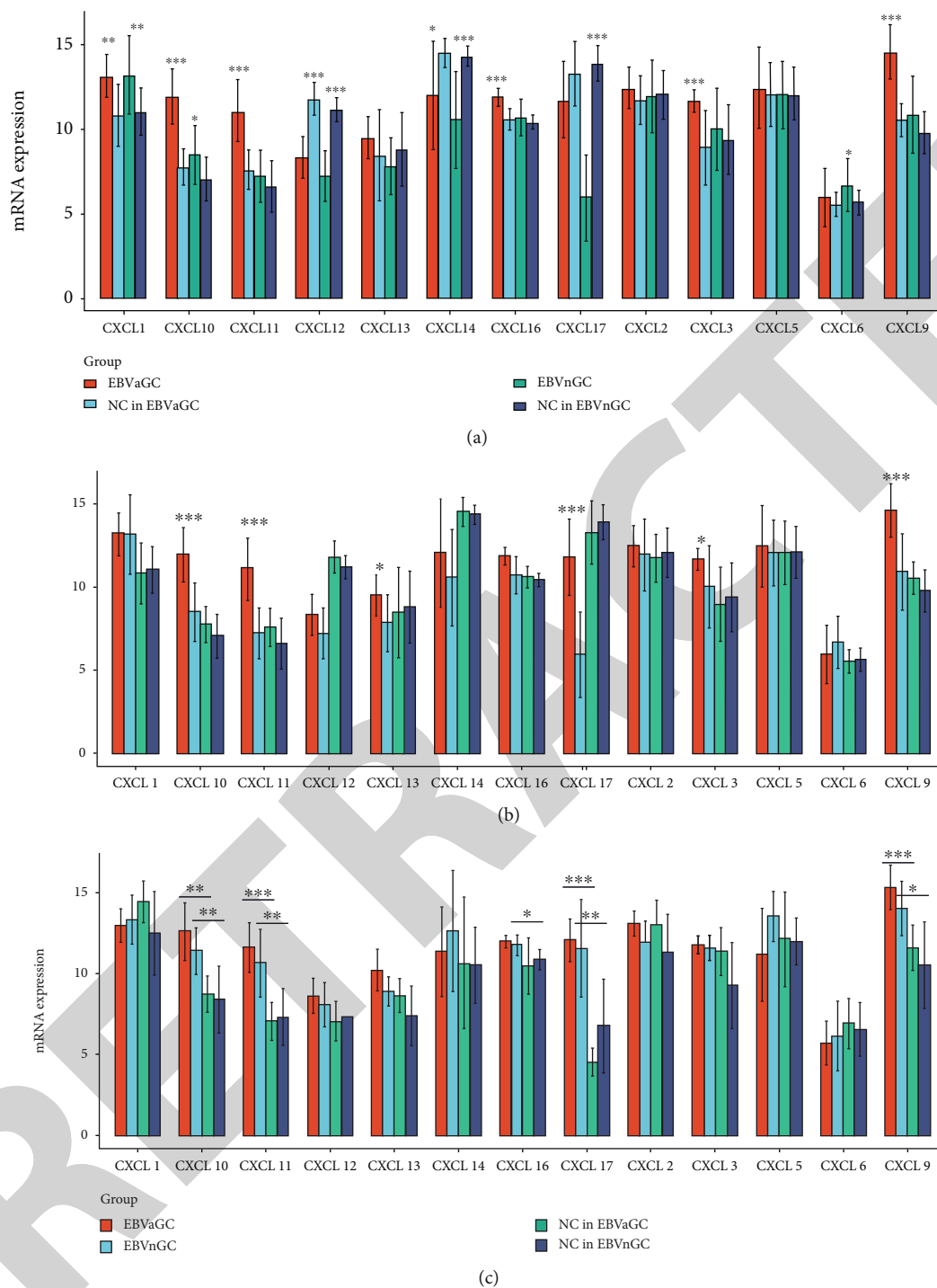


FIGURE 7: Continued.

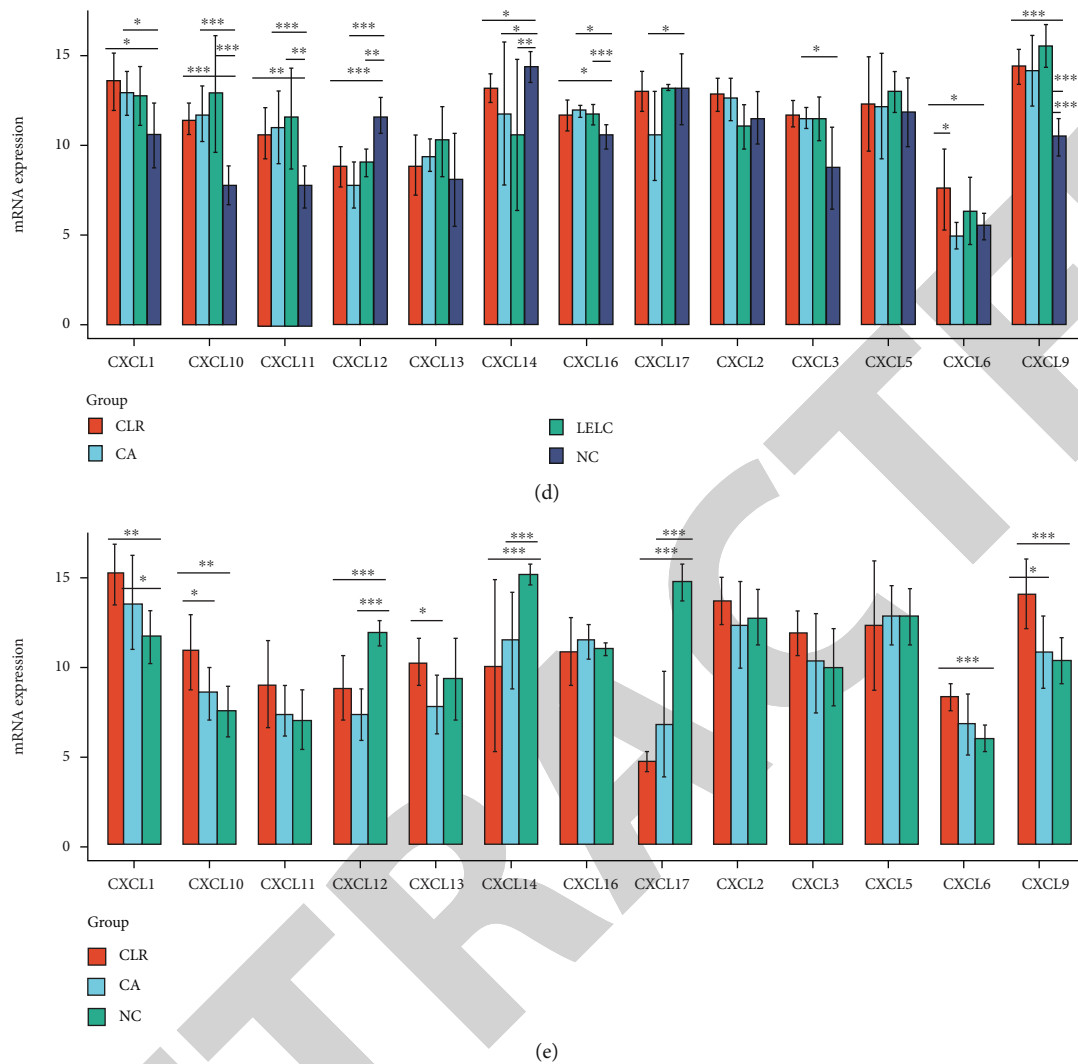


FIGURE 7: CXCL mRNA expression levels between EBVaGC and corresponding normal gastric mucosa based on data from GSE51575.

SLC26A3, and ARC. The KinG database confirms that these TFs are not kinases, indicating that CXCL-associated kinases are not predicted in EBVaGC. In addition, our study evaluated potential miRNAs associated with members of the CXCL family in the PPI network. Using miRWalk and ViRBase databases, we obtained 65 similar miRNAs for CXCL6/9/10/11.

Gene expression microarray technology has been developed and widely used in various studies. However, microarray platforms and protocols are still being refined. The system error is still not fully under control. Quality control is an important issue in gene expression microarray analysis. Therefore, it is necessary to calibrate and standardize gene expression levels in microarray analysis. In this study, quartile segmentation method was used to standardize gene expression level of GSE51575 to verify TCGA results. We found that the mRNA expression level of CXCL1/10/11/14/16 was significantly increased in EBVaGC tissues compared with the corresponding normal gastric mucosa tissues. In contrast, mRNA expression levels of CXCL3/9/12/16 were significantly reduced. In addition, the mRNA expres-

sion level of CXCL3/9/10/11/13/17 was significantly increased in EBVaGC compared with EBVnGC.

C-X-C motif chemokine ligand 6 (CXCL6/GCP2) is a member of the CXC chemokine family and was originally defined as a neutrophil/granulocyte chemokine. The expression of CXCL6 in cancer is rarely studied. Zheng et al. detected the expression of CXCL6 in ESCC tissues by immunohistochemical method and found that CXCL6 was significantly elevated in ESCC compared with the normal control. Upregulated CXCL6 was only significantly associated with differentiation. CXCL6 promoted proliferation, migration, and invasion of ESCC cells in vitro. In nude mice, CXCL6 promoted the growth and metastasis of ESCC cells in vivo. These results suggest that CXCL6 can enhance the growth and metastasis of ESCC cells in vivo and in vitro [35]. CXCL6 is involved in tumor angiogenesis, metastasis, and immune response. Li et al. treated A549 cells with CXCL6 and found that CXCL6 could induce the downregulation of miR-515-5p. Further studies found that CXCL6 was also the target gene of miR-515-5p; that is, CXCL6 and miR-515-5p were in a positive feedback

loop [36]. In vitro and in vivo experiments showed that miR-101-5P overregulation inhibits the progression of NSCLC and cervical cancer cells by targeting CXCL6 [37, 38]. However, whether CXCL6 is involved in the occurrence and development of EBVaGC has not been reported. Our results showed that CXCL6 mRNA expression was enhanced in EBVaGC patients compared with normal mucosal controls of TCGA-STAD. CXCL6 mRNA expression was elevated in patients with advanced EBVaGC. These results suggest that CXCL6 is involved in the development of EBV-dependent GC.

CXCL8, also known as interleukin 8 (IL-8), belongs to the elastin-like recombinant (ELR)+CXC chemokine family and is secreted and expressed by fibroblasts, endothelial cells, epithelial cells, monocytes, macrophages, and cancer cells. The mechanisms of CXCL8 in tumorigenesis and tumor progression have been extensively explored. Studies have shown that CXCL8, a chemokine with multiple tumor-promoting effects in the tumor microenvironment, can stimulate tumor cell proliferation or transformation into mesenchymal phenotype, increase tumor angiogenesis, or recruit more immunosuppressive cells to the tumor [39]. Lin et al. found that CXCL8 could induce PD-L1 +macrophages to form immunosuppressive microenvironment in gastric cancer [40]. The role of CXCL8 in EBV-associated tumors is unclear. Li et al. found in the study of EB virus M81 strain from nasopharyngeal carcinoma that M81 EBER2 could increase the expression of CXCL8, while CXCL8 enhanced the spontaneous lysis replication level of M81-infected B cells [41]. Lo et al. detected 37 pairs of nasopharyngeal carcinoma and normal biopsy tissues and found that the expression level of CXCL8 in nasopharyngeal carcinoma tissues was about 20 times higher than that in surrounding normal tissues [42]. CXCL8 has not been studied in EBV-associated gastric cancer. In this study, we found that CXCL8 mRNA expression was significantly upregulated, and its high expression was significantly related to the prolonged OS time in EBVaGC patients.

C-X-C motif chemokine ligand (CXCL)9/10/11, known as T cell chemokine, recruits antitumor cytotoxic T lymphocytes and inhibits tumor progression through its receptor C-X-C chemokine receptor 3. CXCL9/10/11 is synthesized and released by leukocytes, epithelial cells, endothelial cells, and stromal cells. The production of these chemokines is regulated by interferon- γ (IFN- γ) stimulation [43]. Zhang et al. found that CXCL9/10/11-CXCR3 upregulated the expression of PD-L1 by activating the STAT and PI3K-Akt signaling pathways in GC cells [44]. Zhao et al. showed that CXCL9/10/11/CXCR3 axis is involved in the mechanism of CD68+ CD163-macrophages in the efficacy enhancement of PD-L1/PD-1 blockade [45]. Hsin et al. showed that the expression of CXCL9 in nasopharyngeal carcinoma tissues was significantly higher than that in normal epithelium, and the serum concentration of CXCL9 was also significantly increased, and there was a statistically significant correlation between the concentration of CXCL9 and EBV DNA load. Multivariate logistic regression analysis also showed that higher CXCL9 serum level was an independent prognostic factor for disease-free survival [46]. CXCL9 and CXCL10 genes are often overexpressed in gastric cancer. In this study, we found that the mRNA expression of CXCL9/

10/11 was significantly increased in patients with EBVaGC. In addition, CXCL9/10/11/17 mRNA expression was higher in patients with EBVaGC compared with patients with EBVnGC. CXCL9 mRNA overexpression was significantly associated with better OS time in EBVnGC patients.

In conclusion, our study suggests that CXCL family members are closely associated with the progression of EBV-associated gastric cancer and can be used as markers for EBVaGC. Expression changes of CXCL9/10/11/17 mRNA may be a promising prognostic indicator for EBVaGC patients.

Data Availability

The labeled dataset used to support the findings of this study is available from the corresponding author upon request.

Conflicts of Interest

All authors declare that they have no competing interests.

Acknowledgments

This work was sponsored (supported) by the Natural Science Foundation of Fujian Province (No. 2020J02051) and Fujian Provincial Health Technology Project (No. 2017-CX-28).

References

- [1] H. Sung, J. Ferlay, R. L. Siegel et al., "Global cancer statistics 2020: GLOBOCAN estimates of incidence and mortality worldwide for 36 cancers in 185 countries," *CA: a Cancer Journal for Clinicians*, vol. 71, no. 3, pp. 209–249, 2021.
- [2] J. Ferlay, M. Colombet, I. Soerjomataram et al., "Cancer statistics for the year 2020: an overview," *International Journal of Cancer*, vol. 194, no. 4, pp. 778–789, 2021.
- [3] F. Carneiro, M. Fukayama, H. I. Grabsch, and W. Yasui, "Gastric adenocarcinoma," in *In WHO Classification of Tumours (5th Edition). Digestive System Tumours Edited by the WHO Classification of Tumours Editorial Board*, pp. 85–95, International Agency for Research on Cancer, Lyon (France), 2019.
- [4] S. Pilleron, E. Soto-Perez-de-Celis, J. Vignat et al., "Estimated global cancer incidence in the oldest adults in 2018 and projections to 2050," *International Journal of Cancer*, vol. 148, no. 3, pp. 601–608, 2021.
- [5] J. M. Park, W. S. Ryu, J. H. Kim et al., "Prognostic factors for advanced gastric cancer: stage-stratified analysis of patients who underwent curative resection," *Cancer Research and Treatment*, vol. 38, no. 1, pp. 13–18, 2006.
- [6] L. Necula, L. Matei, D. Dragu et al., "Recent advances in gastric cancer early diagnosis," *World Journal of Gastroenterology*, vol. 25, no. 17, pp. 2029–2044, 2019.
- [7] H. Zu, F. Wang, Y. Ma, and Y. Xue, "Stage-stratified analysis of prognostic significance of tumor size in patients with gastric cancer," *PLoS One*, vol. 8, no. 1, article e54502, 2013.
- [8] T. Kanda, M. Yajima, and K. Ikuta, "Epstein-Barr virus strain variation and cancer," *Cancer Science*, vol. 110, no. 4, pp. 1132–1139, 2019.
- [9] A. P. Burke, T. S. Yen, K. M. Shekitka, and L. H. Sobin, "Lymphoepithelial carcinoma of the stomach with Epstein-Barr virus demonstrated by polymerase chain reaction," *Modern Pathology*, vol. 3, no. 3, pp. 377–380, 1990.

- [10] K. Sun, K. Jia, H. Lv et al., “EBV-positive gastric cancer: current knowledge and future perspectives,” *Frontiers in Oncology*, vol. 10, p. 583463, 2020.
- [11] M. Saito and K. Kono, “Landscape of EBV-positive gastric cancer,” *Gastric Cancer*, vol. 24, no. 5, pp. 983–989, 2021.
- [12] C. E. Hughes and R. J. B. Nibbs, “A guide to chemokines and their receptors,” *The FEBS Journal*, vol. 285, no. 16, pp. 2944–2971, 2018.
- [13] S. Saxena and R. K. Singh, “Chemokines orchestrate tumor cells and the microenvironment to achieve metastatic heterogeneity,” *Cancer Metastasis Reviews*, vol. 40, no. 2, pp. 447–476, 2021.
- [14] M. Vela, M. Aris, L. Llorente, J. A. Garcia-Sanz, and L. Kremer, “Chemokine receptor-specific antibodies in cancer immunotherapy: achievements and challenges,” *Frontiers in Immunology*, vol. 6, 2015.
- [15] Y. Cheng, J. Qu, X. Che et al., “CXCL12/SDF-1 α induces migration via SRC-mediated CXCR4-EGFR cross-talk in gastric cancer cells,” *Oncology Letters*, vol. 14, no. 2, pp. 2103–2110, 2017.
- [16] G. Xu, K. Lu, M. Shen, Q. Zhang, W. Pan, and Z. Tang, “Correlation between chemokine CXCL-12 and its receptor CXCR4 expression is associated with clinical prognosis of gastric cancer,” *Clinical Laboratory*, vol. 66, no. 4, 2020.
- [17] H. Verbeke, K. Geboes, J. Van Damme, and S. Struyf, “The role of CXC chemokines in the transition of chronic inflammation to esophageal and gastric cancer,” *BiochimBiophys Acta*, vol. 1825, no. 1, pp. 117–129, 2012.
- [18] D. Aldinucci and N. Casagrande, “Inhibition of the CCL5/CCR5 axis against the progression of gastric cancer,” *International Journal of Molecular Sciences*, vol. 19, no. 5, p. 1477, 2018.
- [19] W. Tang, D. R. Morgan, M. O. Meyers et al., “Epstein-Barr virus infected gastric adenocarcinoma expresses latent and lytic viral transcripts and has a distinct human gene expression profile,” *Infect Agent Cancer*, vol. 7, no. 1, p. 21, 2012.
- [20] Y. Wei, C. Lin, H. Li et al., “CXCL13 expression is prognostic and predictive for postoperative adjuvant chemotherapy benefit in patients with gastric cancer,” *Cancer Immunology, Immunotherapy*, vol. 67, no. 2, pp. 261–269, 2018.
- [21] Cancer Genome Atlas Research Network, “Comprehensive molecular characterization of gastric adenocarcinoma,” *Nature*, vol. 513, no. 7517, pp. 202–209, 2014.
- [22] A. Lanczky and B. Györfy, “Web-based survival analysis tool tailored for medical research (KMplot): development and implementation,” *Journal of Medical Internet Research*, vol. 23, no. 7, article e27633, 2021.
- [23] V. Mollica Poeta, M. Massara, A. Capucetti, and R. Bonecchi, “Chemokines and chemokine receptors: new targets for cancer immunotherapy,” *Frontiers In Immunology*, vol. 10, p. 379, 2019.
- [24] A. J. Ozga, M. T. Chow, and A. D. Luster, “Chemokines and the immune response to cancer,” *Immunity*, vol. 54, no. 5, pp. 859–874, 2021.
- [25] M. T. Chow and A. D. Luster, “Chemokines in cancer,” *Cancer Immunology Research*, vol. 2, no. 12, pp. 1125–1131, 2014.
- [26] Q. Zhu, X. Han, J. Peng, H. Qin, and Y. Wang, “The role of CXC chemokines and their receptors in the progression and treatment of tumors,” *Journal of Molecular Histology*, vol. 43, no. 6, pp. 699–713, 2012.
- [27] E. Pawluczuk, M. Łukaszewicz-Zajac, and B. Mroczko, “The role of chemokines in the development of gastric cancer - diagnostic and therapeutic implications,” *International Journal of Molecular Sciences*, vol. 21, no. 22, p. 8456, 2020.
- [28] H. J. Lee, I. C. Song, H. J. Yun, D. Y. Jo, and S. Kim, “CXC chemokines and chemokine receptors in gastric cancer: from basic findings towards therapeutic targeting,” *World Journal of Gastroenterology*, vol. 20, no. 7, pp. 1681–1693, 2014.
- [29] X. Chen, R. Chen, R. Jin, and Z. Huang, “The role of CXCL chemokine family in the development and progression of gastric cancer,” *International Journal Of Clinical and Experimental Pathology*, vol. 13, no. 3, pp. 484–492, 2020.
- [30] U. M. Raja, G. Gopal, S. Shirley, A. S. Ramakrishnan, and T. Rajkumar, “Immunohistochemical expression and localization of cytokines/chemokines/growth factors in gastric cancer,” *Cytokine*, vol. 89, pp. 82–90, 2017.
- [31] Y. Li, X. B. Guo, Y. H. Wei, and X. L. Kang, “Serum CXCL13 and PECAM-1 can be used as diagnostic and prognostic markers in elderly patients with gastric cancer,” *Clinical and Translational Oncology*, vol. 23, no. 1, pp. 130–138, 2020.
- [32] H. S. Lee, J. E. Hong, E. J. Kim, and S. H. Kim, “Escin suppresses migration and invasion involving the alteration of CXCL16/CXCR6 axis in human gastric adenocarcinoma AGS cells,” *Nutrition and Cancer*, vol. 66, no. 6, pp. 938–945, 2014.
- [33] Q. Liao, X. Guo, X. Li et al., “Analysis of the contribution of nasopharyngeal epithelial cancer cells to the induction of a local inflammatory response,” *Journal of Cancer Research and Clinical Oncology*, vol. 138, no. 1, pp. 57–64, 2012.
- [34] M. Takahara, T. Kumai, K. Kishibe, T. Nagato, and Y. Harabuchi, “Extranodal NK/T-cell lymphoma, nasal type: genetic, biologic, and clinical aspects with a central focus on Epstein-Barr virus relation,” *Microorganisms*, vol. 9, no. 7, p. 1381, 2021.
- [35] S. Zheng, T. Shen, Q. Liu et al., “CXCL6 fuels the growth and metastases of esophageal squamous cell carcinoma cells both in vitro and in vivo through upregulation of PD-L1 via activation of STAT3 pathway,” *Journal of Cellular Physiology*, vol. 236, no. 7, pp. 5373–5386, 2021.
- [36] J. Li, Z. Tang, H. Wang et al., “CXCL6 promotes non-small cell lung cancer cell survival and metastasis via down-regulation of miR-515-5p,” *Biomedicine & Pharmacotherapy*, vol. 97, pp. 1182–1188, 2018.
- [37] Q. Chen, D. Liu, Z. Hu, C. Luo, and S. L. Zheng, “miRNA-101-5p inhibits the growth and aggressiveness of NSCLC cells through targeting CXCL6,” *Onco Targets and Therapy*, vol. 12, pp. 835–848, 2019.
- [38] W. Shen, X. Y. Xie, M. R. Liu, and L. L. Wang, “MicroRNA-101-5p inhibits the growth and metastasis of cervical cancer cell by inhibiting CXCL6,” *European Review for Medical and Pharmacological Sciences*, vol. 23, no. 5, pp. 1957–1968, 2019.
- [39] K. Fousek, L. A. Horn, and C. Palena, “Interleukin-8: A chemokine at the intersection of cancer plasticity, angiogenesis, and immune suppression,” *Pharmacology & Therapeutics*, vol. 219, p. 107692, 2021.
- [40] C. Lin, H. He, H. Liu et al., “Tumour-associated macrophage-derived CXCL8 determines immune evasion through autonomous PD-L1 expression in gastric cancer,” *Gut*, vol. 68, no. 10, pp. 1764–1773, 2019.
- [41] Z. Li, M. H. Tsai, A. Shumilov et al., “Epstein-Barr virus ncRNA from a nasopharyngeal carcinoma induces an

Retraction

Retracted: Protective Effects of *Amauroderma rugosum* on Doxorubicin-Induced Cardiotoxicity through Suppressing Oxidative Stress, Mitochondrial Dysfunction, Apoptosis, and Activating Akt/mTOR and Nrf2/HO-1 Signaling Pathways

Oxidative Medicine and Cellular Longevity

Received 26 December 2023; Accepted 26 December 2023; Published 29 December 2023

Copyright © 2023 Oxidative Medicine and Cellular Longevity. This is an open access article distributed under the Creative Commons Attribution License, which permits unrestricted use, distribution, and reproduction in any medium, provided the original work is properly cited.

This article has been retracted by Hindawi, as publisher, following an investigation undertaken by the publisher [1]. This investigation has uncovered evidence of systematic manipulation of the publication and peer-review process. We cannot, therefore, vouch for the reliability or integrity of this article.

Please note that this notice is intended solely to alert readers that the peer-review process of this article has been compromised.

Wiley and Hindawi regret that the usual quality checks did not identify these issues before publication and have since put additional measures in place to safeguard research integrity.

We wish to credit our Research Integrity and Research Publishing teams and anonymous and named external researchers and research integrity experts for contributing to this investigation.



The corresponding author, as the representative of all authors, has been given the opportunity to register their agreement or disagreement to this retraction. We have kept a record of any response received.

References

- [1] J. Li, Y. Cheng, R. Li et al., “Protective Effects of *Amauroderma rugosum* on Doxorubicin-Induced Cardiotoxicity through Suppressing Oxidative Stress, Mitochondrial Dysfunction, Apoptosis, and Activating Akt/mTOR and Nrf2/HO-1 Signaling Pathways,” *Oxidative Medicine and Cellular Longevity*, vol. 2022, Article ID 9266178, 24 pages, 2022.

Research Article

Protective Effects of *Amauroderma rugosum* on Doxorubicin-Induced Cardiotoxicity through Suppressing Oxidative Stress, Mitochondrial Dysfunction, Apoptosis, and Activating Akt/mTOR and Nrf2/HO-1 Signaling Pathways

Jingjing Li ^{1,2}, Yanfen Cheng,³ Renkai Li,¹ Xiaoping Wu,¹ Chengwen Zheng,¹ Polly Ho-Ting Shiu,¹ Jacqueline Cho-Ki Chan,¹ Panthakarn Rangsinth,¹ Conghui Liu,¹ Susan Wai-Sum Leung,¹ Simon Ming-Yuen Lee,⁴ Chen Zhang,³ Chaomei Fu,³ Jinming Zhang,³ Timothy Man-Yau Cheung,⁵ and George Pak-Heng Leung ¹

¹Department of Pharmacology and Pharmacy, Li Ka Shing Faculty of Medicine, The University of Hong Kong, Hong Kong SAR, China

²Department of Rehabilitation Sciences, Faculty of Health and Social Sciences, Hong Kong Polytechnic University, Hong Kong SAR, China

³State Key Laboratory of Southwestern Chinese Medicine Resources, School of Pharmacy, Chengdu University of Traditional Chinese Medicine, Chengdu, China

⁴State Key Laboratory of Quality Research in Chinese Medicine and Institute of Chinese Medical Sciences, University of Macau, Macao SAR, China

⁵Tian Ran Healthcare Limited, Hong Kong, China

Correspondence should be addressed to George Pak-Heng Leung; gphleung@hku.hk

Received 24 February 2022; Revised 12 April 2022; Accepted 14 May 2022; Published 1 June 2022

Academic Editor: Shao Liang

Copyright © 2022 Jingjing Li et al. This is an open access article distributed under the Creative Commons Attribution License, which permits unrestricted use, distribution, and reproduction in any medium, provided the original work is properly cited.

Clinical outcomes for doxorubicin (Dox) are limited by its cardiotoxicity but a combination of Dox and agents with cardioprotective activities is an effective strategy to improve its therapeutic outcome. Natural products provide abundant resources to search for novel cardioprotective agents. *Ganoderma lucidum* (GL) is the most well-known edible mushroom within the *Ganodermataceae* family. It is commonly used in traditional Chinese medicine or as a healthcare product. *Amauroderma rugosum* (AR) is another genus of mushroom from the *Ganodermataceae* family, but its pharmacological activity and medicinal value have rarely been reported. In the present study, the cardioprotective effects of the AR extract against Dox-induced cardiotoxicity were studied *in vitro* and *in vivo*. Results showed that both the AR and GL extracts could potentiate the anticancer effect of Dox. The AR extract significantly decreased the oxidative stress, mitochondrial dysfunction, and apoptosis seen in Dox-treated H9c2 rat cardiomyocytes. However, knockdown of Nrf2 by siRNA abolished the protective effects of AR in these cells. In addition, Dox upregulated the expression of proapoptotic proteins and downregulated the Akt/mTOR and Nrf2/HO-1 signaling pathways, and these effects could be reversed by the AR extract. Consistently, the AR extract significantly prolonged survival time, reversed weight loss, and reduced cardiac dysfunction in Dox-treated mice. In addition, oxidative stress and apoptosis were suppressed, while Nrf2 and HO-1 expressions were elevated in the heart tissues of Dox-treated mice after treatment with the AR extract. However, the GL extract had less cardioprotective effect against Dox in both the cell and animal models. In conclusion, the AR water extract demonstrated a remarkable cardioprotective effect against Dox-induced cardiotoxicity. One of the possible mechanisms for this effect was the upregulation of the mTOR/Akt and Nrf2/HO-1-dependent pathways, which may reduce oxidative stress, mitochondrial dysfunction, and cardiomyocyte apoptosis. These findings suggested that AR may be beneficial for the heart, especially in patients receiving Dox-based chemotherapy.

1. Introduction

Doxorubicin (Dox) is one of the most widely used and effective antineoplastic agents for the treatment of various types of cancer, including breast, ovarian, gastric, bladder, and thyroid cancers [1]. However, the cardiotoxicity of Dox limits its clinical applications [2]. Clinical studies have shown that the incidence of cardiotoxicity is approximately 5% when the cumulative dose of Dox is 400 mg/m². However, this incidence can dramatically increase to 26% and 49% when the cumulative dose of Dox is 550 mg/m² and 700 mg/m², respectively [2]. The symptoms of Dox-induced cardiotoxicity include arrhythmia, cardiomyopathy, left ventricular dysfunction, and congestive heart failure [3]. Although the exact mechanisms involved in Dox-induced cardiotoxicity remain elusive, making it difficult to develop appropriate detoxification drugs [4], oxidative stress is considered to be its major causal factor [5]. Dox can stimulate the generation of excessive reactive oxygen species (ROS) in rat cardiomyocytes by increasing the accumulation of intracellular Ca²⁺ [6]. In clinical studies, oxidative stress was markedly increased in heart tissues when the cumulative dosage of Dox exceeded 500 mg/m² [7].

Although oxidative stress is the most widely studied cause, accumulating evidence has indicated that a dysfunction in the nuclear factor erythroid 2-related factor 2 (Nrf2)/Heme oxygenase- (HO-) 1 pathway is also closely involved in the regulation of Dox-induced cardiotoxicity. Nrf2 is a transcription factor responsible for the regulation of cellular redox balance and protective antioxidant and phase II detoxification responses in mammals [8]. Under physiological conditions, Nrf2 combines with proteasomal degradation in the cytosol by the 26S proteasome via the cytoplasmic binding protein kelch-like epichlorohydrin-related protein (Keap) 1 [9]. However, under stressful conditions, Nrf2 is released from Keap1 and translocates to the nucleus. After binding to the antioxidant response element sequence, Nrf2 activates and upregulates the expression of downstream antioxidant proteins and biphasic detoxification enzymes, including HO-1, NAD(P)H:quinone oxidoreductase-1, and glutathione S-transferase, ultimately facilitating intracellular antioxidative responses [10]. It has been reported that the Nrf2-dependent antioxidant response system is suppressed in the hearts of Dox-treated rats, which is consistent with the observed decrease in protein abundance of Nrf2 [11]. Additionally, Dox-induced oxidative stress, cardiomyocyte necrosis, and cardiac dysfunction were found to be exaggerated in Nrf2 knockout mice [12]. Therefore, the Nrf2/HO-1 signaling pathway may be a potential drug target for the prevention and/or treatment of Dox-induced cardiotoxicity.

Natural products provide abundant resources for the discovery of novel cardioprotective agents. Our previous studies have demonstrated that oridonin [13] and glycyrrhetic acid [14, 15] do not only enhance the anticancer efficacy of Dox in breast cancer but also show a potential positive activity in ameliorating Dox-induced cardiotoxicity. *Ganoderma lucidum* (GL), also known as “Lingzhi” in China, is one of the most well-known mushrooms and has been widely used in traditional Chinese medicine for centuries. A prior study has

shown that GL extract can prevent Dox-induced cardiotoxicity by reducing Dox-induced oxidative stress in rats [16]. It has also been reported that GL polysaccharides can ameliorate Dox-induced mitochondrial damage, oxidative stress, proinflammatory cytokine production, and rat cardiomyocyte apoptosis. The underlying mechanism of GL polysaccharides is likely attributed to the rescue of the Nrf2/HO-1 signaling pathway, which is suppressed by Dox [17].

Amauroderma rugosum (AR) is another genus of basidiomycete within the *Ganodermataceae* family. Its cap is black in color and is irregularly wrinkled with thin or blunt edges. Its hymenium has a white surface, which turns dark red when scratched. Because of this, AR is also called “blood Linzhi” in Chinese [18]. AR has been used as a traditional medicine in China and Malaysia for the treatment of inflammation, cancers, gastric disorders, and epilepsy [19]. Although AR is consumed by people in China and South Asia, very few scientific studies have been conducted to explore its medicinal value or its beneficial effects on human health. We have previously reported that AR extract can protect PC12 neuroblastoma cells against 6-OHDA-induced toxicity through its antioxidant and antiapoptotic effects [18]. It has been hypothesized that AR may also influence reducing Dox-induced cardiotoxicity due to its remarkable antioxidant capacity. In the present study, the effect of AR extract on Dox-induced cardiotoxicity and its underlying cardioprotective mechanisms were investigated *in vitro* and *in vivo*, and its efficacy was also compared to that of GL.

2. Materials and Methods

2.1. Ethical Statement. Ethical research considerations were approved by the Chengdu University of Traditional Chinese Medicine. All experimental protocols using animals were conducted in compliance with guidelines established by the Institutional Animal Care and Use Committee (no. CDU2019S121), and animal welfare has been ensured throughout the animal experiments.

2.2. Materials. Dimethyl sulfoxide (DMSO), trypan blue, paraformaldehyde, 3-(4,5-dimethylthiazol-2-yl)-2,5-diphenyltetrazoliumbromide (MTT), ganoderic acid A, ganoderic acid G, lucidenic acid A, and ergosterol were purchased from Sigma-Aldrich (St. Louis, MO, USA). Dulbecco's Modified Eagle Medium, fetal bovine serum, 4',6-diamidino-2-phenylindole dye (DAPI), dihydroethidium (DHE), fluorescein phalloidin dye, annexin-V-conjugated fluorescein isothiocyanate (FITC) dye, 5,5',6,6'-tetrachloro-1,1',3,3'-tetraethylbenzimidazolocarbo-cyanine iodide (JC-1) dye, propidium iodide (PI) dye, bicinchoninic acid assay (BCA) kit, phenylmethylsulphonyl fluoride, CM-H₂DCFDA dye, MitoSOX Red, penicillin/streptomycin, protease inhibitor cocktail, 0.25% (*w/v*) trypsin containing 1 mM EDTA, and phosphate-buffered saline (PBS) were all purchased from Invitrogen (Carlsbad, CA, USA). Terminal deoxynucleotidyl transferase dUTP nick end labelling (TUNEL) and lactate dehydrogenase (LDH) assay kits were obtained from Roche (Basel, Switzerland). Primary antibodies against Nrf2 and Keap1 were obtained from Abcam (Cambridge, UK). Other

primary antibodies and secondary antibodies were purchased from Cell Signaling Technology (Danvers, MA, USA).

2.3. Reflux Extraction of AR and GL. Fruiting bodies of AR and GL were provided by Mytiranran Healthcare Limited (Hong Kong, China), which has been granted an organic crop production certificate by the Hong Kong Organic Resource Centre. The extraction method has been described previously [18]. All extracts were dissolved in water and concentrated in 80 mL with a rotary evaporator and stored at -20°C before use.

2.4. Determination of Total Phenolic Compound, Polysaccharide, Triterpene, and Protein Content. The extracts were filtered and evaporated using a water bath. The residue was dissolved in 5 mL of distilled water, followed by a slow addition of 30 mL of 95% ethanol with stirring, and the samples were shaken and kept at 4°C overnight. After centrifugation, the supernatant was collected for the measurement of total content of phenolic compounds, triterpenes, and proteins. The precipitate was dissolved in hot water in a total volume of 35 mL and kept at 4°C for the detection of the total polysaccharide content. The methodology for determination of total phenolic compound, polysaccharide, and triterpene content has been described previously [18]. Glucose (GE), gallic acid (GAE), and oleonic acid (OA) were used as standards during the chemical analysis of the polysaccharides, phenolic compounds, and triterpenes, respectively.

To measure total protein content in the extracts, a 1 mL sample was added into 4 mL of biuret reagent, mixed, and incubated at room temperature for 30 min. Then, the absorbance at 540 nm was measured with a microplate absorbance reader, and bovine serum albumin (BSA) was used as the standard and results expressed as mg of bovine serum albumin equivalent per g (mg BSA/g).

2.5. High-Performance Liquid Chromatography (HPLC) Analysis of Ganoderic Acid A, Ganoderic Acid G, Lucidenic Acid A, and Ergosterol. HPLC analysis was conducted according to the method described previously [20]. Briefly, the HPLC analysis was performed using an UltiMate 3000 HPLC analysis system (Thermo-Fisher, Waltham, MA, USA) with a DAD 3000 detector, ternary pump of SR3000 Solvent Rack, WPS-3000SL autosampler, TCC-3000SD column temperature controller, and Chromeleon 7.2. Separation and was achieved in a C18 reversed-phase column (Hypersil Gold, particle size $5\ \mu\text{m}$, $250\ \text{mm} \times 4.6\ \text{mm}$, Thermo Scientific). The mobile phase contained acetonitrile (solvent A) and 0.1% phosphoric acid aqueous solution (solvent B). The detailed gradient elution program was as follows: 0–25 min, 25–50% A; 25–30 min, 50–99% B; and 30–50 min, 99–99% B; and HPLC profiling was performed at 30°C at a constant flow rate of 1.0 mL/min. All samples were injected into the system at equal volumes of $10\ \mu\text{L}$. Ganoderic acid A, ganoderic acid G, lucidenic acid A, and ergosterol were used as standards, and an analysis wavelength of 254 nm was selected.

2.6. Cell Culture. Rat cardiomyoblasts H9c2 and human breast adenocarcinoma cells MDA-MB-231 and MCF-7 were obtained from the American Type Culture Collection (Manassas, VA, USA) and cultured in Dulbecco's Modified Eagle Medium. The media was supplemented with 10% heat-inactivated fetal bovine serum and 1% penicillin/streptomycin. All cells were incubated at 37°C in a humidified atmosphere with 5% CO_2 .

2.7. Cell Viability Assay. Cell viability was measured with an MTT assay according to the manufacturer's protocol. Briefly, cell culture medium was replaced with MTT solution (0.5 mg/mL) after drug treatment, and the cells were incubated for an additional 4 h at 37°C . The MTT solution was then discarded, $100\ \mu\text{L}$ of DMSO was added to each well to dissolve the violet formazan crystals formed within the cells, and absorbance at 570 nm was measured with a SpectraMax M5 Multimode Microplate Reader (Molecular Devices, Sunnyvale, CA, USA).

2.8. LDH Assay. Cellular injury was assessed by measuring the activity of LDH released into the culture medium using a commercial kit (Roche, Basel, Switzerland) according to the manufacturer's instructions. Absorbances at 490 nm were measured on a microplate reader.

2.9. Seahorse Assay. Mitochondrial oxygen consumption rates (OCR) were measured using a Seahorse XFe24 Analyzer (Seahorse Biosciences, Billerica, MA, USA). H9c2 cells (8×10^3 cells/well) were seeded into Seahorse XF 24 well culture microplates and incubated overnight at 37°C in a humidified atmosphere with 5% CO_2 . After drug treatment, the culture medium was replaced with Seahorse base medium and incubated in a non- CO_2 incubator for 1 h. H9c2 cells were sequentially treated with $1\ \mu\text{M}$ oligomycin (Oligo), $5\ \mu\text{M}$ carbonyl cyanide-4-(trifluoromethoxy) phenylhydrazone (FCCP), and $1\ \mu\text{M}$ rotenone plus $1\ \mu\text{M}$ antimycin A (R + A). Then, OCR was calculated using Seahorse software (Seahorse Biosciences). After the assay was completed, the cells were lysed with radioimmunoprecipitation assay (RIPA) buffer ($200\ \mu\text{L}$ /well), and the protein concentration was measured using the BCA and OCR values were normalized to the protein content and presented as pmol/min/ μg protein.

2.10. DAPI/Phalloidin and Annexin V/PI Double Staining. Apoptosis was assessed using DAPI/phalloidin and annexin V/PI double staining. H9c2 cells were seeded in 12-well plates (2×10^5 cells/well) overnight and then treated with the appropriate drug. After, the cells were washed twice with ice-cold PBS and stained with DAPI ($2.0\ \mu\text{g}/\text{mL}$) and phalloidin-FITC ($0.5\ \mu\text{M}$) for 20 min at 37°C . Images were then captured using fluorescence microscopy (IN CELL Analyzer; GE Healthcare Life Sciences, Chicago, IL, USA). In addition, the H9c2 cells were harvested and resuspended in binding buffer and stained with annexin V-FITC and PI ($1.0\ \text{mg}/\text{mL}$) for 15 min at 37°C . The stained cells were analyzed using a flow cytometer (BD Biosciences, San Jose, CA, USA) with 10×10^3 events gated for each sample. The data were then analyzed using FlowJo software (BD Biosciences).

2.11. Measurement of Mitochondrial Membrane Potential. H9c2 cells were seeded overnight into 12-well plates (2×10^5 cells/well); and after drug treatment, the cells were washed twice with warm PBS and stained with JC-1 dye ($3 \mu\text{g}/\text{mL}$) for 20 min at 37°C . Images were then captured using a fluorescence microscope. In addition, the H9c2 cells were harvested and resuspended in warm PBS and then the cells were washed twice with warm PBS and examined using a flow cytometry.

2.12. ROS Detection. Intracellular and mitochondrial ROS were detected using CM- H_2DCFDA and MitoSOX Red staining. After drug treatment, H9c2 cells were washed twice with cold PBS and stained with $2 \mu\text{M}$ CM- H_2DCFDA or MitoSOX Red for 15 min. After washing with PBS, a portion of the cells were imaged with a fluorescence microscope, and the remaining cells were harvested and analyzed using flow cytometry.

2.13. siRNA Knockdown of Nrf2. Nrf2 was knocked down specifically using siRNA as previously described [21]. H9c2 cells were transfected with either 100 nM Nrf2 siRNA or nontargeting scrambled siRNA (negative control) using Lipofectamine® 2000 reagent (Invitrogen; Carlsbad, CA, USA) for 24 h according to the manufacturer's protocol.

2.14. Western Blot Analysis. The western blot analysis methodology has been described previously [22]. Briefly, protein was extracted from H9c2 cells or mouse heart tissues with RIPA buffer containing 1% phenylmethylsulphonyl fluoride and 1% protease inhibitor. The cell lysate was then centrifuged for 20 min at $12,500 \times g$ and 4°C to remove the nuclei and unbroken cells. The cytoplasmic and nuclear proteins were extracted using a nuclear and cytoplasmic protein extraction kit (Beyond time, Shanghai, China) according to the manufacturer's instructions. Protein concentrations were measured using BCAs. Equal amounts of protein were separated by electrophoresis using a sodium dodecyl sulphate–polyacrylamide gel and transferred to a polyvinylidene difluoride membrane (Bio-Rad Laboratories, Hercules, CA, USA). Nonspecific antigen binding was blocked with 5% nonfat milk for 1 h at room temperature. The membranes were then probed with primary antibodies against PARP, cleaved-PARP (Asp214), caspase 3, cleaved-caspase 3 (Asp175), caspase 9, cleaved-caspase 9 (Asp315), Bax, Bcl-2, mTOR, phospho-mTOR (Ser2448), Akt, phospho-Akt (Ser473), Nrf2, Keap1, HO-1, or β -actin overnight at 4°C . All primary antibodies were diluted at a ratio of 1:1,000 in Tris-buffered saline with 0.05% Tween 20 (TBST). After washing three times with TBST, the membranes were incubated with horseradish peroxidase-conjugated secondary antibodies (1:2,000 dilution in TBST) for 2 h at room temperature. After multiple washes with TBST, protein bands were developed using enhanced chemiluminescence. Images of the protein bands were captured, and densitometric measurements of signal intensities were collected with a chemiluminescence system (Syngene, Frederick, MD, USA). Protein expression of β -actin was similarly detected with a monoclonal mouse antiactin antibody (Chemicon, Temecula, CA, USA), and the optical density values for the different bands were normalized to those of β -actin.

2.15. Animal Study. Eight-week-old male C57BL/6J mice (~ 25 g) were supplied by the animal centre of Sichuan Provincial Academy of Medical Sciences and kept under a 12 h light/dark cycle at the animal care facility with an ambient temperature controlled at $20 \pm 5^\circ\text{C}$. The animals were fed with a fresh diet (containing 40% corn, 26% bran, 29% soybean cake, 1% salt, 1% bone meal, and 1% lysine) and had free access to water. The mice were acclimated for at least 7 days before the experiments and then divided into four groups ($n = 8$): (i) saline, (ii) Dox, (iii) Dox + AR, and (iv) Dox + GL. The sample size was calculated using the animal sample size calculator InVivoStat (with a power of 90%). The mice in the Dox + AR and Dox + GL groups were first administered AR (250 mg/kg) or GL (250 mg/kg) by oral gavage for 28 consecutive days. Starting from day 13, the mice received intraperitoneal injections of Dox (5 mg/kg) every 3 days until a cumulative dose of Dox (25-mg/kg) was reached to induce cardiotoxicity. The mice in the saline and Dox groups were treated with equal volumes of water for 28 days and received intraperitoneal injections of saline and Dox since day 13. The dose of DOX was chosen based on a previous report [5]. Regarding the dose of AR and GL, a previous report showed that treatment with 50 mg/kg of GL polysaccharide for 14 days had cardioprotective effect on Dox-treated rats [17]. Our chemical analysis showed that the polysaccharide content in AR and GL was approximately 5%, which suggested that 1000 mg/kg of AR and GL should be used. However, since the duration of treatment was 28 days instead of 14 days, the dose should be reduced. Our preliminary studies revealed that there was no significant difference between 250 mg/kg and higher doses in terms of the cardioprotective effect, and therefore, a dose of 250 mg/kg was used in the present study. Body weights and health of the animals were monitored every other day and the experiments would be stopped, and the animals would be removed from the study if they were unable to eat or drink, showed any abnormal behavior, or signs of toxicity, pain, or distress. At the end of the experiment, the mice were euthanized by an overdose of sodium pentobarbital (150 mg/kg), and death was confirmed by the absence of a heartbeat. Then, blood was collected for the assessment of cardiac injury by measuring serum LDH and creatine kinase (CK) levels. The heart tissues were excised, weighed, fixed with 4% (v/v) formaldehyde, dehydrated, and cut into $6 \mu\text{m}$ sections. Then, tissue morphology, oxidative stress, and cell apoptosis were examined by hematoxylin and eosin, DHE, and TUNEL staining. In addition, the sections were immunostained with monoclonal antimouse Nrf2 and HO-1 antibodies to investigate the expression of Nrf2 and HO-1 in heart tissues.

2.16. Survival Rate Analysis. The mean survival time and percentage change in life span were calculated based on mortality of the experimental mice with Dox treatment ($n = 8$). All the animals were allowed a natural death, and animal survival rate was analyzed using a Kaplan-Meier method. Statistical differences were calculated with a log-rank test.

2.17. Echocardiography. To determine cardiac function, the mice were anesthetized with 1% isoflurane in O₂ gas and then placed on a heated imaging platform. Echocardiographic experiments were performed using a Vevo 3100 micro-ultrasound imaging system (Visual Sonics Inc., Toronto, Canada) equipped with a 15 MHz linear transducer. The parameters of left ventricular fractional shortening (LVFS) and left ventricular ejection fraction (LVEF) were analyzed using Vevo LAB software (FUJIFILM VisualSonics, Toronto, ON, Canada).

2.18. Biochemical Analysis. LDH and CK levels in the serum and malondialdehyde (MDA) levels, reduced glutathione (GSH) levels, superoxide dismutase (SOD) activity, and catalase (CAT) activity in the heart tissues were measured using commercial kits (Abcam, Cambridge, UK) following the manufacturer's instructions.

2.19. Statistical Analysis. Data were analyzed in Prism v.5.0 software (GraphPad, La Jolla, CA, USA) and expressed as the mean \pm standard deviation (SD). The differences between groups were compared using one-way ANOVA, and $p < 0.05$ was considered to indicate statistically significant differences.

3. Results

3.1. Chemical Composition of AR and GL Extracts. Chemical assay results showed that the content of total polysaccharides in the AR and GL extracts was 42.45 ± 2.88 and 33.48 ± 2.97 mg GE/g, respectively. The content of total triterpenes included 6.10 ± 0.02 mg OA/g in the AR extract and 4.42 ± 0.134 mg OA/g in the GL extract. The content of total phenolic compounds was 6.60 ± 0.13 mg GAE/g in the AR extract and 3.68 ± 0.21 mg GAE/g in the GL extract. The content of total proteins in the AR and GL extracts was 212.01 ± 8.29 mg BSA/g and 160.02 ± 4.95 mg BSA/g, respectively (Table 1).

3.2. HPLC Analysis of the Major Components Found in AR and GL Extracts. The major components of the AR and GL extracts, including ganoderic acid A, ganoderic acid G, lucidenic acid A, and ergosterol, were quantified using HPLC. The results showed that the amount of ganoderic acid A and lucidenic acid A in the AR extract was lower than that in the GL extract, while the amount of ganoderic acid G and ergosterol in the AR extract was greater than that found in the GL extract (Figure S1). The average amount of ganoderic acid A, ganoderic acid G, lucidenic acid A, and ergosterol in the AR extract was 9.39, 12.20, 15.69, and 1477.68 μ g/g, respectively (Table 2). The average amount of ganoderic acid A, lucidenic acid A, and ergosterol in the GL extract was 41.73, 51.21, and 1070.23 μ g/g, respectively. However, ganoderic acid G could not be detected in the GL extract.

3.3. Effect of AR and GL Extracts on Dox-Induced Toxicity in H9c2 Cells. Cytotoxicity in H9c2 cells was evaluated using MTT and LDH assays, and the results showed that a 24 h treatment with Dox exhibited significant toxicity in H9c2

cells. Viability of H9c2 cells decreased by 54%, and LDH levels increased by 55% after treatment with Dox (Figures 1(a) and 1(b)). However, both the AR and GL extracts showed no toxicity in H9c2 cells at concentrations ranging from 0.125–2 mg/mL (data not shown). The AR extract increased cell viability and decreased LDH levels in a dose-dependent manner at concentrations ranging from 0.5–2 mg/mL in Dox-treated H9c2 cells. However, the GL extract had no effect (Figures 1(a) and 1(b)).

Seahorse assay was performed to evaluate mitochondrial function in H9c2 cells. After a 24 h treatment, Dox significantly induced mitochondrial dysfunction in H9c2 cells by markedly inhibiting basal respiration, ATP-linked respiration, maximal respiration, and spare respiration capacity (Figures 1(c) to 1(g)). By contrast, basal respiration, ATP-linked respiration, maximal respiration, and spare respiration capacity in Dox-treated cells after treatment with the AR extract were increased by 63%, 57%, 181%, and 67%, respectively. However, GL showed no effects on reducing Dox-induced mitochondrial dysfunction in H9c2 cells. In addition, MDA-MB-231 and MCF-7 human breast cancer cells were used to evaluate the impact of the AR and GL extracts on the anticancer effect of Dox. The results showed that both the AR and GL extracts significantly enhanced the anticancer effects of Dox in MDA-MB-231 and MCF-7 breast cancer cells (Figures 1(h) and 1(i)).

3.4. Effect of AR and GL Extracts on Dox-Induced Apoptosis in H9c2 Cells. A reduction in mitochondrial membrane potential (MMP) is an initial and irreversible step towards apoptosis. To evaluate of MMP, H9c2 cells were stained with JC-1 dye, and the changes in MMP were assessed using confocal microscopy and flow cytometry. The AR and GL did not affect MMP in H9c2 cells since no obvious green signals were observed. In contrast, Dox significantly induced the loss of MMP in H9c2 cells as reflected by the change from red to green fluorescence (Figures 2(a) and 2(b)). Quantitative analysis of microscopy images (Figure 2(e)) and flow cytometry (Figure 2(f)) showed that Dox decreased MMP in H9c2 cells by 77% and 48%, respectively. However, Dox-induced loss of MMP was remarkably rescued by the AR but not the GL extract. After AR extract treatment, the MMP from the Dox-treated H9c2 cells was only decreased by 41% and 2% in microscopy images and flow cytometry analysis (Figures 2(e) and 2(f)), respectively.

DAPI/phalloidin double staining was used to evaluate apoptosis in H9c2 cells, and no nuclear condensation or fragmentation was observed in the control, AR, and GL extract-treated cells. In contrast, many bright condensed dots that represent apoptotic bodies were clearly observed in Dox-treated H9c2 cells (Figure 2(c)). Quantitative analysis showed that the number of apoptotic cells was 3.9-fold higher after treatment with 0.5 μ M Dox, and 1.4- and 2.8-fold higher when the H9c2 cells were pretreated with the AR and GL extracts before Dox treatment (Figure 2(g)). The antiapoptotic effect of the AR extract on H9c2 cells was also studied using annexin V-FITC and PI staining and flow cytometry (Figure 2(d)). The number of apoptotic cells was 4.4-fold higher after the treatment with Dox, but

TABLE 1: Analysis of chemical content in AR and GL extracts.

Sample	Polysaccharides (mg GE/g)	Triterpenes (mg OA/g)	Phenols (mg GAE/g)	Proteins (mg BSA/g)
AR	42.45 ± 2.88	6.10 ± 0.02	6.60 ± 0.13	212.01 ± 8.29
GL	33.48 ± 2.97	4.42 ± 0.134	3.68 ± 0.21	160.02 ± 4.95

TABLE 2: HPLC analysis of the major components found in AR and GL extracts.

Sample	Ganoderic acid A ($\mu\text{g/g}$)	Ganoderic acid G ($\mu\text{g/g}$)	Lucidenic acid A ($\mu\text{g/g}$)	Ergosterol ($\mu\text{g/g}$)
AR	9.39	12.20	15.69	1477.68
GL	41.73	Undetected	51.21	1070.23

1.9-fold and 3.7-fold higher when the cells were pretreated with the AR and GL extracts before the Dox treatment (Figure 2(h)).

3.5. Effect of AR and GL Extracts on Proapoptotic Protein Expression in H9c2 Cells. Expression of proteins involved in the apoptotic signaling pathways in H9c2 cells was studied using western blot assays (Figure 3). In comparison with the control group, both the AR and GL extract groups showed a small decrease in the expression of cleaved PARP, cleaved caspase-3, and Bax/Bcl-2 ratio. After a 24 h treatment with Dox (0.5 μM), the ratios of cleaved PARP/PARP, cleaved caspase-3/caspase-3, cleaved caspase-9/caspase-9, and Bax/Bcl-2 were markedly increased by 198%, 191%, 245%, and 78%, respectively. However, the Dox-induced elevation of the ratios of cleaved PARP/PARP, cleaved caspase-3/caspase-3, cleaved caspase-9/caspase-9, and Bax/Bcl-2 were abolished by the AR extract. Dox increased the ratios of cleaved PARP/PARP, cleaved caspase-3/caspase-3, and cleaved caspase-9/caspase-9 by 84%, 51%, and 148% after the treatment with the GL extract, respectively. However, the GL extract had no effect on the Dox-induced Bax/Bcl-2 ratio.

3.6. Effect of AR and GL Extracts on Dox-Induced ROS Generation in H9c2 Cells. Intracellular and mitochondrial ROS accumulation in H9c2 cells were evaluated as shown by staining with DCFDA and MitoSOX fluorescence dyes. The fluorescence signals were detected by confocal microscopy and flow cytometry. The AR and GL extracts showed no effects on intracellular ROS (green fluorescence) or mitochondrial ROS (red fluorescence) generation in H9c2 cells (Figures 4(a)–4(d)). Intracellular ROS generation in H9c2 cells was stimulated to 162% and 466% by Dox (0.5 μM) as determined by confocal microscopy and flow cytometry, respectively (Figures 4(e) and 4(f)). Similarly, mitochondrial ROS generation in H9c2 cells was elevated to 125% and 89% by Dox (0.5 μM) as determined by confocal microscopy and flow cytometry, respectively (Figures 4(g) and 4(h)). The effect of Dox on intracellular and mitochondrial ROS generation was abolished by the AR extract but not the GL extract (Figures 4(e)–4(h)).

3.7. Effect of AR and GL Extracts on Akt/mTOR and Nrf2/HO-1 Signaling Pathways in H9c2 Cells. The Akt/mTOR and Nrf2/HO-1 signaling pathways play vital roles not only

in maintaining cardiomyocyte survival but also in the regulation of cardiomyocyte apoptosis. The expression levels of phospho-Akt, Nrf2, and HO-1 in H9c2 cells were significantly increased by the AR and GL extracts, whereas phospho-mTOR and Keap1 were not affected (Figure 5(a)). Notably, a 24 h treatment with Dox (0.5 μM) inhibited the ratio of p-Akt/Akt, p-mTOR/TOR, Nrf2, and HO-1 by 27%, 75%, 79%, and 67%, respectively, but significantly elevated Keap1 expression by 257% in H9c2 cells (Figures 5(b)–5(f)). After treatment with the AR extract, the ratio of p-Akt/Akt was not decreased, while the ratio of p-mTOR/mTOR and the expression of Nrf2 and HO-1 in Dox-treated cells were decreased by 52%, 28%, and 25%, respectively. In addition, Dox-induced Keap1 expression was increased by 58% after treatment with the AR extract. After treatment with the GL extract, the p-Akt/Akt ratio was not reduced, and Keap1 expression in the Dox-treated H9c2 cells was increased to 65%. No effect of the GL extract on the ratio of p-mTOR/mTOR and expression of Nrf2 and HO-1 was observed (Figures 5(b)–5(f)). Furthermore, protein expression of Nrf2 in the cytosol of H9c2 cells was dose-dependently decreased by the AR extract whereas the protein expression of Nrf2 in the nucleus was significantly elevated by the AR extract (Figures 5(g)–5(h)).

3.8. Effect of Nrf2 Knockdown on the Protective Effect of AR Extract against Dox-Induced Toxicity in H9c2 Cells. To further investigate the role of Nrf2 in the cardioprotective effects of AR extract against Dox-induced cardiotoxicity, Nrf2 expression was knocked down in H9c2 cells using siRNA transfection, and the protective effects of the AR extract were then examined. In comparison with the scramble siRNA-transfected cells, a mild decrease in cell viability and a slight increase in LDH release were observed in Nrf2 siRNA-transfected cells following Dox treatment (Figures 6(a) and 6(b)). AR extract (1 mg/mL) could alleviate Dox-induced cytotoxicity in the scramble siRNA-transfected cells, but it had no effect on Nrf2 siRNA-transfected H9c2s (Figures 6(a) and 6(b)). Similarly, knockdown of Nrf2 increased Dox-induced ROS generation and apoptosis in H9c2 cells (Figures 6(c) to 6(f)). AR could inhibit Dox-induced ROS generation and apoptosis in the scramble siRNA-transfected but not in Nrf2 siRNA-transfected cells (Figures 6(c) to 6(f)).

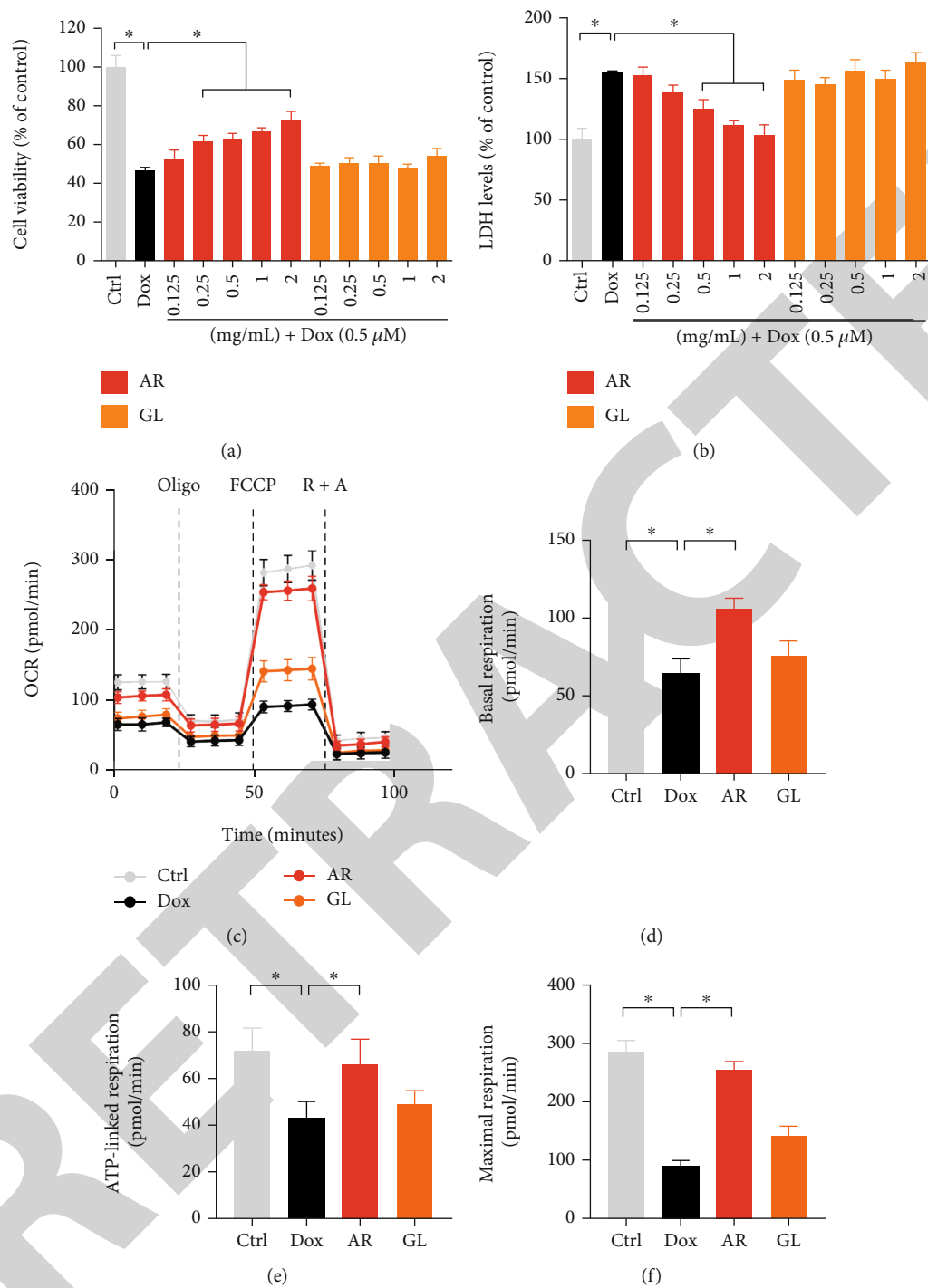


FIGURE 1: Continued.

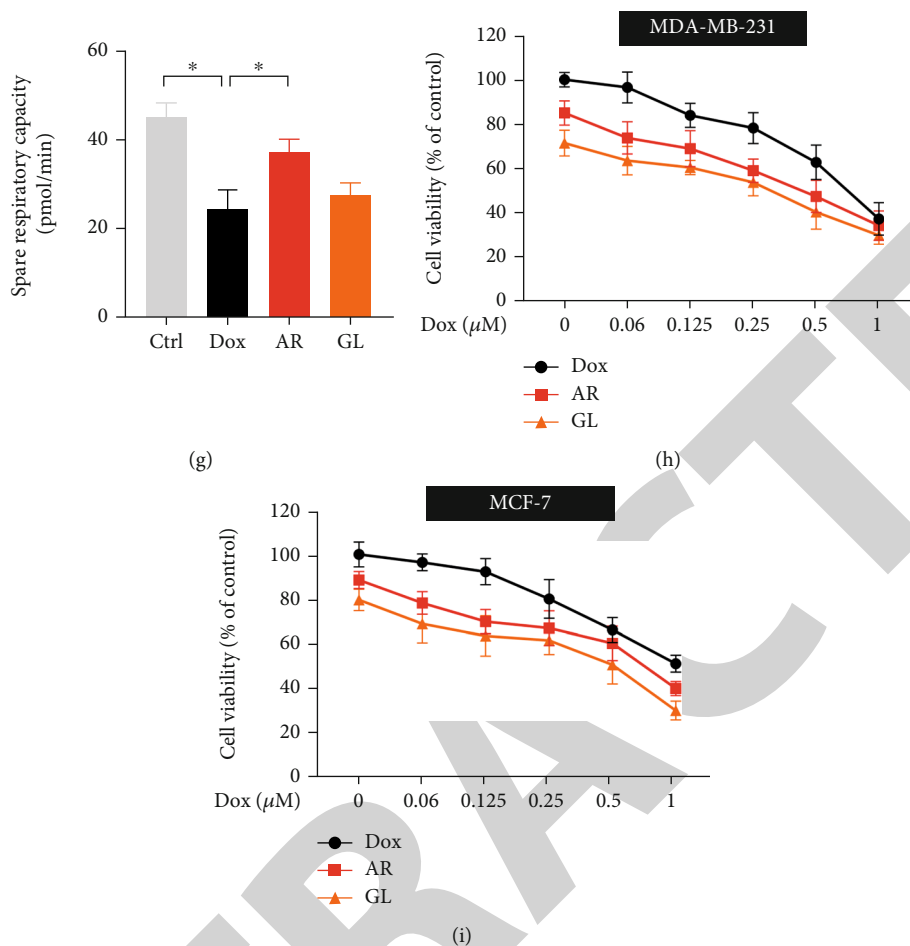


FIGURE 1: Effect of AR and GL extracts on Dox-induced toxicity and mitochondrial dysfunction in H9c2 cells and the anticancer effect of Dox. H9c2 cells were pretreated with various concentrations of AR or GL extracts (0.125–2 mg/mL) for 12 h and then received a 0.5 μ M Dox treatment for a further 24 h. Cell viability and LDH release in H9c2 cells were examined by (a) MTT and (b) LDH assays. (c) Mitochondrial oxygen consumption rate (OCR) was monitored using a Seahorse metabolic analyzer. H9c2 cell response after addition of 1 μ M oligomycin (Oligo), 5 μ M FCCP, and 1 μ M rotenone plus 1 μ M antimycin (R + A) were recorded. (d) Basal respiration, (e) ATP-linked respiration, (f) maximal respiration, and (g) spare respiratory capacity in H9c2 cells were quantified. (h) MDA-MB-231 and (i) MCF-7 human breast cancer cells were treated with various concentrations of Dox (0–1 μ M) in the absence or presence of AR or GL (1 mg/mL) extracts for 48 h. Cell viability was measured using MTT assay, and data are presented as percentage of control group values (mean \pm SD of three independent experiments). * p < 0.05 indicates a statistically significant difference.

3.9. Effect of AR and GL Extracts on Protecting Dox-Induced Cardiotoxicity in Mice. A mouse model of Dox-induced cardiotoxicity was used to further investigate the cardioprotective effects of AR *in vivo*. A cumulative Dox dose of 25 mg/kg was injected into mice to induce cardiotoxicity. Dox induced a reduction in mouse body weight and an increase in the heart weight/body weight ratio (Figures 7(a) and 7(b)). The AR extract (250 mg/kg) alleviated the body weight loss and the increase in heart weight/body weight ratio in mice (Figures 7(a) and 7(b)). Additionally, the AR extract significantly prolonged the survival rate of Dox-treated mice (Figure 7(c)). Mouse cardiac functions were also evaluated using echocardiography (Figure 7(d)). Severe cardiac dysfunction was observed in the hearts of Dox-treated mice, with LVFS and LVEF decreased by 42% and 29%, respectively. Dox-induced cardiac dysfunction was markedly rescued by the AR extract, but not the GL extract. After treatment with the AR extract, LVFS and LVEF in Dox-

treated mice were decreased by 8% and 5%, respectively (Figures 7(e) and 7(f)).

Next, myocardial injury was evaluated by analyzing cardiac damage markers, including LDH and CK. Dox treatment significantly increased the serum levels of LDH and CK in mice, and these effects were markedly reduced by the AR extract but not the GL extract (Figures 7(g) and 7(h)). MDA, SOD, GSH, and CAT levels in the heart tissues were also examined, and we found that MDA levels were elevated by Dox, whereas the increased MDA levels were significantly suppressed by the AR extract (Figure 7(i)). Moreover, SOD activity in the heart was slightly decreased by Dox but significantly elevated after treatment with the AR extract (Figure 7(j)). Furthermore, GSH and CAT activities in the heart were significantly inhibited by Dox, and this inhibition was abolished by AR treatment (Figures 7(k) and 7(m)). Although GL treatment slightly decreased MDA levels and increased SOD, GSH, and CAT activities in Dox-

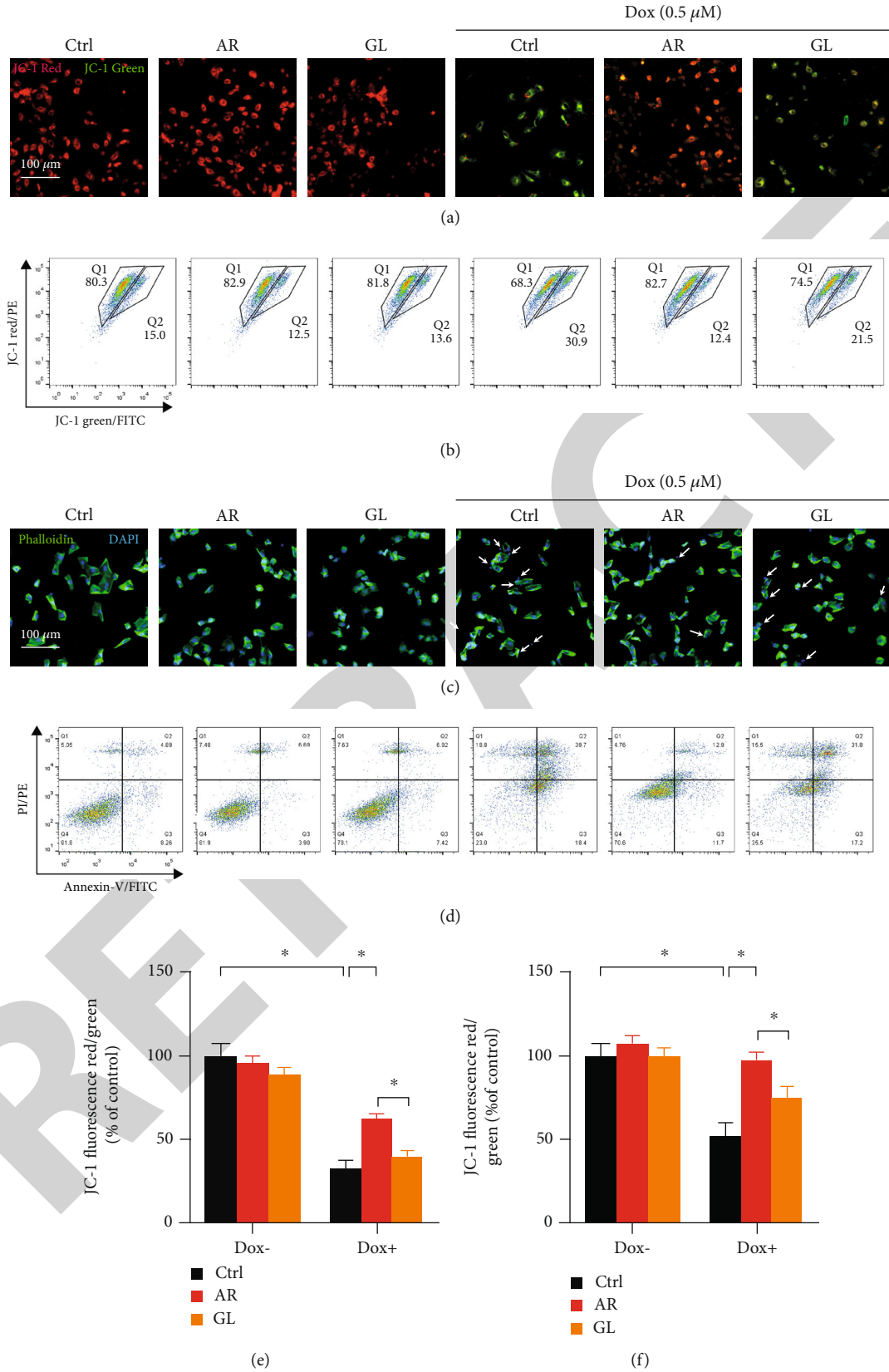


FIGURE 2: Continued.

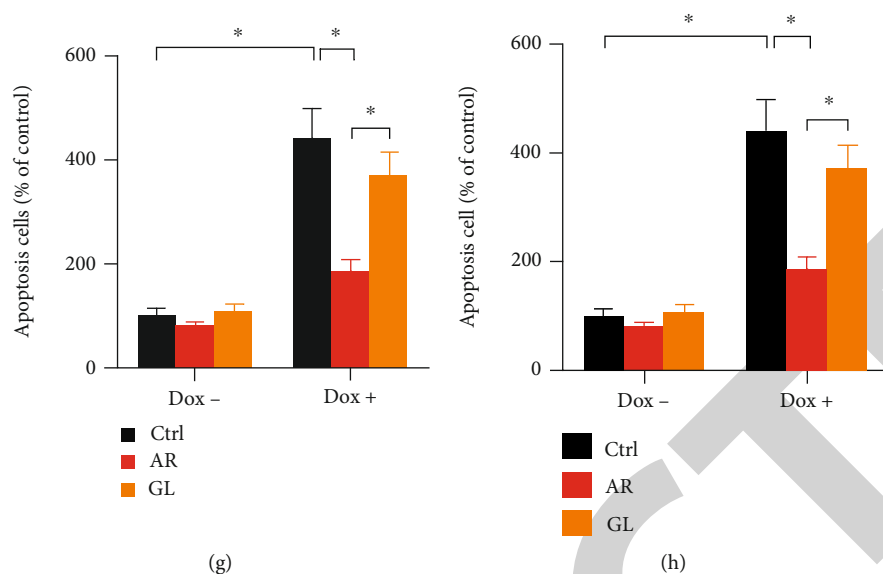


FIGURE 2: Effect of AR and GL extracts on Dox-induced loss of mitochondrial membrane potential and apoptosis in H9c2 cells. H9c2 cells were pretreated with 1 mg/mL of AR or GL extract or vehicle (control) for 12 h and then treated with or without 0.5 μ M Dox for 24 h. (a) Mitochondrial membrane potential in H9c2 cells was then detected using fluorescence microscopy after JC-1 staining. Red and green fluorescence signals indicated JC-1 aggregates (which refers to the loss of mitochondrial membrane potential) and monomers, respectively. Scale bar: 100 μ m. (b) Flow cytometry analysis of mitochondrial membrane potential in H9c2 cells after JC-1 staining. The mitochondrial membrane potential in (e) microscopy images and (f) flow cytometry was quantified. (c) Apoptotic cells were detected by DAPI/phalloidin-FITC double staining. Blue and green signals show nuclei and cytoskeleton of H9c2 cells. White arrows indicate apoptotic cells, and the number of apoptotic cells was counted. Scale bar: 100 μ m. (d) Cells were double stained by annexin V-FITC and PI for 20 min and then analyzed using flow cytometry. The number of apoptotic cells in microscopy images (g) and flow cytometry (h) was quantified. Data are presented as percentage of control group values (mean \pm SD of three independent experiments). * p < 0.05 indicates a statistically significant difference.

treated mice, the difference was not statistically significant. Western blot results for mouse heart tissues showed that the ratio of phosphor-Akt/Akt and expression levels of Nrf2 and HO-1 were decreased by Dox 58%, 48%, and 50%, whereas the Bax/Bcl-2 ratio and cleaved caspase-3/caspase-3 ratio were elevated by Dox to 643% and 204%, respectively, in the mouse heart tissues (Figure 7(l)). With AR extract treatment, the ratio of p-Akt/Akt and the expression of HO-1 could not be reduced, and the expression of Nrf2 could only be decreased by 23% (Figures 7(n)–7(p)). Moreover, the ratio of Bax/Bcl-2 and cleaved caspase-3/caspase-3 could only be increased by 230% and 14%, respectively (Figures 7(q) and 7(r)).

In addition, tissue morphology, ROS accumulation, apoptosis, and expression levels of Nrf2 and HO-1 in the mouse heart were examined using histological analyses. Cardiotoxicity was demonstrated in the Dox-treated mice based on the observation of fewer cardiomyocytes in the cardiac tissues and an increase in nuclear chromatin condensation in these cells (Figure 8(a)). Cardiotoxicity was reduced by the AR extract, but not the GL extract (Figure 8(a)). Dox also induced ROS accumulation and apoptosis in mouse hearts as the positive DHE and TUNEL signals were drastically increased (Figures 8(b) and 8(c)). The expression of Nrf2 and HO-1 in mouse hearts was also suppressed by Dox (Figures 8(d) and 8(e)). However, all the above effects induced by Dox could be reversed by the AR extract, but not the GL extract (Figures 8(f)–8(i)).

4. Discussion

Oxidative stress is considered to be one of the main causes of Dox-induced cardiac injury [23] as an imbalance between ROS and antioxidants can lead to oxidative stress [24, 25]. Sustained oxidative stress caused by Dox can reduce the mitochondrial membrane potential, which induces mitochondrial dysfunction and cell apoptosis and ultimately leads to cardiomyocyte damage [26]. Although the pharmacological effects of AR have rarely been investigated, AR extracts have been shown to inhibit oxidants and proinflammatory mediators such as TNF- α and nitric oxide in LPS-stimulated RAW264.7 cells [27, 28]. Moreover, AR extracts showed potential antioxidant and antiatherosclerotic effects in *in vivo* models by inhibiting low-density lipoprotein (LDL) level, LDL peroxidation, and 3-hydroxy3-methylglutaryl-coenzyme A (HMG-CoA) reductase catalytic activity [29]. Furthermore, a recent study indicated that ethanol extract of AR showed potential gastroprotective effects in rat gastric ulcer models by suppressing inflammation through the inhibition of NF- κ B and NLRP3 gene expression [30]. Our previous study has also demonstrated that AR possessed a remarkable ability to remove ROS and exhibited promising neuroprotective effects in PC12 cells by reducing 6-OHDA-induced oxidative stress, mitochondrial dysfunction, and apoptosis [18]. Although the above studies have suggested an antioxidant property of AR, and heart is well-known to be vulnerable to oxidative stress, the

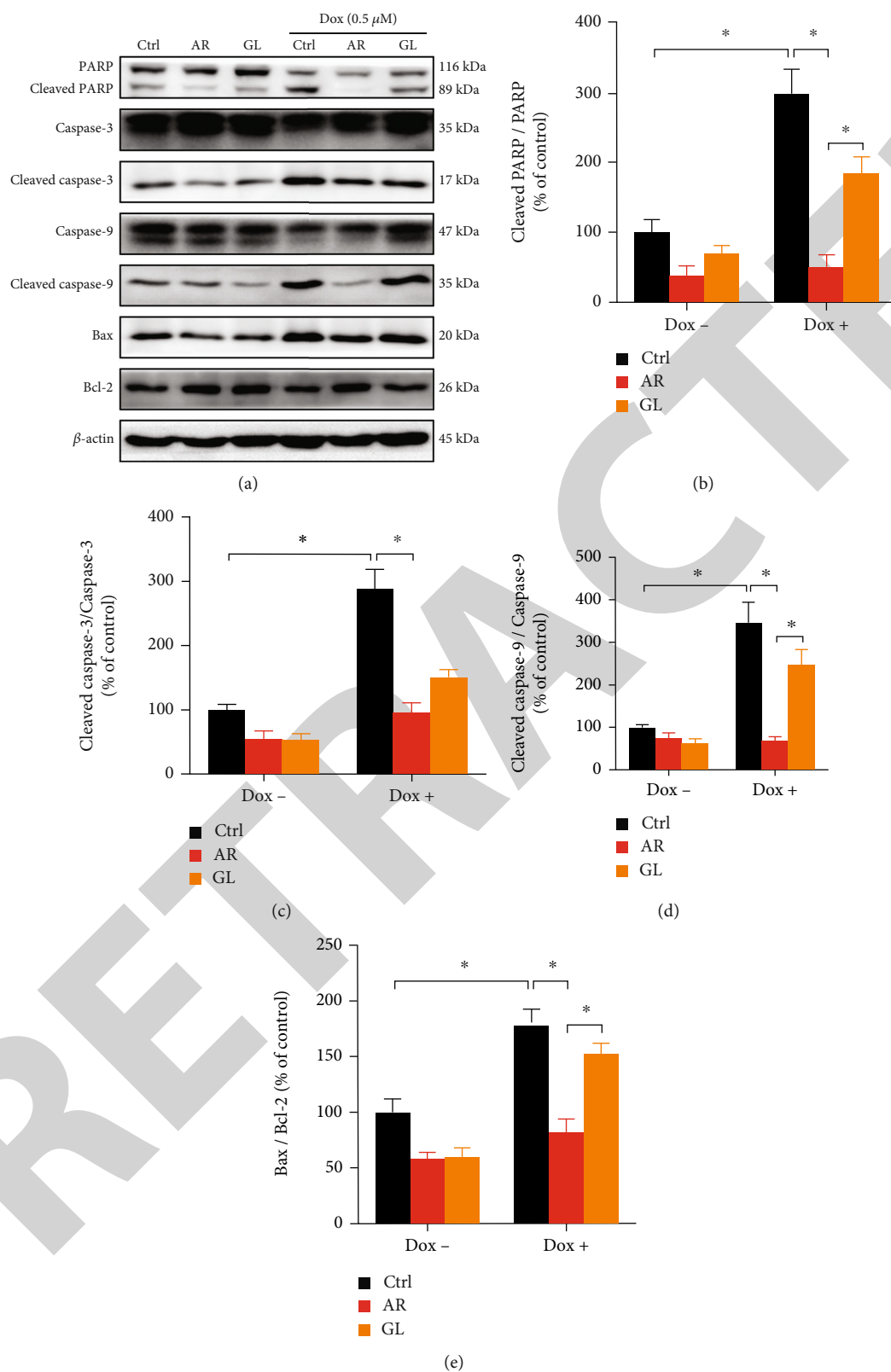


FIGURE 3: Effect of AR and GL extracts on Dox-induced expression of proapoptotic proteins in H9c2 cells. H9c2 cells were pretreated with 1 mg/mL of AR or GL extract or vehicle (control) for 12 h and then treated with or without Dox (0.5 μ M) for 24 h. Protein expression levels of PARP, cleaved-PARP, caspase-3, cleaved caspase-3, caspase-9, cleaved caspase-9, Bax, Bcl-2, and β -actin were examined using western blot analysis. (a) Representative blots. (b–d) Quantitative analysis of the ratios of protein expression level of (b) cleaved PARP/PARP, (c) cleaved caspase-3/caspase-3, (d) cleaved caspase-9/caspase-9, and (e) Bax/Bcl-2. Data are presented as percentage of control group values (mean \pm SD of three independent experiments). * p < 0.05 indicates a statistically significant difference.

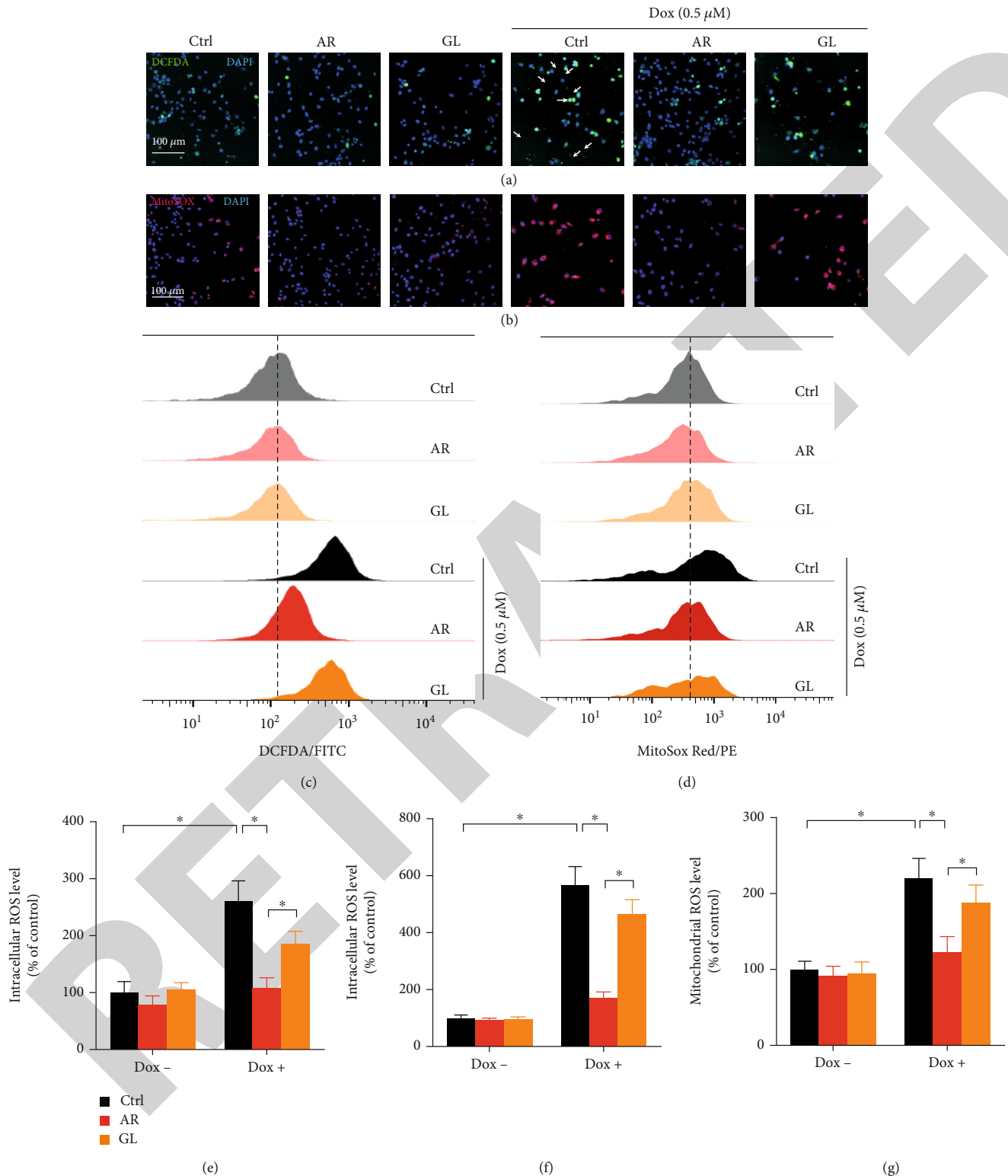


FIGURE 4: Effect of AR and GL extracts on Dox-induced oxidative stress in H9c2 cells. H9c2 cells were pretreated with 1 mg/mL of AR or GL extract or vehicle (control) for 4 h and then treated with or without 0.5 μ M Dox for 4 h. (a) Intracellular ROS and (b) mitochondrial ROS generation in H9c2 cells were detected by fluorescence microscopy after CM-H2DCFDA and MitoSOX red staining. Blue, green, and red signals indicate nuclei, intracellular ROS, and mitochondrial ROS in the H9c2 cells. Scale bar: 100 μ m. Flow cytometry analysis of (c) intracellular ROS and (d) mitochondrial ROS levels in H9c2 cells. Quantitative analysis of (e) intracellular ROS and (g) mitochondrial ROS levels using fluorescent microscopy. (f) Intracellular ROS and (h) mitochondrial ROS levels were quantified using flow cytometry analysis. Data are presented as percentage of control group values (mean \pm SD of three independent experiments). * p < 0.05 indicates a statistically significant difference.

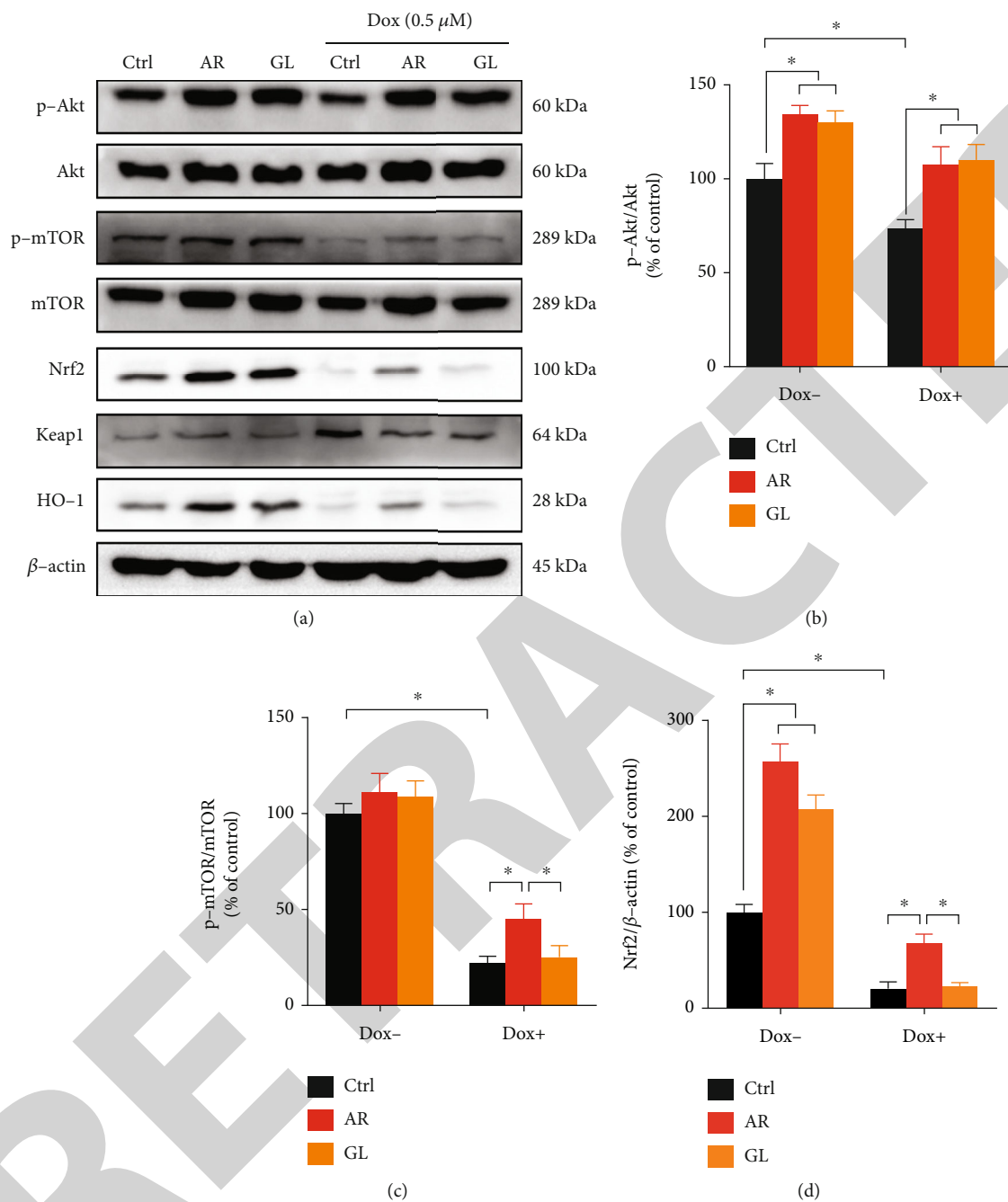


FIGURE 5: Continued.

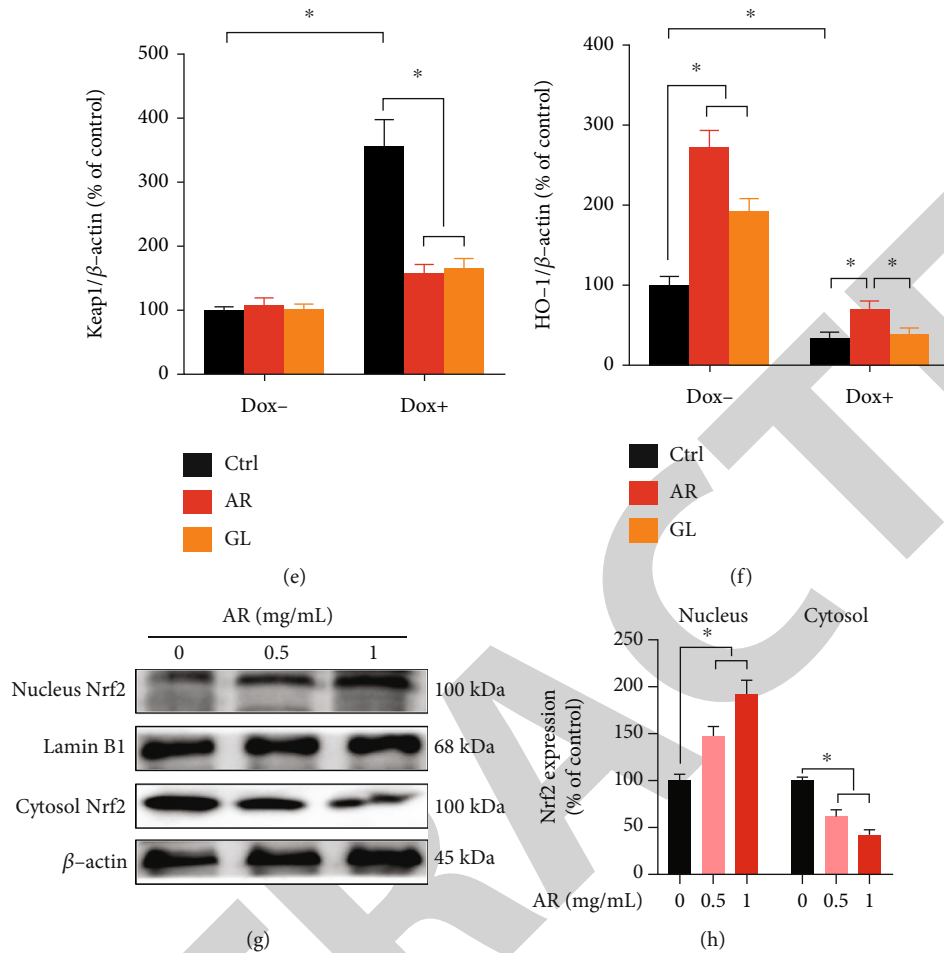


FIGURE 5: Effect of AR and GL extracts on the Akt/mTOR and Nrf2/HO-1 signaling pathways in H9c2 cells. H9c2 cells were pretreated with 1 mg/mL of AR or GL extract or vehicle (control) for 12 h and then treated with or without 0.5 μ M Dox for 24 h. (a) Protein expression levels of p-Akt, Akt, p-mTOR, mTOR, total Nrf2, Keap1, HO-1, and β -actin were examined using western blot analysis. (b)–(f) Quantitative analysis of protein expression levels. (g) H9c2 cells were pretreated with 0.5 and 1 mg/mL of AR for 12 h, and the protein expression levels of Nrf2 in the nucleus and cytosol were examined by western blot analysis. (h) Quantitative analysis of nuclear and cytosolic Nrf2 expression levels. Data are presented as percentage of control group (mean \pm SD of three independent experiments). * $p < 0.05$ indicates a statistically significant difference.

effect of AR on heart has not hitherto been explored. The present study is aimed at filling this research gap, and to our knowledge, we are the first to report that the AR extract could rescue cardiomyocytes from Dox-induced cell death by reducing Dox-induced oxidative stress, mitochondrial dysfunction, and apoptosis.

In terms of the mechanism of cardioprotective action, our results showed that the AR extract may activate the Akt/mTOR signaling pathway, which is known to play a vital regulatory role in cardiomyocyte survival [31]. Phosphorylation of Akt and mTOR was inhibited by Dox in H9c2 cells, but this inhibition could be restored by AR treatment. Moreover, Dox-induced expression of proapoptotic proteins, such as cleaved-PARP, cleaved caspase-3, cleaved caspase-9, and Bax, could be suppressed by the AR extract. Previous studies have also reported that Dox-induced cardiotoxicity is likely due to the downregulation of the Nrf2/HO-1 signaling pathway [11]. Consistently, our results showed that Dox suppressed the expression of Nrf2 and HO-1 in H9c2 cells and mouse heart

tissues, and this downregulation of Nrf2 and HO-1 could be significantly restored by the AR extract. Furthermore, AR also promoted the translocation of Nrf2 from the cytoplasm into nucleus. In addition, the cardioprotective effects of the AR extract against Dox-induced cardiotoxicity was abolished when Nrf2 was knocked down by siRNA. Taken together, our findings suggested that the cardioprotective effect of the AR extract may be related to the activation of both Akt/mTOR and Nrf2/HO-1-mediated mechanisms. Both the Akt/mTOR and Nrf2/HO-1 signaling pathways play important roles in the regulation of cell survival and antioxidative responses in cardiomyocytes [31, 32] and disruption of the Akt/mTOR or Nrf2/HO-1 signaling pathway can induce apoptosis in cardiomyocytes [31, 33]. Interestingly, previous studies have indicated that Akt is the upstream regulator of the Nrf2/HO-1 pathway [34, 35]. Therefore, there should be connection of abnormal expression of different proteins between the Akt/mTOR and Nrf2/HO-1 signaling pathways, which is worth to studying in the future.

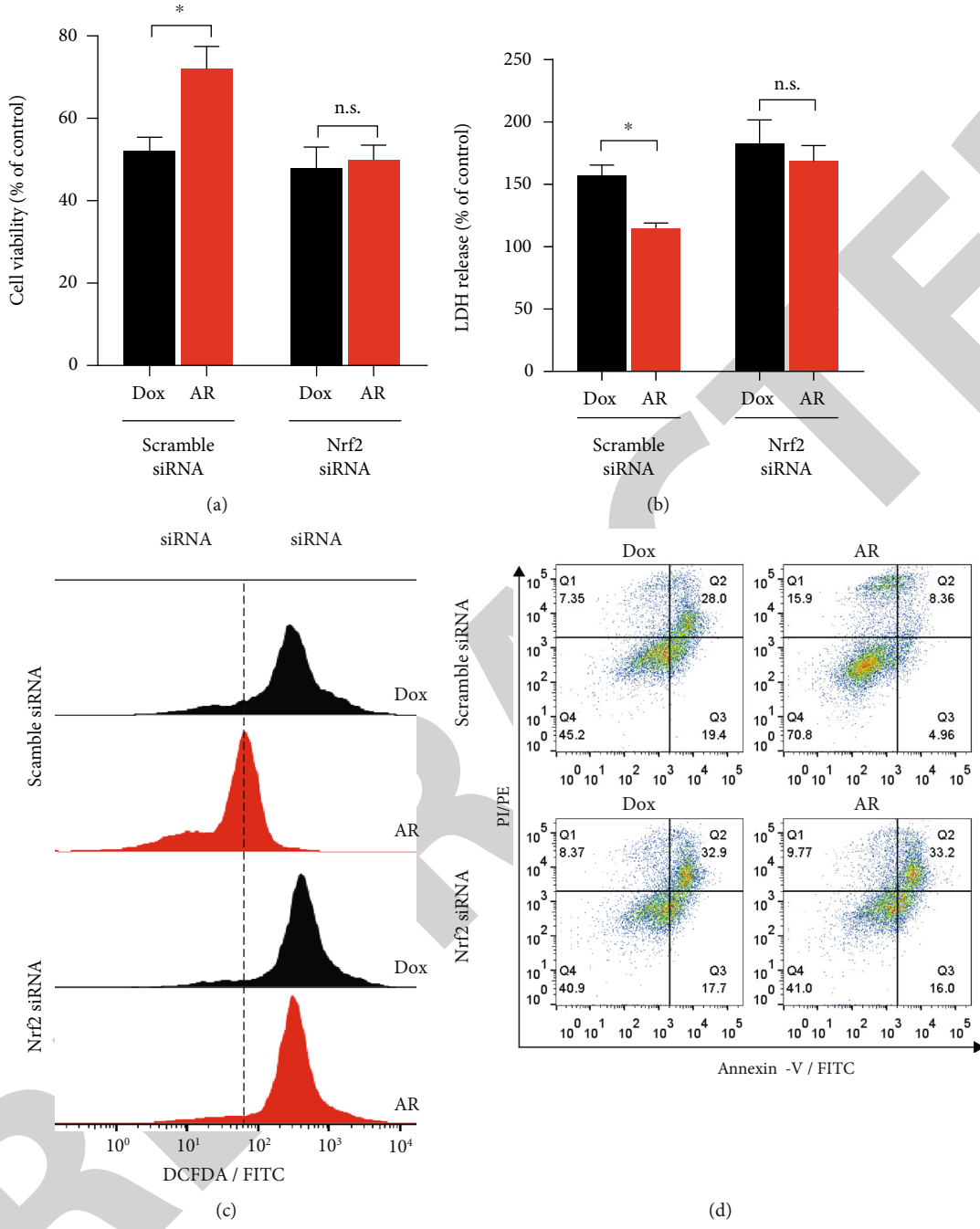


FIGURE 6: Continued.

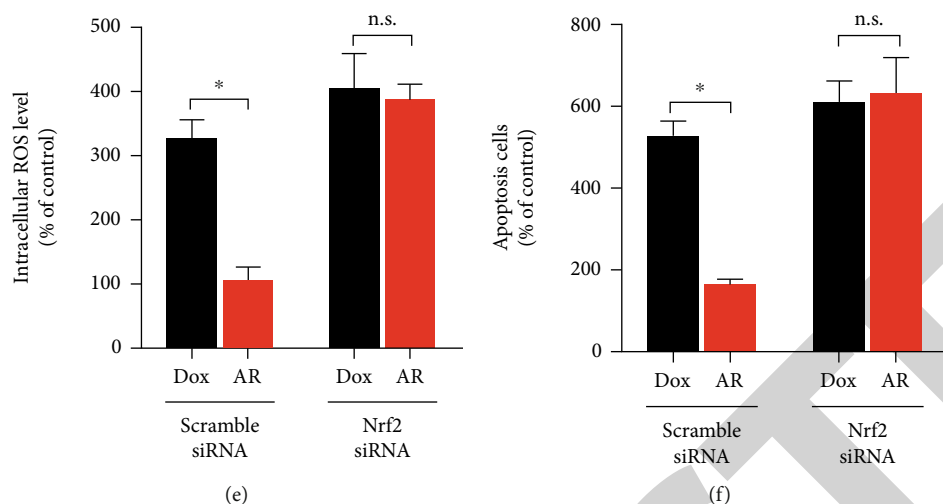


FIGURE 6: Effect of Nrf2 knockdown on the protective effect of AR extract against Dox-induced toxicity in H9c2 cells. The H9c2 cells were transfected with scramble siRNA or siRNA against Nrf2 and pretreated with AR extract (1 mg/mL) or vehicle control (0.1% DMSO) for 12 h and then received a 0.5 μ M Dox treatment for an additional 24 h. Cell viability and LDH levels in the transfected H9c2 cells were examined by (a) MTT and (b) LDH assays. (c) Intracellular ROS generation in H9c2 cells was detected by flow cytometry after CM-H₂DCFDA staining. (d) Cell apoptosis in H9c2 cells was detected using flow cytometry after annexin V-FITC and PI double staining. Quantitative analysis of (e) intracellular ROS levels and (f) apoptosis in transfected H9c2 cells. Data are presented as percentage of control group values (mean \pm SD of three independent experiments). * p < 0.05 indicates a statistically significant difference and n.s. means not significant.

An interesting finding from our study relates to the comparison of cardioprotective effects between the GL and AR water extracts. Previous studies have reported the cardioprotective effects of GL against Dox-induced cardiotoxicity [16, 17], and the present results showed that AR exhibited a greater effect than GL at inhibiting Dox-induced oxidative stress, mitochondrial dysfunction, and cell apoptosis in H9c2 cells. In our animal studies, the AR extract significantly protected the mice from Dox-induced body weight loss, reduced survival rate, and cardiac dysfunction. In our biochemical analyses, the AR extract significantly reversed Dox-induced upregulation of LDH, CK, and MDA levels but downregulated SOD, GSH, and CAT activities. Similarly, in the western blot analysis, the AR extract significantly rescued p-Akt, Nrf2, and HO-1 expression and significantly abolished ROS generation, apoptosis, and proapoptotic protein expression the heart tissue. However, all these protective effects were not observed in GL-treated mice.

The differences in the chemical constituent of AR and GL may provide some hint as to why AR exhibits superior protective effects on Dox-induced cardiotoxicity. A wide variety of constituents, including glycoproteins, polysaccharides, triterpenoids, meroterpenoids, sesquiterpenoids, steroids, alkaloids, benzopyran derivatives, and benzoic acid derivatives, have been found in GL [36]. Among them, polysaccharides are the most abundant component in the water extract [37]. They contribute to the major biological activities and therapeutic effects of GL [38]. It has been reported that GL polysaccharides alleviate Dox-induced cardiotoxicity by reversing Dox-induced cardiomyocyte death, apoptosis, oxidative stress, and proinflammatory cytokine production [17]. Moreover, GL polysaccharides stabilize Nrf2 expression by suppressing Gul3-mediated K48-linked polyubiquitination of Nrf2, leading to HO-1 activation and

inhibition of the NF- κ B signaling pathway [17]. In contrast to these studies, the present results showed that the GL extract was not particularly effective in alleviating Dox-induced cardiotoxicity. This was likely due to the insufficient content of polysaccharides in the water extract. The present data showed that the polysaccharide concentration was equivalent to 33.5 μ g/mL and 42.5 μ g/mL in the GL and AR extracts (1 mg/mL), respectively. The polysaccharide concentration in the GL extract was lower than the effective dose of polysaccharides (i.e., 50 μ g/mL) used in a previous study [17]. Another possibility for the increased potency of the AR extract on cardioprotection may be due to the higher content of triterpenes, phenols, and ergosterol, which are known antioxidants [26]. Interestingly, ganoderic acid G was found in the AR extract but not in the GL extract, and the biological activity of ganoderic acid G has rarely been studied and thus its contribution to cardioprotection warrants further investigation.

In clinical practice, there are two main strategies used to reduce Dox-induced cardiotoxicity: structural modification of Dox using chemical and pharmaceutical methods and pharmacological approaches using drug combinations [26]. Currently, drugs that have been approved for the prevention of Dox-induced cardiotoxicity are rare. Dexrazoxane is the only such cardioprotective agent approved by the U.S. Food and Drug Administration and the European Medicines Agency (EMA) [39]. However, some severe deficiencies have led to restrictions on the use of dexrazoxane in the U.S. and some European countries [40]. As emerging evidence has suggested that dexrazoxane may significantly decrease the response rate of patients with advanced breast cancer receiving Dox treatment [41]. Moreover, dexrazoxane has carcinogenic potential, and its use shows an increased risk of developing acute myeloid leukemia and myelodysplastic

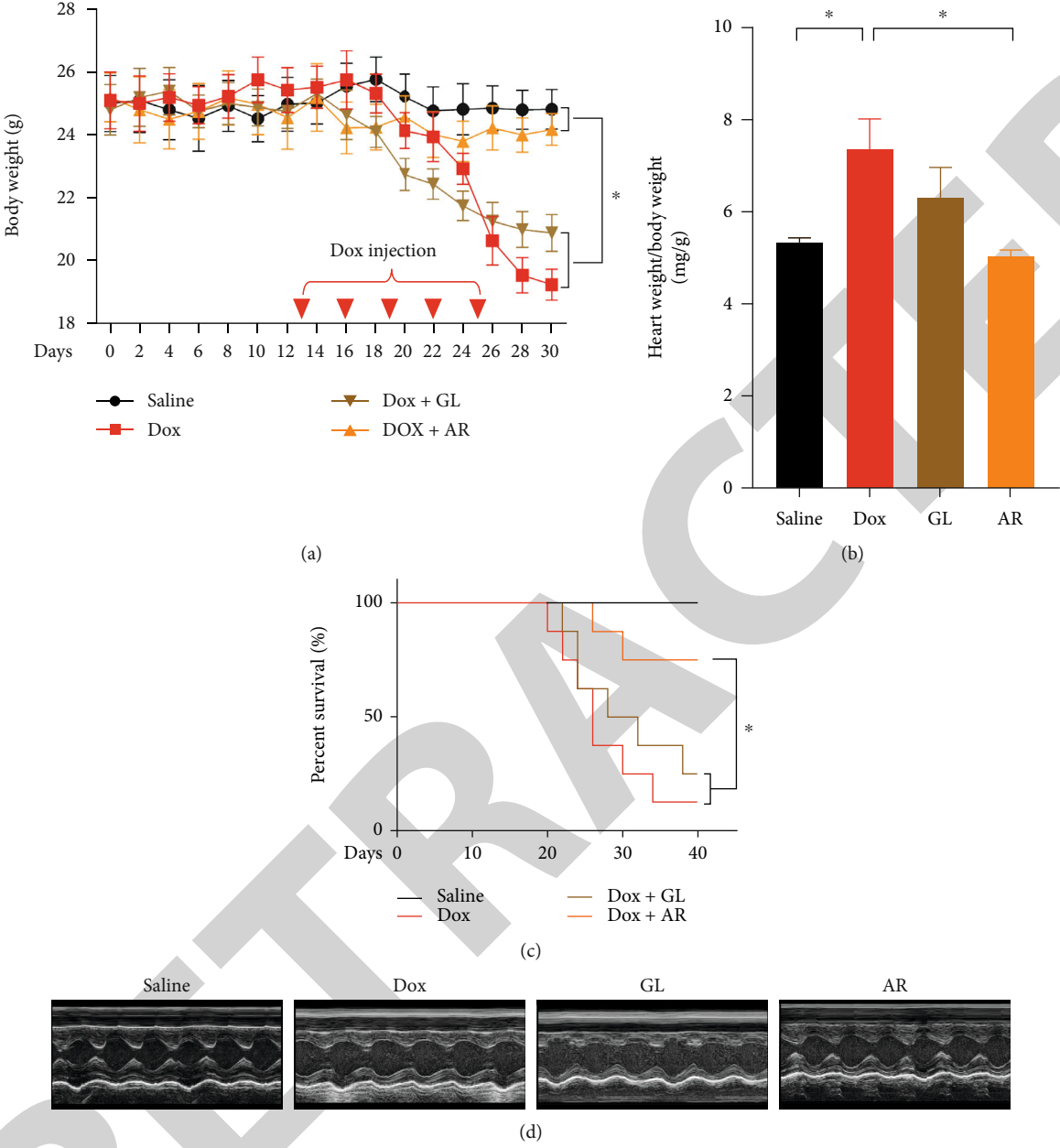


FIGURE 7: Continued.

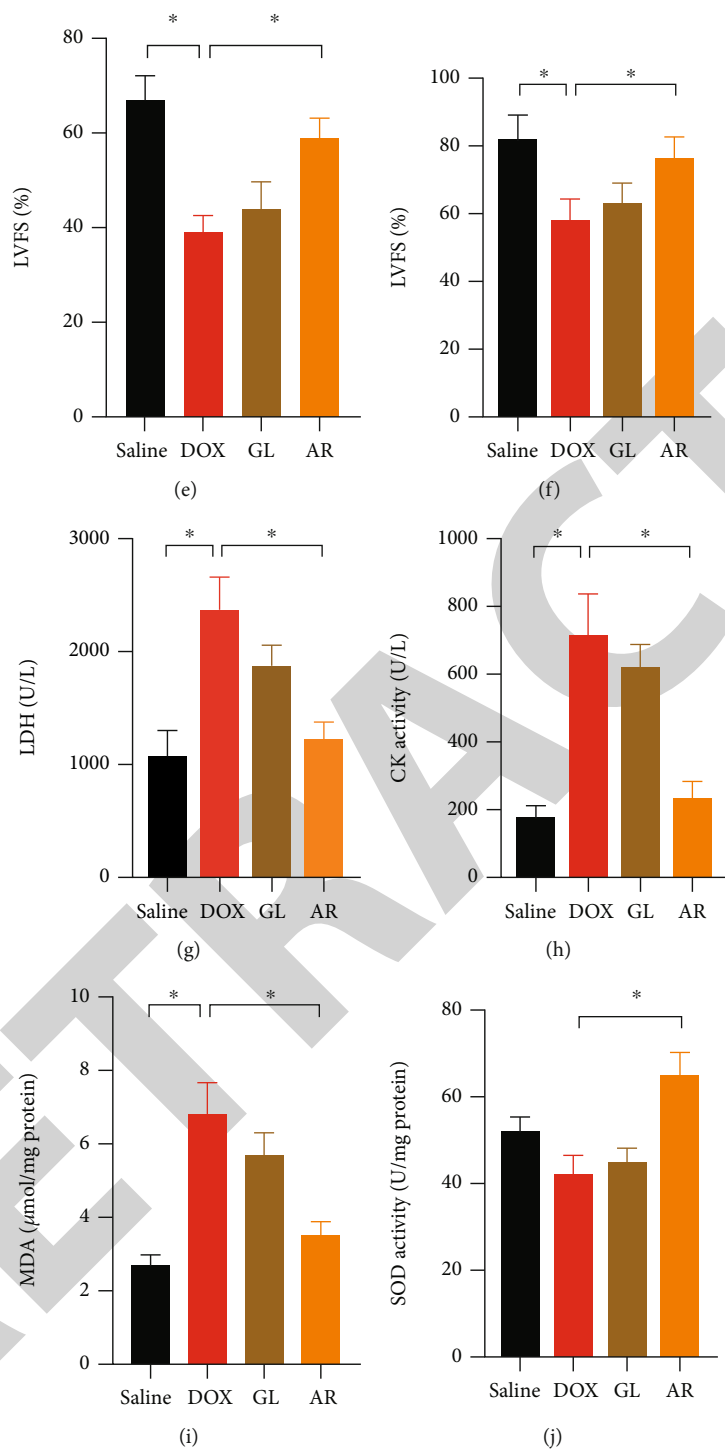


FIGURE 7: Continued.

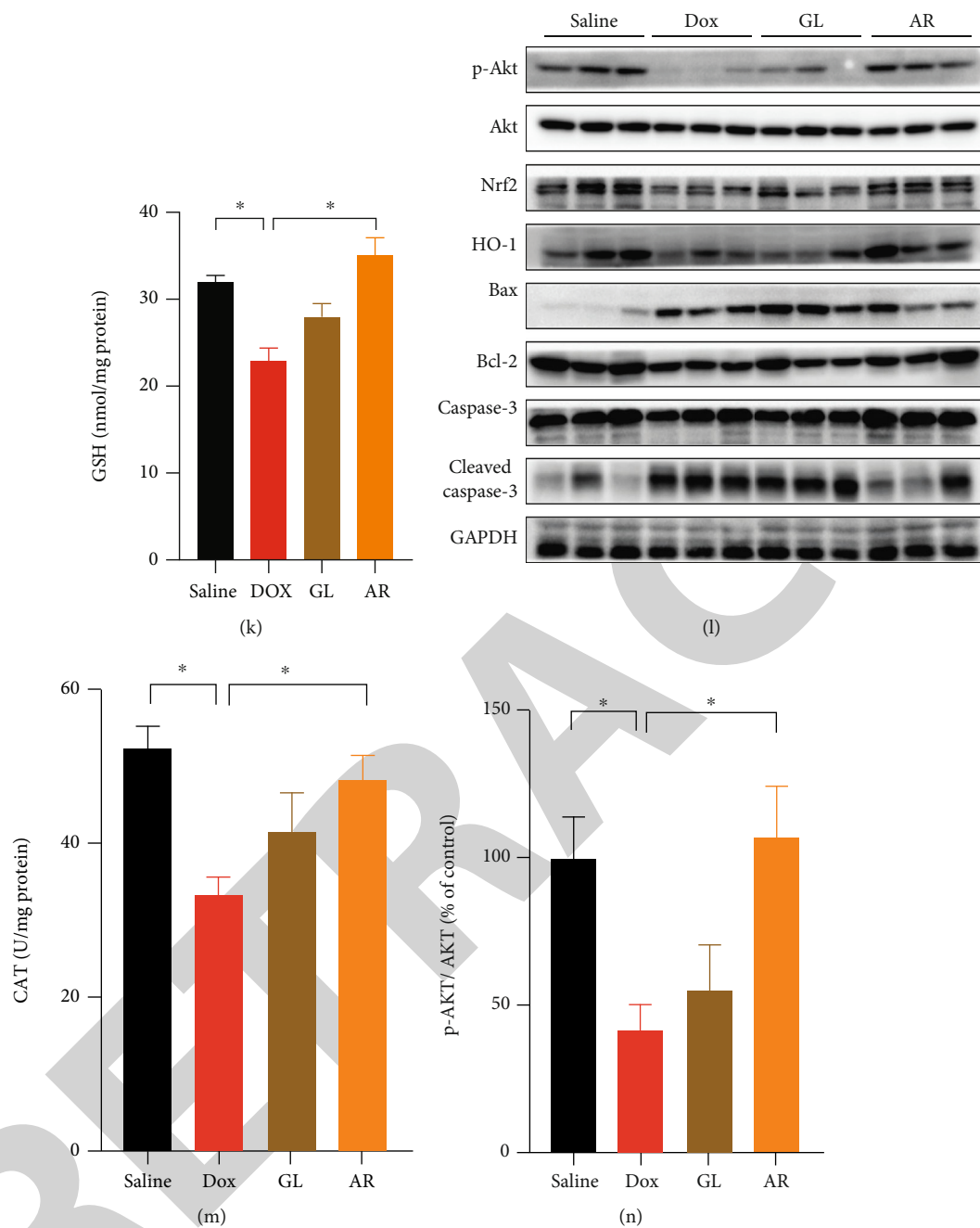


FIGURE 7: Continued.

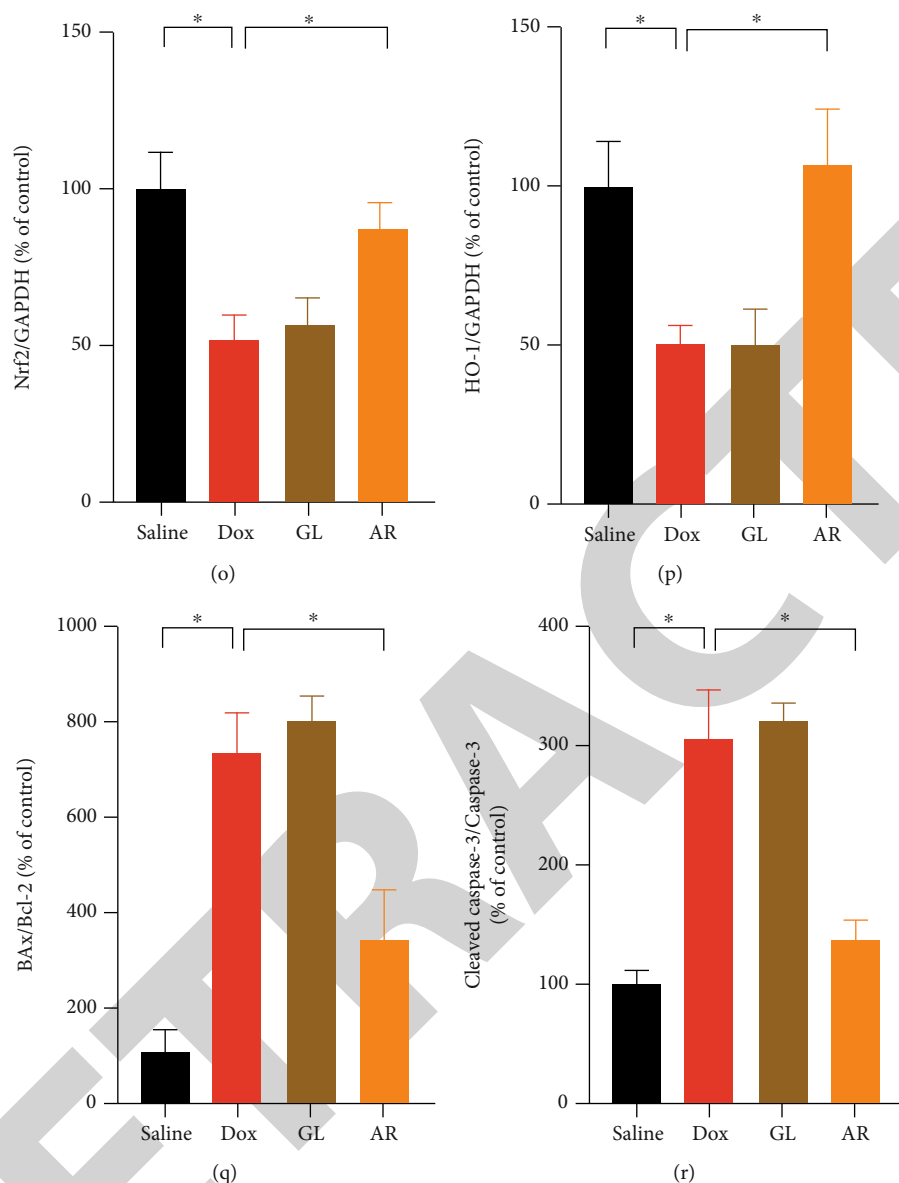


FIGURE 7: Effect of AR and GL extracts on Dox-induced cardiotoxicity in mice. Mice received AR (250 mg/kg) or GL (250 mg/kg) by oral gavage for 28 consecutive days. From day 13, the mice received intraperitoneal injection of Dox (5 mg/kg) every 3 days until a cumulative 25-mg/kg dose of Dox was reached that induced cardiotoxicity. Mice receiving vehicle (instead of AR or GL extract) and saline (instead of Dox) served as the control group. (a) Body weight was monitored every other day during the experimental period. (b) The ratio of heart weight to body weight was determined at the end of the experiment. (c) Kaplan-Meier survival curves for each group ($n = 8$) were monitored during the experiment. Statistical differences ($p < 0.01$) were calculated using the log-rank test. (d) Cardiac function in mice was evaluated as shown by echocardiography. Quantitative analysis of (e) left ventricular fractional shortening (LVFS) and (f) left ventricular ejection fraction (LVEF). (g) LDH and (h) CK activity in mouse serum was measured and quantified. (i) MDA, (j) SOD, (k) GSH, and (m) CAT levels in heart tissues were quantified. (l) Expression levels of p-Akt, Akt, total Nrf2, HO-1, Bax, Bcl-2, caspase-3, cleaved caspase-3, and GAPDH (as internal reference) in heart tissues were detected using western blot analysis. Quantitative analysis of the ratio of protein expression of (n) p-Akt/Akt, (o) Nrf2/GAPDH, (p) HO-1/GAPDH, (q) Bax/Bcl-2, and (r) cleaved caspase 3/caspase-3. Data are presented as percentage of control group values (mean \pm SD of three independent experiments). * $p < 0.05$ indicates a statistically significant difference.

syndrome [42]. Hence, dexrazoxane is contraindicated in children in Europe, and the EMA recommends that the use of dexrazoxane should be restricted in adult patients with advanced or metastatic breast cancer with a high risk of heart failure due to previous receipt of a high cumulative dose of Dox.

Discovery and development of novel drugs that can prevent Dox-induced cardiotoxicity will be of great value in clinical practice. Accumulating evidence has suggested that some natural products, including resveratrol [43], epigallocatechin-3-gallate [44], tanshinone IIA [45], and cardamonin [46], exhibit a remarkable ability to reduce Dox-

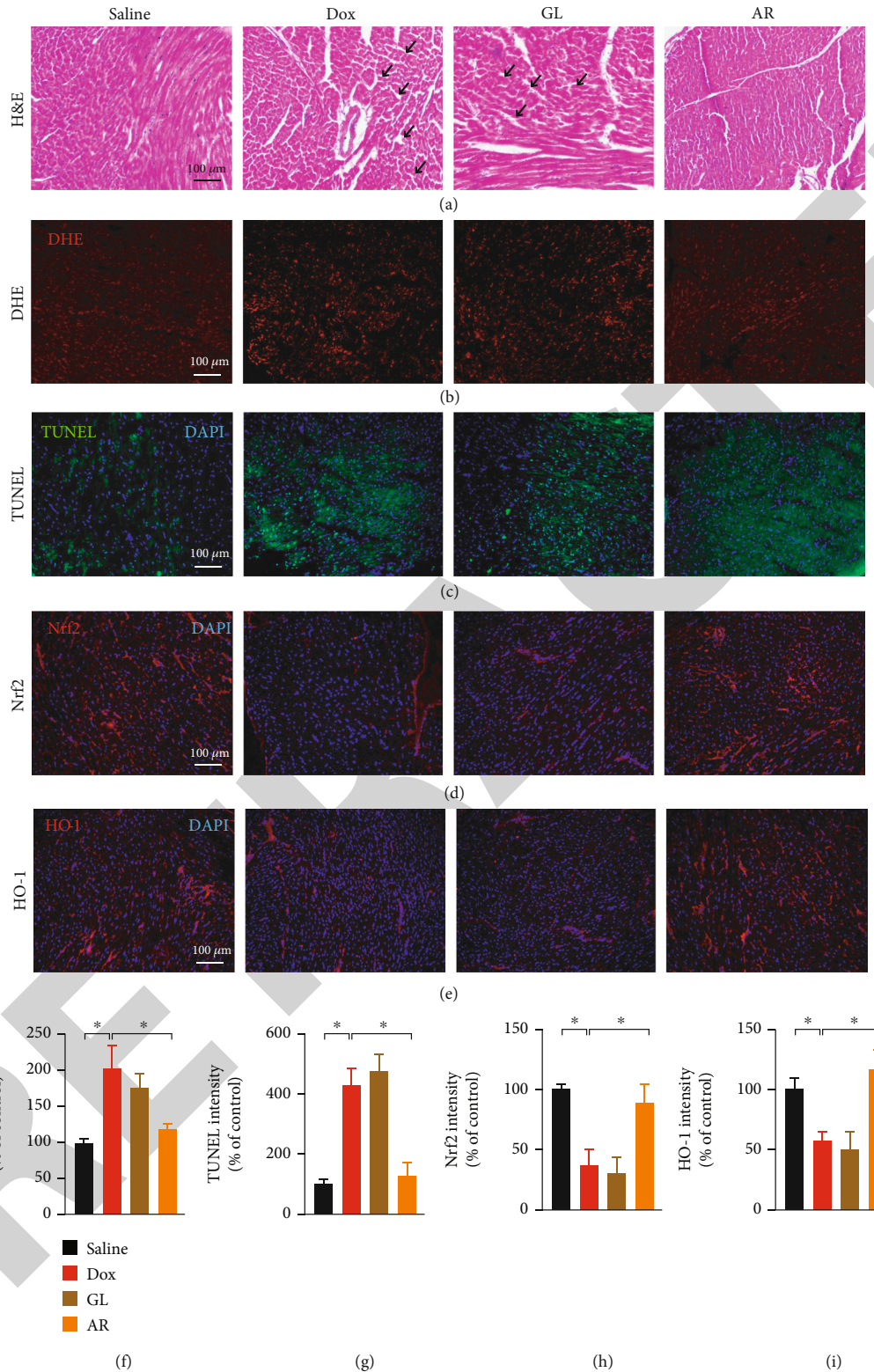


FIGURE 8: Histological analysis of heart tissues in the mouse model. Heart tissue samples ($n = 8$) were fixed with 4% (v/v) formaldehyde and cut into $6 \mu\text{m}$ sections. (a) Sections were stained with hematoxylin and eosin to evaluate tissue architecture. Black arrows indicate lesions in the heart tissues. Sections were also stained with (b) DHE and (c) TUNEL to investigate ROS accumulation and apoptosis in heart cells, respectively. Sections were labeled with (d) anti-Nrf2 and (e) anti-HO-1 antibodies to evaluate oxidative stress in heart tissues. Red and green signals represent positive signals. Blue signals indicate cell nuclei inside the heart tissues. Scale bar: $100 \mu\text{m}$. Quantitative analysis of (f) DHE, (g) TUNEL, (h) Nrf2, and (i) HO-1 signals in heart tissues. Data are presented as the percentage of control (saline) group (mean \pm SD of three independent experiments). * $p < 0.05$ indicates a statistically significant difference.

induced cardiotoxicity. In addition, herbal extracts, including GL [17], *Ginkgo biloba* [47], and *Glycyrrhiza uralensis* [48], have also been demonstrated to possess significant cardioprotective effects against Dox-induced toxicity *in vitro* and *in vivo*. The present study demonstrated that AR extract not only enhanced the anticancer effects of Dox in breast cancer cells but also showed remarkable cardioprotective effects against Dox-induced cardiotoxicity. Therefore, further study on the potential application of AR or its active ingredients in chemotherapy is of great value.

5. Conclusions

In conclusion, the present study demonstrated that AR extract potentiated the cancer effect of Dox and was also a promising protective agent against Dox-induced cardiotoxicity by reducing oxidative stress, mitochondrial dysfunction, and cell apoptosis. The underlying mechanisms for this effect may involve the rescue of the Akt/mTOR and Nrf2/HO-1 signaling pathways. The cardioprotective activity of the AR extract was greater than that of the GL extract, and this was likely due to its higher polysaccharide, triterpene, polyphenol, ganoderic acid G, and ergosterol content. These findings provided valuable information for the future development of AR extracts and their active ingredients for use as a potential adjunct for Dox-based chemotherapy.

Data Availability

The data that support the findings of this study are available from the corresponding author, George Pak-Heng Leung, upon reasonable request.

Conflicts of Interest

The authors declare no conflict of interest.

Authors' Contributions

G.L. and T.C. contributed to the conceptualization. X.W., S.W.L. and S.M.L. C.Z., C.F., and J.Z. contributed to the methodology. J.L., Y.C., and R.L. contributed to the formal analysis. J.L., Y.C., and R.L. contributed to the investigation. T.C. contributed to the resources. J.L., Y.C. R.L. C.W.Z., P.S., J.C. P.R., and C.L. contributed to the data curation. J.L. contributed to the writing (original draft preparation). G.L. contributed to the writing (review and editing). G.L. contributed to the supervision. G.L. contributed to the project administration. G.L. contributed to the funding acquisition. J.L., Y.C., and R.L. contributed equally to the article. Jingjing Li, Yanfen Cheng, and Renkai Li contributed equally to this work.

Acknowledgments

This research work is supported by the Partnership Research Programme of the Innovation and Technology Fund (project no.: PRP/100/20FX).

Supplementary Materials

Figure S1: HPLC chromatograms of major components in AR and GL extract. (a) Mixed reference substances. (b) AR extract sample. (c) GL extract sample. Peak 1: ganoderic acid G; peak 2: ganoderic acid A; peak 3: lucidenic acid A; peak 4: ergosterol. (*Supplementary Materials*)

References

- [1] J. Zhang, J. Li, Z. Shi et al., "pH-sensitive polymeric nanoparticles for co-delivery of doxorubicin and curcumin to treat cancer via enhanced pro-apoptotic and anti-angiogenic activities," *Acta Biomaterialia*, vol. 58, pp. 349–364, 2017.
- [2] J. V. McGowan, R. Chung, A. Maulik, I. Piotrowska, J. M. Walker, and D. M. Yellon, "Anthracycline chemotherapy and cardiotoxicity," *Cardiovascular Drugs and Therapy*, vol. 31, no. 1, pp. 63–75, 2017.
- [3] N. Wenningmann, M. Knapp, A. Ande, T. R. Vaidya, and S. Ait-Oudhia, "Insights into doxorubicin-induced cardiotoxicity: molecular mechanisms, preventive strategies, and early monitoring," *Molecular Pharmacology*, vol. 96, no. 2, pp. 219–232, 2019.
- [4] L. Zhao and B. Zhang, "Doxorubicin induces cardiotoxicity through upregulation of death receptors mediated apoptosis in cardiomyocytes," *Scientific Reports*, vol. 7, no. 1, article 44735, 2017.
- [5] S. Zhang, X. Liu, T. Bawa-Khalfe et al., "Identification of the molecular basis of doxorubicin-induced cardiotoxicity," *Nature Medicine*, vol. 18, no. 11, pp. 1639–1642, 2012.
- [6] S. Y. Kim, S. J. Kim, B. J. Kim et al., "Doxorubicin-induced reactive oxygen species generation and intracellular Ca²⁺ increase are reciprocally modulated in rat cardiomyocytes," *Experimental & Molecular Medicine*, vol. 38, no. 5, pp. 535–545, 2006.
- [7] C. Pereira, G. M. Silva, A. V. Diogo, C. S. Carvalho, F. Monteiro, and J. Oliveira, "Drug-induced cardiac mitochondrial toxicity and protection: from doxorubicin to carvedilol," *Current Pharmaceutical Design*, vol. 17, no. 20, pp. 2113–2129, 2011.
- [8] J. Gutiérrez-Cuevas, M. Galicia-Moreno, H. C. Monroy-Ramírez et al., "The role of NRF2 in obesity-associated cardiovascular risk factors," *Antioxidants*, vol. 11, no. 2, article 235, 2022.
- [9] A. Loboda, M. Damulewicz, E. Pyza, A. Jozkowicz, and J. Dulak, "Role of Nrf2/HO-1 system in development, oxidative stress response and diseases: an evolutionarily conserved mechanism," *Cellular and Molecular Life Sciences*, vol. 73, no. 17, pp. 3221–3247, 2016.
- [10] M. Songbo, H. Lang, C. Xinyong, X. Bin, Z. Ping, and S. Liang, "Oxidative stress injury in doxorubicin-induced cardiotoxicity," *Toxicology Letters*, vol. 307, pp. 41–48, 2019.
- [11] K. K. S. Nordgren and K. B. Wallace, "Disruption of the Keap1/Nrf2-antioxidant response system after chronic doxorubicin exposure *in vivo*," *Cardiovascular Toxicology*, vol. 20, no. 6, pp. 557–570, 2020.
- [12] S. Li, W. Wang, T. Niu et al., "Nrf2 deficiency exaggerates doxorubicin-induced cardiotoxicity and cardiac dysfunction," *Oxidative Medicine and Cellular Longevity*, vol. 2014, Article ID 748524, 15 pages, 2014.

- [13] J. Li, Y. Wu, D. Wang et al., "Oridonin synergistically enhances the anti-tumor efficacy of doxorubicin against aggressive breast cancer via pro-apoptotic and anti-angiogenic effects," *Pharmacological Research*, vol. 146, article 104313, 2019.
- [14] J. Shi, J. Li, J. Li et al., "Synergistic breast cancer suppression efficacy of doxorubicin by combination with glycyrrhetic acid as an angiogenesis inhibitor," *Phytomedicine*, vol. 81, article 153408, 2021.
- [15] J. Li, F. Tang, R. Li et al., "Dietary compound glycyrrhetic acid suppresses tumor angiogenesis and growth by modulating antiangiogenic and proapoptotic pathways *in vitro* and *in vivo*," *The Journal of Nutritional Biochemistry*, vol. 77, article 108268, 2020.
- [16] R. K. Veena, T. A. Ajith, and K. K. Janardhanan, "Lingzhi or Reishi medicinal mushroom, *Ganoderma lucidum* (Agaricomycetes), prevents doxorubicin-induced cardiotoxicity in rats," *International Journal of Medicinal Mushrooms*, vol. 20, no. 8, pp. 761–774, 2018.
- [17] F. Xu, X. Li, X. Xiao et al., "Effects of *Ganoderma lucidum* polysaccharides against doxorubicin-induced cardiotoxicity," *Biomedicine & Pharmacotherapy*, vol. 95, pp. 504–512, 2017.
- [18] J. Li, R. Li, X. Wu et al., "Amauroderma rugosum protects PC12 cells against 6-OHDA-induced neurotoxicity through antioxidant and antiapoptotic effects," *Oxidative Medicine and Cellular Longevity*, vol. 2021, Article ID 6683270, 15 pages, 2021.
- [19] W. Lin, Y. Shi, G. Jia, H. Sun, T. Sun, and D. Hou, "Genome sequencing and annotation and phylogenomic analysis of the medicinal mushroom *Amauroderma rugosum*, a traditional medicinal species in the family Ganodermataceae," *Mycologia*, vol. 113, no. 2, pp. 268–277, 2021.
- [20] C. Zhang, F. Gao, S. Gan et al., "Chemical characterization and gastroprotective effect of an isolated polysaccharide fraction from *Bletilla striata* against ethanol-induced acute gastric ulcer," *Food and Chemical Toxicology*, vol. 131, article 110539, 2019.
- [21] S. W. Lei, G. Cui, G. P. H. Leung et al., "Icaritin protects against oxidative stress-induced injury in cardiac H9c2 cells via Akt/Nrf2/HO-1 and calcium signalling pathways," *Journal of Functional Foods*, vol. 18, pp. 213–223, 2015.
- [22] J. Li, F. Li, F. Tang et al., "AGS-30, an andrographolide derivative, suppresses tumor angiogenesis and growth *in vitro* and *in vivo*," *Biochemical Pharmacology*, vol. 171, article 113694, 2020.
- [23] N. F. Sangweni, K. Gabuza, B. Huisamen, L. Mabasa, D. van Vuuren, and R. Johnson, "Molecular insights into the pathophysiology of doxorubicin-induced cardiotoxicity: a graphical representation," *Archives of Toxicology*, vol. 96, no. 6, pp. 1541–1550, 2022.
- [24] J. Xian, X. Zhong, H. Gu et al., "Colonic delivery of celastrol-loaded layer-by-layer liposomes with pectin/trimethylated chitosan coating to enhance its anti-ulcerative colitis effects," *Pharmaceutics*, vol. 13, no. 12, p. 2005, 2021.
- [25] X. Wang, H. Gu, H. Zhang et al., "Oral core-shell nanoparticles embedded in hydrogel microspheres for the efficient site-specific delivery of magnolol and enhanced antiulcerative colitis therapy," *ACS Applied Materials & Interfaces*, vol. 13, no. 29, pp. 33948–33961, 2021.
- [26] J. Yu, C. Wang, Q. Kong, X. Wu, J. J. Lu, and X. Chen, "Recent progress in doxorubicin-induced cardiotoxicity and protective potential of natural products," *Phytomedicine*, vol. 40, pp. 125–139, 2018.
- [27] P. M. Chan, Y. S. Tan, K. H. Chua, V. Sabaratnam, and U. R. Kuppasamy, "Attenuation of inflammatory mediators (TNF-alpha and nitric oxide) and up-regulation of IL-10 by wild and domesticated *Basidiocarps* of *Amauroderma rugosum* (Blume & T. Nees) torrend in LPS-stimulated RAW264.7 cells," *PLoS One*, vol. 10, no. 10, article e0139593, 2015.
- [28] P. M. Chan, G. Kanagasabapathy, Y. S. Tan, V. Sabaratnam, and U. R. Kuppasamy, "Amauroderma rugosum (Blume & T. Nees) Torrend: nutritional composition and antioxidant and potential anti-inflammatory properties," *Evidence-based Complementary and Alternative Medicine*, vol. 2013, Article ID 304713, 10 pages, 2013.
- [29] C. K. Seng, N. Abdullah, and N. Aminudin, "Antioxidative and inhibitory effects of the fruiting body of black Lingzhi mushroom, *Amauroderma rugosum* (Agaricomycetes), on LDL oxidation and HMG-CoA reductase activity," *International Journal of Medicinal Mushrooms*, vol. 19, no. 9, pp. 797–807, 2017.
- [30] Y. Mai, S. Xu, R. Shen, B. Feng, H. He, and Y. Xu, "Gastroprotective effects of water extract of domesticated *Amauroderma rugosum* against several gastric ulcer models in rats," *Pharmaceutical Biology*, vol. 60, no. 1, pp. 600–608, 2022.
- [31] Z. Q. Lin, P. Zhou, A. von Gise et al., "Pi3kcb links hippo-YAP and PI3K-AKT signaling pathways to promote cardiomyocyte proliferation and survival," *Circulation Research*, vol. 116, no. 1, pp. 35–45, 2015.
- [32] X. He, H. Kan, L. Cai, and Q. Ma, "Nrf2 is critical in defense against high glucose-induced oxidative damage in cardiomyocytes," *Journal of Molecular and Cellular Cardiology*, vol. 46, no. 1, pp. 47–58, 2009.
- [33] T. Matsui, T. Nagoshi, and A. Rosenzweig, "Akt and PI 3-kinase signaling in cardiomyocyte hypertrophy and survival," *Cell Cycle*, vol. 2, no. 3, pp. 219–222, 2003.
- [34] C. Y. Tsai, C. C. Wang, T. Y. Lai et al., "Antioxidant effects of diallyl trisulfide on high glucose-induced apoptosis are mediated by the PI3K/Akt-dependent activation of Nrf2 in cardiomyocytes," *International Journal of Cardiology*, vol. 168, no. 2, pp. 1286–1297, 2013.
- [35] X. Zhang, C. Hu, C. Y. Kong et al., "FNDC5 alleviates oxidative stress and cardiomyocyte apoptosis in doxorubicin-induced cardiotoxicity via activating AKT," *Cell Death and Differentiation*, vol. 27, no. 2, pp. 540–555, 2020.
- [36] R. Ahmad, M. Riaz, A. Khan et al., "Ganoderma lucidum (Reishi) an edible mushroom; a comprehensive and critical review of its nutritional, cosmeceutical, mycochemical, pharmacological, clinical, and toxicological properties," *Phytotherapy Research*, vol. 35, no. 11, pp. 6030–6062, 2021.
- [37] Y. He, Z. Chen, X. Nie et al., "Recent advances in polysaccharides from edible and medicinal *Polygonati rhizoma*: from bench to market," *International Journal of Biological Macromolecules*, vol. 195, pp. 102–116, 2022.
- [38] D. Sohretoglu and S. Huang, "Ganoderma lucidum Polysaccharides as an anti-cancer agent," *Anti-Cancer Agents in Medicinal Chemistry*, vol. 18, no. 5, pp. 667–674, 2018.
- [39] M. Marty, M. Espié, A. Llombart et al., "Multicenter randomized phase III study of the cardioprotective effect of dexrazoxane (Cardioxane®) in advanced/metastatic breast cancer patients treated with anthracycline-based chemotherapy," *Annals of Oncology*, vol. 17, no. 4, pp. 614–622, 2006.
- [40] S. Ganatra, A. Nohria, S. Shah et al., "Upfront dexrazoxane for the reduction of anthracycline-induced cardiotoxicity in adults

Retraction

Retracted: Mild Hypothermia Promotes Ischemic Tolerance and Survival of Neural Stem Cell Grafts by Enhancing Global SUMOylation

Oxidative Medicine and Cellular Longevity

Received 26 December 2023; Accepted 26 December 2023; Published 29 December 2023

Copyright © 2023 Oxidative Medicine and Cellular Longevity. This is an open access article distributed under the Creative Commons Attribution License, which permits unrestricted use, distribution, and reproduction in any medium, provided the original work is properly cited.

This article has been retracted by Hindawi, as publisher, following an investigation undertaken by the publisher [1]. This investigation has uncovered evidence of systematic manipulation of the publication and peer-review process. We cannot, therefore, vouch for the reliability or integrity of this article.

Please note that this notice is intended solely to alert readers that the peer-review process of this article has been compromised.

Wiley and Hindawi regret that the usual quality checks did not identify these issues before publication and have since put additional measures in place to safeguard research integrity.

We wish to credit our Research Integrity and Research Publishing teams and anonymous and named external researchers and research integrity experts for contributing to this investigation.

The corresponding author, as the representative of all authors, has been given the opportunity to register their agreement or disagreement to this retraction. We have kept a record of any response received.

References

- [1] H. Cai, X. Ma, D. Lu et al., “Mild Hypothermia Promotes Ischemic Tolerance and Survival of Neural Stem Cell Grafts by Enhancing Global SUMOylation,” *Oxidative Medicine and Cellular Longevity*, vol. 2022, Article ID 6503504, 13 pages, 2022.

Research Article

Mild Hypothermia Promotes Ischemic Tolerance and Survival of Neural Stem Cell Grafts by Enhancing Global SUMOylation

Heng Cai,^{1,2,3} Xiaofang Ma,^{4,5} Dading Lu,^{1,2,3} Liangyu Chen,^{1,2,3} Xiyun Bian,^{4,5}
Nan Zhang,^{1,2,3} Wei Tang,^{1,2,3} Xiaozhi Liu,^{4,5} and Zhiqing Li^{1,2,3} 

¹Department of Neurosurgery, Shengjing Hospital of China Medical University, Shenyang 110004, China

²Liaoning Clinical Medical Research Center in Nervous System Disease, Shenyang 110004, China

³Key Laboratory of Neuro-oncology in Liaoning Province, Shenyang 110004, China

⁴Central Laboratory, The Fifth Central Hospital of Tianjin, Tianjin 300450, China

⁵Tianjin Key Laboratory of Epigenetics for Organ Development of Preterm Infants, The Fifth Central Hospital of Tianjin, Tianjin 300450, China

Correspondence should be addressed to Zhiqing Li; dr_lizhiqing@163.com

Received 2 March 2022; Revised 7 April 2022; Accepted 18 April 2022; Published 27 May 2022

Academic Editor: Shao Liang

Copyright © 2022 Heng Cai et al. This is an open access article distributed under the Creative Commons Attribution License, which permits unrestricted use, distribution, and reproduction in any medium, provided the original work is properly cited.

Cerebral infarct penumbra due to hypoxia and toxin accumulation is not conducive to the transplantation of neural stem cells (NSCs), although mild hypothermia can improve the local microenvironment of the ischemic penumbra and exert neuroprotective effects. However, insufficient understanding of the molecular mechanism by which mild hypothermia protects the brain limits widespread clinical application. This study evaluated the molecular mechanism of mild hypothermia-induced brain protection from the perspective of global protein small ubiquitin-like modifier (SUMO) modification, with the aim of improving NSC transplant survival rates in the penumbra to enhance neurological function. NSCs from neonatal rats were extracted to detect the effects of hypoxia and mild hypothermia on SUMOylation modification levels, cell stemness, and hypoxia-induced injury. Overexpression and knockdown of UBC9 in NSCs were used to evaluate their ability to maintain stemness and withstand hypoxic injury. Finally, a rat middle cerebral artery occlusion (MCAO) model was used to verify the effect of mild hypothermia treatment and UBC9 overexpression on neural function of NSCs following penumbra transplantation in rats. Results showed that hypoxia and mild hypothermia promoted both the SUMOylation modification and maintenance of NSC stemness. Overexpression of UBC9 enhanced the abilities of NSCs to maintain stemness and resist hypoxic injury, while UBC9 knockdown had the opposite effect. Following transplantation into the ischemic penumbra of MCAO model rats, mild hypothermia and *Ubc9*-overexpressing NSCs significantly reduced cerebral infarct areas and improved neurological function. In conclusion, this study demonstrated that global protein SUMOylation is an important molecular mechanism for NSCs to tolerate hypoxia, and mild hypothermia can further increase the degree of global SUMOylation to enhance the hypoxia tolerance of NSCs, which increases their survival during transplantation in situ and ability to perform nerve repair in the penumbra of cerebral infarction.

1. Introduction

China ranks first in the world for the number of people experiencing stroke and, with the advent of an aging population, this trend is increasing annually [1–3]. According to reports, the prevalence of ischemic stroke in China was 1981 per 100,000 in 2017, with a mortality rate of 149 per

100,000 [2], thus imposing a heavy burden on families and society. Current treatment measures for cerebral infarction involve basic support and monitoring, dehydration to reduce intracranial pressure, anticoagulation, scavenging of free radicals, and nourishing nerves in an attempt to prevent complications and reduce mortality [4, 5]; however, the efficacy of all these methods remains uncertain. Therefore, in

clinical practice, the implementation of an effective treatment plan is particularly important for improving the survival of patients and their quality of life.

In recent years, NSCs have yielded high hopes for the treatment of stroke, especially ischemic cerebrovascular disease [6]. Theoretically, NSCs transplanted into the penumbra at the edge of cerebral infarction will proliferate for a few generations and then differentiate to supplement neurons and glial cells, thereby repairing damage and improving nerve function. However, in fact, the penumbra microenvironment exhibits severe hypoxia and accumulation of large amounts of toxic substances that are extremely unfavorable for the local survival of transplanted NSCs, which severely limits their application. Therefore, improving the survival of transplanted NSCs in the penumbra is key for the treatment of ischemic cerebrovascular disease.

Nowadays, the application of mild hypothermia for brain protection has attracted increasing attention and gradually been implemented in clinical practice. A large number of international trials have confirmed the effectiveness and practicability of mild hypothermia in clinical applications, which can reduce the mortality rate and effectively improve the quality-of-life of patients with ischemic cerebrovascular disease [7–9]. However, as most reports only describe the clinical efficacy and methods of mild hypothermia treatment, the exact mechanism of its action has not been clarified. This restricts its wide acceptance by doctors and, to a certain extent, widespread promotion in clinical practice. Therefore, it is necessary to have a deeper and comprehensive understanding of the molecular mechanism by which mild hypothermia protects the brain to help doctors provide more precise treatment plans for patients with cerebral ischemia.

Small ubiquitin-like modifier- (SUMO-) mediated SUMOylation, a form of posttranslational modification of proteins, is used by cells to respond to external stress and adapt to changes in the internal environment [10]. SUMO modification of proteins requires the cascade reaction of SUMO activating enzyme (E1), conjugating enzyme (E2 and UBC9), and ligase enzyme (E3) [11–13]. Neurons can reportedly antagonize the adverse microenvironment of hypoxia by increasing global SUMOylation of a large number of proteins, such as hypoxia-inducible factor 1 α (HIF-1 α), and mild hypothermia can further increase global SUMOylation in neurons [14–16]. Indeed, this enriches the molecular mechanism underlying mild hypothermia-induced brain protection to a certain extent. At present, no reports describe the effects of hypoxia and mild hypothermia on protein SUMOylation in neural stem cells (NSCs). Moreover, it is unknown whether transplantation of NSCs overexpressing SUMO into the edge of a cerebral infarction, with or without mild hypothermia, can increase the survival rate of NSC grafts and improve prognosis.

Therefore, this study investigated the effects of hypoxia and mild hypothermia on global SUMOylation of NSCs, as well as their proliferation, differentiation, and hypoxia tolerance. We also transplanted NSCs overexpressing UBC9 into the cerebral ischemic penumbra of a rat middle cerebral artery occlusion (MCAO) model to evaluate their survival *in vivo*, as well as effects on the neurological functions of

rats. In summary, the results show that mild hypothermia can promote the ischemic tolerance and survival of NSC grafts by enhancing global SUMOylation and improve the neurological function of rats. These conclusions identify a molecular mechanism supporting the brain protection elicited by mild hypothermia and provide a guide for increasing the survival of NSC grafts to improve the prognosis of patients with cerebral infarction.

2. Materials and Methods

The research conforms to NIH (2011) *Guide for the Care and Use of Laboratory Animals* (8th Edition, Institute for Laboratory Animal Research, Division on Earth and Life Studies, National Research Council of the National Academies Press).

2.1. Experimental Rats. Total number of 60 12-week-old male and 5 new-born (within 1 day) female Sprague-Dawley rats were purchased from SPF Biotechnology Co., Ltd. (Beijing, China). These rats were housed in the Animal Experimental Center of the Fifth Central Hospital of Tianjin (Tianjin, China) with 50% \pm 5% humidity and 20–25°C ambient.

2.2. NSC Culture and Treatment. Rat NSCs were isolated and extracted from the hippocampus of new-born rats (within 1 day) under sterile conditions, digested with 0.05% trypsin for 15 minutes, and carefully pipetted with a dropper to form a single cell suspension at 1000 r/min. Trypsin was removed after centrifugation for 5 min. Neural stem cells were cultured in rat neural stem cell culture medium (Cytogen Biosciences, Suzhou, China). After 5–7 days of culture, the neurospheres were dissociated into single cell suspensions by mechanical separation for subculture, and the cells were seeded at a density of 2×10^5 cells/. Cells of neurospheres were confirmed to be NSCs and propagated for 2 passages to obtain enough NSCs for experiments. Cultures maintained at 37°C and 5% CO₂ in an incubator were recorded as the control group (Con). Hypoxia was performed by placing NSCs in 1% O₂, 94% N₂, 5% CO₂, balanced nitrogen, and 95% humidity for 12 h (designated as H 12 h). For the mild hypothermia group, incubators were set at 33°C (designated as 33°C). All the experiments were carried out after a subsequent 48 h of culture under normal conditions.

2.3. Small Interfering RNA and Gene Transfection. For UBC9 knockdown, UBC9 siRNA (sc-36774) and nonsilencing control siRNA were purchased from Santa Cruz Biotechnology (Dallas, TX, USA, designated as siUBC9 and Con groups). Rat UBC9 cDNA was subcloned into the mammalian expression plasmid pcDNA3.1 (Life Technologies, Waltham, MA, USA), which containing a FLAG tag at the C-terminus (designated as UBC9 or NSC UBC9). siRNA and plasmids were electroporated into NSCs with a Nucleofector instrument (Lonza, Basel, Switzerland). UBC9-transfected NSCs were screened with neomycin (Sigma St. Louis, MO, USA).

2.4. Lactate Dehydrogenase (LDH) Detection, Flow Cytometry, and ECAR Detection. NSCs were collected by centrifugation of $100 \times g$ for 5 min. LDH content in conditioned medium was detected using enzyme-linked immunosorbent assay (ELISA), based on the LDH Activity Assay Kit (Yuanmu Biotechnology Co., Ltd., Shanghai, China) and tested according to the product instructions. The percentage of apoptotic NSCs was determined by flow cytometry assay. After treatments, NSCs were harvested, washed, and then stained with fluorescein isothiocyanate- (FITC-) labeled annexin V and propidium iodide (PI) (Beyotime Biotechnology, Shanghai, China) in dark place for 5 min. After washing for 3 times with phosphate-buffered saline (PBS), percentages of apoptotic were quantified by flow cytometry (NovoCyte D2040R; Hangzhou, China). In addition, the extracellular acidification rates (ECAR) were detected using a Seahorse XF 96 Extracellular Flux Analyzer (Agilent Technologies, Santa Clara, CA, USA) according to instrument description.

2.5. Western Blot Analysis Assay. After extraction of protein from NSCs, the protein concentrations were determined by bicinchoninic acid assay (Thermo Fisher Scientific, Waltham, MA). Twenty micrograms protein of each sample in an equal volume was electrophoresed on 10%–12% polyacrylamide gels, before transfer onto a polyvinylidene fluoride membrane. After blocking the membrane in skim milk for 1 h, antibodies against SUMO1 (ab133352, 1:1000; Abcam, Cambridge, UK), SUMO2/3 (ab3742, 1:1000), UBC9 (ab75854, 1:1000), Oct4 (ab181557, 1:1000), SOX2 (ab92494, 1:1000), caspase-3 (ab184787, 1:1000), and glyceraldehyde-3-phosphate dehydrogenase (GAPDH; ab9485, 1:1000) were incubated overnight at 4°C. Then, the membranes were washed five times with TBST, followed by incubation with horseradish peroxidase-conjugated goat anti-rabbit IgG (111-035-003; 1:2,000; Jackson Immuno Research Laboratories, Inc., West Grove, PA, USA) antibody for 1 h at room temperature. GAPDH was used as internal control. Finally, membranes were exposed using ECL Plus substrate (Thermo Fisher Scientific, Waltham, MA). Data were evaluated by image analysis software (ImageJ version 1.48; National Institutes of Health, Bethesda, MD, USA).

2.6. Cell and Tissue Immunofluorescence. NSCs were mechanically dispersed and seeded on poly-L-lysine-coated coverslips in a 48-well cell culture plate. After being exposed to 4% paraformaldehyde for 15 min, NSCs were permeabilized with 0.2% Triton X-100 for 20 min and blocked with PBS containing 5% goat serum for another 30 min. Coverslips were incubated with antibodies against nestin (ab237036, 1:500) or Neuron-Specific Enolase (NSE; ab79757, 1:500) and Glial Fibrillary Acidic Protein (GFAP; ab279290, 1:500) overnight at 4°C. After washing for 4 times, mixtures of goat anti-mouse IgG H&L (AlexaFluor®488, ab150113, 1:200, Abcam) or goat anti-rabbit IgG H&L (AlexaFluor®594, ab150080, 1:200, Abcam) were dropped onto the coverslips. At last, nuclei were stained with 4',6-diamidino-2-phenylindole (DAPI; Zhongshanjinqiao, Beijing, China) for 10 min. Images were acquired by a fluorescence microscope (Carl Zeiss, Ober-

kochen, Germany). For paraffin sections of rat brain tissues, the fixation, dehydration, embedding, sectioning, and dewaxing steps were added.

2.7. Establishment of Rat MCAO Models. A total number of 60 adult male Sprague-Dawley rats were randomly divided into 5 groups. During the operation, a small-animal ventilator (Shanghai Yuyan Instruments Co., Ltd., Shanghai, China) was used to maintain animals' respiration, and body temperature was monitored by a rectal temperature control. Making a 1 cm longitudinal incision between rat sternum and mandible, then left common carotid artery was isolated, and we found out the external carotid and internal carotid arteries under a stereo microscope (Olympus Corporation, Tokyo, Japan). Next, we ligated the distal heart end of the external carotid artery and the proximal heart end of the carotid artery, and a modified nylon thread (with 0.23 mm head diameter and 0.18 mm trunk diameter) was inserted from the carotid artery to the middle cerebral artery (~12.0 mm deep) and fixed with surgical line.

2.8. Mild Hypothermic Treatment. Rats which underwent surgery without thread insertion were defined as the “sham operation” group. NSCs or UBC9 NSCs were transplanted to the ischemic penumbra after the establishment of MCAO models as reported in literatures [17, 18]. To make mild hypothermia, MCAO rats injected with NSCs were placed on an insulation blanket (Shanghai Yuyan Instruments), and a rectal temperature monitor was to keep body temperature at 32 to 34°C for 12 h. Rats were then removed from blanket and gradually recovered to normal body temperature. After removal, some models' brains were stripped and sliced then incubated in 1% 2,3,5-triphenyl-2H-tetrazolium chloride (TTC, Sigma-Aldrich, St. Louis, MO) for 20 min at 37°C to distinguish the infarct area (white) and the uninfarct area (pink and red). Sections were fixed with 4% paraformaldehyde for 2 h to distinguish stained from unstained areas. The infarcted and uninfarcted areas were analyzed by ImageJ software (National Institutes of Health, Bethesda, MD), and percentages of infarct were calculated as (infarct area)/(area of the whole brain slice) \times 100%. Brain tissues under the same conditions should be collected for paraffin section and immunofluorescence staining assay as described in Section 2.6.

2.9. Neural Function Analysis. Animals recovered from MCAO for 1, 4, 7, 14, 21, or 28 days before assess neurological functions by modified Neurological Severity Scores (mNSS) [19, 20]. The mNSS consisted of balance, movement, sensory function, and reflex tests with a score ranging from 0 to 18 (normal score: 0; maximum defect score: 18). In addition, rotarod testing was performed to evaluate of rat neurological deficits (Zhishuduobao Biotechnology Co., Ltd, Beijing, China). Rats were pretrained for 3 times before MCAO, and the experiment was performed for 7 days after MCAO. The cylinder accelerated from 10 to 40 rpm within 5 min; before rats fell from the rod, the latency to fall was recorded. Mean latency for each rat was calculated from three trials with a 30 min interval between 2 trials.

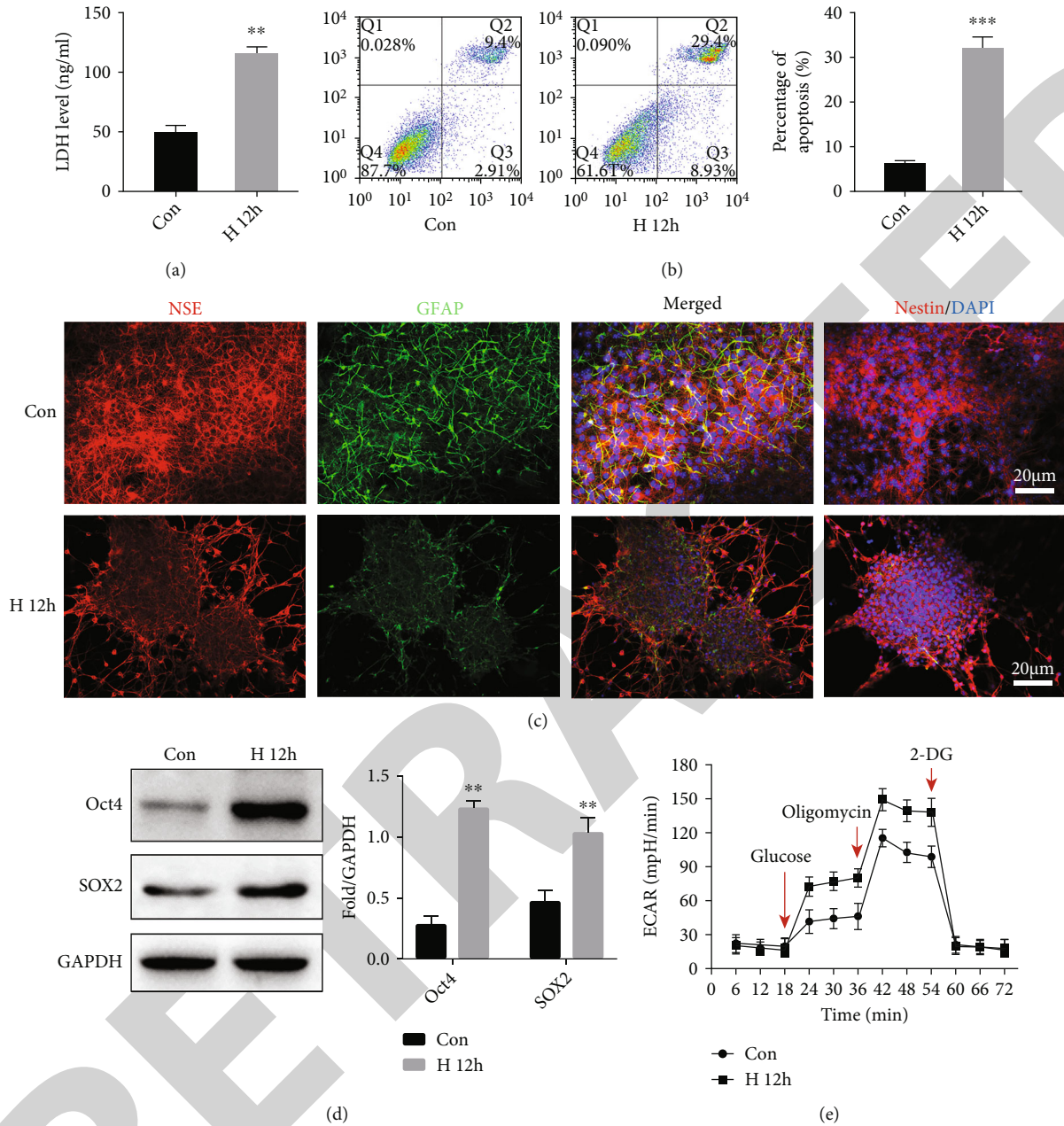


FIGURE 1: Effect of 12 h hypoxia on NSCs. (a) LDH contents of control and hypoxia groups were measured by ELISA. (b) Apoptosis was measured by flow cytometry of the two groups. Data shown indicate mean \pm SD ($n = 4$). (c) Expression of NSE or nestin (red fluorescent signal) and GFAP (green fluorescent signal) in NSCs of the control and hypoxia groups was examined by immunofluorescence; DAPI (blue) was used to stain cell nuclei (scale bar, 20 μ m). (d) Oct4 and SOX2 protein expression was examined by western blotting. GAPDH was used for normalization. Data shown indicate mean \pm SD ($n = 3$). (e) ECAR analysis of the glycolytic capacity of the control and hypoxic NSCs. Data shown indicate mean \pm SD ($n = 5$); ** $P < 0.01$ compared with the control group.

2.10. Rat Behavior Tests. 7 days after MCAO, rats should be tested for behaviors. Spontaneous activity was monitored within 30 min for distance traveled and time spent in corners. Activity was assessed as distance traveled (locomotion), vertical activity (rearing), thigmotaxis, and time spent in corners using behavioral tester (Zhishuduobao Biotechnology Co., Ltd, Beijing, China) equipment. On the 10th day after MCAO, rats were tested for memory and learning abilities in the Morris water maze (Zhishuduobao Biotechnology Co., Ltd, Beijing, China) according to reference [21]. Rats

underwent the visible platform experiment for the first 2 days, the nonvisible platform experiment for the following 3 days, and the probe trial for the last day. Escape latency and swimming paths were measured during the first 5 days. In the probe trial, percentages of time spent in quadrant IV and numbers of platform crossing were recorded.

2.11. Data Statistics and Analysis. Each experiment was performed at least for 3 times. Data are showed as mean \pm standard deviation (SD) and were analyzed using GraphPad

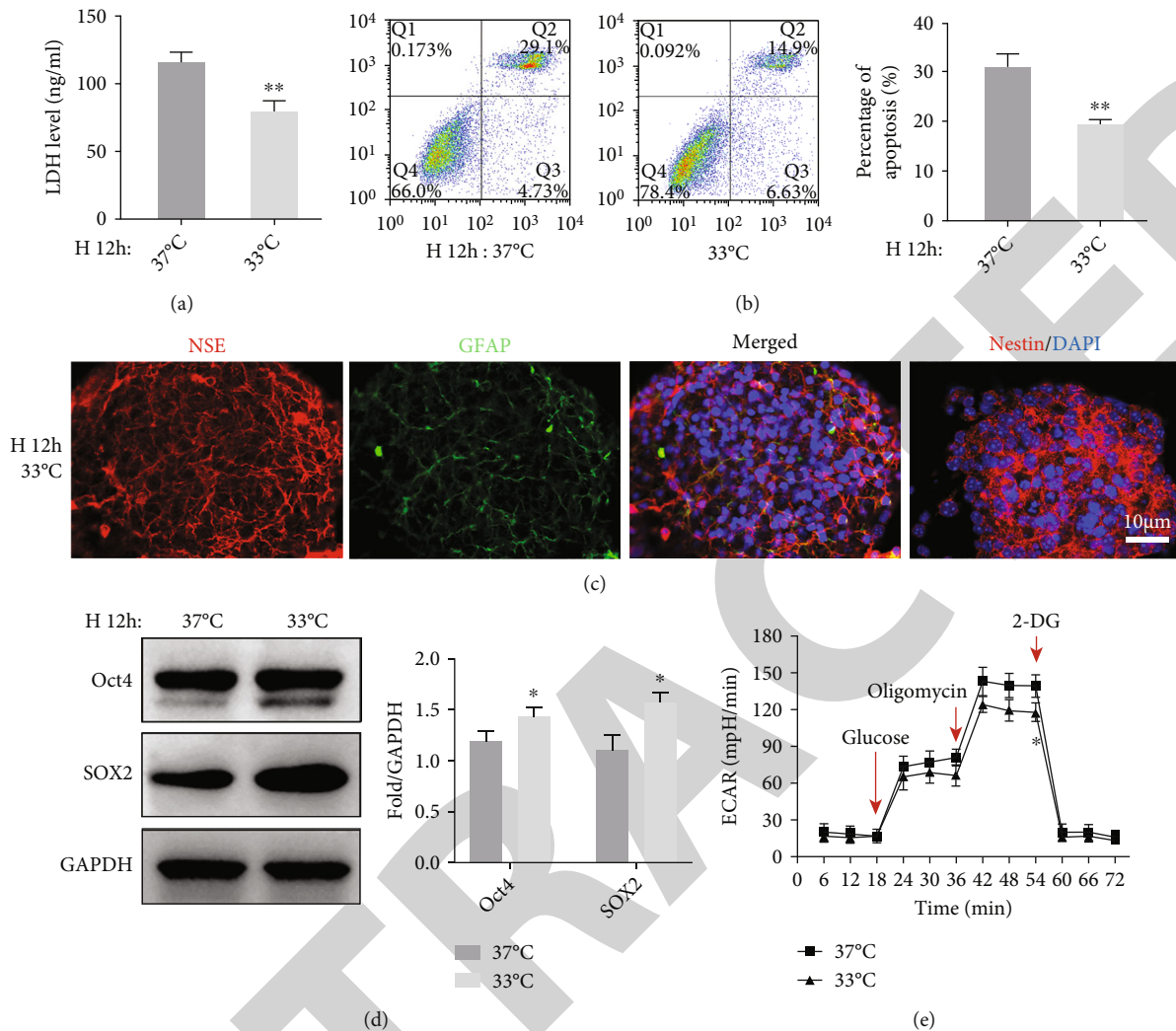


FIGURE 2: Effect of mild hypothermia (33°C) on hypoxic NSCs. (a) LDH contents of the control (37°C) and mild hypothermia groups were measured by ELISA. (b) Apoptosis assays were measured by flow cytometry. Data indicate mean \pm SD ($n = 4$). (c) Expression of NSE or nestin (red fluorescent signal) and GFAP (green fluorescent signal) in the control NSCs or mildly hypothermic and hypoxic NSCs was examined by immunofluorescence; DAPI (blue) was used to stain cell nuclei (scale bar, 10 μ m). (d) Oct4 and SOX2 protein expression was examined by western blotting. Data shown indicate mean \pm SD ($n = 3$). (e) ECAR analysis of the glycolytic capacity of the control NSCs or mildly hypothermic and hypoxic NSCs. Data shown indicate mean \pm SD ($n = 5$); * $P < 0.05$ and ** $P < 0.01$ compared with 37°C group.

Prism 6 software (San Diego, CA). A P value < 0.05 was considered significant difference. One-way ANOVA or the unpaired Student's t test was used to evaluate the significance of differences among treatment groups, as appropriate.

3. Results

3.1. Hypoxia Increased Injury, Inhibited Differentiation, Increased the Stemness Maintenance Potential, and Reduced the Metabolic Capacity of NSCs. After 12 h of hypoxia stimulation, the content of LDH released by NSCs increased significantly, suggesting cell damage (Figure 1(a)). The results showed that the percentage of apoptotic cells reached 30% after hypoxia (Figure 1(b)). Immunofluorescence detection showed that a certain proportion of NSCs spontaneously differentiated under normal conditions. NSE and GFAP were expressed. Nestin, a marker of NSCs, was highly expressed,

and cells showed extensional growth morphology similar to nerve fiber structures. After hypoxia, NSCs exhibited obvious spherical growth, NSE and GFAP expression decreased, and nestin expression significantly increased (Figure 1(c)). Moreover, expression of stem cell markers Oct4 and SOX2 increased significantly (Figure 1(d)). Additionally, we calculated ECAR levels and found that hypoxia could significantly increase the anaerobic hydrolysis level of NSCs (Figure 1(e)).

3.2. Mild Hypothermia Antagonized Hypoxia-Induced Injury, Inhibited Differentiation, and Further Increased the Stemness Potential of NSCs. Mild hypothermia (33°C) significantly inhibited the damage induced by hypoxia at 37°C, significantly decreased the content of LDH, and reeducated the percentage of apoptotic cells to 20% (Figures 2(a) and 2(b)). Immunofluorescence detection showed that mild

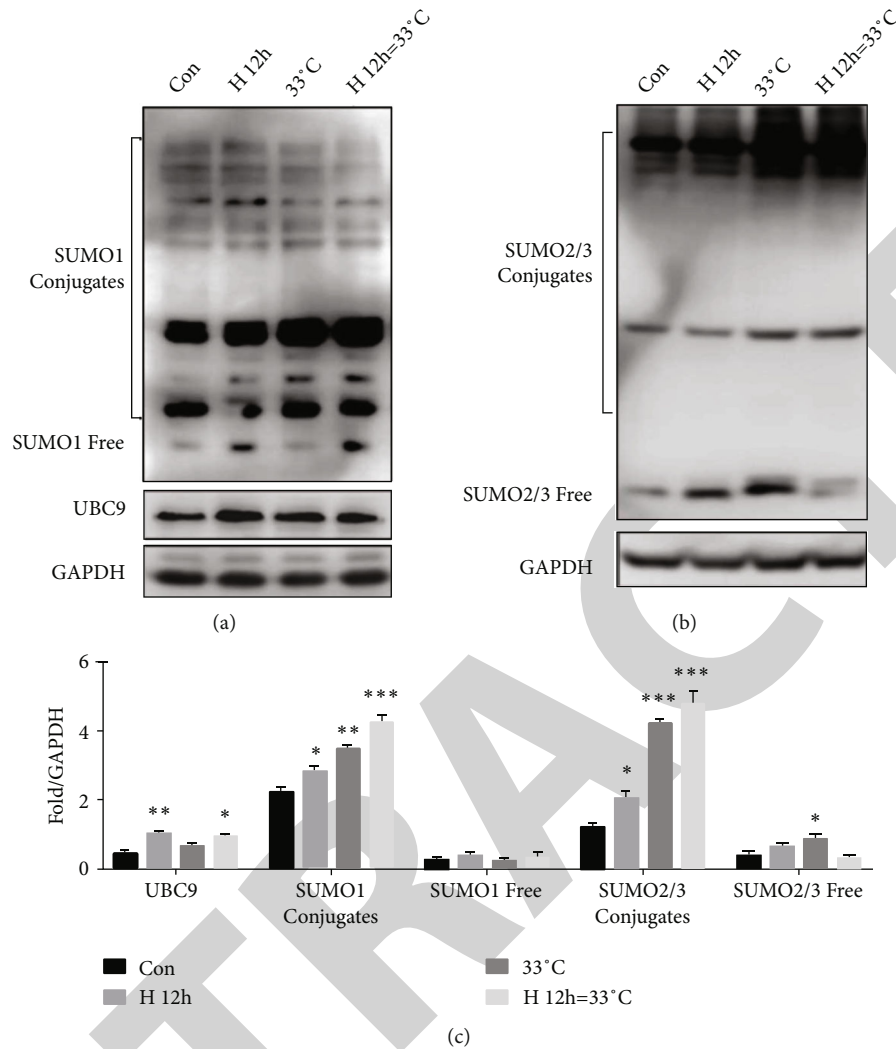


FIGURE 3: Effects of hypoxia (H 12 h) and mild hypothermia (33°C) on whole-protein SUMO modification in NSCs. (a) and (b) Expression of SUMO1 and SUMO2/3 conjugates, free SUMO1 and SUMO2/3, and UBC9 in NSCs after hypoxia and/or moderate hypothermic treatment, as assessed by western blotting. (c) Quantitative data were normalized to GAPDH and are expressed as mean \pm SD ($n = 3$). * $P < 0.05$, ** $P < 0.01$, and *** $P < 0.001$ vs. control.

hypothermia significantly increased the expression of the NSC marker nestin and significantly reduced the expression of NSE and GFAP, and cells showed smooth nerve spherical growth (Figure 2(c)). Expression of Oct4 and SOX2 was also increased by mild hypothermia compared with cells at 37°C exposed to hypoxia (Figure 2(d)). Mild hypothermia could reduce the metabolic level of cells and inhibit hypoxia-induced increases of anaerobic fermentation (Figure 2(e)).

3.3. Hypoxia Increased Whole-Protein SUMOylation in NSCs and Mild Hypothermia further Strengthened SUMOylation Modification. Western blot was used to detect whole-cell levels of the SUMOylation modification under the conditions of hypoxia, mild hypothermia, and their superposition. The results showed that hypoxia and hypothermia could significantly promote the binding of SUMO1 and SUMO2/3 to target proteins and had a superposition effect; however, it had little effect on free SUMOs. Further detection of conju-

gating enzyme E2 (UBC9) showed that hypoxia could promote the expression of this protein (Figures 3(a)–3(c)).

3.4. Overexpression of UBC9 Could Increase the Stemness and Hypoxia Tolerance of NSCs. We transfected NSCs with a plasmid carrying the UBC9 gene sequence and screened clones with high expression of UBC9. Protein detection showed that SUMO1 and SUMO2/3 conjugates in UBC9-overexpressing NSCs were significantly increased, as were the contents of stemness maintenance molecules Oct4 and SOX2 (Figures 4(a)–4(c)). Immunofluorescence detection showed that UBC9 overexpression could significantly increase the expression of the NSC marker nestin and promote spherical growth of cells. Under hypoxia, expression of differentiation markers in NSCs was further reduced, nestin expression was increased, and the cell ball became smaller and round (Figure 4(d)). Compared with the Con group, NSCs overexpressing UBC9 exhibited decreased cell

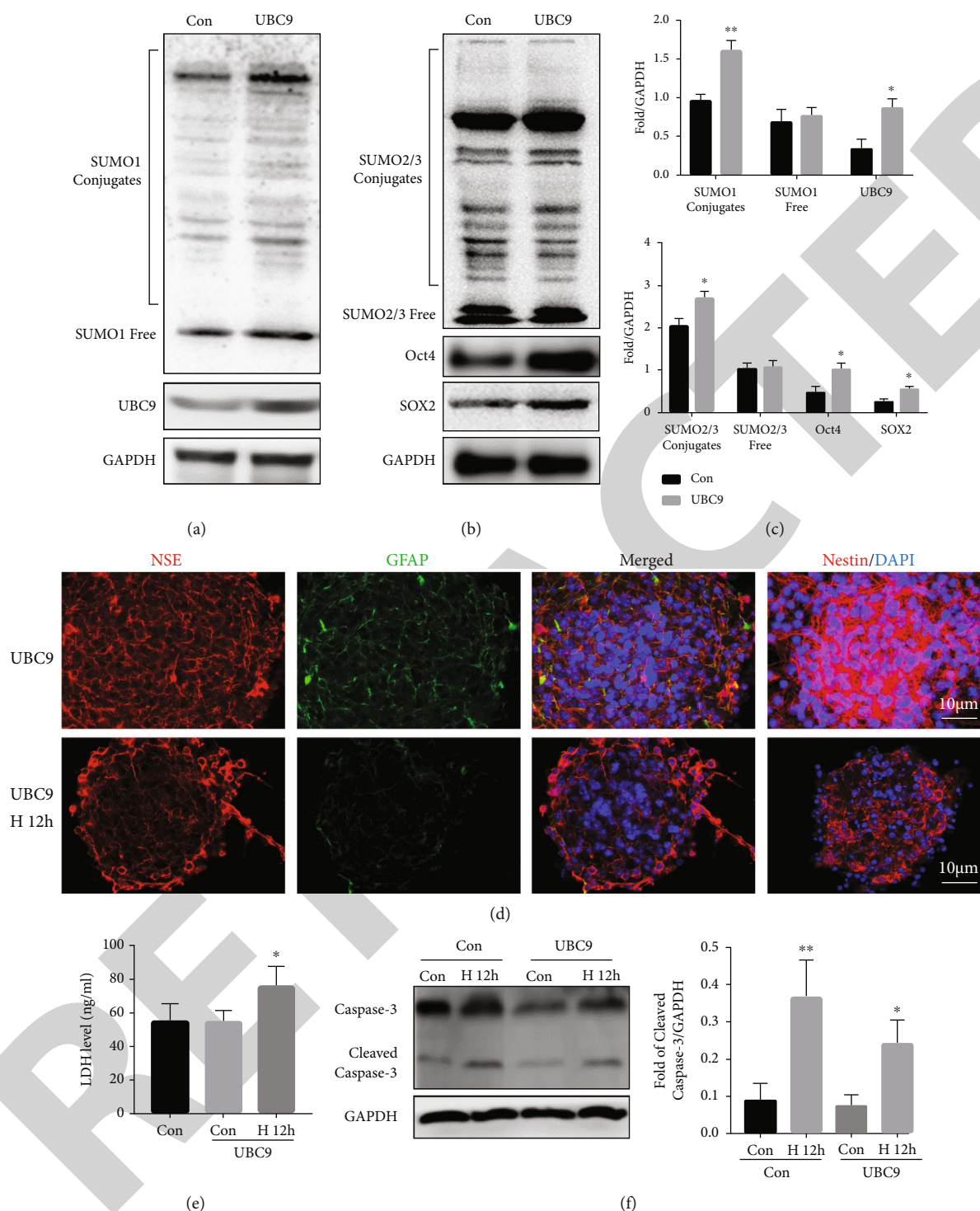


FIGURE 4: Overexpression of UBC9 increased NSC stemness and tolerance to hypoxia. (a) and (b) Expression of SUMO1 and SUMO2/3 conjugates, free SUMO1 and SUMO2/3, UBC9, Oct4, and SOX2 in NSCs overexpressing UBC9, as assessed by western blotting. (c) Quantitative data were normalized to GAPDH and expressed as mean \pm SD ($n = 3$). (d) Expression of NSE or nestin (red fluorescent signal) and GFAP (green fluorescent signal) in NSCs of the UBC9 transgene and Con groups after 12 h hypoxia was examined by immunofluorescence; DAPI (blue) was used to stain cell nuclei (scale bar, 10 μ m). (e) LDH contents were measured by ELISA, and data shown indicate mean \pm SD ($n = 4$). (f) Western blotting to detect cleaved caspase-3 expression in NSCs. Quantitative analysis: cleaved caspase-3 expression was normalized to GAPDH and is expressed as mean \pm SD ($n = 3$). * $P < 0.05$ and ** $P < 0.01$ vs. control.

damage after hypoxia, but there was no significant damage to cells under normoxia (Figure 4(e)). Hypoxia activated the cleaved caspase-3 apoptosis signal in NSCs and pro-

moted apoptosis, but UBC9 overexpression could partially reverse the proapoptotic damage induced by hypoxia (Figure 4(f)).

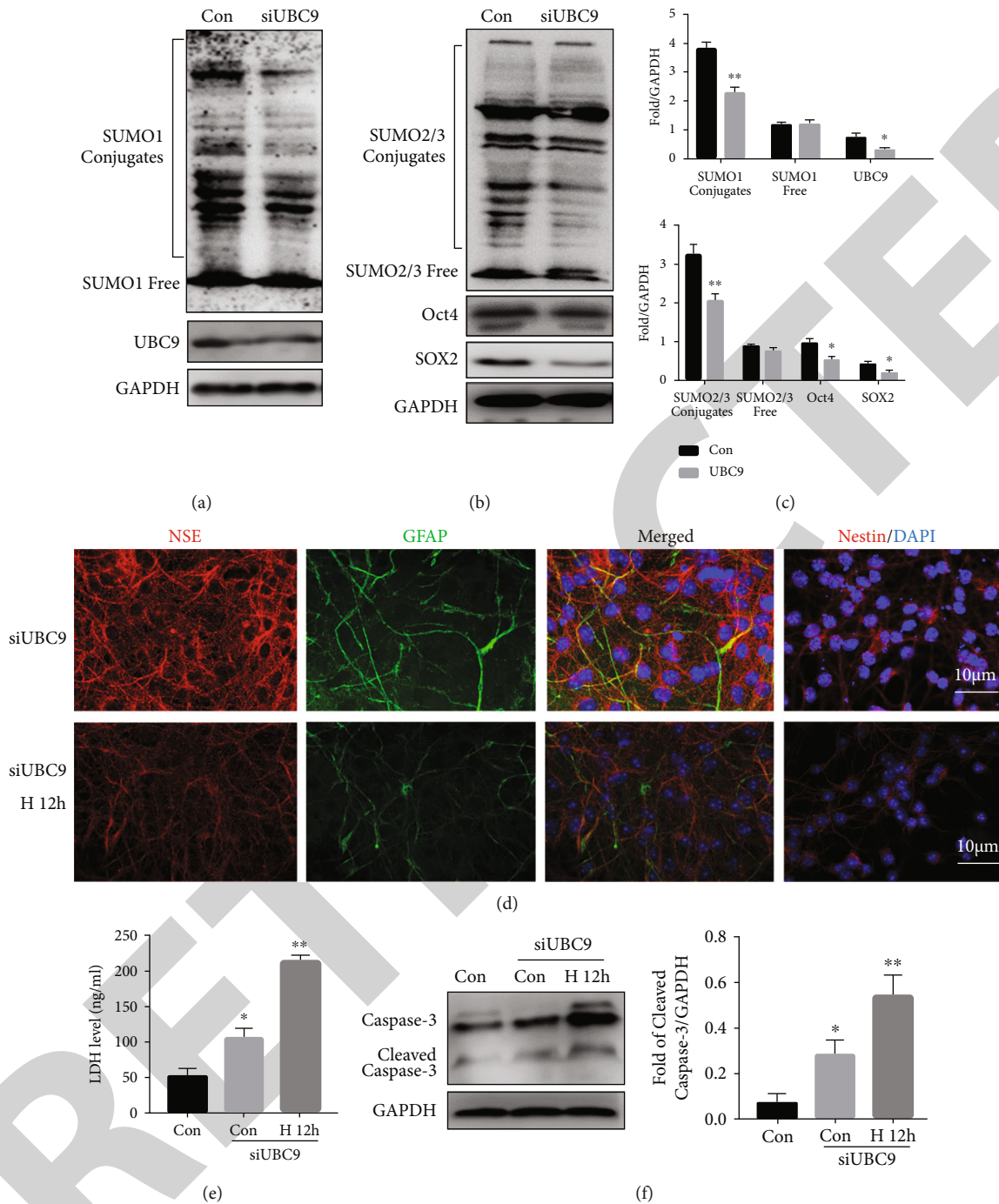


FIGURE 5: UBC9 interference reduced NSC stemness and tolerance to hypoxia. (a) and (b) Expression of SUMO1 and SUMO2/3 conjugates, free SUMO1 and SUMO2/3, UBC9, Oct4, and SOX2 in NSCs after UBC9 interference. (c) Quantitative data were normalized to GAPDH and are shown as mean \pm SD ($n = 3$). (d) Expression of NSE or nestin (red fluorescent signal) and GFAP (green fluorescent signal) in NSCs of the siUBC9 or Con groups after 12 h hypoxia was examined by immunofluorescence; DAPI (blue) was used to stain cell nuclei (scale bar, 10 μ m). (e) LDH contents were measured by ELISA, and data shown indicate mean \pm SD ($n = 4$). (f) Western blotting to detect the expression of cleaved caspase-3 in NSCs. Quantitative analysis: cleaved caspase-3 expression was normalized to GAPDH and is expressed as mean \pm SD ($n = 3$). * $P < 0.05$ and ** $P < 0.01$ vs. control.

3.5. siUBC9 Reduced the Stemness and Hypoxia Tolerance of NSCs. We used small interfering RNA sequences to knock-down UBC9 expression. Protein detection showed that low UBC9 expression inhibited the modification of target proteins by SUMO1 and SUMO2/3 in NSCs, and expression

of the stemness maintenance molecules Oct4 and SOX2 was significantly decreased (Figures 5(a)–5(c)). Immunofluorescence detection showed that low UBC9 expression could significantly inhibit nestin expression and promote cell differentiation. However, under hypoxic conditions, expression

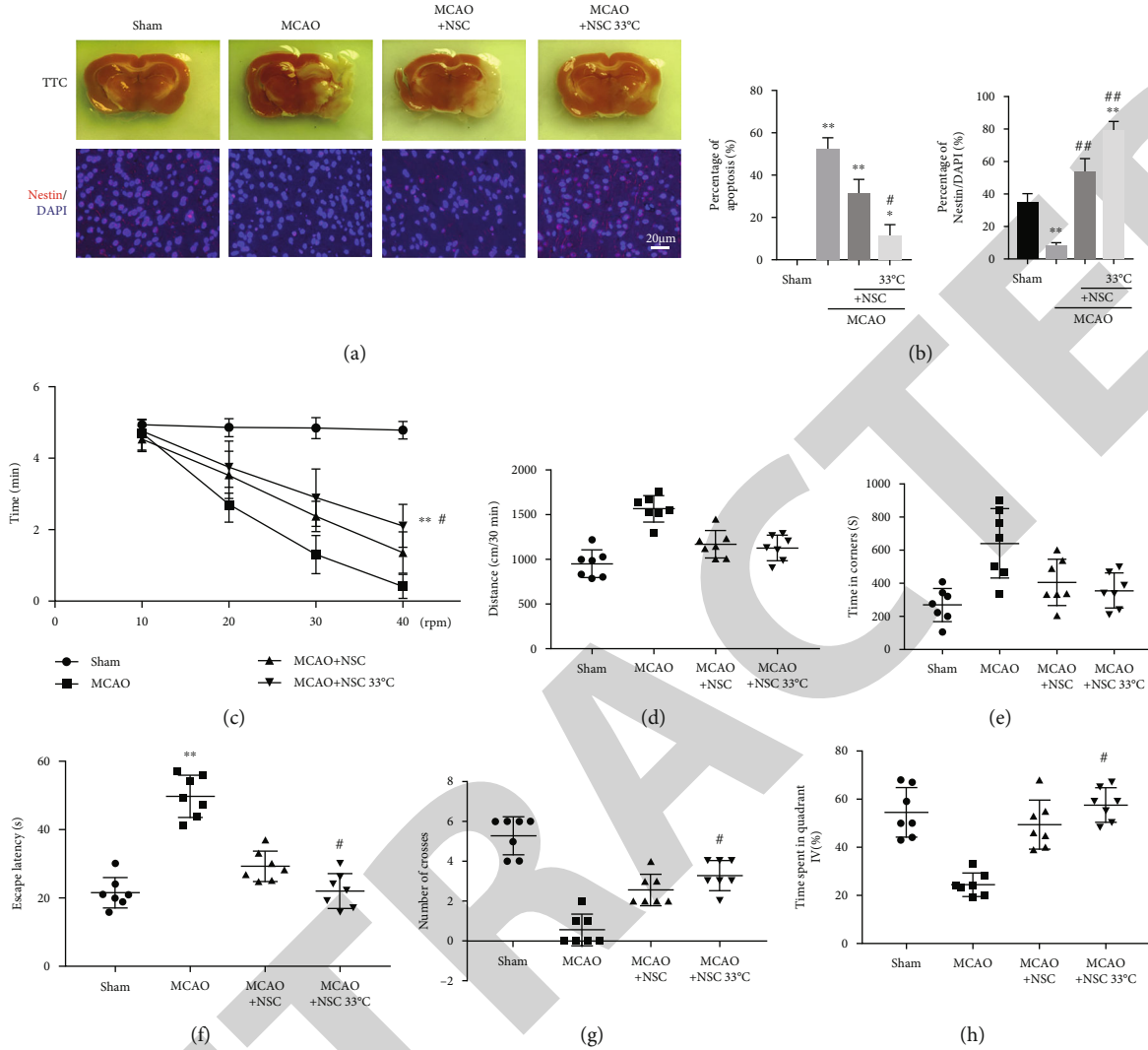


FIGURE 6: Mild hypothermia increased the survival of NSCs transplanted into the ischemic penumbra of rats and improved neuromotor function. (a) Representative TTC-stained coronal brain sections of sham-operated (Sham) rats, MCAO rats, MCAO rats transplanted with NSCs (MCAO+NSC), and MCAO rats transplanted with NSCs kept at 32–34°C for 12 h (MCAO+NSC 33°C). Immunofluorescence staining of cerebral cortex tissue sections (scale bar, 20 μm). (b) Quantification of percentages of cerebral infarct volume ($n = 5$) and proportions of nestin-positive to DAPI-positive cells ($n = 4$); data are expressed as mean \pm SD. (c) Rotarod testing was used to analyze the neurological deficits of rats in each group. (d) Spontaneous activity in the open field over 30 min and (e) time spent in corners. (f)–(h) Escape latency to find the nonvisible platform. Number of crosses in the probe test and time spent in quadrant IV. Data shown indicate mean \pm SD ($n = 7$). * $P < 0.05$ and ** $P < 0.01$ vs. Sham, # $P < 0.05$ and ## $P < 0.01$ vs. MCAO.

TABLE 1: Modified Neurological Severity Score (mNSS) results according to the time after MCAO.

mNSS scores	n	1 d	4 d	7 d	14 d	21 d	28 d
Sham	7	0.57 \pm 0.79	0.43 \pm 0.53	0.57 \pm 0.53	0.43 \pm 0.53	0.43 \pm 0.53	0.71 \pm 0.76
MCAO	7	12.29 \pm 0.95	10.71 \pm 0.76	9.14 \pm 0.90	7.86 \pm 0.69	7.17 \pm 0.75	6.14 \pm 0.90
MCAO+NSC	7	12.29 \pm 1.11	10.29 \pm 0.95	8.29 \pm 0.95	6.43 \pm 0.53	5.43 \pm 0.98	4.29 \pm 0.95
MCAO+NSC 33°C	7	12.14 \pm 1.46	10.57 \pm 1.40	7.43 \pm 1.40	5.74 \pm 2.00	3.29 \pm 0.76 [#]	2.29 \pm 0.76 ^{#&}
MCAO+NSC UBC9	7	11.43 \pm 0.79	10.14 \pm 1.07	9.86 \pm 3.48	4.29 \pm 0.76 [#]	2.86 \pm 0.69 ^{#&}	2.43 \pm 0.98 ^{#&}

of differentiation markers in NSCs was further reduced, as was nestin expression, which may cause irreversible damage to NSCs (Figure 5(d)). Compared with the control group, NSCs with low UBC9 expression exhibited increased LDH

release, which was further increased after hypoxia (Figure 5(e)). Low expression of UBC9 could activate the cleaved caspase-3-mediated apoptosis pathway in cells. Under hypoxia, cleaved caspase-3 activation further

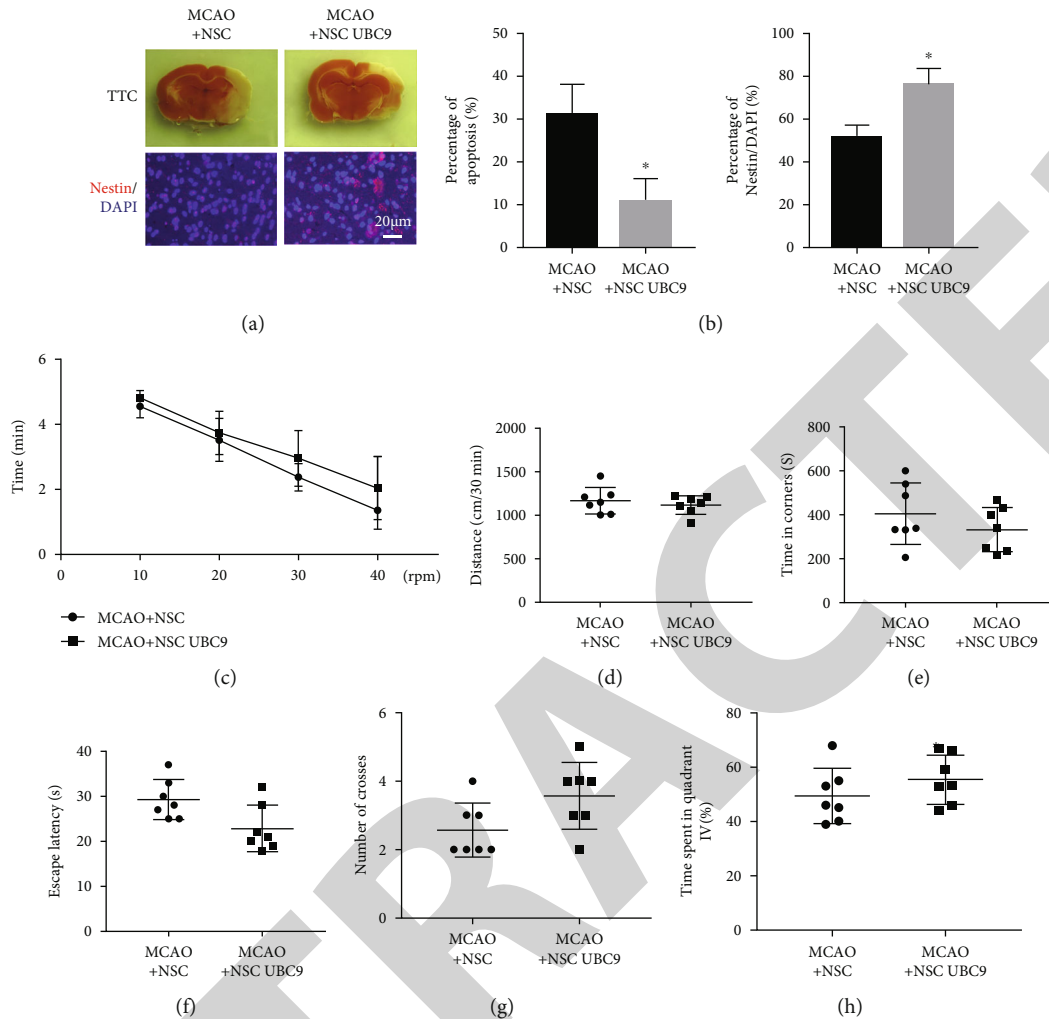


FIGURE 7: UBC9 overexpression increased the survival of NSCs transplanted into the ischemic penumbra of rats and improved neuromotor function. (a) Representative TTC-stained coronal brain sections of MCAO+NSC and MCAO rats transplanted with UBC9-overexpressing NSC (MCAO+NSC UBC9) groups. Immunofluorescence staining of cerebral cortex tissue sections (scale bar, 20 μ m). (b) Quantification of percentages of cerebral infarct volume ($n = 5$) and proportions of nestin-positive to DAPI-positive cells ($n = 4$), and data are expressed as mean \pm SD. (c) Rotarod testing was used to analyze the neurological deficits of rats in each group. (d) Spontaneous activity in the open field over 30 min and (e) time spent in corners. (f)–(h) Escape latency to find the nonvisible platform. Number of crosses in the probe test and time spent in quadrant IV. Data shown indicate mean \pm SD ($n = 7$). * $P < 0.05$ vs. MCAO+NSC.

increased and promoted the expression of its precursor form (Figure 5(f)). Thus, low UBC9 expression significantly aggravated the hypoxic injury of NSCs.

3.6. Mild Hypothermia Increased the Survival of NSCs Transplanted into the Cerebral Ischemic Penumbra of Mice and Improved Neuromotor Function. MCAO could generate infarct areas reaching 50% in rats, and the infarct area could be reduced to 30% after transplantation of NSCs into the penumbra, while mild hypothermia could further reduce the infarct area. Immunofluorescence staining showed that NSC transplantation could significantly increase the density of NSCs in the penumbra, and mild hypothermia could further increase the survival of NSCs (Figures 6(a) and 6(b)). Compared with the MCAO group, the motor and coordination ability of rats transplanted with moderately hypother-

mic NSCs improved after 7 days (Figure 6(c)), and the neural function of rats significantly improved after 21 days (Table 1). Notably, postoperative MCAO rats showed anxiety, which was significantly relieved after NSC transplantation and mild hypothermia (Figures 6(d) and 6(e)). Morris water maze testing showed that the learning and memory function of rats transplanted with NSCs into the penumbra and treated with mild hypothermia improved to varying degrees compared with after MCAO (Figures 6(f)–6(h)).

MCAO rats were treated with NSCs and/or mild hypothermia as follows: Sham, sham operation; MCAO, MCAO model without treatment; MCAO+NSC, MCAO rats transplanted with NSCs; MCAO+NSC 33°C, MCAO rats transplanted NSCs kept at 32–34°C for 12 h; MCAO+NSC UBC9, MCAO rats transplanted with UBC9-overexpressing NSCs. Neurological scores were obtained at 1, 4, 7, 14, 21, and 28

days following surgery in each group. Data are expressed as mean \pm SD ($n = 7$). $^*P < 0.05$ vs. MCAO and $^{\&}P < 0.05$ vs. MCAO+NSC.

3.7. Transplanted NSCs Overexpressing UBC9 in the Cerebral Ischemic Penumbra of Rats Exhibited Higher Survival Rates and Enhanced Neuromotor Function. Compared with simple transplantation of NSCs, UBC9-overexpressing NSCs could reduce the cerebral infarction area of rats from 30% to 12%. Moreover, overexpression of UBC9 could promote the survival of NSCs, as well as their ability to adapt to hypoxic injury of brain (Figures 7(a) and 7(b)). Compared with the NSC-transplanted group, MCAO rats transplanted with NSCs overexpressing UBC9 exhibited significantly improved motor ability and neurological functions (Table 1, Figure 7(c)), reduced anxiety levels, and enhanced learning functions to varying degrees (Figures 7(d)–7(h)).

4. Discussion

In this study, we first examined the effect of hypoxia on NSCs. The results show that although hypoxia damaged NSCs, it increased their potential to maintain stemness, inhibited their neuronal differentiation, and reduced their metabolism. Further studies showed that mild hypothermia antagonized hypoxia-induced damage to NSCs, further inhibiting their differentiation and reducing cell metabolism. To evaluate whether the protective effect of mild hypothermia on NSCs was related to the SUMO modification of proteins, we examined the effect of mild hypothermia on the expression of SUMOs in NSCs. The results show that hypoxia increased global SUMO modifications of NSCs, both SUMO1 and SUMO2/3, and mild hypothermia further strengthened these trends. These results preliminarily validated our hypothesis that hypoxia can increase the hypoxia tolerance of NSCs by increasing global SUMOylation, and mild hypothermia can enhance neuroprotective effects by reinforcing this trend.

To evaluate whether global SUMOylation is indispensable to improving the hypoxia tolerance of NSCs, we next overexpressed and silenced the UBC9 gene (the only E2-binding enzyme in the SUMO modification reaction) [22] in NSCs and evaluated their hypoxia tolerance and stemness maintenance potential. The results show that *Ubc9* overexpression increased both the stemness potential of NSCs and their tolerance to hypoxia; in contrast, silencing UBC9 reduced the stemness of NSCs and decreased their tolerance to hypoxia. These results indicate that global SUMO modification of target proteins is essential to improve the tolerance of NSCs to hypoxia. However, we cannot specify exactly which proteins were SUMO-modified during this event. According to previous studies, we speculate that hypoxia greatly increases SUMO modification levels of numerous target proteins, including HIF-1 α , Oct4, and SOX2. Theoretically, SUMO-modified HIF-1 α , Oct4, and SOX2 cannot be degraded by ubiquitin hydrolase [23–25], thus allowing these proteins to persist and stably exist in the nucleus and cytoplasm of NSCs, whereby they increase hypoxia tolerance and stemness potential.

Finally, we established an MCAO model in rats to investigate the effects of mild hypothermia on survival of NSCs transplanted in the cerebral ischemic penumbra and subsequent improvements of neurological function. The results show that mild hypothermia increased the survival of NSCs transplanted in the cerebral ischemic penumbra of rats and improved their neurological functions, including motor and learning abilities. Finally, we transplanted NSCs overexpressing UBC9 into the cerebral ischemic penumbra of rats and found that these cells exhibited higher survival rates and better improved the neurological function of experimental animals, including motor and learning functions.

These results verify our hypothesis that increasing global SUMOylation of many target proteins, e.g., by overexpressing UBC9, can help NSCs obtain stronger hypoxia tolerance. Moreover, transplantation of NSCs with stronger hypoxia tolerance into the cerebral ischemic penumbra and subsequent mild hypothermia treatment increased the survival of NSCs in the penumbra and enhanced the neurological function of animals.

Although this study has enriched new ideas for the future treatment of ischemic cerebrovascular disease with mild hypothermia therapy combined with NSCs transplantation, there are still many difficult problems to be solved before it is actually applied to the clinic. First, due to the existence of the blood-brain barrier, how to inoculate NSCs into the brain of patients with cerebral ischemia will be a difficult problem for clinicians to face. Second, how to control the time window of hypothermia cooling and rewarming to produce the best therapeutic effect on patients is far from being interpreted. Third, the potential tumorigenic effects brought about by the proliferative characteristics of NSCs are serious side effects that we can never ignore. Last but not the final, SUMOylation can simultaneously intervene in the posttranslational modification of thousands of proteins. How to achieve advantages and avoid disadvantages at the molecular level and protein function will be a problem that researchers attach great importance to. In conclusion, there is still a long way to go before the clinical application of mild hypothermia combined with NSCs transplantation in the treatment of ischemic cerebrovascular disease.

5. Conclusions

Global protein SUMO modification is an important molecular mechanism for NSC tolerance of hypoxia, and mild hypothermia can further increase the degree of global protein SUMO modification in NSCs—a newly discovered molecular mechanism by which mild hypothermia protects the brain. Indeed, mild hypothermia can improve the hypoxia tolerance of NSCs and increase their survival following transplantation in situ, thus yielding better nerve repair effects.

Data Availability

All the data used to support the findings of this study are available from the corresponding authors upon request.

Conflicts of Interest

The authors declare that they have no conflicts of interest.

Authors' Contributions

Heng Cai, Xiaofang Ma and Dading Lu contributed equally to this work and are co-first authors.

Acknowledgments

The present study was supported by the National Natural Science Foundation of China (Grant nos. 81702488 and 81901526), the National Natural Science Foundation Project of Liaoning Province (Grant nos. 2019-ZD-0757 and 2020-KF-12-06), Postdoctoral Research Foundation of China (CN) (No. 2018M641745), Doctoral Start-up Foundation of Liaoning Province (No. 20170520020), Shenyang Science and Technology Bureau (No. 19-112-4-044), 345 Talent Project fund of Shengjing hospital, Tianjin Natural Science Foundation of China (Grant nos. 18JCQNJC12800, 19JCZDJC35200, and 19JCQNJC11900), and Tianjin Special Project of New Generation Artificial Intelligence Technology (No. 18ZXZNSY00260). This study was funded by the Tianjin Key Medical Discipline (Specialty) Construction Project.

References

- [1] S. Wu, C. Jin, S. Li et al., "Aging, arterial stiffness, and blood pressure association in Chinese adults," *Hypertension*, vol. 73, no. 4, pp. 893–899, 2019.
- [2] Y. J. Wang, Z. X. Li, H. Q. Gu et al., "China stroke statistics 2019: a report from the national center for healthcare quality management in neurological diseases, China national clinical research center for neurological diseases, the Chinese stroke association, national center for chronic and non-communicable disease control and prevention, Chinese center for disease control and prevention and institute for global neuroscience and stroke collaborations," *Stroke and vascular neurology*, vol. 5, no. 3, pp. 211–239, 2020.
- [3] X. Cheng, Y. Yang, D. C. Schwebel et al., "Population ageing and mortality during 1990–2017: a global decomposition analysis," *PLoS medicine*, vol. 17, no. 6, article e1003138, 2020.
- [4] R. Jahan, J. L. Saver, L. H. Schwamm et al., "Association between time to treatment with endovascular reperfusion therapy and outcomes in patients with acute ischemic stroke treated in clinical practice," *Journal of the American Medical Association*, vol. 322, no. 3, pp. 252–263, 2019.
- [5] M. Pergakis, N. Badjatia, S. Chaturvedi et al., "BIIB093 (IV glibenclamide): an investigational compound for the prevention and treatment of severe cerebral edema," *Expert opinion on investigational drugs*, vol. 28, no. 12, pp. 1031–1040, 2019.
- [6] M. H. Hamblin and J. P. Lee, "Neural stem cells for early ischemic stroke," *International journal of molecular sciences*, vol. 22, no. 14, p. 7703, 2021.
- [7] A. J. Gunn and M. Thoresen, "Animal studies of neonatal hypothermic neuroprotection have translated well in to practice," *Resuscitation*, vol. 97, pp. 88–90, 2015.
- [8] H. A. Choi, N. Badjatia, and S. A. Mayer, "Hypothermia for acute brain injury—mechanisms and practical aspects," *Nature reviews Neurology*, vol. 8, no. 4, pp. 214–222, 2012.
- [9] N. Alva, J. Palomeque, and T. Carbonell, "Oxidative stress and antioxidant activity in hypothermia and rewarming: can RONS modulate the beneficial effects of therapeutic hypothermia?," *Oxidative medicine and cellular longevity*, vol. 2013, Article ID 957054, 10 pages, 2013.
- [10] B. Lu, I. T. Christensen, T. Yu, C. Wang, Q. Yan, and X. Wang, "SUMOylation evoked by oxidative stress reduced lens epithelial cell antioxidant functions by increasing the stability and transcription of TP53INP1 in age-related cataracts," *Oxidative medicine and cellular longevity*, vol. 2019, Article ID 7898069, 14 pages, 2019.
- [11] K. H. Reiter, A. Ramachandran, X. Xia, L. E. Boucher, J. Bosch, and M. J. Matunis, "Characterization and structural insights into selective E1-E2 interactions in the human and *Plasmodium falciparum* SUMO conjugation systems," *The Journal of biological chemistry*, vol. 291, no. 8, pp. 3860–3870, 2016.
- [12] S. Jentsch and I. Psakhye, "Control of nuclear activities by substrate-selective and protein-group SUMOylation," *Annual review of genetics*, vol. 47, no. 1, pp. 167–186, 2013.
- [13] S. Wiechmann, A. Gartner, A. Kniss et al., "Site-specific inhibition of the small ubiquitin-like modifier (SUMO)-conjugating enzyme Ubc9 selectively impairs SUMO chain formation," *The Journal of biological chemistry*, vol. 292, no. 37, pp. 15340–15351, 2017.
- [14] C. Filippopoulou, G. Simos, and G. Chachami, "The role of SUMOylation in the response to hypoxia: an overview," *Cell*, vol. 9, no. 11, p. 2359, 2020.
- [15] Y. J. Lee, J. D. Bernstock, N. Nagaraja, B. Ko, and J. M. Hallenbeck, "Global SUMOylation facilitates the multimodal neuroprotection afforded by quercetin against the deleterious effects of oxygen/glucose deprivation and the restoration of oxygen/glucose," *Journal of Neurochemistry*, vol. 138, no. 1, pp. 101–116, 2016.
- [16] Y. J. Lee, Y. Mou, D. Klimanis, J. D. Bernstock, and J. M. Hallenbeck, "Global SUMOylation is a molecular mechanism underlying hypothermia-induced ischemic tolerance," *Frontiers in cellular neuroscience*, vol. 8, p. 416, 2014.
- [17] D. Li, Y. Fang, P. Wang, W. Shan, Z. Zuo, and L. Xie, "Autologous transplantation of adipose-derived mesenchymal stem cells attenuates cerebral ischemia and reperfusion injury through suppressing apoptosis and inducible nitric oxide synthase," *International journal of molecular medicine*, vol. 29, no. 5, pp. 848–854, 2012.
- [18] M. M. Daadi, S. H. Lee, A. Arac et al., "Functional engraftment of the medial ganglionic eminence cells in experimental stroke model," *Cell transplantation*, vol. 18, no. 7, pp. 815–826, 2009.
- [19] Y. Hong, Q. Liu, M. Peng et al., "High-frequency repetitive transcranial magnetic stimulation improves functional recovery by inhibiting neurotoxic polarization of astrocytes in ischemic rats," *Journal of Neuroinflammation*, vol. 17, no. 1, p. 150, 2020.
- [20] L. Zhang, X. Yang, M. Yin et al., "An animal trial on the optimal time and intensity of exercise after stroke," *Medicine and science in sports and exercise*, vol. 52, no. 8, pp. 1699–1709, 2020.
- [21] C. V. Vorhees and M. T. Williams, "Value of water mazes for assessing spatial and egocentric learning and memory in rodent basic research and regulatory studies," *Neurotoxicology and teratology*, vol. 45, pp. 75–90, 2014.
- [22] Y. J. Lee and J. M. Hallenbeck, "SUMO and ischemic tolerance," *Neuromolecular medicine*, vol. 15, no. 4, pp. 771–781, 2013.

Retraction

Retracted: Modified Trabeculectomy versus Glaucoma Drainage Implant Surgery: A Retrospective Comparative Study for Refractory Glaucoma Treatment

Oxidative Medicine and Cellular Longevity

Received 8 August 2023; Accepted 8 August 2023; Published 9 August 2023

Copyright © 2023 Oxidative Medicine and Cellular Longevity. This is an open access article distributed under the Creative Commons Attribution License, which permits unrestricted use, distribution, and reproduction in any medium, provided the original work is properly cited.

This article has been retracted by Hindawi following an investigation undertaken by the publisher [1]. This investigation has uncovered evidence of one or more of the following indicators of systematic manipulation of the publication process:

- (1) Discrepancies in scope
- (2) Discrepancies in the description of the research reported
- (3) Discrepancies between the availability of data and the research described
- (4) Inappropriate citations
- (5) Incoherent, meaningless and/or irrelevant content included in the article
- (6) Peer-review manipulation

The presence of these indicators undermines our confidence in the integrity of the article's content and we cannot, therefore, vouch for its reliability. Please note that this notice is intended solely to alert readers that the content of this article is unreliable. We have not investigated whether authors were aware of or involved in the systematic manipulation of the publication process.

In addition, our investigation has also shown that one or more of the following human-subject reporting requirements has not been met in this article: ethical approval by an Institutional Review Board (IRB) committee or equivalent, patient/participant consent to participate, and/or agreement to publish patient/participant details (where relevant).

Wiley and Hindawi regrets that the usual quality checks did not identify these issues before publication and have since put additional measures in place to safeguard research integrity.

We wish to credit our own Research Integrity and Research Publishing teams and anonymous and named external researchers and research integrity experts for contributing to this investigation.

The corresponding author, as the representative of all authors, has been given the opportunity to register their agreement or disagreement to this retraction. We have kept a record of any response received.

References

- [1] Y. He, B. He, Z. Ji et al., "Modified Trabeculectomy versus Glaucoma Drainage Implant Surgery: A Retrospective Comparative Study for Refractory Glaucoma Treatment," *Oxidative Medicine and Cellular Longevity*, vol. 2022, Article ID 3050007, 15 pages, 2022.

Research Article

Modified Trabeculectomy versus Glaucoma Drainage Implant Surgery: A Retrospective Comparative Study for Refractory Glaucoma Treatment

Yuan He ¹, Beilei He ^{1,2}, Zhi Ji,¹ Ruixue Zhang ¹, Zhuoya Quan ¹, Guijun Xie,³ and Xiaoli Pu⁴

¹Department of Ophthalmology, The Second Affiliated Hospital of Xi'an Medical University, Xi'an, 710038 Shaanxi Province, China

²Department of Ophthalmology, Fufeng County People's Hospital, Baoji, 722299 Shaanxi Province, China

³Department of Ophthalmology, Baoji People's Hospital, Baoji, 721006 Shaanxi Province, China

⁴Department of Ophthalmology, Xianyang First People's Hospital, Baoji, 712099 Shaanxi Province, China

Correspondence should be addressed to Yuan He; openji7127@hotmail.com

Received 18 March 2022; Revised 21 April 2022; Accepted 27 April 2022; Published 23 May 2022

Academic Editor: Shao Liang

Copyright © 2022 Yuan He et al. This is an open access article distributed under the Creative Commons Attribution License, which permits unrestricted use, distribution, and reproduction in any medium, provided the original work is properly cited.

Purpose. To observe and compare the efficacy of modified trabeculectomy (TE), Ahmed drainage valve implantation (AGV), and EX-PRESS glaucoma shunt for refractory glaucoma (RG). **Methods.** The study population of this retrospective study comprised 73 patients (76 eyes) who were suffering from RG and treated with modified TE, AGV, and EX-PRESS glaucoma shunt in our hospital from October 2012 to October 2020. The number of cases who underwent modified TE, AVG, and EX-PRESS glaucoma shunt was 36 (38 eyes), 19 (20 eyes), and 18 patients (18 eyes), respectively. The intraocular pressure (IOP), best-corrected visual acuity (BCVA), postoperative antiglaucoma medications, filter bubble morphology, anterior chamber depth (ACD), successful rate, and postoperative complications were recorded and statistically analyzed preoperative and 1 d, 1 w, 1 mon, 3 mon, 6 mon, and the end follow-up after operation. **Results.** The BCVA differed insignificantly among the three cohorts before and 6 months after surgery. Compared to preoperative BCVA, the postoperative BCVA of the three groups had no statistical significance. An obvious reduction in IOP was observed in all the three group after operation ($P < 0.05$). An obvious decrease in antiglaucoma medications was observed after surgery in all the three groups ($P < 0.05$). The AGV group showed deeper ACD postoperatively, while no marked difference was found in postoperative ACD in the other two groups. The total success rates in modified TE and AGV groups were slightly higher than those in the EX-PRESS group. The three groups differed insignificantly in filter bubble morphology after operation. **Conclusion.** Modified TE, AGV, and EX-PRESS glaucoma shunt showed equivalent efficacy for RG, which could validly reduce IOP and postoperative antiglaucoma medications. However, the success rates of modified TE and AGV were slightly higher than those of EX-PRESS glaucoma shunt in the last follow-up, and their complications were slightly less than those of the EX-PRESS glaucoma shunt.

1. Introduction

Glaucoma is an optic neurodegenerative disease and leads to an irreversible blindness, ranking first in the world. It is characterized by progressive visual loss and visual field defect. The risk factors of glaucoma include high intraocular pressure (IOP), age, hypertension, diabetes mellitus, high

myopia, and gene mutation [1]. Pathological intraocular hypertension is the main risk factor. The mainstay of treatment focuses on reducing IOP. The early-stage study about glaucoma showed that the probability of glaucoma progression decreased by 10 percent for every 1 mmHg reduction in IOP, compared to baseline IOP (HR = 0.90; 95%CI = 0.86 ~ 0.94) [2]. Drug laser surgery is a common way to

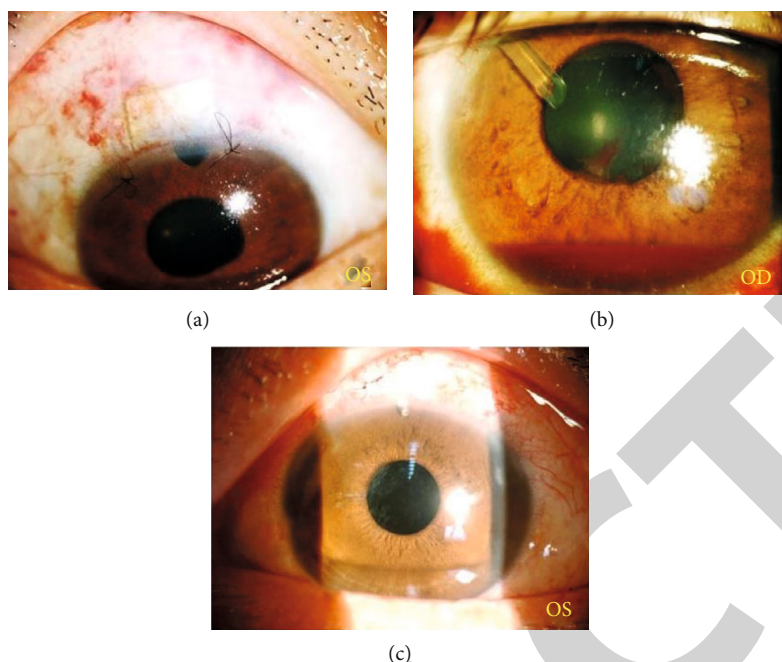


FIGURE 1: Postoperative conditions of the three surgical methods: (a) the modified TE; (b) the Ahmed FP7 glaucoma valve (AGV); (c) the EX-PRESS P50/P200 glaucoma shunt.

TABLE 1: Preoperative demographic characteristics of all patients.

Parameters	Group A (modified trabeculectomy) (<i>n</i> = 38)	Group B (AGV) (<i>n</i> = 20)	Group C (EX-PRESS) (<i>n</i> = 18)	<i>P</i>
Sex, <i>n</i> (%)				0.235
Female	20 (52.63)	5 (25.00)	10 (55.60)	
Male	18 (47.37)	15 (75.00)	8 (44.44)	
Age (years), (mean ± SD)	55.00 ± 15.17	47.30 ± 16.77	49.33 ± 15.97	0.190
Laterality, <i>n</i> (%)				0.653
OD	15 (39.47)	10 (50.00)	9 (50.00)	
OS	23 (60.53)	10 (50.00)	9 (50.00)	
Follow-up time (months), range (mean ± SD)	6-93, 29.89 ± 24.80	6-97, 56.30 ± 39.42	6-45, 26.00 ± 12.25	0.001
IOP (mmHg) (mean ± SD)	47.37 ± 17.55	49.50 ± 15.63	46.78 ± 16.54	0.889
BCVA (logMAR) (mean ± SD)	2.15 ± 0.82	2.07 ± 0.94	1.51 ± 0.30	0.138
No. of preoperative medications (mean ± SD)	3.66 ± 1.24	3.75 ± 0.91	4.22 ± 0.67	0.393
ACD (mm)	2.35 ± 0.93	2.68 ± 0.18	3.25 ± 1.01	0.355
CECC	2450.36 ± 352.52	2328.82 ± 498.53	1966.96 ± 732.91	0.395
Previous surgery, <i>n</i> (%)				
Trabeculectomy	7 (18.42)	1 (5.00)	1 (5.56)	0.207
Keratoplasty	3 (7.89)	3 (15.00)	1 (5.56)	0.558
Hypertension, <i>n</i> (%)	7 (18.42)	1 (5.00)	0 (0.00)	0.071
Diabetes, <i>n</i> (%)	6 (15.79)	4 (20.00)	3 (16.67)	0.920

SD: standard deviation; MD: mean deviation; ACD: anterior chamber depth; CECC: corneal endothelial cell count.

reduce the pressure. The common treatments to reduce IOP included antiglaucoma drugs, lasers, and surgery.

Refractory glaucoma (RG) is a group of disorders with various types of glaucoma associated with very poor progno-

sis [3]. Even though the maximum tolerated dose of anti-glaucoma medications was used for the RG treatment, the long-term outcome was still frustrating. It was difficult to maintain the IOP for target levels. We often needed to

TABLE 2: Glaucoma diagnosis [n (%)].

Diagnosis	Group A (n = 38)	Group B (n = 20)	Group C (n = 18)	Total
NVG	12 (31.58)	9 (45.00)	5 (27.78)	26 (34.21)
Filtration surgery failed	7 (18.42)	1 (5.00)	1 (5.56)	9 (11.84)
Glaucoma after intraocular surgery	3 (7.89)	0 (0.00)	0 (0.00)	3 (3.95)
Glaucoma secondary to chemical burn	2 (5.26)	1 (5.00)	1 (5.56)	4 (5.26)
PKG	3 (7.89)	3 (15.00)	1 (5.56)	7 (9.22)
Glaucoma secondary to trauma	4 (10.53)	0 (0.00)	5 (27.78)	9 (11.84)
UG	2 (5.26)	1 (5.00)	1 (5.56)	4 (5.26)
Steroid-induced glaucoma	1 (2.63)	2 (10.00)	1 (5.56)	4 (5.26)
Juvenile glaucoma	1 (2.63)	0 (0.00)	1 (5.56)	2 (2.63)
ICES	1 (2.63)	0 (0.00)	1 (5.56)	2 (2.63)
PG	0 (0.00)	1 (5.00)	0 (0.00)	1 (1.32)
Glaucoma secondary to keratitis	2 (5.26)	1 (5.00)	1 (5.56)	4 (5.26)
Glaucoma secondary to bullae keratopathy	0 (0.00)	1 (5.00)	0 (0.00)	1 (1.32)
Total	38 (100.00)	20 (100.00)	18 (100.00)	76 (100.00)

NVG: neovascular glaucoma; PKG: postpenetrating keratoplasty glaucoma; UG: uveitic glaucoma; ICES: iridocorneal endothelial syndrome; PG: pigmentary glaucoma. Group A: modified trabeculectomy group; Group B: AGV group; Group C: EX-PRESS group.

TABLE 3: Etiological classification of complex glaucoma.

	I (%)	II (%)	
		Ia (%)	Ib (%)
Group A (n = 38)	8 (21.05%)	18 (47.37%)	12 (31.58%)
Group B (n = 20)	1 (5.00%)	10 (50.0%)	9 (45.00%)
Group C (n = 18)	2 (11.11%)	11 (61.11%)	5 (27.78%)
χ^2		3.113	
P		0.555	

Fisher probabilities were used to analyze the etiological classification. I: primary glaucoma (including failed filtration surgery and juvenile glaucoma); Ia: secondary glaucoma (including glaucoma secondary to chemical burn, PKG, UG, glaucoma after intraocular surgery, glaucoma secondary to trauma, steroid-induced glaucoma, and glaucoma secondary to bullae keratopathy); Ib: NVG.

choose the surgical treatment with the ideal effect of lowering intraocular pressure (IOP), high success rate, and less surgical complications. Trabeculectomy (TE) was first proposed and applied by Cairns in 1968 [4], which was widely regarded as the gold standard for primary open angle glaucoma (POAG) and primary angle-closure glaucoma (PACG). However, the its success rate was about 11-52% [5, 6], and it can lead to some eye complications. At present, modified TE for which traditional TE plus scleral flap adjustable suture or antimetabolites in the intraoperative and postoperative (e.g., MMC and 5-FU) has become a new trend in the clinical treatment of glaucoma. It can reduce the probability of postoperative scarring of the filter bubble, effectively control IOP, and improve operative success rate, which has been applied to treat a variety of RG. The procedure with the most extensive application to lower IOP is TE.

In recent years, many authors suggested that glaucoma drainage implant surgery (GDIS) is a surgical procedure that is preferably used for RG [7]. The most widely used drainage included the Ahmed FP7 glaucoma valve (AGV) and the

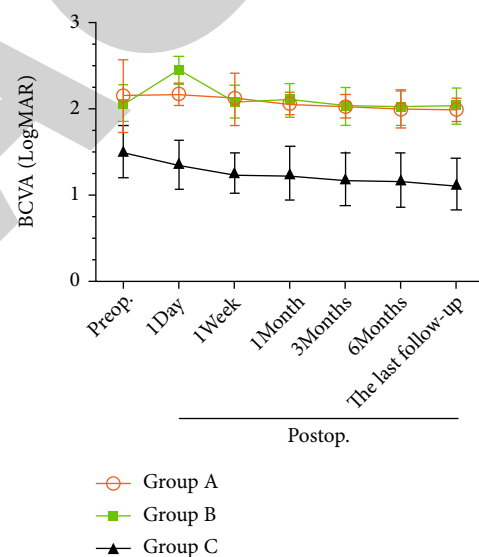


FIGURE 2: The BCVA of the study patients in the modified trabeculectomy, AGV, and EX-PRESS groups before surgery and 1 day, 1 week, 1 month, 3 months, 6 months, and the last follow-up after surgery. There was no significant difference in postoperative BCVA at different follow-up periods compared with preoperative BCVA in the three groups ($P > 0.05$). Group A: modified trabeculectomy group; Group B: AGV group; Group C: EX-PRESS group; preop.: preoperative; postop.: postoperative.

EX-PRESS P50/P200 glaucoma shunt, which were effective in controlling IOP and reducing the incidence of scarring of the filtration bubble. Now, some studies have found that the rate of resurgical treatment for AGV after glaucoma surgery was 9%, compared to that of 29% in the modified TE [8]. A meta-analysis on clinical studies on GDIs and other operations conducted by foreign scholars [9, 10] showed no distinct difference between EX-PRESS shunt and TE in reducing IOP, use of antiglaucoma medications,

Table 4: Postoperative BCVA changes (standard logarithmic visual acuity chart).

Postoperative date		Group A (<i>n</i> = 38) (%)	Group B (<i>n</i> = 20) (%)	Group C (<i>n</i> = 18) (%)	<i>P</i>
1 day	Improve or stay the same	35 (92.11)	15 (75.00)	17 (94.44)	0.137
	Vision reduction	3 (7.89)	5 (25.00)	1 (5.56)	
1 week	Improve or stay the same	35 (92.11)	17 (85.00)	17 (94.44)	0.586
	Vision reduction	3 (7.89)	3 (15.00)	1 (5.56)	
1 month	Improve or stay the same	35 (92.11)	18 (90.00)	17 (94.44)	1.000
	Vision reduction	3 (7.89)	2 (10.00)	1 (5.56)	
3 months	Improve or stay the same	34 (89.47)	18 (90.00)	17 (94.44)	1.000
	Vision reduction	4 (10.53)	2 (10.00)	1 (5.56)	
6 months	Improve or stay the same	34 (89.47)	19 (95.00)	17 (94.44)	0.868
	Vision reduction	4 (10.53)	1 (5.00)	1 (5.56)	
The last follow-up	Improve or stay the same	34 (89.47)	18 (90.00)	16 (88.89)	1.000
	Vision reduction	4 (10.53)	2 (10.00)	2 (11.11)	

Group A: modified trabeculectomy group; Group B: AGV group; Group C: EX-PRESS group.

TABLE 5: Postoperative BCVA changes (difference between preoperative and postoperative values) in the three groups (logMAR, mean \pm SD).

Postoperative date	Group A (<i>n</i> = 38)	Group B (<i>n</i> = 20)	Group C (<i>n</i> = 18)	<i>P</i>
1-day BCVA difference	-0.02 ± 0.37	-0.18 ± 0.60	0.14 ± 0.30	0.166
1-week BCVA difference	0.04 ± 0.42	-0.03 ± 0.33	0.24 ± 0.48	0.255
1-month BCVA difference	0.09 ± 0.44	-0.04 ± 0.31	0.26 ± 0.51	0.218
3-month BCVA difference	0.15 ± 0.42	0.03 ± 0.18	0.32 ± 0.54	0.179
6-month BCVA difference	0.15 ± 0.52	0.05 ± 0.17	0.33 ± 0.57	0.304
The last follow-up BCVA difference	0.16 ± 0.53	0.03 ± 0.19	0.38 ± 0.60	0.179

Group A: modified trabeculectomy group; Group B: AGV group; Group C: EX-PRESS group.

and complete success rate. However, the postoperative complications were significantly less than TE, and the postoperative visual acuity recovered faster. At present, there are long-term follow-up reports regarding the safety and effectiveness of the EX-PRESS shunt in POAG [11]. Zhang et al. [12] also found that for RG, EX-PRESS shunt better reduced IOP with higher effectiveness than AGV. However, the cost of GIDs is relatively higher compared with that of the modified TE, and the financial burden was larger for most patients. Whether the above research conclusions were generally applicable to the Chinese population and the clinical efficacy and safety of GIDs for RG still needed further extensive clinical studies.

Herein, the novelty and motivation of the study is to investigate whether modified TE, AGV, and EX-PRESS shunt were generally applicable to the Chinese population. Meanwhile, we reported our experience in treating RG with modified TE, AGV, and EX-PRESS shunt and analyzed the effectiveness, safety, and success and complication rates of the three procedures.

2. Methods

2.1. Eligibility Criteria [13, 14]. The recruited subjects fulfilled the following inclusion criteria: >18 years old with

IOP > 21 mmHg; postoperative follow-up time < 6 months; IOP control without the use of systemic and local antiglaucoma drugs, and laser and surgical treatments; and drug allergies, noncompliance with antiglaucoma drug therapy, documented progression of visual field defect, and retinal nerve fiber layer (RNFL) thickness reduction. In contrast, those with (1) atrial angle structure deformity or eye tumor, (2) obvious conjunctival scars or adhesions, (3) drainage nail or drainage valve implantation, (4) uncontrolled systemic diseases and any other active eye diseases, (5) poor surgical and medical tolerance, (6) pregnancy or lactation, (7) mental diseases, and (8) serious vital organ dysfunction such as the heart, liver, and kidney were excluded.

2.2. Patients. This retrospective chart review was conducted after obtaining the approval from the Institutional Review Board of the Second Affiliated Hospital of Xi'an Medical College and was conducted in adherence with the tenets laid down in the Declaration of Helsinki. All the participants signed the informed consent. The surgical outcomes of all modified TE, AGV, and EX-PRESS shunt surgeries for RG performed between October 2012 and October 2020 were reviewed. This study enrolled 73 patients (76 eyes) meeting the inclusion criteria. In total, 38 eyes from 36 patients underwent modified TE (group A), and 20 eyes from 19

patients underwent AGV implantation (group B), and 18 eyes from 18 patients received EX-PRESS shunt surgery (group C).

2.3. Preoperative Evaluation. The general information of patients including age, sex, glaucoma diagnosis, and diabetes/hypertension/surgery history was collected. Before the operation, all patients received complete ophthalmological examinations, including best corrected visual acuity (BVCA, converted into logarithm of the minimal angle of resolution: logMAR), slit-lamp microscope examination, IOP measurement with Goldmann applanation tonometry, optical coherence tomography (HD-OCT 4000, ZEISS CIR-RUS, Germany) of the optic disc and RNFL, ultrasound biomicroscopy (MD-300L, Tianjin Maida Company) of the central anterior chamber depth (ACD) examination, and standard automated perimetry using the Swedish interactive threshold algorithm 30-2 (Humphrey Field Analyzer II 850, Carl Zeiss Meditec). Preoperative antiglaucoma drug use was also recorded.

2.4. Modified TE. Local anesthesia was performed with 2 mL of 2% lidocaine after ophthalmic disinfection and towel placement. A fornix- or limbus-based conjunctival flap in the nasal or supertemporal quadrant was followed by fashioning a 4 mm × 4 mm scleral flap. In all cases, 5-FU (25 g/L) was positioned under the scleral and conjunctival flaps for 5 minutes. After anterior chamber (AC) puncture of the clear corneal, viscoelastic (sodium hyaluronate 1.7%; Healon®, Bausch & Lomb Freda Inc., USA) injection was performed to maintain the anterior chamber depth (ACD). Then, TE was carried out under the scleral flap, followed by an iridectomy. After restoring the scleral flap, 10-0 nylon sutures were used to suture 1 needle at the top of each side of the flap for a fixed suture. The two adjustable suture lines were inserted through the superficial scleral, corneoscleral, and cornea at the symmetrical part on both sides of the scleral flap, so that the symmetrical adjustable suture line formed a suture barrier. The AC was formed by the injection of balanced saline, and then, fixation sutures at the top of both sides of the scleral flap were removed. A sterilized dry cotton swab was used to test the tightness of the adjusted sutures, allowing for slow aqueous humor (AH) outflow. Finally, 10-0 nylon sutures were applied for conjunctiva closure. At the end of each surgery, tobramycin dexamethasone ointment was applied for the control of local inflammation.

2.5. AGV. The conjunctival flap based on the limbus was selected under topical anesthesia with 2 mL lidocaine (2%). After sclera exposure via blunt separation of the bulbar conjunctiva and subconjunctival tissues, 5-FU (25 g/L) was placed under the conjunctival flap for 5 minutes. Prior to AGV implantation, normal saline injection was performed through the tail of the drain valve to ensure an unobstructed drainage tube. The drainage disk was then positioned under the separated bulbar conjunctiva and secured on the sclera with sutures. A scleral tunnel 4 mm posterior to the limbus was established with a No. 7 needle, through which the tube was inserted parallel to the AC. Tube positioning and bulbar

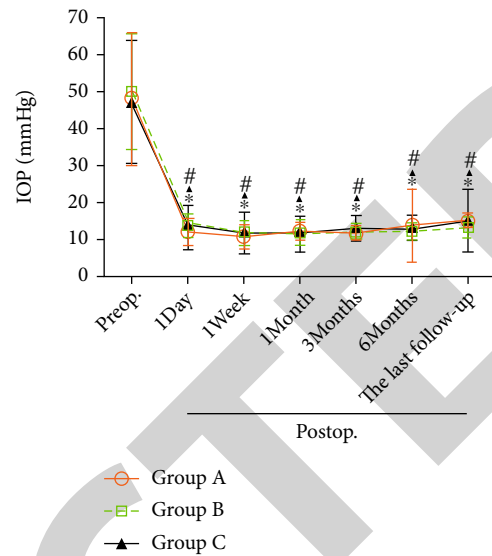


FIGURE 3: IOP of the study patients in the modified trabeculectomy, AGV, and EX-PRESS groups before surgery and 1 day, 1 week, 1 month, 3 months, 6 months, and the last follow-up after surgery. IOP of the study patients in the three groups declined dramatically after surgery ($*P < 0.001$ vs. before surgery in group A; $\Delta P < 0.001$ vs. before surgery in group B; $\#P < 0.001$ vs. before surgery in group C). Group A: modified trabeculectomy group; Group B: AGV group; Group C: EX-PRESS group; preop.: preoperative; postop.: postoperative.

conjunctiva closure were performed using 7-0 absorbable sutures and 10-0 nylon sutures, respectively. At the end of each surgery, tobramycin dexamethasone ointment was applied for the control of local inflammation.

2.6. EX-PRESS Shunt. The limbus-based conjunctival flap was selected under topical anesthesia with 2 mL lidocaine (2%). After preparing a dome-based conjunctival flap (diameter: 3 × 4 mm, thickness: 1/2 of scleral flap), 5-FU (25 g/L) was placed under it for 5 minutes. After penetrating the AC with a No. 7 needle from the scleral flap corneal limbus parallel to the iris surface, a viscoelastic material was injected, followed by the implantation of an EX-PRESS P-50/P-200 drainage device. The scleral flap and the bulbar conjunctiva were restored and fixed using a 10-0 suture. At the end of each surgery, tobramycin dexamethasone ointment was applied for the control of local inflammation.

2.7. Postoperative Follow-Up. Postoperative data including IOP, BCVA, use of antiglaucoma medications, filter bubble morphology, ACD, success rate, and postoperative complications were recorded and statistically analyzed on days 1 and 7, as well as 1, 3, and 6 months postoperatively, until the final follow-up visit.

The surgical outcome was assessed [15]. Complete success was defined as an IOP within the range of 5-21 mmHg and no postoperative application of adjuvant drugs. Qualified success was defined as an IOP within the range of 6-21 mmHg but with antiglaucoma drugs. And failure was indicated in the presence of poorly controlled IOP, use of

TABLE 6: IOP changes (between preoperative and postoperative values and % reduction from preoperative values) in the three groups (mmHg, mean \pm SD).

Postoperative date	Group A ($n = 38$)	Group B ($n = 20$)	Group C ($n = 18$)	P
1 day				
IOP, difference	35.44 \pm 17.76	35.85 \pm 15.80	33.56 \pm 16.64	0.943
% reduction	69.27 \pm 18.60	67.81 \pm 17.99	68.85 \pm 15.07	0.958
1 week				
IOP, difference	36.68 \pm 17.95	37.80 \pm 15.05	34.89 \pm 17.64	0.913
% reduction	71.99 \pm 18.67	73.22 \pm 13.45	71.40 \pm 15.81	0.953
1 month				
IOP, difference	35.05 \pm 16.88	37.60 \pm 15.05	35.22 \pm 15.81	0.845
% reduction	68.91 \pm 17.18	72.48 \pm 14.50	73.44 \pm 12.55	0.603
3 months				
IOP, difference	35.66 \pm 17.33	37.65 \pm 14.91	33.67 \pm 15.12	0.818
% reduction	69.78 \pm 17.81	72.93 \pm 12.01	69.82 \pm 9.91	0.749
6 months				
IOP, difference	33.47 \pm 20.71	37.15 \pm 15.77	33.56 \pm 16.19	0.765
% reduction	63.68 \pm 31.68	70.62 \pm 16.61	68.83 \pm 11.33	0.603
The last follow-up				
IOP, difference	32.29 \pm 17.58	36.30 \pm 14.98	31.67 \pm 15.90	0.648
% reduction	60.88 \pm 22.79	69.76 \pm 13.54	65.87 \pm 15.36	0.259

Group A: modified trabeculectomy group; Group B: AGV group; Group C: EX-PRESS group.

antiglaucoma drugs, need of another antiglaucoma surgery, IOP < 6 mmHg for ≥ 2 months, serious complications (retinal detachment, endophthalmitis, severe choroidal detachment, malignant glaucoma, etc.), loss of light perception, or atrophy of the eyeball.

2.8. Statistical Processing. Statistical analysis was conducted via SPSS 20.0 (SPSS, Inc., Chicago, IL, USA). The categorical variables were described in percentages and frequencies. Chi-square (χ^2) test or Fischer's exact test was performed for them. Intergroup comparisons of continuous variables represented by mean \pm standard deviation (SD) employed independent sample t -test, whereas intragroup comparisons adopted the independent sample t -test or paired sample t -test. One-way ANOVA was used for the difference values between groups, followed by the Bonferroni post hoc test. The correlation between the preoperative and the postoperative IOP decline was analyzed by Pearson correlation. Analysis of complete success used the Kaplan–Meier survival analysis. Significant differences were assumed at $P < 0.05$.

3. Results

3.1. General Conditions. This study enrolled 73 patients (76 eyes) meeting the inclusion criteria. In total, 38 eyes from 36 patients underwent modified TE (group A), 20 eyes from 19 patients underwent AGV implantation (group B), and 18 eyes from 18 patients received EX-PRESS shunt surgery (group C) (Figure 1). Patients' preoperative demographic and ocular characteristics can be found in Table 1. Patients

were of mean age of 55 ± 15.17 , 47.3 ± 16.77 , and 49.33 ± 15.97 years for modified TE, AGV, and EX-PRESS glaucoma shunt, respectively. The mean follow-up periods were 29.89 ± 24.80 months (range, 6-93 months), 56.30 ± 39.42 months (range, 6-97 months), and 26.00 ± 12.25 months (range, 6-45 months), and significant differences were observed between the follow-up times ($P = 0.001$). The three cohorts were age- ($P = 0.190$), gender- ($P = 0.235$), and laterality-matched ($P = 0.653$), showing no statistical difference. Nor were there any obvious difference in IOP, BCVA, number of antiglaucoma medications used, and ACD before operation among the three groups ($P > 0.05$).

3.2. Etiology of RG. The RG in the study included NVG; failed filtration surgery; iridocorneal endothelial syndrome (ICES); pigmentary glaucoma (PG); juvenile glaucoma and secondary glaucoma, such as glaucoma secondary to chemical burn; postpenetrating keratoplasty glaucoma (PKG); uveitic glaucoma (UG); glaucoma after intraocular surgery; and glaucoma secondary to trauma and steroid-induced glaucoma. Among them, NVG (34.24%), failed filtration surgery (11.84%), glaucoma secondary to trauma (11.84%), and PKG (9.21%) were the main causes. The most prevalent type of RG was NVG (31.58%, 45%) in the modified TE group and AGV group. The most prevalent type of glaucoma was glaucoma secondary to trauma (27.78%) and NGV (27.78%) (Table 2).

We divided RG into I and II categories according to the etiology of glaucoma. Primary glaucoma including filtration surgery failed, and juvenile glaucoma is classified as category

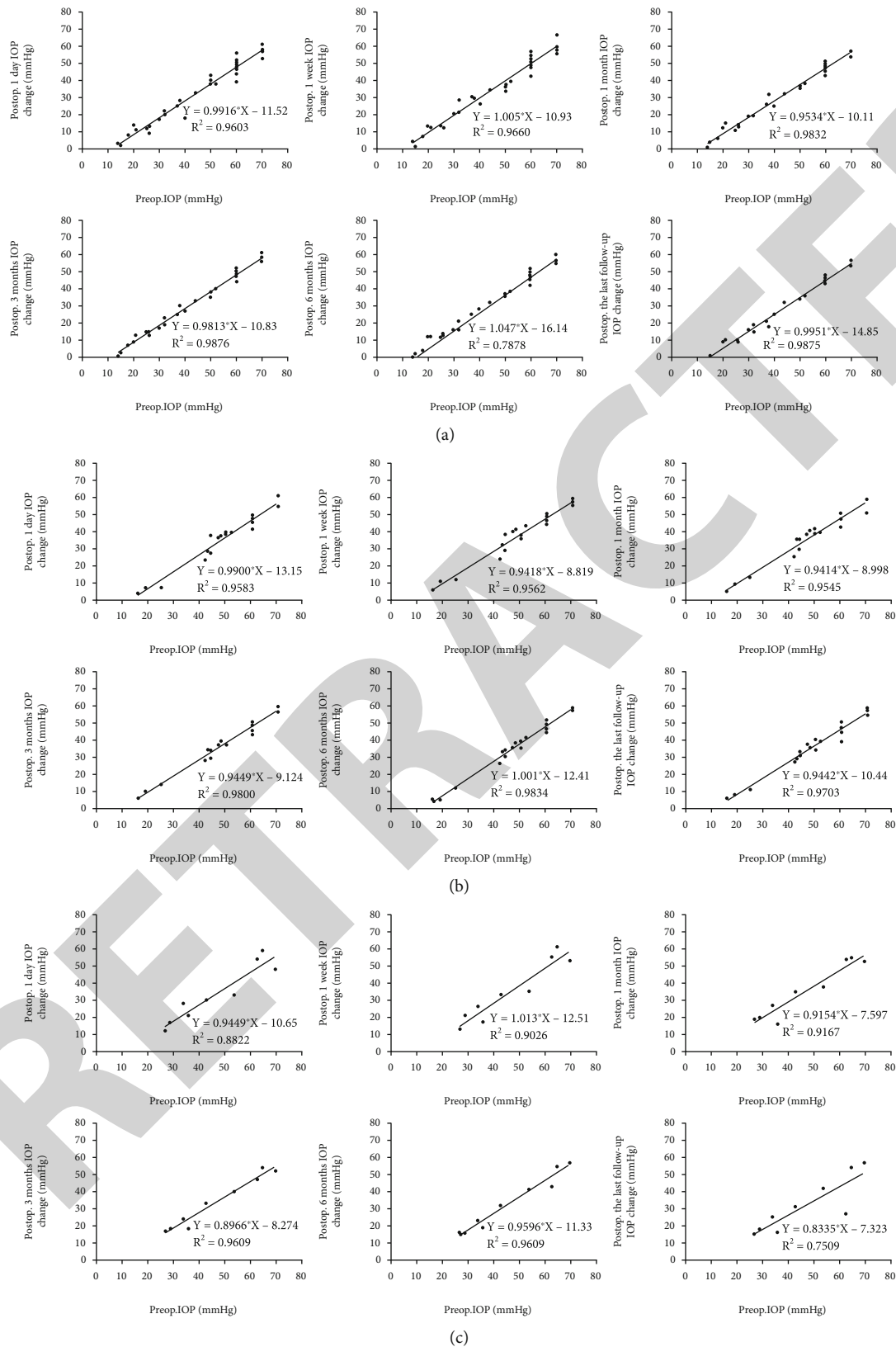


FIGURE 4: Pearson correlation analysis of postoperative IOP decline at 1 day, 1 week, 1 month, 3 months, 6 months, and the last follow-up and preoperative IOP. The R values of the three groups at different follow-up times ranged from 0.867 to 0.992, and there was significant correlation between the drop in IOP after operation in different follow-up times and preoperative IOP in the three groups: (a) modified trabeculectomy group; (b) AGV group; (c) EX-PRESS group. preop.: preoperative; postop.: postoperative.

I. Secondary glaucoma is classified as category IIa, and NVG is classified as category IIb. Fisher probabilities were used to analyze the etiological classification of patients in the three groups, and there was no statistical significance in the results ($P = 0.555$) (Table 3).

3.3. Comparisons of BCVA in the Three Groups. In the modified TE group, the BCVA was 2.15 ± 0.82 logMAR at baseline, which was then changed to 2.17 ± 0.13 logMAR at day 1, 2.12 ± 0.80 logMAR at day 7, 2.06 ± 0.13 logMAR at 1 month, 2.03 ± 0.13 logMAR at 3 months, 2.00 ± 0.81 logMAR at 6 months, and 1.99 ± 0.13 logMAR at the end of follow-up. And BCVA reduction was observed in 3 eyes (7.87%) at day 1, day 7, and 1 month and 4 eyes (10.53%) at 3 months, 6 months, and the last follow-up. No marked difference was found in postoperative BCVA at different periods compared with the baseline ($P > 0.05$) (Figure 2, Table 4). In the AGV group, preoperative BCVA was 2.07 ± 0.21 logMAR and postoperative BCVA was 2.45 ± 0.16 logMAR at 1 day, 2.09 ± 0.19 logMAR at 1 week, 2.10 ± 0.19 logMAR at 1 month, 2.04 ± 0.21 logMAR at 3 months, 2.02 ± 0.21 logMAR at 6 months, and 2.04 ± 0.21 logMAR at the last follow-up. And BCVA reduction was observed in 5 eyes (25%) at day 1, 3 eyes (15%) at day 7, 2 eyes (10%) at 1 month and 3 months, 1 eyes (5%) at 6 months, and 2 eyes (10%) at the last follow-up. The BCVA at different postoperative periods showed no marked difference in comparison with the baseline ($P > 0.05$) (Figure 2, Table 4). In the EX-PRESS group, the BCVA was 1.51 ± 0.30 logMAR preoperatively, while postoperatively, it was 1.36 ± 0.28 logMAR at day 1, 1.26 ± 0.93 logMAR at day 7, 1.25 ± 0.31 logMAR at 1 month, 1.19 ± 0.30 logMAR at 3 months, 1.18 ± 0.3 logMAR at 6 months, and 1.13 ± 0.30 logMAR at the last follow-up. And BCVA reduction was observed in 1 eye (5.56%) at day 1, day 7, 1 month, 3 months, and 6 months and 2 eyes (11.11%) at the last follow-up. The BCVA at different postoperative periods showed no marked difference in comparison with the baseline ($P > 0.05$) (Figure 2, Table 4).

We also compared the difference in BCVA between preoperative and postoperative values in the three groups during the same period. The BCVA of the EX-PRESS group at day 1, day 7, 1 month, 6 months, and the last follow-up after surgery were all higher than those of the other two groups at the same period after operation. However, the three groups presented no marked difference in BCVA changes in the same period ($P > 0.05$) (Table 5).

3.4. Comparative Analysis of IOP. In the modified TE group, the preoperative IOP was 47.37 ± 17.55 mmHg. This was reduced to 11.92 ± 3.54 mmHg at 1 day, 10.68 ± 3.31 mmHg at 1 week, 12.32 ± 2.34 mmHg at 1 month, 11.71 ± 1.96 mmHg at 3 months, 13.89 ± 9.58 mmHg at 6 months, and 15.08 ± 1.96 mmHg at the last follow-up ($*P < 0.001$). In the AGV group, the preoperative IOP was 49.50 ± 15.63 mmHg. This was reduced to 13.65 ± 3.32 mmHg at 1 day, 11.70 ± 3.38 mmHg at 1 week, 11.90 ± 3.34 mmHg at 1 month, 11.85 ± 2.28 mmHg at 3 months, 12.35 ± 2.03 mmHg at 6 months, and 13.20 ± 2.73 mmHg at the last

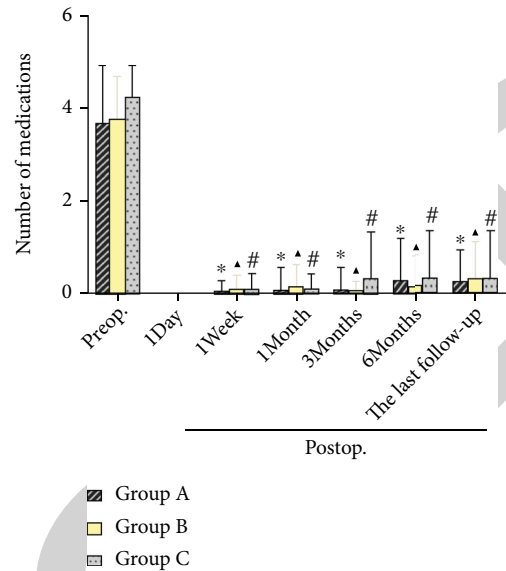


FIGURE 5: Mean number of antiglaucoma medications before surgery and during follow-up time. The number of medications of patients in the three groups was dramatically decreased after surgery ($*P < 0.001$ vs. before surgery in group A; $\Delta P < 0.001$ vs. before surgery in group B; $\#P < 0.05$ vs. before surgery in group C). Group A: modified trabeculectomy group; Group B: AGV group; Group C: EX-PRESS group; preop.: preoperative; postop.: postoperative.

follow-up ($\Delta P < 0.001$). The IOP of the EX-PRESS group before surgery was 41.22 ± 20.66 mmHg. This was reduced to 13.22 ± 5.78 mmHg at 1 day, 13.87 ± 9.92 mmHg at 1 week, 11.56 ± 4.77 mmHg at 1 month, 13.11 ± 3.44 mmHg at 3 months, 12.89 ± 2.98 mmHg at 6 months, and 14.22 ± 8.24 mmHg at the last follow-up ($\#P < 0.001$) (Figure 3).

Postoperative IOP changes are shown in Table 6. The percentage reduction of IOP in the three groups during different follow-up times was more than 60%. However, the three cohorts showed no distinct difference in IOP change and percentage change at each follow-up visit ($P > 0.05$). Pearson correlation analysis was performed between postoperative IOP decline and preoperative IOP (Figure 4). The R values ranged from 0.867 to 0.992 in the three cohorts at different follow-ups, with statistical significance ($P < 0.001$). The results showed the presence of a close connection between IOP decrease at different postoperative follow-ups and preoperative IOP in the three groups.

3.5. Application of Antiglaucoma Medications before and after Operation. In the modified TE group, the quantity of antiglaucoma drugs used was 3.66 ± 1.24 medications at baseline, which was decreased to 0.00 ± 0.00 at day 1, 0.05 ± 0.23 at day 7, 0.08 ± 0.49 at 1 month, 0.08 ± 0.49 at 3 months, 0.29 ± 0.89 at 6 months, and 0.24 ± 0.68 at the last follow-up. The quantity of antiglaucoma medications used in the AGV group decreased from 3.75 ± 0.91 medications at baseline to 0.00 ± 0.00 at day 1, 0.10 ± 0.31 at day 7, 0.15 ± 0.49 at 1 month, 0.05 ± 0.22 at 3 months, 0.15 ± 0.67 at 6 months, and 0.30 ± 0.80 at the last follow-up. In EX-PRESS group, the quantity of antiglaucoma medications

TABLE 7: Number of antiglaucoma medication changes (between preoperative and postoperative values and % reduction from preoperative values) in the three groups.

Postoperative date	Group A (n = 38)	Group B (n = 20)	Group C (n = 18)	P
1 day				
No. of med difference (mean ± SD)	3.66 ± 1.24	3.75 ± 0.91	4.22 ± 0.67	0.381
% reduction	100%	100%	100%	
1 week				
No. of med difference (mean ± SD)	3.60 ± 1.24	3.75 ± 0.91	4.22 ± 0.67	0.319
% reduction	98.36%	100%	100%	
1 month				
No. of med difference (mean ± SD)	3.58 ± 1.43	3.65 ± 0.99	4.11 ± 1.60	0.507
% reduction	97.81%	97.33%	97.39%	
3 months				
No. of med difference (mean ± SD)	3.58 ± 1.43	3.60 ± 1.09	4.11 ± 1.60	0.509
% reduction	97.81%	96.00%	97.39%	
6 months				
No. of med difference (mean ± SD)	3.36 ± 1.60	3.70 ± 0.92	3.89 ± 0.93	0.481
% reduction	91.80%	98.67%	92.18%	
The last follow-up				
No. of med difference (mean ± SD)	3.34 ± 1.58	3.60 ± 1.35	3.89 ± 0.93	0.553
% reduction	91.26%	96.00%	92.18%	

Group A: modified trabeculectomy group; Group B: AGV group; Group C: EX-PRESS group.

applied was decreased from 4.22 ± 0.67 to 0.00 ± 0.00 at day 1, 0.11 ± 0.33 at day 7, 0.11 ± 0.33 at 1 month, 0.33 ± 1.00 at 3 months, 0.33 ± 1.00 at 6 months, and 0.33 ± 1.00 at the end follow-up. Compared with preoperative medications, a statistical reduction in the quantity of antiglaucoma medications used was observed in the three cohorts at each postoperative follow-up (* $P < 0.001$, $\Delta P < 0.001$, and $\#P < 0.05$) (Figure 5, Table 7).

As shown in Table 5, the differences of the quantity of antiglaucoma drugs used (between preoperative and postoperative values) and percentage reduction in each group at the same follow-up time were compared, and we found that there were no significant differences ($P > 0.05$).

3.6. Comparison of Anterior Chamber Depth (ACD). At 6 months after operation, the ACD was increased from 2.35 ± 0.93 mm to 2.83 ± 0.67 mm in the modified TE group, from 2.68 ± 0.18 mm to 3.15 ± 0.23 mm in the AGV group, and from 3.26 ± 1.01 mm to 3.57 ± 0.48 mm in the EX-PRESS group. However, the degree of postoperative ACD deepening in the AGV group was more significant ($P < 0.05$) (Figure 6).

3.7. Postoperative Follicular Conditions. The Kronfeld scale was used to evaluate the follicular function [16]: I, microcystic type; II, diffuse flat type; III, scar type; and IV, package type (Figure 7). Types I and II were thought to be functional follicles; types III and IV were considered as nonfunctional follicles. The proportion of functional follicles in the three groups at different follow-up times after surgery is shown in Table 8. At 6 months after operation, the proportion of

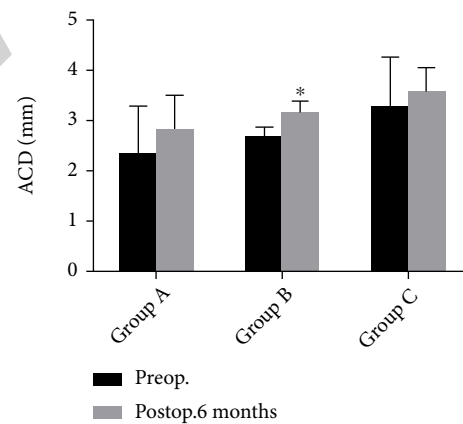


FIGURE 6: The anterior chamber depth (ACD) before surgery and at 6 months after surgery. The postoperative ACD in the three groups was deeper than that before operation. However, the postoperative ACD in the AGV group increased significantly ($P < 0.05$ vs. before surgery). Group A: modified trabeculectomy group; Group B: AGV group; Group C: EX-PRESS group; preop.: preoperative; postop.: postoperative. * $P < 0.05$ vs. preoperative.

functional follicles in the modified TE, AGV, and EX-PRESS groups was 97.37%, 95%, and 88.89%, respectively. At the last follow-up, the proportion of functional follicles was 97.37%, 95%, 88.89%, respectively, in the three groups. The three cohorts showed no evident difference in the proportion of functional follicles at different follow-ups.

3.8. Success Rate. See Figure 8 for the comparison of success rate among the three cohorts. In the modified TE group, the complete success rate was 97.37% at 3 months, 89.47% at 6

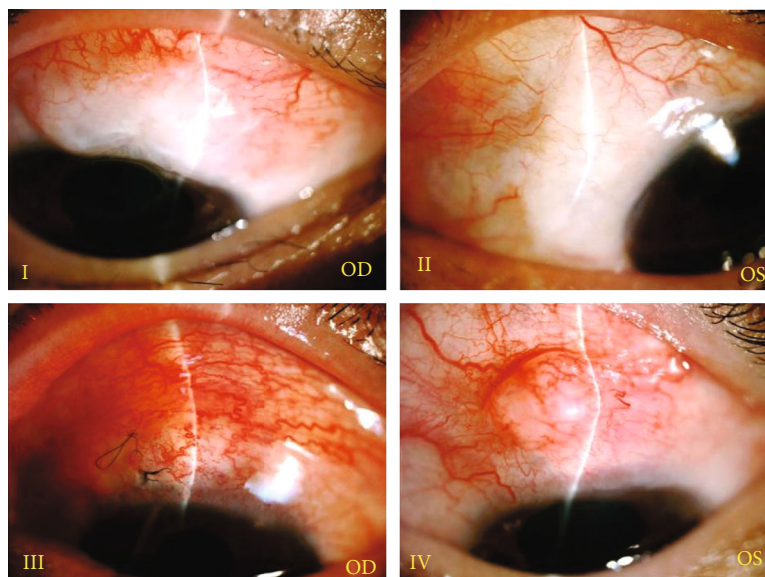


FIGURE 7: The different types of filtration bubbles after operation. The Kronfeld scale was used to evaluate the follicular function—I: microcystic type; II: diffuse flat type; III: scar type; IV: package type. I and II types were considered as functional follicles; III and IV types were defined as nonfunctional follicles.

TABLE 8: Postoperative functional follicular in the three groups.

Postoperative date	Group A (<i>n</i> = 38)	Group B (<i>n</i> = 20)	Group C (<i>n</i> = 18)	<i>P</i>
1 day, <i>n</i> (%)	38 (100.00)	20 (100.00)	18 (100.00)	1.000
1 week, <i>n</i> (%)	38 (100.00)	20 (100.00)	18 (100.00)	1.000
1 month, <i>n</i> (%)	38 (100.00)	20 (100.00)	18 (100.00)	1.000
3 months, <i>n</i> (%)	38 (100.00)	19 (95.00)	16 (88.89)	0.344
6 months, <i>n</i> (%)	37 (97.37)	19 (95.00)	16 (88.89)	0.347
The last follow-up, <i>n</i> (%)	37 (97.37)	19 (95.00)	16 (88.89)	0.347

Group A: modified trabeculectomy group; Group B: AGV group; Group C: EX-PRESS group.

months, and 84.21% at the last follow-up, and the total success rate was 100%, 97.37%, and 94.73%, respectively. The complete success rate in the AGV group was 95% at 3 months, 90% at 6 months, and 90% at the last follow-up, with the total success rate of 100%, 100%, and 95%, respectively. In the EX-PRESS group, the complete success rate at 3 months, 6 months, and the last follow-up was 88.89%, and the total success rate was 100%, 100%, and 88.89%, respectively. The success rate of the three groups decreased to different degrees with the follow-up time, while the three cohorts showed no evident difference in complete and total success rates ($P > 0.05$) (Table 9). The complete success rates throughout the 6-month follow-up period were visualized by Kaplan–Meier survival curves (Figure 8).

3.9. Surgical Complications. Postoperative complications during and after operation were listed in Figure 9, including shallow AC (27%), hypertony (22%), scarring filtration bleb (14%), hyphema (13%), hypotony (13%), and choroidal detachment (11%). No severe complications occurred in all patients. We defined complications occurring within 1 mo after surgery as early complications and occurring more than 1 mo after surgery as late complications. Early compli-

cations included shallow anterior chamber, hyphema, hypotony, early hypertony, and choroidal detachment in the three groups. Late complications were hypertony and scarring filtration bleb. All the complications were recovered after symptomatic treatment, except for the uncontrollable IOP in one eye of the modified TE group due to scarring of the filtration bubble. The three cohorts differed insignificantly in total, early, and late complications (Table 10).

4. Discussion

RG is different from primary glaucoma. The causes of it are complex and changeable, and the pathogenesis is mixed. It is often accompanied by systemic diseases in addition to ocular manifestations. Most patients have impaired visual function and even blindness due to long-term high IOP damage to the optic nerve. In China, the number of patients with RG is about 2.2 million to 4.4 million [17]. NVG is one of the most common causes of RG, which is mainly caused by retinal ischemia and hypoxia. Studies have found that retinal ischemia can produce a large number of neovascularization-related factors in the eye [18–20], resulting in the imbalance between stimulant and inhibitory factors for angiogenesis.

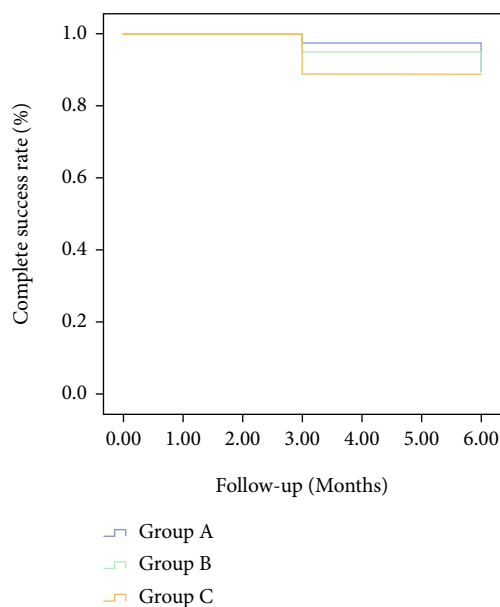


FIGURE 8: Kaplan-Meier survival curve showed that there was no statistically significant difference in complete success rate among the modified trabeculectomy group, AGV group, and EX-PRESS group at 6 months after surgery ($P > 0.05$). Group A: modified trabeculectomy group; Group B: AGV group; Group C: EX-PRESS group.

Neovascularization and neovascularization membrane are formed in the fundus iris atrium. The main mechanisms of glaucoma secondary to trauma include posttraumatic hematocele of the AC, atrial angle regression, traumatic lens dislocation, iris adhesion caused by inflammation, occlusion of the pupil membrane, or obstruction of the trabecular meshwork caused by inflammatory substances, which would lead to obstruction of AH outflow pathway [21]. Juvenile glaucoma may be due to abnormal development of the atrial angle. Abnormal structure and function of trabecular meshwork and Schlemm tube result in blocked outflow of AH and increase IOP [22]. Because of these complex etiologies and pathogenesises, different surgical methods are often used in clinical practice. They mainly include salvage surgical methods, such as TE and GDI implantation, and destructive surgical methods, such as cyclocryotherapy, cyclophotocoagulation (CPC), and cyclodynamic therapy. At present, modified TE, GDIS, ciliary body destruction, and MIGS are the most commonly used surgical options.

In this study, we treated RG patients with modified TE, AGV, and EX-PRSS. The results showed that no statistical difference was found in the composition ratio of the etiological classification of glaucoma in the three cohorts before surgery ($P > 0.05$). In the present research, NVG (34.21%) was the most common cause of RG. According to data statistics, NVG patients account for 0.7%~5.1% of the Asian glaucoma population [23], which agrees with our statistical results. Meanwhile, patients' sex and mean age were compared. Patients were slightly older in the modified TE group (55 ± 15.17 years), as compared to the AGV group (47.3 ± 16.77 years) and the EX-PRESS group

(49.33 ± 15.97 years). This may be related to the fact that the patients were younger, required less invasive surgery, and wanted to have better vision years after surgery. The surgeon recommended GDIS.

This paper investigated the safety and effectiveness of three surgical methods in treating RG. At the last follow-up, 4 eyes (10.53%) had vision reduction and 1 eye had vision loss in the modified TE group, 2 eyes (10%) had vision reduction and 1 eye had vision loss in the AGV group, and 2 eyes (11.11%) had vision loss in the EX-PRESS group. Post-operative visual loss may be due to the following reasons: (1) the IOP was not controlled below the target value after surgery, and the optic nerve was still damaged. (2) Most of patients who were middle-aged and elderly may have cataracts before surgery, and surgery may accelerate the progression of cataracts, leading to loss of vision. Besides, we compared the mean postoperative BCVA and found no marked difference among the three cohorts at different follow-ups and before surgery. And the BCVA difference in preoperative and postoperative values was not significant among the three cohorts at different follow-ups. However, the BCVA of the EX-PRESS group was slightly improved compared with the AGV and the modified TE groups. This may be related to the difference of patient selection. Preoperative diagnosis found that patients in the EX-PRESS group mainly had secondary glaucoma (IIa, 61.11%), who had less optic nerve damage and better visual acuity before surgery. The primary glaucoma (I, filtration surgery and juvenile glaucoma) and NVG (IIb) were the main diagnosis in the AGV and modified TE groups. Patients with both types of glaucoma have more damage to the optic nerve. In addition, patients with NVG were often accompanied by fundus lesions, such as diabetic retinopathy and macular edema, which led to poor preoperative visual acuity. Due to the good IOP control in the three groups after surgery, the BCVA improvement was relatively better in the EX-PRESS group.

The IOP of all patients at different postoperative follow-ups decreased significantly compared with that before surgery, with a decrease rate of more than 60%. The higher the patient's IOP before surgery, the greater the decrease of postoperative IOP. These results indicated that the three surgical methods could significantly reduce IOP and decrease antiglaucoma drug use in all RG patients. Some studies have also obtained similar results [13, 24]. However, the three cohorts differed insignificantly in the decrease range and rate of IOP at different follow-ups. The result indicated that the three surgical methods had similar effects on controlling IOP in patients with RG. However, AGV and EX-PRESS were slightly better than modified TE in IOP control only at 6 months and the last follow-up after surgery. The better IOP control in the AGV and EX-PRESS groups may be attributed to the mechanism of reducing IOP. The primary purpose of both EX-PRESS and TE that are follicle-dependent surgeries is to drain the AH into the subconjunctival space. The amplitude of descending IOP is related to the status and function of the filtration bubble. EX-PRESS has a certain controllability and predictability for the outflow of AH. In addition, it has good biocompatibility, which can reduce the postoperative inflammatory response of patients

TABLE 9: Success rate in the three groups.

	Group A (<i>n</i> = 38)	Group B (<i>n</i> = 20)	Group C (<i>n</i> = 18)	<i>P</i>
3 months, success rate, <i>n</i> (%)				
Total	38 (100)	20 (100)	18 (100)	1.000
Complete	37 (97.37)	19 (95.00)	16 (88.89)	0.347
Qualified	1 (2.63)	1 (5.00)	2 (11.11)	
Failure	0 (0.00)	0 (0.00)	0 (0.00)	
6 months, success rate, <i>n</i> (%)				
Total	37 (97.37)	20 (100)	18 (100)	1.000
Complete	34 (89.47)	18 (90.00)	16 (88.89)	1.000
Qualified	3 (7.89)	2 (10.00)	2 (11.11)	
Failure	1 (2.63)	0 (0.00)	0 (0.00)	
The last follow-up, success rate, <i>n</i> (%)				
Total	36 (94.73)	19 (95.00)	16 (88.89)	0.705
Complete	32 (84.21)	18 (90.00)	16 (88.89)	0.908
Qualified	4 (10.53)	1 (5.00)	0 (0.00)	
Failure	2 (5.26)	1 (5.00)	2 (11.11)	

Group A: modified trabeculectomy group; Group B: AGV group; Group C: EX-PRESS group.

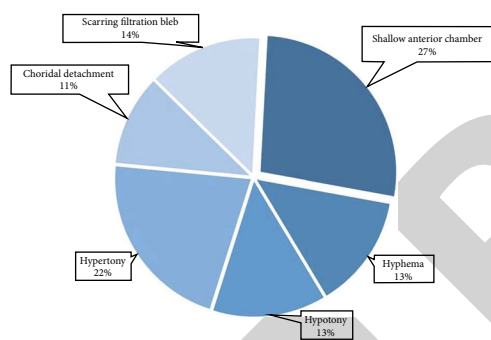


FIGURE 9: Postoperative complications during and after operation. The complications included shallow anterior chamber, hypertony, scarring filtration bleb, hypyema, hypotony, and choroidal detachment at the end of follow-up.

and the probability of scarring of the filter aisle [25]. AGV is postfiltered, which drains the AH to the back of Tenon's capsule and is absorbed by the vessels and lymphatics of the intraocular vein, and it does not significantly block the outflow of AH. However, the decrease of IOP in the three groups was basically the same in the early postoperative period, which is possibly related to the early adjustment of sutures, massage filtration bubble, and proportion of the functional filtration bubble in the modified TE group. Other studies have suggested that AGV and EX-PRESS have similar efficacy on RG, but EX-PRESS had a better control of postoperative IOP than AGV [14]. It may be related to the differences in types of RG cases and the number of samples between groups.

Our research showed no significant differences in the complete and total success rates among the three groups at the last follow-up ($P > 0.05$); however, the total success rates of the modified TE and AGV groups were slightly higher than that of the EX-PRESS group. Because of the frequent

scarring of the filtration bubble after routine filtration surgery for RG, the success rate of the surgery is about 11%~52% [5, 6]. An obviously higher success rate of modified TE compared with traditional TE was determined in this study. This may be related to the modified surgical methods. We used bilateral symmetrical adjustable sutures through the cornea, keratosis margin, and sclera and no fixed scleral flap sutures. We observed during the operation that bilateral symmetrical adjustable sutures could completely prevent the outflow of AH, thus avoiding ocular hypotony and flat AC caused by the excessive outflow of AH in the early postoperative scleral flap without fixed sutures. In the middle and late postoperative periods, we reduced the resistance of the outflow of AH in the filter channel and increased the outflow of AH by removing the adjustable sutures to prevent scar formation of the filtration bubble. Therefore, the modified TE group in this study had a high ratio of the postoperative functional filtration bubble (97.37%) and a high success rate of surgery. In addition, patients with RG generally had poor preoperative ocular surface conditions, and some patients had a history of multiple surgeries or medications. Because of these reasons, the traditional TE was prone to scarring of the filtration bubble, and the failure rate of surgery was greatly increased (48%~89%) [5, 6].

Waisbourd et al.'s study [26] found that the cumulative success rate was about 83.9% in the EX-PRESS group and 75.8% in the AGV group over 4.5 years after surgery in 57 patients with RG, showing no statistical difference between groups. In the present research, a basically similar success rate of the EX-PRESS group while a much higher success rate of the AGV group was determined. Meanwhile, foreign literature has reported a total success rate of about 70% in controlling IOP by AGV. The reason may be related to the characteristics of the included cases. The majority of patients included in this study was NVG and had a poor prognosis after traditional filtration, with a success rate of only 11%

TABLE 10: Postoperative complications in all patients.

	Group A (<i>n</i> = 38) (%)	Group B (<i>n</i> = 20) (%)	Group C (<i>n</i> = 18) (%)	<i>P</i>
Total postop. complications	13 (34.21)	7 (35.00)	8 (44.44)	0.745
Early postop. complications	11 (28.95)	6 (30.00)	6 (33.33)	0.945
Shallow anterior chamber	4 (10.53)	4 (20.00)	2 (11.11)	0.611
Hyphemia	1 (2.63)	3 (15.00)	1 (5.56)	0.177
Hypotony	4 (10.53)	0 (0.00)	1 (5.56)	0.422
Early hypertony	0 (0.00)	1 (5.00)	2 (11.11)	0.071
Choroidal detachment	3 (7.89)	0 (0.00)	1 (5.56)	0.671
Late postop. complications	2 (5.26)	1 (5.00)	2 (11.11)	0.705
Hypertony	2 (5.26)	1 (5.00)	2 (11.11)	0.705
Scarring filtration bleb	2 (5.26)	1 (5.00)	2 (11.11)	0.705

Group A: modified trabeculectomy group; Group B: AGV group; Group C: EX-PRESS group.

to 33% [27]. It has also been pointed out that glaucoma drainage valves can rapidly reduce IOP in NVG patients, but the postoperative effect is not as good as other glaucoma types [28]. Foreign studies have also shown that the success rate after modified TE for NVG patients is only about 62.6% at 1 year after surgery [29]. However, all NVG patients included in this study were treated with anti-VEGF before surgery and antimetabolic medications during surgery, and the systemic disease and other factors causing NVG were actively controlled after surgery. These procedures improved the efficacy of the AGV group, as well as the modified TE and EX-PRESS groups.

The three cohorts differed insignificantly in the incidence of complications ($P > 0.05$). The shallow AC was a common complication in the early filtration surgery and was usually associated with strong postoperative filtration, choroidal detachment, and filtration bubble leakage [30]. High IOP of the shallow AC may also occur. Previous studies have reported that the incidence of shallow AC after glaucoma filtration was 2% to 41% [31]. In this study, the incidence of shallow AC was found to be 10.53%, 20%, and 11.11% in the modified TE group, AGV group, and EX-PRESS group, respectively. The shallow AC was caused by strong filtration. Excluding 1 eye with AC puncture, the AC of 9 eyes was recovered after conservative treatment. Meanwhile, we also measured ACD at 6 months after surgery and found that the postoperative ACD of the AGV group was statistically deeper versus the preoperative ACD. The result was consistent with the decrease of IOP in the group. The reason may be that when the ACD is normal, the AH circulation is normal, thus reducing the IOP [32]. The results were consistent with those of some domestic scholars [33].

In this study, the incidence of hyphemia was 2.63% in the modified TE group, 15% in the AGV group, and 5.56% in the EX-PRESS group. All patients' injuries were caused by rupture of iris neovascularization, and hemostasis was absorbed after symptomatic treatment. We analyzed the causes of postoperative hyphemia: (1) bleeding from the wound caused by resection of trabeculae and iris tissue during surgery and (2) preoperative IOP was not controlled, resulting in hyperemia of the eyeball. After incision of the

AC, the sudden decrease of IOP caused the rupture of capillaries in the eye, resulting in bleeding. (3) The ciliary body was damaged. (4) Iris neovascularization did not completely recede after anti-VEGF therapy in NVG patients, and the rupture of neovascularization resulted in hyphemia. Some studies have found that when patients were given anti-VEGF therapy 6-8 days before TE, only the neovascularization on the surface of the iris was reduced, and the vessels in the stromal layer still existed. The risk of hyphemia after surgery could not be greatly decreased. However, anti-VEGF therapy was given at 10 ± 11 days before surgery, and the risk of hyphemia was significantly decreased [34]. Hyphemia is considered to be the most common complication of antiglaucoma surgery for NVG patients, with an incidence of 34.3%-63% [35].

Hypotony is also a common complication. It usually occurs in conjunction with choroidal detachment and may also be associated with antimetabolic medications, strong filtration, filtration bubble wrapping, and inflammatory reactions [32, 36]. The incidence of hypotony in this study was 4 eyes (10.53%) and 1 eye (5.56%) in the modified TE group and the EX-PRESS group, respectively. Choroidal detachment was observed in 4 eyes, except for 1 eye which was considered to be related to strong filtration. Studies have found that persistent hypotony can cause idiopathic hypotony maculopathy [37]. The choroid of all patients with hypotony was recovered, and IOP returned to normal after conservative treatment. It has been reported that the incidence of hypotony after glaucoma filtration was only 1.6%~12.4% in clinical trials [38, 39] and 7.2%~42.2% in observational studies [36, 40, 41]. Hypertony after glaucoma filtration may be related to inflammatory reaction, hyphemia, malignant glaucoma, and encapsulation or scarring of filter bubbles. In this study, hypertony occurred in both the early and late postoperative periods. The incidence of early hypertony was 5% in the AGV group and 11.11% in the EX-PRESS group. In the modified TE group, 1 eye was found to have uncontrollable hypertony due to filtration bleb scarring, so modified TE was performed again to control IOP. There was 1 eye each with filter bubble wrapping in the modified TE group and the AGV group, while 2 eyes in the EX-PRESS group. All patients with filter bubble

wrapping had hypertony. At present, scarring of filtration bleb was widely considered to be an important cause of failure in glaucoma filtration surgery. The medications, such as 5-FU or MMC, were used intraoperatively and postoperatively to effectively reduce the rate of scarring formation of filtration bubbles. Zhou et al. [7] observed the surgical effect of the MCC treatment of drainage valve implantation and found statistically less fibrosis of the filtration bubble in the treatment group (2.6%) compared with the untreated group (19.5%). Cui et al. [42] also retrospectively analyzed 50 patients who underwent drainage valve implantation and found an obviously higher success rate in the treatment group with antimetabolic medications compared with the untreated group (86% vs. 58%). We also used 5-FU during the operation, and all patients of NVG were treated with anti-VEGF medications before operation. The chance of the filtration bubble scar was reduced, and the success rate of the operation was improved.

5. Conclusion

In conclusion, the modified TE can validly reduce IOP in RG patients, decrease antiglaucoma drug use, significantly improve the success rate of traditional TE, and reduce the incidence of postoperative complications. The operative effect was comparable to AGV and EX-PRESS implantation. However, the cost of modified TE was lower than that of the other two surgical methods, and the modified TE should be promoted. Due to the complicated etiology of these patients, a reasonable surgical method must be selected according to the specific situation of the patients. The present study has some limitations. First, the small sample size may limit the identification of differences in values. Second, the duration of observation is not long enough. Therefore, the efficacy and safety of the three surgical methods for RG patients need to be further demonstrated by long-term observation and a larger sample size study.

Data Availability

The simulation experiment data used to support the findings of this study are available from the corresponding author upon request.

Conflicts of Interest

The authors declare no competing interests.

Authors' Contributions

Yuan He, Beilei He, and Zhi Ji contributed equally to this work.

Acknowledgments

This study was supported by the National Natural Science Foundation of China (Nos. 81770929 and 82070964), Shaanxi Provincial Education Department Service for Local Scientific Research Program 2018 (No. 18JC026), Shaanxi Provincial Science and Technology Agency Project (No. 2019SF-162),

Shaanxi Provincial Department of Education Project (No. 19JK0758), and Xi'an Science and Technology Bureau Project (No. 2019114613YX001SF041-(3)).

References

- [1] A. K. Schuster, C. Erb, E. M. Hoffmann, T. Dietlein, and N. Pfeiffer, "The diagnosis and treatment of glaucoma," *Deutsches Ärzteblatt International*, vol. 117, no. 13, article 225, 2020.
- [2] M. C. Leske, A. Heijl, M. Hussein et al., "Factors for glaucoma progression and the effect of treatment: the early manifest glaucoma trial," *Archives of Ophthalmology*, vol. 121, pp. 48–56, 2003.
- [3] C. K. Lee, K. T. Ma, Y. J. Hong, and C. Y. Kim, "Long-term clinical outcomes of Ahmed valve implantation in patients with refractory glaucoma," *PLoS One*, vol. 12, article e0187533, 2017.
- [4] J. Cairns, "Trabeculectomy: preliminary report of a new method," *American Journal of Ophthalmology*, vol. 66, pp. 673–679, 1968.
- [5] E. Ansari, "An update on implants for minimally invasive glaucoma surgery (MIGS)," *Ophthalmology and therapy*, vol. 6, pp. 233–241, 2017.
- [6] M. M. Bikbov and I. I. Khusnitdinov, "The results of the use of Ahmed valve in refractory glaucoma surgery," *Journal of Current Glaucoma Practice*, vol. 9, article 86, 2015.
- [7] M. Zhou, W. Wang, W. Huang, and X. Zhang, "Use of mitomycin c to reduce the incidence of encapsulated cysts following Ahmed glaucoma valve implantation in refractory glaucoma patients: a new technique," *BMC Ophthalmology*, vol. 14, pp. 1–7, 2014.
- [8] H. Saheb, S. J. Gedde, J. C. Schiffman, W. J. Feuer, and Tube Versus Trabeculectomy Study Group, "Outcomes of glaucoma reoperations in the tube versus trabeculectomy (TVT) study," *American Journal of Ophthalmology*, vol. 157, pp. 1179–1189, 2014.
- [9] W. Wang, M. Zhou, W. Huang, and X. Zhang, "Ex-PRESS implantation versus trabeculectomy in uncontrolled glaucoma: a meta-analysis," *PLoS One*, vol. 8, article e63591, 2013.
- [10] W. Wang and X. Zhang, "Meta-analysis of randomized controlled trials comparing Ex-PRESS implantation with trabeculectomy for open-angle glaucoma," *PLoS One*, vol. 9, article e100578, 2014.
- [11] L. de Jong, A. Lafuma, A. S. Aguadé, and G. Berdeaux, "Five-year extension of a clinical trial comparing the EX-PRESS glaucoma filtration device and trabeculectomy in primary open-angle glaucoma," *Clinical Ophthalmology (Auckland, NZ)*, vol. 5, article 527, 2011.
- [12] M. Zhang, B. Li, and Y. Sun, "EX-PRESS and Ahmed glaucoma valve in treatment of refractory glaucoma," *Acta Ophthalmologica*, vol. 94, pp. e382–e383, 2016.
- [13] M. G. Altinel, A. Y. Kanra, R. Karadag, and H. Bayramlar, "EX-PRESS implantation for different types of glaucoma," *International Journal of Ophthalmology*, vol. 12, article 1290, 2019.
- [14] W. Bo, D. Dai, and F. Sun, "Observation of curative effects of Ex-PRESS and AGV implantation in the treatment of refractory glaucoma," *Experimental and Therapeutic Medicine*, vol. 15, pp. 4419–4425, 2018.
- [15] M. Wilczynski, I. Drobniewski, A. Synder, and W. Omulecki, "Evaluation of early corneal endothelial cell loss in bimanual

Retraction

Retracted: Fibroblasts in Scar Formation: Biology and Clinical Translation

Oxidative Medicine and Cellular Longevity

Received 1 August 2023; Accepted 1 August 2023; Published 2 August 2023

Copyright © 2023 Oxidative Medicine and Cellular Longevity. This is an open access article distributed under the Creative Commons Attribution License, which permits unrestricted use, distribution, and reproduction in any medium, provided the original work is properly cited.

This article has been retracted by Hindawi following an investigation undertaken by the publisher [1]. This investigation has uncovered evidence of one or more of the following indicators of systematic manipulation of the publication process:

- (1) Discrepancies in scope
- (2) Discrepancies in the description of the research reported
- (3) Discrepancies between the availability of data and the research described
- (4) Inappropriate citations
- (5) Incoherent, meaningless and/or irrelevant content included in the article
- (6) Peer-review manipulation

The presence of these indicators undermines our confidence in the integrity of the article's content and we cannot, therefore, vouch for its reliability. Please note that this notice is intended solely to alert readers that the content of this article is unreliable. We have not investigated whether authors were aware of or involved in the systematic manipulation of the publication process.

Wiley and Hindawi regrets that the usual quality checks did not identify these issues before publication and have since put additional measures in place to safeguard research integrity.

We wish to credit our own Research Integrity and Research Publishing teams and anonymous and named external researchers and research integrity experts for contributing to this investigation.

The corresponding author, as the representative of all authors, has been given the opportunity to register their agreement or disagreement to this retraction. We have kept a record of any response received.

References

- [1] H. Qian, Y. Shan, R. Gong et al., "Fibroblasts in Scar Formation: Biology and Clinical Translation," *Oxidative Medicine and Cellular Longevity*, vol. 2022, Article ID 4586569, 11 pages, 2022.

Review Article

Fibroblasts in Scar Formation: Biology and Clinical Translation

Huan Qian ¹, Yihan Shan,² Ruicheng Gong,³ Danfeng Lin,⁴ Mengwen Zhang,¹ Chen Wang,¹ and Lu Wang ³

¹Department of Plastic Surgery, The Second Affiliated Hospital, School of Medicine, Zhejiang University, Hangzhou, China

²Wenzhou Medical University, Wenzhou, China

³Starbody plastic surgery Clinic, Hangzhou, China

⁴Department of Breast Surgery, The First Affiliated Hospital of Wenzhou Medical University, Wenzhou, China

Correspondence should be addressed to Huan Qian; huanqian@zju.edu.cn and Lu Wang; wlu104@gmail.com

Received 16 March 2022; Revised 20 April 2022; Accepted 28 April 2022; Published 12 May 2022

Academic Editor: Shao Liang

Copyright © 2022 Huan Qian et al. This is an open access article distributed under the Creative Commons Attribution License, which permits unrestricted use, distribution, and reproduction in any medium, provided the original work is properly cited.

Scarring, which develops due to fibroblast activation and excessive extracellular matrix deposition, can cause physical, psychological, and cosmetic problems. Fibroblasts are the main type of connective tissue cells and play important roles in wound healing. However, the underlying mechanisms of fibroblast in reaching scarless wound healing require more exploration. Herein, we systematically reviewed how fibroblasts behave in response to skin injuries, as well as their functions in regeneration and scar formation. Several biocompatible materials, including hydrogels and nanoparticles, were also suggested. Moreover, factors that concern transformation from fibroblasts into cancer-associated fibroblasts are mentioned due to a tight association between scar formation and primary skin cancers. These findings will help us better understand skin fibrotic pathogenesis, as well as provide potential targets for scarless wound healing therapies.

1. Introduction

Many situations can cause skin injuries, and most human skin wounds heal with the process of scarring. While some scars reach complete regeneration, many others undergo pathological tissue repairs, which occur with hypertrophic and keloid scars [1]. Treatment often involves surgical resection, laser therapy, radiation therapy, physical therapy (i.e., pressure therapy), and medication (i.e., triamcinolone injections) [2–5]. Currently, a number of animal studies have reported the molecular basis of scar-free healing [6–9]. Several factors, including growth factors, cytokines, cells (especially fibroblasts), and the extracellular matrix (ECM), contribute to scar formation. However, any preventive and therapeutic strategies to date remain unsatisfactory [10], which brings significant challenges to clinical practice. Additionally, differentiation towards cancer-associated fibroblasts (CAFs) may have an adverse function in skin healing. Yet,

given the rapid development of nanotechnology, the use of nanodrugs may facilitate scar-free wound healing [11, 12].

2. Fibroblasts in Wound Healing and Pathological Scar Repair

2.1. Wound Healing Process. The wound healing proceeds across three partially overlapping phases, including inflammation, re-epithelialization, and tissue remodeling [13]. It is considered to be a rather complex, but well-organized physiological process that involves mediators, ECM components, growth factors, and proteinases [12, 14].

The inflammation often occurs within 48 h after injury and is characterized by a hypoxic and ischemic environment [15]. A fibrin clot is formed, and platelets are able to be activated by release of several growth factors, including transforming growth factor (TGF- α and TGF- β), epidermal

growth factor (EGF), platelet-derived growth factor (PDGF), and fibroblast growth factor (FGF) [16–18]. Neutrophils and macrophages are also activated and summoned to curb the infection [19]. The re-epithelialization stage is characterized by the formation of new tissues. The early event involved the migration of keratinocytes to cover the skin surface [20]. Under stimulation of PDGF and FGF from previously attracted inflammatory cells, granulation tissue is gradually formed by involvement of angiogenesis, as well as migration of fibroblasts [21]. With the accumulation, differentiation, and proliferation of fibroblasts, new ECM is produced, and wounds become slowly contracted [22]. The remodeling phase can last for a year or even longer, and apoptosis develops in most endothelial cells, macrophages, and fibroblasts, at this stage [23]. The collagen III in the newly synthesized ECM is gradually replaced by more robust collagen I, which enhances tensile strength of the healed skin [24].

2.2. Fibroblasts in Wound Healing. Fibroblasts, which are known as connective-tissue-resident cells that generate ECM the scaffolding of the body, play important roles in wound healing [25]. The normal dermis can be divided into three layers containing different fibroblasts, including the papillary dermis (with papillary fibroblasts), reticular dermis (with reticular fibroblasts), and hypodermis/white adipose layer (with preadipocytes and adipocytes) [26, 27]. The histological structure of skin scars can be quite distinguishable. Numerous active fibroblasts and lymphocytes are located within the superficial dermis, while the middle layer contains abundant fibroblasts and ECM. Only a few dermal cells lie within the deep layer [28]. After injuries, the reticular fibroblasts gather and produce ECM [26, 29]. By expressing α -smooth muscle actin (α -SMA) and large amounts of ECM proteins, dermal regeneration is initiated. This phenomenon was observed by Driskell et al. and Emanuel et al. [27, 30]. The papillary fibroblasts are then recruited in the subsequent re-epithelialization phase [27]. Goss et al. suggested that, unlike reticular fibroblasts, papillary lineage-derived fibroblasts significantly enhance the regeneration of blood vessel-associated pericytes, which indicates a higher angiogenic potential during the second phase of wound healing. This result is also supported by Emanuel et al. [31, 32]. Additionally, modulation of developmental pathways, including canonical wntless-related integration site (Wnt) transcription factor lymphoid enhancer factor 1 (Lef1) in papillary fibroblasts, enables better skin repair [33].

The resident fibroblasts can also facilitate skin repair by wound contraction and crosstalk with immune cells by differentiating themselves into myofibroblasts, which are the major force in scarring [34, 35]. As they are a distinct subpopulation of myofibroblasts, adipocyte precursors have been proven to contribute to wound repair and ECM production and regulation [35, 36]. Maksim et al. have also indicated that new hair follicles in a wound can reprogram the myofibroblasts into adipocyte differentiation by activating the bone morphogenetic protein signaling pathway [37].

Besides the afore-mentioned fibroblasts, other types of fibroblasts have also been reported to affect skin repair. For

example, fascia fibroblasts help scarring by swarming to the skin surface in the case of deep wounds [38]. Among chronic open wounds, however, Engrailed-1 (En1-)-positive fibroblasts were detected both in the skin, as well as in the underneath fascia, which can help prevent fascia fibroblasts from migrating upwards, thus inhibiting wound repair [38].

2.3. Fibroblasts in Pathological Scar Repair. Pathological scar formation (i.e., hypertrophic scarring or keloids) may develop as long-term sequelae of delayed wound healing [39]. It is mainly featured by excessive proliferation of fibroblasts, as well as massive deposition of ECM (mostly collagen), reduced tensile strength and elasticity, and a lack of hair follicles [40].

Fibroblasts are heterogeneous cells, whether by cell lineage or by molecular phenotype [25]. For example, fibroblasts that are derived from embryonic precursors that express En1 have been reported to be the culprit in skin fibrosis, and targeted suppression/inhibition can effectively reduce formation of scars during wound healing [41]. Leavitt et al. demonstrated the inherent fibrotic characteristics of paired-related homeobox-1 (Prrx1-)-expressing fibroblasts during wound repair by lineage tracing and single-cell transcriptomics technology [42]. Deeper understanding of skin fibroblast lineages may help provide increased clues with regard to regenerative therapies that target subpopulations [43].

Surface markers are often frequently utilized to further identify and isolate fibroblast populations. For example, the upper (papillary) and lower (reticular) dermis can be subdivided by differentially expressed markers [27]. As is confirmed by lineage tracing, the papillary fibroblasts are characterized by an $\alpha 8$ integrin subunit, dipeptidyl peptidase 4 (Dpp4), Lrig1, and B lymphocyte-induced maturation protein 1 (Blimp1), while Dlk1 and Sca1 are selective markers for the lower dermis [27, 29, 44]. Functional analysis and expression profiling studies have suggested that FAP+CD90- cells represent a population of papillary fibroblasts that display proliferative potential. On the other hand, FAP-CD90+ fibroblasts from the reticular lineage may undergo adipogenic differentiation [45].

Myofibroblasts, the primary effector cells in scar formation, mainly derive from fibroblasts with distinct markers and functions. According to a study led by Shook et al., the most abundant populations include adipose precursors (Aps) that express CD26, as well as cells with highly expressed CD29 on the surface (CD29-High) in the wound bed [35]. The significant upregulation of Connexin 43 (Cx43) in specialized fascia fibroblasts are known to be responsible for scar formation, while inhibition of Cx43 prevents collective migration of fascia En1-positive fibroblasts, which disrupts the repair of deep injuries [46]. Other wound-associated biomarkers include SMA α +, FAP+, and FSP1+ [22]. Meanwhile, high expression of FOXF2 is measured in scar fibroblasts, and knockdown of FOXF2 demonstrates declined scars and reduced collagen I. In contrast to normal skin, abnormal scars fail to drop the immature scar phenotype, which is characterized by a CD34 and α -SMA dermal region [47].

3. Regulation of Fibroblasts in Wound Healing and Scar Formation

3.1. Microenvironment. The microenvironment in the wound area often regulates behaviors of fibroblasts through the use of mechanical forces, interaction with other cells (i.e., keratinocytes), and numerous substances, including cytokines. Mechanical forces are able to cause scarring via myofibroblast differentiation and collagen overproduction. The shift of fibroblasts towards profibrotic phenotypes is driven by ERK-YAP activation in human cells [48]. Consisting of more than 80% of epithelial cells, keratinocytes make a great contribution to not only skin protection, but also to re-epithelialization and wound closure after injuries [49]. The secretion of the high-mobility group box chromosomal protein 1 (HMGB1) by keratinocytes is known to trigger an α -smooth muscle actin promoter by motivating fibroblasts by promoting the nuclear import of MRTF-A, as well as increasing nuclear accumulation of MRTF-A/SRF complexes [50]. Interestingly, thinner skin and reduced collagen density were found among mice with focal adhesion kinase (FAK)-deleted keratinocytes, which actively participate in mechano-transduction and ECM production [51, 52].

In addition, cytokines and cell adhesion molecules are also reported to play roles in ECM deposition, fibroblast differentiation, and cell migration. TGF- β -induced release of IL-11 is significantly upregulated in hypertrophic scars, which activates the enrichment of CD39+ fibroblasts within the upper dermis and secretes a large amount of ECM [53]. CD44 is a cell surface adhesion receptor that has been implicated in leukocyte recruitment, T cell extravasation, and hyaluronic acid metabolism. Mice that lack CD44 exhibit reduced collagen degradation, which leads to increased accumulation during and after wound closure [54]. CXCL4 has been validated to stimulate endothelial-to-mesenchymal transition in fibrotic tissues. Myofibroblast differentiation and collagen synthesis are directly induced, indicating that CXCL4 may be a potential therapeutic target for the treatment of fibrosis and scars [55]. Meanwhile, N-cadherin has been shown to be critical in injury-triggered swarming, as well as migration of fascia fibroblasts that progressively contract the skin and form scars [56].

3.2. Signaling Pathway. Key aspects of fibroblast biology, which consists of cell differentiation, migration, proliferation, and ECM secretion, are regulated by several signaling pathways during wound healing and scar formation. In general, aggravated scarring is thought to be associated with c-Jun N-terminal kinase (JNK), TGF- β , Wnt, and Hippo pathways (with enhanced fibroblast migration, increased transition into myofibroblasts, and ECM rearrangement), whereas JUN is related to better repair. Contractile myofibroblast state transition is needed for fibroblasts to fully function, while the aberrant and sustained switch contributes to both scarring, as well as the development of certain cancers.

As previously reported, differentiation is dominantly controlled by the TGF- β pathway. TGF- β pathway controls a wide variety of cellular processes, ranging from cell prolifer-

ation and differentiation to tissue homeostasis and regeneration via SMAD-dependent (canonical) and independent (noncanonical) signaling [57, 58]. Based on functional analysis, boosted myofibroblast differentiation and excessive deposition of ECM have been observed due to increased levels of TGF- β 1, mediated by Dpp4 and urokinase (PLAU) *in vitro* [59].

Relative therapeutic strategies include targeted inhibition of TGF- β at the genetic and cellular levels. As a TGF- β profibrotic signaling-related microRNA, MiR-125b is known to be required for fibroblast-to-myofibroblast transition [60]. The suppression of miR-1224-5p is indicated to decrease proliferation, as well as invasion of keloid fibroblasts, by inhibiting the TGF- β 1/Smad3-related pathways, thereby further emphasizing the importance of miRNAs as the potential target [61]. Similar activation of the myofibroblast transition has been suggested in other signaling pathways. For example, scars can develop when the translocation of β -catenin in fibroblasts is enhanced by Wnt, thereby leading to proliferation, migration, and transition of fibroblasts into myofibroblasts, as well as deposition of type I collagen [62]. Reduced expression of collagen I and III was observed in a biomimetic nanodrug delivery system with increased efficacy on hypertrophic scars by regulating Wnt/ β -catenin and JAK2/STAT3 pathways [63]. Interestingly, Sun et al. recently discovered that activation of sonic hedgehog can eliminate the negative effect brought by long-term Wnt signaling [64]. In another study, David et al. demonstrate that induced fibroblast activation and upregulated expression of myofibroblast marker proteins are present in samples that are treated with extracellular signal regulated kinase (ERK) or JNK inhibitors and that treatment with a p38 inhibitor can sufficiently inhibit fibroblast activation [65]. It is also worth mentioning that the activation of fibroblasts differentiation mediated by ERK or JNK inhibition can be partially antagonized by cotreatment with a small molecule inhibitor of TGF- β R1, indicating that there is underlying crosstalk between these various signaling pathways [66]. In the meantime, stimulation on other fibroblast subpopulations is also proposed. Hippo signaling pathway has emerged as being central to regeneration, in which an elevated nuclear level of YAP and TAZ has been observed [67]. On the other hand, YAP inhibition blocks activation of En1 and promotes ENF-mediated repair, which induces recovery of normal dermal ultrastructure [68]. Additionally, administration with the nuclear Yap-TEAD inhibitor verteporfin prolonged myofibroblast persistence and converted tissue regeneration to fibrosis *in vivo* [69]. JUN initiates hypertrophic scar formation by regulating CD36, modulating distinct fibroblast subpopulations, boosting reticular fibroblasts, and decreasing levels of lipofibroblasts [70].

Given the role of fibroblasts and signaling pathways, any abnormalities that concern fibroblasts (dysregulation of gene expression, altered differentiation, adverse microenvironment, and deflected signaling pathways) can affect regeneration and even cause pathological scarring. For instance, both *in vivo* and *in vitro* experiments conducted by Schulz et al. indicated that a lack of α 11 β 1 related to defective TGF- β -dependent JNK signaling prevents effective

conversion from dermal fibroblasts to myofibroblasts, causing poor collagen remodeling [71]. In another study, fibroblasts with conjugation-deficient ISG15 were associated with increased reactive oxygen species (ROS) levels and fewer ROS scavengers, which manifested as ulcerating skin lesions [72]. It has also been shown that selective loss of fibroblasts from the upper dermis after acute and chronic ultraviolet radiation can cause skin injury [73].

4. Fibroblasts and Cancer-Associated Fibroblasts

Despite the mechanisms that are involved in regeneration and scar formation, the dysfunction of fibroblasts can lead to a worse case—cancer. It is known that the process of wound healing (scarring in particular) and cancer progression shares several common characteristics, including promoting proliferation and migration of epithelial cells and activation of fibroblasts and excessive ECM deposition, angiogenesis, and lymphangiogenesis, as well as increase in levels of various types of immune cells [74, 75]. From this phenomenon, we can draw the hypothesis that cancers and scarring may share some similar mechanisms.

The microenvironment plays a significant role in both wound healing and tumorigenesis through intracellular communication. The past decade has witnessed a soaring interest in studies that concern the tumor microenvironment and CAFs, a major component and the main cell type that produces ECM. CAFs derive from a diverse group of cells (mainly intrinsic fibroblasts and stellate cells) under either endogenous or exogenous stimulation. Although some biomarkers of CAFs, such as fibroblast activation protein (FAP), α -SMA, fibroblast specific protein 1 (FSP1), and platelet-derived growth factor receptor (PDGFR), have been proposed, the complex heterogeneity has not yet been fully revealed [76].

Recent studies demonstrate the process and effect of reprogramming of skin fibroblasts into CAFs [77, 78]. A notable example is the strong upregulation of tumor necrosis factor (TNF)-receptor associated factor 6 (TRAF6) in CAFs in melanoma, which enhances proliferation and migration of fibroblasts, and is accompanied by increased expression of matrix metalloproteinase and α -SMA. Furthermore, FGF19 has been shown to be a key cytokine regulated by TRAF6 through NF- κ B [79]. Twist1, another key regulator of CAFs, can directly upregulate Prrx1 expression, and subsequently enhance expression of Tenascin-C (TNC), which, in turn, increases the expression of Twist1. Thus, a Twist1-Prrx1-TNC positive feedback loop (PFL) is developed, which leads to the sustained activation of fibroblasts, and the transformation into CAFs [80]. Notch1 is capable of blocking DNA damage response and ensures growth arrest by suppression of ATM-FOXO3a association and the downstream signaling cascade. The amplification of Notch1 is observed in CAFs from squamous cell carcinomas, as well as normal dermal fibroblasts (to a lesser extent), and exposure to UVA (ultraviolet A) expands the effect in normal dermal fibroblasts, while the squamous cell carcinomas appear to be resistant [81]. Activin A is overexpressed in different skin

cancers, including basal cell carcinomas, squamous cell carcinomas [82], and melanoma [83–85]. It has been reported to reprogram fibroblasts into protumorigenic CAFs via a Smad2-mediated transcriptional regulation of the formin mDia2, promoting filopodia formation and cell migration. Blockade of this paracrine activin A-mDia2 axis suppresses cancer cell malignancy and squamous carcinogenesis *in vitro* and *in vivo* [86, 87]. As for facilitated invasiveness, keloid tissue-derived fibroblasts (KF) with upregulated LARP6 expression demonstrates enhanced cell proliferation and invasive behavior in cell culture system, while knock-down of LARP reverses this effect, with reduced deposition of type I collagen and inhibition of proliferation and invasion ability [88]. In another study, Tan et al. revealed the role of PPAR β/δ in the epithelial-mesenchymal communication involved in cellular redox homeostasis. Mice with PPAR β/δ -deleted fibroblasts indicated retarded growth of tumors [89]. Decreased melanoma invasion is detected, with an upregulation of collagen-cleaving MMP1 expression and subsequent degradation of local collagen (COL1A1) due to damaged dermal fibroblasts by UVR [90].

On the other hand, substances that enhance the genomic stability are likely to prevent CAF transformation. E3 ubiquitin ligase Smurf2 protects human dermal fibroblasts (HDFs) from malignant transformation by regulating E3 ubiquitin ligase RNF20 and histone methyltransferase EZH2, thereby stabilizing chromatin. Depletion of Smurf2 converts HDFs into a tumorigenic entity [91]. Down-modulation of CSL/RBP-J κ , the effector of canonical NOTCH signaling, with intrinsic transcription repressive function, harms genomic stability and causes conversion of dermal fibroblasts into CAFs [92]. A deficiency of CLEC2A, the ligand of activating NK cell receptor NKp65, may participate in the fibroblast reprogramming process. The expression of CLEC2A on fibroblasts may be downregulated by TNF- α , IL-1 α , and IL-1 β , but not by TGF- β *in vitro*. It has been suggested that CLEC2A can accelerate the engulfment of cancer cells by NK cells at early tumorigenesis stages, at which time fibroblasts do not change to the CAF phenotype [93].

5. Materials in Scarless Wound Healing

As mentioned above, wound repair is an extremely well-organized process that is mainly conducted by fibroblasts, and scars are the result of dysregulation with excessive ECM deposition and fibroblast proliferation. The primary goal of wound therapy is to help prevent serious infection postinjury, as well as pathological scar formation to accelerate wound healing. Classic options include medication (i.e., intralesional corticosteroids and intralesional fluorouracil), cryotherapy, surgical excision, and perioperative therapies and laser therapy. Although some of them have proven to be effective, many patients undergoing these treatments suffer from a lot of pain or can be bothered by a high risk of recurrence [94–97]. Thus, developing novel technologies is required. Recent findings on fibroblasts and nanoscale materials may help provide a promising future in scarless wound healing. This strategy largely includes inhibition of fibroblast

proliferation, modulation of cell differentiation, and alteration of ECM components.

Generally, fibroblast-related technologies refer to detection and identification of pathological skin repair and wound healing-associated therapy. Regarding pathological diagnosis involving the analysis of mRNA expression, materials include NanoFlares and nucleic-acid-based probe. Through the use of NanoFlares, a type of imaging nanoprobes designed for live-cell detection of mRNA, D.C. Yeo et al. distinguished hypertrophic and keloidal fibroblasts from normal fibroblasts by measuring the expression of connective tissue growth factor (CTGF) [98]. Similarly, Zeng et al. utilized a novel nucleic-acid-based probe in order to achieve this type of distinction. The probe is generally utilized for diagnosis and spontaneous regulation of the abnormal expression (by suppressing the mRNA expression of TGF β RI and CTGF) of fibrosis-related mRNA in scar-derived skin fibroblasts [99]. Therefore, these techniques can serve as means of biopsy-free scar diagnosis and eventually help make treatment decisions.

With regard to treatment, fibroblast-related technologies involve skin substitutes, controlled release, and exosomes. With regard to skin substitutes, bioengineered scaffold, hybrid membrane, and marine-derived films are invented. A trilayer PCL-gelatin scaffold mimicking the actual skin structure displayed improved regeneration with an ideal mechanical strength by maintaining a porosity gradient and conducting proper microenvironments [100]. Meanwhile, Li et al. proposed an innovative approach that combines graphene oxide with collagen I and N-acetyl cysteine (NAC), both of which allowed the continuous release of antioxidant NAC. The hybrid membrane exhibits a better antiscar effect, which demonstrates with decreased mRNA expression of profibrotic factors, as well as overexpression of antifibrotic factors [101]. Moreover, application of astaxanthin incorporated collagen film (ACF) and gentamicin incorporated collagen film (GCF) in order promote epithelialization in Wistar rats with full thickness excision and linear incision [102].

The second strategy, controlled release, refers to regulating the same substance across different phases towards opposite effects. This strategy refers to various methods, including multilayered structures, porous design, and photo-induced release. Nanotechniques that play different roles at various stages of wound healing promote regeneration and suppress scarring. A modified formulation of poly (γ -glutamic acid), according to electrospun photocrosslinkable hydrogel fibrous scaffolds combined with ginsenoside Rg3 (GS-Rg3), has developed for improved tissue repair function. Reduced scar formation was observed due to sustained release of GS-Rg3, which allows fibroblast proliferation at an early stage but abated angiogenesis and collagen accumulation later [103]. As TGF- β signaling pathway participates during whole process, from the activation of transcription factors to fibroblast differentiation and α -SMA production, it remains a promising target with regard to scarless wound healing. The exogenous growth factor delivery platform based on coacervate achieves scarless skin regeneration via dual release of TGF- β 3 and IL-10 at differ-

ent stages [104]. This type of results is also demonstrated by Zhang et al. using an integrated photocrosslinking strategy. A microcapsule platform is developed with pulsatile release of TGF- β inhibitors, demonstrating spatiotemporal specificity across both murine skin wounds and large animal models [105]. Similarly, the controlled release of metformin hydrochloride forms a three-layer scaffold, which alleviates scar formation by downregulating expression of fibrosis-involved genes, including TGF- β 1, collagen type 1 and 3, fibronectin, and α -SMA [106].

Regarding their last strategy, exosomes comprising mRNAs, miRNAs, cytokines, and growth factors are isolated, and their effects on the behavior of fibroblasts are evaluated. The use of exosomes also exerts promising clinical translation [11]. For example, transplantation of exosomes from the human umbilical cord blood plasma (UCB-Exos) accelerates cutaneous wound healing through miR-21-3p-mediated promotion of angiogenesis and fibroblast function [107]. A group of umbilical cord-derived MSCs-derived exosomes demonstrate antiscarring functions via suppression of myofibroblast formation, which may be associated with inhibition of TGF- β 2/SMAD2 pathway [108].

Other methods that promote scarless wound healing include induction of MSCs-differentiated fibroblast [109], regulation of angiogenesis [110] and TGF- β 3 expression [111], and M1-M2 phenotype switching of macrophages [112]. Moreover, the silk nanofiber hydrogels loaded with asiaticoside (AC) have been shown to improve efficiency compared to previous liposome systems in reaching scarless wound healing by regulating inflammatory reactions and angiogenesis [113].

6. Clinical Trials

Several clinical trials have been carried out or are ongoing that can help clarify the safety, feasibility, and efficacy of fibroblast-based therapeutics in wound healing and skin regeneration. Although clinical guidelines have not included use of fibroblasts, many studies have shown the great potential of fibroblast therapy in clinical applications (Table 1).

A study that enrolled 49 volunteers with circular 5-mm full-thickness wound of unblemished skin underneath both arms who were treated with α -CT1 demonstrated dose-dependent decreases in fibroblast movement directionality, which resulted in increased randomness during the migration paths [114]. Meuli et al. recruited seven patients, each with seven wounds. Three wounds were administered fibroblast injection, while the other three wounds used fibroblasts that were seeded on amniotic membrane scaffolds (FAMS). The last one was treated with standard wound care (SWC) (Vaseline gauze). Although increased wound healing was achieved using the first two methods, the fibroblast injection was proven to be superior to FAMS, and a continuous collagen layer was established with better microscopic effects in completely healed wounds [115]. ICX-RHY-013 is an investigational medicinal product that is comprised of viable allogeneic human dermal fibroblast (HDFs) cells that were suspended in HypoThermosol[®]-FRS. Rubin and colleagues conducted a clinical trial that included eight participants.

TABLE 1: The clinical trials of fibroblast-based therapy in wound healing and scarring.

Conditions	Interventions	Status	Results
Acne scarring of the face	Biological: autologous human fibroblasts (azficel-T)	Completed	Reduced scars in autologous fibroblast cheeks
Restrictive scar contracture	ICX-RHY-013	Terminated	Safe
Restrictive hypertrophic scar			
Burn scar contractures	AbobotulinumtoxinA 500 UNT	Active, not recruiting	Ongoing
Burn scar			
Hypertrophic scarring	Dermal fibroblasts	Completed	Ongoing
Trophic ulcer			
Nonhealing wound	LED phototherapy	Completed	Ongoing
Nonhealing ulcer of skin			
Burns	Fibroblasts and keratinocytes	Completed	Ongoing
Wound scars	Connexin 43 carboxyl terminal mimetic peptide α CT1	Completed	Decreased directionality of fibroblast movement, and the generation of a 3D collagen matrix postwounding that is similar to unwounded skin
Dystrophic epidermolysis bullosa	Fibroblast injection Amniotic membrane scaffolds (FAMS) Vaseline gauze (SWC)	Completed	Establishment of a continuous collagen layer and better microscopic effects

The participants were divided into two cohorts according to their wound types (cohort 1 with an abdominal incision scar and cohort 2 burn scars with restrictive scar contractures). There were no life-threatening events observed, but there were mild adverse events, including redness and itching. In order to investigate the safety and efficacy of autologous fibroblasts towards severe facial acne scarring, 109 patients were selected and administered with autologous fibroblasts and placebo on either sides of their cheeks, respectively. The autologous fibroblast-treated cheeks earned better scores of Evaluator Live Acne Scarring Assessment (ELASA) and Subject Live Acne Scarring Assessment (SLASA), thereby indicating improved healing conditions with autologous fibroblast treatment.

7. Discussion

Skin wound repair is a complex process that can accomplish two major tasks. First, wound repair attenuates skin barrier functions, which effectively protects skin stability and prevents infection. Moreover, wound healing restores the physiological and mechanical properties of skin. Fibroblasts are expected to contract wounds and secrete ECM during the process, but uncontrolled proliferation of fibroblasts and excessive deposition of ECM contributes to the scar formation and should be avoided.

During recent years, numerous studies have been carried out in the field of inhibiting scar formation and have achieved some promising results. Fibroblast heterogeneity, intracellular crosstalk, and signaling pathways have provided some innovative thoughts. However, the exact mechanisms

that are involved are still not revealed. Limitations, such as the lack of detection in dynamic change of fibroblast phenotypes and the obscurity of how these lineages are interconnected, remain unsolved. Therefore, further tests during clinical samples are still needed. The treatment of pathological scars remains a thorny and daunting challenge, as most of the current studies, especially clinical trials, have not shown any beneficial effect of treating scarless wound healing. Nevertheless, the recently progressive application of biomaterials has brought some insight into this issue. Special probes are designed as diagnostic tools for pathological scars, and significant therapeutic effects were found in fibroblasts-based technologies concerning skin substitutes, controlled release, and exosomes. Meanwhile, novel techniques and methods, such as lineage tracing, intravital microscopy, single-cell transcription, and epigenetic profiling, can help uncover the underlying mechanisms of skin scarring and provide potential therapeutic targets for regenerative treatment of skin injuries.

The TGF- β signaling pathway participates in wound healing, scar formation, and fibroblast reprogramming towards CAFs. While elevated expression of TGF- β at the re-epithelialization stage seems to promote wound repair, the continued upregulation at the remodeling phase is related to scarring. While administration of TGF- β antibodies during remodeling and the resolution stage can cause significant improvement of skin scarring, treatment at an early stage may cause later cutaneous wound healing [116]. This suggests the importance of the timing of intervention. Meanwhile, TGF- β expression is reported to be upregulated in skin cancers such as melanoma. It is worth mentioning

that fibroblast sensitivity to TGF- β in keloids is higher than normal skin fibroblasts, which causes increased secretion of ECM. On the other hand, melanoma cells appear to be less sensitive to the growth inhibiting effect of TGF- β . Therefore, the controlled inhibition of TGF- β can be applied clinically as an intervention.

Activated fibroblasts during wound healing, especially scarring and CAFs, share many common cellular features and signaling pathways, but with distinct characteristics. These fibroblasts associated with ECM have a primary role in tissue repair and tumor proliferation. Normal skin fibroblasts can be converted to CAFs under certain condition, with TRAF6, Twist1-Prrx1-TNC loop, and LARP6 acting as inducers, while CLEC2A, SMURF2, and CSL can be used as inhibitors. Therefore, it is likely that controlling proliferation and activities of CAFs may limit tumor progression and improve response to antitumor therapies. In addition, we hypothesize that preventing the transformation of CAFs may reduce progression of tumor at an early stage. Moreover, therapeutic strategies that are aimed at reducing scars may also work in the suppression of cancer. However, a deeper understanding of the main role of fibroblasts in tumors and scars is needed.

Data Availability

No data were used to support this study.

Conflicts of Interest

The authors declare that there are no potential conflicts of interest.

Authors' Contributions

Huan Qian and Yihan Shan wrote the manuscript. Lu Wang and Danfeng Lin conceived and supervised this work. Danfeng Lin, Mengwen Zhang, Chen Wang, and Ruicheng Gong revised the manuscript. All authors approved the final version.

Acknowledgments

This study was funded by the Zhejiang Provincial Natural Science Foundation of China (LGD21H150001).

References

- [1] R. A. F. Clark, M. Musillo, and T. Stransky, "Chapter 70-Wound repair: basic biology to tissue engineering," in *Principles of Tissue Engineering (Fifth Edition)*, R. Lanza, R. Langer, J. P. Vacanti, and A. Atala, Eds., pp. 1309–1329, Academic Press, 2020.
- [2] K. Dastagir, D. Obed, F. Bucher, T. Hofmann, K. I. Koyro, and P. M. Vogt, "Non-invasive and surgical modalities for scar management: a clinical algorithm," *Journal of Personalized Medicine*, vol. 11, no. 12, p. 1259, 2021.
- [3] C. K. Sen, "Human wound and its burden: updated 2020 compendium of estimates," *Advances in Wound Care*, vol. 10, no. 2021, pp. 281–292, 2021.
- [4] B. Guix, I. Henríquez, A. Andrés, F. Finestres, J. I. Tello, and A. Martínez, "Treatment of keloids by high-dose-rate brachytherapy: a seven-year study," *International Journal of Radiation Oncology • Biology • Physics*, vol. 50, no. 1, pp. 167–172, 2001.
- [5] T. H. Park, S. W. Seo, J. K. Kim, and C. H. Chang, "Outcomes of surgical excision with pressure therapy using magnets and identification of risk factors for recurrent keloids," *Plastic and Reconstructive Surgery*, vol. 128, no. 2, pp. 431–439, 2011.
- [6] C. Soo, F. Y. Hu, X. Zhang et al., "Differential expression of fibromodulin, a transforming growth factor-beta modulator, in fetal skin development and scarless repair," *The American Journal of Pathology*, vol. 157, no. 2, pp. 423–433, 2000.
- [7] S. R. Beanes, F.-Y. Hu, C. Soo et al., "Confocal microscopic analysis of scarless repair in the fetal rat: defining the transition," *Plastic and Reconstructive Surgery*, vol. 109, no. 1, pp. 160–170, 2002.
- [8] M. W. J. Ferguson and S. O'Kane, "Scar-free healing: from embryonic mechanisms to adult therapeutic intervention," *Philosophical Transactions of the Royal Society of London. Series B, Biological Sciences*, vol. 359, no. 1445, pp. 839–850, 2004.
- [9] A. S. Colwell, T. M. Krummel, M. T. Longaker, and H. P. Lorenz, "An in vivo mouse excisional wound model of scarless healing," *Plastic and Reconstructive Surgery*, vol. 117, no. 7, pp. 2292–2296, 2006.
- [10] H. J. Lee and Y. J. Jang, "Recent understandings of biology, prophylaxis and treatment strategies for hypertrophic scars and keloids," *International Journal of Molecular Sciences*, vol. 19, no. 3, p. 711, 2018.
- [11] D. Bian, Y. Wu, G. Song, R. Azizi, and A. Zamani, "The application of mesenchymal stromal cells (MSCs) and their derivative exosome in skin wound healing: a comprehensive review," *Stem Cell Research & Therapy*, vol. 13, no. 1, p. 24, 2022.
- [12] W. Wang, K.-J. Lu, C.-H. Yu, Q.-L. Huang, and Y.-Z. Du, "Nano-drug delivery systems in wound treatment and skin regeneration," *Journal of Nanobiotechnology*, vol. 17, no. 1, p. 82, 2019.
- [13] G. C. Gurtner, S. Werner, Y. Barrandon, and M. T. Longaker, "Wound repair and regeneration," *Nature*, vol. 453, no. 7193, pp. 314–321, 2008.
- [14] J. M. Reinke and H. Sorg, "Wound repair and regeneration," *European Surgical Research*, vol. 49, no. 1, pp. 35–43, 2012.
- [15] P. Martin, "Wound healing - aiming for perfect skin regeneration," *Science*, vol. 276, no. 5309, pp. 75–81, 1997.
- [16] W. K. Stadelmann, A. G. Digenis, and G. R. Tobin, "Physiology and healing dynamics of chronic cutaneous wounds," *American Journal of Surgery*, vol. 176, no. 2, pp. 26S–38S, 1998.
- [17] R. Braund, S. Hook, and N. J. Medlicott, "The role of topical growth factors in chronic wounds," *Current Drug Delivery*, vol. 4, no. 3, pp. 195–204, 2007.
- [18] G. Gainza, S. Villullas, J. L. Pedraz, R. M. Hernandez, and M. Igartua, "Advances in drug delivery systems (DDSs) to release growth factors for wound healing and skin regeneration," *Nanomedicine: Nanotechnology, Biology and Medicine*, vol. 11, pp. 1551–1573, 2015.
- [19] S. A. Eming, T. Krieg, and J. M. Davidson, "Inflammation in wound repair: molecular and cellular mechanisms," *The*

- Journal of Investigative Dermatology*, vol. 127, no. 3, pp. 514–525, 2007.
- [20] P. Rousselle, F. Braye, and G. Dayan, “Re-epithelialization of adult skin wounds: cellular mechanisms and therapeutic strategies,” *Advanced Drug Delivery Reviews*, vol. 146, pp. 344–365, 2019.
- [21] Y. Qian, L. Li, Y. Song et al., “Surface modification of nanofibrous matrices via layer-by-layer functionalized silk assembly for mitigating the foreign body reaction,” *Biomaterials*, vol. 164, pp. 22–37, 2018.
- [22] K. M. McAndrews, T. Miyake, E. A. Ehsanipour et al., “Dermal α SMA myofibroblasts orchestrate skin wound repair via β 1 integrin and independent of type I collagen production,” *The EMBO Journal*, vol. 41, no. 7, article e109470, 2022.
- [23] A. Young and C.-E. McNaught, “The physiology of wound healing,” *Surgery*, vol. 29, no. 10, pp. 475–479, 2011.
- [24] H. Pratsinis, E. Mavrogonatou, and D. Kletsas, “Scarless wound healing: from development to senescence,” *Advanced Drug Delivery Reviews*, vol. 146, pp. 325–343, 2019.
- [25] S. Mascharak and M. T. Longaker, “Fibroblast heterogeneity in Wound healing: hurdles to clinical translation,” *Trends in Molecular Medicine*, vol. 26, no. 12, pp. 1101–1106, 2020.
- [26] R. R. Driskell and F. M. Watt, “Understanding fibroblast heterogeneity in the skin,” *Trends in Cell Biology*, vol. 25, no. 2, pp. 92–99, 2015.
- [27] R. R. Driskell, B. M. Lichtenberger, E. Hoste et al., “Distinct fibroblast lineages determine dermal architecture in skin development and repair,” *Nature*, vol. 504, no. 7479, pp. 277–281, 2013.
- [28] C. D. Marshall, M. S. Hu, T. Leavitt, L. A. Barnes, H. P. Lorenz, and M. T. Longaker, “Cutaneous scarring: basic science, current treatments, and future directions,” *Advances in Wound Care*, vol. 7, no. 2, pp. 29–45, 2018.
- [29] J. M. Sorrell and A. I. Caplan, “Fibroblast heterogeneity: more than skin deep,” *Journal of Cell Science*, vol. 117, no. 5, pp. 667–675, 2004.
- [30] E. Rognoni, A. O. Pisco, T. Hiratsuka et al., “Fibroblast state switching orchestrates dermal maturation and wound healing,” *Molecular Systems Biology*, vol. 14, no. 8, article e8174, 2018.
- [31] G. Goss, E. Rognoni, V. Salameti, and F. M. Watt, “Distinct fibroblast lineages give rise to NG2+ pericyte populations in mouse skin development and repair,” *Frontiers In Cell and Developmental Biology*, vol. 9, article 675080, 2021.
- [32] E. Rognoni, “Dermal hedgehog signaling in papillary fibroblasts: an emerging key player in skin regeneration,” *The Journal of Investigative Dermatology*, 2022.
- [33] Q. M. Phan, G. M. Fine, L. Salz et al., “Lef1 expression in fibroblasts maintains developmental potential in adult skin to regenerate wounds,” *eLife*, vol. 9, 2020.
- [34] J. J. Tomasek, G. Gabbiani, B. Hinz, C. Chaponnier, and R. A. Brown, “Myofibroblasts and mechano: regulation of connective tissue remodelling,” *Nature Reviews Molecular Cell Biology*, vol. 3, no. 5, pp. 349–363, 2002.
- [35] B. A. Shook, R. R. Wasko, G. C. Rivera-Gonzalez et al., “Myofibroblast Proliferation and Heterogeneity Are Supported by Macrophages during Skin Repair,” *Science*, vol. 362, no. 6417, p. 362, 2018.
- [36] G. Donati, V. Proserpio, B. M. Lichtenberger et al., “Epidermal Wnt/ β -catenin signaling regulates adipocyte differentiation via secretion of adipogenic factors,” *Proceedings of the National Academy of Sciences of the United States of America*, vol. 111, no. 15, pp. E1501–E1509, 2014.
- [37] M. V. Plikus, C. F. Guerrero-Juarez, M. Ito et al., “Regeneration of Fat Cells from Myofibroblasts during Wound Healing,” *Science*, vol. 355, no. 6326, pp. 748–752, 2017.
- [38] D. Correa-Gallegos, D. Jiang, S. Christ et al., “Patch repair of deep wounds by mobilized fascia,” *Nature*, vol. 576, no. 7786, pp. 287–292, 2019.
- [39] B. Ter Horst, G. Chouhan, N. S. Moiemien, and L. M. Grover, “Advances in keratinocyte delivery in burn wound care,” *Advanced Drug Delivery Reviews*, vol. 123, pp. 18–32, 2018.
- [40] M. Monavarian, S. Kader, S. Moeinzadeh, and E. Jabbari, “Regenerative scar-free skin wound healing,” *Tissue Engineering Part B: Reviews*, vol. 25, pp. 294–311, 2019.
- [41] Y. Rinkevich, G. G. Walmsley, M. S. Hu et al., “Skin fibrosis. Identification and isolation of a dermal lineage with intrinsic fibrogenic potential,” *Science*, vol. 348, article aaa2151, 2015.
- [42] T. Leavitt, M. S. Hu, M. R. Borrelli et al., “Prrx1 fibroblasts represent a pro-fibrotic lineage in the mouse ventral dermis,” *Cell Reports*, vol. 33, no. 6, article 108356, 2020.
- [43] R. Takagi, J. Ishimaru, A. Sugawara et al., “Bioengineering a 3D integumentary organ system from iPS cells using an in vivo transplantation model,” *Science Advances*, vol. 2, no. 4, p. e1500887, 2016.
- [44] D. G. Janson, G. Saintigny, A. van Adrichem, C. Mahé, and A. El Ghalbzouri, “Different gene expression patterns in human papillary and reticular fibroblasts,” *The Journal of Investigative Dermatology*, vol. 132, no. 11, pp. 2565–2572, 2012.
- [45] A. Korosec, S. Frech, B. Gesslbauer et al., “Lineage identity and location within the dermis determine the function of papillary and reticular fibroblasts in human skin,” *The Journal of Investigative Dermatology*, vol. 139, no. 2, pp. 342–351, 2019.
- [46] L. Wan, D. Jiang, D. Correa-Gallegos et al., “Connexin43 gap junction drives fascia mobilization and repair of deep skin wounds,” *Matrix Biology*, vol. 97, pp. 58–71, 2021.
- [47] G. C. Limandjaja, J. M. Belien, R. J. Scheper, F. B. Niessen, and S. Gibbs, “Hypertrophic and keloid scars fail to progress from the CD34-/ α -smooth muscle actin (α -SMA)+ immature scar phenotype and show gradient differences in α -SMA and p16 expression,” *The British Journal of Dermatology*, vol. 182, no. 4, pp. 974–986, 2020.
- [48] K. Chen, S. H. Kwon, D. Henn et al., “Disrupting biological sensors of force promotes tissue regeneration in large organisms,” *Nature Communications*, vol. 12, no. 1, p. 5256, 2021.
- [49] I. Pastar, O. Stojadinovic, N. C. Yin et al., “Epithelialization in wound healing: a comprehensive review,” *Advances in Wound Care*, vol. 3, no. 7, pp. 445–464, 2014.
- [50] J. Zhao, J. Yu, Y. Xu et al., “Epidermal HMGB1 activates dermal fibroblasts and causes hypertrophic scar formation in reduced hydration,” *The Journal of Investigative Dermatology*, vol. 138, no. 11, pp. 2322–2332, 2018.
- [51] V. W. Wong, R. K. Garg, M. Sorkin et al., “Loss of keratinocyte focal adhesion kinase stimulates dermal proteolysis through upregulation of MMP9 in wound healing,” *Annals of Surgery*, vol. 260, no. 6, pp. 1138–1146, 2014.
- [52] M. Januszyk, S. H. Kwon, V. W. Wong et al., “The role of focal adhesion kinase in keratinocyte fibrogenic gene expression,” *International Journal of Molecular Sciences*, vol. 18, no. 9, p. 1915, 2017.

- [53] X. Huang, S. Gu, C. Liu et al., “CD39⁺ fibroblasts enhance myofibroblast activation by promoting IL-11 secretion in hypertrophic scars,” *The Journal of Investigative Dermatology*, vol. 142, no. 4, pp. 1065–1076.e19, 2022.
- [54] P. Govindaraju, L. Todd, S. Shetye, J. Monslow, and E. Puré, “CD44-dependent inflammation, fibrogenesis, and collagenolysis regulates extracellular matrix remodeling and tensile strength during cutaneous wound healing,” *Matrix Biology*, vol. 75–76, pp. 314–330, 2019.
- [55] A. J. Affandi, T. Carvalho, A. Ottria et al., “CXCL4 drives fibrosis by promoting several key cellular and molecular processes,” *Cell Reports*, vol. 38, no. 1, article 110189, 2022.
- [56] D. Jiang, S. Christ, D. Correa-Gallegos et al., “Injury triggers fascia fibroblast collective cell migration to drive scar formation through N-cadherin,” *Nature Communications*, vol. 11, no. 1, p. 5653, 2020.
- [57] E. J. Macarak, P. J. Wermuth, J. Rosenbloom, and J. Uitto, “Keloid disorder: fibroblast differentiation and gene expression profile in fibrotic skin diseases,” *Experimental Dermatology*, vol. 30, no. 1, pp. 132–145, 2021.
- [58] S. Chawla and S. Ghosh, “Regulation of fibrotic changes by the synergistic effects of cytokines, dimensionality and matrix: towards the development of an in vitro human dermal hypertrophic scar model,” *Acta Biomaterialia*, vol. 69, pp. 131–145, 2018.
- [59] V. Vorstandlechner, M. Laggner, D. Copic et al., “The serine proteases dipeptidyl-peptidase 4 and urokinase are key molecules in human and mouse scar formation,” *Nature Communications*, vol. 12, no. 1, p. 6242, 2021.
- [60] V. Nagpal, R. Rai, A. T. Place et al., “MiR-125b is critical for fibroblast-to-myofibroblast transition and cardiac fibrosis,” *Circulation*, vol. 133, no. 3, pp. 291–301, 2016.
- [61] X. Yao, X. Cui, X. Wu et al., “Tumor suppressive role of miR-1224-5p in keloid proliferation, apoptosis and invasion via the TGF- β 1/Smad3 signaling pathway,” *Biochemical and Biophysical Research Communications*, vol. 495, no. 1, pp. 713–720, 2018.
- [62] M. F. Griffin, J. Huber, F. J. Evan, N. Quarto, and M. T. Longaker, “The role of Wnt signaling in skin fibrosis,” *Medicinal Research Reviews*, vol. 42, no. 1, pp. 615–628, 2022.
- [63] T. Wu, X. Hou, J. Li et al., “Microneedle-mediated biomimetic cyclodextrin metal organic frameworks for active targeting and treatment of hypertrophic scars,” *ACS Nano*, vol. 15, no. 12, pp. 20087–20104, 2021.
- [64] C. H. Lim, Q. Sun, K. Ratti et al., “Hedgehog stimulates hair follicle neogenesis by creating inductive dermis during murine skin wound healing,” *Nature Communications*, vol. 9, no. 1, p. 4903, 2018.
- [65] D. M. Dolivo, S. A. Larson, and T. Dominko, “Crosstalk between mitogen-activated protein kinase inhibitors and transforming growth factor- β signaling results in variable activation of human dermal fibroblasts,” *International Journal of Molecular Medicine*, vol. 43, no. 1, pp. 325–335, 2019.
- [66] G. Nikoloudaki, S. Brooks, A. P. Peidl, D. Tinney, and D. W. Hamilton, “JNK signaling as a key modulator of soft connective tissue physiology, pathology, and healing,” *International Journal of Molecular Sciences*, vol. 21, no. 3, p. 1015, 2020.
- [67] A. Dey, X. Varelas, and K.-L. Guan, “Targeting the hippo pathway in cancer, fibrosis, wound healing and regenerative medicine,” *Nature Reviews. Drug Discovery*, vol. 19, no. 7, pp. 480–494, 2020.
- [68] S. Mascharak, H. E. desJardins-Park, M. F. Davitt et al., “Preventing Engrailed-1 activation in fibroblasts yields wound regeneration without scarring,” *Science*, vol. 372, no. 6540, 2021.
- [69] C. M. Brewer, B. R. Nelson, P. Wakenight et al., “Adaptations in Hippo-Yap signaling and myofibroblast fate underlie scar-free ear appendage wound healing in spiny mice,” *Developmental Cell*, vol. 56, no. 19, pp. 2722–2740.e6, 2021.
- [70] M. F. Griffin, M. R. Borrelli, J. T. Garcia et al., “JUN promotes hypertrophic skin scarring via CD36 in preclinical in vitro and in vivo models,” *Science Translational Medicine*, vol. 13, no. 609, article eabb3312, 2021.
- [71] J.-N. Schulz, C. Zeltz, I. W. Sørensen et al., “Reduced granulation tissue and wound strength in the absence of α 11 β 1 integrin,” *The Journal of Investigative Dermatology*, vol. 135, no. 5, pp. 1435–1444, 2015.
- [72] M. N. H. Malik, S. F. Waqas, J. Zeitvogel et al., “Congenital deficiency reveals critical role of ISG15 in skin homeostasis,” *The Journal of Clinical Investigation*, vol. 132, no. 3, 2022.
- [73] E. Rognoni, G. Goss, T. Hiratsuka et al., “Role of distinct fibroblast lineages and immune cells in dermal repair following UV radiation-induced tissue damage,” *eLife*, vol. 10, 2021.
- [74] E. N. Arwert, E. Hoste, and F. M. Watt, “Epithelial stem cells, wound healing and cancer,” *Nature Reviews Cancer*, vol. 12, no. 3, pp. 170–180, 2012.
- [75] M. Cangkrama, M. Wietecha, and S. Werner, “Wound repair, scar formation, and cancer: converging on activin,” *Trends in Molecular Medicine*, vol. 26, no. 12, pp. 1107–1117, 2020.
- [76] X. Chen and E. Song, “Turning foes to friends: targeting cancer-associated fibroblasts,” *Nature Reviews Drug Discovery*, vol. 18, no. 2, pp. 99–115, 2019.
- [77] K. Shiga, M. Hara, T. Nagasaki, T. Sato, H. Takahashi, and H. Takeyama, “Cancer-associated fibroblasts: their characteristics and their roles in tumor growth,” *Cancers*, vol. 7, no. 4, pp. 2443–2458, 2015.
- [78] E. Cukierman, “A reflection on how carcinoma-associated fibroblasts were recognized as active participants of epithelial tumorigenesis,” *Cancer Research*, vol. 81, no. 18, pp. 4668–4670, 2021.
- [79] Y. Guo, X. Zhang, W. Zeng et al., “TRAF6 activates fibroblasts to cancer-associated fibroblasts through FGF19 in tumor microenvironment to benefit the malignant phenotype of melanoma cells,” *The Journal of Investigative Dermatology*, vol. 140, no. 11, pp. 2268–2279.e11, 2020.
- [80] S.-Y. Yeo, K.-W. Lee, D. Shin, S. An, K.-H. Cho, and S.-H. Kim, “A positive feedback loop bi-stably activates fibroblasts,” *Nature Communications*, vol. 9, no. 1, p. 3016, 2018.
- [81] A. Katarkar, G. Bottoni, A. Clocchiatti et al., “NOTCH1 gene amplification promotes expansion of cancer associated fibroblast populations in human skin,” *Nature Communications*, vol. 11, no. 1, p. 5126, 2020.
- [82] V. Madan, J. T. Lear, and R. M. Szeimies, “Non-melanoma skin cancer,” *The Lancet*, vol. 375, no. 9715, pp. 673–685, 2010.
- [83] M. Heinz, H. L. Niederleithner, E. Puujalka et al., “Activin A is anti-lymphangiogenic in a melanoma mouse model,” *The Journal of Investigative Dermatology*, vol. 135, no. 1, pp. 212–221, 2015.
- [84] M. Antsiferova, M. Huber, M. Meyer et al., “Activin enhances skin tumorigenesis and malignant progression by inducing

- a pro-tumourigenic immune cell response,” *Nature Communications*, vol. 2, no. 1, p. 576, 2011.
- [85] P. Donovan, O. A. Dubey, S. Kallioinen et al., “Paracrine activin- α signaling promotes melanoma growth and metastasis through immune evasion,” *The Journal of Investigative Dermatology*, vol. 137, no. 12, pp. 2578–2587, 2017.
- [86] M. Cangkruma, M. Wietecha, N. Mathis et al., “A paracrine activin A-mDia2 axis promotes squamous carcinogenesis via fibroblast reprogramming,” *EMBO Molecular Medicine*, vol. 12, no. 4, article e11466, 2020.
- [87] R. Samain and V. Sanz-Moreno, “Cancer-associated fibroblasts: activin A adds another string to their bow,” *EMBO Molecular Medicine*, vol. 12, no. 4, article e12102, 2020.
- [88] L. Chen, Y. Su, B. Yin et al., “LARP6 regulates keloid fibroblast proliferation, invasion, and ability to synthesize collagen,” *The Journal of Investigative Dermatology*, 2022.
- [89] M. W. Y. Tan, M. K. Sng, H. S. Cheng et al., “Deficiency in fibroblast PPAR β/δ reduces nonmelanoma skin cancers in mice,” *Cell Death and Differentiation*, vol. 27, no. 9, pp. 2668–2680, 2020.
- [90] T. Budden, C. Gaudy-Marqueste, A. Porter et al., “Ultraviolet light-induced collagen degradation inhibits melanoma invasion,” *Nature Communications*, vol. 12, no. 1, p. 2742, 2021.
- [91] D. Manikoth Ayyathan, P. Koganti, V. Marcu-Malina et al., “SMURF2 prevents detrimental changes to chromatin, protecting human dermal fibroblasts from chromosomal instability and tumorigenesis,” *Oncogene*, vol. 39, no. 16, pp. 3396–3410, 2020.
- [92] G. Bottoni, A. Katarkar, B. Tassone et al., “CSL controls telomere maintenance and genome stability in human dermal fibroblasts,” *Nature Communications*, vol. 10, no. 1, p. 3884, 2019.
- [93] M. Gonçalves-Maia, Y. Gache, M. Basante et al., “NK cell and fibroblast-mediated regulation of skin squamous cell carcinoma invasion by CLEC2A is compromised in Xeroderma pigmentosum,” *The Journal of Investigative Dermatology*, vol. 140, no. 9, pp. 1723–1732, 2020.
- [94] B. Hirshowitz, D. Lerner, and A. R. Moscona, “Treatment of keloid scars by combined cryosurgery and intralesional corticosteroids,” *Aesthetic Plastic Surgery*, vol. 6, no. 3, pp. 153–158, 1982.
- [95] B. Berman and H. C. Bielely, “Adjunct therapies to surgical management of keloids,” *Dermatologic Surgery*, vol. 22, no. 2, pp. 126–130, 1996.
- [96] J. A. Ledon, J. Savas, K. Franca, A. Chacon, and K. Nouri, “Intralesional treatment for keloids and hypertrophic scars: a review,” *Dermatologic Surgery*, vol. 39, no. 12, pp. 1745–1757, 2013.
- [97] D. B. Lumenta, E. Siepmann, and L.-P. Kamolz, “Internet-based survey on current practice for evaluation, prevention, and treatment of scars, hypertrophic scars, and keloids,” *Wound Repair and Regeneration*, vol. 22, no. 4, pp. 483–491, 2014.
- [98] D. C. Yeo, C. Wiraja, A. S. Paller, C. A. Mirkin, and C. Xu, “Abnormal scar identification with spherical-nucleic-acid technology,” *Nature Biomedical Engineering*, vol. 2, no. 4, pp. 227–238, 2018.
- [99] M. Zheng, C. Wiraja, D. C. Yeo et al., “Oligonucleotide molecular sprinkler for intracellular detection and spontaneous regulation of mRNA for theranostics of scar fibroblasts,” *Small*, vol. 14, no. 49, article e1802546, 2018.
- [100] S. Haldar, A. Sharma, S. Gupta, S. Chauhan, P. Roy, and D. Lahiri, “Bioengineered smart trilayer skin tissue substitute for efficient deep wound healing,” *Materials Science & Engineering. C, Materials for Biological Applications*, vol. 105, article 110140, 2019.
- [101] J. Li, C. Zhou, C. Luo et al., “N-acetyl cysteine-loaded graphene oxide-collagen hybrid membrane for scarless wound healing,” *Theranostics*, vol. 9, no. 20, pp. 5839–5853, 2019.
- [102] A. Veeruraj, L. Liu, J. Zheng, J. Wu, and M. Arumugam, “Evaluation of astaxanthin incorporated collagen film developed from the outer skin waste of squid *Doryteuthis singhalensis* for wound healing and tissue regenerative applications,” *Materials Science & Engineering. C, Materials for Biological Applications*, vol. 95, pp. 29–42, 2019.
- [103] T. Xu, R. Yang, X. Ma et al., “Bionic poly(γ -glutamic acid) electrospun fibrous scaffolds for preventing hypertrophic scars,” *Advanced Healthcare Materials*, vol. 8, no. 13, article e1900123, 2019.
- [104] U. Park, M. S. Lee, J. Jeon et al., “Coacervate-mediated exogenous growth factor delivery for scarless skin regeneration,” *Acta Biomaterialia*, vol. 90, pp. 179–191, 2019.
- [105] J. Zhang, Y. Zheng, J. Lee et al., “A pulsatile release platform based on photo-induced imine-crosslinking hydrogel promotes scarless wound healing,” *Nature Communications*, vol. 12, no. 1, p. 1670, 2021.
- [106] F. Chogan, T. Mirmajidi, A. H. Rezayan et al., “Design, fabrication, and optimization of a dual function three-layer scaffold for controlled release of metformin hydrochloride to alleviate fibrosis and accelerate wound healing,” *Acta Biomaterialia*, vol. 113, pp. 144–163, 2020.
- [107] Y. Hu, S. S. Rao, Z. X. Wang et al., “Exosomes from human umbilical cord blood accelerate cutaneous wound healing through miR-21-3p-mediated promotion of angiogenesis and fibroblast function,” *Theranostics*, vol. 8, no. 1, pp. 169–184, 2018.
- [108] S. Fang, C. Xu, Y. Zhang et al., “Umbilical cord-derived mesenchymal stem cell-derived exosomal microRNAs suppress myofibroblast differentiation by inhibiting the transforming growth factor- β /SMAD2 pathway during wound healing,” *Stem Cells Translational Medicine*, vol. 5, no. 10, pp. 1425–1439, 2016.
- [109] Y. Xiao, J. Peng, Q. Liu et al., “Ultrasoft CuS@BSA nanoparticles with mild photothermal conversion synergistically induce MSCs-differentiated fibroblast and improve skin regeneration,” *Theranostics*, vol. 10, no. 4, pp. 1500–1513, 2020.
- [110] W. Ma, H. Ma, P. Qiu et al., “Sprayable β -FeSi₂ composite hydrogel for portable skin tumor treatment and wound healing,” *Biomaterials*, vol. 279, article 121225, 2021.
- [111] C. Kalirajan and T. Palanisamy, “A ZnO-curcumin nanocomposite embedded hybrid collagen scaffold for effective scarless skin regeneration in acute burn injury,” *Journal of Materials Chemistry B*, vol. 7, no. 38, pp. 5873–5886, 2019.
- [112] X. Zheng, Z. Ding, W. Cheng et al., “Microskin-inspired injectable MSC-laden hydrogels for scarless wound healing with hair follicles,” *Advanced Healthcare Materials*, vol. 9, no. 10, article e2000041, 2020.
- [113] L. Liu, Z. Ding, Y. Yang, Z. Zhang, Q. Lu, and D. L. Kaplan, “Asiaticoside-laden silk nanofiber hydrogels to regulate inflammation and angiogenesis for scarless skin regeneration,” *Biomaterials Science*, vol. 9, no. 15, pp. 5227–5236, 2021.

Retraction

Retracted: Perioperative Management and Long-Term Outcomes in Ocular Cicatricial Pemphigoid Patients Undergoing Cataract Surgery

Oxidative Medicine and Cellular Longevity

Received 26 September 2023; Accepted 26 September 2023; Published 27 September 2023

Copyright © 2023 Oxidative Medicine and Cellular Longevity. This is an open access article distributed under the Creative Commons Attribution License, which permits unrestricted use, distribution, and reproduction in any medium, provided the original work is properly cited.

This article has been retracted by Hindawi following an investigation undertaken by the publisher [1]. This investigation has uncovered evidence of one or more of the following indicators of systematic manipulation of the publication process:

- (1) Discrepancies in scope
- (2) Discrepancies in the description of the research reported
- (3) Discrepancies between the availability of data and the research described
- (4) Inappropriate citations
- (5) Incoherent, meaningless and/or irrelevant content included in the article
- (6) Peer-review manipulation

The presence of these indicators undermines our confidence in the integrity of the article's content and we cannot, therefore, vouch for its reliability. Please note that this notice is intended solely to alert readers that the content of this article is unreliable. We have not investigated whether authors were aware of or involved in the systematic manipulation of the publication process.

Wiley and Hindawi regrets that the usual quality checks did not identify these issues before publication and have since put additional measures in place to safeguard research integrity.

We wish to credit our own Research Integrity and Research Publishing teams and anonymous and named external researchers and research integrity experts for contributing to this investigation.





The corresponding author, as the representative of all authors, has been given the opportunity to register their agreement or disagreement to this retraction. We have kept a record of any response received.

References

- [1] Y. He, Z. Quan, R. Zhang et al., "Perioperative Management and Long-Term Outcomes in Ocular Cicatricial Pemphigoid Patients Undergoing Cataract Surgery," *Oxidative Medicine and Cellular Longevity*, vol. 2022, Article ID 2496649, 24 pages, 2022.

Research Article

Perioperative Management and Long-Term Outcomes in Ocular Cicatricial Pemphigoid Patients Undergoing Cataract Surgery

Yuan He ¹, Zhuoya Quan ¹, Ruixue Zhang ¹, Zhi Ji,¹ Jun Jia,¹ Huifeng Liu,¹ Chuntao Zhang,¹ Beilei He,¹ Yuan Ren,¹ and Yun Feng ²

¹The Second Affiliated Hospital of Xi'an Medical University, Eye Center, Ocular Immunology and Inflammation Institute, Shaanxi Provincial Clinical Research Center for Ophthalmology, Xi'an 710038, China

²Department of Ophthalmology, Peking University Third Hospital, Beijing Key Laboratory of Restoration of Damaged Ocular Nerve, Peking University Third Hospital, Beijing 100191, China

Correspondence should be addressed to Yuan He; openji7127@hotmail.com and Yun Feng; fengyun@bjmu.edu.cn

Received 18 February 2022; Revised 23 March 2022; Accepted 1 April 2022; Published 30 April 2022

Academic Editor: Shao Liang

Copyright © 2022 Yuan He et al. This is an open access article distributed under the Creative Commons Attribution License, which permits unrestricted use, distribution, and reproduction in any medium, provided the original work is properly cited.

Objective. To observe the outcomes of cataract surgery in ocular cicatricial pemphigoid (OCP) patients and explore routine perioperative medical treatments. **Design.** Retrospective case series. **Methods.** Fourteen eyes of 8 patients were included in the study. Foster's stage 1-4 OCP patients were given human intravenous immunoglobulin, whereas patients with active inflammation were treated with prednisone tablets and methotrexate. Those who were intolerant to methotrexate and had severe inflammatory symptoms were treated with cyclophosphamide. Cataract surgery was performed for all patients after three months of systemic treatment under stable conditions. The conjunctival biopsy was evaluated by immunofluorescence microscopy. Then, patients were divided into individuals with or without ankyloblepharon. Records were reviewed for OCP stage, type of surgery, best-corrected visual acuity (BCVA), Schirmer I test, corneal fluorescein sodium staining, meibomian gland coloboma range, and ocular surface disease index (OSDI) scores. Follow-up was for the duration of taking topical and systemic medication. **Results.** Nine female (64.29%) and 4 male (35.71%) eyes were diagnosed with OCP by biopsy. The mean follow-up time was 60.64 ± 35.62 months. Thirteen eyes (92.86%) of 7 patients underwent phacoemulsification. One eye underwent phacoemulsification combined with amniotic membrane transplantation. The intracapsular extraction of cataract was applied to one eye. The BCVA improved significantly in all the patients, which remained stable until the last follow-up. The Schirmer I test was higher than that before the surgery. Corneal fluorescein sodium staining after surgery showed a decrease in score compared to the preoperative score. The BCVA of the patients after surgery increased significantly. The OSDI scores of patients with ankyloblepharon were significantly higher than for those without it. Postoperative symblepharon showed no significant difference compared to the preoperative symblepharon. **Conclusions.** In this series, OCP patients with cataracts were able to undergo phacoemulsification surgery, whereas routine use of immunosuppression and closed postoperative follow-up were necessary.

1. Introduction

Mucous membrane pemphigoid (MMP) is a systemic autoimmune bullous skin disease which mainly affects mucosal tissues, such as the conjunctiva, nasal cavity, oropharynx, esophagus, trachea, skin, and genitals [1]. Approximately 70% of patients with ocular damage as the main clinical symptom have bilateral [2], asymmetric, and chronic pro-

gressive fibrosis and inflammatory conjunctivitis, known as ocular cicatricial pemphigoid (OCP) [3]. According to relevant reports, OCP is a rare and potentially blinding disease. One of its characteristics is that it destroys the adhesion between the conjunctival epithelium and the subepithelial tissues, thereby causing the subepithelial tissues to form blisters [2]. The incidence rate of OCP is 1-5/60,000, mainly in women (male to female ratio is approximately 1:2). The

average age of onset of patients was 65 years old, and all ethnic groups were roughly the same [4, 5]. Patients affected by this autoimmune disease will eventually develop conjunctival scarring. If the patient does not receive proper treatment or is not treated, it may cause ocular corneal opacity and permanent vision damage and loss [6]. OCP is an autoimmune chronic cicatricial conjunctivitis, and abnormal immune system regulation is an important feature of OCP [4]. Thus, ocular MMP treatment guidelines are designed to control immune-mediated inflammatory diseases, prevent fibrosis, and manage ocular surface diseases [7]. Mycophenolate mofetil, azathioprine, and methotrexate can be used for the treatment of moderate disease. Of these drugs, mycophenolate mofetil had the best safety profile and was well tolerated, with the lowest withdrawal rate among the drugs used. The recommended dose is 1 gram twice daily, and the treatment can be controlled in 59% of patients [8, 9].

Surgical operations may stimulate the patient's immune response, which had entered the cessation period of inflammation [10]. Such patients should be treated with preservative-free artificial tear eye drops, topical steroids, or immunosuppressants. In the stable period of inflammation, OCP and Stevens-Johnson syndrome (SJS) or toxic epidermal necrolysis (TEN) are safe for cataract extraction [11, 12]. Cataracts are visual impairments caused by decreased transparency and refractive power of the lens. When cataracts become obvious, surgery is the only certain treatment. Patients without other complications usually have excellent postoperative vision after cataract surgery [13]. The reported success rates for improved visual acuity in age-related cataract surgeries range from 91% to 98.5% [14, 15]. When cataracts are associated with other ocular surface diseases, such as Steven-Johnson syndrome (SJS), OCP, silkworm corneal ulcer, spring keratoconjunctivitis, and limbal stem cell deficiency, the prognosis of visual quality is rarely reported [15]. Puranik et al.'s study reported the outcomes of cataract surgery in ocular cicatricial pemphigoid and found that cataract surgery could be safely performed with no major intra- or postoperative complications [11]. However, OCP patients often present common causes of cataracts, which may result in visual loss through aging, medication-induced or complex cataracts. Age-related cataracts are more common in OCP patients because they tend to occur at an older age [6]. Drug-induced cataracts may be caused by local and systemic steroids used to treat conjunctival inflammation, and complex cataracts may be caused by uveitis associated with keratitis [16]. Vision improvement of such patients after cataract surgery may not be comparable to that of patients with senile cataract alone. Many studies have shown that surgical interventions such as cataract removal often trigger excessive inflammation in the eyes of OCP patients, leading to disease deterioration. In most patients, it is difficult to observe cataracts through the opaque cornea, which could increase the risk and difficulty of the surgical process [17]. At the same time, the risk of complications after surgery is also increased with a higher degree of scar adhesion or aggravated corneal disease after surgery. Previous studies have shown that cataract surgery can achieve certain success after complete control of conjunctival inflammation before

surgery [18]. However, due to the progressive scar formation of the disease itself, the benefits of improved vision are short-lived [17].

The significance of cataract surgery in patients with OCP, the opportunity for surgery, and the choice of methods have always been controversial. Improper perioperative medication can aggravate existing ocular symptoms in OCP [15]. Therefore, the motivation and purpose of our study are to indicate the safety and effectiveness of such patients after cataract surgery and to provide guidelines for clinical research and treatment in OCP patients through evaluating ocular manifestations and symptoms of OCP stage, BCVA, Schirmer I test, corneal fluorescein sodium staining, meibomian gland coloboma range, and OSDI scores after surgery. We suggest that the routine use of immunosuppression and postoperative close follow-up are necessary.

2. Methods

2.1. General Data. The study was a retrospective cohort case study. A total of 14 eyes from 8 patients diagnosed with OCP who underwent cataract surgery in the Department of Ophthalmology, at the Second Affiliated Hospital of Xi'an Medical University from 2010 to 2018, were included and followed up for at least 2 years. The described research adhered to the tenets of the Declaration of Helsinki, and Ethics Committee approval of the Second Affiliated Hospital of Xi'an Medical University was obtained. All patients met the diagnostic criteria of ocular cicatrix pemphigoid disease with lens opacity [19]. The basic information of the patients and the detailed medication history related to the disease were collected. Every patient underwent evaluation, including BCVA (LogMAR), slit lamp examination, Goldmann applanation tonometry, and indirect funduscopy before surgery. Ocular surface disease index (OSDI), Foster's staging system (Table 1), stage of keratopathy (Table 2), stage of the symblepharon degree (Table 3), corneal sodium fluorescein dyeing (Table 4), score of meibomian gland coloboma range (Table 5), aqueous flare, and Schirmer I test were compared before and after surgery. The surgical procedure, serological markers, and postoperative complications were recorded for each patient.

Inclusion criteria: (1) patients who met the diagnosis of OCP based on ocular manifestations, with ocular symptoms including red eyes, blepharospasm, lacrimonia, photophobia, decreased vision, burning, foreign body sensations, itching, and heavy eyelids associated with dry eye. (2) A slit lamp was used to evaluate the ocular lesions in detail. Trichiasis, dichiasis, blepharoglandular dysfunction and blepharitis, conjunctival congestion, papillary hyperplasia, and follicular formation were observed. In severe cases, conjunctival keratosis with subepithelial fibrosis, fornix shortening, and conjunctival scarring may be present. (3) Local eye conjunctiva was taken for lab examination. Direct immunofluorescence microscopy showed linear fluorescence along the conjunctival epithelial basement membrane region. (4) In accordance with the diagnostic criteria of cataract (LOCS III), after the pupil was dilated at least 5 mm, the lens was examined by ophthalmoscope or slit lamp microscope with the opacity

TABLE 1: The stage of ocular cicatricial pemphigoid (Foster's staging system).

Stage	Clinical feature
I	Conjunctival congestion, subconjunctival fibrosis, chronic nonspecific conjunctivitis
II	Except for conjunctival scar, the lower fornix is shortened and the corneal epithelium is punctate stained
III	Significant eyelid adhesion, especially at the epicanthus, conjunctival scar thickening, corneal infiltration, scar, neovascularization, and dry eye
IV	Eyelid adhesions, corneal epithelial keratosis, corneal neovascularization, trichiasis, eyelash disorder, rabbit eye, varus

TABLE 2: The stage of keratopathy.

Stage	Clinical feature
0	Normal cornea
1	Mild to moderate superficial punctate keratitis
2	Severe superficial punctate keratitis
3	Mild to moderate scarring and/or neovascularization
4	Severe scarring and/or neovascularization

TABLE 3: The stage of the symblepharon degree.

Stage	Clinical feature
0	No symblepharon
1	Symblepharon only involves the conjunctival surface
2	The formation of symblepharon involves less than half of the corneal surface
3	The formation of symblepharon involves more than half of the corneal surface

accompanied by painless vision loss. (5) Consent for the operation was provided and the informed consent was signed. (6) The cataract surgery indications were met. (7) All patients were diagnosed for the first time without taking relevant therapeutic drugs. (8) All patients were followed up with for more than 2 years. Exclusion criteria: (1) patients with other serious physical or tumor diseases; (2) people with mental illness; (3) patients with insufficient medical records; (4) patients with follow-up less than 2 years.

2.2. Treatment Protocols. Patients with Foster's stages I-IV were given 2-3 g/kg human immunoglobulin (IVIG) systemic intravenous injection within 4-5 h per day and divided into three equal parts for at least three days. Cataract surgery was performed after ocular surface inflammation was in the quiescence phase (no conjunctival congestion or secretions and no progress in subconjunctival scar formation). Patients with active inflammation are routinely treated with prednisone tablets (starting at 1 mg/kg/d) in combination with methotrexate, with the doses ranging from 5 to 10 mg/week. Folic acid (5 mg) was taken orally the next day after methotrexate administration, to reduce its adverse reactions. Cataract surgery was performed after 3 months when the inflammation was stable. Methotrexate intolerance and stage IV fosters were treated with prednisone tablets (starting dose 1 mg/kg/d) combined with cyclophosphamide (1-2 mg/kg/d).

TABLE 4: Corneal fluorescein sodium dyeing score.

Score	Degree of dyeing
0	Nonfluorescent dyeing
1	Fluorescein dyeing sites < 5
2	Corneal fluorescein dyeing sites < 30 and ≥ 5 and/or dyeing range no more than 2 quadrants
3	Corneal fluorescein dyeing sites ≥ 30 and/or corneal injury area 2 quadrants or above and fusion of dyeing sites

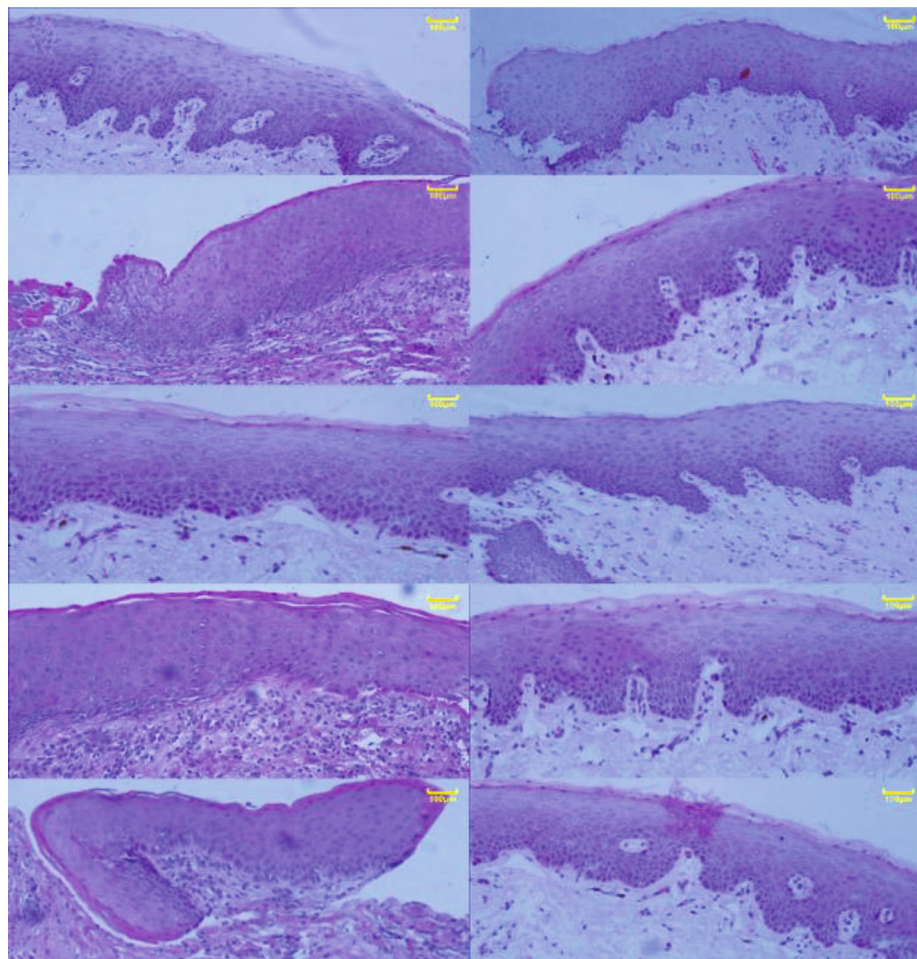
TABLE 5: The score of meibomian gland coloboma range.

Score	Meibomian gland coloboma range
0	No coloboma
1	<1/3 proportion
2	1/3~2/3 proportion
3	>2/3 proportion

Prednisone tablets (1 mg/kg/d) were taken orally for all patients 1 week before surgery, and levofloxacin eye drops were given to the eyes 3 days before surgery, 4 times per day. Compound tropicamide eye drops (0.5%) were applied to the eyes to fully dilate the pupils before surgery. The dosage of prednisone tablets was reduced after 4-16 weeks when the inflammation was stable, by withholding one to two tablets every two to four weeks until the dosage was 10 mg daily, and then reduced to one tablet every 4-8 weeks. Prednisone was withdrawn until the condition of OCP patients was stable. The patients who were treated with immunosuppressants before surgery continued to take them after surgery.

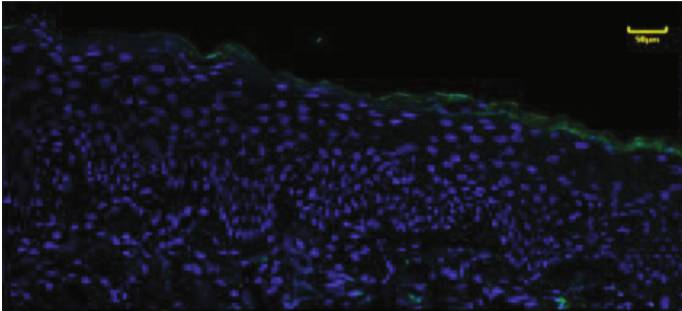
2.3. Biological Sample Processing. A 2 mm \times 6 mm inferior fornix of conjunctiva sample was obtained with sterilized smooth forceps and ocular surgical scissors after topical anesthesia for cataract surgery. The conjunctival sample was divided into two equal parts: one used for immunofluorescence microscopy and the other for hematoxylin-eosin (HE) staining. The samples were inserted into optimal cutting temperature compound (OCT) for embedding and quickly in liquid nitrogen. After quick freezing, the tissues were cut into serial sections with a cryostat at minus 20°C and stored for subsequent testing.

2.4. HE Staining. The slices were incubated at room temperature and stained with hematoxylin for 5 min. The slices were then differentiated in 1% hydrochloric acid ethanol

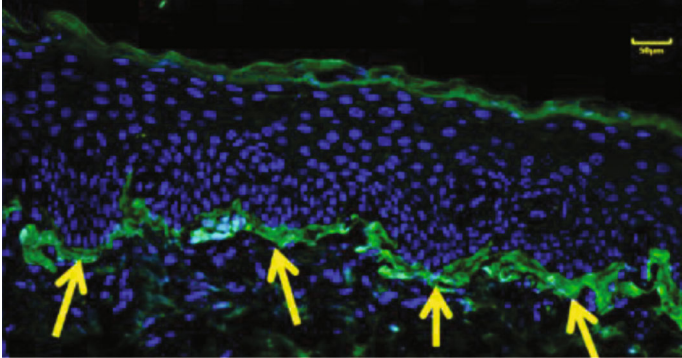


(a)

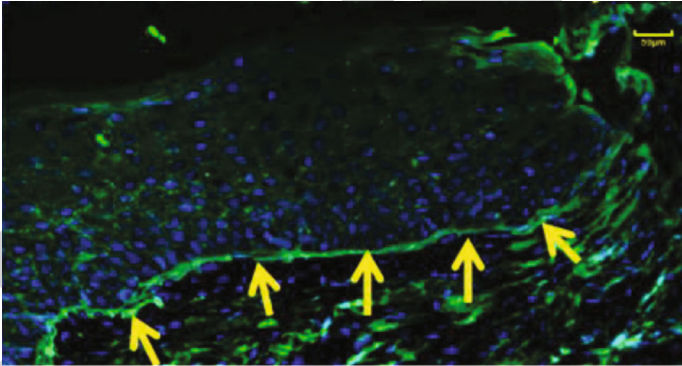
FIGURE 1: Continued.



(b)

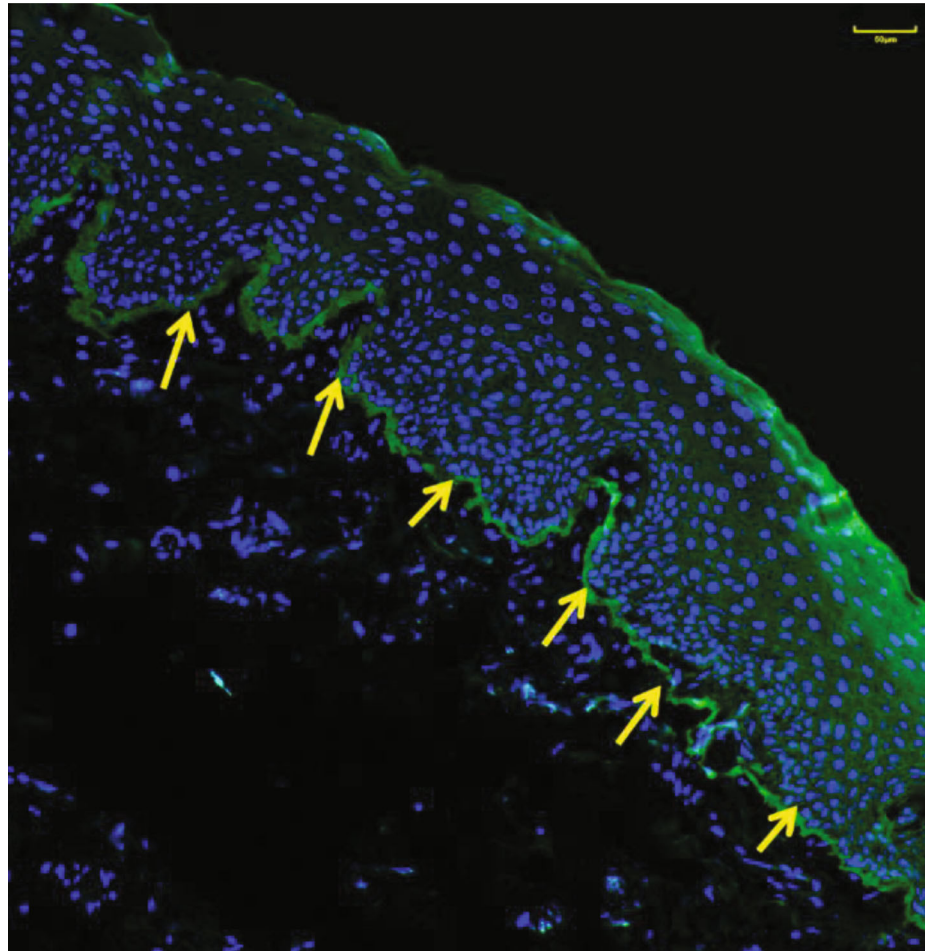


(c)



(d)

FIGURE 1: Continued.



(e)

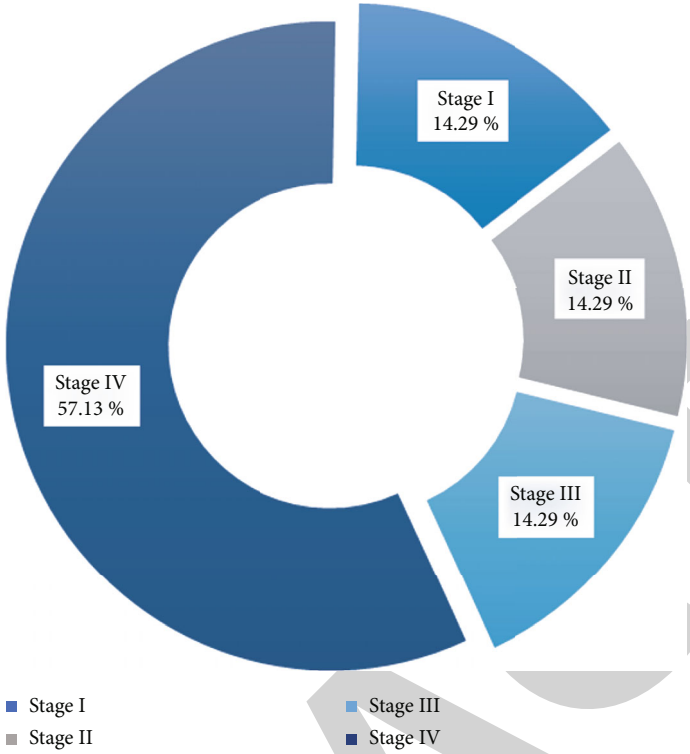
FIGURE 1: HE staining and immunofluorescence assay. (a) The histology of OCP conjunctiva. Multiple infiltrating immune cells were observed in the HE-stained slides from 10 eyes of 8 patients. (b) Control group. There was no staining along the conjunctival basement membrane zone. (c–e) Positive results of brilliant IgM, IgA, and IgG fluorescent staining along the basement membrane zone.

for a few seconds and dehydrated with 95% alcohol for 30 s. The same procedure was used for eosin alcohol staining solution for approximately 3 min. The excess dye was rinsed with water and differentiated with 85% alcohol. The slices were successively dehydrated with different concentrations of alcohol. Finally, the slices were added to xylene to make them transparent and sealed with neutral gum and then were examined with a light microscope (Olympus, Japan) and photographed with a digital camera.

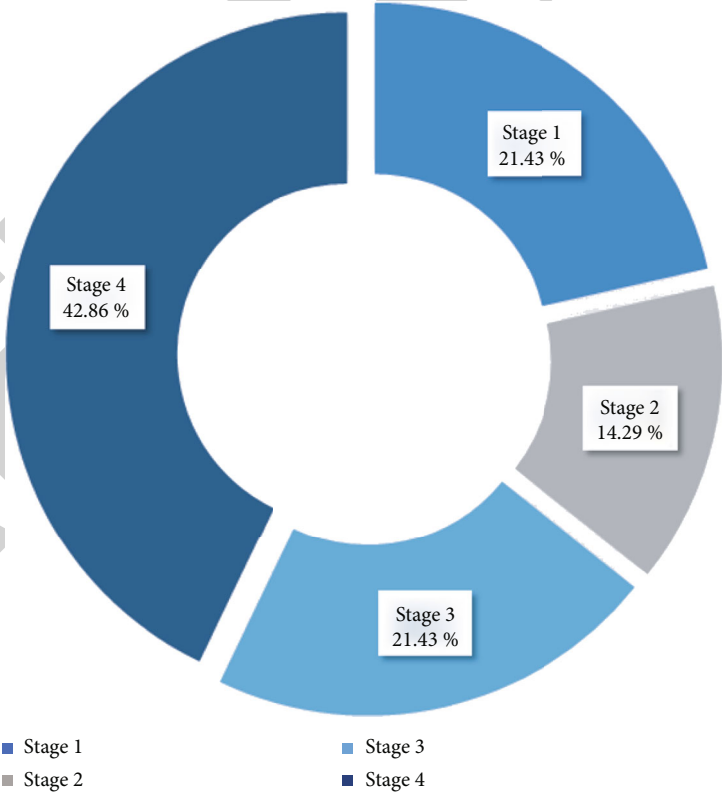
2.5. Immunofluorescence Microscopy. After cryoembedding at -20°C , the slices were ventilated to remove water vapor, fixed with 4% paraformaldehyde fixing solution, and washed with PBS three times. After the antigens were heated, they were naturally cooled at room temperature and incubated with goat serum for 1 h. Anti-IgA (1:100, Abcam, UK), IgG (1:300, Abcam, UK), and IgM (1:1000, Abcam, UK) antibodies were then added overnight at 4°C . Fluorescence isothiocyanate- (FITC-) labeled sheep anti-human antibodies IgA, IgG, and IgM were added followed by incubation in the dark, at room temperature for 1 h. After washing with

PBS, the nuclei were stained with DAPI, and the anti-bleaching agent was used to seal the slices. The slices were then observed under a confocal microscope (Nikon, Japan).

2.6. OSDI Score. According to the subjective feelings of the patients, the OSDI scoring scale [20] was used to self-test the patients. The completion of the questionnaire was carried out under the strict professional guidance of ophthalmologists in our hospital. This questionnaire contained a total of 12 questions, for example: whether the patients have photophobia, pain, and foreign body sensation and other eye discomfort symptoms; whether there was blurred vision and visual fluctuations in the daily reading, writing, driving, the use of computers and television; and whether eyes in the sand, dry, and air conditioning environment felt uncomfortable. Each question was followed by five possible answers: 0 (never experienced such symptoms), 1 (occasional occurrence of such symptoms), 2 (had such symptoms about half the time), 3 (most of the time), and 4 (this kind of symptom occurred all the time). Patients answered the questions selectively but responded to at least two items. Each score will be



(a)



(b)

FIGURE 2: Continued.

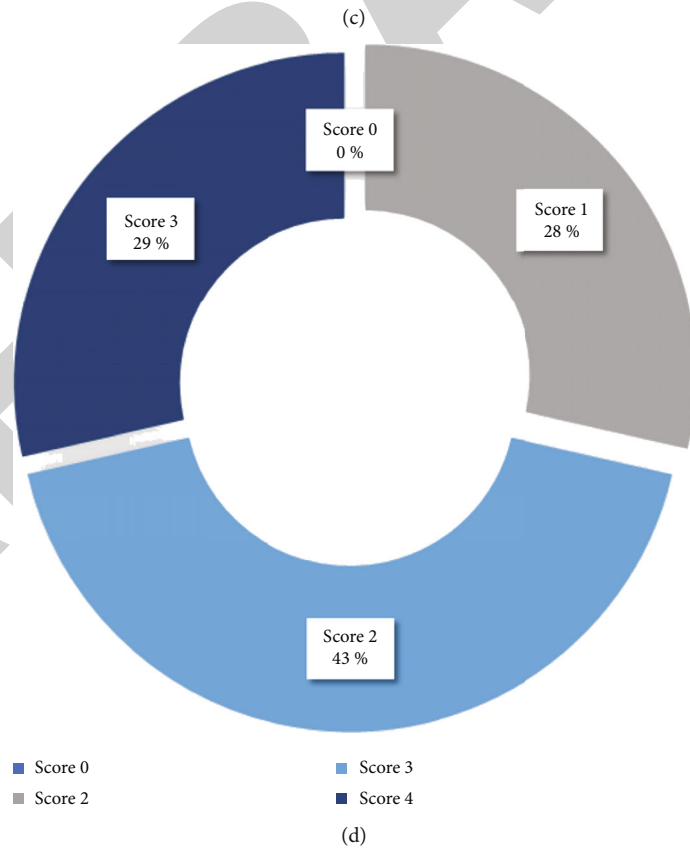
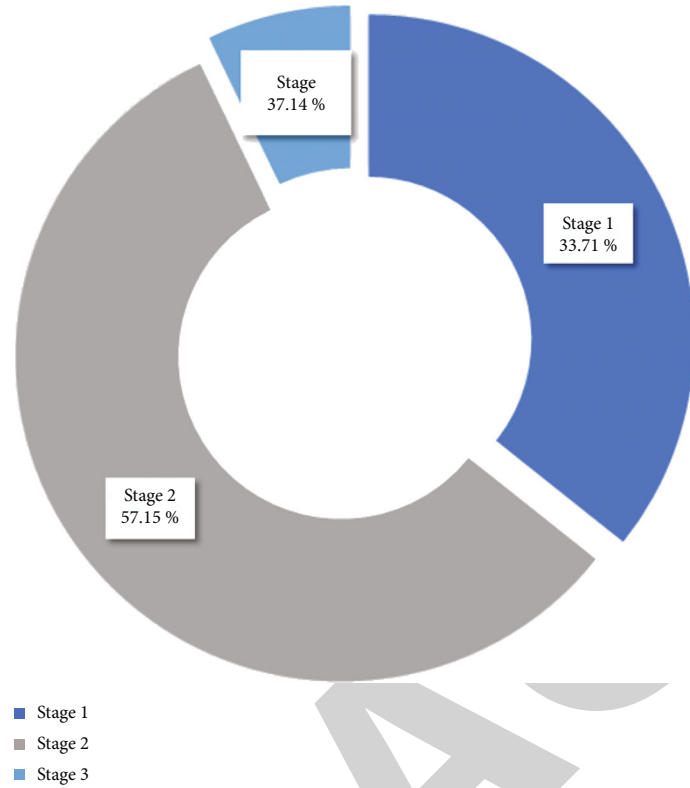


FIGURE 2: Preoperative and postoperative stage and score of OCP patients. (a) Foster's stage I-IV. (b) Keratopathy stage 1-4. (c) Symblepharon stage 1-3. (d) Meibomian gland coloboma range score 0-3.

TABLE 6: Preoperative information of patients.

Patient	Age/sex	Eye	OCP	Aqueous flare	Symblepharon	Keratopathy	BCVA	Meibomian gland coloboma range	Schirmer I test
1	51/M	OD	I	0	1	3	1	1	3
	51	OS	I	0	1	4	1.3	1	4
2	68/F	OD	IV	0	2	3	2	2	18
	67	OS	IV	0	2	1	1.9	2	7
3	64/F	OD	IV	0	2	2	1.1	2	4
	64	OS	IV	0	2	4	1.4	2	3
4	72/F	OD	III	0	2	3	1.2	2	15
	72	OS	III	0	1	2	1.3	2	10
5	71/F	OS	IV	2	2	4	0.0025	3	2
6	71/M	OD	IV	2	3	4	0.005	3	3
7	65/M	OD	IV	2	2	4	0.005	3	5
	66	OS	IV	2	2	4	0.005	3	5
8	66/F	OD	II	0	1	1	0.4	1	12
	66	OS	II	0	1	1	0.5	1	15

The aqueous flare: 0: no; 1: have; 2: not clear.

summarized with a score range of 0~100, calculated by the following formula: OSDI score = (total score × 25)/number of questions.

2.7. Follow-Up Observation Indices. LogMAR visual acuity was recorded at 1 day, 1 week, 1 month, 3 months, 6 months, 1 year, and 2 years and at the final follow-up after surgery. The conjunctiva, cornea, and anterior segment were examined with a slit lamp. Ankyloblepharon and inflammation were examined and compared with those before the operation. The OSDI score was used to distinguish between patients with normal eye and dry eye. Perioperative doses and the durations of local and systemic immunosuppressive agents were recorded. Complications before, during, and after cataract extraction and other surgical interventions were also recorded. Patients were divided into two groups according to Foster's staging system and ankyloblepharon. The first group (without ankyloblepharon) included mild to moderate patients with OCP stages I, II, and III. The second group included severe patients (ankyloblepharon group) with OCP stage IV. The changes in OSDI score, Schirmer I test, corneal sodium fluorescein staining, meibomian gland coloboma range, and BCVA were compared before and after surgery among patients with different grades at different times. Routine blood and urine examinations were performed every week. Liver and kidney function examinations were also recorded every half a month. Blood pressure and blood glucose of OCP patients were kept within normal ranges.

2.8. Statistical Analysis. All data were analyzed by SPSS 20.0 software. Paired sample *t*-tests were used for intragroup comparisons, ANOVA was used for intergroup comparisons, repeated measure ANOVA was used to analyze intragroup differences in OSDI scores before and after surgery, and group *t*-tests or Wilcoxon rank sum tests were used for comparisons between groups. $P < 0.05$ was considered to be statistically significant.

3. Results

3.1. Demography of Patients. Seventeen eyes of 10 OCP patients underwent cataract surgery. Two of them were inadequate after follow-up and were excluded. Finally, 14 eyes of 8 patients were analyzed, including 9 eyes of 5 female patients (64.29%) and 5 eyes of 3 male patients (35.71%). The average age of the patients was 66.11 ± 6.33 years, and the mean follow-up time was 60.64 ± 35.62 months. The shortest follow-up time was 24 months, and the longest continuous follow-up time was 120 months.

3.2. HE Staining and Indirect Immunofluorescence Assay. Fourteen eyes of 8 patients were diagnosed with OCP and included in this study. None of them received any treatment or took medication before diagnosis. All patients underwent conjunctival biopsy during cataract surgery. Multiple typical infiltrated immune cells, such as lymphocytes, plasma cells, and white blood cells, were observed by HE staining (Figure 1(a)). A positive result with linear direct immunofluorescence labeling (green) of autoantibodies was staining along the basement membrane zone. (Figures 1(c)–1(e)). Since the time between the binocular operations was no more than three months, conjunctival tissue was excised from only one eye of 4 patients for HE staining.

3.3. Other Ocular Surgeries. One eye (7.14%) was unable to undergo phacoemulsification because of severe corneal opacity, and intracapsular cataract extraction (ICCE) was finally applied (patient 5). One patient (7.14%) underwent phacoemulsification combined with amniotic membrane transplantation (patient 6). One patient with a case of binoculus (14.28%) underwent upper eyelid surgical treatment of entropion and trichiasis (patient 2).

3.4. Comparison of Patient Information before and after Surgery. Foster's stage, corneal fluorescein sodium staining, and meibomian gland coloboma range did not change pre- and postoperatively (Figures 2(a)–2(d)). Table 6 shows the

TABLE 7: The postoperation outcomes of patients after one week.

Patient	Eye	OCP	Aqueous flare		Symblepharon		Keratopathy		Meibomian gland coloboma range		BCVA	
			Postoperation	Difference	Postoperation	Difference	Postoperation	Difference	Postoperation	Difference	Preoperation	Postoperation
1	OD	I	0	0	1	0	3	0	1	0	1.0	0.7
	OS	I	0	0	1	0	4	0	1	0	1.3	1.8
2	OD	IV	0	0	2	0	3	0	2	0	2.0	1.2
	OS	IV	0	0	2	0	1	0	2	0	1.9	0.4
3	OD	IV	1	1	2	0	2	0	2	0	1.1	0.8
	OS	IV	0	0	2	0	4	0	2	0	1.4	0.9
4	OD	III	1	1	2	0	3	0	2	0	1.2	0.5
	OS	III	1	1	1	0	2	0	2	0	1.3	0.3
5	OS	IV	2	0	2	0	4	0	3	0	0.0025	0.005
6	OD	IV	2	0	3	0	4	0	3	0	0.005	0.005
	OD	IV	2	0	2	0	4	0	3	0	0.005	0.014
	OS	IV	2	0	2	0	4	0	3	0	0.005	0.014
	OD	II	0	0	1	0	1	0	1	0	0.4	0
	OS	II	0	0	1	0	1	0	1	0	0.5	0

The aqueous flare: 0: no; 1: have; 2: not clear.

TABLE 8: The outcomes of patients after operation in three months.

Patient	Eye	OCP	Aqueous flare		Symblepharon		Keratopathy		Meibomian gland coloboma range		BCVA		Schirmer I test
			Postoperation	Difference	Postoperation	Difference	Postoperation	Difference	Postoperation	Difference	Preoperation	Postoperation	
1	OD	I	0	0	1	0	3	0	1	0	1.0	0.6	11
	OS	I	0	0	1	0	4	0	1	0	1.3	0.7	15
2	OD	IV	0	0	2	0	3	0	2	0	2.0	1.0	17
	OS	IV	0	0	2	0	1	0	2	0	1.9	0.4	11
3	OD	IV	0	0	2	0	2	0	2	0	1.1	0.8	10
	OS	IV	0	0	2	0	4	0	2	0	1.4	0.9	13
4	OD	III	0	0	2	0	3	0	2	0	1.2	0.4	18
	OS	III	0	0	1	0	2	0	2	0	1.3	0.3	16
5	OS	IV	2	0	2	0	4	0	3	0	0.0025	0.005	5
	OD	IV	2	0	3	0	4	0	3	0	0.005	0.014	8
7	OD	IV	2	0	2	0	4	0	3	0	0.005	0.014	6
	OS	IV	2	0	2	0	4	0	3	0	0.005	0.014	5
8	OD	II	0	0	1	0	1	0	1	0	0.4	0	14
	OS	II	0	0	1	0	1	0	1	0	0.5	0	15

The aqueous flare: 0: no; 1: have; 2: not clear.

TABLE 9: The outcome of patients after operation in six months.

Patient	Eye	OCP	Aqueous flare		Symblepharon		Keratopathy		Meibomian gland coloboma range		BCVA		Schirmer I test
			Postoperation	Difference	Postoperation	Difference	Postoperation	Difference	Postoperation	Difference	Preoperation	Postoperation	
1	OD	I	0	0	1	0	3	0	1	0	1.0	0.6	11
	OS	I	0	0	1	0	4	0	1	0	1.3	0.7	15
2	OD	IV	0	0	2	0	3	0	2	0	2.0	1.0	17
	OS	IV	0	0	2	0	1	0	2	0	1.9	0.4	11
3	OD	IV	0	0	2	0	2	0	2	0	1.1	0.8	10
	OS	IV	0	0	2	0	4	0	2	0	1.4	0.9	13
4	OD	III	0	0	2	0	3	0	2	0	1.2	0.4	18
	OS	III	0	0	1	0	2	0	2	0	1.3	0.3	16
5	OS	IV	2	0	2	0	4	0	3	0	0.0025	0.005	5
6	OD	IV	2	0	3	0	4	0	3	0	0.005	0.014	8
7	OD	IV	2	0	2	0	4	0	3	0	0.005	0.014	6
	OS	IV	2	0	2	0	4	0	3	0	0.005	0.014	5
8	OD	II	0	0	1	0	1	0	1	0	0.4	0	14
	OS	II	0	0	1	0	1	0	1	0	0.5	0	15

The aqueous flare: 0: no; 1: have; 2: not clear.

TABLE 10: The outcomes of patients after operation in final time.

Patient	Eye	Time	OCP	Aqueous flare		Symblepharon		Keratopathy		Meibomian gland coloboma range		BCVA		Schirmer I test
				Postoperation	Difference	Postoperation	Difference	Postoperation	Difference	Postoperation	Difference	Preoperation	Postoperation	
1	OD	120	I	0	0	1	0	3	0	1	0	1.0	0.5	9
	OS	120	I	0	0	1	0	4	0	1	0	1.3	0.6	19
2	OD	55	IV	0	0	2	0	3	0	2	0	2.0	1.0	16
	OS	55	IV	0	0	2	0	1	0	2	0	1.9	0.4	13
3	OD	79	IV	0	0	2	0	2	0	2	0	1.1	0.8	13
	OS	79	IV	0	0	2	0	4	0	2	0	1.4	0.9	15
4	OD	82	III	0	0	2	0	3	0	2	0	1.2	0.3	19
	OS	73	III	0	0	1	0	2	0	2	0	1.3	0.3	14
5	OS	24	IV	2	0	2	0	4	0	3	0	0.002	0.05	6
6	OD	76	IV	2	0	3	0	4	0	3	0	0.005	0.014	7
7	OD	24	IV	2	0	2	0	4	0	3	0	0.005	0.014	9
	OS	31	IV	2	0	2	0	4	0	3	0	0.005	1	5
8	OD	24	II	0	0	1	0	1	0	1	0	0.4	0	15
	OS	24	II	0	0	1	0	1	0	1	0	0.5	0	17

The aqueous flare: 0: no; 1: have; 2: not clear.

TABLE 11: Antibody detection, types, and complications.

Patient	Eye	Type	Serological markers	Postoperation conjunctival complications	Postoperation corneal complications
1	OD	Phaco+PCIOL	Antibody to pemphigoid (+)	—	—
	OS	Phaco+PCIOL		—	—
2	OD	Phaco+PCIOL	Antibody to pemphigoid (+)	Conjunctival congestion	Conjunctival congestion
	OS	Phaco+PCIOL	Rheumatoid factors (+)	—	—
3	OD	Phaco+PCIOL	Antibody to pemphigoid (+)	Conjunctival congestion	Corneal edema
	OS	Phaco+PCIOL		—	—
4	OD	Phaco+PCIOL	Antibody to pemphigoid (+)	—	—
	OS	Phaco+PCIOL		—	—
5	OS	ICCE	Antibody to pemphigoid (+)	Conjunctival congestion	Neovascularization
6	OD	Phaco	Antibody to pemphigoid (+)	Conjunctival congestion	Corneal edema
7	OD	Phaco	Antibody to pemphigoid (+)	Conjunctival congestion	Corneal edema
	OS	Phaco		—	Neovascularization
8	OD	Phaco+PCIOL	Antibody to pemphigoid (+)	—	—
	OS	Phaco+PCIOL		—	—

Phaco: phacoemulsification; PCIOL: posterior chamber intraocular lens; ICCE: intracapsular cataract extraction.

TABLE 12: Steroid hormones and immunosuppressant.

Patient	Eye	Medicine				
		Admission	Preoperation	Before one week	Postoperation	Final
				After one week	After three months	
1	OD	Mtx	Mtx, IVIG, Pred	Mtx, Pred, FML, I α -2aI	Mtx, FML	Mtx
	OS	Mtx		Pred, FML, I α -2aI	Mtx, FML	Mtx
2	OD	Mtx	Mtx, IVIG, Pred	Mtx, Pred	Mtx	Mtx
	OS	Mtx		Mtx, Pred	Mtx	Mtx
3	OD	Mtx	Mtx, IVIG, I α -2aI, CED, Pred	Mtx, CED, Pred	Mtx	Mtx
	OS	Mtx		Mtx, I α -2aI, IVIG, CED, Pred	Mtx, CED, Pred	Mtx
4	OD	Mtx	Mtx, IVIG, I α -2aI, Pred	Mtx, I α -2aI, Pred	Mtx	Mtx
	OS	Mtx		Mtx, IVIG, Pred	Mtx, Pred	Mtx
5	OS	Mtx	Mtx, IVIG, Pred	Mtx, Pred	Mtx	Mtx
6	OD	I α -2bED, Pred, CED, Cyc	IVIG, I α -2bED, Pred, CED, FML, Cyc	I α -2bED, Pred, CED, Cyc	Mtx, CED, Cyc	Cyc
7	OD	Mtx	Mtx, IVIG, Pred	Pred, Mtx	Mtx	Mtx
	OS	Mtx		Mtx, IVIG, Pred	Pred, Mtx	Mtx
8	OD	Mtx	Mtx, IVIG, Pred	Mtx, Pred	Mtx	Mtx
	OS	Mtx		Mtx, IVIG, Pred	Mtx, Pred	Mtx

Cyc: cyclophosphamide; Mtx: methotrexate; Pred: prednisone tablets; IVIG: intravenous immunoglobulin; FML: fluorometholone; I α -2aI: recombinant human interferon α -2a injection; I α -2bED: recombinant human interferon α 2b eye drop; CED: cyclosporine eye drops.

basic information of preoperative OCP patients. Six patients underwent binocular cataract surgery (12 eyes, 85.71%), and two patients underwent monocular cataract surgery (2 eyes, 14.29%). The BCVA of patient 5 was light perception preoperatively. The BCVA of patient 8 was 0.4 in the right eye and 0.5 in the left eye. For the Schirmer I test, 9 eyes (64.29%) were hyposecreted before the operation, and 6 eyes (42.86%) were dry eyes. Foster's staging system, stage of ker-

atopathy, stage of the symblepharon degree, and score of meibomian gland coloboma range after operation were very stable compared with those before operation, and there was no significant difference between pre- and postoperative states Table 7.

Compared to the preoperative values, the BCVA of all patients improved to varying degrees after surgery. The Schirmer I test and corneal fluorescein sodium staining were

TABLE 13: BCVA distribution statistics in pre- and postoperation.

BCVA	Preoperation (n%)				Postoperation (n%)			
	>2	1.4-2	1-1.3	<2	>1	0.7-1	0.4-0.6	<0.4
BCVA	4 (28.57)	4 (28.57)	3 (21.43)	3 (21.43)	3 (21.43)	4 (28.57)	3 (21.43)	4 (28.57)

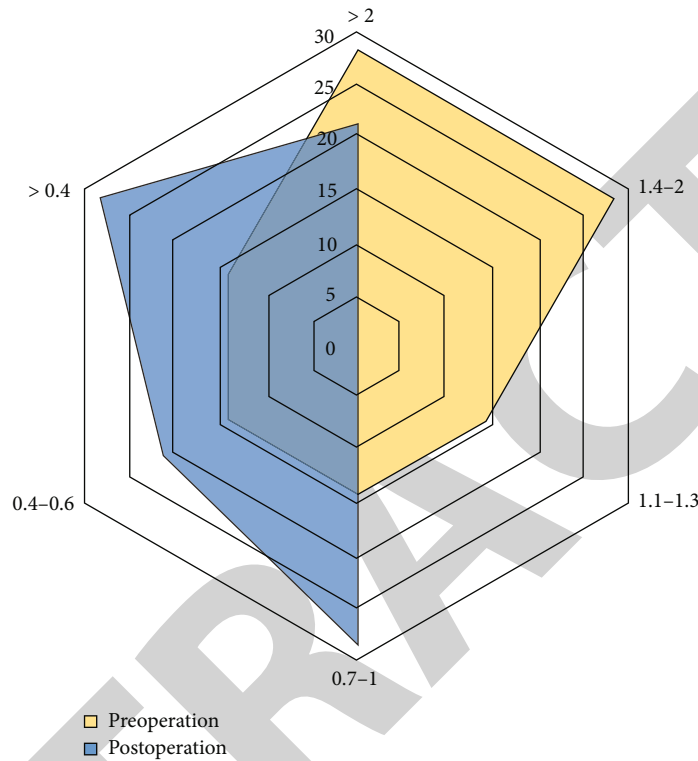


FIGURE 3: Preoperative and postoperative radar images of the BCVA in OCP patients. The postoperative BCVA of the standard logarithmic visual acuity chart above 0.1 was significantly increased.

not performed within 3 months after surgery to avoid ocular infection. The postoperative results 3 months after surgery are shown in Table 8. Compared with one week after the operation, the BCVA of 5 eyes (35.71%) was still improving. The aqueous flare disappeared in some patients, which may be related to the postoperative fade of corneal edema. The Schirmer I test showed that only 4 eyes (28.57%) remained hyposecreted after the operation, and there were no dry eyes. Table 9 analyzes the results of BCVA and Schirmer I test after operation in six months. Between 3 months and the final follow-up time, no changes in aqueous flare, keratopathy, symblepharon degree, or meibomian gland coloboma range were observed (Table 10). The BCVA in 2 eyes of one patient (14.29%) after the operation was 0. The BCVA improved by 7 lines in one eye of one patient (7.14%). There was no significant difference in the existing Foster's stage postoperatively compared to preoperatively.

3.5. Patient's Antibody Detection, Types, and Complications. The patient's surgical types, serological markers, and early and late complications before and after surgery are summa-

rized in Table 11. Pemphigoid antibodies can be detected in the serum of all patients. Patient 2 (12.5%) showed a positive result for rheumatoid factor. Ten eyes (71.43%) underwent phacoemulsification and intraocular lens implantation. Three eyes (21.43%) were without intraocular lens implantation. One eye (7.14%) did not receive regular medication one year after ICCE and developed progressive conjunctival hyperemia 24 months later. Conjunctival complications occurred in 5 eyes (35.71%) after surgery, manifested as conjunctival hyperemia, which disappeared after 3 days. Corneal edema occurred in 5 eyes (35.71%). After the application of hypertonic saline eye drops and recombinant bovine basic fibroblast growth factor eye gel, corneal edema disappeared. Two patients with 2 eyes present (14.28%) did not take medicine regularly after the operation and their cornea neovascularization was worse than preoperation, but the OCP stage did not improve.

3.6. The Medicine of Perioperative Period. All patients took oral immunosuppressive agents at the beginning of treatment. Seven of them received oral methotrexate (87.5%),

TABLE 14: Comparison of inspection result in pre- and postoperation.

Type	Eye	Statistical	Preoperation	Postoperative day	Time							Final
					1 week after operation	1 month after operation	3 months after operation	6 months after operation	1 year after operation	2 years after operation		
BCVA	14	Mean \pm SD	1.5 \pm 0.70	1.14 \pm 0.80	0.99 \pm 0.79	0.95 \pm 0.74	0.93 \pm 0.74	0.93 \pm 0.75	0.84 \pm 0.71	0.84 \pm 0.71	0.84 \pm 0.71	
		<i>P</i>	—	<0.001	<0.001	<0.001	<0.001	<0.001	<0.001	<0.001	<0.001	
		<i>t</i>	—	5.579	7.041	8.261	8.42	8.42	8.42	7.632	7.632	7.632
Schirmer I test	14	Mean \pm SD	7.57 \pm 5.39	—	—	—	11.71 \pm 4.43	11.36 \pm 4.16	11.71 \pm 4.21	11.21 \pm 3.79	12.64 \pm 4.68	
		<i>P</i>	—	—	—	—	0.001	0.006	0.003	0.019	0.001	
		<i>t</i>	—	—	—	—	4.146	3.267	3.64	2.684	4.252	
Corneal fluorescein sodium dyeing	14	Mean \pm SD	2.86 \pm 2.63	—	—	—	2.64 \pm 2.50	2.29 \pm 2.33	2.29 \pm 2.33	2.14 \pm 2.25	2.14 \pm 2.45	
		<i>P</i>	—	—	—	—	0.082	0.006	0.006	0.006	0.006	
		<i>t</i>	—	—	—	—	1.883	3.309	3.309	3.309	3.238	

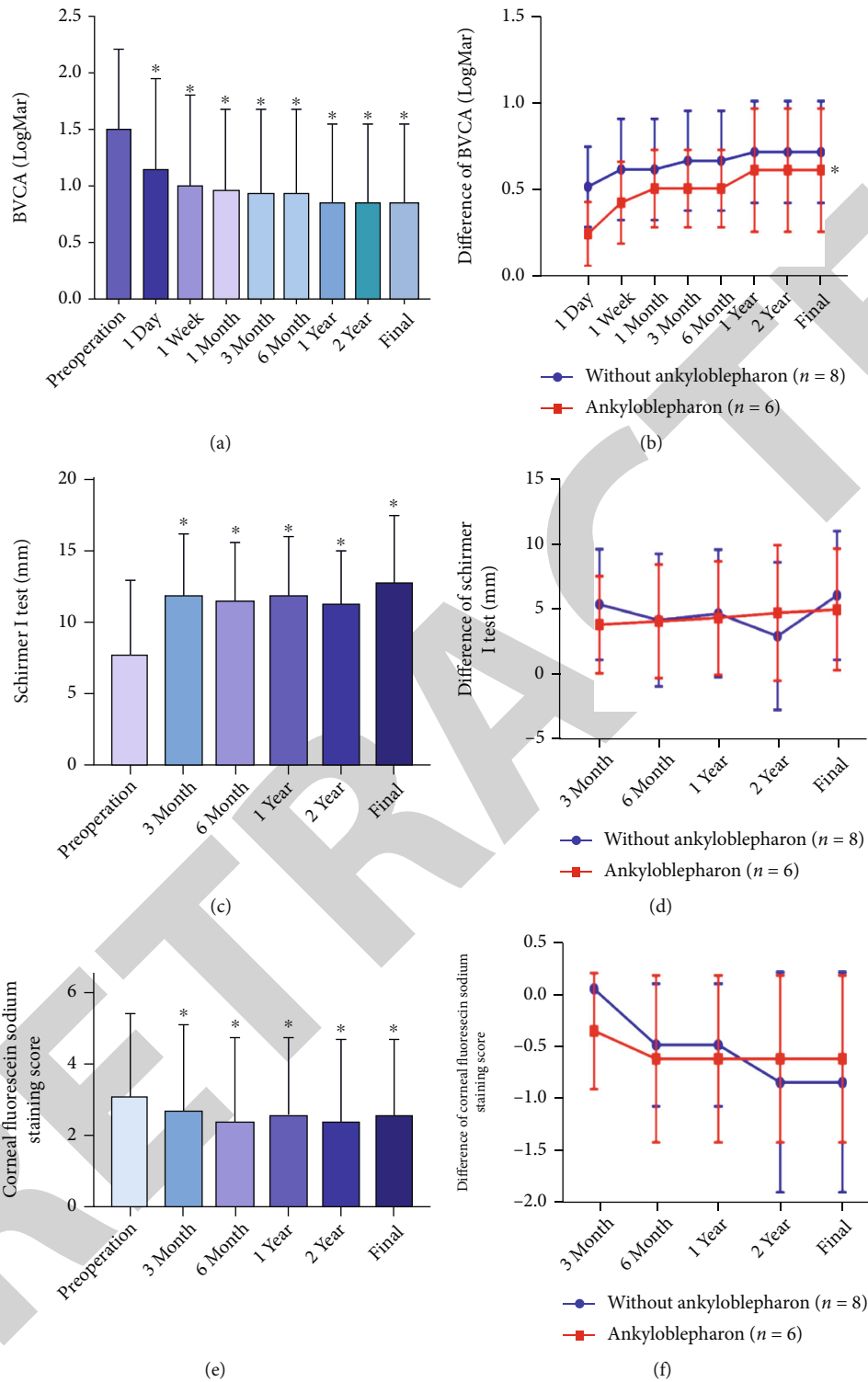


FIGURE 4: The BCVA, Schirmer I test, and corneal fluorescein sodium staining preoperative and postoperative. (a) The BCVA preoperative and postoperative (compared to preoperative, $*P < 0.001$, $n = 14$). (b) The difference in BCVA between preoperative and postoperative patients (compared to the group without ankyloblepharon, $*P < 0.05$). (c) The Schirmer I test preoperative and postoperative (compared to preoperative, $*P < 0.001$, $n = 14$). (d) The difference in the Schirmer I test between preoperative and postoperative values. (e) Preoperative and postoperative corneal fluorescein sodium staining (compared to preoperative, $*P < 0.001$, $n = 14$). (f) The difference in corneal fluorescein sodium dyeing between preoperative and postoperative samples.

TABLE 15: Comparison of BCVA pre- and postoperation.

	3 months after operation	6 months after operation	1 year After operation	2 years After operation	Final
Ankyloblepharon ($n = 6$)	5.00 ± 4.10	3.83 ± 4.91	4.33 ± 4.71	2.66 ± 5.47	5.67 ± 4.76
Without ankyloblepharon ($n = 8$)	3.50 ± 3.60	3.75 ± 4.20	4.00 ± 4.21	4.38 ± 5.01	4.63 ± 4.50
<i>F</i>	0.532	0.001	0.019	0.369	0.175
<i>P</i>	0.480	0.973	0.891	0.555	0.683

TABLE 16: Comparison of Schirmer I test differences pre- and postoperation.

	Postoperative day	1 week after operation	1 month after operation	3 months after operation	6 months after operation	1 year After operation	2 years After operation	Final
Ankyloblepharon ($n = 6$)	0.52 ± 0.23	0.62 ± 0.29	0.62 ± 0.29	0.67 ± 0.29	0.67 ± 0.29	0.72 ± 0.29	0.72 ± 0.29	0.72 ± 0.29
Without ankyloblepharon ($n = 8$)	0.24 ± 0.18	0.42 ± 0.24	0.50 ± 0.22	0.50 ± 0.22	0.50 ± 0.22	0.61 ± 0.36	0.61 ± 0.36	0.61 ± 0.36
<i>F</i>	6.062	1.847	0.647	1.392	0.340	0.340	0.340	0.340
<i>P</i>	0.030	0.199	0.437	0.261	0.570	0.570	0.570	0.570

TABLE 17: Comparison of corneal fluorescein sodium dyeing differences pre- and postoperation.

	3 months after operation	6 months after operation	1 year After operation	2 years After operation	Final
Ankyloblepharon ($n = 6$)	0 ± 0	-0.50 ± 0.55	-0.50 ± 0.55	-0.83 ± 0.98	-0.83 ± 0.98
Without ankyloblepharon ($n = 8$)	-0.38 ± 0.52	-0.63 ± 0.74	-0.63 ± 0.74	-0.63 ± 0.74	-0.63 ± 0.74
<i>F</i>	3.086	0.120	0.120	0.205	0.205
<i>P</i>	0.104	0.735	0.735	0.659	0.659

and one patient received oral cyclophosphamide (12.5%). All patients were intravenously injected with immunoglobulin, and prednisone tablets were taken one week before the operation. The patients stopped taking oral prednisone three months postoperation. Immunoglobulin was discontinued after the operation. Patient 1 was given cyclosporine eye drops before the surgery, and recombinant human interferon α -2 injection ($I\alpha$ -2a1) was used for 2 weeks after surgery. Fluorometholone eye drops were applied until the ocular symptom condition was stable (Table 12).

3.7. Comparison of Eye Conditions. The BCVA (Table 13, Figure 3) was lower than 2 in only 3 eyes (21.43%) before the operation, while the number of patients was increased to 11 eyes after the operation (78.67%). The BCVA was significantly improved after the operation in all patients compared to preoperative values (Table 14, Figure 4(a)) ($P < 0.001$). The difference between the BCVA between the with and without ankyloblepharon groups was statistically significant on the first day after surgery ($P < 0.05$). There

was no statistically significant difference in the subsequent days (Table 15, Figure 4(b)). Schirmer I test numerical value in all postoperative patient increased and improved compared to preoperative (Table 14, Figure 4(c)) and was statistically significant ($P < 0.01$). There was no statistical significance in the comparison of the difference of Schirmer I test between the group with or without ankyloblepharon after operation (Table 16, Figure 4(d)). The positive rate of corneal sodium fluorescein dyeing at 6 months, 1 year, 2 years, and the final follow-up time decreased significantly compared to preoperatively (Table 14, Figure 4(e)) ($P < 0.01$). The difference in corneal sodium fluorescein dyeing between the group with or without ankyloblepharon was not statistically significant after surgery (Table 17, Figure 4(f)). The meibomian gland coloboma range in all patients remained unchanged after surgery (Table 14). Figure 5 shows the difference in OSDI score between preoperative and postoperative samples. Figures 6–8 show the preoperative and postoperative images of the partial anterior segment.

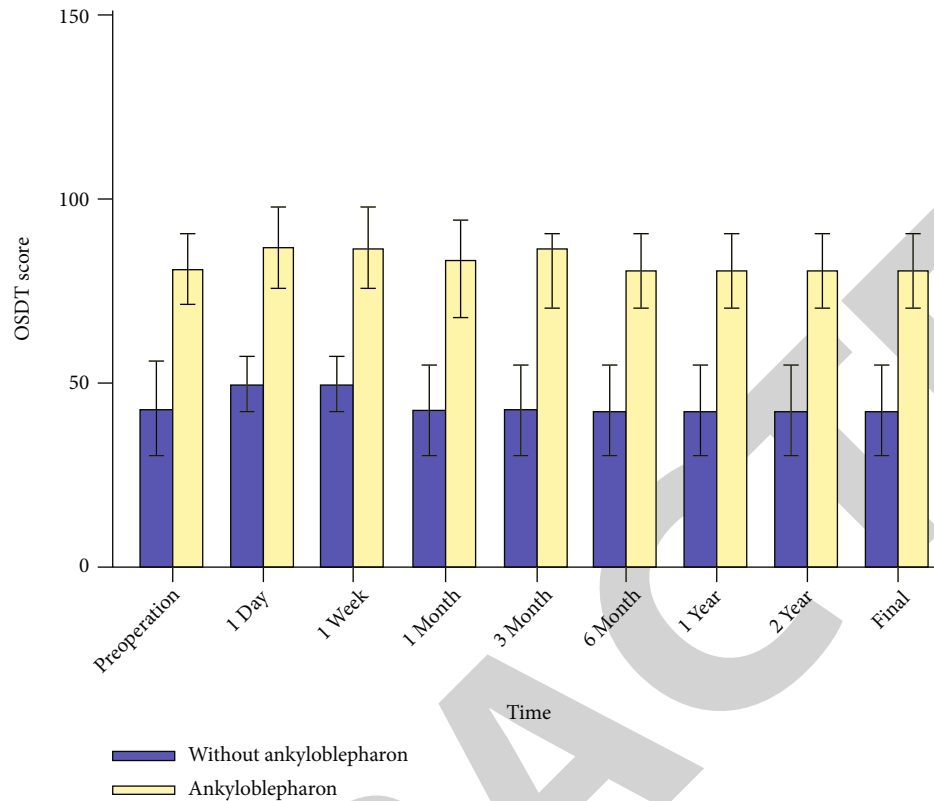


FIGURE 5: The difference in OSDI score between preoperative and postoperative samples. There was statistically significant difference between the group without ankyloblepharon and the group with ankyloblepharon (* compared to preoperative $P < 0.01$, the group with ankyloblepharon $n = 6$, the group without ankyloblepharon $n = 8$).

3.8. OSDI Questionnaire Survey Analysis. The OSDI scores of patients with OCP stages I, II, and III were significantly higher at 1 day and 1 week postoperation than preoperation. The OSDI scores of patients with OCP stage IV were higher at 1 day, 1 week, and 1 month after surgery. The score significantly increased before operation and then began to decrease until it eventually reached the same level as preoperation, but there was no statistically significant difference between each group before and after treatment ($P > 0.05$). The average OSDI scores of patients with preoperative and postoperative OCP stages I, II, and III were significantly higher than those of grade IV patients ($P < 0.01$) (Table 18).

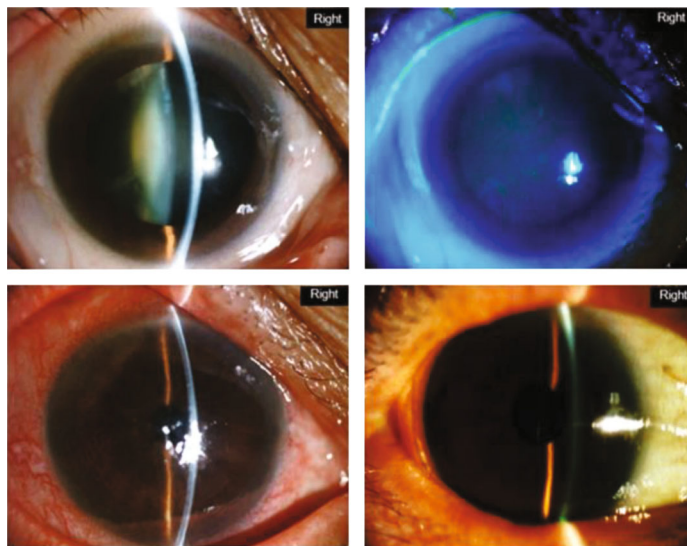
4. Discussion

MMP is a skin disease with chronic, recurrent, and multisystemic autoimmune dysfunction. Inflammation and scar formation on mucosal surfaces are characteristic pathological clinical manifestations of OCP [21]. It has been reported that the visual acuity of patients with OCP combined with cataracts improves poorly after phacoemulsification [6]. The main reason for the poor prognosis of vision is the progression of the disease and subsequent scarring. Maza et al. [18] reported that twenty OCP patients received systemic immunosuppression before cataract surgery and none of the patients showed disease progression during an average of 22 months of follow-up, indicating that cataract surgery

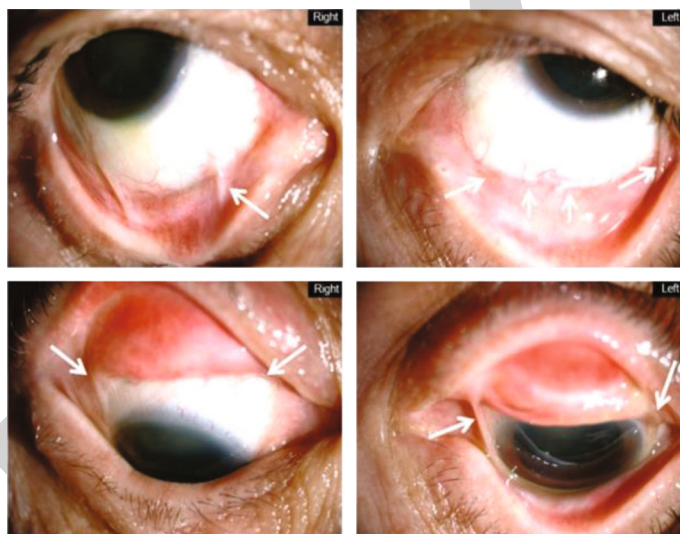
can be performed safely with complete remission of the diseases.

The commonly used immunosuppressants for OCP patients are cyclophosphamide, azathioprine, methotrexate, and dapsone. Patients should be given less effective medicines after diagnosis and gradually change a medical prescription. It has been reported that preoperative and postoperative use of artificial tears and autologous serum eye drops can help stabilize the ocular surface condition [21]. All of our patients were treated preoperatively and postoperatively. Bissen-Miyajima and his team reported that the combination of limbal and amniotic membrane transplantation for ocular surface reconstruction and cataract surgery showed a faster visual rehabilitation effect in SJS patients [22]. One eye of our patients was treated with amniotic membrane transplantation combined with cataract surgery, and the BCVA improved significantly.

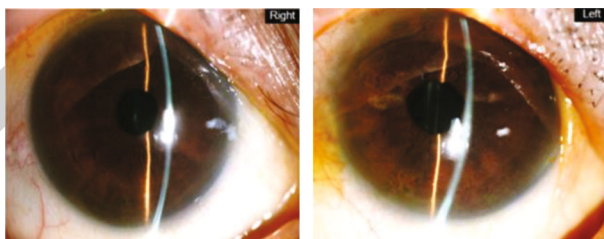
According to the visual acuity statistics in our study, the postoperative BCVA was 57.14% higher than the preoperative BCVA. The BCVA of 5 of 14 eyes (36%) met the legal criteria for “blindness” before surgery, but navigated visual acuity was achieved in all eyes after surgery. This result shows that OCP patients with well-controlled inflammation can obtain good visual benefits after cataract surgery. Control of long-term medication can maintain good visual acuity. The BCVA of one patient in their right eye improved from 1 to 0.5 after 120 months of follow-up after surgery. The BCVA of the left eye improved from 1.3 to 0.6. All



(a)



(b)



(c)

FIGURE 6: Continued.

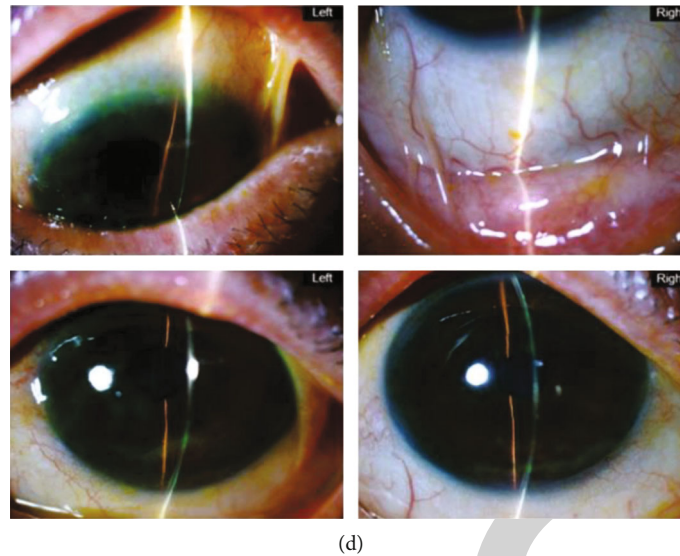


FIGURE 6: Anterior segment image of the patient in the OCP stage of Foster's stage II and III. (a) Cortical and nuclear opacifications were found in the lens after dilatation before the operation of the eighth patient in the OCP stage of Foster's stage II. Sodium fluorescein staining before surgery of the eighth patient in the OCP stage of Foster's stage II, anterior segment image 1 month and 6 months after surgery. (b) Anterior segment image of the fourth patient in the OCP stage of Foster's stage III before surgery, the double frontal fornix becomes shallower preoperatively, and there are obvious symblepharons, which are especially evident in the inner and outer canthus. (c) Anterior segment image of the fourth patient in the OCP stage of Foster's stage III in 6 months after surgery. (d) Anterior segment image of the fourth patient in the OCP stage of Foster's stage III in 2 years after surgery.

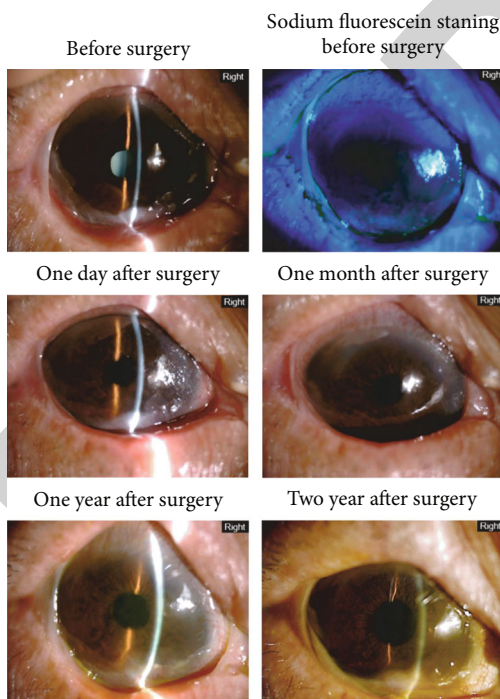


FIGURE 7: The anterior segment image of the second patient in the OCP stage of Foster's stage IV.

patients' BCVA improved postoperatively, and the *P* values were less than 0.001. The BCVA on the first postoperative day between patients with or without eyelid adhesions was significantly different. This was mainly because the patients

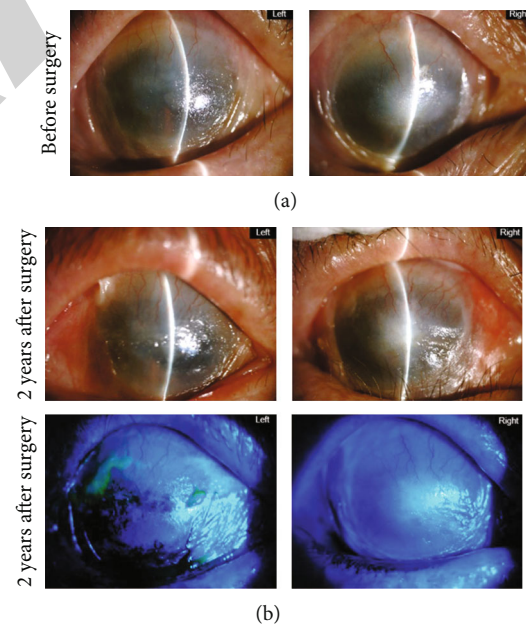


FIGURE 8: Anterior segment image of the fifth patient in the OCP stage of Foster's stage IV. (a) Both eyes showed corneal neovascularization before surgery. (b) Anterior segment image and sodium fluorescein staining image of both eyes 2 years after ICCE surgery.

without eyelid adhesions and cataracts had milder lesions. Phacoemulsification energy had little effect on the cornea, due to a lower probability of corneal edema after surgery and a faster recovery speed.

TABLE 18: Comparison of OSDI scores in OCP patients before and after surgery.

	Preoperation	After 1 day	After 1 week	After 1 month	After 3 months	After 6 months	After 12 months	After 24 months	Final	F	P
Without ankyloblepharon	42.86 ± 12.19	49.20 ± 7.23	49.80 ± 7.23	42.86 ± 12.19	42.86 ± 12.19	42.86 ± 12.19	42.86 ± 12.19	42.86 ± 12.19	42.86 ± 12.19	4	0.184
Ankyloblepharon	80.54 ± 9.66	86.82 ± 10.75	86.82 ± 10.75	82.64 ± 11.7	80.5 ± 9.66	80.54 ± 9.66	80.54 ± 9.66	80.54 ± 9.66	80.54 ± 9.66	4.51	0.065
<i>t</i>	4.879	5.217	5.217	5.217	4.667	4.879	4.879	4.879	4.879		
<i>P</i>	0.003	0.002	0.002	0.003	0.003	0.003	0.003	0.003	0.003		

Ankyloblepharon *n* = 6; without ankyloblepharon *n* = 8.

It has been reported that patients with dry eye have poor BCVA due to late corneal complications, endophthalmitis, and other causes after cataract surgery [23]. The Schirmer I test of our patients increased from 7.57 ± 5.39 mm to 12.64 ± 4.68 mm after surgery. The OCP stage had no effect on the Schirmer I test results. Although there was a short-term decline in postoperative results, the long-term results were gratifying. This may be because the patients paid more attention to their eyes after surgery than before. However, Schirmer I test results alone cannot evaluate dry eye symptoms of OCP patients.

The Foster stage, meibomian gland coloboma range, corneal fluorescein sodium staining, keratopathy stage, and symblepharon degree of patients did not change after surgery. Short-term complications occurred in 6 eyes of 5 patients (42.86%). After treatment, conjunctival hyperemia and corneal edema disappeared. Corneal neovascularization appeared in 2 eyes of 2 patients (14.29%) and was aggravated compared to preoperation. After immunosuppressive treatment, the symptoms were relieved without affecting visual acuity. Cataract surgery did not cause corneal surface injury and even improved after standard treatment, independent of the degree of symblepharon, also confirmed by the OSDI score scale. However, the OSDI scores of patients with ankyloblepharon were higher than those of patients without ankyloblepharon. Cataract surgery did not affect the subjective perception between the two groups of patients. The reason why the OSDI scores before and after did not improve may be because most of the patients were middle-aged and had a low demand for driving and reading. The OSDI score scale does not fully reflect the benefits of vision correction.

With the improvement of modern cataract surgery refinement and technology, cataract extraction surgery has become safer than before. The decision of whether stage IV OCP patients should undergo cataract surgery still needs to be cautiously determined. Finally, OCP patients must consider the level of vision loss caused by cataracts. Surgeons must try to balance the risk of intraoperative or postoperative complications. All patients must be followed up in time to prevent irreversible disease progression. Therefore, preoperative treatment and advanced surgical techniques by ophthalmologists are necessary.

This study still obtains some limitations; due to the fact that this is a retrospective case study, it is not allowed to randomize the patients into groups which might jeopardize the similarity of patients in groups. Meanwhile, the treatment effect of patients administered novel medicines such as rituximab during the operation period has not been evaluated which may be one of the potential therapeutic medicines that can replace immunosuppressants or other large clinical side effects for OCP patients in the future. Besides, this study had few objective evaluations of postoperative results.

5. Conclusion

With complete control of ocular surface inflammation, patients with a low stage of OCP could obtain greater postoperative BCVA improvement. Standardized perioperative

medication and detailed surgical plans resulted in fewer postoperative adverse reactions and complications and improved patient satisfaction. After successful elimination of active conjunctival inflammation in OCP patients with systemic steroids and immunosuppressants, there was a low risk of disease activity due to surgical trauma. Since there was no conclusive evidence about the quiescent period of OCP inflammation, the best time for surgical treatment was waiting for at least 3 months after active inflammation subsided. The prospect of this study is to provide reliable efficacy and safety support for the surgical treatment of OCP patients complicated with cataract.

Data Availability

The labeled dataset used to support the findings of this study are available from the corresponding author upon request.

Conflicts of Interest

The authors declare no competing interests.

Authors' Contributions

Yuan He, Zhuoya Quan, and Ruixue Zhang contributed equally to this work.

Acknowledgments

This research was funded by the National Natural Science Foundation of China (Nos. 81770929 and 82070964), Shaanxi Provincial Education Department Service for Local Scientific Research Program 2018 (No. 18JC026), Shaanxi Provincial Science and Technology Agency Project (2019SF-162), Shaanxi Provincial Department of Education Project (No. 19JK0758), and Xi'an Science and Technology Bureau Project (No. 2019114613YX001SF041-(2)).

References

- [1] S. Taurone, M. Spoletini, M. Ralli et al., "Ocular mucous membrane pemphigoid: a review," *Immunologic Research*, vol. 67, no. 2-3, pp. 280-289, 2019.
- [2] L. S. Chan, A. R. Ahmed, G. J. Anhalt et al., "The first international consensus on mucous membrane pemphigoid: definition, diagnostic criteria, pathogenic factors, medical treatment, and prognostic indicators," *Archives of Dermatology*, vol. 138, no. 3, pp. 370-379, 2002.
- [3] M. Kirzhner and F. A. Jakobiec, "Ocular cicatricial pemphigoid: a review of clinical features, immunopathology, differential diagnosis, and current management," in *Presented at Seminars in ophthalmology*, vol. 26, pp. 270-277, Taylor & Francis, 2011.
- [4] M. Ahmed, G. Zein, F. Khawaja, and C. S. Foster, "Ocular cicatricial pemphigoid: pathogenesis, diagnosis and treatment," *Progress in Retinal and Eye Research*, vol. 23, no. 6, pp. 579-592, 2004.
- [5] D. S. Holsclaw, "Ocular cicatricial pemphigoid," *International Ophthalmology Clinics*, vol. 38, no. 4, pp. 89-106, 1998.
- [6] P. H. Blomquist, "Methicillin-resistant *Staphylococcus aureus* infections of the eye and orbit (an American Ophthalmological

Retraction

Retracted: The Correlation between the Increased Expression of Aquaporins on the Inner Limiting Membrane and the Occurrence of Diabetic Macular Edema

Oxidative Medicine and Cellular Longevity

Received 1 August 2023; Accepted 1 August 2023; Published 2 August 2023

Copyright © 2023 Oxidative Medicine and Cellular Longevity. This is an open access article distributed under the Creative Commons Attribution License, which permits unrestricted use, distribution, and reproduction in any medium, provided the original work is properly cited.

This article has been retracted by Hindawi following an investigation undertaken by the publisher [1]. This investigation has uncovered evidence of one or more of the following indicators of systematic manipulation of the publication process:

- (1) Discrepancies in scope
- (2) Discrepancies in the description of the research reported
- (3) Discrepancies between the availability of data and the research described
- (4) Inappropriate citations
- (5) Incoherent, meaningless and/or irrelevant content included in the article
- (6) Peer-review manipulation

The presence of these indicators undermines our confidence in the integrity of the article's content and we cannot, therefore, vouch for its reliability. Please note that this notice is intended solely to alert readers that the content of this article is unreliable. We have not investigated whether authors were aware of or involved in the systematic manipulation of the publication process.

In addition, our investigation has also shown that one or more of the following human-subject reporting requirements has not been met in this article: ethical approval by an Institutional Review Board (IRB) committee or equivalent, patient/participant consent to participate, and/or agreement to publish patient/participant details (where relevant).

Wiley and Hindawi regrets that the usual quality checks did not identify these issues before publication and have since put additional measures in place to safeguard research integrity.

We wish to credit our own Research Integrity and Research Publishing teams and anonymous and named external researchers and research integrity experts for contributing to this investigation.

The corresponding author, as the representative of all authors, has been given the opportunity to register their agreement or disagreement to this retraction. We have kept a record of any response received.

References

- [1] Y. Chen, H. Chen, C. Wang et al., "The Correlation between the Increased Expression of Aquaporins on the Inner Limiting Membrane and the Occurrence of Diabetic Macular Edema," *Oxidative Medicine and Cellular Longevity*, vol. 2022, Article ID 7412208, 11 pages, 2022.

Research Article

The Correlation between the Increased Expression of Aquaporins on the Inner Limiting Membrane and the Occurrence of Diabetic Macular Edema

Yiqi Chen,¹ Huan Chen,² Chenxi Wang,¹ Jiafeng Yu,¹ Jiwei Tao,² Jianbo Mao,¹ and Lijun Shen ¹

¹Center for Rehabilitation Medicine, Department of Ophthalmology, Zhejiang Provincial People's Hospital (Affiliated People's Hospital, Hangzhou Medical College), Hangzhou, Zhejiang, China

²Department of Retina Center, Affiliated Eye Hospital of Wenzhou Medical University, Hangzhou, 310000 Zhejiang Province, China

Correspondence should be addressed to Lijun Shen; shenlj89@163.com

Received 17 February 2022; Revised 23 March 2022; Accepted 1 April 2022; Published 28 April 2022

Academic Editor: Shao Liang

Copyright © 2022 Yiqi Chen et al. This is an open access article distributed under the Creative Commons Attribution License, which permits unrestricted use, distribution, and reproduction in any medium, provided the original work is properly cited.

Purpose. Diabetic macular edema (DME) is a major cause of vision loss in patients with diabetic retinopathy; this study is aimed at comparing the expression of aquaporins (AQPs) on the inner limiting membranes (ILMs) of various vitreoretinal diseases and investigating the role of aquaporins expressed on the ILMs in mediating the occurrence of DME. **Methods.** The whole-mounted ILM specimens surgically excised from patients with various vitreoretinal diseases (idiopathic macular hole, myopic traction maculopathy, and diabetic retinopathy) were analyzed by immunohistochemistry (IHC). The distribution and morphology of AQP4, AQP7, and AQP11 on the ILMs were correlated with immunohistochemical staining characteristics. Moreover, immunofluorescence of AQP4 was performed on the ILM specimens of the patient in four groups: the control group, negative control group, no DME group, and DME group. The immunofluorescence intensity value of AQP4 was measured using ImageJ. The difference between the four groups and the correlation between the immunofluorescence value and central foveal thickness (CFT) were analyzed. **Results.** In IHC sections, the expression of AQP4, AQP7, and AQP11 on ILMs of diabetic retinopathy (DR) with macular edema, respectively, seemed to be more abundant than in the idiopathic macular hole (iMH) and myopic traction maculopathy (MTM). Moreover, markedly higher fluorescence intensity of AQP4 of ILMs was determined in the DME group (51.05 ± 5.67) versus the other three groups ($P < 0.001$). A marked positive association was identified between the fluorescence intensity of AQP4 and CFT ($r = 0.758$; $P = 0.011$). **Conclusions.** AQP4, AQP7, and AQP11 can be expressed on human ILM in vivo. The increased expression of AQPs on the ILMs of DR may be associated with the occurrence of DME. Moreover, the degree of DME may be positively correlated with the expression of AQP4 on the ILMs.

1. Introduction

For retina, a vital sensory tissue, delicate fluid balance is required for the maintenance of cellular homeostasis and proper tissue functions. The water transport of cells through the plasma membrane is a vital molecular process, which enables glandular tissue to secrete fluid, fluid flow in tissues to exchange nutrients and metabolites, and cell volume modulation [1]. Aquaporin (AQP) is an important type of protein that regulates osmotic gradients and hydrostatic pressure to control the bidirectional movement of water

across cell membranes [1]. It is repeatedly documented in animal models that AQP is implicated in the nosogenesis of retinal vascular disease, retinal nerve injury, and diabetic retinopathy [1–9]. Moreover, Vujosevic et al. has demonstrated that the biomarkers AQP1 and AQP4 in the aqueous humor of diabetic patients with diabetic retinopathy were significantly higher than nondiabetic patients, indicating that diabetes might have a strong effect on Müller cells [10].

Previous studies have shown that the internal limiting membrane (ILM) is anatomically organized by the basement membrane of Müller cells, located at the vitreoretinal

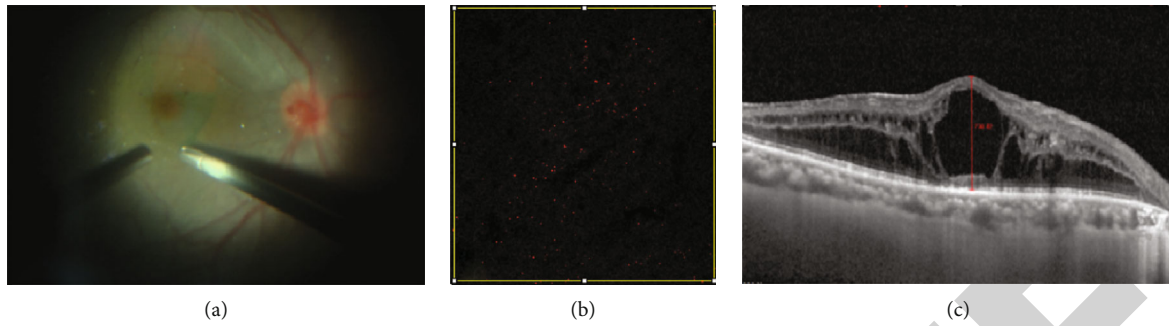


FIGURE 1: Experimental methods and data acquisition. (a) The peeling of ILM was performed within 2PD of macular fovea with the aid of 0.17% ICG. (b) ImageJ was used to measure immunofluorescence value; all images chosen 8 bit type and set threshold and then traced an rectangular box of similar size where the fluorescence intensity was uniformed by wand tool to measure immunofluorescence intensity values. (c) The distance between the inner limiting membrane (ILM) and the surface of retinal pigment epithelium (RPE) at the fovea was used to record the CFT (central foveal thickness). Magnification: (b) $\times 400$.

interface [11]. The mRNA expression of all AQPs, namely, AQP0 to AQP12, can be detected in the human retina [12], while only AQP4, AQP7, and AQP11 can be detected on human ILMs in vitro [13–15]. As the only human living retinal tissue currently available, there have not been many studies on the correlation between AQP and the pathogenesis of eye diseases. Therefore, the motivation of this study is to investigate whether AQPs on ILMs will undergo pathological changes in various vitreoretinal diseases, or whether these changes are related to the pathogenesis. Due to the unknown mechanism in the change of AQPs on ILMs and the undefined relationship between them and the occurrence of the disease, the content of this research constitutes its novelty.

This study is aimed at comparing the expression of AQPs on ILMs of various vitreoretinal diseases and investigating the role of AQPs expressed on the ILMs in mediating the occurrence of diabetic macular edema.

2. Materials and Methods

2.1. Subjects. A total of 64 eyes of 64 patients who had undergone vitrectomy with ILM peeling due to various vitreoretinal diseases were enrolled, including 19 patients with idiopathic macular hole (iMH), 9 patients with myopic traction maculopathy (MTM), and 36 patients with diabetic retinopathy (DR). Inclusion criteria for DR are as follows: patients with stage IV and above who underwent pars plana vitrectomy (PPV) for traction retinal detachment, vitreous hemorrhage (VH), etc. Inclusion criteria for MTM are as follows: (1) MTM diagnosed by optical coherence tomography (OCT), (2) highly myopic eyes defined as an axis length ≥ 26 mm or a spherical equivalent refractive error ≥ -6.00 D, and (3) patients without other general diseases and can undergo surgery. Inclusion criteria for iMH are as follows: (1) OCT diagnosed as a full-thickness macular hole and (2) patients without other general diseases and can undergo surgery. Exclusion criteria are as follows: (1) previously received anti-VEGF drug therapy or macular laser photocoagulation and (2) previously received PPV treatment. The Institutional Review Board of Zhejiang Eye Hospital ratified the study, together with the module for patients' informed consent.

The distribution and morphology of AQP4, AQP7, and AQP11 on ILMs were obtained by immunohistochemical staining. There were 3 specimens for each of the following three groups including the iMH group, MTM group, and DR group. The immunofluorescence staining of AQP4 was performed on ILM specimens of other patients. The corresponding study consists of four groups, with 8 iMH specimens in the control group, 2 iMH specimens and 6 DR specimens in the negative control group, 9 specimens in the no diabetic macular edema (DME) group, and 12 specimens in the DME group.

2.2. Surgical Techniques. Under retrobulbar anesthesia plus intravenous anesthesia, all operations were completed by the same surgeon. All patients underwent standard 3-port 23- or 25-gauge PPV. With the purpose of reducing phototoxicity and photoactivation of indocyanine green (ICG) while ensuring adequate surgical field, the endoillumination levels were adjusted to a minimum of $<40\%$. After core vitrectomy, the posterior vitreous cortex was stained with triamcinolone acetonide (TA; 0.1 mL with the concentration of 0.1 mL/4 mg) and the residual vitreous was then removed as completely as possible. Epiretinal membrane was then peeled if present. After that, ILM was peeled within 2 papillary diameters (PD) of macular fovea with the aid of 0.17% ICG (Figure 1(a)). Excessive ICG was aspirated at once after injection to minimize possible toxicity to the tissue. For patients without DME, the residual posterior vitreous cortex in macular area was peeled together with the ILMs to prevent postoperative preretinal proliferation in macular area.

2.3. Tissue Preparation for Immunohistochemical (IHC) and Immunofluorescence (IF) Microscopy. Surgically excised ILM specimens for IHC and IF staining were placed onto glass slides and being processed with the use of a stereomicroscope (MS 5; Leica, Wetzlar, Germany). Precleaned microscope slides were prepared by adhering two secure seal spacers to each slide face, allowing two flat mounts per slide. Thereafter, the specimens were subjected to unfolding in 0.1 M phosphate-buffered saline (PBS; pH 7.4) and then immediate 4% paraformaldehyde immobilization (4°C) for ≥ 24 hours.

TABLE 1: Clinical data of patients.

Case	Eye	Age	Gender	Diagnosis	Method
1	OS	55	M	DR, VH, DME	Immunohistochemistry AQP4
2	OS	59	M	DR, DME, VH	Immunohistochemistry AQP4
3	OD	56	F	DR, VH, DME	Immunohistochemistry AQP4
4	OS	54	M	iMH	Immunohistochemistry AQP4
5	OS	69	F	iMH	Immunohistochemistry AQP4
6	OS	65	F	iMH, ERM	Immunohistochemistry AQP4
7	OS	49	F	MHRD	Immunohistochemistry AQP4
8	OS	68	F	MHRD	Immunohistochemistry AQP4
9	OS	56	M	MHRD	Immunohistochemistry AQP4
10	OS	46	F	DR, VH, DME	Immunohistochemistry AQP7
11	OD	50	F	DR, DME	Immunohistochemistry AQP7
12	OS	63	F	DR, DME, VH, ERM	Immunohistochemistry AQP7
13	OS	62	M	iMH	Immunohistochemistry AQP7
14	OD	35	M	iMH	Immunohistochemistry AQP7
15	OS	77	F	iMH, ERM	Immunohistochemistry AQP7
16	OS	61	F	MHRD	Immunohistochemistry AQP7
17	OD	49	F	MHRD	Immunohistochemistry AQP7
18	OD	53	F	MHRD, ERM	Immunohistochemistry AQP7
19	OS	66	M	DR, VH, DME	Immunohistochemistry AQP11
20	OD	64	F	DR, VH, DME	Immunohistochemistry AQP11
21	OD	56	F	DR, VH, DME	Immunohistochemistry AQP11
22	OS	69	M	iMH	Immunohistochemistry AQP11
23	OD	67	M	iMH, ERM	Immunohistochemistry AQP11
24	OD	56	F	iMH	Immunohistochemistry AQP11
25	OD	53	F	MHRD	Immunohistochemistry AQP11
26	OD	49	F	MHRD	Immunohistochemistry AQP11
27	OD	53	F	MHRD, ERM	Immunohistochemistry AQP11

OD: right eye; OS: left eye; iMH: idiopathic macular hole; DR: diabetic retinopathy; VH: vitreous hemorrhage; MHRD: macular hole retinal detachment; DME: diabetic macular edema; ERM: epiretinal macular membrane; AQP: aquaporin.

2.4. Immunohistochemistry (IHC) of Flat-Mounted ILM Specimens. Various antibodies were applied to label the AQPs that were in interest (anti-AQP4, 1 : 100, Thermo; anti-AQP7, 1 : 300, Novus; anti-AQP11, 1 : 50, Abcam). After tissue immobilization, specimens were treated with 3 rinses using 0.1 M PBS (pH 7.4) before approximately 5 min of indoor incubation with 3% H₂O₂. Then, the sections were subjected to another 3 rinses using 0.1 M PBS, followed by 1-2 hours or overnight incubation (4°C) with the primary antibodies at ambient temperature. After 3 PBS washes (3 min/time), the specimens were treated with the enhance labeled polymer system ELPS (Envision, Beijing Zhongshan Jinqiao Biotechnology Co. Ltd.) for 15-20 min at indoor temperature. After 15-20 min of immersion in the horseradish enzyme at room temperature, specimens were treated with 3 PBS washes (3 min/time) and then placed into the color developing agents for 3-15 min of incubation. After thorough rinsing, counterstaining, dehydration, hyalinization, and sealing, the sections were observed with optical microscopy.

2.5. Immunofluorescence of Flat-Mounted ILM Specimens. After fixation in 4% paraformaldehyde (PFA) overnight,

the specimens were incubated in 0.3% BSA and 1% Triton X-100 for 30 minutes. Then, a 30 μ L (1 : 240) diluent primary antibody, Aquaporin 4 Polyclonal Antibody) was added and incubated with the specimens overnight at 4°C. After that, excess primary antibodies were washed away after 3 rinses (5 min/time) with 0.01 M PBS (pH 7.4) on a shaking table. Then, the specimens were incubated in 30 μ L (1 : 300) secondary antibody (Goat Anti-rabbit IgG/PE antibody (bs-0295G-PE)) for 1.5 hours at 37°C in darkroom. Finally, specimens were subjected to 3 rinses (5 min/time) with 0.01 M PBS on the shaking table in darkroom.

To prepare the specimens in the negative control group (the 2 iMH specimens and 6 DR specimens), the primary antibody was substituted with diluent and specimens were incubated with the secondary antibody alone. All other procedures were identical to the procedures illustrated above.

Images were acquired using a confocal microscope (LSM880 with AiryScan+TP; ZEISS). All the acquisition parameters were kept the same at all times.

2.6. The Measurement of Fluorescence Intensity. After obtaining immunofluorescence images using ZEN (a

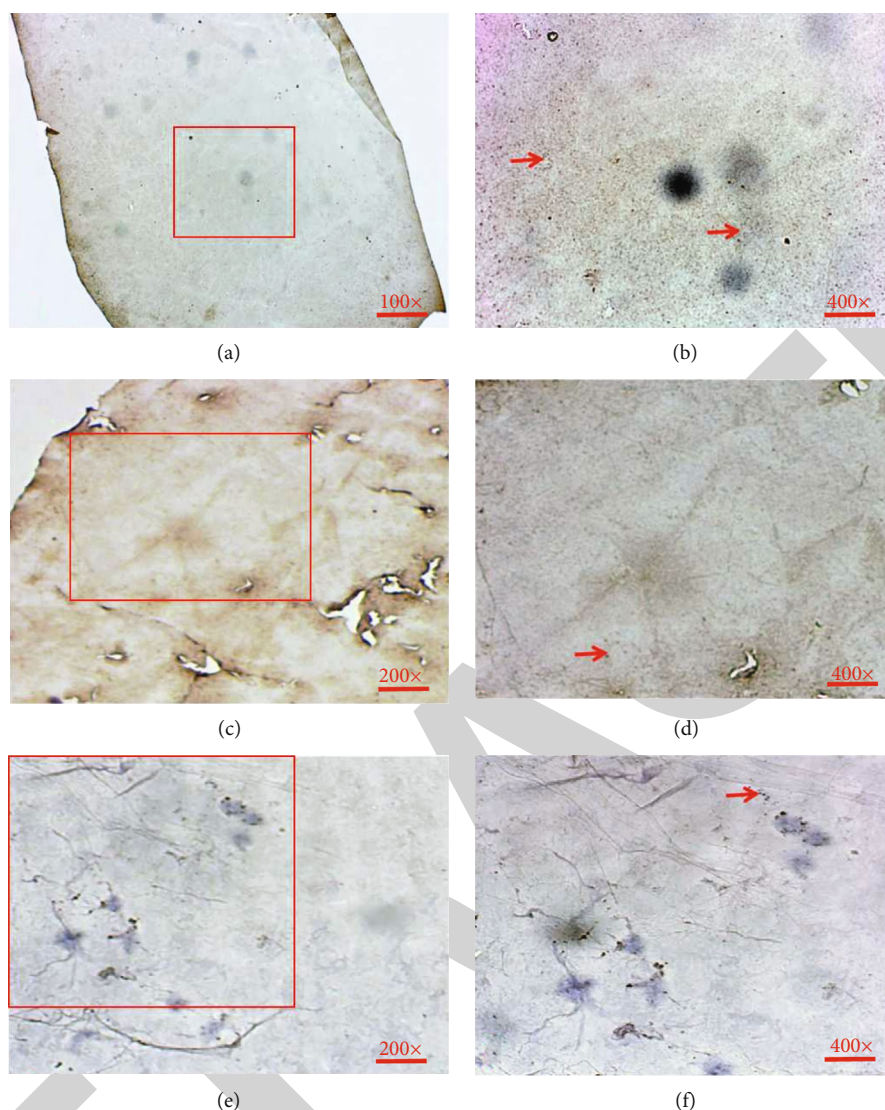


FIGURE 2: Flat-mount preparation of the ILMs for immunohistochemistry of AQP4. (a, b) On the ILM of DR with DME, AQP4-positive reactions are abundant, irregularly gather, and form clusters (arrowheads). (c–f) On the ILM of iMH or MHRD, AQP4-positive reactions are detected (arrowheads). Magnification: (a) $\times 100$, (b, d, f) $\times 400$, and (c, e) $\times 200$. The area circled by the square is the positive area, which is also the enlarged display area in the next figure.

supporting software of confocal microscope), the open access software ImageJ was used to measure the fluorescence intensity of the proteins on ILM specimens that were positively stained. All images were transformed to 8-bit type and a threshold was set. Then, traced a rectangular box of similar size where the fluorescence intensity was uniformed by wand tool to measure values of the fluorescence intensity (Figure 1(b)).

2.7. Measurement of Central Foveal Thickness. With the use of the Spectralis optical coherence tomography (OCT; Heidelberg, Germany) instrument, retinal images were obtained from DR patients who could successfully completed the pre-operative macular OCT scan. The central foveal thickness (CFT) corresponds to the distance from the ILM to the sur-

face of the retinal pigment epithelium (RPE) at the fovea (Figure 1(c)). An average value was obtained from three consecutive CFT measurements.

2.8. Statistical Processing. SPSS v22.0 for Windows (SPSS, Inc., Chicago, IL) was responsible for statistical analysis. According to variance homogeneity of the fluorescence intensity of AQP4 evaluated by Levene's test, the analysis was parametric and was displayed as mean \pm standard deviation. One-way analysis of variance was employed for the determination of significant differences in AQP4 fluorescence intensity between the 4 groups. Correlation analysis between the AQP4 fluorescence value and CFT was made by Spearman's rank correlation coefficients. P values < 0.05 were considered statistically significant.

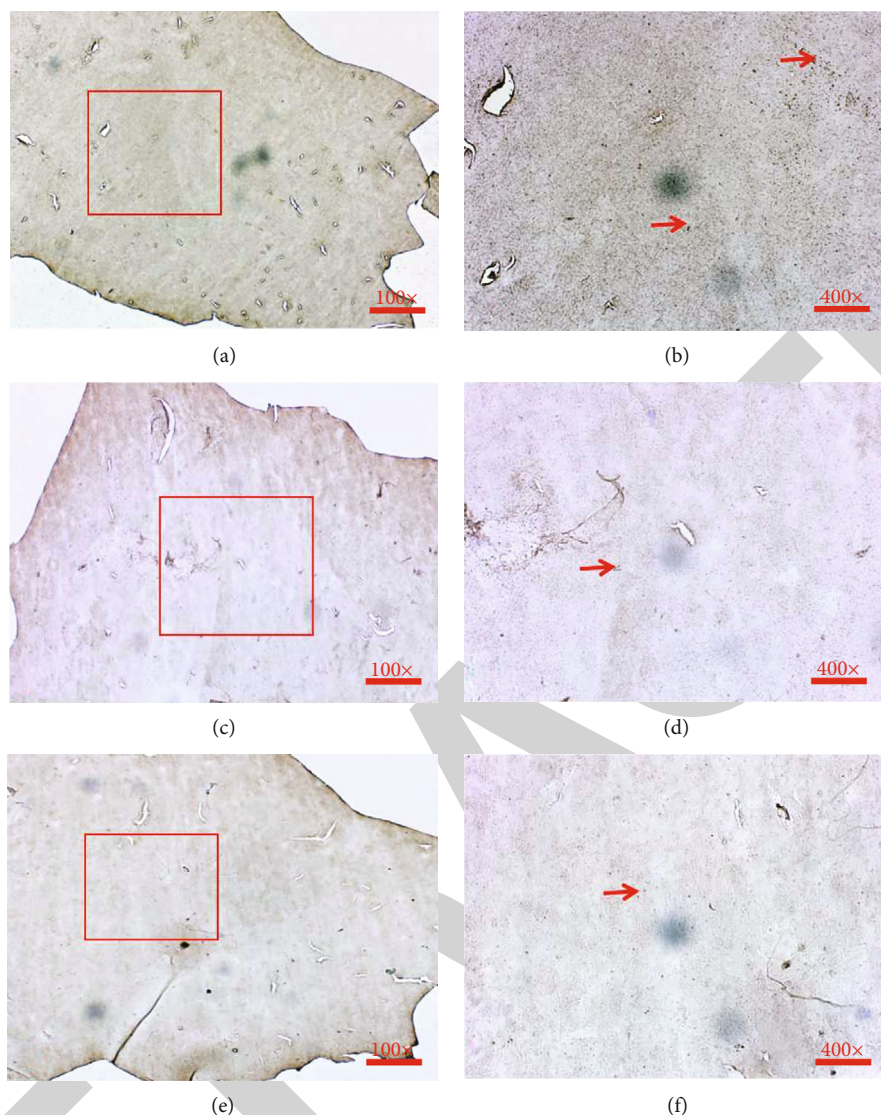


FIGURE 3: Flat-mount preparation of the ILMs for immunohistochemistry of AQP7. (a, b) On the ILM of DR with DME, AQP7-positive reactions are abundant, irregularly gather and form clusters (arrowheads). (c–f) On the ILM of iMH or MHRD, AQP7-positive reactions are detected (arrowheads). Magnification: (a, c, e) $\times 100$ and (b, d, f) $\times 400$. The area circled by the square is the positive area, which is also the enlarged display area in the next figure.

3. Results

3.1. IHC. An immunohistochemical study was conducted on the ILM specimens of 9 patients separately with iMH, MTM, or DR with DME. The basic characteristics of these patients are summarized in Table 1. As shown in Figures 2–4, AQP4-positive, AQP7-positive, and AQP11-positive reactions were all abundantly observed on the ILMs of the DR with the DME group (Figures 2(a), 2(b), Figures 3(a), 3(b), Figures 4(a) and 4(b)). Some brown particles of AQP4-positive, AQP7-positive, and AQP11-positive reactions were irregularly gathered on the dense specimens, forming clusters on the ILMs of the DR with DME group (Figures 2(a), 2(b), Figures 3(a), 3(b), Figures 4(a), and 4

(b)). Compared to the ILMs of iMH and MTM, on the three ILM specimens of DR with DME, respectively, seemed to be stained markedly positive for AQP4, AQP7, and AQP11 antibodies, indicating the possible association between the AQPs and macular edema.

3.2. Immunofluorescence. Another thirty-seven ILM specimens were collected for the AQP4 immunofluorescence study. They included 8 patients with iMH as the control group, 2 patients with iMH and 6 patients with DR as the negative control group, 9 patients with DR as the no DME group, and 12 patients with DME as the DME group. See Table 2 for patient basic characteristics.

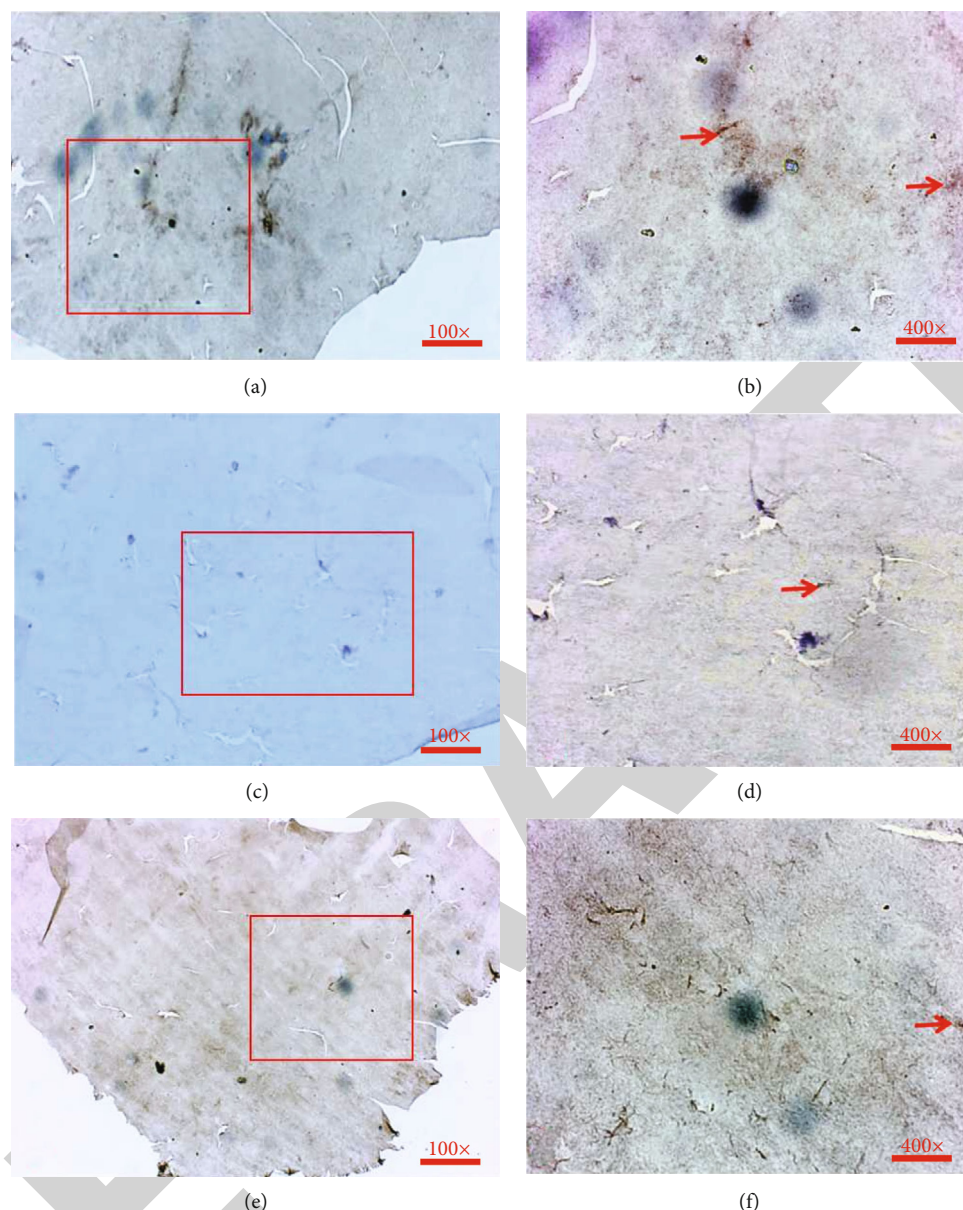


FIGURE 4: Flat-mount preparation of the ILMs for Immunohistochemistry of AQP11. (a, b) On the ILM of DR with DME, AQP11-positive reactions are abundant, irregularly gather and form clusters (arrowheads). (c–f) On the ILM of iMH or MHRD, AQP11-positive reactions are detected (arrowheads). Magnification: (a, c, e) $\times 100$ and (b, d, f) $\times 400$. The area circled by the square is the positive area, which is also the enlarged display area in the next figure.

As shown in Table 3 and Figure 5, the value of fluorescence intensity of AQP4 on ILMs in the negative control group (17.37 ± 5.81) was statistically lower versus the other three groups (control group, no DME group, and DME group, all $P < 0.001$), indicating that AQP4 can be expressed on human ILM, though there may be differences in the degree of expression in different diseases. Moreover, the value of fluorescence intensity of AQP4 on ILMs in the DME group (51.05 ± 5.67) was evidently higher versus the other three groups (control group, negative control group, and no DME group, all $P < 0.001$). However, there was no statistical difference between the value of fluorescence intensity of AQP4 on ILMs between the no DME

group (36.79 ± 6.60) and the control group (38.01 ± 5.04 ; $P = 0.669$).

3.3. The Correction between AQP4 Immunofluorescence Intensity Value and CFT. A total of twelve DR with DME patients were able to successfully complete preoperative macular OCT scan. The CFT value ranged from 212 to 730 μm (mean $491.36 \pm 146.36 \mu\text{m}$). As indicated by Figure 6, a marked positive association was determined between CFT and immunofluorescence intensity values of AQP4 ($r = 0.758$; $P = 0.011$).

There was a significant positive correlation between the AQP4 immunofluorescence intensity value and CFT.

TABLE 2: Clinical data of patients of four groups.

Case	Group	Eye	Age	Gender	Diagnosis	Intraoperative medications
1	Control	OD	47	F	iMH	TA/ICG
2	Control	OS	57	F	iMH	TA/ICG
3	Control	OD	57	F	iMH	TA/ICG
4	Control	OD	64	M	iMH	TA/ICG
5	Control	OD	46	F	iMH	TA/ICG
6	Control	OD	56	F	iMH	TA/ICG
7	Control	OS	77	F	iMH	TA/ICG
8	Control	OD	67	M	iMH	TA/ICG
9	Negative control	OS	69	F	iMH	TA/ICG
10	Negative control	OD	71	F	iMH	TA/ICG
11	Negative control	OS	49	F	PDR, DME	TA/ICG
12	Negative control	OS	56	M	PDR	TA/ICG
13	Negative control	OS	67	M	PDR	TA/ICG
14	Negative control	OD	47	F	DR, DME	TA/ICG
15	Negative control	OD	59	M	DR, DME	TA/ICG
16	Negative control	OD	56	F	DR	TA/ICG
17	No DME	OD	48	M	DR	TA/ICG
18	No DME	OS	69	F	DR	TA/ICG
19	No DME	OD	64	F	DR	TA/ICG
20	No DME	OS	51	M	DR	TA/ICG
21	No DME	OD	73	F	DR	TA/ICG
22	No DME	OD	48	F	DR	TA/ICG
23	No DME	OS	56	M	PDR	TA/ICG
24	No DME	OS	66	F	PDR	TA/ICG
25	No DME	OS	69	F	VH, DR	TA/ICG
26	DME	OS	52	M	DR, DME	TA/ICG
27	DME	OS	66	M	VH, DME	TA/ICG
28	DME	OD	59	M	VH, DME	TA/ICG
29	DME	OS	54	M	VH, DME	TA/ICG
30	DME	OS	52	F	DR, DME	TA/ICG
31	DME	OD	56	M	DR, DME	TA/ICG
32	DME	OS	79	M	DR, DME	TA/ICG
33	DME	OS	55	M	DR, DME	TA/ICG
34	DME	OS	50	F	DR, DME	TA/ICG
35	DME	OD	73	M	DR, DME	TA/ICG
36	DME	OS	59	M	PDR, DME	TA/ICG
37	DME	OS	63	F	PDR, DME	TA/ICG

OD: right eye; OS: left eye; iMH: idiopathic macular hole; PDR: proliferative diabetic retinopathy; DR: diabetic retinopathy; VH: vitreous hemorrhage; DME: diabetic macular edema; ICG: indocyanine green; TA: triamcinolone acetonide.

4. Discussion

For the purpose of addressing the limitations of conventional sectioning and embedding preparation, this study analyzes AQPs IHC and immunofluorescence on ILMs using flat-mount preparations, a procedure that makes the enface visualization of the whole ILM specimen possible. Unlike conventional sectioning preparations, flat-mount preparations can even detect the formation of single small

cell clusters of ILM specimens that might be missed by serial-sectioning preparations [16].

In the present study, the result of AQPs IHC showed that AQP4, AQP7, and AQP11 could be detected on ILMs of various vitreoretinal diseases, confirming that AQP4, AQP7, and AQP11 can be expressed on the human ILMs in vivo for the first time. Moreover, the expression of AQP4, 7 and 11 on ILMs of DR with DME seemed all higher than the ILMs of iMH and MTM, indicating the increased

TABLE 3: Comparison of the AQP4 immunofluorescence intensity values of four groups.

Group	AQP4 immunofluorescence intensity value
Control group, $n = 8$	38.01 ± 5.04
Negative control group, $n = 8$	$17.37 \pm 5.81^*$
No DME group, $n = 9$	36.79 ± 6.60
DME group, $n = 12$	$51.05 \pm 5.67^*$
<i>P</i> value	<0.0001

Values are displayed as mean \pm standard deviation. *P* values were computed with one-way analysis of variance; * $P < 0.05$, compared to the other three groups. DME: diabetic macular edema; AQP4: aquaporin 4; *n*: number.

expression of AQPs on the ILMs of DR may be associated with the occurrence of DME. Under normal conditions, AQP7 is involved in maintaining the osmotic gradient across the outer membrane in the retina, which regulates the transport of water through the RPE into the choroid, thereby preventing patients from retinal detachment and subretinal edema [17]. Yakata et al. [18] indicated that AQP11 has a lower water permeability and is essential for maintaining endoplasmic reticulum homeostasis of vascular endothelial cells under the metabolic stress state of the liver and kidney [19]. In addition, pathogens, inflammatory factors, radiation, and other stress effects regulate AQP11 through signaling pathways such as JNK/NF κ B, which in turn affect the differentiation process of lipid cells [20]. Previous studies indicated that AQP7 and AQP11 are mainly involved in the outflow channel of tissue water in the retinal nerve fiber layer and RPE layer, and AQP11 deletion at Müller glia plasma cell membranes may result in weakened capacity of cells to reduce cell volume through water outflow, which gives rise to cell swelling and consequently fatal retinal edema in ERU and other retinal diseases as well like DME [8]. However, in this study, AQP7 and AQP11 were increased on the ILM of diabetic retinopathy with macular edema compared with other patients.

Therefore, we hypothesize that AQP7 and AQP11 on the ILM may also participate in the water absorption process. The increase in water absorption causes an accumulation of water in the retina, while the expression of AQP7 and AQP11 in other retinal tissues is downregulated, decreases the outflow of water, and finally causes the retinal edema. Compared with AQP4, the water absorption function of AQP7 and AQP11 should be much weaker; therefore, the changes of AQP7 and AQP11 in the ILM of DR with DME are not significant. However, the regulation mechanism of AQPs is not completely clear by far, and further investigation is required. AQP7 and AQP11 are colocalized in the Müller cell endfeet at the ILM, while AQP4 is polarized distributed in Müller cells and mainly expressed in the endfeet membranes [12, 21]. According to the results of AQPs' IHC in this study, AQP4 seemed to be, qualitatively, the most abundant among the three AQPs expressed on the ILMs, so we selected AQP4 as the protein for immunofluorescence detection.

The results of AQP4 immunofluorescence in this study identified statistically higher AQP4 fluorescence intensity in the DME group versus the other three groups. Moreover, there was a significant positive correlation between the AQP4 immunofluorescence intensity value and CFT, indicating that the increased expression of AQP4 on the ILMs of DR may be associated with the occurrence of DME, and the degree of DME may be positively correlated with the expression of AQP4 on the ILMs. Vujosevic et al. have demonstrated that diabetes might have a strong effect on Müller cells [10]. Functionally, expressing voltage-gated channels and neurotransmitter receptors, Müller cells can modulate neuronal viability via modulating the extracellular content of neuroactive substances (K^+ , glutamate, GABA, H^+ , etc.). Around the retinal vessels, there are Müller cell endfeet. AQP4 has abundant expression in the glial processes facing retinal capillaries, and the contact between end-feet with capillary endothelium can release K^+ , acid equivalents, and water, [22] which is in keeping with the role of AQP4 in water release to the capillaries, thus helping to maintain extracellular osmolality during neuronal activity. Oku et al. [7] have confirmed that nitric oxide (NO) increased not only AQP4 expression but also the volume of optic nerve astrocytes via the cGMP/protein kinase G axis. Therefore, we assume that osmotic pressure, oxygen concentration, hormones, neurotransmitters, cytokines, and other factors affect the expression of AQP4 through cGMP/PKG, MAPK [23], and other signaling pathways, thereby affecting the blood-retinal barrier and active transfer of water, K^+ , etc., leading to the formation of ischemia and edema in patients with diabetic retinopathy.

As an important type of protein that relies on osmotic gradients and hydrostatic pressure to control the bidirectional motion of water through the membrane, AQPs may be essential in the pathogenic mechanism of DME. Recently, PPV combined with ILM peeling was performed for refractory macular edema, with ideal clinical effects [24–26]. In previous studies, the authors indicated that the removal of ILM may release the mechanical traction on macula, exert interference with nutrition or oxygenation of retina, and remove the proteins and cytokines related to DME on the inner limiting membrane [26]. According to the results of this study, the increase in AQP expression on ILMs of DR may be associated with the occurrence of DME; therefore, the use of AQP antagonists or the inhibitors of the proteins related to the mechanism of AQP may have a preventive or therapeutic effect on DME, instead of just using anti-VEGF or corticosteroids on the conservative treatment. Cui et al. [27] found that intravitreal injection of AQP4 protein inhibitor such as AQP4 shRNA (R) lentivirus particles or negative lentivirus particles could enhance AQP4 expression in diabetic rat retina. So, the regulation of AQP4 on retinal function may reduce diabetic retinopathy.

As the only human living retinal tissue currently available [1], the ILM, located at the vitreoretinal interface, can be used as a medium to study abnormal changes of vitreous body and retina. So, this study attempted to analyze the abnormal expression of AQPs on the ILMs of various vitreoretinal human diseases for the first time and to explore

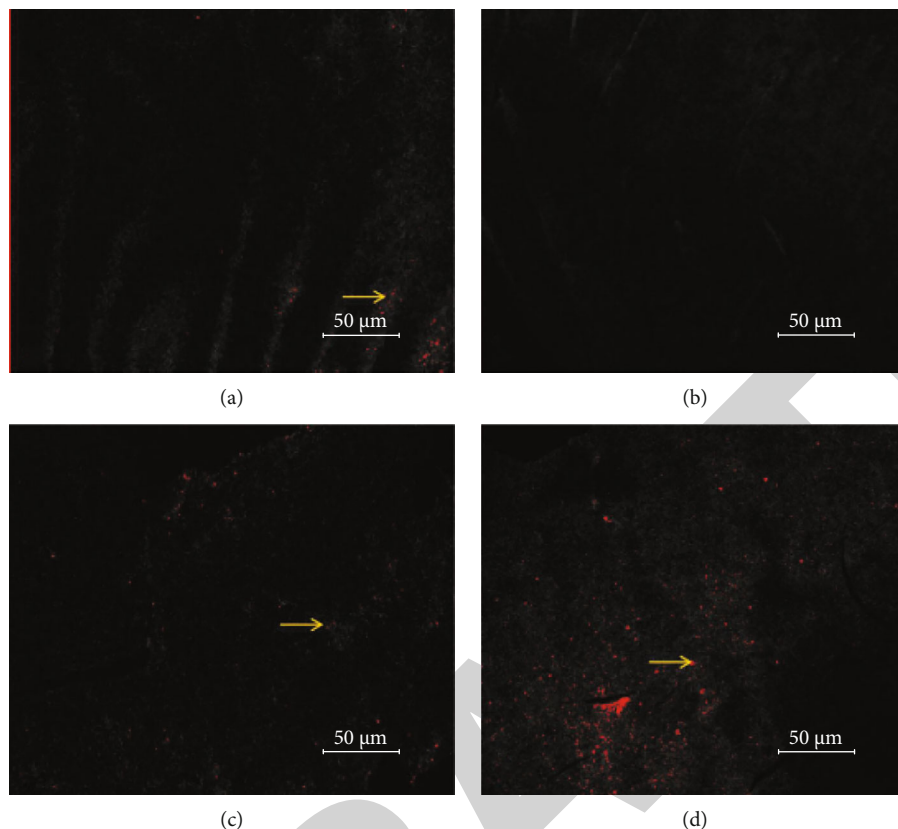


FIGURE 5: Flat-mount preparation of the ILMs for AQP4 immunofluorescence. (a) Low-intensity AQP4-positive reactions are uniformly scattered and evenly distributed on the ILM of a patient of the control group (arrow). (b) No AQP4-positive reactions are detected on the ILM of a patient of the negative control group. (c) Compared with the control group, higher intensity AQP4-positive reactions are detected and more densely distributed in the no DME group (arrow); (d) In the DME group, AQP4-positive reactions are most abundant, irregularly gather and form clusters (arrow).

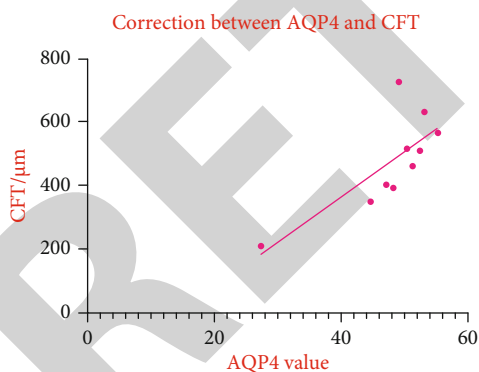


FIGURE 6: The correction between AQP4 immunofluorescence intensity Value and CFT.

the correction between the degree of DME and the expression of AQP4 on the ILMs. This study still obtains some deficiencies and shows some room for improvement. Firstly, the sample size should be expanded, and the ILMs of DR patients without DME should be included in particular. Secondly, in this study, only preoperative OCT was observed. For some patients who could not complete the scan due to VH or severe cataract before surgery, it can be combined with intraoperative OCT. Thirdly, in the subsequent study,

it can be combined with the patient’s follow-up. The prospect of this study is to further investigate whether AQP can be a treatment target on human retina disease and find out its clinical value.

5. Conclusions

In conclusion, AQP4, AQP7, and AQP11 can be expressed on the ILM of human in vivo. The increase in AQP expression on ILMs of DR may be associated with the occurrence of DME. Moreover, the degree of DME may be positively correlated with the expression of AQP4 on the ILMs.

Data Availability

The data that support the findings of this study are available from the corresponding author upon request.

Conflicts of Interest

All authors declare that there is no conflict of interest regarding the publication of this paper.

Authors' Contributions

Yiqi Chen and Huan Chen conceived and designed the experiments. Huan Chen, Chenxi Wang, Jiafeng Yu, and Jiwei Tao performed the experiments and contributed with reagents/materials/analysis tools. Jianbo Mao and Lijun Shen provided guidance and corrections for research design, result analysis and data statistics. Huan Chen and Yiqi Chen wrote the paper. All contributing authors have read and approved the final version of the manuscript. Yiqi Chen and Huan Chen contributed equally to this work and are co-first authors.

Acknowledgments

The authors are grateful to Dr. Joseph Chan Yau Kei (University of Hong Kong), Xiaoxin Zhang (Zhejiang Provincial People's Hospital), and Bin Xie (Wenzhou Medical University) for their valuable contributions. This work was supported by the National Natural Science Foundation of China (81700884), Zhejiang Public Welfare Technology Application Project (LGF21H120005), and Scientific Research Foundation of National Health and Health Commission (WKJ-ZJ-2037).

References

- [1] K. L. Schey, Z. Wang, J. L. Wenke, and Y. Qi, "Aquaporins in the eye: expression, function, and roles in ocular disease," *Biochimica et Biophysica Acta (BBA)-General Subjects*, vol. 1840, no. 5, pp. 1513–1523, 2014.
- [2] K. Kaneko, K. Yagui, A. Tanaka et al., "Aquaporin 1 is required for hypoxia-inducible angiogenesis in human retinal vascular endothelial cells," *Microvascular Research*, vol. 75, no. 3, pp. 297–301, 2008.
- [3] M. Hollborn, S. Dukic-Stefanovic, T. Pannicke et al., "Expression of aquaporins in the retina of diabetic rats," *Current Eye Research*, vol. 36, no. 9, pp. 850–856, 2011.
- [4] A. Miki, A. Kanamori, A. Negi, M. Naka, and M. Nakamura, "Loss of aquaporin 9 expression adversely affects the survival of retinal ganglion cells," *The American Journal of Pathology*, vol. 182, no. 5, pp. 1727–1739, 2013.
- [5] H. Suzuki, H. Oku, T. Horie et al., "Changes in expression of aquaporin-4 and aquaporin-9 in optic nerve after crushing in rats," *PLoS One*, vol. 9, no. 12, article e114694, 2014.
- [6] M. Dal Monte, G. Nicchia, M. Cammalleri et al., "Aquaporin 4 is required to induce retinal angiogenesis in a mouse model of oxygen-induced retinopathy," *Acta Ophthalmologica*, vol. 92, 2014.
- [7] H. Oku, S. Morishita, T. Horie et al., "Nitric oxide increases the expression of aquaporin-4 protein in rat optic nerve astrocytes through the cyclic guanosine monophosphate/protein kinase g pathway," *Ophthalmic Research*, vol. 54, no. 4, pp. 212–221, 2015.
- [8] C. A. Deeg, B. Amann, K. Lutz et al., "Aquaporin 11, a regulator of water efflux at retinal müller glial cell surface decreases concomitant with immune-mediated gliosis," *Journal of Neuroinflammation*, vol. 13, pp. 1–12, 2016.
- [9] S. Lassiale, F. Valamanesh, C. Klein, D. Hicks, M. Abitbol, and C. Versaux-Botteri, "Changes in aquaporin-4 and Kir4.1 expression in rats with inherited retinal dystrophy," *Experimental Eye Research*, vol. 148, pp. 33–44, 2016.
- [10] S. Vujosevic, A. Micera, S. Bini, M. Berton, G. Esposito, and E. Midena, "Aqueous humor biomarkers of Müller cell activation in diabetic eyes," *Investigative Ophthalmology & Visual Science*, vol. 56, no. 6, pp. 3913–3918, 2015.
- [11] N. Matsunaga, H. Ozeki, Y. Hirabayashi, S. Shimada, and Y. Ogura, "Histopathologic evaluation of the internal limiting membrane surgically excised from eyes with diabetic maculopathy," *Retina*, vol. 25, no. 3, pp. 311–316, 2005.
- [12] S. Tenckhoff, M. Hollborn, L. Kohen, S. Wolf, P. Wiedemann, and A. Bringmann, "Diversity of aquaporin mRNA expressed by rat and human retinas," *Neuroreport*, vol. 16, no. 1, pp. 53–56, 2005.
- [13] M. J. Goodyear, S. G. Crewther, and B. M. Junghans, "A role for aquaporin-4 in fluid regulation in the inner retina," *Visual Neuroscience*, vol. 26, no. 2, pp. 159–165, 2009.
- [14] T. L. Tran, T. Bek, M. la Cour et al., "Altered aquaporin expression in glaucoma eyes," *APMIS*, vol. 122, no. 9, pp. 772–780, 2014.
- [15] B. Amann, K. J. Kleinwort, S. Hirmer et al., "Expression and distribution pattern of aquaporin 4, 5 and 11 in retinas of 15 different species," *International Journal of Molecular Sciences*, vol. 17, no. 7, article 1145, 2016.
- [16] R. G. Schumann, K. H. Eibl, F. Zhao et al., "Immunocytochemical and ultrastructural evidence of glial cells and hyalocytes in internal limiting membrane specimens of idiopathic macular holes," *Investigative Ophthalmology & Visual Science*, vol. 52, no. 11, pp. 7822–7834, 2011.
- [17] T. L. Tran, T. Bek, L. Holm et al., "Aquaporins 6–12 in the human eye," *Acta Ophthalmologica*, vol. 91, no. 6, pp. 557–563, 2013.
- [18] K. Yakata, K. Tani, and Y. Fujiyoshi, "Water permeability and characterization of aquaporin-11," *Journal of Structural Biology*, vol. 174, no. 2, pp. 315–320, 2011.
- [19] A. Rojek, E.-M. Füchtbauer, A. Füchtbauer et al., "Liver-specific Aquaporin 11 knockout mice show rapid vacuolization of the rough endoplasmic reticulum in periportal hepatocytes after amino acid feeding," *American Journal of Physiology-Gastrointestinal and Liver Physiology*, vol. 304, pp. G501–G515, 2013.
- [20] J. D. Chiadak, T. Arsenijevic, F. Gregoire et al., "Involvement of JNK/NFκB signaling pathways in the lipopolysaccharide-induced modulation of aquaglyceroporin expression in 3T3-L1 cells differentiated into adipocytes," *International Journal of Molecular Sciences*, vol. 17, no. 10, article 1742, 2016.
- [21] E. A. Nagelhus, Y. Horio, A. Inanobe et al., "Immunogold evidence suggests that coupling of K⁺ siphoning and water transport in rat retinal Müller cells is mediated by a coenrichment of Kir 4.1 and AQP4 in specific membrane domains," *Glia*, vol. 26, no. 1, pp. 47–54, 1999.
- [22] S. Hamann, T. Zeuthen, M. L. Cour et al., "Aquaporins in complex tissues: distribution of aquaporins 1–5 in human and rat eye," *American Journal of Physiology-Cell Physiology*, vol. 274, no. 5, pp. C1332–C1345, 1998.
- [23] Y. Zheng, L. Wang, M. Chen, A. Pei, L. Xie, and S. Zhu, "Upregulation of mir-130b protects against cerebral ischemic injury by targeting water channel protein aquaporin 4 (AQP4)," *American Journal of Translational Research*, vol. 9, no. 7, pp. 3452–3461, 2017.
- [24] Y. Asahina, N. Tachi, Y. Asahina, K. Yoshimura, Y. Ueta, and Y. Hashimoto, "Six-month postoperative outcomes of

Retraction

Retracted: Cryptotanshinone Protects against PCOS-Induced Damage of Ovarian Tissue via Regulating Oxidative Stress, Mitochondrial Membrane Potential, Inflammation, and Apoptosis via Regulating Ferroptosis

Oxidative Medicine and Cellular Longevity

Received 26 September 2023; Accepted 26 September 2023; Published 27 September 2023

Copyright © 2023 Oxidative Medicine and Cellular Longevity. This is an open access article distributed under the Creative Commons Attribution License, which permits unrestricted use, distribution, and reproduction in any medium, provided the original work is properly cited.

This article has been retracted by Hindawi following an investigation undertaken by the publisher [1]. This investigation has uncovered evidence of one or more of the following indicators of systematic manipulation of the publication process:

- (1) Discrepancies in scope
- (2) Discrepancies in the description of the research reported
- (3) Discrepancies between the availability of data and the research described
- (4) Inappropriate citations
- (5) Incoherent, meaningless and/or irrelevant content included in the article
- (6) Peer-review manipulation

The presence of these indicators undermines our confidence in the integrity of the article's content and we cannot, therefore, vouch for its reliability. Please note that this notice is intended solely to alert readers that the content of this article is unreliable. We have not investigated whether authors were aware of or involved in the systematic manipulation of the publication process.

Wiley and Hindawi regrets that the usual quality checks did not identify these issues before publication and have since put additional measures in place to safeguard research integrity.

We wish to credit our own Research Integrity and Research Publishing teams and anonymous and named external researchers and research integrity experts for contributing to this investigation.

The corresponding author, as the representative of all authors, has been given the opportunity to register their

agreement or disagreement to this retraction. We have kept a record of any response received.

References

- [1] H. Liu, J. Xie, L. Fan et al., "Cryptotanshinone Protects against PCOS-Induced Damage of Ovarian Tissue via Regulating Oxidative Stress, Mitochondrial Membrane Potential, Inflammation, and Apoptosis via Regulating Ferroptosis," *Oxidative Medicine and Cellular Longevity*, vol. 2022, Article ID 8011850, 21 pages, 2022.

Research Article

Cryptotanshinone Protects against PCOS-Induced Damage of Ovarian Tissue via Regulating Oxidative Stress, Mitochondrial Membrane Potential, Inflammation, and Apoptosis via Regulating Ferroptosis

Honglin Liu ¹, Jiani Xie ¹, Limin Fan ², Yue Xia ¹, Xia Peng ¹, Jianhua Zhou ¹, and Xiaorong Ni ¹

¹Department of Gynecology, Shanghai University of Traditional Chinese Medicine, Shanghai Traditional Chinese Medicine Hospital, 274 Middle Zhi Jiang Rd, Shanghai 200071, China

²The Institute for Biomedical Engineering and Nano Science Tongji University School of Medicine, No. 1239, Siping Road, Shanghai 200092, China

Correspondence should be addressed to Xiaorong Ni; nixr2015@163.com

Received 9 February 2022; Revised 24 February 2022; Accepted 1 March 2022; Published 4 April 2022

Academic Editor: Shao Liang

Copyright © 2022 Honglin Liu et al. This is an open access article distributed under the Creative Commons Attribution License, which permits unrestricted use, distribution, and reproduction in any medium, provided the original work is properly cited.

Polycystic ovary syndrome (PCOS) is the most common endocrine disorder in women of childbearing age. Cryptotanshinone (CRY) has been shown to be effective in reversing reproductive disorders, but whether it can be used in the treatment of polycystic ovary syndrome remains unclear. We aimed to explore whether the mechanism of cryptotanshinone (CRY) in the treatment of polycystic ovary syndrome (PCOS) can be driven via regulating ferroptosis. A rat model of PCOS was established by daily injection of human chorionic gonadotropin and insulin for 22 days. An in vitro model of ischemia-reperfusion (IR) of granulosa cells was established. The in vitro and rat models of PCOS were subjected to different treatments including ferroptosis activators and inhibitors, CRY, and MAPK inhibitor. Oxidative stress was evaluated by measuring the activities of SOD, MDA, and GSH-PX. Total body weight and ovarian weight, as well as the levels of LH and the LH to FSH ratio, significantly increased in rats with PCOS, compared with controls. The expression of Bax was increased in PCOS tissues while PGC1 α , NFR1, GPX4, catalase p-ERK, and Bcl-2 were all downregulated. Ferroptosis activator, erastin, had effects similar to those of PCOS while the contrary was found with CRY and ferroptosis inhibitor treatment groups. In vitro, CRY inhibited oxidative stress, MMP, and NF- κ B and activated MAPK/ERK signaling by regulating ferroptosis. Overall, this study indicated that CRY protects against PCOS-induced damage of the ovarian tissue, via regulating oxidative stress, MMP, inflammation, and apoptosis via regulating ferroptosis.

1. Introduction

Polycystic ovary syndrome is an endocrine disease affecting 15%-20% of women of childbearing age [1]. The etiology and pathogenesis of PCOS are unknown, and the diagnosis is often delayed. The repercussions of PCOS are varied and include psychological, gynecological, and metabolic disorders such as insulin resistance, type II diabetes, cardiovascu-

lar risks, and obesity; PCOS is also one of the causes of infertility in women due to the ovulatory disorders it triggers [2–6]. To date, there is no effective treatment to cure PCOS and the proposed treatments are symptomatic and are aimed at correcting the symptoms related to hyperandrogenism, restoring the menstrual cycle to increase the chances of fertility, and correcting metabolic abnormalities [7–9]. For PCOS patients with infertility, infertility treatment options

TABLE 1: List of primers used in this study.

	Forward primer 5' → 3'	Reverse primer 5' → 3'
PGC1a	AGGTCCCCAGGCAGTAGAT	CGTGCTCATTGGCTTCATA
NRF1	TGGTGTCAGTGGGCTCAATC	GTCTCAAGCTCTGGCCGAAT
GPX4	GGGACAAAGAGCCGGTAG	GGTTACTGGGACCTAGGGGA
Catalase	CCACTCTCTCAGGAATCCGC	GGGTTTCAGCTGTGCTGACT
ERK	CAGGCGCTGAGAGGAGAAAA	TGCTGCTAAGCCCATGGAAA
UCP2	CAATGTTGCCCGAAATGCCA	AGTTGGGTGAGGGGATCCAA
BAX	CTGAGACACTCGCTCAGCTT	TTGCTACAGGGGTGAGTGTG
BCL2	CCCCACAATGGTATGGCACT	CTGCAACACTGCTCTTTGCC
SOD1	AGCCCTATTGGTGAAGCAGA	TGTTTCCTTGCTCGTGGCTA
NF-κB	CAACGCTGTCTCTCACTGGT	GACTGCCTTGACTTCCGTGA
MAPK	GGAGGGGCTCCTTTGAACTT	TGCTCCCTTCATATCCCACA
Actin	AGGGAAATCGTGCGTGACAT	ACAACACTACAGGGCTGACCAC

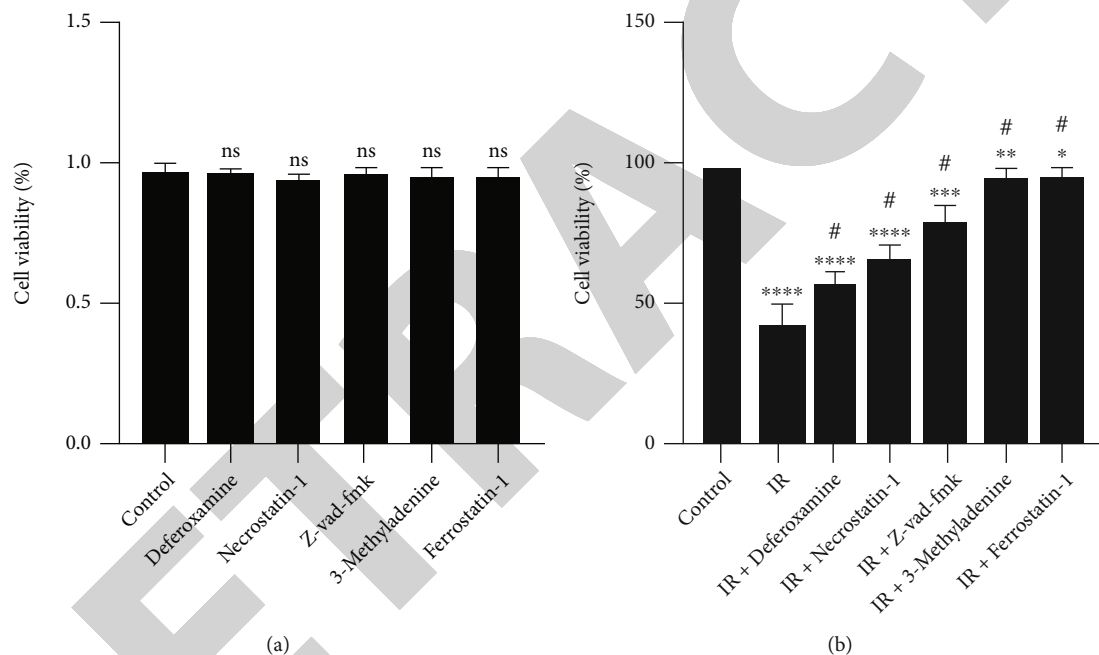


FIGURE 1: Ferroptosis is activated in ischemia-reperfusion- (IR-) induced injury of granulosa cells. (a) Effect of different ferroptosis inhibitors on cell viability. (b) Effect of IR alone or in combination with ferroptosis inhibitors on cell viability. ns: nonsignificant. * $p < 0.05$, ** $p < 0.01$, *** $p < 0.001$, and **** $p < 0.0001$, compared to control; # $p < 0.05$ compared to IR.

such as drugs (letrozole, clomiphene citrate, and gonadotropins), surgery, and in vitro fertilization are offered to patients [10, 11]. Therefore, given the urgency of the situation, it is necessary to look for ways to develop effective treatments for PCOS.

Cryptotanshinone is one of the major bioactive molecules extracted from the plant *Salvia miltiorrhiza* Bunge (Danshen), a plant recognized in traditional Chinese medicine for its virtues in the treatment of various diseases [12]. Previous studies have shown that CRY has biological activities for the treatment of diseases such as coronary heart disease, kidney failure, Alzheimer's disease, cancers, obesity, ageing, diabetes, and fibrosis of the liver, lungs, heart, and kidneys [13–23]. A limited amount of research has shown

that CRY may be effective in the treatment of PCOS and some molecular mechanisms have been proposed [24–27]. In our previous study [28], we also demonstrated the efficacy of CRY in the treatment of PCOS and proposed that its mode of action is mediated by its effect on the regulation of the HMGB1/TLR4/NF-kappaB signaling pathway. However, given the complexity of the pathogenesis and pathophysiology of PCOS, it is important to further investigate the molecular mechanisms underlying PCOS and to explore the mechanisms of action of CRY in order to propel this molecule in the treatment of PCOS.

Ferroptosis is a type of necrotic cell death that has been implicated in the pathogenesis of various diseases such as cancers, cardiovascular diseases, neurodegenerative diseases,

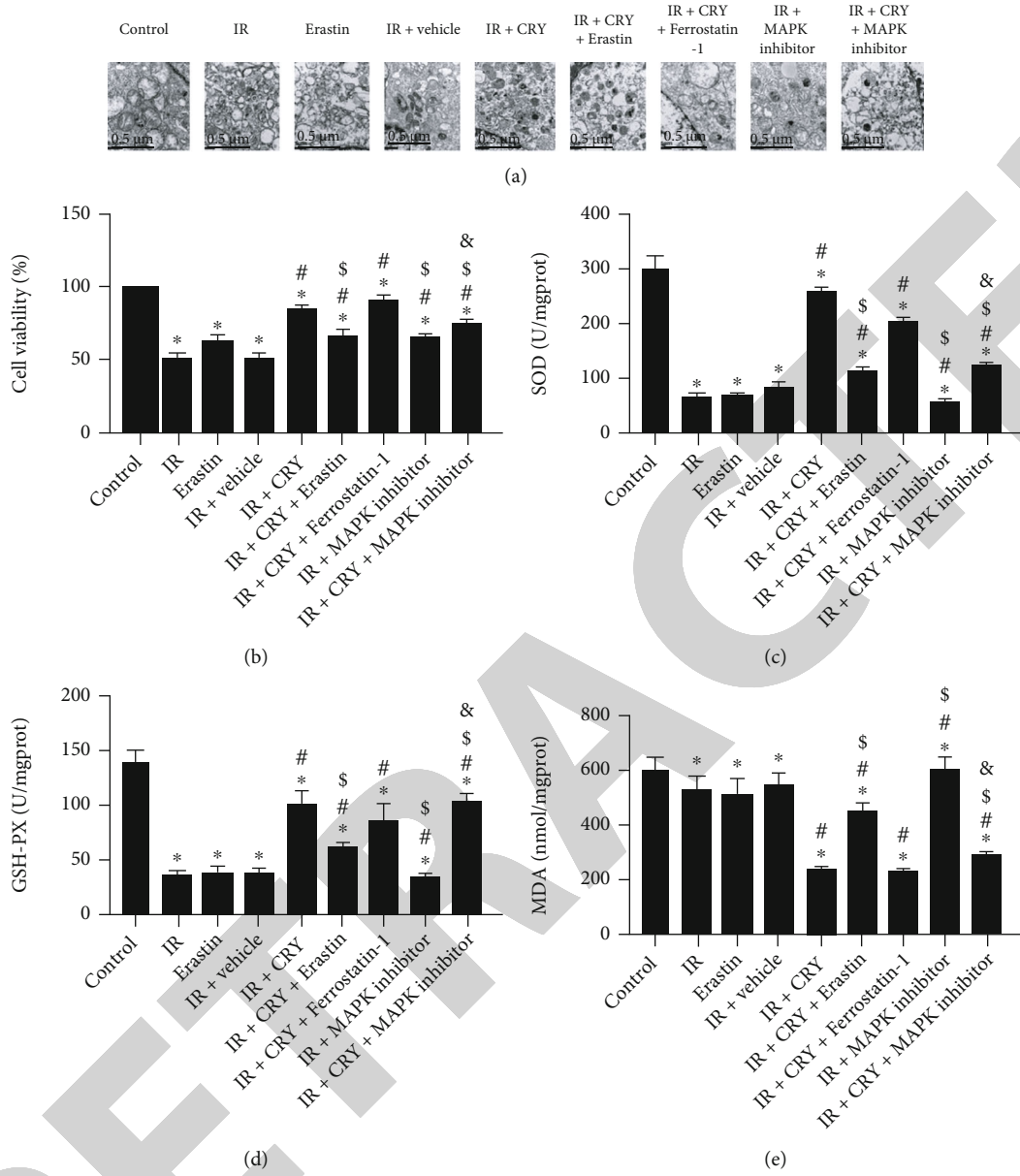


FIGURE 2: Continued.

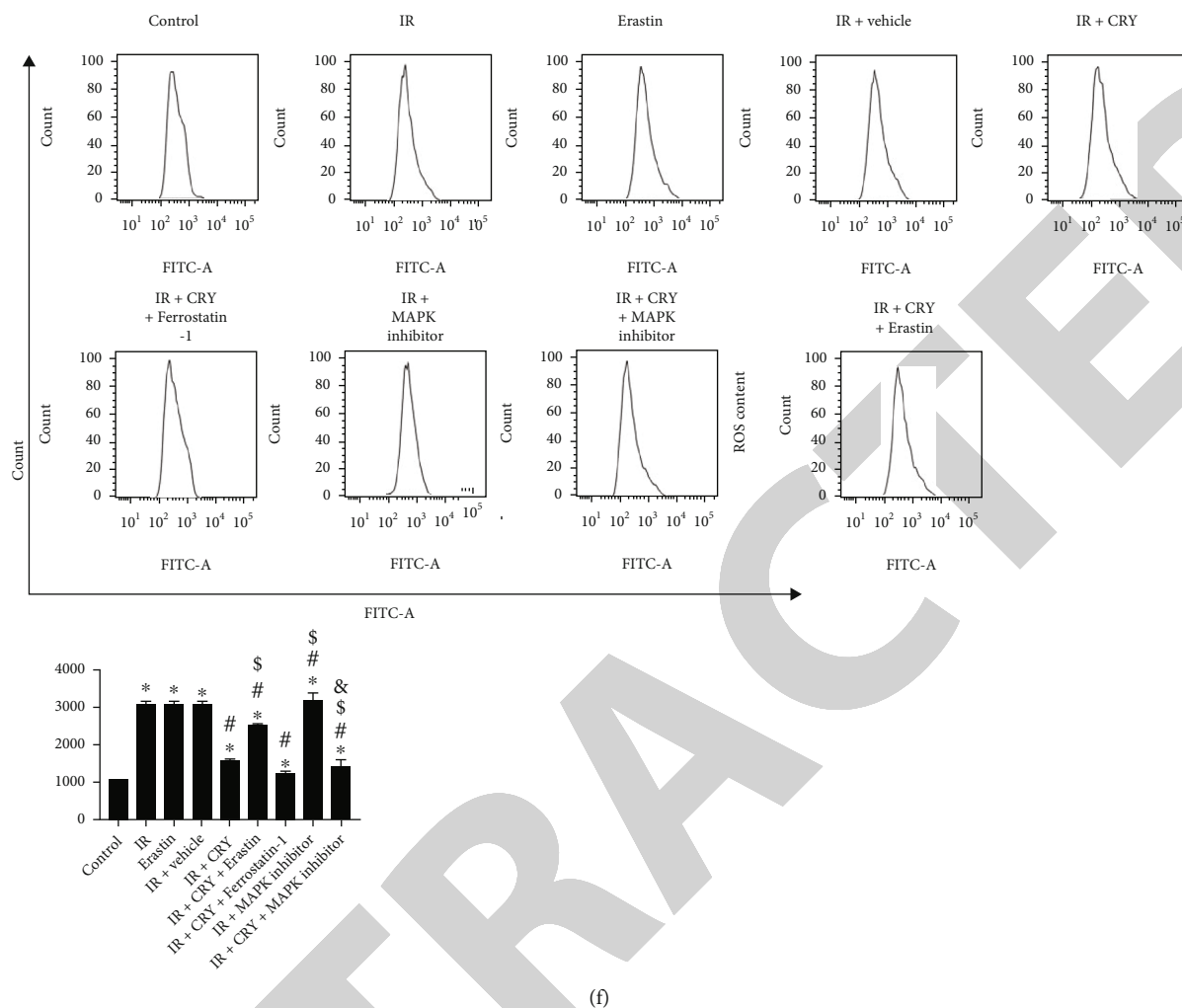


FIGURE 2: Cryptotanshinone inhibits ischemia-reperfusion-induced oxidative stress by regulating ferroptosis via the MAKP signaling pathway in granulosa cells. (a) Ultrastructural analysis of GCs by transmission electron microscopy. (b) Effect of different treatments on cell viability. (c) Effect of different treatments on SOD. (d) Effect of different treatments on MDA. (e) Effect of different treatments on GSH-PX. (f) Effect of different treatments on ROS production. ns: nonsignificant. * $p < 0.05$, compared to control; # $p < 0.05$ compared to IR; \$ $p < 0.05$ compared to IR+CRY; & $p < 0.05$ compared to IR+CRY+ferrostatin-1.

diabetes, and renal failure [29–36]. Studies have shown that ferroptosis is at the center of a multitude of metabolic pathways [31, 33], which gives it a key role in understanding and developing therapeutics. Indeed, studies have demonstrated an interconnection between ferroptosis and biological processes such as oxidative stress and mitochondrial function [37–39]. The current trend suggests that modulation of ferroptosis, either through its inhibition or activation, could be beneficial for the treatment of many diseases. However, although few studies have suggested the involvement of ferroptosis in processes related to ovarian disorders, the role of ferroptosis in PCOS remains unknown. In addition, it has been reported that cryptotanshinone against lung cancer cells is through ferroptosis [40]. Also, cryptotanshinone may increase the accumulation of ROS by inhibiting the expression of xCT and GPX4 to induce the ferroptosis of HepG2 cells [41]. Furthermore, despite the potential of CRY in the treatment of various diseases, no published study, to the best of our knowledge, has yet scrupulously

analyzed whether ferroptosis could be a target of the mechanism of action of CRY in the treatment of PCOS or other diseases. Thus, the novelty and motivation of this study are to expand our knowledge on the mechanisms of action of CRY and its impact on ferroptosis in PCOS would be of great importance in the treatment of PCOS and various diseases.

Thus, in the present study, we set out to extend our previous research by exploring the effect of CRY on ferroptosis and related biological processes such as oxidative stress and mitochondrial function.

2. Material and Methods

2.1. The Rats Used in the Experiments. The rats used in this study were commercially acquired from the Shanghai Laboratory Animal Center, Co. Ltd. The weight of the rats was in the range of 174–210 g, and their average age was 87.8 days. The rats were housed and acclimatized in a temperature-

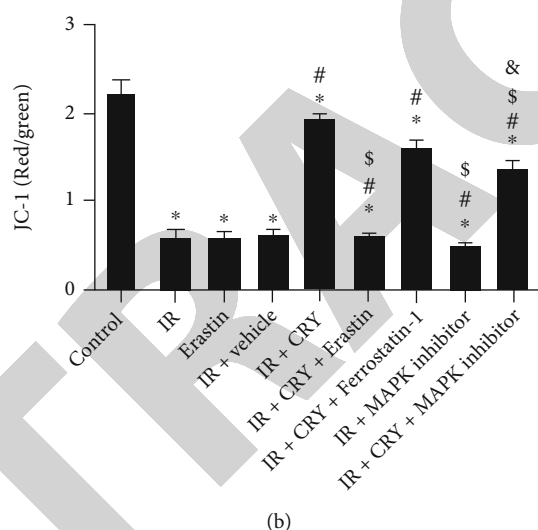
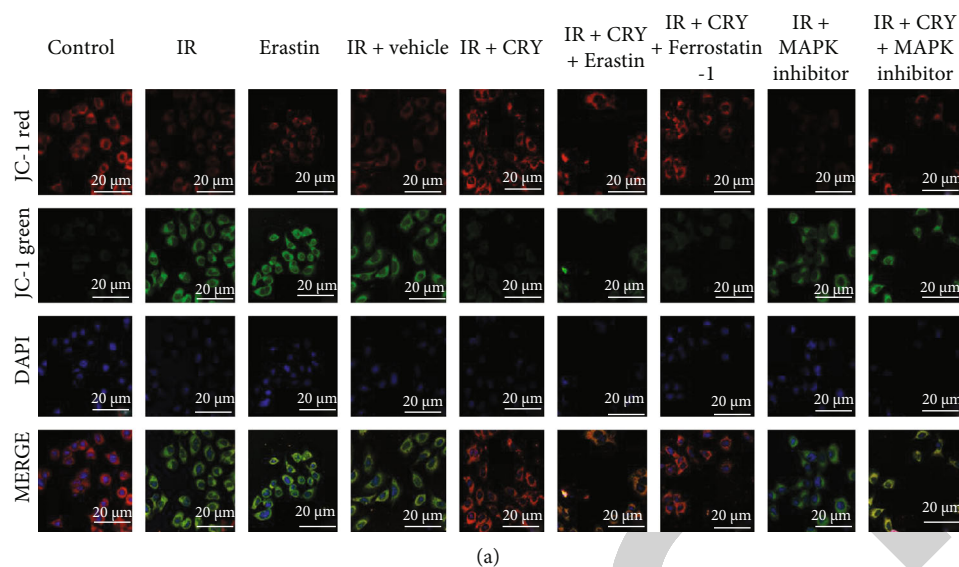


FIGURE 3: Cryptotanshinone regulates ischemia-reperfusion-induced mitochondrial membrane potential by regulating ferroptosis via the MAPK signaling pathway in granulosa cells. (a) Fluorescence image of GCs stained with JC-1 after different treatments. (b) Numerical data of green/red fluorescence-positive GCs. * $p < 0.05$, compared to control; # $p < 0.05$ compared to IR; \$ $p < 0.05$ compared to IR+CRY; & $p < 0.05$ compared to IR+CRY+ferrostatin-1.

controlled environment of $25 \pm 2^\circ\text{C}$ with alternating cycles of 12 h of darkness and 12 h of light under humidity conditions of $55 \pm 15\%$. The animals had free access to food and water. The experimental protocols were in accordance with the standards of the Chinese Ministry of Science and Technology for the Care and Use of Laboratory Animals after approval by the Animal Care and Experiment Review Board of Shanghai Traditional Chinese Medicine Hospital (Shanghai, China) (approval no. 20190103).

2.2. Establishment of the PCOS Rat Model and Treatments. The rats were divided into nine batches of 12 rats each: (1) the control group consisting of rats intragastrically administered with physiological saline; (2) the PCOS group consisting of PCOS rats with intragastric administration of

physiological saline; (3) the PCOS+vehicle group containing of PCOS rats with administration of DMSO in physiological saline; (4) the PCOS+CRY group containing PCOS rats with daily intragastric administration of CRY; (5) the PCOS+ferrostatin-1 group containing PCOS rats with daily intragastric administration of saline and daily intraperitoneal administration of ferrostatin-1, the ferroptosis inhibitor; (6) the PCOS+CRY+erastin group containing PCOS rats with daily intragastric administration of CRY (27 mg/kg) and intraperitoneal administration of erastin; (7) the PCOS+MAPK inhibitor group containing all PCOS rats with daily intraperitoneal administration of 100 μL Skepinone-L (10 mg/kg; China); and (8) the PCOS+CRY+Skepinone-L (selective p38 α -MAPK inhibitor) group containing all PCOS rats with daily intraperitoneal administration of 100 μL

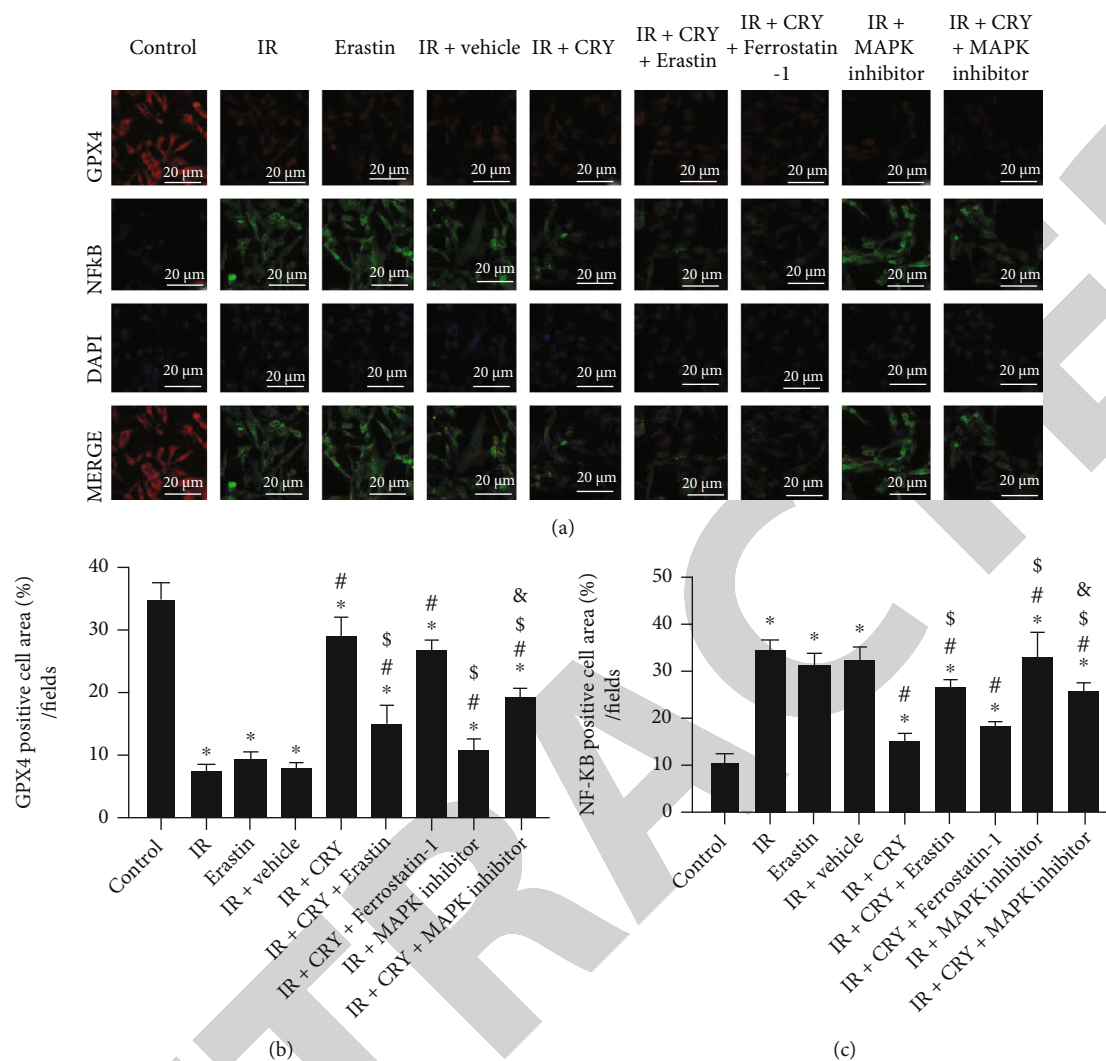


FIGURE 4: Immunofluorescence analysis of GPX4 and NF-κB regulated by cryptotanshinone under ischemia-reperfusion injury. (a) Fluorescence image of GCs stained with GPX4 and NF-κB after different treatments. The photograph shows GPX4 and NF-κB and merge images. (b) Numerical data of the expression of GPX4-positive cells. (c) Numerical data of the expression of NF-κB-positive cells. * $p < 0.05$, compared to control; # $p < 0.05$ compared to IR; \$ $p < 0.05$ compared to IR+CRY; & $p < 0.05$ compared to IR+CRY+ferrostatin-1.

Skepinone-L (10 mg/kg; China). Ferrostatin-1 and erastin were dissolved in DMSO and diluted in physiological saline (0.9% NaCl).

The PCOS model was established as described in our previous study. Briefly, rats were administered by 2 daily subcutaneous injections with HCG (3.0 IU/day) and insulin for a duration of 22 days. The insulin dose was gradually increased from 0.5 to 3 U/day from days 1 to 11 and maintained at 3 U/day from days 12 to 22. Rats in the control group were treated with 2 skin injections of physiological saline. At the beginning of the experiment, water was replaced by 5% dextrose solution. Rats were weighed weekly, and vaginal swabs were taken daily from day 1 to day 23. Confirmation of PCOS was confirmed by the loss of regularity of the estrous cycle.

2.3. Assessment of Body Mass Index, Lee's Index, and Ovarian Quotient. At the end of the experiment, the length

of the rats from the nose to the anus was measured and used to calculate Lee's index [42] and body mass index [43]. The formula for calculating Lee's index was as follows: Lee's index = $\text{weight}^{1/3} \times 10^3 / \text{length}$. The formula for calculating the body mass index was $\text{BMI} = \text{weight} / \text{length}^2$. The unit of length was in centimeter while weight was in grams (g). Ovarian quotient was calculated as the quotient of ovarian mass to body mass and expressed in milligrams per 100 g.

2.4. Collection of Samples. At the end of the experiment, the rats were anaesthetized by intraperitoneal injection of sodium pentobarbital (55 mg/kg) after an overnight fast. Blood (5-7 mL) was collected from the abdominal aorta and subjected to centrifugation (4°C; 1,500 × g; 20 min) for serum collection. After this, pentobarbital sodium (250 mg/kg) was used to kill the animals and death was confirmed by exsanguination. Dissection of the ovaries was then performed, followed by weighing. For the immediate

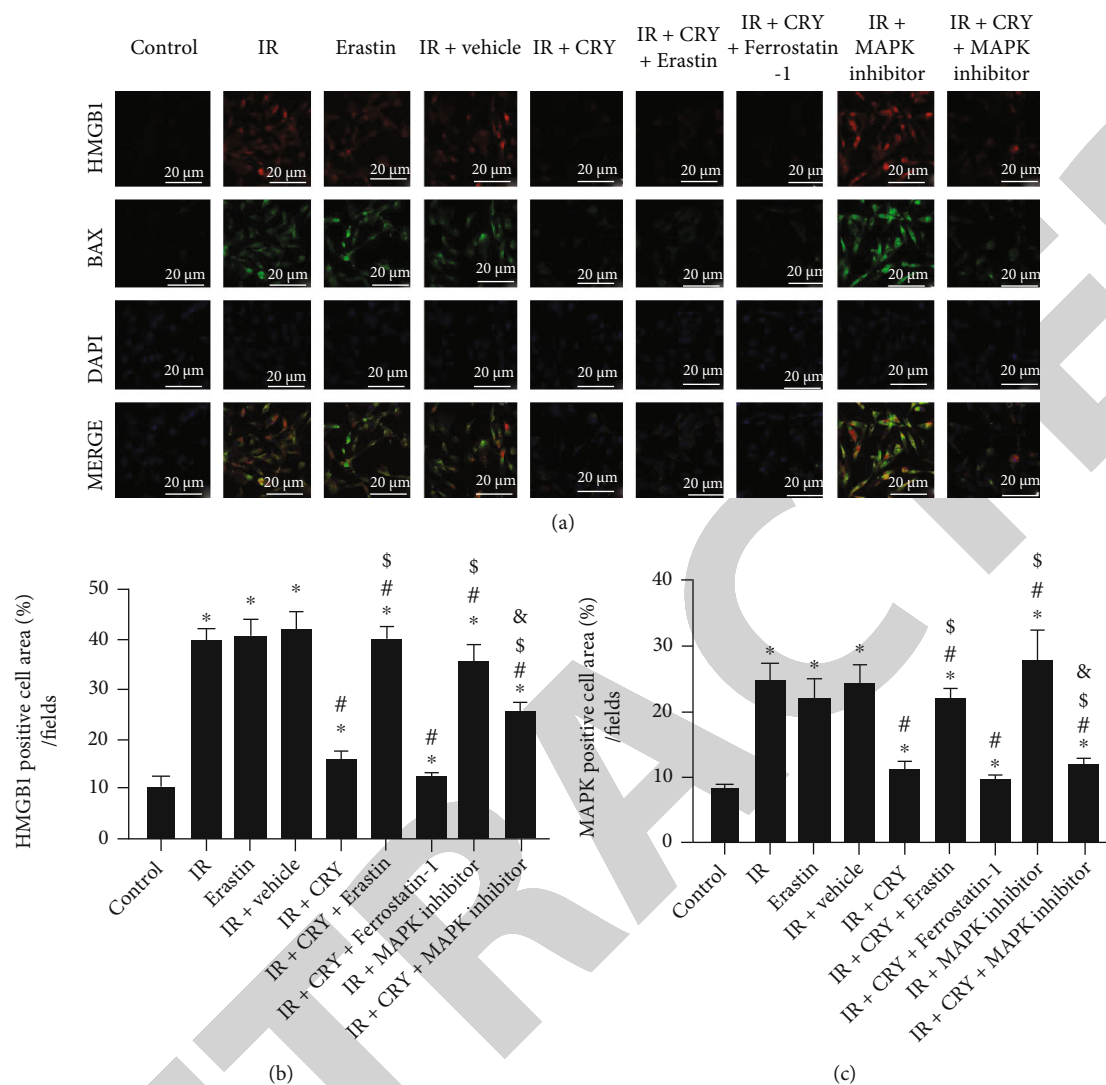


FIGURE 5: Immunofluorescence analysis of BAX and HMGB1 regulated by cryptotanshinone under ischemia-reperfusion injury. (a) Fluorescence image of GCs stained with BAX and HMGB1 after different treatments. The photograph shows MAPK and HMGB1 and merge images. (b) Numerical data of the expression of MAPK-positive cells. (c) Numerical data of the expression of HMGB1-positive cells. * $p < 0.05$, compared to control; # $p < 0.05$ compared to IR; \$ $p < 0.05$ compared to IR+CRY; & $p < 0.05$ compared to IR+CRY +ferrostatin-1.

experiments, a part of the samples was fixed in a 4% paraformaldehyde solution at 25°C for 24 hours. The rest of the samples were stored in a refrigerator at -80°C.

2.5. Histopathological Analysis. For histomorphometric analysis, the tissues were successively dehydrated in graded concentrations of ethanol (50, 70, 80, 90, and 100%) for 30 sec. Afterwards, the tissues were washed in xylene and embedded in paraffin to make 4 μm thick slices. The slices thus made were subjected to picric acid staining at room temperature for 30 min and hematoxylin-eosin staining at room temperature for 15 min. Finally, the stained sections were examined under a fluorescence microscope with the Leica DM5000 platform (Leica Microsystems, Inc.; magnification, ×100).

2.6. Immunohistochemistry. Protein expression was assessed by the immunohistochemical approach. Tissues were first fixed for 24 h in 4% paraformaldehyde at 4°C, embedded in

paraffin, and cut into small 4 μm thick slices. Subsequently, the tissues were blocked in 0.5% BSA solution followed by incubation with primary antibodies to GPX4 (1:200; cat. no. ab125066; Abcam), BAX (1:250; cat. no. ab32503; Abcam), NF-κB (1:2000; cat. no. ab32536; Abcam), and HMGB1 (1:200; cat. no. Ab92310; Abcam) overnight. Revealing was done by visualization with biotin-conjugated secondary antibodies (1:300; cat. no. ab7176; Abcam) after half an hour incubation at 25°C using the Dako EnVision+ Detection System kit in strict accordance with the manufacturer's guidelines. Counterstaining of the coverslips was done by hematoxylin-eosin staining for 5 min at 25°C, and microscopic observation was done with the Leica DM5000 microscope (Leica Microsystems, Inc.; magnification, ×100).

2.7. Isolation and Culture of Rat Ovarian Granulosa Cells. Young female rats between 21 and 25 days of age were used

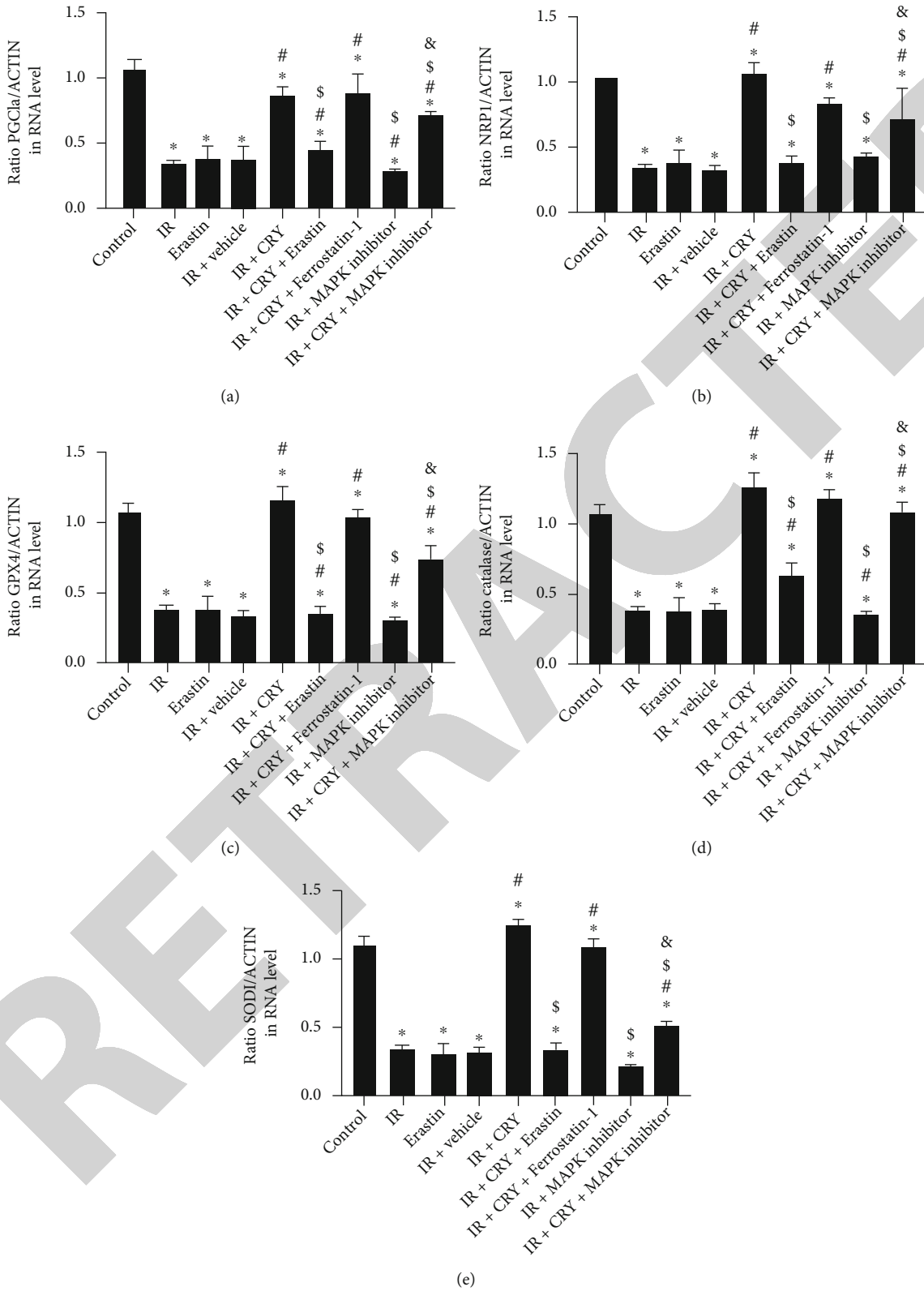


FIGURE 6: Continued.

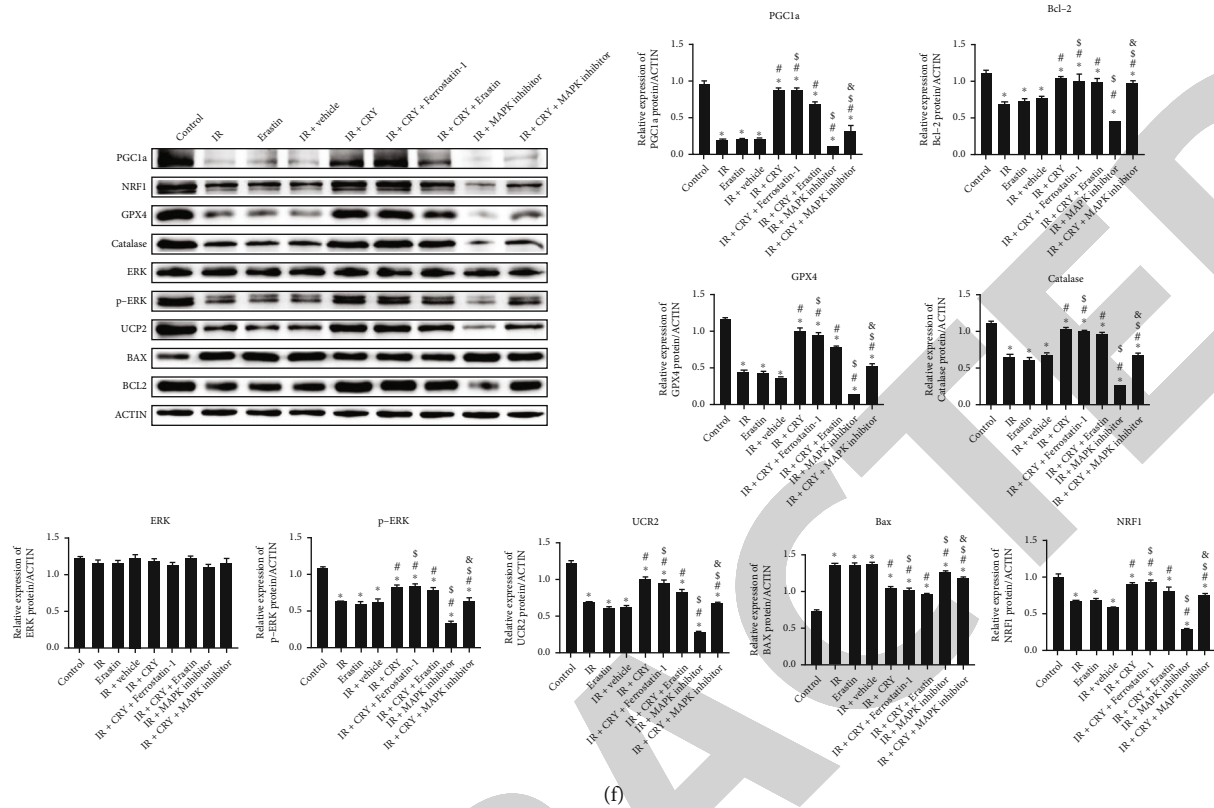


FIGURE 6: mRNA and protein expression regulated by cryptotanshinone under ischemia-reperfusion injury. (a) mRNA expression of PGC1a as determined by RT-qPCR. (b) mRNA expression of NRF1 as determined by RT-qPCR. (c) mRNA expression of GPX4 as determined by RT-qPCR. (d) mRNA expression of catalase gene as determined by RT-qPCR. (e) mRNA expression of SOD1 as determined by RT-qPCR. (f) Blot images and numeric quantification of protein expression of PGC1a, NRF1, GPX4, catalase, ERK, p-ERK, UCP2, BAX, and BCL2 as determined by western blotting. * $p < 0.05$, compared to control; # $p < 0.05$ compared to IR; \$ $p < 0.05$ compared to IR+CRY; & $p < 0.05$ compared to IR+CRY+ferrostatin-1.

to isolate granulosa cells from the ovary. The rats used in this study were commercially acquired from Shanghai Laboratory Animal Center, Co. Ltd. For this purpose, the rats were subjected to a subcutaneous injection of pregnant mare serum gonadotropin (PMSG) (150 IU/kg). 48 h after the injection, the rats were dissected and the ovaries were removed and subjected to follicular puncture as described above for the isolation of granulosa cells, after filtration and centrifugation for 5 min at $200 \times g$ at 4°C . Subsequently, the supernatant was discarded and the cells were resuspended in Dulbecco's modified Eagles medium (Thermo Fisher Scientific, Inc.) to which compounds such as insulin, gentamicin, selenium, and transferrin were added. Cell culture was performed in 6-well plates at a density of 5×10^4 cells/mL in an incubator set to a humidified atmosphere containing 5% CO_2 for 24 h at 37°C .

2.8. Application of Ischemia-Reperfusion [28] to Granulosa Cells. Establishment of ischemia-reperfusion was done by treating granulosa cells with $1 \mu\text{mol/L}$ dexamethasone for a period of 72 h, followed by determination of glucose and sucrose concentration with appropriate kits according to the vendor's recommendations.

2.9. Treatment and Determination of Cell Viability. Cells were subjected to different treatments including ischemia-

reperfusion as described above, CRY, erastin, ferrostatin-1, and MAPK inhibitor. In other cases, several ferroptosis inhibitors were used. The treated cells were grown in 96-well plates at a density of 1×10^4 cells per well. For the assessment of cell viability, the cells were treated with MTT reagent (0.2 mg/mL MTT) which was added to each well, followed by incubation in a humidified atmosphere containing 5% CO_2 for 4 h at 37°C . Then, the formazan crystals were dissolved by treatment with DMSO and the absorbance at 490 nm was measured spectrophotometrically with microplate readers (Safire 2, Tecan Group, Ltd.).

2.10. Analysis of the Ultrastructure of Granulosa Cells. The ultrastructural changes of cells from different groups were analyzed using a transmission electron microscope. Briefly, GCs from different treatment groups were collected and after successive fixing in 2.5% glutaraldehyde and 1% phosphate-buffered osmium tetroxide, the GCs were embedded and colored using uranyl acetate and lead citrate. The transmission electron microscope (JEOL, Tokyo, Japan) was finally applied for microscopic imaging as well as analysis.

2.11. Intracellular ROS Measurement. The fluorescent 2',7'-dichlorofluorescein diacetate probes (DCFH-DA) (Sigma-Aldrich, Poznan, Poland) were employed for the assessment

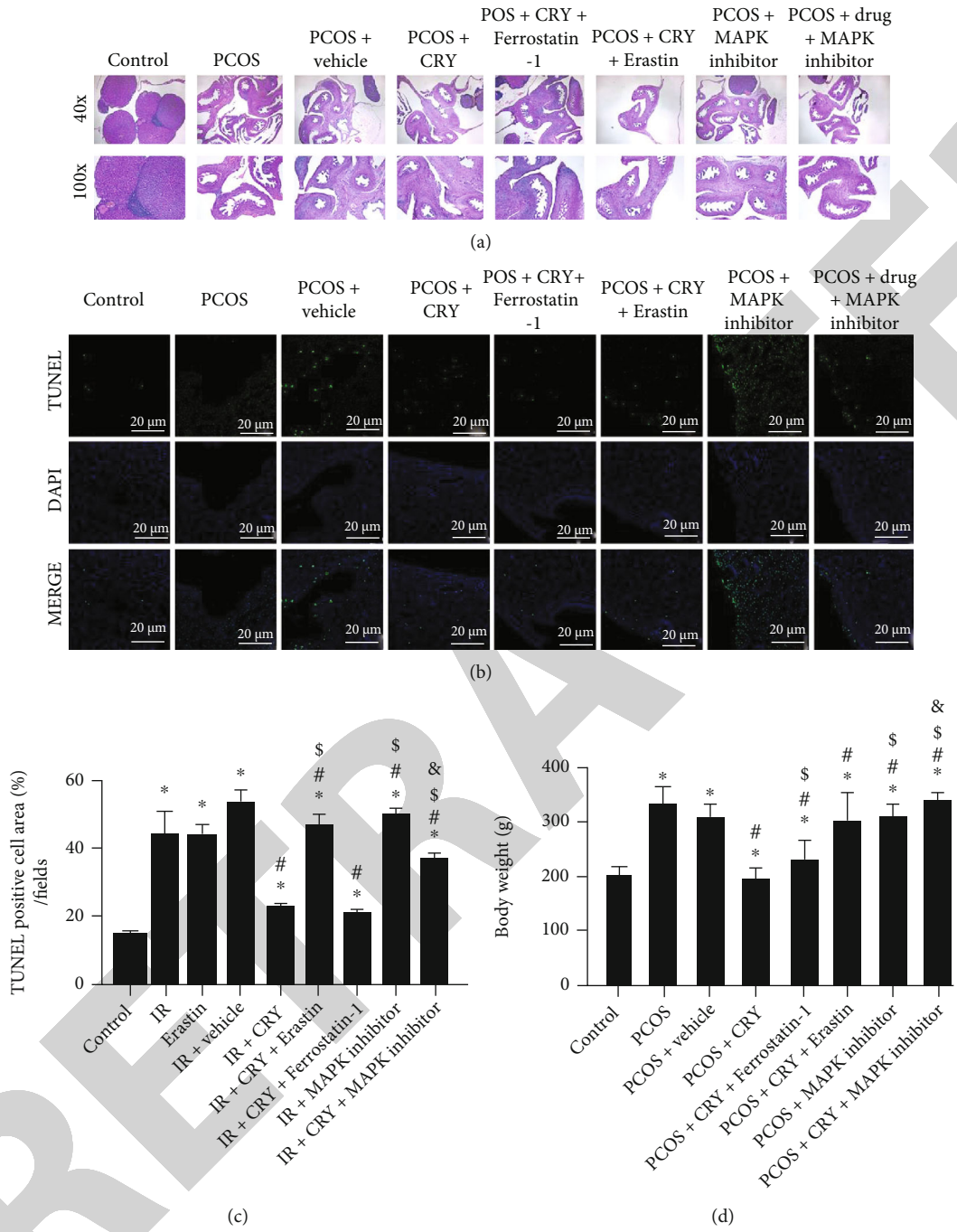


FIGURE 7: Continued.

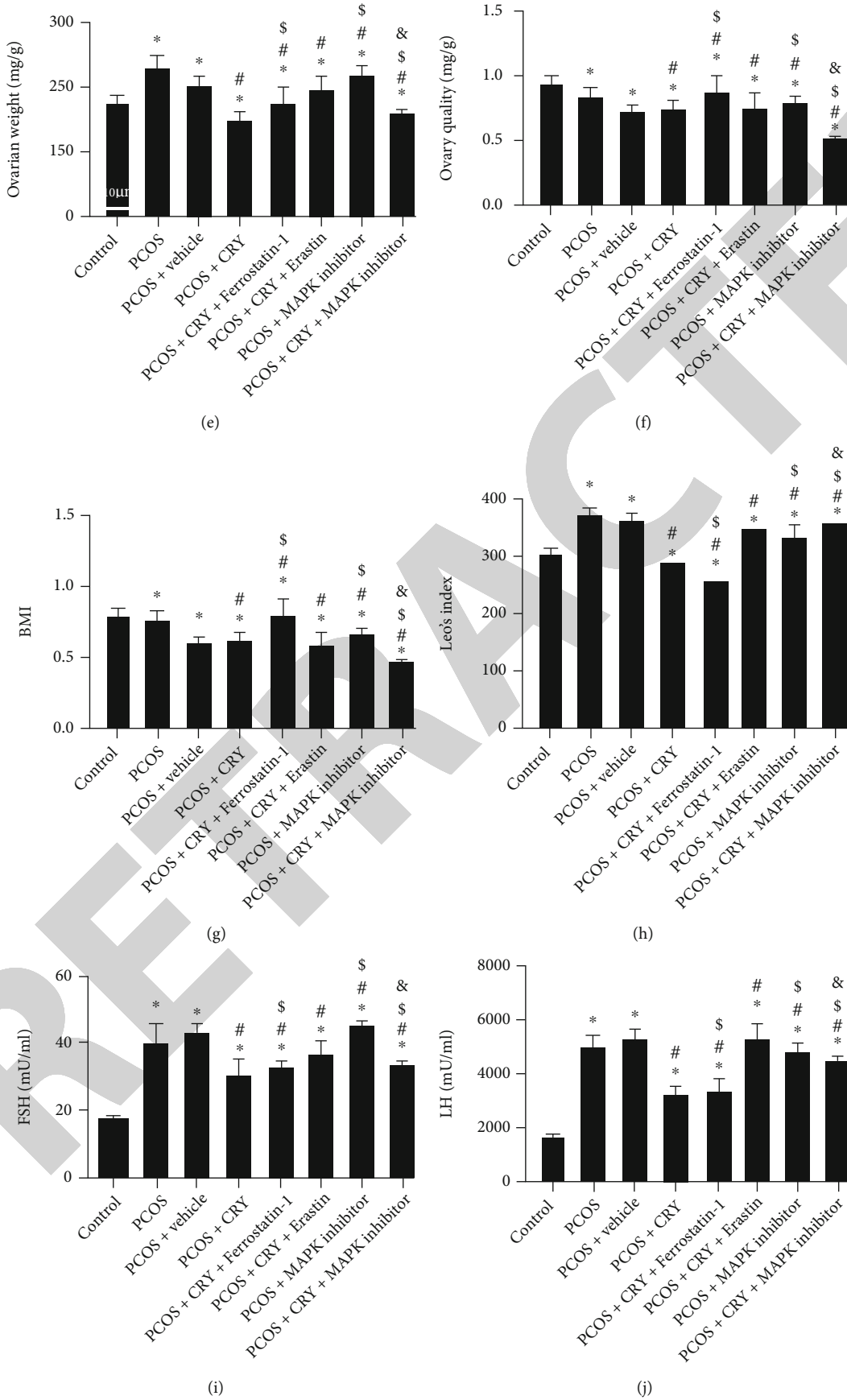


FIGURE 7: Continued.

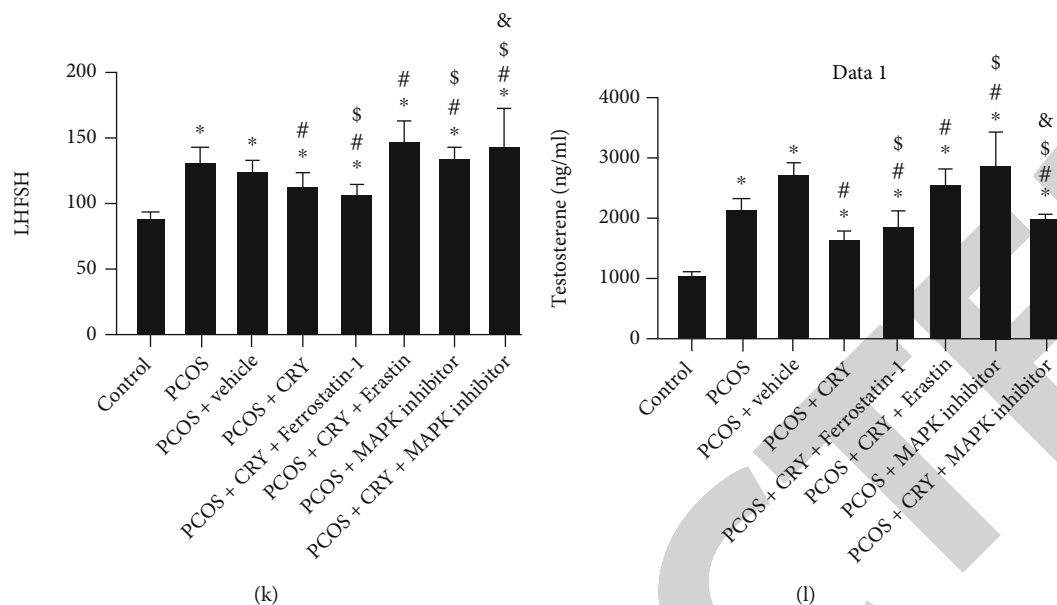


FIGURE 7: Cryptotanshinone protects against the deleterious effects underlying PCOS through inhibition of ferroptosis and activation of MAPK. (a) Histopathological analysis of ovary tissues obtained from different treatment groups. (b) TUNEL staining of ovary tissues obtained from different treatment groups. (c) Proportion of TUNEL-positive cells of ovary tissues obtained from different treatment groups. (d) Body weight of animals in different groups, (e) Ovarian weight from different groups. (f) Ovary quotiety in different groups. (g) Lee's index. (h) BMI of animals in different groups. (i) FSH level in different groups. (j) LH level in different groups. (k) LH/FSH ratio in different groups. (l) Testosterone level in different groups. * $p < 0.05$, compared to control; # $p < 0.05$ compared to IR; \$ $p < 0.05$ compared to IR+CRY; & $p < 0.05$ compared to IR+CRY+ferrostatin-1.

of intracellular ROS. The GCs from different treatment groups were incubated in the dark with DCFH-DA (10 mM) at 37°C. Next, after rinsing three times, the cells were observed with the Olympus BX51 fluorescence microscope (Tokyo, Japan) for the detection of intracellular ROS fluorescence.

2.12. Terminal Deoxynucleotidyl Transferase dUTP Nick-End Labeling (TUNEL) Assay. A TUNEL-specific antibody was used for the histochemical staining of 6 μm ovary sections. The sections were deparaffinized using Histo-Clear. Afterwards, following permeabilization in 0.3% Triton X-100, the DeadEnd™ Colorimetric TUNEL System (Promega, Madison, USA) was used for the detection of apoptosis in ovary tissues following the recommendations provided by the manufacturer. The Olympus IX81 microscope (Olympus America Inc., Center Valley, PA) was used for microscopic analysis, and green fluorescence was used for the identification of TUNEL-positive cells; counterstaining with the diamidino-2-phenylindole (DAPI) was used for the identification of nuclei.

2.13. RNA Extraction and RT-qPCR. RNA was extracted with the conventional method using the TRIzol extraction kit. The extracted RNA was retrotranscribed to cDNA using the GoScript™ Reverse Transcription System Kit (Promega Corporation) and following the protocols recorded therein. Amplification was done using the SYBR-Green PCR master mix platform supplied by Thermo Fisher Scientific, Inc. Thermal cycler settings were as follows: activation step at 50°C, denaturation at 95°C (30 seconds), 40 amplification

cycles (95°C, 5 seconds), and termination (60°C, 30 seconds). The sequences of the primers used in the reaction mixture were recorded in Table 1.

2.14. Western Blot. For the western blot experiment, proteins were first extracted from the samples using RIPA reagent (cat. no. ab7937; Abcam). The protein-containing lysates were centrifuged and then subjected to quantification using BCA reagent (cat. no. 23227; Thermo Fisher Scientific, Inc.). Next, an aliquot of 50 μg of protein was electrophoretically separated on 12% SDS-PAGE, followed by loading onto PVDF membranes and incubation in 25% skim milk for 120 min. The membranes were then contacted with solutions of primary antibodies directed against the indicated proteins. The antibodies used were PGC1a monoclonal antibody (1:5000, cat. no. 66369-1-Ig) from Proteintech, anti-NRF1 antibody (1:1000, cat. no. ab175932) from Abcam, GPX4 monoclonal antibody (1:1000, cat. no. 67763-1-Ig) from Proteintech, catalase monoclonal antibody (1:2000, cat. no. 66765-1-Ig) from Proteintech, ERK monoclonal antibody (1E5) (1:2000; MA5-15896) from Thermo Fisher, Phospho-p44/42 MAPK (Erk1/2) (Thr202/Tyr204) antibody #9101 (1:1000) from Cell Signaling Technology, anti-UCP2 antibody (1:1000, cat. no. sc-390189) from Santa Cruz, anti-Bax antibody (1:1000, cat. no. sc-7480) from Santa Cruz, BCL2 monoclonal antibody (1:2000, cat. no. 60178-1-Ig) from Proteintech, SOD1 monoclonal antibody (1:5000, cat. no. 67480-1-Ig) from Proteintech, Anti-NF- κB p65 antibody [E379] (1:1000, ab32536) from Abcam, p38 MAPK (D13E1) XP® Rabbit mAb #8690 (1:1000) from Cell Signaling, and anti-beta Actin antibody (1:1000, ab8227) from

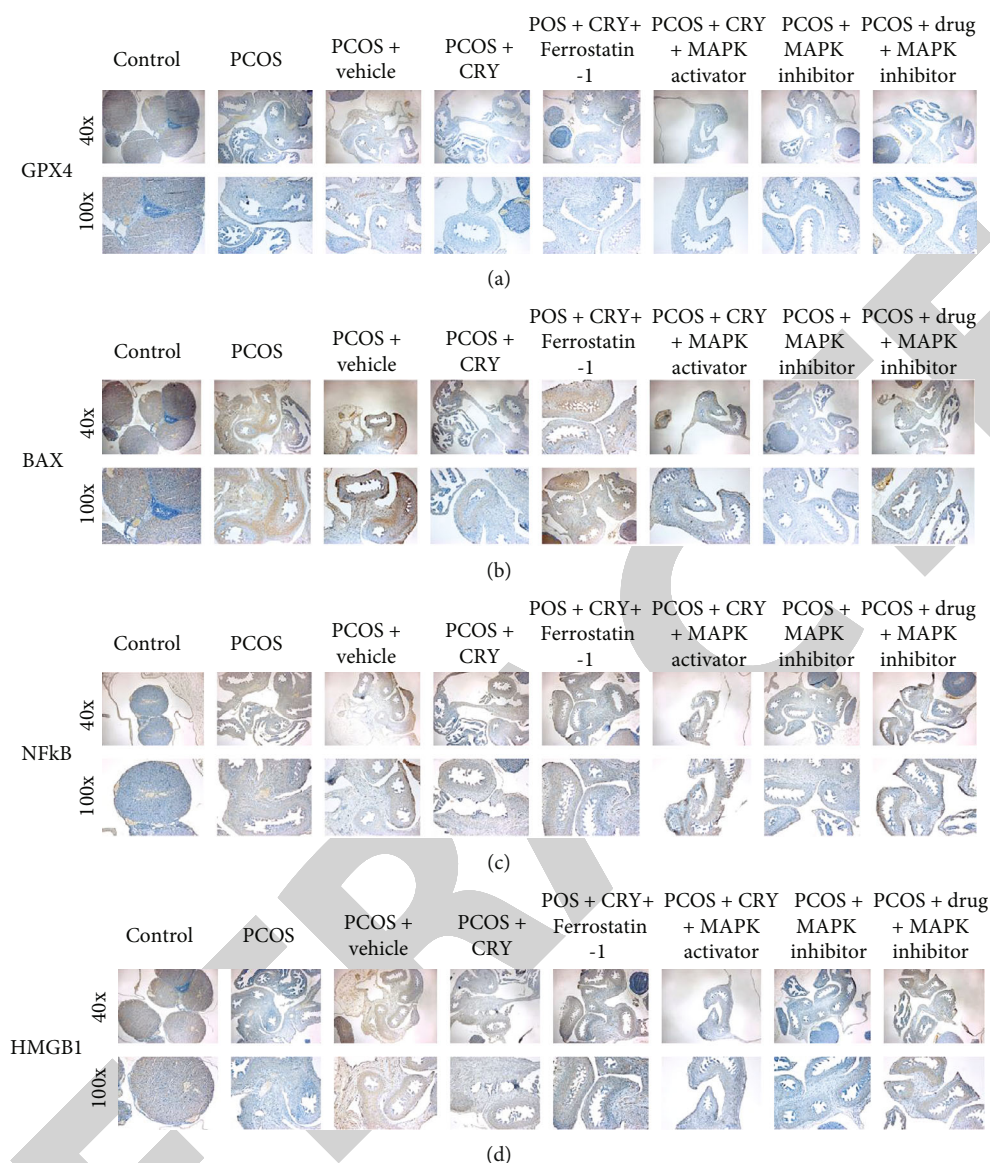


FIGURE 8: Immunohistochemistry analysis of proteins. (a) Immunohistochemistry analysis of GPX4 protein of ovary tissues obtained from different treatment groups. (b) Immunohistochemistry analysis of BAX protein of ovary tissues obtained from different treatment groups. (c) Immunohistochemistry analysis of NF- κ B protein of ovary tissues obtained from different treatment groups. (d) Immunohistochemistry analysis of HMGB1 protein of ovary tissues obtained from different treatment groups.

Abcam. After incubation, the membranes were washed three times with TBST and incubated with the HRP-coupled secondary antibody solutions (1:5000; cat. no. ab7097; Abcam) at 25°C for 60 min. The revelation of the signals corresponding to the immune complexes was performed using the ECL reagent (cat. no. WBKLS0050; EMD Millipore). Finally, ImageJ software (Image J, National Institutes of Health, Bethesda, MD) was used for densitometric analysis of the bands. The ImageJ results were then used to calculate the relative expression of the proteins with reference to the Actin protein.

2.15. Immunofluorescence Staining. For protein (GPX4, BAX, NF- κ B, and HMGB1) expression in cells, GCs were subjected to immunofluorescence. GCs from different treat-

ment groups were washed, and after fixing and incubation for blocking in 1% bovine serum albumin (BSA), GCs were incubated with primary antibodies (anti-GPX4, anti-BAX, anti-NF- κ B, and anti-HMGB1) at 4°C overnight. Then, the incubation with the secondary antibodies was performed in the dark for 1 h at 37°C. Finally, DAPI was used for counterstaining and examination under the Olympus BX51 fluorescence microscope.

2.16. Statistical Analysis. Data were expressed as mean \pm sd. For comparison between two, the *T*-test was used. For analyses involving more than two groups, the one-way ANOVA test was performed; for comparative analyses between different groups, the Bonferroni post hoc test was applied following the one-way ANOVA. All analyses and graphs were

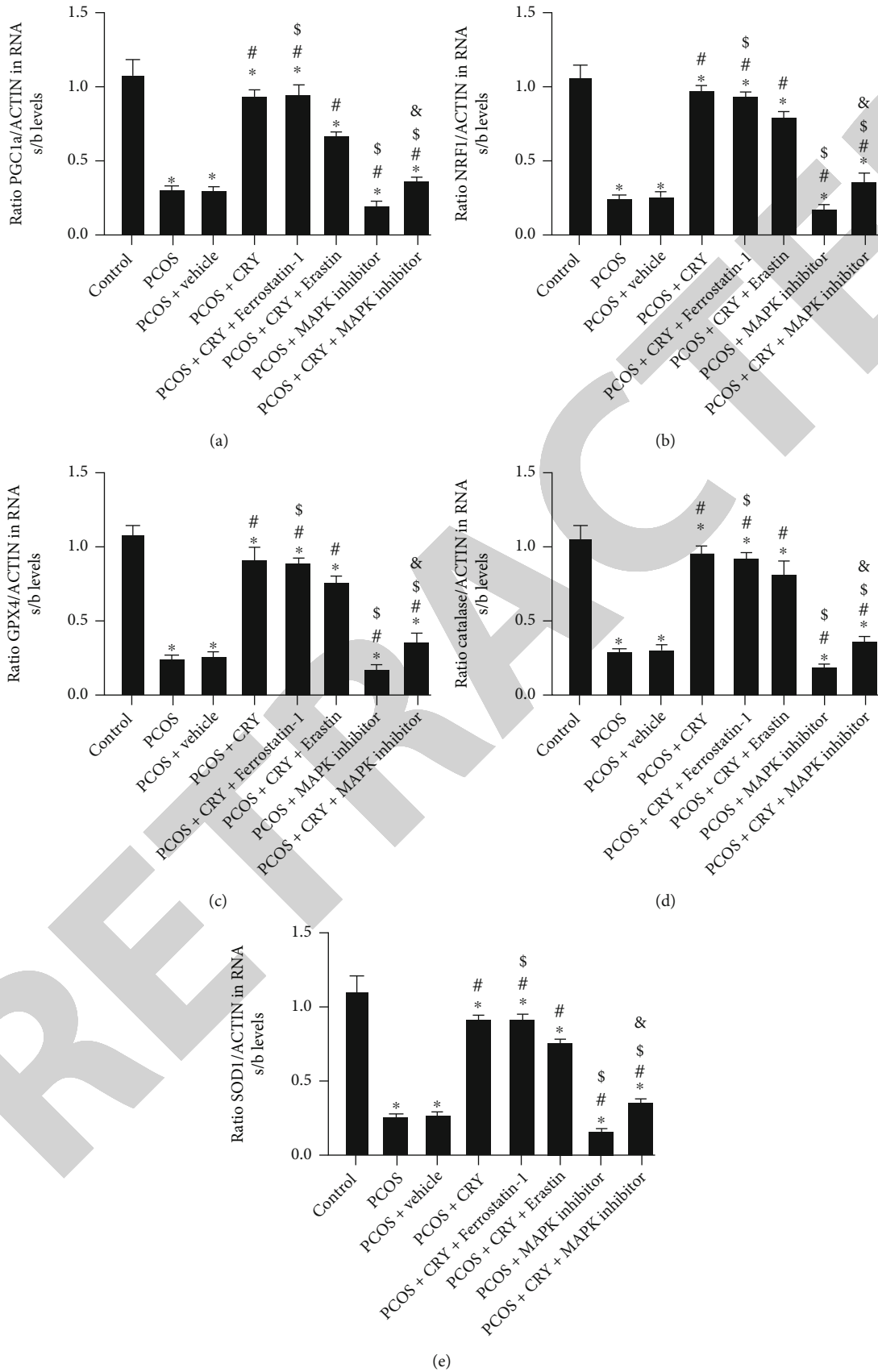


FIGURE 9: Continued.

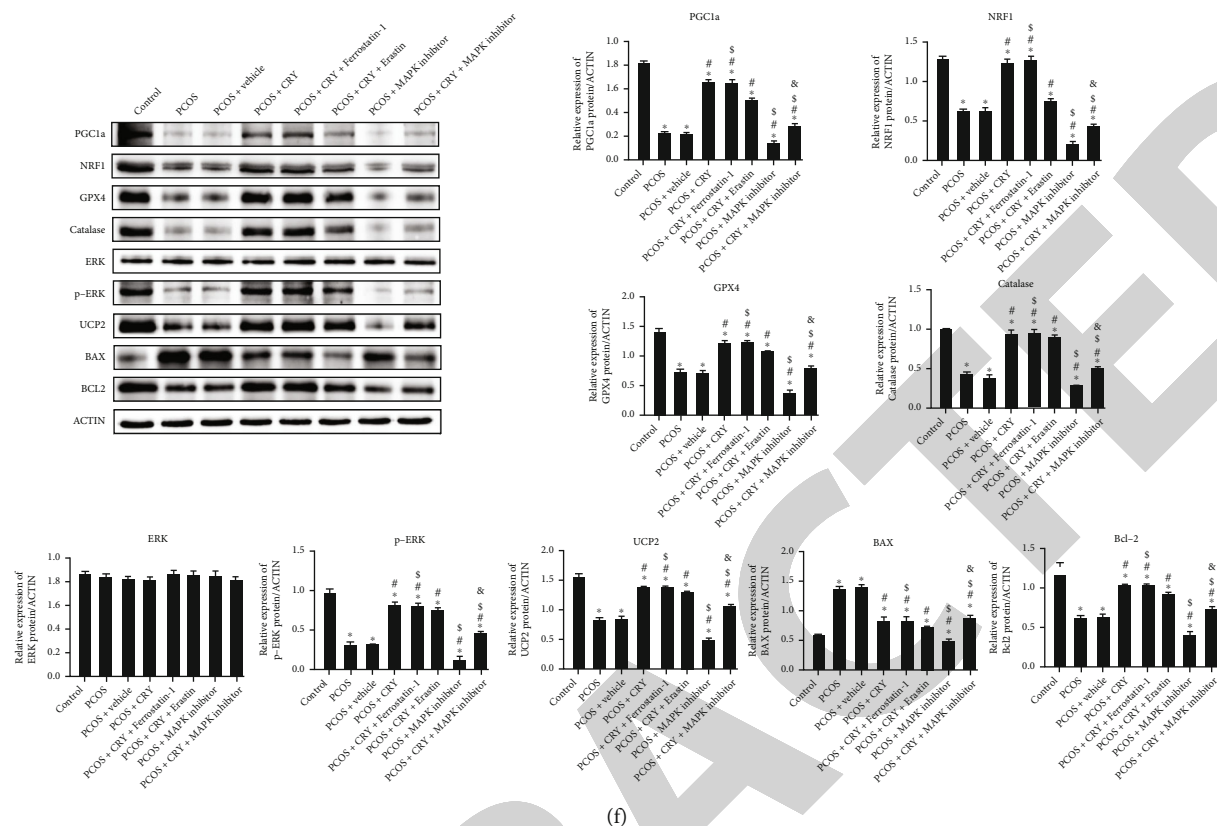


FIGURE 9: mRNA and protein expression regulated by cryptotanshinone in PCOS. (a) mRNA expression of PGC1a as determined by RT-qPCR. (b) mRNA expression of NRF1 as determined by RT-qPCR. (c) mRNA expression of GPX4 as determined by RT-qPCR. (d) mRNA expression of catalase gene as determined by RT-qPCR. (e) mRNA expression of SOD1 as determined by RT-qPCR. (f) Blot images and numeric quantification of protein expression of PGC1a, NRF1, GPX4, catalase, ERK, p-ERK, UCP2, BAX, and BCL2 as determined by western blotting. * $p < 0.05$, compared to control; # $p < 0.05$ compared to IR; \$ $p < 0.05$ compared to IR+CRY; & $p < 0.05$ compared to IR +CRY+ferrostatin-1.

produced with GraphPad Prism version 9 statistical software (GraphPad Software, Inc.).

3. Results

3.1. Ferroptosis Is Activated in Ovarian Granulosa Cells Subjected to Ischemia-Reperfusion. In order to investigate the probable involvement of ferroptosis in PCOS, we first treated granulosa cells with different ferroptosis inhibitors. The results showed that ferroptosis inhibitors had no cytotoxic effect on granulosa cells (Figure 1(a)). However, after ischemia-reperfusion, treatment of granulosa cells with the inhibitors showed different effects. Indeed, ischemia-reperfusion was followed by a remarkable decrease in cell viability (Figure 1(b)); but treatment with the different ferroptosis inhibitors was followed by a reversal of the effect of ischemia-reperfusion on cell viability. In addition, we found that the abrogation of the effect of ischemia-reperfusion was most pronounced after treatment with ferrostatin. Therefore, ferrostatin was selected as a ferroptosis inhibitor for further studies. These results indicated that ferroptosis activation may play a key role in the pathogenesis of PCOS.

3.2. CRY Inhibits Oxidative Stress by Regulating Ferroptosis via the MAPK Signaling Pathway. In order to elucidate the mechanism of action of CRY on the pathological processes involved in PCOS, we measured the effect of CRY on oxidative stress in the IR-induced PCOS model in vitro. The ultrastructural analysis indicated contracted mitochondria in the IR group and erastin groups while CRY and CRY+ferrostatin-1 treatment markedly improved the morphology of mitochondria (Figure 2(a)). In addition, the cotreatment of CRY with MAPK inhibitor or erastin significantly counteracted the effect of CRY on IR-induced cells (Figure 2(a)). The results also showed that IR and treatment with the ferroptosis stimulator, erastin, led to a decrease in cell viability (Figure 2(b)) and the activities of SOD (Figure 2(c)) and GSH-PX (Figure 2(d)). On the contrary, the level of MDA released in the PCOS model and in the erastin treatment group was increased compared to that in the control group (Figure 2(e)). Further study showed that ROS production was increased by PCOS or by erastin treatment (Figure 2(f)). In addition, we noted that treatment with CRY was followed by a reversal of the effects of erastin and PCOS on SOD, GSH-PX, MDA, and ROS (Figures 2(b)–2(f)). In addition, treatment with ferroptosis (ferrostatin) or MAPK inhibitor was followed by an effect similar to that of CRY.

However, cotreatment with CRY and the ferroptosis activator (erastin) on the one hand and CRY and the MAPK inhibitor on the other was followed by a significant abrogation of the effect of CRY on PCOS. These results indicated that CRY inhibits PCOS-induced oxidative stress by regulating ferroptosis via the MAKP signaling pathway.

3.3. CRY Inhibits Mitochondrial Membrane Potential through Regulation of Ferroptosis via the MAKP Signaling Pathway. In order to detect whether CRY regulates oxidative stress through modulation of mitochondrial dynamics, JC-1 staining was performed. As shown in Figures 3(a) and 3(b), a significant decrease in red fluorescence was remarkable in the PCOS and erastin groups, leading to a drop in the ratio of red to green fluorescence, compared to the control group. In contrast, treatment with CRY alone or together with ferrostatin counteracted this effect. However, cotreatment of CRY with erastin or the treatment MAPK inhibitor reversed the effect of CRY on the ratio of red to green fluorescence. These results suggested that CRY inhibits mitochondrial membrane potential through the regulation of ferroptosis via the MAKP pathway.

3.4. CRY Inhibits GPX4 Expression and Activates NF- κ B via the MAKP Signaling Pathway in the PCOS Cell Model. In order to detect whether CRY regulates GPX4 and inflammation in the pathogenic processes of PCOS, immunofluorescence of GPX4 and NF- κ B was performed. As shown in Figures 4(a) and 4(b), a significant decrease in GPX4 expression was observed in the PCOS and erastin groups while NF- κ B expression was significantly increased in both groups compared to the control group. On the contrary, CRY and ferrostatin reversed the effect of erastin and IR-induced PCOS. However, cotreatment of CRY with erastin or the MAPK inhibitor inhibited the effect of CRY on GPX4 and NF- κ B expression levels. These results suggest that CRY inhibits PCOS-induced inflammation via the regulation of ferroptosis via the MAKP signaling pathway (Figure 4(c)).

3.5. CRY Inhibits HMGB1 and BAX Expression via Inhibition of Ferroptosis in the IR-Induced PCOS Cell Model. Immunofluorescence of HMGB1 and BAX was performed. As shown in Figures 5(a) and 5(b), significant activation of HMGB1 and BAX expression was observed in the IR and erastin groups. In contrast, CRY alone or in combination with ferrostatin abrogated the effect of erastin and IR on HMGB1 and BAX. However, cotreatment of CRY with erastin or the MAPK inhibitor inhibited the effect of CRY on HMGB1 and BAX expression levels (Figure 5(c)). These results suggest that CRY inhibits IR-induced HMGB1 and BAX expression via the regulation of ferroptosis.

3.6. Effect of CRY on Gene and Protein Expression In Vitro. In order to further confirm the mode of action of CRY, we determined the effect of CRY on the expression of genes involved in various biological processes associated with PCOS pathogenesis. At the transcriptional level (Figures 6(a)–6(e)), RT-PCR results showed that compared to the control group, IR treatment was followed by an inhibition of the expression of PGC1 α , NRF1, GXP4, catalase, and SOD

genes. Similar results were recorded with the ferroptosis activator, erastin (Figures 6(a)–6(e)). Furthermore, after treatment with CRY alone or in combination with the ferroptosis inhibitor (ferrostatin-1), the transcriptional levels of these genes increased compared to the IR group (Figure 6(a)), indicating an abrogation of the effect of IR and the ferroptosis inhibitor on these genes. In addition, treatment with the MAPK inhibitor abrogated the effect of cryptotanshinone, indicating an important role for MAPK in the mode of action of CRY (Figures 6(a)–6(e)). At the protein expression level, western blot results showed that the expression levels of PGC1 α , NRF1, GXP4, catalase, SOD, p-ERK, UCP2, and Bcl2 were inhibited by treatment with IR and erastin but these inhibitory effects were reversed by treatment with cryptotanshinone alone or in combination with ferrostatin (Figure 6(f)). The effect of cryptotanshinone was also abrogated by treatment with the MAPK inhibitor (Figure 6(f)). A reverse trend was observed for Bax expression while no significant change was observed for ERK expression in the different groups (Figure 6(f)).

3.7. CRY Protects against the Deleterious Effects Underlying PCOS through Inhibition of Ferroptosis and Activation of MAPK. To verify the mode of action of CRY on PCOS in vivo, a rat model of PCOS was established. As shown in Figure 7(a), a regular structure of the rat ovary was observed in the control group, with numerous follicles (luteal, pre-antral, and antral) made of multiple layers with visible oocytes and corona radiata. In the PCOS and vehicle groups, microscopic examination showed cystic dilatation of the follicles with the presence of small layers of granulosa cells, the presence of corpora lutea, and lipid inclusions in the cytoplasm. However, treatment with CRY alone or with ferrostatin was followed by the presence of various follicles at different developmental stages and the presence of oocyte and corona in the mature follicles; corpora lutea growth and a regular layer of granulosa cells were also observed. The effect of CRY was abrogated by MAPK inhibitor.

In addition, we sought to verify the effect of cryptotanshinone and ferroptosis on cell apoptosis in vivo (Figures 7(b) and 7(c)). The TUNEL assay was used, and staining of ovarian tissue sections showed that in the PCOS model, cell apoptosis was increased compared to the control group. Treatments with vehicle led to similar results. However, treatments with CRY alone or in combination with ferrostatin led to a decrease in cell apoptosis. In addition, MAPK inhibitor increased the apoptosis rate in the PCOS model and reversed the effect of CRY on cell apoptosis.

In addition, the body weight (Figure 7(d)), ovarian weight (Figure 7(e)), and ovary quotiety (Figure 7(f)) were all increased in PCOS model but decreased by the treatment with CRY alone or in combination with ferrostatin. MAPK inhibitor reversed the effect of CRY on uterus body weight (Figure 7(d)), ovarian weight (Figure 7(e)), and ovary quotiety (Figure 7(f)). Moreover, hormonal tests indicated that Lee's index (Figure 7(g)) and BMI (Figure 7(h)) were all increased in the PCOS group but reversed by the treatment with CRY and CRY+ferrostatin-1; the effect of CRY was counteracted by the treatment with MAPK inhibitor. In

addition, hormonal tests indicated that FSH (Figure 7(i)), LH (Figure 7(j)), and LH/FSH (Figure 7(k)) ratio as well as the testosterone (Figure 7(l)) levels were all increased in the PCOS group but reversed by the treatment with CRY and CRY+ferrostatin-1; however, treatment with the MAPK inhibitor counteracted the effect of CRY.

Immunohistochemistry was used to check the expression of proteins such as GPX4, BAX, NF- κ B, and HMGB1. As shown in Figures 8(a) and 8(b), in the PCOS group and after treatments with erastin and MAPK inhibitor, a decrease in the expression of GPX4, BAX, NF- κ B, and HMGB1 was observed in ovarian tissues whereas treatment with CRY and ferrostatin-1 was followed by an abrogation of this effect characterized by an increase in cells staining positive for these proteins. Moreover, the effect of CRY was counteracted by the treatment with the MAPK inhibitor (Figures 8(c) and 8(d)).

In order to further confirm the mode of action of CRY *in vivo*, we determined the effect of CRY on the expression of genes involved in various biological processes associated with the pathogenesis of PCOS. At the transcriptional level (Figures 9(a)–9(e)), RT-PCR results showed that compared to the control group, an inhibition of the expression of PGC1 α , NRF1, GXP4, catalase, and SOD genes was observed in the PCOS group. Furthermore, after treatment with CRY or CRY+ferrostatin-1, the transcriptional levels of these genes increased compared to the PCOS group (Figures 9(a)–9(e)), indicating an abrogation of the effect of PCOS on these genes. In addition, treatment with the MAPK inhibitor abrogated the effect of CRY, indicating an important role for MAPK in the mode of action of CRY (Figures 9(a)–9(e)). At the protein expression level, western blot results showed that the expression levels of PGC1 α , NRF1, GXP4, catalase, SOD, p-ERK, UCP2, and Bcl2 were inhibited by treatment with PCOS and erastin but these inhibitory effects were reversed by treatment with CRY or CRY+ferrostatin-1 (Figure 9(f)). The effect of CRY was also abrogated by treatment with the MAPK inhibitor (Figure 9(f)). A reverse trend was observed for Bax expression while no significant change was observed for ERK expression in the different groups (Figure 9(f)).

4. Discussion

Recent studies have demonstrated the crucial importance of ferroptosis in various biological processes such as cancers and cardiovascular and neurodegenerative diseases [33, 35, 44–47]. Studies have also shown that ferroptosis could affect the therapeutic efficacy of various drugs in the treatment of these diseases by promoting drug resistance [48–50]. In one of our previous studies, we proved the efficacy of CRY in the treatment and prevention of PCOS [28]. Other researchers have also reported the efficacy of CRY in the treatment of various ovarian conditions, including PCOS [24–27]. In addition, some undetailed studies by other investigators have suggested that ferroptosis may play an important role in the pathogenesis of PCOS [51, 52]. Thus, in the present study, we proposed to investigate the role of ferroptosis in the mechanisms underlying PCOS and to verify

whether the mechanism of action of CRY could be mediated by its inhibitory action on ferroptosis. In this line, we conducted *in vitro* experiments by subjecting granulosa cells to ischemia-reperfusion and to treatments with CRY, inhibitors, and activators of ferroptosis and of the inhibitor of MAPK signaling pathway. Our results demonstrated *in vitro* and *in vivo* that ferroptosis was increased in cells subjected to IR *in vitro* and in the PCOS model *in vivo*. In addition, treatment with the ferroptosis activator and the MAPK inhibitor showed results with trends similar to the PCOS model. In contrast, treatments with CRY and the ferroptosis inhibitor were followed by a reversal of the effect observed in the PCOS model. In addition, the same trends were reported with respect to MMP, ROS, and expression of oxidative stress-related genes as well as apoptosis. These results indicate that the mechanism of action of CRY in the treatment of PCOS relies on its mediating effect on cellular ferroptosis. These results are of great value in the treatment and prevention of PCOS.

The results of the present study showed that ferroptosis levels were increased in granulosa cells subjected to IR and in the PCOS model *in vivo*. To date, specific studies investigating the role of ferroptosis in PCOS have not been reported. Only a few studies have reported the role of ferroptosis in ovarian cells or pathological conditions related to PCOS. An earlier study reported that uterine or placental ferroptosis can be modulated by insulin resistance and hyperandrogenism [51]. The sensitivity of clear cells found in the kidney and ovary to ferroptosis was also reported in another study which indicated that this sensitivity is based on the inhibition of GPX4 [52]. Proteomic analysis of CD4 + T cells from infertile PCOS patients showed that key proteins were involved in the ferroptosis pathway [50]. Differential gene expression analysis also demonstrated that crosstalk between autophagy, apoptosis, and ferroptosis is involved in the initiation of follicular atresia in pig ovaries [53]. Treatment of ovarian cells with the ferroptosis inhibitor reverses cellular cytotoxicity [54]. In view of the above, our study is the first of its kind to elucidate the involvement of ferroptosis in PCOS.

The effects of ferroptosis inhibitor and activator on MMP, ROS, and the expression of proteins involved in oxidative stress, inflammation, and apoptosis suggest that activation of ferroptosis in PCOS follows a deregulation of mitochondrial dynamics, promotion of inflammatory stimulation, and exacerbation of oxidative stress. These results corroborate those of a large body of literature showing an interconnection between ferroptosis and oxidative stress [55]. Furthermore, our results are consistent with other studies suggesting that oxidative stress is induced during the process of ferroptosis [56, 57]. Other studies have shown that during the regulation of ferroptosis, consequent changes occur at the mitochondrial level, including morphological changes, change in energy metabolism, change in iron metabolism, and change in lipid metabolism [58]; these results are in line with the results of the present study showing an effect of depolarization of MMPs by induction of ferroptosis. Our results are in line with those of other researchers also indicating that oxidative stress is induced

by free radicals released during ferroptosis [59]. In this context, oxidative stress is induced by mitochondrial ROS release [59], which is consistent with the results of the present study showing the induction of ROS production by the activator of ferroptosis. However, the present study could only demonstrate the role of ferroptosis on oxidative stress and mitochondrial dynamics. Further studies are needed to confirm the directionality of the regulation between ferroptosis and oxidative stress as this outcome is equivocal. Indeed, although the studies cited above have confirmed the trend of our results, other researchers have shown that oxidative stress is a positive regulator of ferroptosis. For example, it has been reported that induction of oxidative stress by arsenite leads to induction of ferroptosis [60]. It has also been shown that oxidative stress induces ferroptosis and mitochondrial dysfunction in the retinal pigment cells PC12 [38, 61, 62].

CRY is known to have therapeutic and prophylactic benefits in a variety of diseases including ovarian, colon, bladder, and lung cancers and pulmonary fibrosis [12, 63–66]. CRY has also been reported to be effective against ovarian disorders, including PCOS [28, 67]. In many diseases, studies have demonstrated the mode of action of CRY by assessing its effect on a number of biological processes and signaling pathways. However, no study has evaluated the effect of CRY on disease-associated ferroptosis, especially in PCOS. Our present study therefore has the merit of demonstrating that CRY inhibits cell death by ferroptosis in PCOS. These results are of paramount importance as ferroptosis is considered a promising pharmacological therapeutic target for various diseases. Inflammation also plays an important role in PCOS. Many studies have shown a stimulation of inflammation in PCOS. In our previous study, we demonstrated that CRY inhibits inflammation by inhibiting metabolic pathways involving the NF- κ B protein. These results were confirmed in the present study. In addition, numerous studies have shown that ferroptosis involves inflammatory pathways involving the inflammasome. Although we did not measure the effect of CRY on the inflammasome, the regulation of NF- κ B by CRY is an indication that activated cellular ferroptosis in PCOS may be the result of an inflammasome activation cascade. Further study involving the NLRP3 inflammasome may clarify this hypothesis in our future studies.

We also noticed that CRY inhibits the MAPK/ERK pathway via inhibition of ferroptosis. Many studies have shown the connection between ferroptosis and the MAPK/ERK signaling pathway. According to the results of these studies, in case of ferroptosis, the MAPK/ERK pathway is activated. The activation of MAPK/ERK is also induced by the production of ROS in the medium. Here, we also noticed that HMGB1 protein was also upregulated in the PCOS model but inhibited by treatment with CRY and the ferroptosis inhibitor. Previous studies have shown a regulatory link between HMGB1 and the MAPK/ERK pathway. Therefore, we deduce that CRY exerts its therapeutic effect on PCOS by inhibiting the HMGB1/MAPK/ERK pathway via the induction of ferroptosis. There are still some limitations that remain to be solved in this study. Although CRY can

decrease the expression of HMGB1 and NF- κ B in rats with PCOS, the underlying mechanism remains unclear. Besides, the protective effects of CRY on IR-induced ovarian granulosa cells were not confirmed through validation experiments other than cell viability detection. Still, cryptotanshinone may be a potential treatment option for polycystic ovary syndrome and the efficacy and safety of this mechanism need to be further studied.

5. Conclusions

In conclusion, the present study explored the mode of action of CRY on PCOS. The results demonstrate for the first time that ferroptosis is upregulated in PCOS and that the therapeutic or protective effect of CRY may be mediated by inhibition of this process which is a regulator of the HMGB1/MAPK/ERK pathway involved in the regulation of many pathological processes. This study provides a new perspective on understanding the pathogenesis of PCOS and offers hope in the search for therapeutic compounds for PCOS.

Abbreviations

PCOS:	Polycystic ovary syndrome
CRY:	Cryptotanshinone
ROS:	Reactive oxygen species
IR:	Ischemia-reperfusion
MMP:	Mitochondrial membrane potential
LH:	Luteinizing hormone
FSH:	Follicle-stimulating hormone.

Data Availability

All data generated or analyzed during this study are included in this published article.

Ethical Approval

The rats used in this study were commercially acquired from Shanghai Laboratory Animal Center, Co. Ltd. The experimental protocols were in accordance with the standards of the Chinese Ministry of Science and Technology for the Care and Use of Laboratory Animals after approval by the Animal Care and Experiment Review Board of Shanghai Traditional Chinese Medicine Hospital (Shanghai, China) (approval no. 20190103).

Conflicts of Interest

The authors declare that they have no competing interests.

Authors' Contributions

Honglin Liu, Jiani Xie, Jianhua Zhou, Yue Xia and Xia Peng contributed to the writing of the manuscript and data analysis. Xiaorong Ni and Limin Fan supervised the work and designed the study. All the authors have read and agreed to the final version to be published. Honglin Liu and Jiani Xie contributed equally to this work and share first authorship.

Acknowledgments

This work was supported by the National Youth Science and National Natural Science Foundation of China (grant number 81804136).

References

- [1] S. Susan and P. Kirsten, "Epidemiology, diagnosis, and management of polycystic ovary syndrome," *Clinical Epidemiology*, vol. 2013, pp. 1–13, 2013.
- [2] A. Pa, A. Bct, and B. Rpk, "Polycystic ovarian syndrome (PCOS): long-term metabolic consequences," *Long-term metabolic consequences*, vol. 86, pp. 33–43, 2018.
- [3] V. Cappelli, M. C. Musacchio, A. Bulfoni, G. Morgante, and V. D. Leo, "Natural molecules for the therapy of hyperandrogenism and metabolic disorders in PCOS," *European Review for Medical & Pharmacological Sciences*, vol. 21, pp. 15–29, 2017.
- [4] H. F. Escobar-Morreale, "Polycystic ovary syndrome: definition, aetiology, diagnosis and treatment," *Nature Reviews Endocrinology*, vol. 14, no. 5, pp. 270–284, 2018.
- [5] G. Morgante, M. G. Massaro, A. Di Sabatino, V. Cappelli, and V. De Leo, "Therapeutic approach for metabolic disorders and infertility in women with PCOS," *Gynecological Endocrinology*, vol. 34, no. 1, pp. 4–9, 2018.
- [6] W. Beata, Z.-K. Agnieszka, and N.-B. Julita, "Metabolic disorders in polycystic ovary syndrome," *Pediatric Endocrinology, Diabetes, and Metabolism*, vol. 23, no. 4, pp. 204–208, 2017.
- [7] J. P. Christ and T. Falcone, "Bariatric surgery improves hyperandrogenism, menstrual irregularities, and metabolic dysfunction among women with polycystic ovary syndrome (PCOS)," *Obesity Surgery*, vol. 28, no. 8, pp. 2171–2177, 2018.
- [8] A. L. Marca, A. C. Artensio, G. Stabile, and A. Volpe, "Metformin treatment of PCOS during adolescence and the reproductive period," *European Journal of Obstetrics & Gynecology & Reproductive Biology*, vol. 121, no. 1, pp. 3–7, 2005.
- [9] V. Tagliaferri, D. Romualdi, E. Scarinci et al., "Melatonin treatment may be able to restore menstrual cyclicity in women with PCOS: a pilot study," *Reproductive Sciences*, vol. 25, pp. 269–275, 2018.
- [10] M. F. Costello, M. L. Misso, A. Balen, J. Boyle, and H. J. Teede, "A brief update on the evidence supporting the treatment of infertility in polycystic ovary syndrome," *Australian and New Zealand Journal of Obstetrics and Gynaecology*, vol. 59, no. 6, pp. 867–873, 2019.
- [11] T. Tanbo, J. Mellembakken, S. Bjercke, E. Ring, T. Åbyholm, and P. Fedorcsak, "Ovulation induction strategies in polycystic ovary syndrome," *Acta Obstetrica et Gynecologica Scandinavica*, vol. 98, pp. 1162–1167, 2018.
- [12] Y. H. Wu, Y. R. Wu, B. Li, and Z. Y. Yan, "Cryptotanshinone: a review of its pharmacology activities and molecular mechanisms," *Fitoterapia*, vol. 145, article 104633, 2020.
- [13] S. Huang, G. Chen, Y. Lu, and W. Chen, "Molecular evidence of cryptotanshinone for treatment and prevention of human cancer," *Anti-Cancer Agents in Medicinal Chemistry Formerly Current Medicinal Chemistry-Anti-Cancer Agents*, vol. 13, no. 7, pp. 979–987, 2013.
- [14] S. H. Lo, C. T. Hsu, H. S. Niu, C. S. Niu, J. T. Cheng, and Z. C. Chen, "Cryptotanshinone inhibits STAT3 signaling to alleviate cardiac fibrosis in type 1-like diabetic rats," *Phytotherapy Research*, vol. 31, no. 4, pp. 638–646, 2017.
- [15] S. Ma, D. Yang, K. Wang, B. Tang, D. Li, and Y. Yang, "Cryptotanshinone attenuates isoprenaline-induced cardiac fibrosis in mice associated with upregulation and activation of matrix metalloproteinase-2," *Molecular Medicine Reports*, vol. 6, pp. 145–150, 2012.
- [16] A. Nagappan, J. H. Kim, D. Y. Jung, and M. H. Jung, "Cryptotanshinone from the *Salvia miltiorrhiza* Bunge attenuates ethanol-induced liver injury by activation of AMPK/SIRT1 and Nrf2 signaling pathways," *International Journal of Molecular Sciences*, vol. 21, no. 1, p. 265, 2020.
- [17] M. Song, L. Chen, L. Zhang, C. Li, and H. Wang, "Cryptotanshinone enhances wound healing in type 2 diabetes with modulatory effects on inflammation, angiogenesis and extracellular matrix remodelling," *Pharmaceutical Biology*, vol. 58, no. 1, pp. 845–853, 2020.
- [18] N. Wang, X. Dong, D. Shi, N. Li, and Q. Zhang, "Cryptotanshinone ameliorates placental oxidative stress and inflammation in mice with gestational diabetes mellitus," *Archives of Pharmacological Research*, vol. 43, no. 7, pp. 755–764, 2020.
- [19] W. Wang, P. H. Zhou, W. Hu et al., "Cryptotanshinone hinders renal fibrosis and epithelial transdifferentiation in obstructive nephropathy by inhibiting TGF- β 1/Smad3/integrin β 1 signal," *Oncotarget*, vol. 9, no. 42, pp. 26625–26637, 2018.
- [20] X. Y. Yu, S. G. Lin, X. Chen et al., "Transport of cryptotanshinone, a major active triterpenoid in *Salvia miltiorrhiza* Bunge widely used in the treatment of stroke and Alzheimer's disease, across the blood-brain barrier," *Current Drug Metabolism*, vol. 8, no. 4, pp. 365–377, 2007.
- [21] Q. Zhang, C. Gan, H. Liu, L. Wang, and T. Ye, "Cryptotanshinone reverses the epithelial-mesenchymal transformation process and attenuates bleomycin-induced pulmonary fibrosis," *Phytotherapy Research*, vol. 34, no. 10, pp. 2685–2696, 2020.
- [22] Y. Zhang, W. Lu, X. Zhang, J. Lu, and P. Liu, "Cryptotanshinone protects against pulmonary fibrosis through inhibiting Smad and STAT3 signaling pathways," *Pharmacological Research*, vol. 147, article 104307, 2019.
- [23] Y. Zhang, F. Luo, H. Zhang, W. He, and G. Shi, "Cryptotanshinone ameliorates cardiac injury and cardiomyocyte apoptosis in rats with coronary microembolization," *Drug Development Research*, vol. 82, pp. 581–588, 2021.
- [24] Y. Huang, W. Li, C. C. Wang, X. Wu, and J. Zheng, "Cryptotanshinone reverses ovarian insulin resistance in mice through activation of insulin signaling and the regulation of glucose transporters and hormone synthesizing enzymes," *Fertility & Sterility*, vol. 102, no. 2, pp. 589–596, 2014.
- [25] Y. Xia, P. Zhao, H. Huang, Y. Xie, and L. Dong, "Cryptotanshinone reverses reproductive disturbances in rats with dehydroepiandrosterone-induced polycystic ovary syndrome," *American Journal of Translational Research*, vol. 9, no. 5, pp. 2447–2456, 2017.
- [26] X. Yang, Y. Zhang, X. Wu et al., "Cryptotanshinone reverses reproductive and metabolic disturbances in prenatally androgenized rats via regulation of ovarian signaling mechanisms and androgen synthesis," *American Journal of Physiology. Regulatory, Integrative and Comparative Physiology*, vol. 300, no. 4, pp. R869–R875, 2011.
- [27] J. Yu, D. Zhai, L. Hao et al., "Cryptotanshinone reverses reproductive and metabolic disturbances in PCOS model rats via regulating the expression of CYP17 and AR," *Evidence-Based*

- Complementary and Alternative Medicine*, vol. 2014, article 670743, pp. 1–10, 2014.
- [28] Y. Yang, L. Yang, C. Qi, G. Hu, and X. Ni, "Cryptotanshinone alleviates polycystic ovary syndrome in rats by regulating the HMGB1/TLR4/NF- κ B signaling pathway," *Molecular Medicine Reports*, vol. 22, no. 5, pp. 3851–3861, 2020.
- [29] M. M. Capelletti, H. Manceau, H. Puy, and K. Peoc'H, "Ferroptosis in liver diseases: an overview," *International Journal of Molecular Sciences*, vol. 21, no. 14, p. 4908, 2020.
- [30] J. Li, F. Cao, H. L. Yin, Z. J. Huang, and G. Wang, "Ferroptosis: past, present and future," *Cell Death & Disease*, vol. 11, no. 2, p. 88, 2020.
- [31] Y. Mou, J. Wang, J. Wu et al., "Ferroptosis, a new form of cell death: opportunities and challenges in cancer," *Journal of Hematology & Oncology*, vol. 34, 2019.
- [32] X. Song and D. Long, "Nrf2 and ferroptosis: a new research direction for neurodegenerative diseases," *Frontiers in Neuroscience*, vol. 14, p. 267, 2020.
- [33] B. R. Stockwell, X. Jiang, and W. Gu, "Emerging mechanisms and disease relevance of ferroptosis," *Trends in Cell Biology*, vol. 30, no. 6, pp. 478–490, 2020.
- [34] S. Tang and X. Xiao, "Ferroptosis and kidney diseases," *International Urology and Nephrology*, vol. 52, pp. 497–503, 2020.
- [35] A. Weiland, Y. Wang, W. Wu et al., "Ferroptosis and its role in diverse brain diseases," *Molecular Neurobiology*, vol. 56, no. 7, pp. 4880–4893, 2019.
- [36] H. Yu, P. Guo, X. Xie, Y. Wang, and G. Chen, "Ferroptosis, a new form of cell death, and its relationships with tumorous diseases," *Journal of Cellular & Molecular Medicine*, vol. 21, no. 4, pp. 648–657, 2017.
- [37] N. Sumneang, N. Siri-Angkul, S. Kumfu, S. C. Chattapakorn, and N. Chattapakorn, "The effects of iron overload on mitochondrial function, mitochondrial dynamics, and ferroptosis in cardiomyocytes," *Archives of Biochemistry and Biophysics*, vol. 680, article 108241, 2020.
- [38] C. Wu, W. Zhao, J. Yu, S. Li, and X. Chen, "Induction of ferroptosis and mitochondrial dysfunction by oxidative stress in PC12 cells," *Scientific Reports*, vol. 8, no. 1, p. 574, 2018.
- [39] J. Zhu, Y. Xiong, Y. Zhang, J. Wen, and W. Zhang, "The molecular mechanisms of regulating oxidative stress-induced ferroptosis and therapeutic strategy in tumors," *Oxidative Medicine and Cellular Longevity*, vol. 2020, 14 pages, 2020.
- [40] X. Li, W. Li, P. Yang, H. Zhou, and L. Ma, "Anticancer effects of cryptotanshinone against lung cancer cells through ferroptosis," *Arabian Journal of Chemistry*, vol. 14, no. 6, article 103177, 2021.
- [41] J. L. Liu, L. Tong, Y. Luo, and Y. J. Gao, "Cryptotanshinone may induce ferroptosis of human liver cancer HepG2 cells," *Acta Academiae Medicinae Sinicae*, vol. 43, no. 3, pp. 366–370, 2021.
- [42] M. He, C. Tu, Q. Huang, P. Li, and W. Peng, "Approach on exerting Lee's index to evaluate the obese degree of mature rats," *Chinese Journal of Clinical Pharmacology and Therapeutics*, vol. 177, 1997.
- [43] M. Garrouste-Orgeas, G. Troché, E. Azoulay et al., "Body mass index," *Intensive Care Medicine*, vol. 30, no. 3, pp. 437–443, 2004.
- [44] L. Mahoney-Sánchez, H. Bouchaoui, S. Ayton, D. Devos, and J. C. Devedjian, "Ferroptosis and its potential role in the pathophysiology of Parkinson's disease," *Progress in Neurobiology*, vol. 196, article 101890, 2021.
- [45] D. Martin-Sanchez, M. Fontecha-Barriuso, J. M. Martinez-Moreno et al., "Ferroptosis y nefropatia," *Nefrología English Edition*, vol. 40, no. 4, pp. 384–394, 2020.
- [46] N. Yan and J. J. Zhang, "Iron metabolism, ferroptosis, and the links with Alzheimer's disease," *Frontiers in Neuroscience*, vol. 13, pp. 1443–1443, 2020.
- [47] S. M. Elgendy, S. K. Alyammahi, D. W. Alhamad, S. M. Abdin, and H. A. Omar, "Ferroptosis: an emerging approach for targeting cancer stem cells and drug resistance," *Critical Reviews in Oncology/Hematology*, vol. 155, article 103095, 2020.
- [48] J. Angeli, D. V. Krysko, and M. Conrad, "Ferroptosis at the crossroads of cancer-acquired drug resistance and immune evasion," *Nature Reviews Cancer*, vol. 19, no. 7, pp. 405–414, 2019.
- [49] H. Zhang, T. Deng, R. Liu, T. Ning, and Y. Ba, "CAF secreted miR-522 suppresses ferroptosis and promotes acquired chemo-resistance in gastric cancer," *Molecular Cancer*, vol. 19, no. 1, 2020.
- [50] Y. Zhang, M. Hu, W. Jia, G. Liu, and H. Billig, "Hyperandrogenism and insulin resistance modulate gravid uterine and placental ferroptosis in PCOS-like rats," *Journal of Endocrinology*, vol. 246, pp. 247–263, 2020.
- [51] F. Nasri, M. Zare, M. Doroudchi, and B. Ghareasi-Fard, "Proteome analysis of CD4+ t cells reveals differentially expressed proteins in infertile polycystic ovary syndrome patients," *Endocrine, Metabolic & Immune Disorders-Drug Targets Formerly Current Drug Targets-Immune, Endocrine & Metabolic Disorders*, vol. 21, 2021.
- [52] Y. Zou, M. J. Palte, A. A. Deik, H. Li, and S. L. Schreiber, "A GPX4-dependent cancer cell state underlies the clear-cell morphology and confers sensitivity to ferroptosis," *Nature Communications*, vol. 10, no. 1, p. 1617, 2019.
- [53] J. Zhang, Y. Liu, W. Yao, Q. Li, H. L. Liu, and Z. Pan, "Initiation of follicular atresia: gene networks during early atresia in pig ovaries," *Reproduction*, vol. 156, 2018.
- [54] A. L. Greenshields, T. G. Shepherd, and D. W. Hoskin, "Contribution of reactive oxygen species to ovarian cancer cell growth arrest and killing by the anti-malarial drug artesunate," *Molecular Carcinogenesis*, vol. 56, no. 1, pp. 75–93, 2017.
- [55] D. Galaris, A. Barbouti, and K. Pantopoulos, "Iron homeostasis and oxidative stress: an intimate relationship," *Cell Research*, vol. 1866, no. 12, article 118535, 2019.
- [56] W. Qi, Z. Li, L. Xia, J. Dai, and S. Xu, "LncRNA GABPB1-AS1 and GABPB1 regulate oxidative stress during erastin-induced ferroptosis in HepG2 hepatocellular carcinoma cells," *Scientific Reports*, vol. 9, no. 1, p. 16185, 2019.
- [57] L.-J. Su, J.-H. Zhang, H. Gomez et al., "Reactive oxygen species-induced lipid peroxidation in apoptosis, autophagy, and ferroptosis," *Oxidative Medicine and Cellular Longevity*, vol. 2019, Article ID 5080843, 13 pages, 2019.
- [58] H. Wang, C. Liu, Y. Zhao, and G. Gao, "Mitochondria regulation in ferroptosis," *European Journal of Cell Biology*, vol. 99, article 151058, 2020.
- [59] F. Kuang, J. Liu, D. Tang, and R. Kang, "Oxidative damage and antioxidant defense in ferroptosis," *Frontiers in Cell and Developmental Biology*, vol. 8, 2020.
- [60] M. A. Pan, A. Sz, B. Xj et al., "Arsenite induces testicular oxidative stress *in vivo* and *in vitro* leading to ferroptosis," *Ecotoxicology and Environmental Safety*, vol. 194, p. 110360, 2020.
- [61] S. Yun, Z. Yingfeng, W. Chunxiao, and L. Yizhi, "Glutathione depletion induces ferroptosis, autophagy, and premature cell

Research Article

Nauclea orientalis (L.) Bark Extract Protects Rat Cardiomyocytes from Doxorubicin-Induced Oxidative Stress, Inflammation, Apoptosis, and DNA Fragmentation

Jayasinghe A. N. Sandamali ¹, Ruwani P. Hewawasam ², Kamani A. P. W. Jayatilaka ², and Lakmini K. B. Mudduwa ³

¹Department of Medical Laboratory Science, Faculty of Allied Health Sciences, University of Ruhuna, 80000, Sri Lanka

²Department of Biochemistry, Faculty of Medicine, University of Ruhuna, 80000, Sri Lanka

³Department of Pathology, Faculty of Medicine, University of Ruhuna, 80000, Sri Lanka

Correspondence should be addressed to Ruwani P. Hewawasam; ruwaniph@yahoo.com

Received 31 October 2021; Revised 22 January 2022; Accepted 27 January 2022; Published 14 February 2022

Academic Editor: Ana Lloret

Copyright © 2022 Jayasinghe A. N. Sandamali et al. This is an open access article distributed under the Creative Commons Attribution License, which permits unrestricted use, distribution, and reproduction in any medium, provided the original work is properly cited.

The therapeutic efficacy of anthracycline antibiotic, doxorubicin (Dox), is hampered due to the dose-dependent cardiotoxicity. The objective of the study was to explore the counteraction of aqueous bark extract of *Nauclea orientalis* in Dox-induced cardiotoxicity in Wistar rats. The acute and subchronic toxicity study performed with 2.0 g/kg of the plant extract revealed biochemical and haematological parameters to be within the physiological range, and no histological alterations were observed in any organs isolated. Screening of plant extract for the protection of the myocardium from Dox-induced oxidative stress, inflammation, and apoptosis was performed on five groups of rats: control, plant extract control, Dox control (distilled water (D.H₂O) 2 weeks + on the 11th day single injection of Dox, 18 mg/kg), plant + Dox (2.0 g/kg plant extract 2 weeks + on the 11th day Dox, 18 mg/kg), and positive control, dexrazoxane. A significant increase in cardiac biomarkers and lipid peroxidation ($p < 0.001$) and a significant decrease in antioxidant parameters ($p < 0.001$) were observed in the Dox control group. All these parameters were reversed significantly ($p < 0.05$) in the plant-pretreated group. The histopathological assessment of myocardial damage provided supportive evidence for the biochemical results obtained. Inflammatory markers, myeloperoxidase, expression of TNF α and caspase-3, and DNA fragmentation (TUNEL positive nuclei) were significantly elevated ($p < 0.05$), and expression of Bcl-2 was significantly decreased ($p < 0.05$) in the Dox control; however, all these parameters were significantly reversed in the plant extract-treated group. In conclusion, the aqueous bark extract of *Nauclea orientalis* (2.0 g/kg) has the ability to attenuate the Dox-induced oxidative stress, inflammation, apoptosis, and DNA fragmentation in Wistar rats.

1. Introduction

Doxorubicin (Dox), the anthracycline antibiotic, is a widely accepted chemotherapeutic agent in the treatment of diverse malignancies [1]. Unfortunately, its long-term usage is restricted by the multiorgan toxicity including severe cardiotoxicity [2]. Dox-induced dose-dependent cardiotoxicity could be manifested by various changes within the heart like cardiac arrhythmias, electrocardiographic alterations, permanent degenerative cardiomyopathy, and

congestive heart failure [3]. Several molecular mechanisms have been identified in the pathogenesis of acute and chronic Dox-induced cardiotoxicity including oxidative stress, altered iron metabolism, dysregulation in calcium homeostasis, structural alterations in sarcomeres, modulation of gene expression, and apoptosis [4]. However, one of the foremost important mechanisms is the oxidative stress caused by the generation of free radicals which subsequently cause the lipid peroxidation, reduction of sulfhydryl groups, and depletion of antioxidant enzymes [3].

Additionally, inflammation, apoptosis, and impairment of DNA arise in the myocardium.

The main reason for oxidative stress caused by Dox is the imbalance between reactive oxygen species and the endogenous antioxidant defence system [4]. Radical formation in Dox-induced cardiotoxicity occurs by two main pathways: a nonenzymatic pathway via iron and an enzymatic pathway via mitochondrial respiratory chain [5]. Dox is converted to a Dox semiquinone form by reduced flavoenzymes such as nicotinamide adenine dinucleotide phosphate hydrogen- (NADPH-) cytochrome P450 reductase [5, 6]. This reduced form is in a position to make a complex with iron (Fe^{2+}) which has the ability to impulsively reduce molecular oxygen to superoxide. In the enzymatic pathway, free oxygen radicals are also produced when Dox gets reduced at complex I of the electron transport chain by accepting electrons from nicotinamide adenine dinucleotide (NADH) or NADPH [5]. The redox cycling that happens might also be very harmful since a small amount of Dox was found to be adequate for the formation of the large amount of superoxide radicals. As Dox has high affinity to cardiolipin, Dox enters the mitochondria and suppresses respiratory chain by binding to cardiolipin, which is identified as a cardiac-specific, polyunsaturated fatty acid-rich phospholipid found within the mitochondrial internal membrane [5, 7]. Dox is also capable of reducing the action of cardiac enzymes like glutathione S-transferase, superoxide dismutase (SOD), and catalase. Moreover, the myocardial tissues are more vulnerable to be injured by Dox-induced free radicals because the antioxidants available in the heart tissues are low in comparison to other organs [7].

Furthermore, generation of ROS results in activation of the mitochondria-mediated apoptotic signalling pathway which consequently activates caspase-3-mediated intrinsic cardiomyocyte apoptosis [8]. In addition to the activation of extrinsic apoptotic pathway, death ligands like tumour necrosis factor α ($\text{TNF}\alpha$) also contribute to the apoptosis in cardiomyocytes.

As Dox remains a highly effective anticancer drug for various malignancies, several therapeutic approaches are tested to scale back the occurrence of cardiotoxicity including the administration of defensive agents like antioxidants, iron chelators, and radical scavengers [4]. *Nauclea orientalis* (L.) L. that belongs to the family Rubiaceae is a useful medicinal plant which has a high antioxidant effect. Consistent with previous reports, the root and the bark of this plant contain constituents such as β -sitosterol and phenolic substances which play a crucial role in scavenging free radicals in addition to the metal chelating and anticarcinogenic properties [9]. A study led by Daoa et al. has also revealed that the bark of *Nauclea orientalis* (L.) L. has significant DPPH radical scavenging and inhibitory action on lipid peroxidation [10]. Therefore, the aqueous bark extract of *Nauclea orientalis* (L.) L. was selected to determine the cardioprotective effect against Dox-induced cardiotoxicity in Wistar rats.

2. Methods

2.1. Collection of *Nauclea orientalis* (L.) L. Bark. The identified bark of *Nauclea orientalis* (L.) L. consistent with the

study of Jayaweera [11] was collected from the Southern province, Sri Lanka, and authenticated at the National Herbarium, Royal Botanical Gardens, Peradeniya, Sri Lanka.

2.2. Pharmacognostic Standardization

2.2.1. Determination of Physicochemical Parameters and Phytochemical Profile. Heavy metal analysis, extractable matter, and moisture content were determined following WHO guidelines [12]. Morphological features were examined using a microscope following WHO (2011) guidelines on quality control and standardization of plant materials [13].

D.H₂O or organic extraction of the *Nauclea orientalis* (L.) L. bark was used for the phytochemical screening tests in the identification of compounds including glycosides (anthracene, cyanogenic, and cardenoloid), polyphenols, flavonoids, alkaloids, saponin, tannins, reducing sugars, and proteins [14, 15].

2.3. Determination of Total Polyphenol Content and In Vitro Antioxidant Activity of *Nauclea orientalis* (L.) L. Bark

2.3.1. Preparation of Aqueous Extract. A *Nauclea orientalis* bark (2.50 g) was dried at 40°C and coarsely ground. Then it was added to D.H₂O (60 mL) and extracted by refluxing for 3 h. Then the mixture was kept in a rotary evaporator for 1 h at 100 rpm. After that, the mixture was filtered through muslin cloth, and the filtrate was concentrated through evaporation on a water bath at 100°C. The final extract was weighed (0.33 g, percentage yield was 13.2%) and stored. Subsequent assays were performed on a concentration series (1–500 $\mu\text{g}/\text{mL}$) of the extract.

2.3.2. Estimation of Total Polyphenol Content. The aqueous bark extract of *Nauclea* was subjected to determine the polyphenol content based on the spectrophotometric method using the Folin-Ciocalteu reagent [16]. The plant extract (1.0 mL) was added into a solution mixture containing 95% ethanol, D.H₂O, and the newly prepared 50% Folin-Ciocalteu reagent. After five minutes, the mixture was incubated with sodium carbonate (Na_2CO_3) at 27°C for one hour. The absorbance was determined (725 nm), and the results were mentioned as milligrams of gallic acid equivalent per gram of extract dry weight (mgGAE/g dw).

2.3.3. 2,2-Diphenyl-1-Picrylhydrazyl (DPPH) Free Radical Scavenging Activity. The method of Bhuiyan et al. [17] was modified to assess the DPPH radical scavenging activity of the aqueous bark extract of *Nauclea*. The concentration series of the bark extract and the standard (L-ascorbic acid) were incubated in 0.004% DPPH solution (3.0 mL) at 25°C, and the absorbance was measured (517 nm). The absorbance of the control was obtained from 0.004% DPPH solution. The radical scavenging ability (percentage inhibition of free radicals) was calculated by the below-mentioned equation.

$$\begin{aligned} \text{Radical scavenging activity(\%)} \\ = [(\text{Abs control} - \text{Abs test})/(\text{Abs control})] \times 100. \end{aligned} \quad (1)$$

The IC_{50} value (concentration of the plant extract or standard required to inhibit DPPH radical formation by 50%) was finally calculated to measure the antioxidant activity of the aqueous bark extract of *Nauclea orientalis*.

2.3.4. Nitric Oxide (NO) Radical Scavenging Activity. Sodium nitroprusside which has the ability to react with oxygen generates nitric oxide; hence, it is used as the NO^{\bullet} generator. The NO radical scavenging activity of *Nauclea* bark was assessed by the modified Griess reaction [18]. The buffered sodium nitroprusside (10 mM) was incubated with the concentration series of aqueous plant extract (1 mL) and the L-ascorbic acid (standard) at 25°C for 180 min. Then they were mixed with the Griess reagent in equal volume. The absorbance of the pink colour formed during the reaction was measured by a spectrophotometer (550 nm). Radical scavenging activity was estimated by Equation (1).

2.3.5. Ferric Reducing Antioxidant Power (FRAP) Assay. The FRAP assay was performed based on the method published by Zahin et al. [19]. In the reaction, $Fe^{3+}(CN^{-})_6$ is reduced to $Fe^{2+}(CN^{-})_6$, and the addition of excess ferric ions in the medium develops a Perl's Prussian blue complex. The concentration series of the aqueous bark extract was added into the mixture of potassium ferricyanide (1%, $K_3Fe(CN)_6$) and the phosphate buffer (pH 6.6) and incubated for 20 min (at 50°C). After the addition of 10% trichloroacetic acid and 0.1% $FeCl_3$, the mixture was again incubated at room temperature for 20 min, and absorbance was measured (700 nm).

2.4. Experimental Animals. Wistar albino rats (6-8 weeks old), weighing 175 ± 25 g, were procured from the Medical Research Institute (MRI), Sri Lanka. The rats were housed in stainless-steel cages in a controlled environment, temperature at $23 \pm 2^{\circ}C$, and humidity $55 \pm 5\%$ under a 12-hour light-dark cycle. They were fed with a standard laboratory diet of rat pellets and water ad libitum. The animal experiments were followed obeying the CIOMS international guiding principles [20] under the approval of the Ethics Committee of the Faculty of Medicine, University of Ruhuna, Sri Lanka.

2.5. Dose-Response Effect of Aqueous Bark Extract of *Nauclea orientalis* (L.) L. against Dox-Induced Cardiotoxicity In Vivo. The following treatment protocol was followed in seven groups of 10 animals in each: group I (control): oral dose of D_2O (10 mL/kg) for 2 weeks and single intraperitoneal (IP) injection of saline on the 11th day; group II (Dox control): oral dose of D_2O (10 mL/kg) for 2 weeks and single IP injection of Dox (18 mg/kg) on the 11th day; and groups III to VII; oral dose of freeze-dried aqueous bark extract of *Nauclea orientalis* (L.) L. (0.125, 0.25, 0.5, 1.0, and 2.0 g/kg) for 2 weeks and single IP injection of Dox (18 mg/kg) on the 11th day; IP injections were given after 16 h fasting in each animal. 72 h after the administration of IP injections, serum was collected from the blood for the detection of cardiac troponin I (cTnI), aspartate aminotransferase (AST, EC 2.6.1.1), and lactate dehydrogenase (LDH, EC 1.1.1.27), and

myocardial tissues were fixed in 10% buffered formalin for histological assessment of myocardial damage.

2.6. Evaluation of Acute and Subchronic Toxicity of Plant Extract. Toxicity studies were followed on the optimum concentration of the aqueous bark extract which showed the very best cardio protection within the dose-response study. Both acute and chronic toxicity studies were performed following the principles of the Organization for Economic Cooperation and Development (OECD) [21, 22]. Two groups of Wistar rats were used in the acute toxicity study, and one group (control group) was administered with a single dose of water (10 mL/kg) orally. The second group was treated with a single dose (2.0 g/kg) of aqueous extract of *Nauclea orientalis* (L.) bark. Individual animals were inspected during the initial half an hour, then from time to time within the first 24 h, giving special attention during the initial 4 h. Then they were observed daily for 2 weeks by giving attention to changes in the mucous membranes, eyes, skin, fur, and general behaviours. Further, the signs of toxicity such as lethargy, salivation, diarrhoea, tremors, sleep, convulsions, and coma were also observed.

Healthy rats were randomly assigned into two groups in the subchronic toxicity study. The control group of rats was given an oral dose of D_2O daily throughout one month, and the second group of rats received freeze-dried aqueous bark extract of *Nauclea orientalis* (L.) L. (2.0 g/kg) daily throughout one month via oral route. The experimental rats were inspected during the one-month period for the signs of toxicity and mortality. After 24 h of the last dose, the animals were sacrificed after 16 h fasting, and blood samples were collected into two tubes: one with EDTA for the assessment of haematological parameters including red blood cell (RBC) count, white blood cell (WBC) count, platelet count, haematocrit, haemoglobin concentration, mean corpuscular haemoglobin (MCH), mean corpuscular volume (MCV), and mean corpuscular haemoglobin concentration (MCHC) and the other without additives for the assessment of biochemical parameters including AST, alanine aminotransferase (ALT), alkaline phosphatase (ALP), creatinine, and blood urea. The weighed organs (heart, lungs, kidney, liver, small intestine, and spleen) were fixed in 10% buffered formalin for the detection of histologic evidences of toxicity.

2.7. Screening of *Nauclea orientalis* (L.) L. Aqueous Bark Extract for Cardioprotective Effect against Dox-Induced Oxidative Stress, Inflammation, and Apoptosis In Vivo. Five groups ($n = 10$) of Wistar albino rats were subjected to the following test protocol. This study uses the method of Sandamali et al., and the method description partly reproduces their wording [23]. Figure 1 shows the summary procedure of the treatment protocol used in the study.

Group I received D_2O by gastric gavage daily for 2 weeks, and an IP injection of normal saline was given on the 11th day after a fasting period (16 h). Rats in group II were given a daily oral dose of freeze-dried aqueous bark extract (2.0 g/kg) for 2 weeks while an IP injection of normal saline was introduced on the 11th day after a 16 h of fasting period. Group III and group V were also administered with

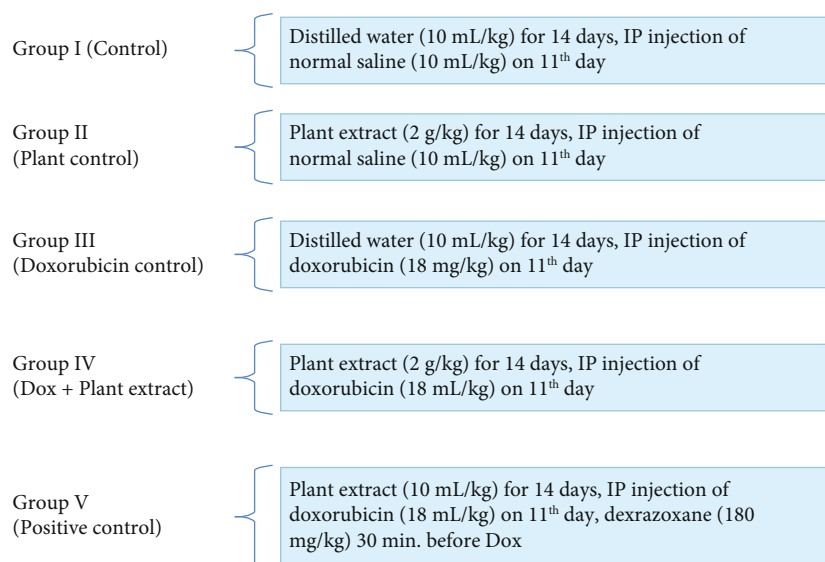


FIGURE 1: Treatment protocol.

an oral dose of D.H₂O for 2 weeks, and in the 11th day, both groups were injected with a single IP injection of Dox while the positive control group received single IP injection of dexrazoxane (180 mg/kg) half an hour before the introduction of Dox. Rats in group IV were given aqueous bark extract of *Nauclea orientalis* (2.0 g/kg) daily for 2 weeks, and a single respective dose of IP injection of Dox was administered after 16 h of fasting on the 11th day.

At the end of the two weeks, all animals were sacrificed after 16 h of fasting, and blood samples were collected into tubes with no additives (plain tubes) for the determination of N terminal-pro-brain natriuretic peptide (NT-pro BNP), cTnI concentration, AST activity, and LDH activity, and the results were compared among the five groups utilized in the study.

The antioxidant parameters (glutathione peroxidase (GPx, EC 1.11.1.9), reduced glutathione (GSH), glutathione reductase (GR, EC 1.8.1.7), SOD (EC 1.15.1.1) activity, catalase (EC 1.11.1.6) activity, and total antioxidant level) and lipid peroxidation as an oxidative stress biomarker were determined using the homogenate (tissue weight to homogenization buffer: 1:10) of heart tissues prepared by half of the heart collected into ice-cold phosphate-buffered saline (PBS), and the results were compared among the five groups.

The rest of the heart tissues fixed in 10% buffered formalin were used in the determination of histological evidences of cardiac damage, in the immunohistochemical analysis of inflammatory and apoptotic markers, and in the terminal deoxynucleotidyl transferase-mediated dUTP nick-end labelling (TUNEL) assay.

The myeloperoxidase (MPO, EC 1.11.2.2) activity which was used as a biochemical inflammatory marker was measured in the serum of experimental rats.

2.7.1. Collection of Blood (Cardiac Puncture) and Heart Tissues. Experimental Wistar rats were anesthetized using isoflurane inhalation and euthanized by cardiac exsanguina-

tion [24]. They were placed in the recumbent supine position on the animal operation table; an incision was made on the ventral aspect of the thoracic wall just above the diaphragm by using a surgical scissor, and the thoracic cavity was opened. Then the blood sample was collected slowly using a 21G needle from the ventricles. After that, the heart was collected from the mediastinum by dissecting it out from the major blood vessels. The heart was washed in saline, soaked in a blotting paper to extract the blood, and fixed in 10% buffered formalin. The myocardial tissue was sampled for histological assessment from the ventricle, 5 mm above the apex of the heart of all animals.

2.7.2. Histological Assessment of Cardiac Damage. The heart tissues fixed in 10% buffered formalin were processed and embedded in paraffin. Then they were sectioned at 3 μ m thickness and stained with haematoxylin and eosin (H&E) [23]. The sections were examined by a histopathologist blinded to the treatments under the compound light microscope, and histological features of the necrosis were scored. The grading system was prepared by the authors of the study by inspecting the myocardium of rat tissues (section with 5 mm diameter) as follows: absence of any myocardial cells with features of necrosis: 0; \leq 10 myocardial cells with features of necrosis: 1; 11-50 myocardial cells with features of necrosis: 2; 51-100 myocardial cells with features of necrosis: 3; and >100 myocardial cells with features of necrosis: 4.

Necrotic myocytes were identified with the features including hypereosinophilic cytoplasm, without striations and changes in the nucleus such as pyknosis, karyolysis, or karrheorhexis. Necrotic myocytes were counted separately in the subendocardial region and peripheral region of the rat myocardium.

2.7.3. Immunohistochemical Analysis of Inflammatory Markers, TNF α and Apoptotic Markers, Caspase-3, and Bcl-2. Immunohistochemical analysis was followed on the basis

of a modified method explained by Bulut et al. [25]. Antigen retrieval from the heart tissue sections was performed by placing them in a citrate buffer (pH 6.0). Then the sections were subjected to overnight incubation with the primary antibodies for TNF α , Bcl-2, and caspase-3 at 4°C. They were treated with the streptavidin peroxidase substrate solution, and then chromogen and diaminobenzidine (DAB) were applied followed by the counterstain haematoxylin. The breast carcinoma tissue (for TNF α), reactive lymph node tissue (for Bcl-2), and colon tissue (for caspase-3) were used as positive controls for immunostaining. The freely downloadable Image J 1.53a (2015) software [26] was applied to measure the area of expression of the respective markers which showed the brown colour staining on the tissue sections, and finally, the average area (in m^2) of brown-stained area was calculated.

2.7.4. TUNEL Assay. DNA fragmentation considered one of the features of apoptosis was detected using the TUNEL technique [27]. The DeadEnd™ Colorimetric TUNEL System detection kit (Promega Corporation, USA) was used, and the manufacturer's protocol was followed. In the presence of terminal deoxynucleotidyl transferase, 3'-OH ends of the fragmented DNA in apoptotic cells were labelled with biotinylated nucleotide. Then horseradish peroxidase-labelled streptavidin was bound to the biotinylated nucleotide and was detected using the hydrogen peroxide and stable chromogen, diaminobenzidine which gave the brown colour. Then the number of apoptotic nuclei in the 10 high-power field ($\times 400$ magnification) was counted.

2.8. Statistical Analysis. Data were expressed as the mean \pm standard deviation (SD). For a statistical analysis of the data, the group means were compared by the one-way analysis of variance with post hoc analysis (SPSS 26.0 software). Dunnett's post hoc test was applied to identify significance among groups; $p < 0.05$ was considered statistically significant.

3. Results

3.1. Standardization of Plant Material

3.1.1. Physicochemical and Phytochemical Analysis. The physicochemical analysis of *Nauclea orientalis* (L.) L. bark is shown in Supplementary data Table 1. The highest quantity of extractable matters was detected in hot water. Heavy metals including arsenic (As), cadmium (Cd), lead (Pb), and mercury (Hg) were absent in the *Nauclea orientalis* bark. The microscopic appearance of the bark is also included in Table 1 (Supplementary data).

The phytochemical profile of the *Nauclea orientalis* (L.) L. bark is shown in the Supplementary data Table 1. Polyphenols, tannins, alkaloids, and reducing sugars were detected in the bark. However, the *Nauclea* bark was negative for cyanogenic glycosides, anthracene glycosides, and cardenoloid glycosides. Saponin, flavonoids, and proteins were also not detected in the *Nauclea* bark.

3.2. In Vitro Antioxidant Activity of the *Nauclea orientalis* (L.) L. Bark. The *ex vivo* antioxidant activity and polyphenol content of the aqueous extract of *Nauclea orientalis* are included in Table 2 (Supplementary data). The correlation between the polyphenol content and the *in vitro* antioxidant activities of aqueous plant extract was determined using the linear regression analysis, and results are shown in Figure 2. A considerable positive correlation was detected between the polyphenolic content and antioxidant activities ($R^2 = 0.9325$, $R^2 = 0.8961$, and $R^2 = 0.86$, respectively). Therefore, it is evident that there is a substantial impact of phenolic substances to the antioxidant activity detected in the aqueous bark extract of *Nauclea orientalis*.

3.3. Dose-Response Effect of Aqueous Bark Extract of *Nauclea orientalis* (L.) L. for Cardioprotective Effect against Dox-Induced Cardiotoxicity In Vivo. Rats in the Dox control group showed a momentous rise ($p < 0.001$) in the serum cTnI level at 156.76 pg/mL in comparison to the control at 0 pg/mL (Figure 3(a)). After the administration of *Nauclea orientalis* bark extract, a considerable decrease ($p < 0.05$) in cTnI concentration was detected in all rat groups in comparison to the Dox control (groups III-VII: 41.04, 38.96, 17.75, 13.75, and 13.0 pg/mL). A significant increase ($p < 0.001$) in the enzyme activities of AST and LDH was also observed in rat groups administered with Dox in comparison to the normal control (Figures 3(b) and 3(c)). Although the rat groups treated with all concentrations of *Nauclea orientalis* bark extract showed significant changes ($p < 0.05$) against the Dox control group of rats for the LDH activity, a significant difference ($p < 0.05$) in the AST activity was detected only in rat groups treated with higher doses including 0.5, 1.0, and 2.0 g/kg.

Cross-section of the tissues of the myocardium of the normal control group exhibited normal morphology (Figures 4(a) and 4(b)). Rats administered with Dox alone exhibited the maximum score (7.9) for the early changes of necrosis showing greater damage to the peripheral and sub-endocardium of the myocardial tissues (Figures 4(a)–4(c)). All groups of rats subjected to the treatment of different doses of plant extract (group III-VII) showed a regular decrease in the score of myocardial cells with early changes of necrosis with the increase of the dosages of plant extract (Figure 4(c)). Additionally to the necrosis, other histological changes including congestion of blood vessels, intracellular vacuoles, interstitial oedema, haemorrhages, inflammatory infiltrations, and wavy myocardial fibers were also seen in the rats treated only with Dox (Supplementary data Table 3, Figure 4(d)). Groups of rats administered with different doses of plant extract exhibited different degrees of above histologic changes while haemorrhages, interstitial oedema, and inflammatory infiltrations were totally absent in groups of rats administered with higher dosages of the plant extract. Supporting the collective results obtained for biochemical parameters and histopathological assessment of cardiac damage, 2.0 g/kg of *Nauclea orientalis* bark extract was considered the optimum dosage to be used for the determination of cardioprotective activity against Dox-induced cardiotoxicity.

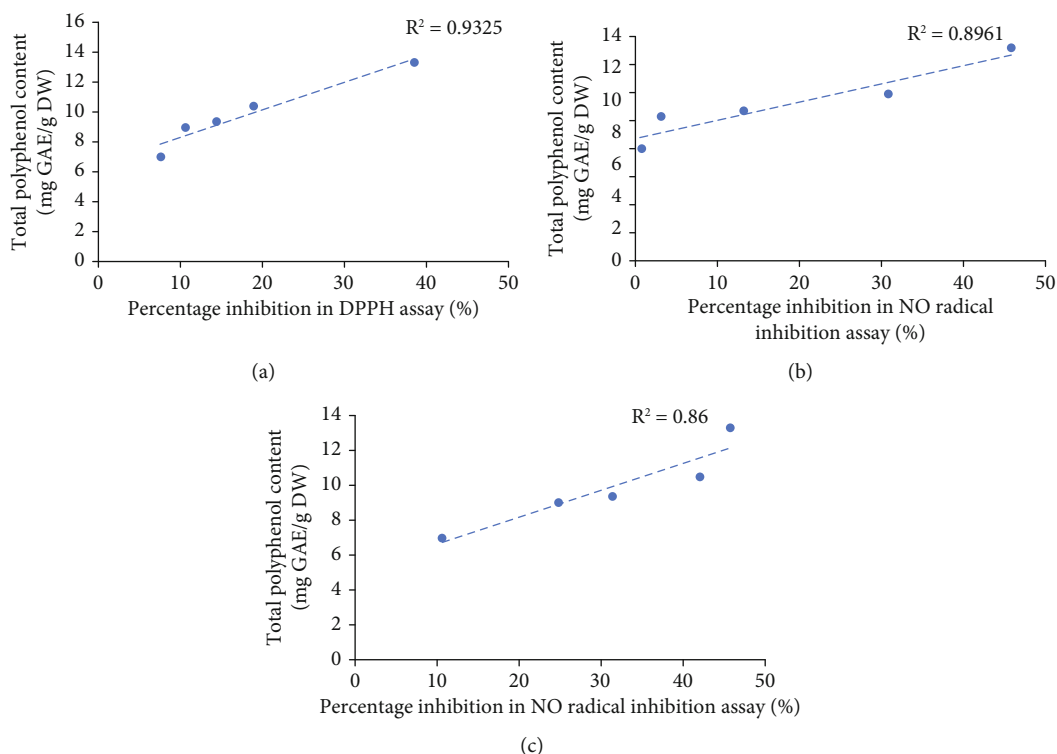


FIGURE 2: *In vitro* antioxidant activity as determined by the total polyphenol content of freeze-dried aqueous extract of *Nauclea orientalis* bark. (a) Correlation between polyphenol amount and the percentage inhibition in DPPH assay. (b) Correlation between polyphenol amount and the percentage inhibition in NO assay. (c) Correlation between polyphenol amount and the FRAP assay results. R^2 : correlation coefficient. DPPH: 2,2'-diphenyl-2-picrylhydrazyl hydrate. NO: nitric oxide. FRAP: ferric reducing antioxidant power.

3.4. Acute and Subchronic Toxicity Evaluation of Plant Extract. The acute toxicity study revealed that rats treated with a single dose of *Nauclea* bark extract (2.0 g/kg) did not show mortality or morbidity throughout the 14-day period. No changes were observed in the morphology of the eyes, nose, fur, and skin. The respiratory and central nervous system effects such as tremors, convulsions, salivation, diarrhoea, and lethargy were also not examined in animals that were administered with a single dose of bark extract, and they did not show any unusual behaviour throughout the observation period.

Oral administration of freeze-dried aqueous extract of *Nauclea orientalis* bark daily for 30 days did not produce any conspicuous symptoms of toxicity in experimental Wistar rats. There was no treatment-related mortality reported in rats treated with the plant extract. No changes were observed in food and water intake during the period of investigation. Changes in body weight during the period of investigation are presented in Supplementary data, Table 4. Statistically significant changes ($p > 0.05$) in the gain of body weight were not detected between the control and the plant extract-treated group.

The subchronic administration of *Nauclea orientalis* bark extract on the changes in haematological parameters was presented in Supplementary data, Table 5. The measured haematology parameters were within the physiological range during the 30-day period of investigation, and a significant difference ($p > 0.05$) was not detected in comparison to the rats in the control group.

Liver function (AST, ATL, and ALP activities) and kidney function (blood urea and creatinine) test results of the study groups are shown in Supplementary data, Table 6. Statistically considerable changes ($p > 0.05$) were not examined in those biochemical tests between the rats in the control group and the plant extract-administered group.

Absolute and relative organ weights of *Nauclea*-administered rats and control rats were shown in Supplementary data, Table 7. A significant change was not observed between the plant extract-treated group and the control group. No evidences of histological changes were examined in the six organs isolated (Supplementary data, Figure 1). The microscopic examination of the heart, kidneys, lungs, liver, small intestine, and spleen did not show any structural changes in the cells when viewed under the compound light microscope with multiple magnifications.

3.5. Screening of *Nauclea orientalis* (L.) L. Aqueous Bark Extract for Cardioprotective Effect against Dox-Induced Oxidative Stress, Inflammation, and Apoptosis *In Vivo*

3.5.1. Cardiac Biomarkers in Serum. The intracellular cTnI is released into the circulation when there is damage to the cardiomyocytes. The rat group treated with Dox (Dox control) showed the maximum concentration of cTnI among the groups of rats utilized in this experiment indicating that Dox causes damage to the myocardium as shown in Table 1. Rats pretreated with *Nauclea orientalis* bark extract followed by Dox presented a substantial reduction ($p < 0.05$)

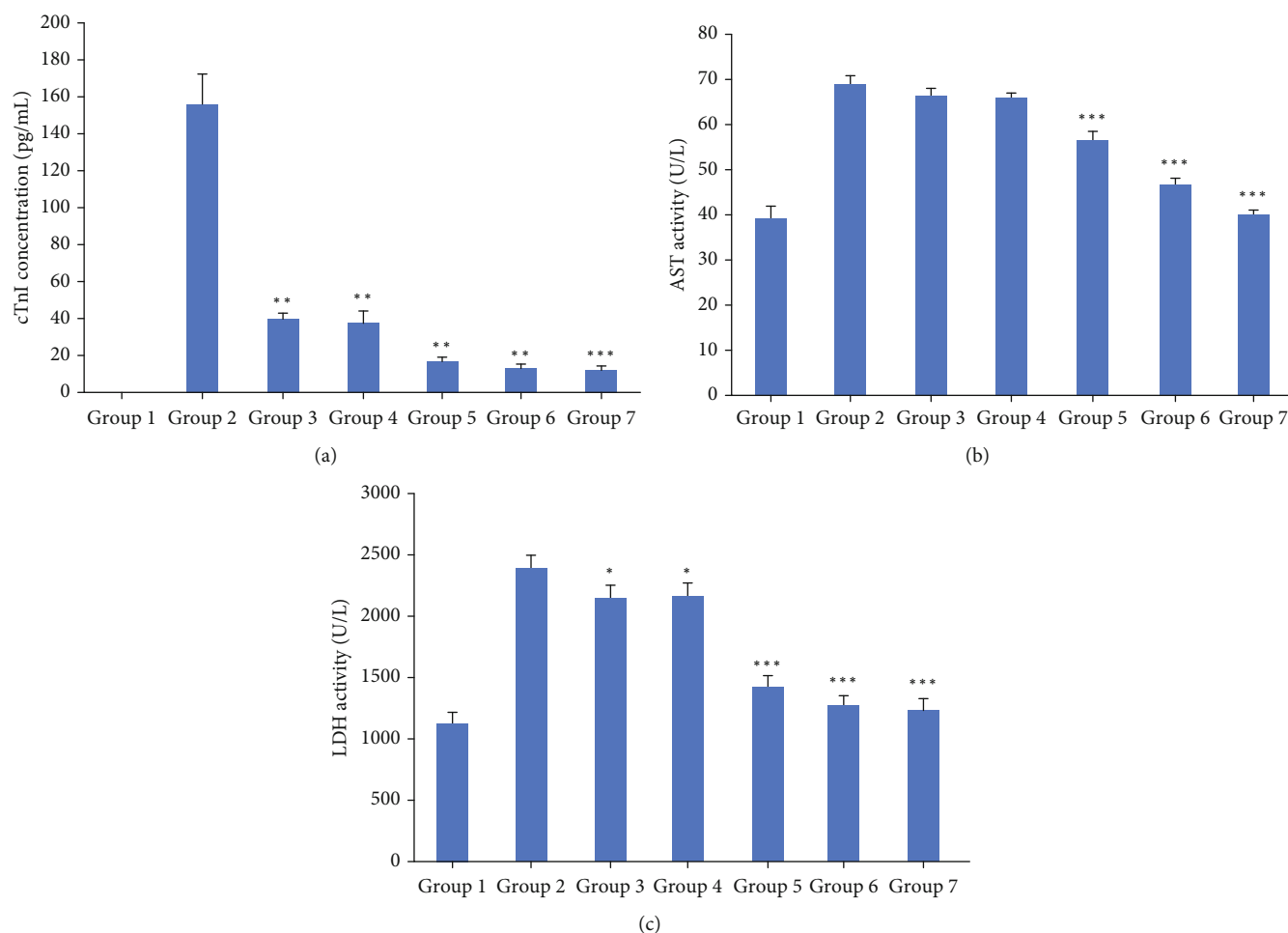


FIGURE 3: Biochemical investigation of the dose-response effect of freeze-dried aqueous *Nauclea orientalis* bark extract in Wistar rats treated with Dox. (a) Cardiac troponin I (cTnI) concentration in rats' serum. (b) Aspartate aminotransferase (AST) level in rats' serum. (c) Lactate dehydrogenase (LDH) level in rats' serum. Group 1: normal control, group 2: Dox control, group 3: rats treated with Dox (18 mg/kg) and *Nauclea* bark extract (0.125 g/kg), group 4: rats treated with Dox (18 mg/kg) and *Nauclea* bark extract (0.25 g/kg), group 5: rats treated with Dox (18 mg/kg) and *Nauclea* bark extract (0.50 g/kg), group 6: rats treated with Dox (18 mg/kg) and *Nauclea* bark extract (1.0 g/kg), and group 7: rats treated with Dox (18 mg/kg) and *Nauclea* bark extract (2.0 g/kg). Each column represents the mean \pm SD ($n = 10$). * $p < 0.05$, ** $p < 0.01$, *** $p < 0.001$, significant difference compared to the Dox control.

in cTnI concentration in comparison to the Dox control. The rats in plant control group did not show significant change ($p < 0.05$) in cTnI concentration compared to the control group of rats. The rat group treated with *Nauclea* bark extract and Dox and the positive control group showed a significant change ($p < 0.001$) in cTnI concentration compared to the control group of rats.

NT-pro BNP is similarly measured as a suitable biomarker in the identification of cardiotoxicity. Considering the results, it could be noticed that NT-pro BNP concentration is significantly augmented ($p < 0.05$) in rats treated with Dox compared to the control group as exhibited in Table 1. Rats pretreated with aqueous *Nauclea* bark extract followed by Dox treatment exhibited a significantly low ($p < 0.05$) value in comparison to the rats in the Dox control group. The rats treated with *Nauclea* bark extract which was considered the plant control did not show any noteworthy change ($p < 0.05$) in the NT-pro BNP concentration related to the rats in the control group. However, the rat group

treated with plant extract and Dox and the positive control group showed a significant increase ($p < 0.001$) in the NT-pro BNP concentration compared to the control.

AST and LDH are valuable cardiac enzymes which are released into the circulation when there is necrosis. The rats in the plant control group did not show any important difference ($p < 0.05$) in AST and LDH activities in relation to the rats in the control group as exhibited in Table 1. The AST and LDH activities were considerably elevated ($p < 0.05$) in Dox-administered rats in comparison to the rats in the control group. The rats in the plant extract-pretreated group followed by Dox injection exhibited a significant decrease ($p < 0.05$) in AST and LDH activities in comparison to the rats in the Dox control group. Although the rats in group IV (*Nauclea* + Dox) showed a significant elevation ($p < 0.05$) in AST and LDH activities compared to the control, the positive control group did not show a significant elevation ($p > 0.05$) compared to the control.

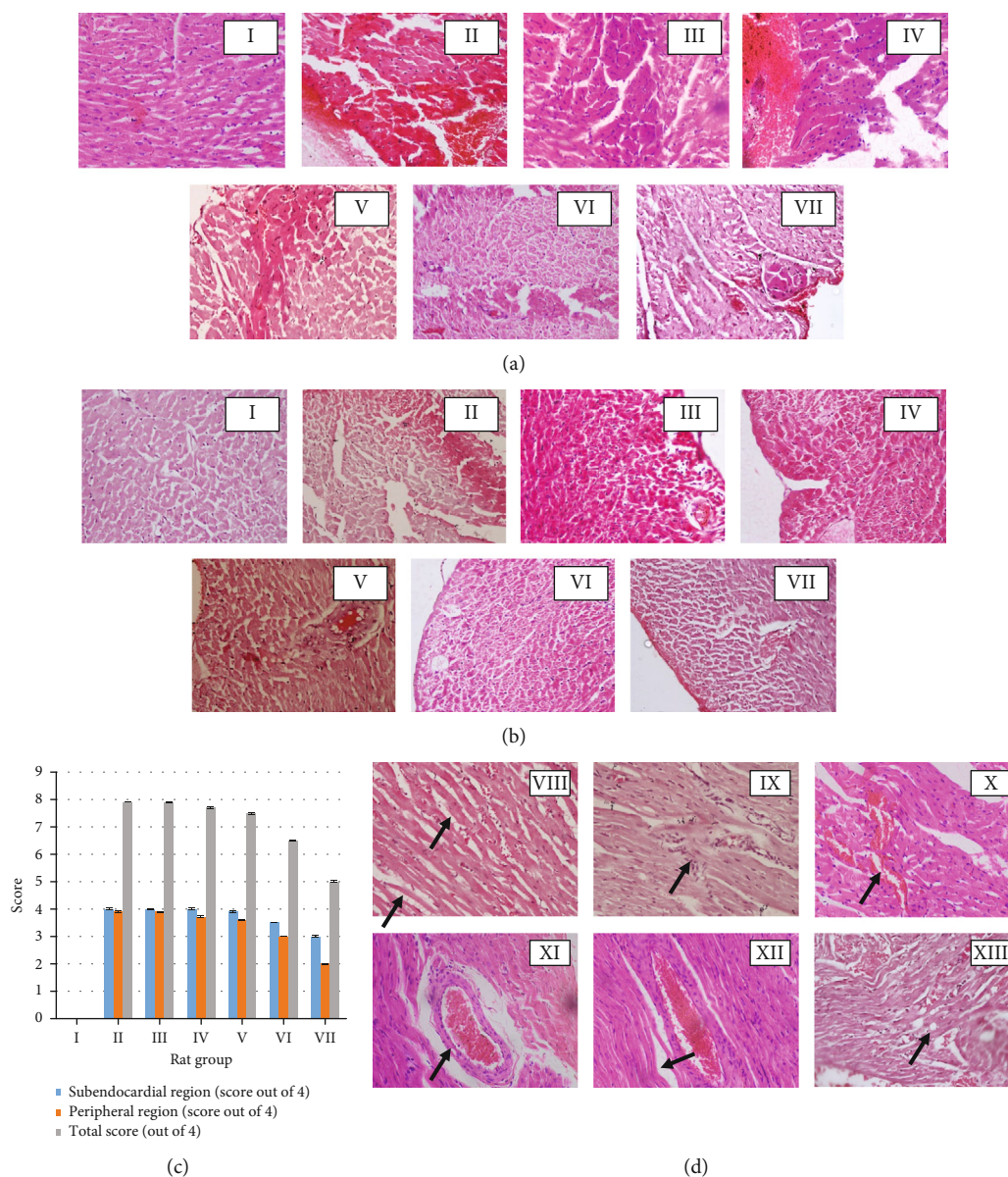


FIGURE 4: Histological investigation of the dose-response effect of freeze-dried aqueous *Nauclea orientalis* bark extract in Wistar rats treated with Dox (H&E, 10×40). (a) Cardiac myocytes with early changes of necrosis in the subendocardial region. (b) Cardiac myocytes with early changes of necrosis in the peripheral region. (c) Average grading of cardiac myocytes with early changes of necrosis (absence of any myocardial cells with features of necrosis: 0; ≤ 10 myocardial cells with features of necrosis: 1; 11-50 myocardial cells with features of necrosis: 2; 51-100 myocardial cells with features of necrosis: 3; and >100 myocardial cells with features of necrosis: 4). I: control, II: Dox control, III: rats administered with Dox (18 mg/kg) and *Nauclea* bark extract (0.125 g/kg), IV: rats administered with Dox (18 mg/kg) and *Nauclea* bark extract (0.25 g/kg), V: rats administered with Dox (18 mg/kg) and *Nauclea* bark extract (0.5 g/kg), VI: rats administered with Dox (18 mg/kg) and *Nauclea* bark extract (1.0 g/kg), and VII: rats administered with Dox (18 mg/kg) and *Nauclea* bark extract (2.0 g/kg). (d) Dox-induced reversible histologic changes in the myocardium of Wistar rats. VIII: interstitial oedema, IX: inflammatory infiltrations, X: haemorrhages, XI: congestion of blood vessel, XII: wavy myocardial fibers, and XIII: intracellular vacuoles. Arrows indicate reversible cellular changes. Each column represents the mean \pm SD ($n = 10$).

3.5.2. Antioxidant Parameters in Homogenate of Heart Tissue. The results of GSH, GPx, and GR activities among the groups of rats utilized in this experiment are shown in Figures 5(a) and 5(b). The glutathione system has a key role in protecting the cells against oxidative damage. Dox induces damage to the myocardium due to oxidative stress generated by ROS, and this was reinforced by the results found in the

present study as well revealing a considerable reduction ($p < 0.001$) in GSH, GPx, and GR enzyme activities in myocardial tissues of Wistar rats subjected to the treatment of Dox and D.H₂O compared to the rats of the control group. However, the rats in the pretreated plant extract group followed by the Dox injection showed a significant ($p < 0.05$) elevation in the GSH level as well as other two

TABLE 1: Investigation of cardiac biomarkers in the screening of aqueous extract of *Nauclea orientalis* (L.) L. bark for the potential cardioprotective effect.

Serum cardiac biomarkers	Group I	Group II	Group III	Group IV	Group V
cTnI (pg/mL)	0.00	0.00	145.15 ± 10.77 ^c	38.92 ± 3.08 ^{***,c}	11.46 ± 2.59 ^{***,c}
NT-pro BNP (pg/mL)	41.57 ± 7.29	44.43 ± 4.27	371.14 ± 9.69 ^c	233.29 ± 11.12 ^{***,c}	159.43 ± 12.39 ^{***,c}
AST (U/L)	25.71 ± 1.41	25.12 ± 1.74	66.10 ± 2.07 ^c	34.98 ± 2.14 ^{***,c}	26.90 ± 1.26 ^{***}
LDH (U/L)	1057.21 ± 38.6	1181.06 ± 36.30	1584.19 ± 83.4 ^c	1308.96 ± 68.8 ^{***,c}	1104.97 ± 58.7 ^{***}

cTnI: cardiac troponin I, NT-pro BNP: N terminal-pro-brain natriuretic peptide, AST: aspartate aminotransferase, LDH: lactate dehydrogenase. Group I: control group, group II: *Nauclea orientalis* plant control, group III: Dox control, group IV: rats received *Nauclea orientalis* bark extract + Dox, and group V: positive control. *p* values * < 0.05, ** < 0.01, and *** < 0.001 were considered significant (compared to the Dox control). *p* values ^a< 0.05, ^b< 0.01, and ^c< 0.001 were considered significant (compared to the control).

antioxidant enzyme (GPx and GR) activities in relation to the rats in the Dox control group. Rats in the plant extract control group did not exhibit any substantial difference ($p > 0.05$) in the GSH level and other two enzyme activities in comparison to the rats in the control. However, the rats in group IV (*Nauclea* + Dox) showed a significant reduction ($p < 0.05$) in GSH, GR, and GPx activities while the positive control showed a significant reduction ($p < 0.05$) only in GPx and GR activities.

In the present study, antioxidant enzymes which detoxify oxygen radicals like catalase and SOD also displayed a significant rise ($p < 0.05$) in the rats in the Dox control group in comparison to the rats in the normal control group as shown in Figure 5(c) representing free radical formation following Dox treatment. However, rats pretreated with freeze-dried aqueous extract of *Nauclea orientalis* bark followed by Dox injection were capable of significantly augmenting ($p < 0.05$) the SOD and catalase enzyme levels in comparison to the rats in the Dox control group. Considerable differences ($p > 0.05$) could not be detected in these two enzyme activities in the heart tissues of rats treated with aqueous *Nauclea* bark extract alone (plant control) when compared to the control group of rats. The positive control group and rat group treated with plant extract and Dox showed significant reductions ($p < 0.05$) in SOD and catalase activities compared to the control.

The total antioxidant status assessed among the groups of experimental rats is shown in Figure 5(d). Wistar rats in the Dox control group exhibited the significant drop ($p < 0.001$) in total antioxidant status when compared with the control group of rats confirming that Dox causes the exhaustion of antioxidants within the myocardial tissues. However, Wistar rats pretreated with the *Nauclea* bark extract followed with Dox injection were capable of significantly increasing ($p < 0.001$) the total antioxidant status in comparison to the Wistar rats in Dox control indicating its high antioxidant effect. The plant extract control did not show a significant difference ($p > 0.05$) in total antioxidant activity compared to the control. However, rats treated with *Nauclea* bark extract and Dox showed a significant reduction ($p < 0.001$) in total antioxidant activity compared to the control.

3.5.3. Analysis of Lipid Peroxidation in Homogenate of Heart Tissue. Results of lipid peroxidation by means of malondial-

dehyde (MDA) concentration are presented in Figure 5(e). The *Nauclea* bark extract control group did not exhibit any considerable difference ($p > 0.05$) in the lipid peroxidation compared to the normal control. Rats in the Dox control exhibited a significant rise ($p < 0.05$) in lipid peroxidation in comparison to the rats in the control group indicating that Dox treatment increases the lipid peroxidation. Although the rats in the group pretreated with freeze-dried aqueous plant extract followed by Dox treatment showed a significant increase ($p < 0.001$) in lipid peroxidation compared to the control, they exhibited a substantial decrease ($p < 0.001$) in the MDA level in comparison to the rats in the Dox control group.

3.5.4. MPO Activity in Serum. Inflammation is another obvious outcome of the Dox treatment which is evident by increased MPO activity. The results of the MPO activity among the experimental groups of the present study are shown in Figure 6. The plant extract control group did not show a considerable difference ($p > 0.05$) in MPO activity when compared with the control group. Wistar rats in the Dox control group showed a significant rise ($p < 0.001$) in MPO activity in comparison to the rats in the control group, and it was the highest concentration among the five groups of rats. However, rats in the group pretreated with the plant extract followed by Dox treatment showed a considerable reduction ($p < 0.001$) in the MPO activity compared to the rats in the Dox control group.

Rats in the positive control group were treated with dexrazoxane as it is the accepted protective agent in the clinical setting to be used to treat the Dox-induced cardiotoxicity. When considering the biochemical results of the present experiment, a significant difference ($p < 0.001$) was observed between the rats in the positive control group and the Dox control in all parameters tested.

3.5.5. Histological Assessment of the Myocardial Damage. The myocardial tissues of the rats in the control group exhibited the general architecture in the peripheral and sub-endocardial regions of the myocardium (Figures 7(a) and 7(b)). A large number of cells with early changes of necrosis were observed in both regions (peripheral and subendocardium) of the myocardium of the Dox control group of rats, and they exhibited the highest score (7.8) among the five groups of rats used in the present study (Figure 7(c)).

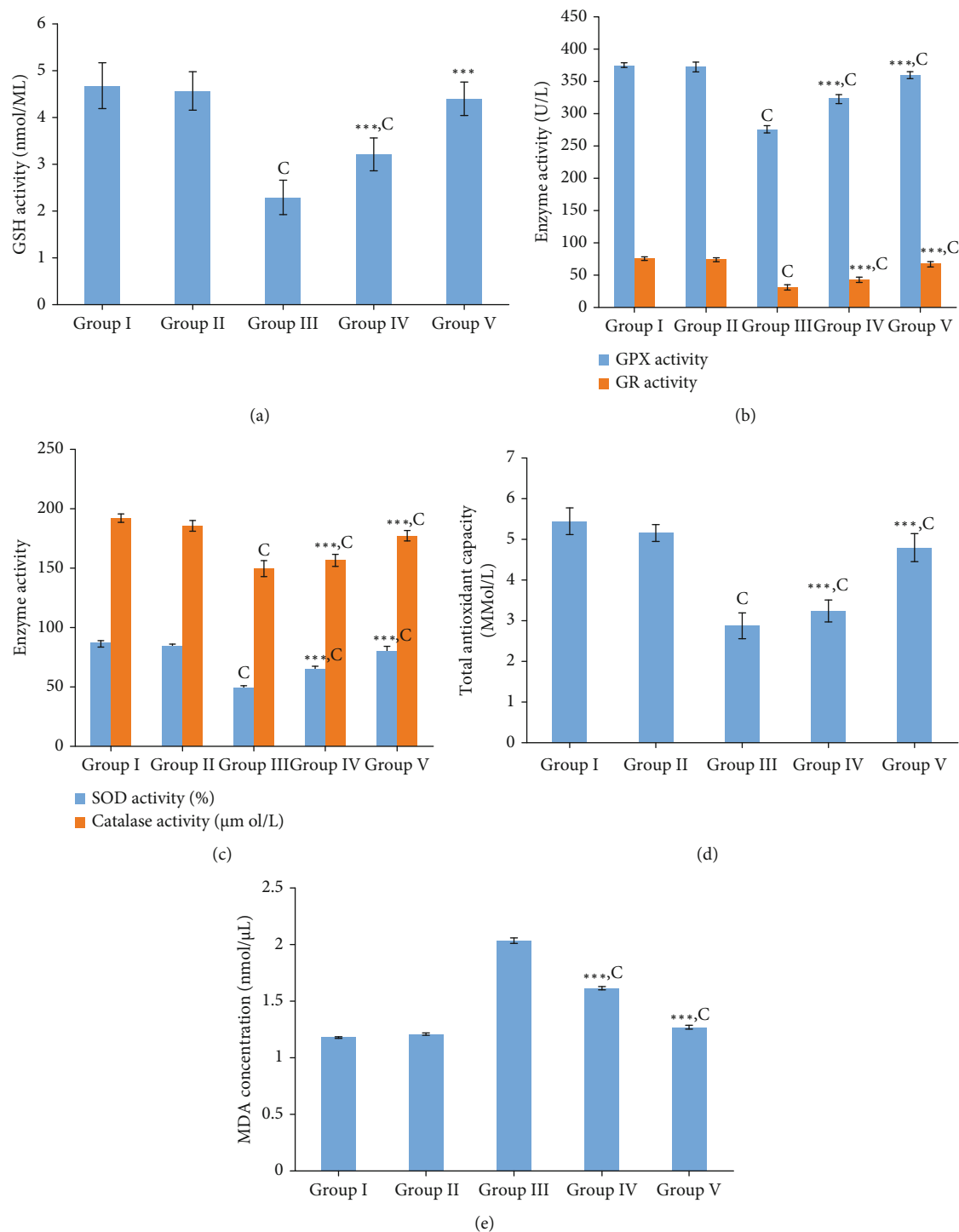


FIGURE 5: Investigation of oxidative stress biomarkers in the screening of aqueous extract of *Nauclea orientalis* (L.) L. bark for the cardioprotective effect. (a) Effect of plant extract on GSH activity of homogenate heart tissues. (b) Effect of plant extract on GPx and GR activity of homogenate heart tissues. (c) Effect of plant extract on SOD and catalase activity of homogenate heart tissues. (d) Effect of plant extract on total antioxidant activity of homogenate heart tissues. (e) Effect of plant extract on lipid peroxidation in the homogenate heart tissues. Group I: control group, group II: *Nauclea orientalis* plant control, group III: Dox control, group IV: rats received *Nauclea orientalis* bark extract + Dox, and group V: positive control (rats received dexrazoxane + Dox). p values $^* < 0.05$, $^{**} < 0.01$, and $^{***} < 0.001$ were considered significant (compared to the Dox control); p values $^a < 0.05$, $^b < 0.01$, and $^c < 0.001$ were considered significant (compared to the control). Each column represents the mean \pm SD ($n = 10$). GSH: reduced glutathione, GPx: glutathione peroxidase, GR: glutathione reductase, SOD: superoxide dismutase, and MDA: malondialdehyde (end product of lipid peroxidation).

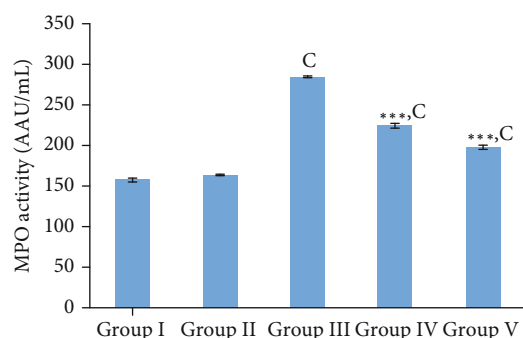


FIGURE 6: Investigation of serum inflammatory marker (MPO activity) in the screening of aqueous extract of *Nauclea orientalis* (L.) L. bark for the cardioprotective effect. Group I: control group, group II: *Nauclea orientalis* plant control, group III: Dox control, group IV: rats received *Nauclea orientalis* bark extract + Dox, and group V: positive control (rats received dexrazoxane + Dox). p values $^* < 0.05$, $^{**} < 0.01$, and $^{***} < 0.001$ were considered significant (compared to the Dox control); p values $^a < 0.05$, $^b < 0.01$, and $^c < 0.001$ were considered significant (compared to the control). Each column represents the mean \pm SD ($n = 10$). MPO: myeloperoxidase.

However, a number of cells with necrotic changes were more visible in the subendocardial region when compared with the peripheral region (Figures 7(a) and 7(b)). Features of cell injury including intracellular vacuoles, congestion of blood vessels, interstitial oedema, haemorrhages, and wavy myocardial fibers (Supplementary data Table 8, Figure 4(d)) were observed in rats of the Dox control group. Pretreatment with the freeze-dried *Nauclea orientalis* bark extract reduced the early changes of necrosis as evident by the lesser number of necrotic cells being visible with a score of 4.5 (Figure 7(c)). However, cells with early changes of necrosis were more noticeable in the subendocardial region. Only a few reversible changes of cell injury including occasional intracellular vacuoles, congestion of blood vessels, and wavy myocardial fibers were observed while interstitial oedema, inflammatory cell infiltrations, and haemorrhages were absent in the rat group which underwent pretreatment with plant extract followed by Dox treatment (Supplementary data Table 8). The plant extract control group (group II) did not show any histological changes in the myocardium and were the same as the control group (Figures 7(a) and 7(b)). The Wistar rats in the positive control group showed well-preserved myocardium with a minimum score in the necrosis scale, and the intracellular vacuoles were observed as the only reversible histological changes of cell injury.

3.5.6. Immunohistochemical Analysis of Inflammatory Markers (TNF α) and Apoptotic Markers (Caspase-3 and Bcl-2). Expression of respective inflammatory and apoptotic markers was visualized in brown colour in immunostained cardiomyocytes. The microscopic appearance of expression of TNF α is shown in Figure 8(a). Expression of TNF α which is an inflammatory marker was absent in the control group of rats and rats treated with *Nauclea orientalis* bark extract (plant control) alone. However, the expression of TNF α was markedly elevated in rats administered with Dox, and

they showed the highest amount of cytokine expression with an average area of expression of 0.85 m² among the experimental groups as shown in Figure 8(b). Pretreatment with lyophilized aqueous *Nauclea orientalis* bark extract in rats treated with Dox showed a considerable ($p < 0.001$) decrease in the expression of TNF α when compared with the Dox control as evident in the reduction of area which expresses the TNF α (Figure 8(b)). Dexrazoxane-treated rats (positive control group) also exhibited a significant decrease ($p < 0.001$) in the expression of TNF α in comparison with the Dox control group.

Caspase-3 is a key protein marker expressed in apoptosis. Microscopic evidence of expression of caspase-3 is shown in Figure 8(c). Expression of caspase-3 was not observed in the control group of rats and rats treated with the plant extract alone. Treatment with Dox (Dox control) markedly increased the level of caspase-3 as shown in Figure 8(d), and this group of rats showed the highest expression of caspase-3 among the study groups which was evident by the highest area (0.37 m²) of expression. Interestingly, pretreatment with aqueous bark extract of *Nauclea orientalis* significantly reduced ($p < 0.001$) the area of expression of caspase-3 protein compared to the Dox control group as shown in Figure 8(d). The positive control group that underwent dexrazoxane treatment showed the lowest level of caspase-3 which was evident by the lowest area of expression.

Bcl-2 is considered an antiapoptotic marker. Figure 8(e) shows the microscopic observations of Bcl-2 expression. Expression of Bcl-2 marker was absent in the control group as well as in the rat group treated only with the aqueous plant extract. A markedly increased level of Bcl-2 marker (average area of expression was 0.24 m²) was observed in the positive control group of rats that were treated with dexrazoxane. On the other hand, the lowest expression of antiapoptotic marker, Bcl-2, was observed in rats treated with Dox alone (Dox control) which was evident with the lowest area (0.03 m²) of expression. However, a significant increase ($p < 0.001$) in Bcl-2 expression was observed in rats pretreated with aqueous bark extract of *Nauclea orientalis* that were exposed to Dox injection compared to the Dox control group as shown in Figure 8(f).

3.5.7. TUNEL Assay. TUNEL assay detects DNA cleavage which is considered an early nuclear change of apoptosis. The microscopic appearance of the TUNEL stained myocardium is shown in Figure 8(g). Some rats in the control group as well as the plant extract control group showed very few numbers of TUNEL-positive nuclei, and the results are shown in Figure 8(h). The Dox control group of rats showed significantly ($p < 0.001$) increased the number of TUNEL-positive nuclei compared to the control group, and the average number of TUNEL-positive nuclei per 10 high-power fields was 59.6. However, pretreatment with lyophilized aqueous bark extract of *Nauclea orientalis* in rats treated with Dox showed a significant reduction ($p < 0.01$) in apoptotic nuclei compared to the Dox control group, and the average number of apoptotic nuclei in 10 high-power fields was 33.8. The positive control group of rats treated with

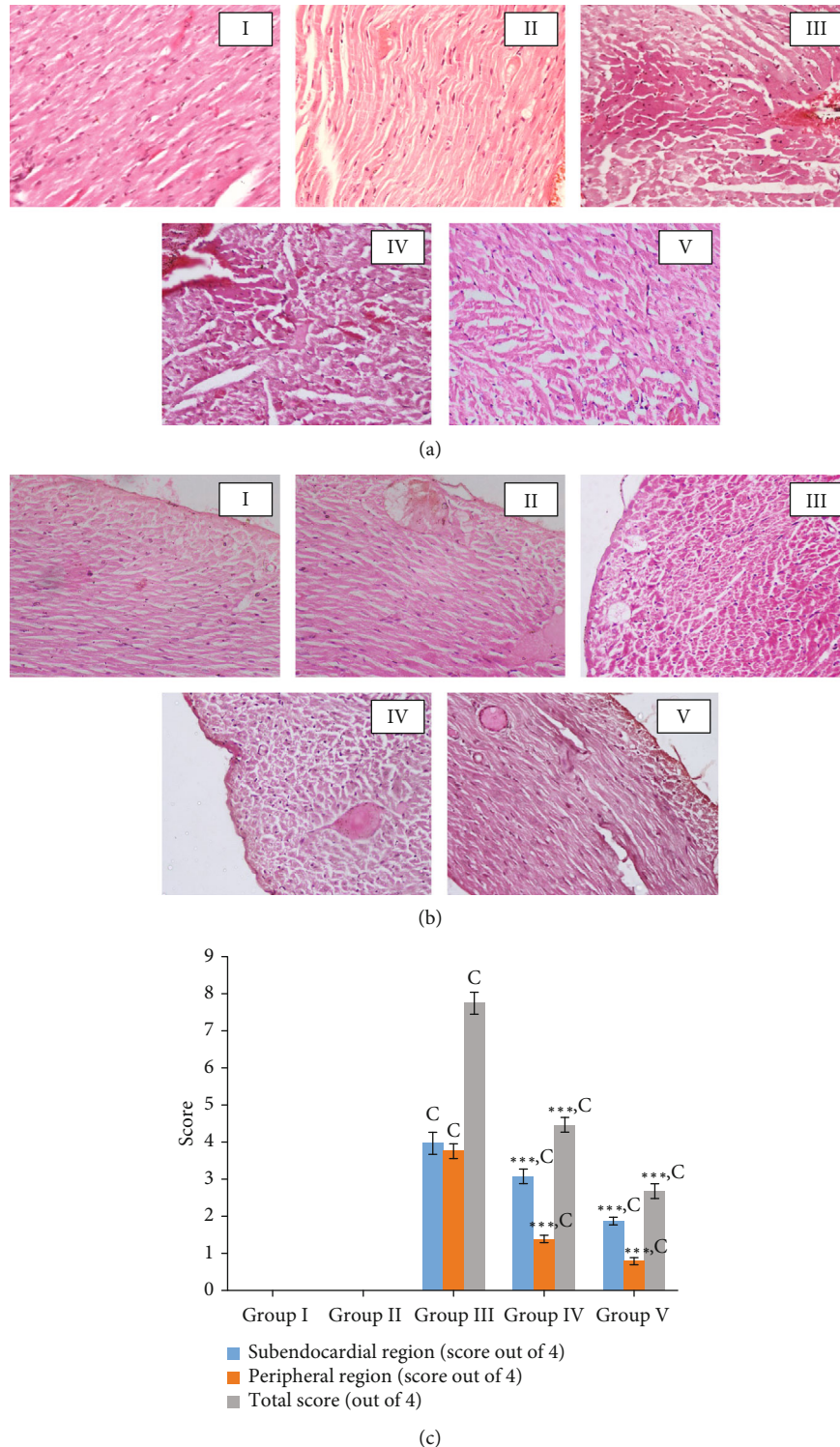


FIGURE 7: Histological investigation in the screening of aqueous extract of *Nauclea orientalis* (L.) L. bark for the cardioprotective effect. (a) Cardiac myocytes with early changes of necrosis in the subendocardial region (H&E, 10×40). (b) Cardiac myocytes with early changes of necrosis in the peripheral region (H&E, 10×40). (c) Average grading of cardiac myocytes with necrotic changes (absence of any myocardial cells with features of necrosis: 0; ≤ 10 myocardial cells with features of necrosis: 1; 11-50 myocardial cells with features of necrosis: 2; 51-100 myocardial cells with features of necrosis: 3; and >100 myocardial cells with features of necrosis: 4). Group I: control group, group II: *Nauclea orientalis* plant control, group III: Dox control, group IV: rats received *Nauclea orientalis* bark extract + Dox, and group V: positive control (rats received dexrazoxane + Dox). p values $^* < 0.05$, $^{**} < 0.01$, and $^{***} < 0.001$ were considered significant (compared to the Dox control); p values $^a < 0.05$, $^b < 0.01$, and $^c < 0.001$ were considered significant (compared to the control). Each column represents the mean \pm SD ($n = 10$).

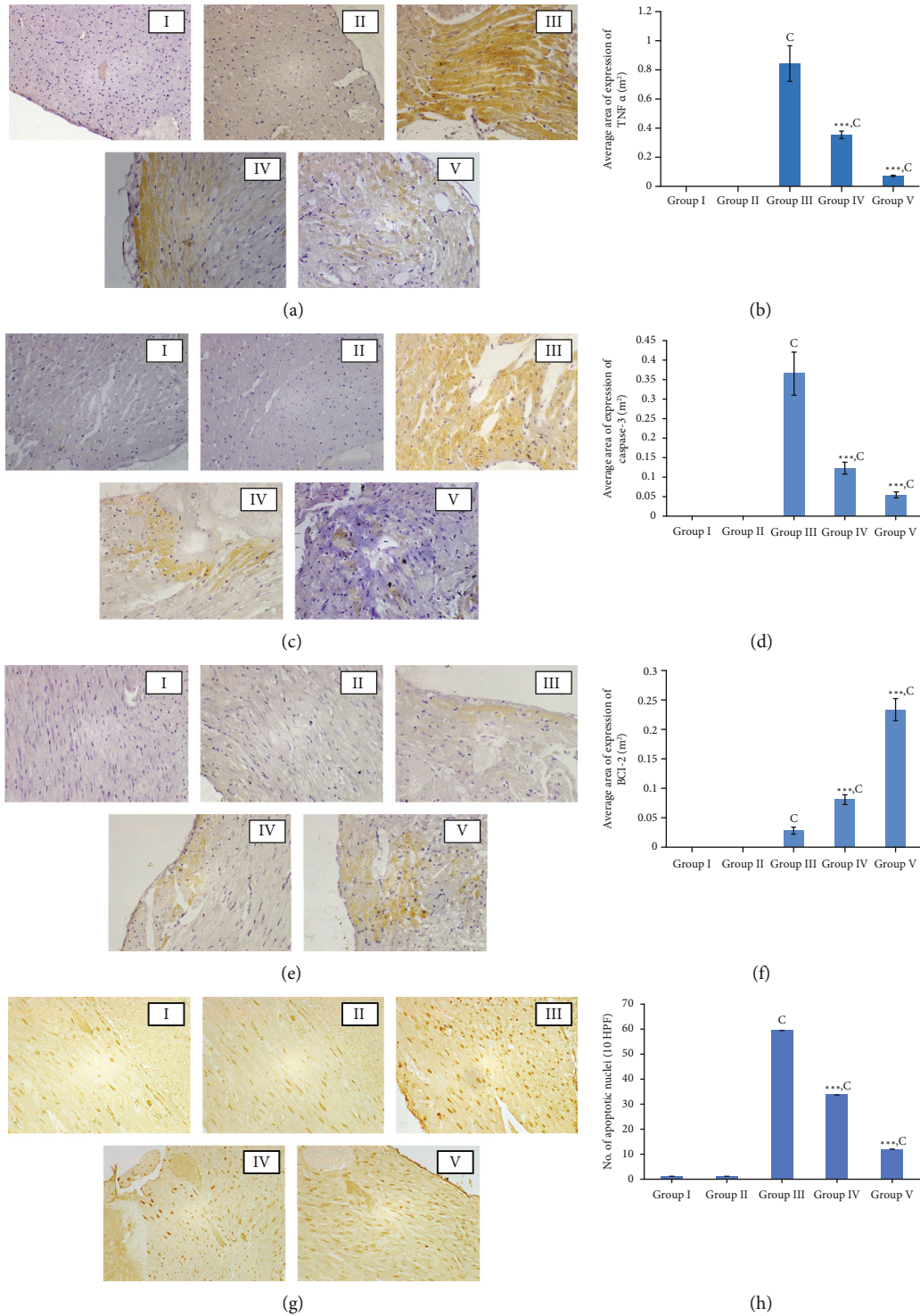


FIGURE 8: Immunohistochemical analysis of inflammatory markers (TNF α) and apoptotic markers (caspase-3 and Bcl-2) and TUNEL assay. (a) Microscopic observation of immunohistochemical analysis of TNF α (10 \times 40). (b) Average area of expression of TNF α in myocardial tissues of rats. (c) Microscopic observation of immunohistochemical analysis of caspase-3 (10 \times 40). (d) Average area of expression of caspase-3 in myocardial tissues of rats. (e) Microscopic observation of immunohistochemical analysis of Bcl-2 (10 \times 40). (f) Average area of expression of Bcl-2 in myocardial tissues of rats. (g) Microscopic analysis of TUNEL-positive nuclei (10 \times 40). (h) Average number of TUNEL-positive nuclei in myocardial tissues of rats. Group I: control group, group II: *Nauclea orientalis* plant control, group III: Dox control, group IV: rats received *Nauclea orientalis* bark extract + Dox, and group V: positive control (rats received dexrazoxane + Dox). *p* values * <0.05 , ** <0.01 , and *** <0.001 were considered significant (compared to the Dox control); *p* values ^a <0.05 , ^b <0.01 , and ^c <0.001 were considered significant (compared to the control). Each column represents the mean \pm SD (*n* = 10). TNF α : tumour necrosis factor α , Bcl-2: B-cell lymphoma 2, and TUNEL: terminal deoxynucleotidyl transferase dUTP nick-end labelling.

dexrazoxane also showed a significant reduction ($p < 0.001$) in the number of apoptotic nuclei compared to the Dox control group.

4. Discussion

Dox, the most potent anthracycline chemotherapeutic agent, exhibits acute and chronic cardiotoxicity which leads to left ventricular dysfunction and subsequent heart failure [28]. A solid body of evidence suggests that oxidative stress, inflammation, and apoptosis are main mechanisms involved in the pathogenesis of Dox-induced cardiotoxicity [29].

The molecular mechanism of cardiotoxicity is multifactorial, and the most accepted mechanism is the generation of ROS related to oxidative stress [5]. Due to the importance of oxidative stress in the occurrence of Dox-induced cardiotoxicity, strategies that are capable of reducing oxidative stress have been identified as effective approaches to prevent cardiotoxicity [7]. Based on this, combination therapies of drugs with antioxidants have been investigated in many studies. Therefore, in the present study, a medicinal plant which showed a higher antioxidant activity was selected to be screened against Dox-induced cardiotoxicity.

Although oxidative stress plays a major role in the pathogenesis of Dox-induced cardiotoxicity, Dox-induced inflammatory effects on the myocardium and the vasculature are mediated through the upregulation of NF- κ B expression [30]. Furthermore, there is accumulated evidence to suggest that mechanisms of programmed cell death, such as apoptosis which is characterized by nuclear and chromosomal DNA fragmentation, cell shrinkage, and blebbing as well as autophagy, also play an important role in the pathogenesis of cardiotoxicity [30, 31]. Therefore, assessment of markers for cardiac damage, oxidative stress, inflammation, apoptosis, and DNA fragmentation is important in the diagnosis of anthracycline-induced cardiotoxicity as well as in the determination of mechanism of action of therapeutic interventions used against them. In this study, we determined the effect of the aqueous bark extract of *Nauclea orientalis* on the oxidative stress, inflammation, apoptosis, and DNA fragmentation induced by the administration of Dox in Wistar rats.

According to the recommendations given in OECD guidelines to perform limit tests, a higher dose of 2.0 g/kg must be used to investigate the acute and subchronic toxicity of plant extracts [22, 23]. Previous studies have revealed that severe growth depression may occur due to reduced food intake which is a common phenomenon if plant extracts are toxic to the experimental animals [32]. In this study, in addition to the absence of any signs of acute toxicity, the consumption of food and intake of water were not changed between the control and treatment groups suggesting that this plant extract neither induced nor suppressed appetite in healthy rats. Further, a significant difference was not observed in the body weights of the test group compared to the control group. The analysis of biochemical and haematological parameters is also relevant for the evaluation of risk as they are widely used as predictors of toxicity of medicinal plant extracts to humans and animals [32]. The

rat group treated with *Nauclea orientalis* bark extract did not show any significant changes in haematological parameters, liver function, and kidney function parameters suggesting that subchronic administration of plant extract had no toxic effects in Wistar rats. The histological assessment of the body tissues is considered the gold standard for the evaluation of treatment-related pathological changes in different tissues [33]. The microscopic examination of organs including the heart, kidneys, lungs, liver, small intestine, and spleen did not show any alterations in cell structure or any unfavourable effects when viewed under the light microscope using multiple magnifications confirming the non-toxic effect of *Nauclea orientalis* bark extract.

It is already proven that oxidative stress is the major cause of cardiotoxicity, and cardiomyocytes are more prone to this damage if their antioxidant defence mechanism is compromised [27, 34, 35]. Further, it is proven that supplementation of an exogenous antioxidant provides protection against cardiac injury. Therefore, *Nauclea orientalis* bark extract was screened for the potential cardioprotective effects against Dox-induced cardiotoxicity *in vivo*. Cardiotoxicity induced by Dox is manifested by increased activities of cTnI, NT-pro BNP, AST, and LDH which are released from damaged cardiomyocytes in response to the degree of cardiac injury, ischaemia, and infarction [34]. In the present study, it was revealed that *Nauclea orientalis* bark extract has the potential to significantly reduce the cardiac biomarkers increased in response to Dox administration suggesting that it is an effective approach to attenuate Dox-induced cardiotoxicity. Consistent with our results, a study done by Sergazy et al. has shown that Dox causes increased activity of AST and cardiac troponin T, and administration of grape polyphenol concentrate significantly reduced the release of these two parameters [36]. Another study done by El-Sayed et al. has shown that serum creatine kinase-MB activity and LDH activity increased with Dox treatment in rats, and *Curcuma longa* L. extract which has an antioxidant effect had the ability to significantly reduce the two cardiac biomarkers [37]. Afsar et al. also corroborated our results showing that *Acacia hydasypica* R. Parker significantly reduced the AST, LDH, and creatine kinase-MB activities which were increased by Dox treatment [34].

Elevated level of lipid peroxidation and alterations in the enzymatic and nonenzymatic antioxidant systems are considered the signs of oxidative stress induced by Dox [38]. GSH, GPx, GR, SOD, and catalase are the common antioxidant compounds found in tissues which protect tissues from oxidative stress injury. GSH is the most abundant intracellular antioxidant molecule, and the deficiency of GSH observed in the Dox-treated group could be due to the consumption of GSH during the interaction between Dox-induced free radicals with biological membranes, macromolecules, and subsequent lipid peroxidation [39]. In the present study, oxidative damage was observed in the Dox control group as shown by the markedly elevated MDA concentration and reduced GSH, GPx, GR, catalase, and SOD levels, but the aqueous *Nauclea* bark extract could significantly increase all antioxidant enzyme activities in plant extract-treated group suggesting its high antioxidant activity.

According to the results of the present study, important phytochemicals such as polyphenols, alkaloids, and tannins were present in the *Nauclea orientalis* bark while toxic phytochemicals were absent. It was already reported that plants with high polyphenol content have significant antioxidant activity [40]. Results of this study also revealed that the *Nauclea orientalis* bark has a considerable polyphenol content which may have contributed to its antioxidant activity. A previous study conducted in Sri Lanka also reported that the aqueous extract of *Nauclea orientalis* bark extract possesses high antioxidant activity which corroborates the results obtained in our study [33]. A study done by Gnana-Pragasam et al. also confirmed this mechanism showing that *Centella asiatica* which has high antioxidant activity has the ability to significantly increase GSH and GPx activities in heart tissues after the administration of Dox [41]. SOD and catalase are also important antioxidant enzymes in the first-line defence mechanism which protect the biological systems from oxidative stress damages [42]. Dox treatment causes depletion of these enzyme activities as it produces many oxygen radicals [40]. A study done by Liu et al. reported that *Panax notoginseng* has a significant effect on the increase of SOD and catalase activities in mice injected with Dox [43]. Hence, results reported in many other studies are consistent with that of the present study as they have also shown that natural compounds with high antioxidant activities have the potential to attenuate Dox-induced cardiotoxicity [27, 35–38]. The formation of ROS in Dox metabolism can cause lipid peroxidation of the cell membrane which can increase the MDA concentration in the myocardial tissues [44]. A study done by Singh et al. also showed that administration of Dox causes significant increase in MDA concentration, and the aqueous extract of *Terminalia arjuna* bark which has significant antioxidant effect greatly reduced the lipid peroxidation which was evident by the low MDA concentration reported [35]. Several other studies have also confirmed the results reported by Singh et al. [27, 36–38]. The results of the present study were also in line with the above test results showing that *Nauclea orientalis* bark extract also has a significant capacity to reduce MDA production subsequent to Dox administration and could be an effective approach to reduce cardiotoxicity induced by Dox.

Histopathological evidence of cellular necrosis is considered the gold standard in the identification of Dox-induced cardiotoxicity in rodents [3, 45]. In the present study, the aqueous extract of the *Nauclea orientalis* bark significantly decreased the histological changes such as necrosis, intracellular vacuoles, congestion of blood vessels, and wavy myocardial fibers while histological changes including haemorrhages, oedema, and inflammatory infiltrations were completely absent in the plant-treated group indicating its cardioprotective activity. Consistent with our findings, a previous study done by Sun et al. also showed that myocardial fibrosis and necrosis are evident after the administration of Dox [46]. Further, Sun et al. showed that scutellarin, which has an antioxidant effect, significantly reduced the histological changes of myocardial damage [46]. Another study done by Zang et al. also showed that an antioxidant compound, oxymatrine, effectively reduced the histological changes such

as necrosis, intracellular oedema, damaged mitochondria, and wavy cardiac fibers in Dox-treated rats [47]. Iqbal et al. reported that telmisartan attenuated the histological changes including focal necrosis, oedema, haemorrhage, and congestions in rat heart induced by a single dose of Dox [48].

Dox-induced cardiotoxicity is a multimolecular mechanism which is mainly led by oxidative stress, inflammation, and apoptosis. Previous studies reported that Dox-induced cardiotoxicity is initiated by the production of ROS. As Dox enters the body, it binds tightly to cardiolipin which is located in the inner mitochondrial membrane and accumulates in mitochondria. This affects the synthesis of ROS and reactive nitrogen species via the electron transport chain which subsequently cause mitochondrial and cellular membrane damage and diminished antioxidant defence system leading to cellular apoptosis [49]. Mitochondrial damage also initiates an imbalance in the intracellular Ca^{2+} concentration, which further affects the apoptosis pathways causing myocardial cell death [50]. Because of this molecular mechanism, it is expected that the use of plant extract which has a high antioxidant effect is capable of attenuating the apoptosis in cardiac tissues without obstructing the anticancer effect of Dox mainly led by DNA intercalation [5].

Dox-induced myocytic necrosis evokes an inflammatory response in the cardiac tissues by upregulating the expression of NF- κ B signalling which increases the secretion of inflammatory cytokines including TNF α , interleukin 1 β , and interleukins 6 and 8. These cytokines subsequently cause profound pathological alterations which lead to cardiomyopathy [29]. Therefore, to investigate some of these mechanisms further, inflammatory markers were analysed where MPO activity was estimated in the serum, and the immunohistochemical analysis of TNF α was performed in the myocardial tissues. The results of the present study showed a significant reduction in the serum inflammatory marker, MPO, and expression of TNF α in myocardial tissues suggesting that *Nauclea orientalis* bark may also have significant anti-inflammatory activities. Consistent with the results obtained in this study, the study done by Zhang et al. showed that Dox treatment increases the inflammatory mediators including TNF α and interleukin 6 (IL-6) in the serum of mice, and injection of “shenmai” which is composed of *Panax ginseng* and *Ophiopogon japonicus* (Thunb.) suppressed the expression of TNF α and IL-6 [50]. Other studies done by Hijazi et al. and Hamza et al. also showed similar results [51, 52]. Programmed cell death, apoptosis, also plays a major role in Dox-induced cardiotoxicity which increases the cytochrome c, Bax expression, and caspase-3 activity [49]. Dox reduces the expression of Bcl-2, a major antiapoptotic protein which inhibits apoptosis for the protection of structure and function of mitochondria. In the present study, the TUNEL assay was performed to detect DNA fragmentation that results in apoptosis, and immunohistochemical markers for caspase-3 and Bcl-2 were used to identify involvement of apoptosis in Dox-induced cardiotoxicity. The TUNEL assay identifies DNA fragments which result in apoptosis [46]. Although DNA fragmentation is not specific to apoptosis as it occurs in necrosis as well, the use of

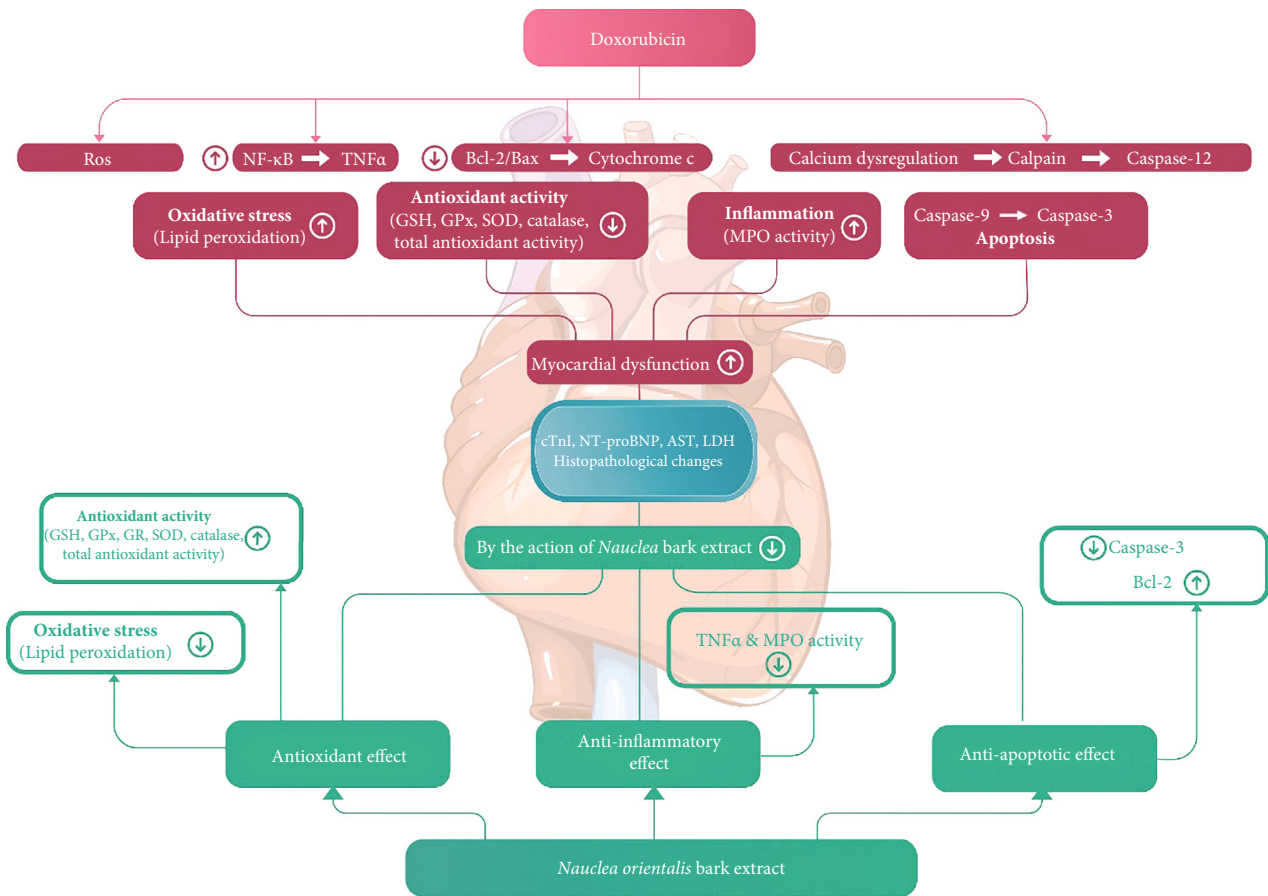


FIGURE 9: Schematic representation of cardioprotective effect of *Nauclea orientalis* bark extract.

TUNEL assay together with the upregulation of caspase-3 and downregulation of Bcl-2 which are known markers of apoptosis provides evidence for the presence of apoptosis [53]. In the present study, the Dox control group showed a marked elevation of TUNEL-positive nuclei, and the expression of caspase-3 and reduction in Bcl-2 expression compared to the control group confirmed the presence of apoptosis in Dox-treated rats. Pretreatment with aqueous extract of *Nauclea orientalis* bark showed a significant reduction in caspase-3 activity and TUNEL-positive nuclei as well as an elevation in expression of Bcl-2 marker showing that *Nauclea* bark may also have an antiapoptotic effect. Previous study done by Zhang et al. corroborated the results obtained in our study and has shown that luteolin which is a flavonoid found in vegetables and fruits attenuates the Dox-induced cardiotoxicity by upregulating the AKT/Bcl-2 pathway [54]. Several other studies also showed that natural compounds with antioxidant and antiapoptotic effects have the ability to attenuate Dox-induced cardiotoxicity [27, 55–58].

In the present study, dexrazoxane was used as the positive control as it is the only cardioprotective drug approved by the FDA for the prevention of anthracycline-induced cardiotoxicity [59]. However, when the results of the rat group treated with the plant extract were compared with the positive control, a significant difference ($p < 0.05$) was observed.

This may be due to the differences in the mechanisms of action triggered by the active constituents in the plant extract and dexrazoxane to attenuate Dox-induced cardiotoxicity. Although the mechanism of dexrazoxane is not completely understood, numerous studies have proven that it is due to iron chelation which decreases the generation of ROS [60, 61]. But, in the present study, we assume that the cardioprotective effect of *Nauclea orientalis* bark is due to the replenishment of cardiomyocytes with antioxidants provided by the plant.

In the present study, cardiac biomarkers were analysed to detect the structural abnormalities in the heart of Wistar rats. However, cardiac function tests such as ECG analysis and echocardiography analysis could not be performed due to limited resources, and it is considered a limitation of this study.

In summary, as shown in Figure 9, formation of ROS during Dox metabolism induces the oxidative stress and also upregulates the inflammatory and apoptotic pathways in myocardial tissues. However, *Nauclea orientalis* bark extract which has high antioxidant activity significantly reduced the oxidative stress in the cardiac tissues. The current study also provided evidence that the *Nauclea orientalis* bark extract protected the cardiomyocytes of Wistar rats against Dox-induced cardiotoxicity via a synergistic effect through the suppression of oxidative stress, inflammation, and apoptosis.

5. Conclusion

In conclusion, administration of standardized aqueous bark extract of *Nauclea orientalis* (2.0 g/kg) attenuated the Dox-induced oxidative stress, inflammation, apoptosis, and DNA fragmentation, and it has the potential to be developed as an adjunct against Dox-induced cardiotoxicity in cancer patients who undergo anthracycline chemotherapy.

Data Availability

The datasets used and/or analysed during the current study are available from the corresponding author on reasonable request.

Conflicts of Interest

The authors declare that there is no conflict of interest regarding the publication of this paper.

Acknowledgments

This work was supported by the National Research Council of Sri Lanka (grant No.: 18-050) and University Grant Commission (UGC) (UGC/VC/DRIC/PG2015(III)/RUH/01). Mr. G.H.J.M. Priyashantha and Mr. E.G. Rukman Asiri of the Department of Biochemistry, Faculty of Medicine, University of Ruhuna, Galle, Sri Lanka, are acknowledged for their assistance in the animal house.

Supplementary Materials

Table S1: physicochemical properties and phytochemical analysis of *Nauclea orientalis* bark. Table S2: total polyphenol content and the in vitro antioxidant activity of aqueous bark extract of *Nauclea orientalis* (L.) L. bark. Table S3: dose-response effect on reversible histological changes of cardiac tissues of Wistar rats exposed to different doses of *Nauclea orientalis* bark extracts. Table S4: effect of subchronic oral administration of *Nauclea orientalis* (L.) L. aqueous bark extract on the average body weight of rats. Table S5: effect of subchronic oral administration of *Nauclea orientalis* (L.) L. aqueous bark extract on haematological parameters of rats. Table S6: effect of subchronic oral administration of *Nauclea orientalis* (L.) L. aqueous bark extract on biochemical parameters of rats. Table S7: effect of subchronic oral administration of *Nauclea orientalis* (L.) L. aqueous bark extract on absolute and relative organ weight of rats. Table S8: screening of *Nauclea orientalis* (L.) L. aqueous bark extract for cardioprotective effect: histological assessment of reversible histological changes. Figure S1: histological investigation of the effect of subchronic oral administration of *Nauclea orientalis* bark extract in Wistar rats (H&E, 10 × 10). (a) Histological investigation in the control group of rats, (b) histological investigation in the rat group treated with *Nauclea orientalis* bark extract. i: Heart tissue, ii: kidney tissue, iii: liver tissue, iv: lung tissue, v: small intestine tissue, and vi: spleen tissue. (*Supplementary Materials*)

References

- [1] J. V. McGowan, R. Chung, A. Maulik, I. Piotrowska, J. M. Walker, and D. M. Yellon, "Anthracycline chemotherapy and cardiotoxicity," *Cardiovascular Drugs and Therapy*, vol. 31, no. 1, pp. 63–75, 2017.
- [2] E. Sadurska, "Current views on anthracycline cardiotoxicity in childhood cancer survivors," *Pediatric Cardiology*, vol. 36, pp. 1112–1119, 2015.
- [3] M. Volkova and R. Russell, "Anthracycline cardiotoxicity: prevalence, pathogenesis and treatment," *Current Cardiology Reviews*, vol. 7, no. 4, pp. 214–220, 2011.
- [4] D. S. dos Santos and R. C. dos Santos Goldenberg, "Doxorubicin-Induced cardiotoxicity: from mechanisms to development of efficient therapy," *Intech Open*, 2018.
- [5] M. Mobaraki, A. Faraji, M. Zare, P. Dolati, M. Ataei, and H. R. D. Manshadi, "Molecular mechanisms of cardiotoxicity: a review on major side-effect of Dox," *Indian Journal of Pharmaceutical Sciences*, vol. 79, no. 3, pp. 335–344, 2017.
- [6] M. A. Mitry and J. G. Edwards, "Dox induced heart failure: phenotype and molecular mechanisms," *International Journal Cardiology Heart & Vasculature*, vol. 10, pp. 17–24, 2016.
- [7] V. M. Torres and V. D. Simic, "Dox-induced oxidative injury of cardiomyocytes – do we have right strategies for prevention?," *Intech Open*, 2012.
- [8] J. Shi, E. Abdelwahid, and L. Wei, "Apoptosis in anthracycline cardiomyopathy," *Current Paediatric Reviews*, vol. 7, no. 4, pp. 329–336, 2011.
- [9] S. T. V. Raghavamma, N. R. Rao, K. R. S. S. S. Rao, and G. D. Rao, "In Vitro antioxidant potential of crude extract from leaves of *Nauclea orientalis* Linn," *Journal of Pharmacy Research*, vol. 4, no. 5, pp. 1548–1549, 2011.
- [10] P. T. A. Daoa, T. L. Quanb, and N. T. T. Maib, "Constituents of the stem of *Nauclea orientalis*," *Natural Product Communications*, vol. 10, no. 11, pp. 1901–1903, 2015.
- [11] D. M. A. Jayaweera, *Medicinal Plants (Indigenous and Exotic) Used in Ceylon*, National Science Foundation in Sri Lanka, Sri Lanka, 1982.
- [12] World Health Organization, *Guidelines for the Assessment of Herbal Medicines*, WHO Technical Report Series, World Health Organization, Geneva, 1996, https://www.who.int/traditional-complementary-integrative-medicine/publications/trs1010_annex2.pdf?ua=1.
- [13] World Health Organization, *Quality Control Methods for Herbal Materials*, WHO Press, World Health Organization, Geneva, Switzerland, 2011, https://apps.who.int/iris/bitstream/handle/10665/44479/9789241500739_eng.pdf;jsessionid=698837D8E9627AA38A9A831738FC6F95?sequence=1.
- [14] G. E. Trease and W. C. Evans, *Pharmacognosy*, Bailliere Tindall Ltd, London, 16th edition, 2009.
- [15] A. Mushtaq, S. Akbar, M. A. Zargar et al., "Phytochemical screening, physicochemical properties, acute toxicity testing and screening of hypoglycaemic activity of extracts of *Eremurus himalaicus* baker in normoglycaemic Wistar strain albino rats," *BioMed Research International*, vol. 2014, 2014.
- [16] V. L. Singleton, R. Ortofer, and R. M. Lamuda-raventos, "Analysis of total phenols and other oxidation substrates and antioxidants by means of Folin-Ciocalteu reagent," *Methods in Enzymology*, vol. 299, pp. 152–178, 1999.

- [17] M. A. R. Bhuiyan, M. Z. Hoque, and S. J. Hossain, "Free radical scavenging activities of *Zizyphus mauritiana*," *World Journal of Agricultural Sciences*, vol. 5, no. 3, pp. 318–322, 2009.
- [18] F. Boora, E. Chirisa, and S. Mukanganyama, "Evaluation of nitrite radical scavenging properties of selected Zimbabwean plant extracts and their phytoconstituents," *Journal of Food Processing*, vol. 2014, 2014.
- [19] M. Zahin, F. Aqil, F. M. Husain, and I. Ahmad, "Antioxidant capacity and antimutagenic potential of *Murraya koenigii*," *BioMed Research International*, vol. 2013, Article ID 263509, 2013.
- [20] Council for International Organizations of Medical Sciences (CIOMS) and The International Council for Laboratory Animal Science, *International Guiding Principles for Biomedical Research Involving Animals (1985)*, 2012, https://grants.nih.gov/grants/olaw/guiding_principles_2012.pdf.
- [21] Organization of Economic Co-operation and Development (OECD), *Test No. 423: Acute Oral Toxicity—Acute Toxic Class Method, OECD Guidelines for the Testing of Chemicals, Section 4*, OECD Publishing, Paris, doi, 2002.
- [22] Organization of Economic Co-operation and Development (OECD), *Test No. 407: Repeated Dose 28-Day Oral Toxicity Study in Rodents, OECD Guidelines for the Testing of Chemicals, Section 4*, OECD Publishing, Paris, 2008.
- [23] J. A. N. Sandamali, R. P. Hewawasam, K. A. P. W. Jayatilaka, and L. K. B. Mudduwa, "Cardioprotective potential of *Murraya koenigii*(L.) Spreng. leaf extract against Doxorubicin-Induced cardiotoxicity in rats," *Evidence Based Complementary and Alternative Medicine*, vol. 2020, pp. 1–16, 2020.
- [24] S. C. Williams, M. A. Linske, and K. C. Stafford, "Humane use of cardiac puncture for non-terminal phlebotomy of wild-caught and released *Peromyscus* spp.," *Animals*, vol. 10, no. 5, p. 826, 2020.
- [25] S. Bulut, H. Uslu, B. H. Özdemir, and O. E. Bulut, "Expression of caspase-3, p53 and Bcl-2 in generalized aggressive periodontitis," *Head & Face Medicine*, vol. 2, no. 1, 2006.
- [26] T. J. Collins, "ImageJ for microscopy," *BioTechniques*, vol. 43, no. 1S, pp. S25–S30, 2007.
- [27] A. Hamza, A. Amin, and S. Daoud, "The protective effect of a purified extract of *Withania somnifera* against doxorubicin-induced cardiac toxicity in rats," *Cell Biology and Toxicology*, vol. 24, no. 1, pp. 63–73, 2008.
- [28] W. Zhu, M. H. Soonpaa, H. Chen et al., "Acute Doxorubicin cardiotoxicity is associated with p53-induced inhibition of the mammalian target of rapamycin pathway," *Circulation*, vol. 119, no. 1, pp. 99–106, 2009.
- [29] E. M. Mantawy, W. M. El-Bakly, A. Esmat, A. M. Badr, and E. El-Demerdash, "Chrysin alleviates acute doxorubicin cardiotoxicity in rats via suppression of oxidative stress, inflammation and apoptosis," *European Journal of Pharmacology*, vol. 728, pp. 107–118, 2014.
- [30] Y. Gao, Y. Xu, S. Hua, S. Zhou, and K. Wang, "ALDH2 attenuates Dox-induced cardiotoxicity by inhibiting cardiac apoptosis and oxidative stress," *International Journal of Clinical and Experimental Medicine*, vol. 8, no. 5, pp. 6794–6803, 2015.
- [31] O. Tacar, S. Indumathy, M. L. Tan, S. Baidur-Hudson, A. M. Friedhuber, and C. R. Dass, "Cardiomyocyte apoptosis vs autophagy with prolonged Dox treatment: comparison with osteosarcoma cells," *Journal of Pharmacy and Pharmacology*, vol. 67, no. 2, pp. 231–243, 2015.
- [32] R. P. Hewawasam, K. A. P. W. Jayatilaka, L. K. B. Mudduwa, and C. Pathirana, "Toxicological evaluation of five Sri Lankan medicinal plants: a biochemical, haematological and histopathological assessment," *International Journal of Pharmaceutical Sciences and Research*, vol. 7, no. 10, pp. 4014–4021, 2016.
- [33] A. P. Attanayaka and K. A. P. W. Jayatilaka, "Evaluation of antioxidant properties of 20 medicinal plant extracts traditionally used in Ayurvedic medicine in Sri Lanka," *Indian Journal of Traditional Knowledge*, vol. 15, pp. 50–56, 2016.
- [34] T. Afsar, S. Razak, K. M. Batoo, and M. R. Khan, "Acacia hydaspica R. Parker prevents doxorubicin-induced cardiac injury by attenuation of oxidative stress and structural cardiomyocyte alterations in rats," *BMC Complementary and Alternative Medicine*, vol. 17, no. 1, 2017.
- [35] G. Singh, A. T. Singh, A. Abraham et al., "Protective effects of *Terminalia arjuna* against Doxorubicin-induced cardiotoxicity," *Journal of Ethnopharmacology*, vol. 117, no. 1, pp. 123–129, 2008.
- [36] S. Sergazy, Z. Shulgau, G. Fedotovskikh et al., "Cardioprotective effect of grape polyphenol extract against Dox induced cardiotoxicity," *Scientific Reports*, vol. 10, no. 1, p. 14720, 2020.
- [37] E. M. El-Sayed, A. S. A. El-azeem, A. A. Afify, M. H. Shabana, and H. H. Ahmed, "Cardioprotective effects of *Curcuma longa* L. extracts against Dox-induced cardiotoxicity in rats," *Journal of Medicinal Plants Research*, vol. 5, no. 17, pp. 4049–4058, 2011.
- [38] G. Khan, S. E. Haque, T. Anwer, M. N. Ahsan, M. M. Safhi, and M. F. Alam, "Cardioprotective effect of green tea extract on Dox-induced cardiotoxicity in rats," *Acta Poloniae Pharmaceutica-Drug Research*, vol. 71, no. 5, pp. 861–868, 2014.
- [39] Z. X. Du, H. Y. Zhang, X. Meng, Y. Guan, and H. Q. Wang, "Role of oxidative stress and intracellular glutathione in the sensitivity to apoptosis induced by proteasome inhibitor in thyroid cancer cells," *BMC Cancer*, vol. 9, 2009.
- [40] N. Saeed, M. R. Khan, and M. Shabbir, "Antioxidant activity, total phenolic and total flavonoid contents of whole plant extracts *Torilis leptophylla* L.," *BMC Complementary and Alternative Medicine*, vol. 12, 2012.
- [41] A. Gnanapragasam, S. Yogeeta, R. Subhashini, K. K. Ebenezer, V. Sathish, and T. Devaki, "Adriamycin induced myocardial failure in rats: protective role of *Centella asiatica*," *Molecular and Cellular Biochemistry*, vol. 294, no. 1-2, pp. 55–63, 2007.
- [42] O. M. Ighodaro and O. A. Akinloye, "First line defence antioxidants-superoxide dismutase (SOD), catalase (CAT) and glutathione peroxidase (GPX): their fundamental role in the entire antioxidant defence grid," *Alexandria Journal of Medicine*, vol. 54, no. 4, pp. 287–293, 2018.
- [43] L. Liu, R. Shi, Q. Shi, Y. Cheng, and Y. Huo, "Protective effect of saponins from *Panax notoginseng* against Dox-induced cardiotoxicity in mice," *Planta Medica*, vol. 74, no. 3, pp. 203–209, 2008.
- [44] S. Hrelia, D. Fiorentini, T. Maraldi et al., "Doxorubicin induces early lipid peroxidation associated with changes in glucose transport in cultured cardiomyocytes," *Biochimica et Biophysica Acta*, vol. 1567, no. 1-2, pp. 150–156, 2002.
- [45] J. Dudka, R. Gieroba, A. Korga et al., "Different effects of resveratrol on dose-related Dox-induced heart and liver toxicity," *Evidence-based Complementary and Alternative Medicine*, vol. 2012, Article ID 606183, 2012.
- [46] X. P. Sun, L. L. Wan, Q. J. Yang, Y. Huo, Y. L. Han, and C. Guo, "Scutellarin protects against Dox-induced acute cardiotoxicity and regulates its accumulation in the heart," *Archives of Pharmacal Research*, vol. 40, no. 7, pp. 875–883, 2017.

- [47] Y. Y. Zhang, M. Yi, and Y. P. Huang, "Oxymatrine ameliorates Doxorubicin-Induced cardiotoxicity in rats," *Cellular Physiology and Biochemistry*, vol. 43, no. 2, pp. 626–635, 2017.
- [48] M. Iqbal, K. Dubey, T. Anwer, A. Ashish, and K. K. Pillai, "Protective effects of telmisartan against acute Dox-induced cardiotoxicity in rats," *Pharmacological Reports*, vol. 60, no. 3, pp. 382–390, 2008.
- [49] L. Guo, X. Zheng, E. Wang, X. Jia, G. Wang, and J. Wen, "Iri-genin treatment alleviates Dox (Dox)-induced cardiotoxicity by suppressing apoptosis, inflammation and oxidative stress via the increase of miR-425," *Biomedicine & Pharmacotherapy*, vol. 125, article 109784, 2020.
- [50] S. Zhang, Z. You, L. Yang et al., "Protective effect of Shenmai injection on Dox-induced cardiotoxicity via regulation of inflammatory mediators," *BMC Complementary and Alternative Medicine*, vol. 19, 2019.
- [51] M. A. Hijazi, H. A. Jambi, B. M. Aljehany, and M. A. Althai-ban, "Potential protective effect of *Achillea fragrantissima* against adriamycin-induced cardiotoxicity in rats via an anti-oxidant and anti-inflammatory pathway," *BioMed Research International*, vol. 2019, Article ID 5269074, 2019.
- [52] A. A. Hamza, M. M. Ahmed, H. M. Elwey, and A. Amin, "Melissa officinalis protects against Dox-induced cardiotoxi-city in rats and potentiates its anticancer activity on MCF-7 cells," *Plo S One*, vol. 11, no. 11, 2016.
- [53] A. Saraste and K. Pulkki, "Morphologic and biochemical hall-marks of apoptosis," *Cardiovascular Research*, vol. 45, no. 3, pp. 528–537, 2000.
- [54] Y. Zhang, C. Ma, C. Liu, and F. Wei, "Luteolin attenuates Dox-induced cardiotoxicity by modulating the PHLPP1/AKT/Bcl-2 signalling pathway," *PeerJ*, vol. 8, 2020.
- [55] M. Ueno, Y. Kakinuma, K. Yuhki et al., "Doxorubicin induces apoptosis by activation of caspase-3 in cultured cardiomyo-cytes in vitro and rat cardiac ventricles in vivo," *Journal of Pharmacological Sciences*, vol. 101, no. 2, pp. 151–158, 2006.
- [56] X. Yu, L. Cui, Z. Zhang, Q. Zhao, and S. Li, "Linolenic acid attenuates doxorubicin-induced cardiotoxicity in rats through suppression of oxidative stress and apoptosis," *Acta Biochi-mica et Biophysica Sinica*, vol. 45, no. 10, pp. 817–826, 2013.
- [57] X. Jiang, Y. Hong, D. Zhao et al., "Low dose radiation prevents Dox-induced cardiotoxicity," *Oncotarget*, vol. 9, no. 1, pp. 332–345, 2017.
- [58] J. X. Xue, X. Q. Zhang, W. H. Bian, and C. Yao, "Alleviation of Dox-induced cardiotoxicity by Hong Huang decoction may involve a reduction in myocardial oxidative stress and activa-tion of Akt/FoxO3a pathways," *International Journal of Clinical and Experimental Medicine*, vol. 11, no. 10, pp. 10574–10584, 2018.
- [59] X. Yu, Y. Ruan, T. Shen, Q. Qiu, M. Yan, and S. Sun, "Dexra-zoxane protects cardiomyocyte from doxorubicin-induced apoptosis by modulating miR-17-5p," *BioMed Research Inter-national*, vol. 2020, 2020.
- [60] B. Chen, X. Peng, L. Pentassuglia, C. C. Lim, and D. B. Sawyer, "Molecular and cellular mechanisms of anthracycline cardio-toxicity," *Cardiovascular Toxicology*, vol. 7, no. 2, pp. 114–121, 2007.
- [61] L. Zhou, R. Y. T. Sung, K. Li, N. H. Pong, P. Xiang, and J. Shen, "Cardioprotective effect of dexrazoxane in a rat model of myo-cardial infarction: anti-apoptosis and promoting angiogene-sis," *International Journal of Cardiology*, vol. 152, no. 2, pp. 196–201, 2011.

Retraction

Retracted: Ginsenoside Rg3 Alleviates Antithyroid Cancer Drug Vandetanib-Induced QT Interval Prolongation

Oxidative Medicine and Cellular Longevity

Received 26 December 2023; Accepted 26 December 2023; Published 29 December 2023

Copyright © 2023 Oxidative Medicine and Cellular Longevity. This is an open access article distributed under the Creative Commons Attribution License, which permits unrestricted use, distribution, and reproduction in any medium, provided the original work is properly cited.

This article has been retracted by Hindawi, as publisher, following an investigation undertaken by the publisher [1]. This investigation has uncovered evidence of systematic manipulation of the publication and peer-review process. We cannot, therefore, vouch for the reliability or integrity of this article.

Please note that this notice is intended solely to alert readers that the peer-review process of this article has been compromised.

Wiley and Hindawi regret that the usual quality checks did not identify these issues before publication and have since put additional measures in place to safeguard research integrity.

We wish to credit our Research Integrity and Research Publishing teams and anonymous and named external researchers and research integrity experts for contributing to this investigation.

The corresponding author, as the representative of all authors, has been given the opportunity to register their agreement or disagreement to this retraction. We have kept a record of any response received.

References

- [1] J. Zhang, D. Luo, F. Li et al., "Ginsenoside Rg3 Alleviates Antithyroid Cancer Drug Vandetanib-Induced QT Interval Prolongation," *Oxidative Medicine and Cellular Longevity*, vol. 2021, Article ID 3520034, 14 pages, 2021.

Research Article

Ginsenoside Rg3 Alleviates Antithyroid Cancer Drug Vandetanib-Induced QT Interval Prolongation

Juan Zhang,¹ Dan Luo,¹ Fang Li,¹ Zhiyi Li,¹ Xiaoli Gao,¹ Jie Qiao,¹ Lin Wu ^{1,2},
and Miaoling Li ¹

¹Key Laboratory of Medical Electrophysiology of Ministry of Education, Medical Electrophysiology Key Lab of Sichuan Province, Institute of Cardiovascular Research, Southwest Medical University, Luzhou 646000, China

²Department of Cardiology, Peking University First Hospital, Beijing, China

Correspondence should be addressed to Lin Wu; lin_wu@163.com and Miaoling Li; limiaolingcc@swmu.edu.cn

Received 30 May 2021; Accepted 31 August 2021; Published 7 October 2021

Academic Editor: Shao Liang

Copyright © 2021 Juan Zhang et al. This is an open access article distributed under the Creative Commons Attribution License, which permits unrestricted use, distribution, and reproduction in any medium, provided the original work is properly cited.

Inhibition of human ether-a-go-go-related gene (hERG) potassium channel is responsible for acquired long QT syndromes, which leads to life-threatening cardiac arrhythmia. A multikinase inhibitor, vandetanib, prolongs the progression-free survival time in advanced medullary thyroid cancer. However, vandetanib has been reported to induce significant QT interval prolongation, which limits its clinical application. Some studies have showed that ginsenoside Rg3 decelerated hERG K(+) channel tail current deactivation. Therefore, in this study, we aim to confirm whether ginsenoside Rg3 targeting hERG K(+) channel could be used to reverse the vandetanib-induced QT interval prolongation. Electrocardiogram (ECG) and monophasic action potential (MAP) were recorded using electrophysiology signal sampling and analysis system in Langendorff-perfused rabbit hearts. The current clamp mode of the patch-clamp technique was used to record transmembrane action potential. The whole-cell patch-clamp technique was used to record the hERG K⁺ current. In Langendorff-perfused hearts, vandetanib prolonged the QT interval in a concentration-dependent manner with an IC₅₀ of 1.96 μmol/L. In human-induced pluripotent stem cell-derived cardiomyocytes (hiPSC-CMs), vandetanib significantly prolonged the action potential duration at 50%, 70%, and 90% repolarization (APD₅₀, APD₇₀, and APD₉₀). In stable transfected human hERG gene HEK293 cells, vandetanib caused concentrate-dependent inhibition in the step and tail currents of hERG. As expected, ginsenoside Rg3 relieved vandetanib-induced QT interval prolongation in Langendorff-perfused heart and reversed vandetanib-induced APD prolongation in hiPSC-CMs. Furthermore, ginsenoside Rg3 alleviated vandetanib-induced hERG current inhibition and accelerated the process of the channel activation. Ginsenoside Rg3 may be a promising cardioprotective agent against vandetanib-induced QT interval prolongation through targeting hERG channel. These novel findings highlight the therapeutic potential of ginsenoside to prevent vandetanib-induced cardiac arrhythmia.

1. Introduction

Medullary thyroid cancer (MTC) is a rare neuroendocrine tumor, which originates from thyroid parafollicular cells (C cells) [1]. Sporadic MTC is usually diagnosed as an advanced disease because of no symptoms. In recent years, with the development of targeted drugs, a variety of multitarget small-molecular tyrosine kinase inhibitors have been reported to be effective against unresectable locally advanced MTC, including vandetanib, cabozantinib, lenvatinib, anlotinib, sulfatinib, and axitinib.

Vandetanib is a once-daily oral (300 mg/day) small molecular kinase inhibitor, by targeting on vascular endothelial growth factor receptor (VEGFR), rearranged during transfection (RET), epidermal growth factor receptor EGFR [2–4], and v-kit Hardy-Zuckerman 4 feline sarcoma viral oncogene (v-kit) [5]. Vandetanib was demonstrated to be the most preferred drug for MTC treatment with regard to progression-free survival [6, 7]. In 2011, the United States Food and Drug Administration (FDA) and the European Medicines Agency (EMA) approved vandetanib for the treatment of progressive, symptomatic, inoperable locally

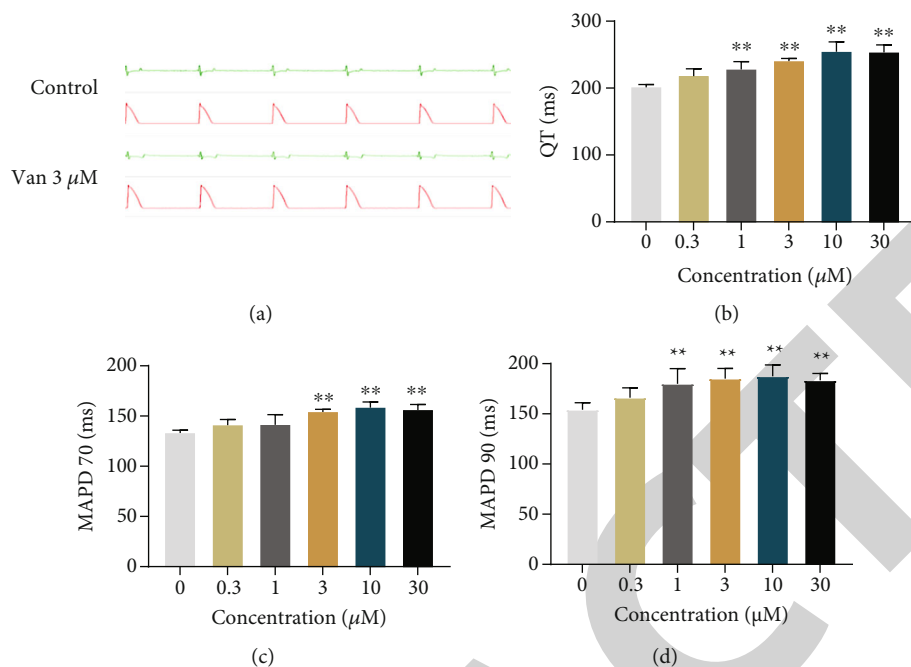


FIGURE 1: Effects of vandetanib on QT and MAPD in rabbit hearts. Vandetanib prolonged QT interval and MAPD in a concentration-dependent manner. (a) Representative recording traces of monophasic action potential and ECG in Langendorff-perfused rabbit hearts; (b) QT interval statistical chart; (c, d) statistical chart of MAPD₇₀ and MAPD₉₀. Data are represented by the means \pm SEM. *Compared with the control group, * $P < 0.05$ and ** $P < 0.01$; #compared with the 3 μM Van group, # $P < 0.05$ and ## $P < 0.01$.

advanced or metastatic MTC [8, 9]. Nevertheless, QTc interval prolongation is one of the major adverse effects of this drug. The data from nine trials with 2,188 patients showed that the total occurrence rate of all-grade and high-grade QTc interval prolongation was 16.4% (95% CI, 8.1-30.4%) and 3.7% (8.1-30.4%), respectively [10]. Clinical application of vandetanib is limited by cardiotoxicity (QTc interval prolongation), and the exact mechanisms are unclear [10–12]. Therefore, it is of great value for clinical treatment to study the mechanism of antitumor drug-induced cardiotoxicity and try to find agents which could alleviate the cardiotoxicity during the period of chemotherapy. The rapid component of the delayed rectifier K^+ current (I_{Kr} , encoded by the hERG gene) is one of the most crucial ion channels in myocardium repolarization, which dysfunction leads to QT interval prolongation [13–15]. It has been reported that ginsenoside Rg3 (Gin Rg3) can increase the current amplitude of hERG and slow the deactivation of tail current. Therefore, we speculated that the combination of Gin Rg3 and vandetanib could reverse vandetanib-induced hERG current inhibition and then alleviated the prolongation of QT interval induced by vandetanib.

2. Materials and Methods

2.1. Drugs and Reagents. Vandetanib (Van, #HY-1284) and Gin-Rg3 (#HY-N1376) were purchased from MedChemExpress company (MCE, USA). All chemicals for solution preparation were purchased from Sangon Biotech (Shanghai, China).

2.2. Animals and Management. Animal experiments were carried out in compliance with the Laboratory Animal Management Rules of China and approved by the Animal Care and Use Committee of Peking University. Twenty-four New Zealand white rabbits with a body weight of 2.5-3.5 kg were used in this study. First, the rabbits were heparinized (heparin sodium, 1000 U/kg) for 10 min and then anaesthetized with urethane (20% \times 5 mL/kg) for about 5-10 min. Immediately, the heart was isolated and perfused from the aorta using a Langendorff perfusion apparatus (37°C, oxygenated with 95% O_2 and 5% CO_2) with Tyrode solution (mM 118 NaCl, 4.8 KCl, 2.0 pyruvic acid sodium salt, 2.5 CaCl_2 , 1.2 MgSO_4 , 0.5 $\text{Na}_2\text{-EDTA}$, 25 NaHCO_3 , 5.5 glucose, 1.2 KH_2PO_4 , and pH 7.4 with NaOH). The rabbit experiments were divided into 3 groups: (1) control group, only perfusion with Tyrode solution; (2) vandetanib-treated group, perfusion with various concentrations of van (0.3, 1, 3, 10, and 30 $\mu\text{mol/L}$); (3) Van+Gin-Rg3-treated group, perfusion with van 3 $\mu\text{mol/L}$ +various concentrations of Gin-Rg3 (0.3, 1, 3, 10, and 30 $\mu\text{mol/L}$); monophasic action potential duration at 50% (MAPD₅₀), 70% (MAPD₇₀), and 90% (MAPD₉₀) and ECG recording were measured by the multichannel electrophysiological recording system (BIOPAC, MP150, USA) [16]. **hiPSC-CM culture.** hiPSC-CMs used for action potential recording were purchased from Help Stem Cell Innovations (Nanjing, China). In this study, hiPSCs at differentiation day 40 were selected to record action potential. Before recording, hiPSC-CMs were seeded onto 1% matrigel-coated coverslips with 24-well plates at a lower density for more than 48 h.

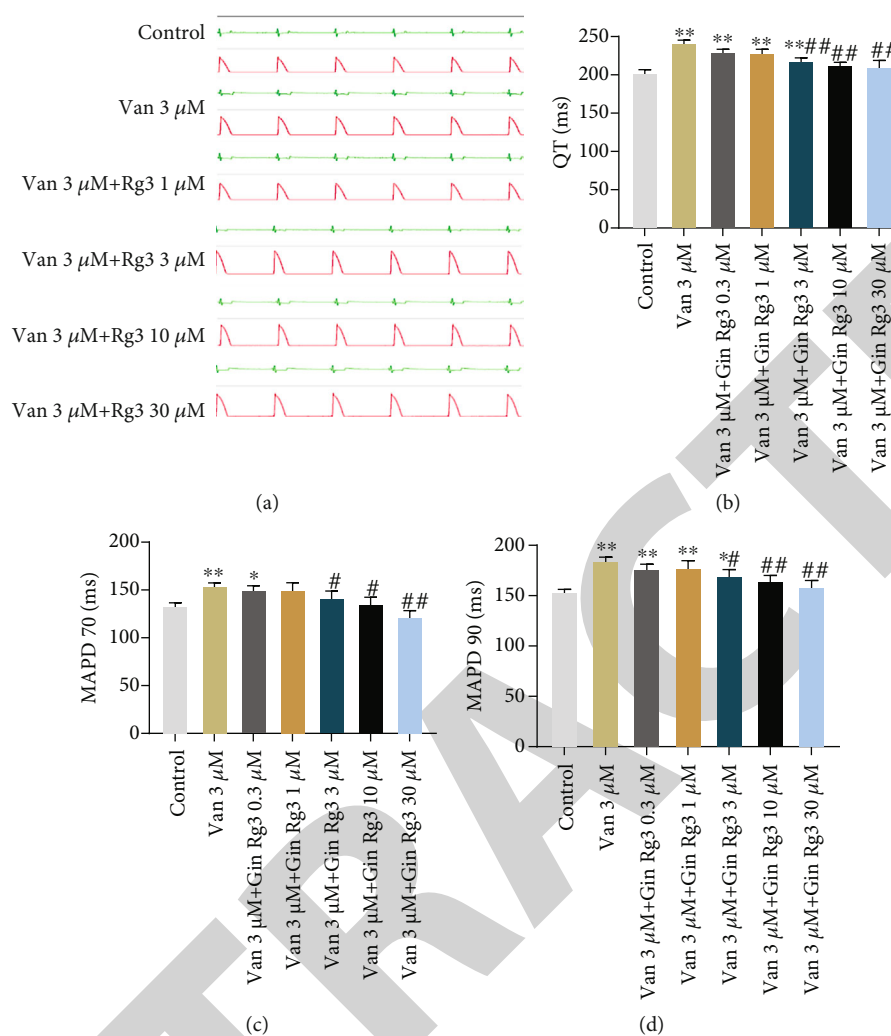


FIGURE 2: Rg3 alleviated vandetanib-induced prolongation of QTc interval and MAPD in rabbit hearts. (a) Representative monophasic action potential map and simulated ECG tracing. (b) Statistical chart of QT interval. (c, d) Statistical chart of MAPD70 and MAPD90, respectively. Data are represented by the means \pm SEM. *Compared with the control group, * $P < 0.05$ and ** $P < 0.01$; #compared with the 3 μM van group, # $P < 0.05$ and ## $P < 0.01$.

2.3. Action Potential Recording by Patch-Clamp Technique.

The hiPSC-CMs on coverslips were placed onto a temperature-controlled (35–37°C) recording chamber and perfused continuously with an extracellular solution (mmol/L 140 NaCl, 40 KOH, 5 KCl, 1 MgCl₂, 5 HEPES, 1.8 CaCl₂, 140 NaH₂PO₄, and pH 7.35 with NaOH). The pipette electrodes with tip resistances of 4–6 M Ω were pulled from borosilicate glass capillaries (WPI, USA) and filled with pipette solution (mmol/L 5.4 KCl, 136 K-aspartate, 5 Mg₂-ATP, 1 MgCl₂, 5 K₂-EGTA, 1 HEPES, 5 Na-phosphocreatine, and pH 7.2 with KOH). Action potentials (APs) were recorded by using current-clamp mode with Multiclamp 700B microelectrode amplifier (Axon, USA). APs were evoked by a stimulus current of 800–1000 pA for 10 ms at a frequency of 1 Hz with a current injection of 50 pA. The resting membrane potential (RMP), AP amplitude (APA), and the AP duration at 50% (APD₅₀), 70% (APD₇₀), and 90% (APD₉₀) repolarization were measured before or after treatment with vandetanib 3 micromolar/L (abbreviated as μM) and vandetanib with Gin Rg3 (1, 3, and 10 μM).

2.4. Cell Culture and Transfection. hERG cDNA plasmid was stably transfected in human embryonic kidney (HEK293, ATCC, USA) cells by using lipofectamine 3000 reagent (Invitrogen, Carlsbad, CA). Then, HEK293 cells were cultured in DMEM with 10% fetal bovine serum. For electrophysiology experiment, cells were available after being seeded on coverslips for more than 24 h.

2.5. hERG K⁺ Current Recording. For recording hERG K⁺ current, the bath solution contained (mmol/L) 140 NaCl, 40 KOH, 5 KCl, 1 MgCl₂, 5 HEPES, 1.8 CaCl₂, 140 NaH₂PO₄, and adjusted pH to 7.35 with NaOH. The pipette solution contained (mmol/L) 0.1 GTP, 110 D-aspartic acid, 5 Mg₂-ATP, 110 KOH, 20 KCl, 1 MgCl₂, 5 K₂-EGTA, 10 HEPES, 5 Na-phosphocreatine, and adjusted pH to 7.2 with KOH. hERG currents were recorded by using the whole-cell voltage-clamp technique at room temperature. The microelectrode resistance of the tip was about 2–4 M Ω . When high impedance seal was formed, the series resistance was compensated up to 70% or so. The sampling frequency was

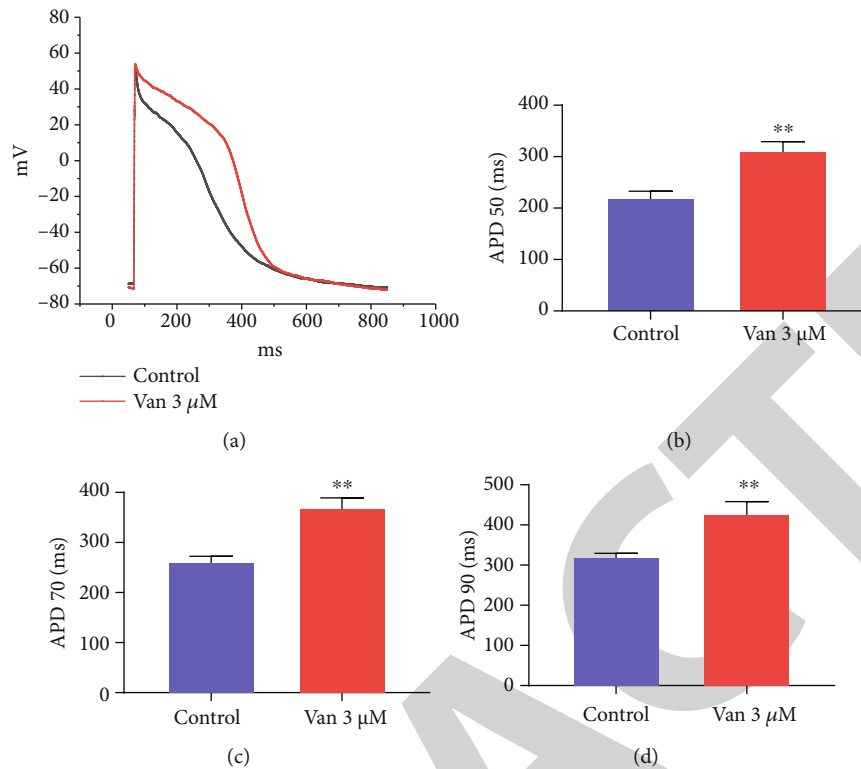


FIGURE 3: Effects of vandetanib on APD in hiPSC-CMs. (a) Representative action potential traces of human iPSC-induced differentiated cardiomyocytes (hiPSC-CMs). (b–d) Statistical chart of APD₅₀, APD₇₀, and APD₉₀, respectively. Data are represented by the means \pm SEM. *Compared with the control group, ** $P < 0.01$.

10 kHz. The data was analyzed with Clampfit 10.4 (Axon, USA) and plotted with Origin 8.0 software (OriginLab, USA).

2.6. Statistical Analysis. Data are expressed as mean \pm standard error of mean (SEM). Statistical analysis comparison was performed by using Student's *t*-test. For comparisons among multiple groups, one-way ANOVA was used. A $P < 0.05$ was considered significant difference.

3. Results

3.1. Vandetanib Prolonged QT Interval and MAPD in Rabbit Hearts. In Langendorff-perfused New Zealand rabbit hearts, electrocardiograph (ECG) and monophasic action potential duration (MAPD) can be simultaneously recorded with the multichannel electrophysiological recording system. Data showed (Figure 1) that vandetanib concentration dependently (0, 0.3, 1, 3, 10, 30 μM) prolonged QT interval, MAPD₇₀ and MAPD₉₀. Vandetanib 1, 3, 10, and 30 μM significantly prolonged QT interval, respectively, from 202.25 \pm 4.43 ms (control, $n = 16$) to 228.8 \pm 11.78 ms ($n = 5$, 1 μM, $P < 0.01$), 241.38 \pm 4.11 ms ($n = 16$, 3 μM, $P < 0.01$), 255.33 \pm 14.73 ms ($n = 6$, 10 μM, $P < 0.01$), and 254.33 \pm 11.32 ms ($n = 6$, 30 μM, $P < 0.01$). The IC₅₀ value of vandetanib on QT interval prolongation was 1.96 μM by Hill equation fitting from a dose-response curve (Figure 1(b)). Vandetanib prolonged MAPD₇₀ from 133.70 \pm 2.963 ms (control, $n = 11$) to 154.69 \pm 2.79 ms ($n = 11$, 3 μM, $P < 0.01$), 159.11 \pm 5.71 ms ($n = 5$, 10 μM, $P < 0.01$), and 156.77

\pm 5.54 ($n = 5$, 30 μM, $P < 0.01$) (Figure 1(c)). Meanwhile, van increased MAPD₉₀ from 154.14 \pm 6.89 ms (control, $n = 11$) to 185.07 \pm 10.12 ms ($n = 11$, 3 μM, $P < 0.01$), 187.40 \pm 11.32 ms ($n = 5$, 10 μM, $P < 0.01$), and 183.38 \pm 6.90 ms ($n = 5$, 30 μM, $P < 0.01$) (Figure 1(d)). Van had no significant effect on the prolongation of APD₅₀ ($n = 5$, $P > 0.05$).

3.2. Gin Rg3 Alleviated Vandetanib-Induced QT Interval and MAPD Prolongation in Rabbit Hearts. In Langendorff-perfused rabbit hearts, after treatment of 3 μM vandetanib for 10 min, then perfused Gin Rg3 (1, 3, 10, 30 μM) with vandetanib 3 μM for 10 min. Figure 2 illustrates that Gin Rg3 dose-dependent decreased vandetanib-induced QT interval and MAPD prolongation in rabbit hearts. Compared to the treatment of 3 μM vandetanib on QT interval, Rg3 (10 μM) significantly decreased QT interval from 241.38 \pm 3.98 ms to 212.31 \pm 4.07 ms ($n = 13$, $P < 0.01$). The effect began at a concentration of 3 μM and stabilizes at 30 μM of Gin Rg3. Compared to the treatment of vandetanib 3 μM on MAPD, 3 μM ($n = 13$, $P < 0.01$), 10 μM, and 30 μM of Gin Rg3 displayed significantly decreased MAPD₇₀ and MAPD₉₀.

3.3. Gin Rg3 Improved Vandetanib-Induced APD Prolongation in hiPSC-CMs. In this study, the current-clamp mode of the whole-cell patch-clamp technique was used to record action potential with hiPSCs at differentiation day 40. hiPSC-CMs without spontaneous contraction were selected to record action potential with a stimulated

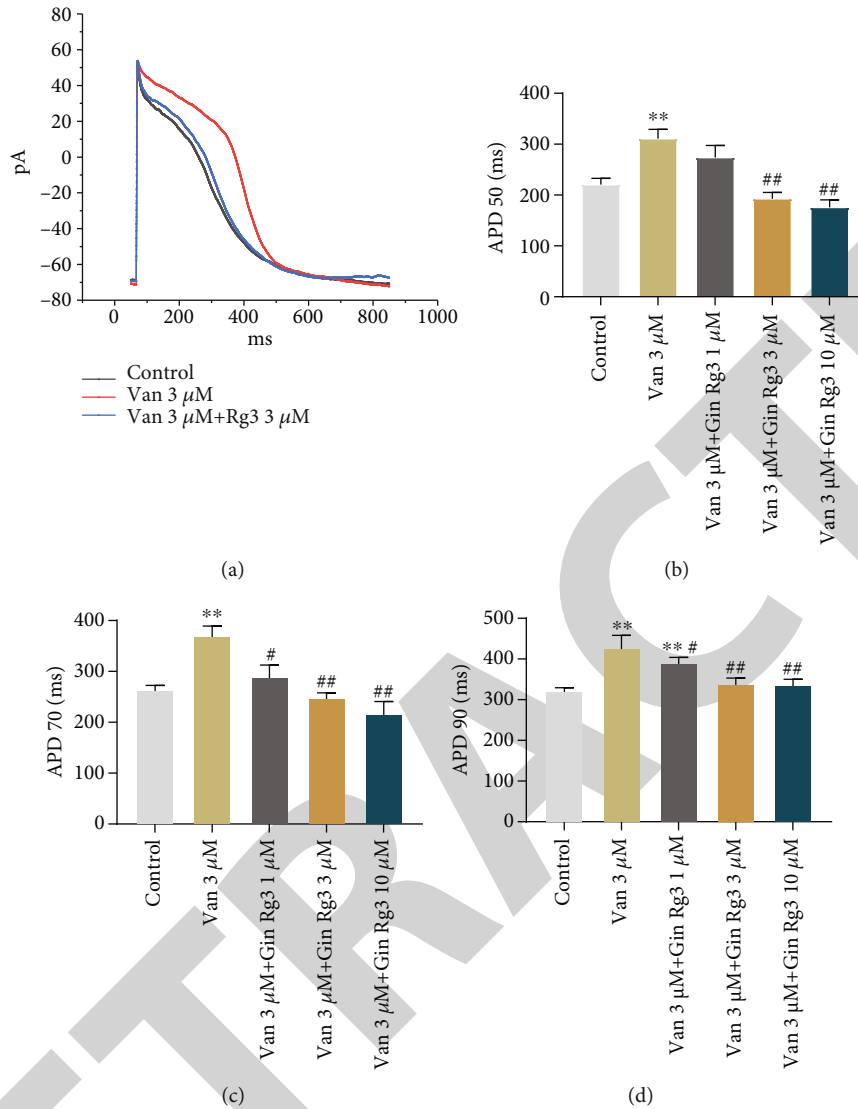


FIGURE 4: Effects of Rg3 on vandetanib-induced APD prolongation in hiPSC-CMS. (a) Representative action potential traces of hiPSC-CMS in control, vandetanib 3 μM, and vandetanib 3 μM with Gin Rg3 3 μM. (b–d) Statistical chart of APD50, APD70, and APD90, respectively. Data are represented by the means ± SEM. *Compared with the control group, * $P < 0.05$ and ** $P < 0.01$; #compared with the 3 μM van group, # $P < 0.05$ and ## $P < 0.01$.

frequency of 1 Hz. Compared to the control group, vandetanib prolonged APD₅₀, APD₇₀, and APD₉₀ in a concentration-dependent manner (Figure 3, $n = 7$, $P < 0.01$). In order to illustrate whether Gin Rg3 could reverse vandetanib-mediated action potential duration prolongation, Gin Rg3 was reperused for 15 min to maximum effect on APD after the treatment of vandetanib (Figure 4). The vandetanib (3 μM) group and the vandetanib (3 μM) with Gin Rg3 (3 μM) group both had no significant effect on resting membrane potential (RMP). In comparison with the treatment of vandetanib (3 μM), Gin Rg3 remarkably improved the APD₅₀ (310.82 ± 18.23 ms vs. 192.80 ± 12.22 ms, $n = 6$, $P < 0.01$), APD₇₀ (370.20 ± 18.83 ms vs. 248.12 ± 9.79 ms, $n = 6$, $P < 0.01$), and APD₉₀ (428.36 ± 11.20 ms vs. 340.69 ± 12.32 ms, $n = 6$, $P < 0.01$), respectively. These results indicated that vandetanib plays a prolonged role on APD in hiPSC-CMS,

the prolonged effect can be reversed by combination of Gin Rg3 with vandetanib.

3.4. Inhibition of I_{hERG} in Stable Transfected HEK293 Cells by Vandetanib. To confirm whether APD prolongation by vandetanib is involved in the inhibition of myocardial repolarization, I_{hERG} was recorded by the whole-cell patch-clamp technique in stably transfected HEK293 cells at room temperature. For recording I_{hERG} , the holding potential was maintained at -80 mV and the voltage steps of depolarization were initiated from -50 mV to $+60$ mV for 3 s; the tail currents were initiated by repolarization to -60 mV for 3 s. Figure 5(a) shows the representative current traces of I_{hERG} . The first 3 s was used to record the step current, and another 3 s was used to record the tail currents. Vandetanib dose-dependently inhibited $I_{hERG,tail}$

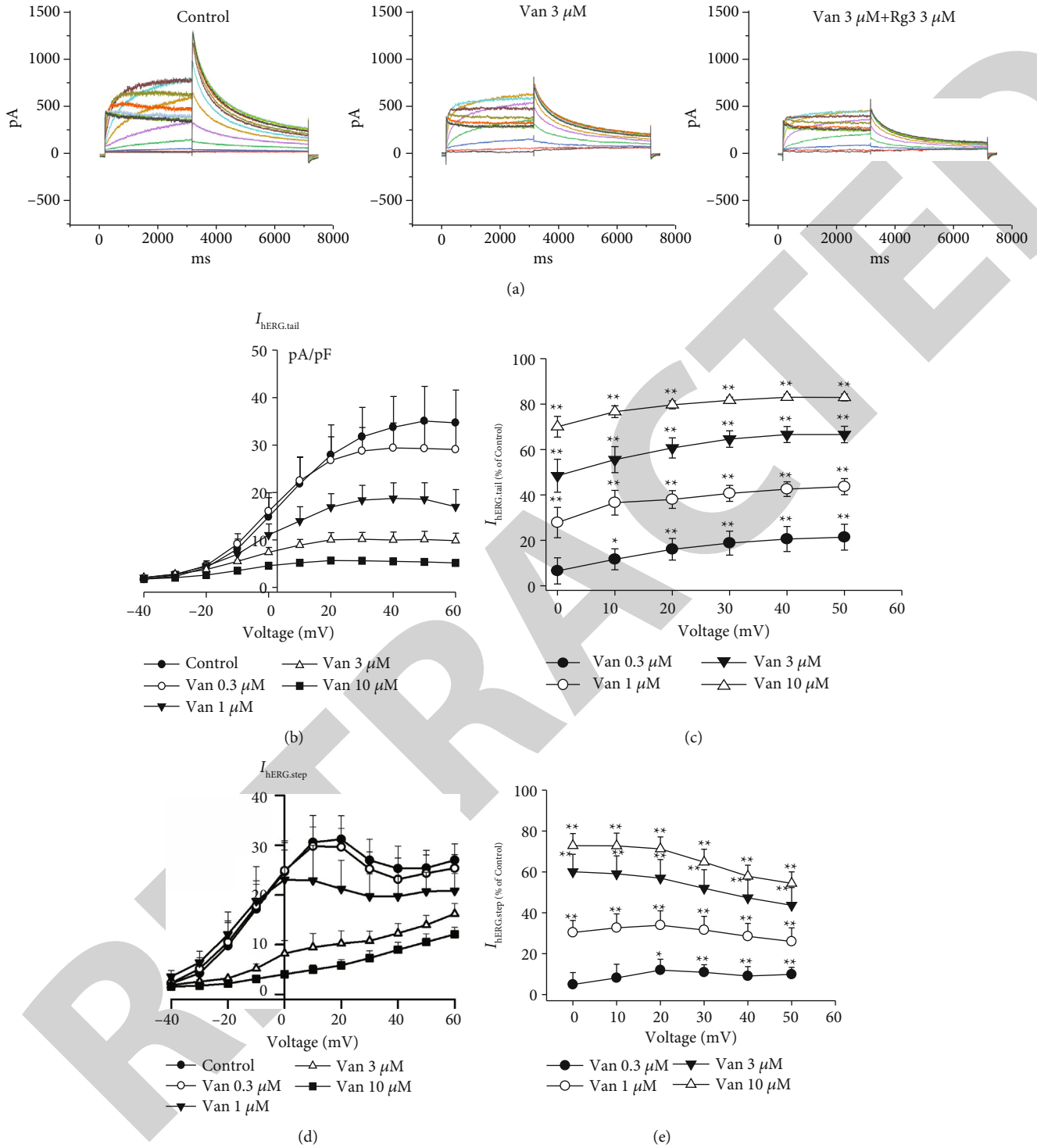


FIGURE 5: Effect of vandetanib on I_{hERG} in stable transfected HEK293 cells. (a) Representative hERG current traces in HEK293 cells. (b) I-V curve of hERG tail current, vandetanib inhibits hERG current in a concentration-dependent manner ($n = 6$). (c) The rate of inhibition of vandetanib on $I_{hERG,tail}$ at different concentrations ($n = 8$). (d) I-V curve of hERG step current. (e) The rate of inhibition of vandetanib on $I_{hERG,step}$ at different concentrations ($n = 8$). Data are represented by the means \pm SEM. *Compared to the control group, * $P < 0.05$ and ** $P < 0.01$.

(Figures 5(b) and 5(c)). Compared to the control group (Figure 5(c)), vandetanib suppressed $I_{hERG,tail}$ by $18.7 \pm 5.28\%$ ($0.3 \mu\text{M}$), $40.69 \pm 3.52\%$ ($1 \mu\text{M}$), $64.63 \pm 3.64\%$ ($3 \mu\text{M}$), and $81.78 \pm 1.36\%$ ($10 \mu\text{M}$), respectively. IC_{50} of

vandetanib on $I_{hERG,tail}$ is approximately $1.89 \mu\text{M}$ ($n = 8$, $P < 0.01$). Furthermore, in Figures 5(d) and 5(e), vandetanib also dose-dependently inhibited $I_{hERG,step}$ with IC_{50} of around $2.79 \mu\text{M}$ ($n = 6$, $P < 0.01$).

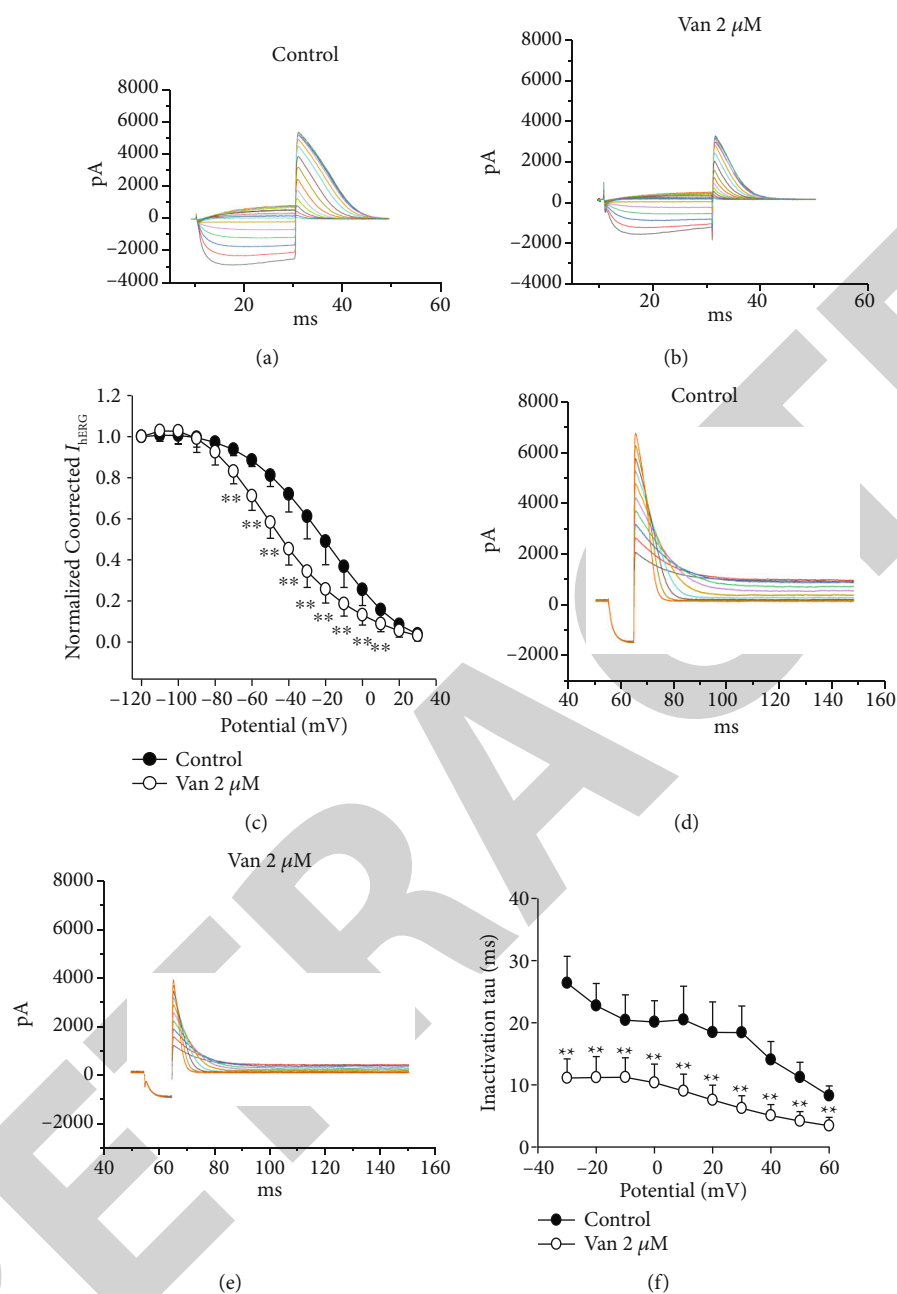


FIGURE 6: Effect of vandetanib on steady-state inactivation process of hERG channels in HEK293 cells. (a, b) The steady-state inactivation curves of the control and 2 μ M vandetanib group, respectively. (c) Statistical diagram of steady-state inactivation. (d, e) The curves of inactivation time constants of the control and 2 μ M vandetanib group. (f) The statistics of inactivation time constant. Data are represented by the means \pm SEM. *Compared with control, * $P < 0.05$ and ** $P < 0.01$.

3.5. Vandetanib Inhibited Steady-State Inactivation Process of hERG K^+ Channels in HEK293 Cells. In addition to the effect of vandetanib on the hERG current amplitude, the role of vandetanib on the hERG channel inactivation process is also a point that needs to be concerned. Figure 6 displays the representative traces of hERG channel steady-state inactivation. Compared with the control group in Figure 6(c), the treatment with vandetanib (2 μ M) caused a significantly leftward shift in a steady-state inactivation curve. The time constant of inactivation process reflects the charging and discharging speed of cell membrane capacity and the rate

of inactivation. As shown in Figure 6(f), the inactivation time constant was shortened by treatment with vandetanib, which indicated that vandetanib can accelerate the inactivation process of the hERG K^+ channel.

3.6. Vandetanib Blocking on Activation and Time-Dependence Process of hERG K^+ Channels in HEK293 Cells. The activation and inactivation of the hERG K^+ channel almost occur simultaneously. In this study, we used a special envelope of tail current protocol to measure the activation dynamics of the channel. In the process of repeated

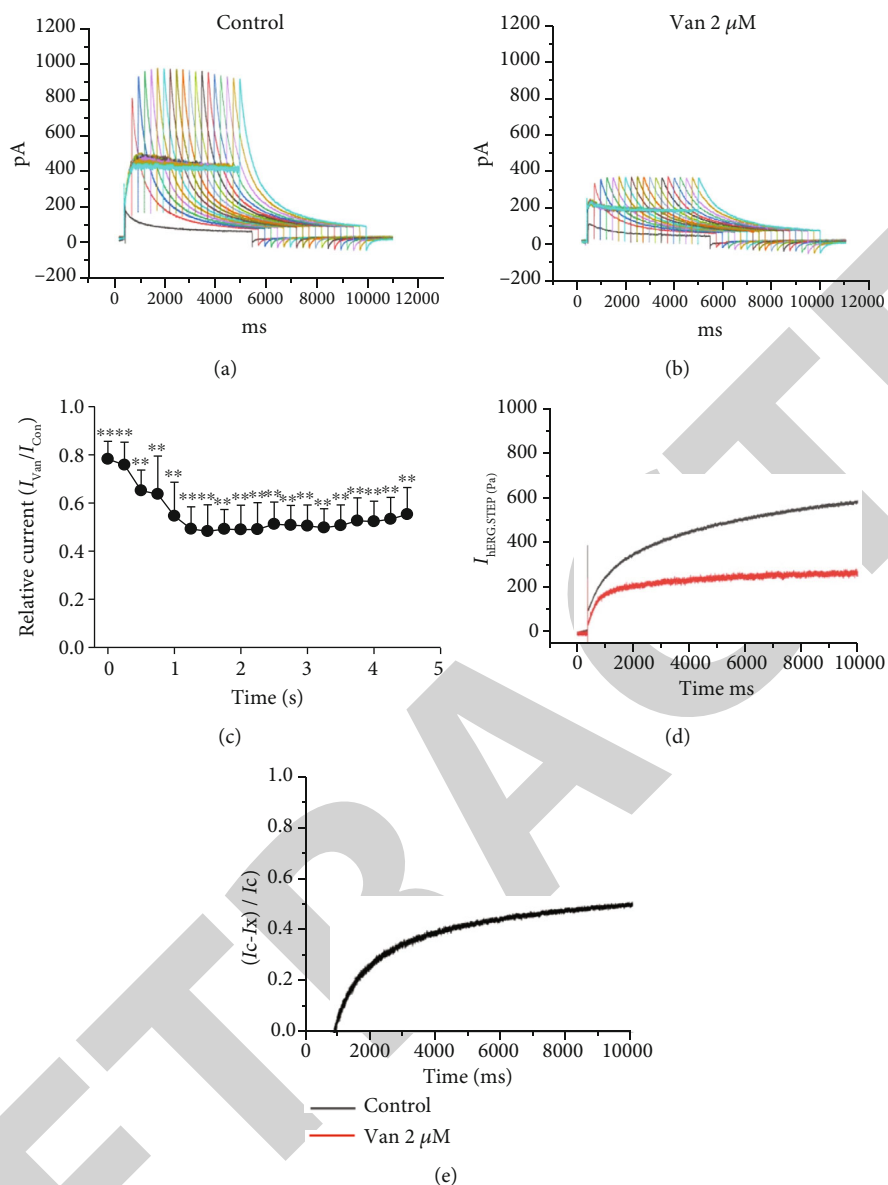


FIGURE 7: The development of vandetanib block of hERG channels was further assessed using an envelope of tail test in HEK293 cells. (a, b) Envelope tail protocol and representative hERG current before (control) and after application of 2 μ M vandetanib. Cells were held at a holding potential of -80 mV and pulsed to depolarizing voltage ($+30$ mV) for variable durations from 50 to 4800 ms in 250 ms increments. $I_{HERG-tail}$ was recorded upon repolarization to -50 mV. (c) A plot of relative tail current with 2 μ M vandetanib versus the depolarizing duration. The time-dependent decay in relative tail current was fitted by a single exponential function. (d) Voltage clamp pulse protocol and representative recordings of hERG current before and after exposure of the cell to 2 μ M vandetanib. (e) Drug-sensitive current expressed as a proportion of the current in the absence and the presence of 2 μ M vandetanib. Data are represented by the means \pm SEM. *Compared with control, * $P < 0.05$ and ** $P < 0.01$.

stimulation, the stimulus time course of depolarization gradually increases.

The effect of vandetanib on the development of the hERG channel was further assessed using an envelope of tail current measurement procedure (Figures 7(a) and 7(b)). The relative tail current was obtained by comparing the tail current of the control group (Figure 7(a)) with that of the 2 μ M vandetanib group (Figure 7(b)). The relative tail current is attenuated in a time-dependent manner. The initial value of the relative tail current activated by vandetanib was used to estimate the blocking effect on hERG current. The initial

relative tail current (Figure 7(c)) at 50 ms was 78.22 ± 7.39 % (inhibited by 21.78%) and the steady-state tail current was 55.31 ± 9.01 % (total inhibition by 44.69%) at 4200 ms with 2 μ M vandetanib. Therefore, the percentage of vandetanib inhibition to hERG channel was 21.78%, while the ratio of 2 μ M vandetanib to open channel was 22.91%. The results showed that vandetanib exerts blocking effects on both the opening and closing states of hERG channels.

The time-dependent effect of vandetanib on hERG channel blocking was produced by the whole-cell patch-clamp technique. The voltage was depolarized from -80 mV to

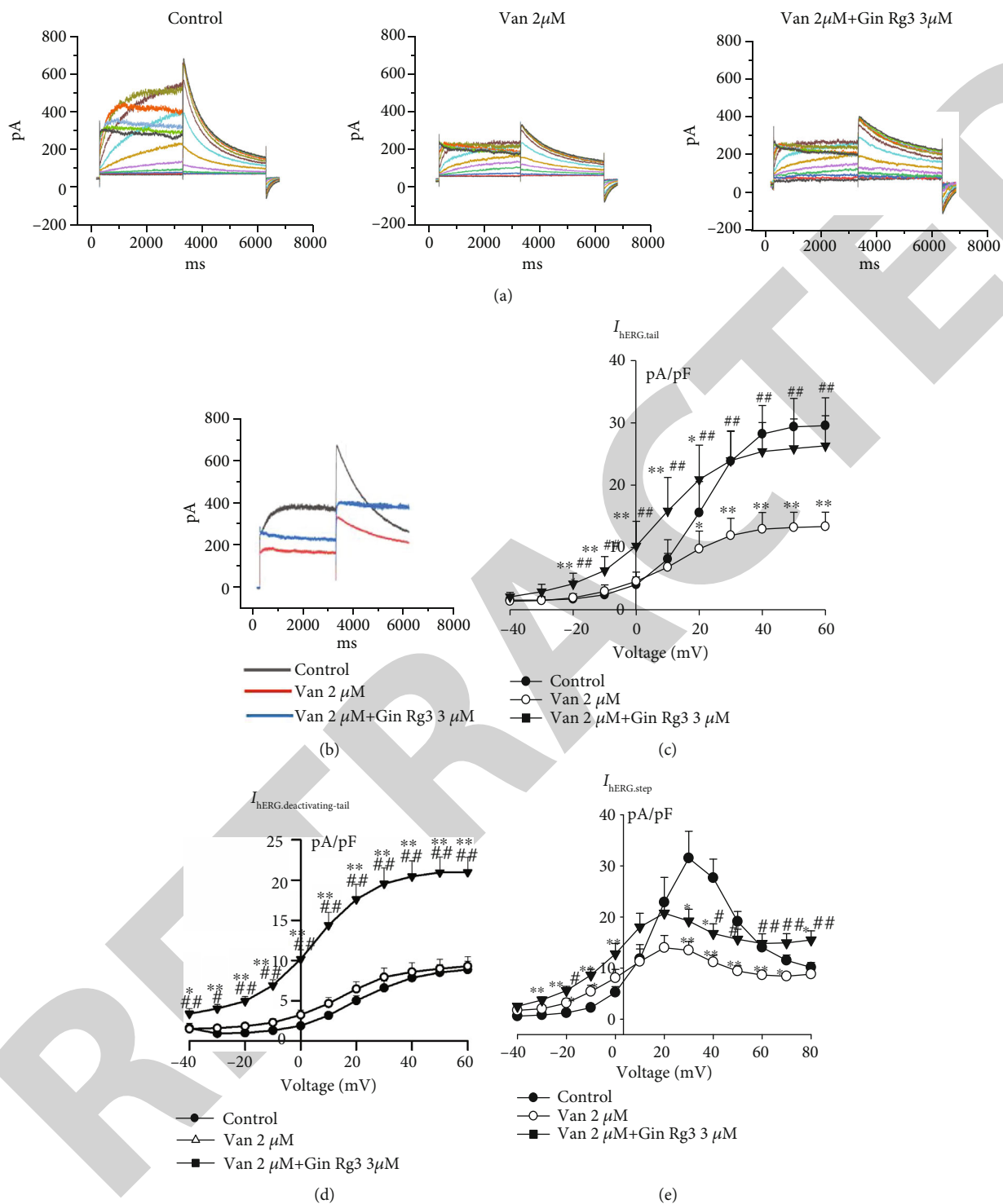


FIGURE 8: The effect of Gin Rg3 on vandetanib-induced inhibition of hERG channels in HEK293 cells. (a) Representative hERG current traces in HEK293 cells. (b) Representative hERG current trace at +30 mV by treatment of control, vandetanib 2 μM, and vandetanib 2 μM along with the Gin Rg3 3 μM group. (c–e) I–V curve of hERG tail current, deactivation of hERG tail current, and hERG step current of control, vandetanib 2 μM, and vandetanib 2 μM with the Gin Rg3 3 μM group ($n = 10$). *Compared with control, $*P < 0.05$ and $**P < 0.01$. #Compared with 2 μM vandetanib, $#P < 0.05$ and $##P < 0.01$.

0 mV with a step of 10 s. The current traces are shown in Figure 7(d). Compared to the control group, vandetanib significantly inhibited the depolarization current and showed a

blocking effect on the hERG channel. The effect of vandetanib on open channel blocking was analyzed by the formula: $[(I_C - I_{van})/I_C]$, where I_{van} represents before and after

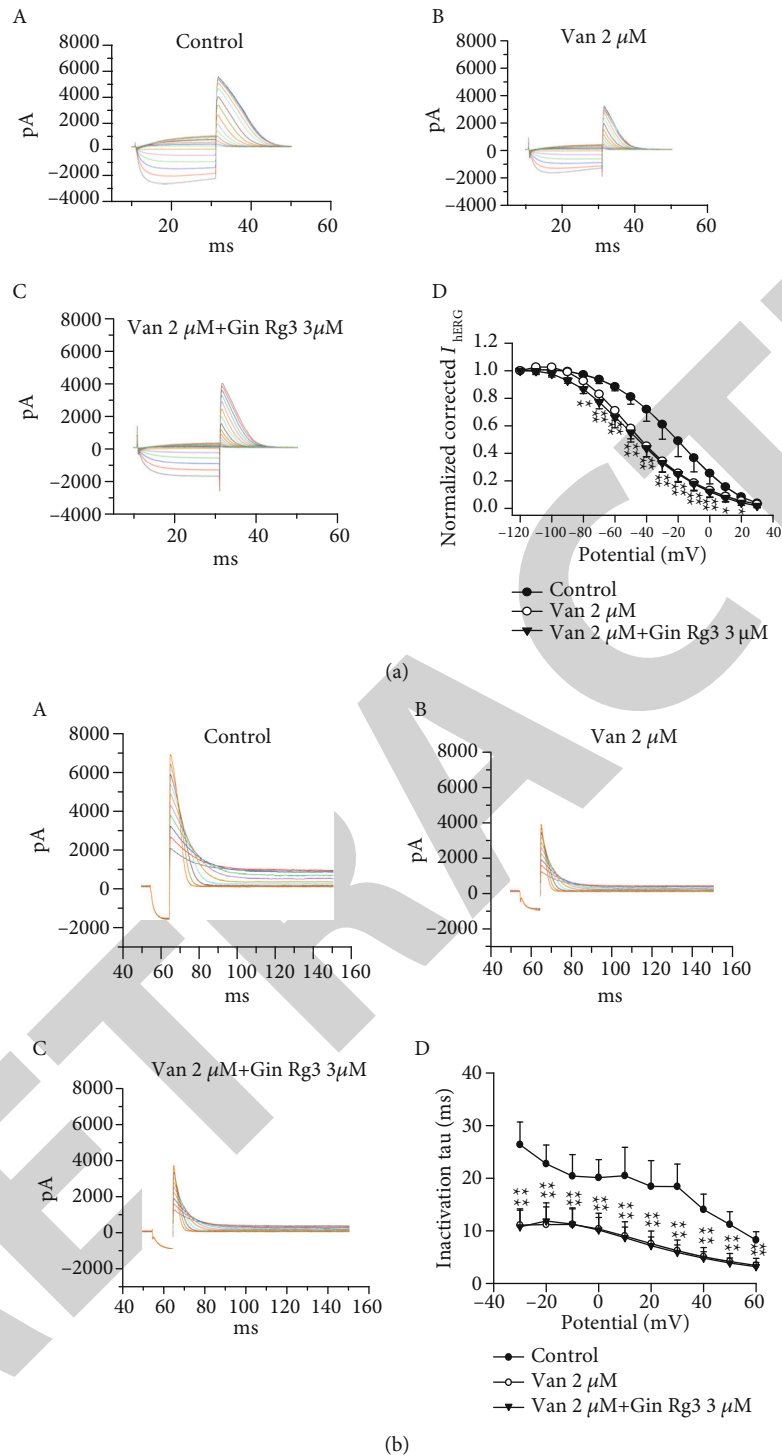


FIGURE 9: Effect of Rg3 on vandetanib-induced inhibition on steady-state inactivation process of hERG K^+ channels in HEK293 cells. (a) hERG channel current steady-state inactivation curve. The steady-state inactivation current diagram of different groups of hERG channels including control (A), vandetanib 2 μ M (B), and vandetanib 2 μ M with Gin Rg3 3 μ M (C). hERG channel current steady-state inactivation fit curve (D). (b) The curves of inactivation time constants of control (A), vandetanib 2 μ M (B), and vandetanib 2 μ M with Gin Rg3 3 μ M (C). (D) The statistics of inactivation time constant. Data are represented by the means \pm SEM. *Compared with control, * $P < 0.05$ and ** $P < 0.01$.

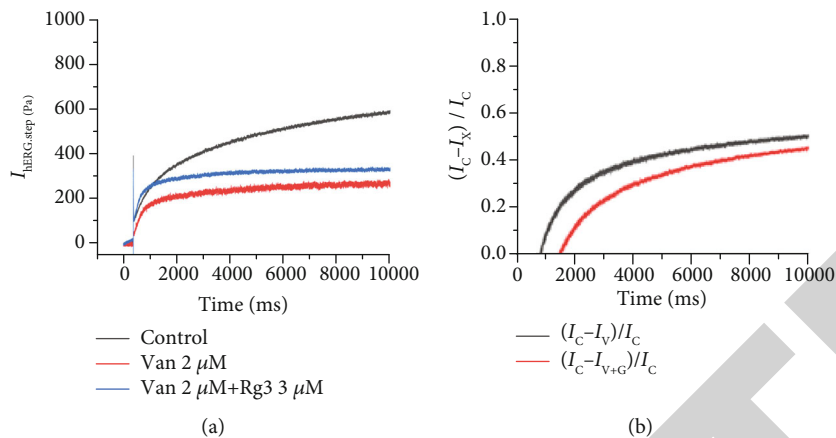


FIGURE 10: (a) Voltage clamp pulse protocol and representative recordings of hERG current before and after exposure of the cell to 2 μM vandetanib and 2 μM vandetanib with 3 μM Gin Rg3. (b) Drug-sensitive current expressed as a proportion of the current in the absence and the presence of 2 μM vandetanib.

vandetanib 2 μM treatment. The data was fitted by a single exponential equation (Figure 7(e)). The drug sensitivity current was increased with time increasing. The results showed that open channel blocking is involved in the inhibition of vandetanib on hERG K^+ channels.

3.7. Gin Rg3 Reversed Vandetanib-Induced I_{hERG} Inhibition in HEK293 Cells. Figure 8(a) shows the representative current traces of control and vandetanib (2 μM) with or without Rg3 (3 μM). In Figure 8(b), Gin Rg3 remarkably reversed vandetanib-induced I_{hERG} inhibition at +30 mV ($n = 10$, $P < 0.05$). The I-V curve of tail current is shown in Figure 8(c). Compared with the treatment of vandetanib, Gin Rg3 displayed an increasing effect on the tail current amplitude ($I_{\text{hERG,tail}}$). The end of repolarization during recording the $I_{\text{hERG,tail}}$ represents the deactivating tail current ($I_{\text{hERG,deactivating-tail}}$). Compared with the control group, vandetanib did not significantly change $I_{\text{hERG,deactivating-tail}}$ ($n = 10$, $P > 0.05$). However, Gin Rg3 caused a significant increase in $I_{\text{hERG,deactivating-tail}}$ (Figure 8(d), $n = 10$, $P < 0.01$) in comparison to the control group and the vandetanib group. The I-V curve of $I_{\text{hERG,step}}$ is shown in Figure 8(e). These results indicated that Gin Rg3 reversed van-induced inhibition of $I_{\text{hERG,tail}}$, $I_{\text{hERG,step}}$, and $I_{\text{hERG,deactivating-tail}}$.

3.8. Gin Rg3 Improved Vandetanib-Induced Inhibition on Steady-State Inactivation Process of hERG K^+ Channels in HEK293 Cells. The current traces in Figure 9(a), A–C were used to evaluate the inactivation time constant of Gin Rg3 and van on hERG channels. Compared with the control group (Figure 9(a), B and C), Gin Rg3 (3 μM) with vandetanib (2 μM) decreased the inactivation time constant with the voltages from -30 mV to +60 mV, and the difference was statistically significant. Compared with vandetanib 2 μM , Gin Rg3 3 μM with vandetanib 2 μM had no effect on the inactivation time constant (Figure 9(a), D). These results suggest that van accelerated hERG channel inactivation, and Gin Rg3 3 μM had no effect on hERG channel inactivation induced by vandetanib. The effects of vandetanib and

Gin Rb3 on the steady-state inactivation of the hERG channel are shown in Figure 9(a), D. Compared with the control group, the half-inactivation potential of van and Rg3 with van both shifted to the left, which showed obvious leftward shift between +10 mV and -70 mV, and the difference has statistical significance. Compared with van, Rg3 had no effect on hERG channel inactivation. The results showed that vandetanib accelerated hERG channel inactivation.

The representative current traces are shown in Figure 9(b), A–C, the time constant of inactivation process. As shown in Figure 9(b), D, the inactivation time constant was shortened by treatment with vandetanib with or without Gin Rg3; no effect was acted on the group between vandetanib and vandetanib with Gin Rg3, which indicated that vandetanib could accelerate the inactivation process of the hERG channel, while Rg3 has no action to reverse the effect on van-induced inactivation time constant shortening.

3.9. The Time Dependence of Gin Rg3 on Vandetanib-Induced hERG Channel Blocking. Vandetanib induced suppression of the current during in depolarization, while Gin Rg3 reversed it (Figure 10(a)). The trigger of open channel block was produced by using the drug-sensitive formula as follows: $[(I_C - I_X) / I_C]$, where I_C represents the current of control and I_X represents the currents of vandetanib with or without Gin Rg3. The data was fitted by monoexponential equation. Compared with the vandetanib 2 μM , the current amplitude of vandetanib 2 μM with Gin Rg3 3 μM was increased, while the sensitivity current of the combined application was decreased. The drug sensitivity current of van and van with Gin Rg3 was increased with time. The results showed that inhibition of van on hERG channels is involved in open channel blocking. Gin Rg3 reversed van-mediated hERG channel inhibition.

4. Discussion

Our study demonstrated that ginsenoside Rg3 can reverse vandetanib-induced QT interval prolongation by targeting on the hERG K^+ channel.

Vandetanib targets multiple cell-signaling pathways, which is involved in the molecular pathogenesis of advanced thyroid cancer. Vascular endothelial growth factor receptor (VEGFR), epidermal growth factor receptor (EGFR), and rearranged during transfection receptor (RET) are the main targets of vandetanib on MTC treatment [17]. Vandetanib is regarded as a class of tyrosine kinase inhibitors (TKIs), which has been used for the treatment of thyroid cancer in clinic with a good therapeutic effect. In recent decades, increasing evidence is emerging for reports of vandetanib involving diarrhea, rash, and photosensitivity, especially LQT syndrome which occurs, which limits its clinical application [18, 19]. Abnormal T wave and QT interval prolongation are susceptible to cause the clinical syndrome of malignant ventricular arrhythmia, syncopal, and sudden death [20, 21]. In this study, we demonstrated that vandetanib prolonged the QT interval in Langendorff perfusion rabbit hearts. Also, vandetanib can prolong the cardiac action potential in rabbit heart and hiPSC-CMs, which are consistent with the results reported in the literature [22]. Malignant arrhythmias caused by QT interval prolongation pose a serious threat to patient's life safety and then limit their clinical application. Although QT interval prolongation induced by vandetanib is uncommon, drug-induced QT interval prolongation is associated with life-threatening arrhythmias and sudden death. Therefore, studies on the molecular mechanism of anticancer drug-induced LQT and searching for new drug to reverse LQT will provide a new choice for the drug therapy of clinical cancer patients.

The underlying mechanism of cardiotoxicity induced by vandetanib is unclear. Studies have reported that vandetanib can prolong hiPSC-CM action potential and inhibit hERG current, as well as inhibit both sodium current and calcium current [22]. The dynamic characteristics of hERG channel caused by vandetanib have not been analyzed. In this study, we analyzed the hERG current dynamics induced by vandetanib, including activation, inactivation, and deactivation. By analyzing the hERG channel dynamics of vandetanib, we further clarified the mechanism of QT interval prolongation.

Gin Rg3, a monomer extract from ginseng, is one of the effective components of ginseng. It has been reported that it plays beneficial roles on antitumor [23, 24], oxidation [25], anti-inflammatory [26], and other effects. Jiang et al. demonstrated that ginsenoside Rg3 can reduce the levels of transforming growth factor β 1, tumor necrosis factor- α , interleukin 6, interleukin 1, and endothelin-1 in hypertensive rats [27]. Thus, Gin Rg3 has a protective effect on cardiovascular disease [28]. Gin Rg3 can be used as an adjuvant in conventional cancer therapy, which can improve the efficacy and reduce adverse reactions through synergistic activity [29–31]. Therefore, we speculate that the combination of Gin Rg3 and vandetanib has a protective effect on the arrhythmias induced by vandetanib.

Our results showed that the combined application of Gin Rg3 and vandetanib could reverse vandetanib-induced action potential duration prolongation, which may be directly related to the effect of Rg3 on repolarized potassium channels.

Kv11.1 (hERG) is the molecular basis of I_{Kr} in cardiomyocytes and plays an important role in cardiac repolarization [32, 33]. The hERG K^+ channel current is the main current of action potential phase 3. hERG K^+ channel mutations can lead to hereditary arrhythmic syndrome characterized by prolongation or shorten QT interval and increased incidence of life-threatening arrhythmia [34–36]. Lee et al. [22] found that vandetanib inhibited hERG current, I_{Na} and I_{Ca-L} . However, the dynamic characteristics of hERG channel current were not studied, and the specific mechanism of prolongation of action potential was not clear.

In this study, we analyzed the hERG current dynamic characteristics of vandetanib and found that vandetanib concentration-dependent inhibited the activation of hERG current and the end current of depolarization. Meanwhile, the inactivation time constant decreased, the steady-state inactivation voltage shifted to the left, and the deactivation current did not change. This suggests that vandetanib prolongs the duration of cardiac action potential by affecting the activation and inactivation of hERG current. The combined application of Gin Rg3 and vandetanib had no effect on hERG current activation, inactivation time constant, and steady-state inactivation, and the deactivation current increased significantly. Choi et al. [37] found that ginsenoside Rg3 had no significant effect on the tail current of hERG K^+ channel, and ginsenoside Rg3 could increase in deactivation tail of hERG channel, which was consistent with our results, indicating that ginsenoside Rg3 could increase the deactivation current of hERG K^+ channel, thus alleviating vandetanib-mediated action potential duration prolongation.

In conclusion, vandetanib prolonged the monophasic action potential of New Zealand rabbits and the action potential of human regenerated cardiomyocytes by affecting the activation and inactivation of hERG current. Gin Rg3 can shorten the duration of vandetanib-mediated action potential by affecting the deactivation current. Therefore, it is helpful to clarify the cardiac toxicity mechanism of vandetanib and discover the protective effect of ginsenoside Rg3 on the heart, which can guide rational clinical drug use.

Data Availability

The data used to support the findings of this study are available from the corresponding authors upon request.

Conflicts of Interest

The authors declare that there is no conflict of interests.

Authors' Contributions

Juan Zhang, Dan Luo, Fang Li, Zhiyi Li, and Xiaoli Gao carried out the experiments. Miaoling Li and Lin Wu designed the experiments and wrote the manuscript. Juan Zhang, Dan Luo, and Fang Li contributed equally to this work.

Acknowledgments

This work was supported by the Fund of Science & Technology Department of Sichuan Province (19YYJC1958), Education Department of Sichuan Province (16ZA0192), and Science and Technology Strategic Cooperation Project of Government of Luzhou and Southwest Medical University (2019LZXNYDF02 and 2019LZNYDJ30).

References

- [1] M. Kim and B. H. Kim, "Current guidelines for management of medullary thyroid carcinoma," *Journal of Korean Endocrine Society*, vol. 36, no. 3, pp. 514–524, 2021.
- [2] A. Morabito, M. C. Piccirillo, R. Costanzo et al., "Vandetanib: an overview of its clinical development in Nscl and other tumors," *Drugs of Today (Barcelona, Spain: 1998)*, vol. 46, no. 9, pp. 683–698, 2010.
- [3] S. S. Terzyan, T. Shen, X. Liu et al., "Co-crystal structure of RET and nintedanib complex," *Journal of Biological Chemistry*, vol. 294, no. 27, pp. 10428–10437, 2019.
- [4] E. N. Klein Hesselink, D. Steenvoorden, E. Kapiteijn et al., "Therapy of endocrine disease: response and toxicity of small-molecule tyrosine kinase inhibitors in patients with thyroid carcinoma: a systematic review and meta-analysis," *European Journal of Endocrinology*, vol. 172, no. 5, pp. R215–R225, 2015.
- [5] R. Elisei, M. J. Schlumberger, S. P. Müller et al., "Cabozantinib in progressive medullary thyroid cancer," *Journal of Clinical Oncology*, vol. 31, no. 29, pp. 3639–3646, 2013.
- [6] M. Schlumberger, B. Jarzab, M. E. Cabanillas et al., "A phase ii trial of the multitargeted tyrosine kinase inhibitor lenvatinib (E7080) in advanced medullary thyroid cancer," *Clinical Cancer Research: An Official Journal of the American Association for Cancer Research*, vol. 22, no. 1, pp. 44–53, 2016.
- [7] M. R. Cooper, S. Y. Yi, W. Alghamdi, D. J. Shaheen, and M. Steinberg, "Vandetanib for the treatment of medullary thyroid carcinoma," *The Annals of Pharmacotherapy*, vol. 48, no. 3, pp. 387–394, 2014.
- [8] H. Deshpande, S. Roman, J. Thumar, and J. A. Sosa, "Vandetanib (Zd6474) in the treatment of medullary thyroid cancer," *Clinical Medicine Insights: Oncology*, vol. 5, pp. CMO.S6197–CMO.S6221, 2011.
- [9] D. A. Liebner and M. H. Shah, "Thyroid cancer: pathogenesis and targeted therapy," *Therapeutic Advances in Endocrinology and Metabolism*, vol. 2, no. 5, pp. 173–195, 2011.
- [10] J. Zang, S. Wu, L. Tang et al., "Incidence and risk of Qtc interval prolongation among cancer patients treated with vandetanib: a systematic review and meta-analysis," *PloS One*, vol. 7, no. 2, article e30353, 2012.
- [11] M. Santoni, F. Guerra, A. Conti et al., "Incidence and risk of cardiotoxicity in cancer patients treated with targeted therapies," *Cancer Treatment Reviews*, vol. 59, pp. 123–131, 2017.
- [12] B. B. Hasinoff and D. Patel, "The lack of target specificity of small molecule anticancer kinase inhibitors is correlated with their ability to damage myocytes in vitro," *Toxicology and Applied Pharmacology*, vol. 249, no. 2, pp. 132–139, 2010.
- [13] J. I. Vandenberg, M. D. Perry, M. J. Perrin, S. A. Mann, Y. Ke, and A. P. Hill, "hERG K(+) channels: structure, function, and clinical significance," *Physiological Reviews*, vol. 92, no. 3, pp. 1393–1478, 2012.
- [14] H. M. Lee, M. S. Yu, S. R. Kazmi et al., "Computational determination of hERG-related cardiotoxicity of drug candidates," *BMC Bioinformatics*, vol. 20, Supplement 10, p. 250, 2019.
- [15] A. Garrido, A. Lepailleur, S. M. Mignani, P. Dallemagne, and C. Rochais, "hERG toxicity assessment: useful guidelines for drug design," *European Journal of Medicinal Chemistry*, vol. 195, p. 112290, 2020.
- [16] Q. Zhang, J. H. Ma, H. Li et al., "Increase in CO₂ levels by upregulating late sodium current is proarrhythmic in the heart," *Heart Rhythm*, vol. 16, no. 7, pp. 1098–1106, 2019.
- [17] P. Fallahi, S. M. Ferrari, M. R. Galdiero et al., "Molecular targets of tyrosine kinase inhibitors in thyroid cancer," in *Seminars in Cancer Biology*, Academic Press, 2020.
- [18] P. Fallahi, F. Di Bari, S. M. Ferrari et al., "Selective use of vandetanib in the treatment of thyroid cancer," *Drug Design, Development and Therapy*, vol. 9, pp. 3459–3470, 2015.
- [19] T. Oba, T. Chino, A. Soma et al., "Comparative efficacy and safety of tyrosine kinase inhibitors for thyroid cancer: a systematic review and meta-analysis," *Endocrine Journal*, vol. 67, no. 12, pp. 1215–1226, 2020.
- [20] M. L. Ponte, G. A. Keller, and G. Di Girolamo, "Mechanisms of drug induced Qt interval prolongation," *Current Drug Safety*, vol. 5, no. 1, pp. 44–53, 2010.
- [21] H. Zhao, J. F. Strasburger, B. F. Cuneo, and R. T. Wakai, "Fetal cardiac repolarization abnormalities," *The American Journal of Cardiology*, vol. 98, no. 4, pp. 491–496, 2006.
- [22] H. A. Lee, S. A. Hyun, B. Byun, J. H. Chae, and K. S. Kim, "Electrophysiological mechanisms of vandetanib-induced cardiotoxicity: comparison of action potentials in rabbit Purkinje fibers and pluripotent stem cell-derived cardiomyocytes," vol. 13, no. 4, Article ID e0195577, 2018.
- [23] X. Yang, J. Zou, H. Cai et al., "Ginsenoside Rg3 inhibits colorectal tumor growth via down-regulation of C/EBP β /NF- κ B signaling," *Biomedicine & Pharmacotherapy = Biomedecine & Pharmacotherapie*, vol. 96, pp. 1240–1245, 2017.
- [24] H. Y. Sun, J. H. Lee, Y. S. Han et al., "Pivotal roles of ginsenoside Rg3 in tumor apoptosis through regulation of reactive oxygen species," *Anticancer Research*, vol. 36, no. 9, pp. 4647–4654, 2016.
- [25] J. Geng, W. Fu, X. Yu et al., "Ginsenoside Rg3 alleviates ox-Ldl induced endothelial dysfunction and prevents atherosclerosis in Apoe(-/-) mice by regulating Ppar γ /Fak signaling pathway," *Frontiers in Pharmacology*, vol. 11, p. 500, 2020.
- [26] L. Ma, L. Y. Li, and T. L. Zhao, "Anti-inflammatory effects of ginsenoside Rg3 on the hypertrophic scar formation via the Nf-Kb/Ikb signaling pathway in rabbit ears," *Die Pharmazie*, vol. 75, no. 2, pp. 102–106, 2020.
- [27] Y. Jiang, M. Li, Z. Lu et al., "Ginsenoside Rg3 induces ginsenoside Rb1-comparable cardioprotective effects independent of reducing blood pressure in spontaneously hypertensive rats," *Experimental and Therapeutic Medicine*, vol. 14, no. 5, pp. 4977–4985, 2017.
- [28] W. Fan, Y. Huang, H. Zheng et al., "Ginsenosides for the treatment of metabolic syndrome and cardiovascular diseases: pharmacology and mechanisms," *Biomedicine & Pharmacotherapy = Biomedecine & Pharmacotherapie*, vol. 132, article 110915, 2020.
- [29] M. Sun, Y. Ye, L. Xiao, X. Duan, Y. Zhang, and H. Zhang, "Anticancer effects of ginsenoside Rg3 (review)," *International Journal of Molecular Medicine*, vol. 39, no. 3, pp. 507–518, 2017.